VOL 1
PART 1

TD 155

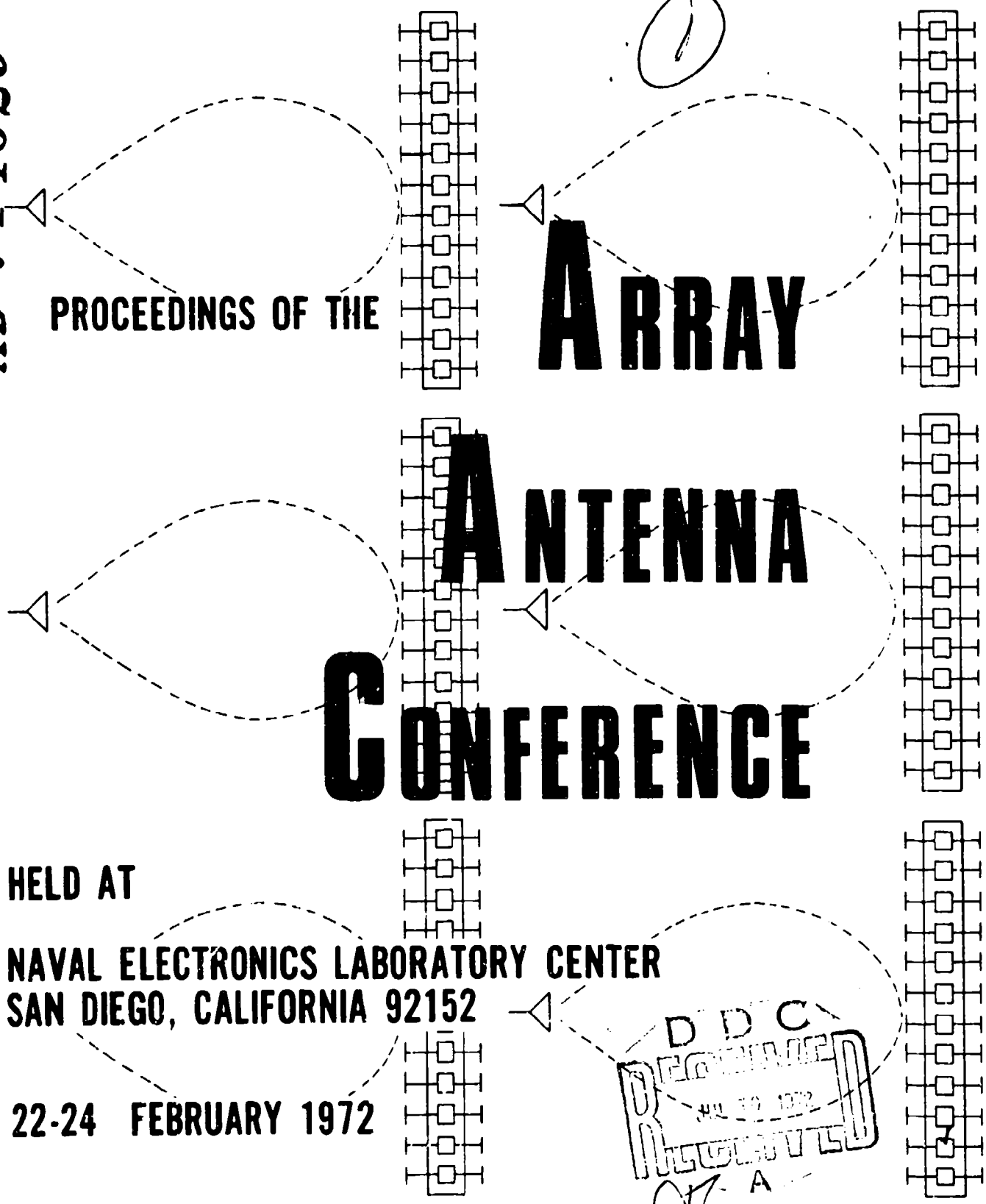

PROCEEDINGS OF THE ARRAY ANTENNA CONFERENCE

HELD AT

NAVAL ELECTRONICS LABORATORY CENTER
SAN DIEGO, CALIFORNIA 92152

22-24 FEBRUARY 1972

CONTENTS

1. PHASED ARRAYS -- A FUTURE?

by

J. H. Provencher

Code 2300

Naval Electronics Laboratory Center
San Diego, California 92152

for

ARRAY ANTENNA CONFERENCE

22, 23, 24 February 1972

1. PHASED ARRAYS – A FUTURE?

Traditionally, the Navy has had a major interest in antennas and in the research and development related to them. The Naval Research Laboratory (NRL) was instrumental in the development of the early Navy radars. Since its inception at the end of World War II, the Naval Electronics Laboratory (NEL) and later the Naval Electronics Laboratory Center (NELC) has had a continuing interest in the development of Fleet antennas.

Let us look back about 25 years and examine some of the antenna problems present at that time. In January, 1946 a conference was held at NEL:

"To acquaint contractor representatives and government people with general antenna problems."

From 22-26 July 1946, another conference was held at NEL with the objective:

"To consider in detail certain specific problems connected with the antenna improvement program."

Some of the problems discussed at that time (and still with us) were:

1. "Determining the vertical polar diagrams of shipboard and other antennas,
2. "Broadband antennas, 2-20 MHz and 225-400 MHz,
3. "Impairment of the beam of a radar antenna by looking through an adjacent mast."

Another comment at that time was that

"An active program of experimentation is underway at NEL." The emphasis at that time appeared to be on the communications frequencies.

Such names as Schelkunoff, Silver, Van Atta, T. Taylor, Bonert, Whinnery, Bolljahn, P. Carter, Sinclair, and others denote those who contributed their ideas to the various problems.

Another conference was held on 9-11 October 1947 to discuss:

1. Shore station antennas,
2. Shipboard antennas,
3. Antenna theory, and
4. Instrumentation for measurements.

Again the familiar problems were present, for example,

"Problems of modeling a ground surface,"

"Broadband sleeve antenna,"

"The antenna program for submarines," and

"Around-the-mast antennas."

The radar frequencies discussed included L, S, C bands and 35 GHz, and indications of the problem of crowding of antennas generated some comments:

"The number of electronic equipments has multiplied many times, and the demand for antennas constantly increases until at present some ships have as many as 150 antennas to be installed over a deck space less than 600 feet long and 90 feet wide."

"Existing submarine antenna systems are inadequate."

" . . . problem of providing efficient antennas in new frequency ranges for the new electronic equipments being installed in our fleet boats . . . "

And also at that conference, comments about multiple use of the same equipment to perform several tasks:

Due to " . . . limits in mast and space facilities, the Bureau of Ships . . . the 1200-MHz and 6000-MHz surface search and 1000-MHz IFF could be mounted on a common pedestal."

At that same conference, Dr. Van Atta of NRL suggested:

"All of these problems [hemispheric radar search, DF and gun direction] require rapid scanning, and it cannot be done by a purely mechanical means that moves a parabola through an angular motion."

Up to this time, there did not appear to be any discussion of arrays. However, a highlight of the 1948 conference, as summed up by Dr. T. J. Keary was:

"Thinking should not be restrained to putting antennas on the structures of ships as they exist today."

This thinking led to the departure from traditional design, as in the case of the ENTERPRISE and the LONG BEACH, and with the advent of the phased array, signalled a new era for the Navy. However, the trend did not continue, even though the arrays performed well. What, then, is the reason that phased arrays, with their many favorable attributes, have not had widespread use?

At the 1947 conference in a discussion of future trends, CAPT Berkley, BUSHIPS, said:

"In future wars, the ships will be supporting devices operating in the air. Microwave elements will get lots of attention in the future. Radar will be used to guide a missile to its target, to determine whether it is enemy or friendly, and to determine where it is coming from.

"The use of microwaves will help in the solving of communication security and other security problems."

Certainly his predictions have come to pass; the need for phased arrays is established; the limited space on ships and aircraft is a fact of life. Technology has shown that phased arrays can be built. What is the limiting factor?

It appears that perhaps the future of phased arrays is closely tied to the dollar. There have been isolated examples of phased arrays, usually one or two of a kind, but not in large quantities, where a cost reduction program could be effective.

Let us look at a typical phased array as in figure 1-1. If the array is divided into three major portions, consisting of the:

1. Radiating structure,
2. Phase shifter or phasor, and
3. Logic and driver,

it can be seen from the figure that these portions account for over 75 percent of the total array cost. If there is to be a cost reduction in the overall array cost, it is obvious that emphasis should be placed in these areas.

One approach is aimed to:

1. reduce costs, and
2. reduce the number of antennas on the ship.

This approach is the use of the multiple-array radiating aperture. A slotted multifrequency array using frequencies of 3.0 GHz and 0.42 GHz was proposed in 1963 by NEL and is shown in figure 1-2. NRL and NELC have investigated this approach and, for some applications, the technique shows promise. Other approaches to the multiple simultaneous use of an aperture radiating structure have been proposed, but have received little attention to date.

Other techniques which show promise for possible cost reduction make use of the Microwave Integrated Circuits (MIC) and the hybrid circuit technology. Considerable progress has been made in these areas in the recent past, and although material losses tend to restrict the overall use of MIC techniques for phasors at present, future prospects for low cost and high reproducibility and reliability are excellent.

The driver for the phasor and associated element circuitry is amenable to the hybrid circuit techniques. An examination of figure 1-3 shows that elimination, consolidation, or combination of some of the components will result in a substantial cost reduction for arrays having thousands of elements. These techniques also appear promising. They are amenable to mass production techniques, and could result in a reduction in the overall weight of the array.

I have tried to give you some possible areas which I feel offer promise to reduce the cost of phased-array antennas. NELC is actively working in these areas, and although some progress has been made, considerable work remains.

A primary objective of this conference is to bring together the recent technology in array antennas, not only in the technical areas but also in the cost-effective area. Unless

1. significant cost reductions can be made in component cost, or
2. techniques can be developed to reduce the number of components, or
3. techniques are developed to exploit multiple use of the aperture, then

I feel that the future for widespread use of phased arrays is dim.

I have not discussed the prospects of the solid-state array, as I am sure that this area will be adequately covered in the next few days. However, I urge you all to orient your technical appraisal along with a dollar appraisal and ask, "Can we afford to build these arrays in large quantities for widespread use?" If we can answer this question, affirmatively, then certainly, phased arrays have a very bright future.

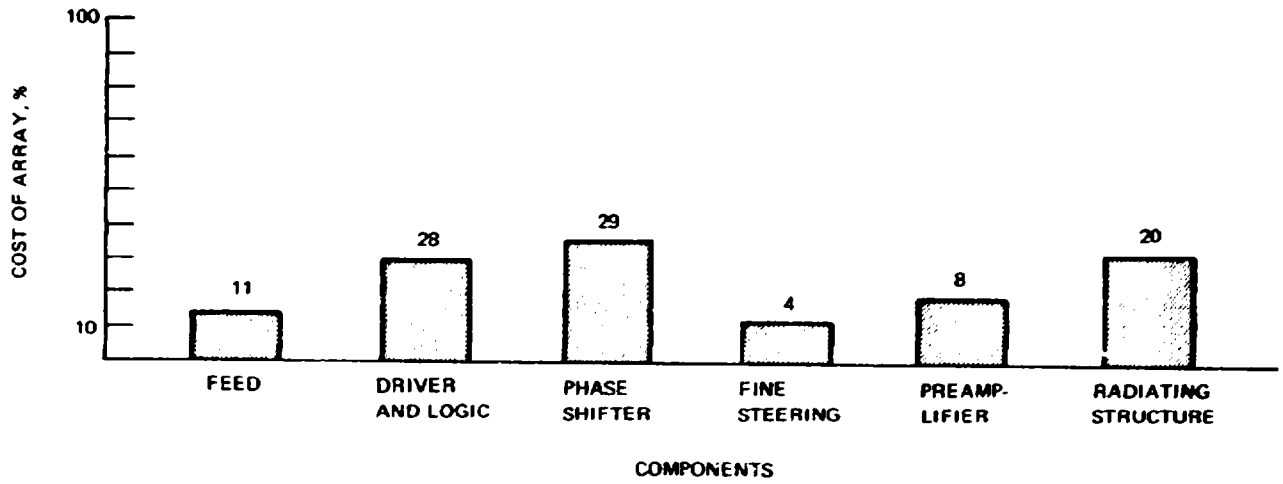

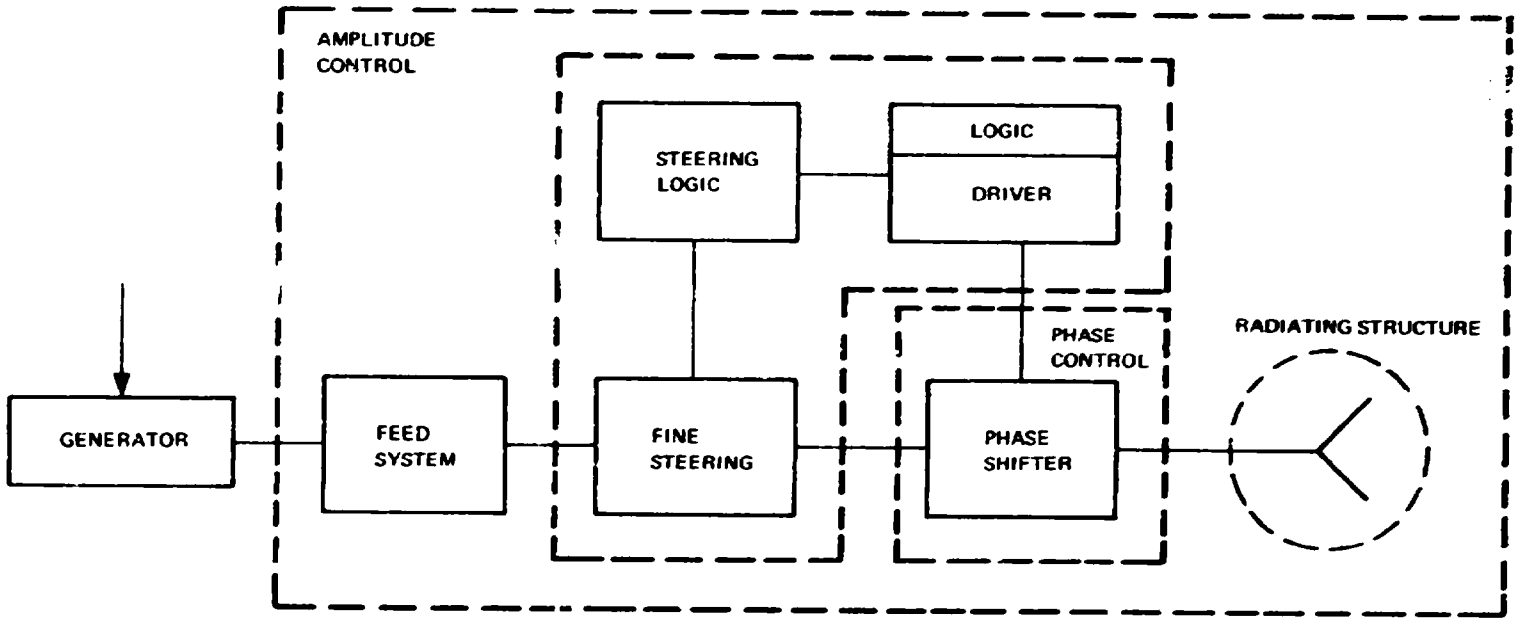

Figure 1-1. Typical phased array.

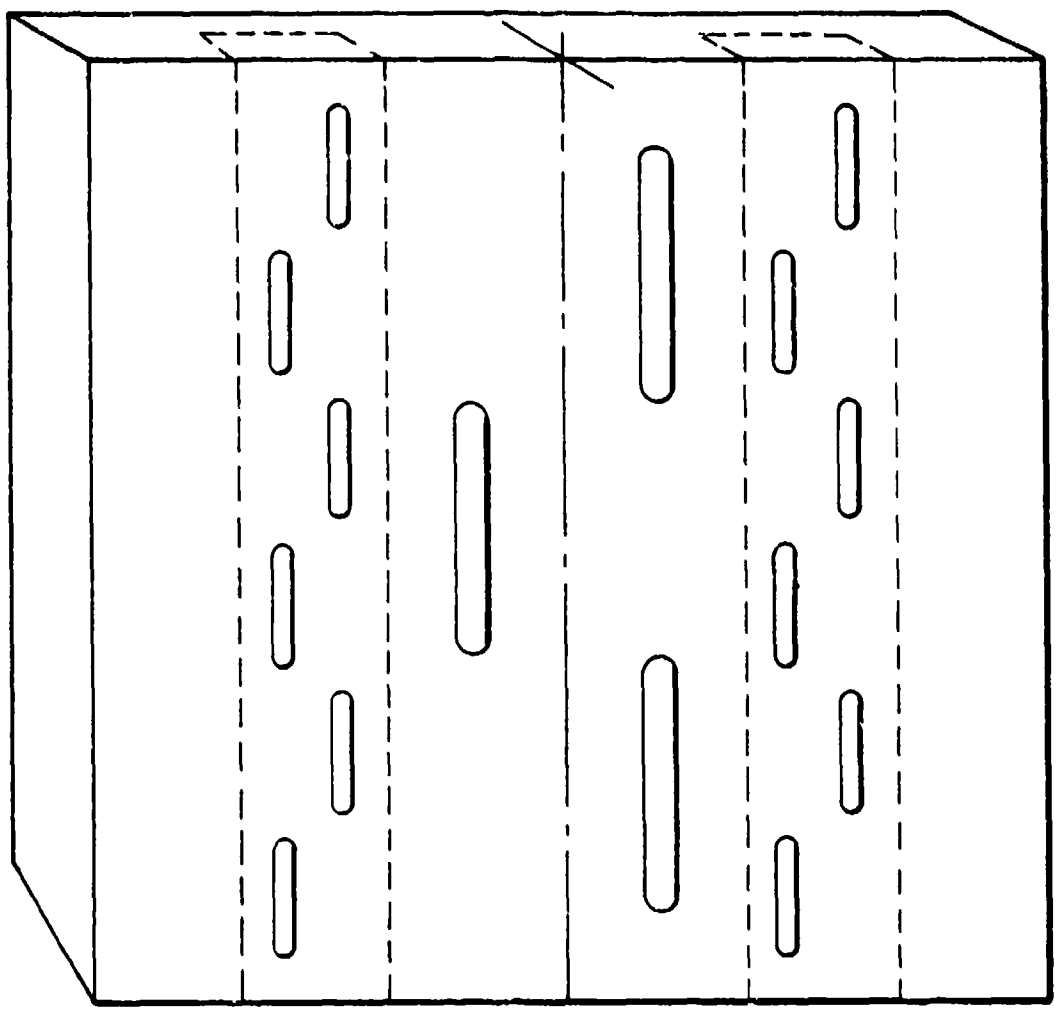

Figure 1-2. Slotted multifrequency array.

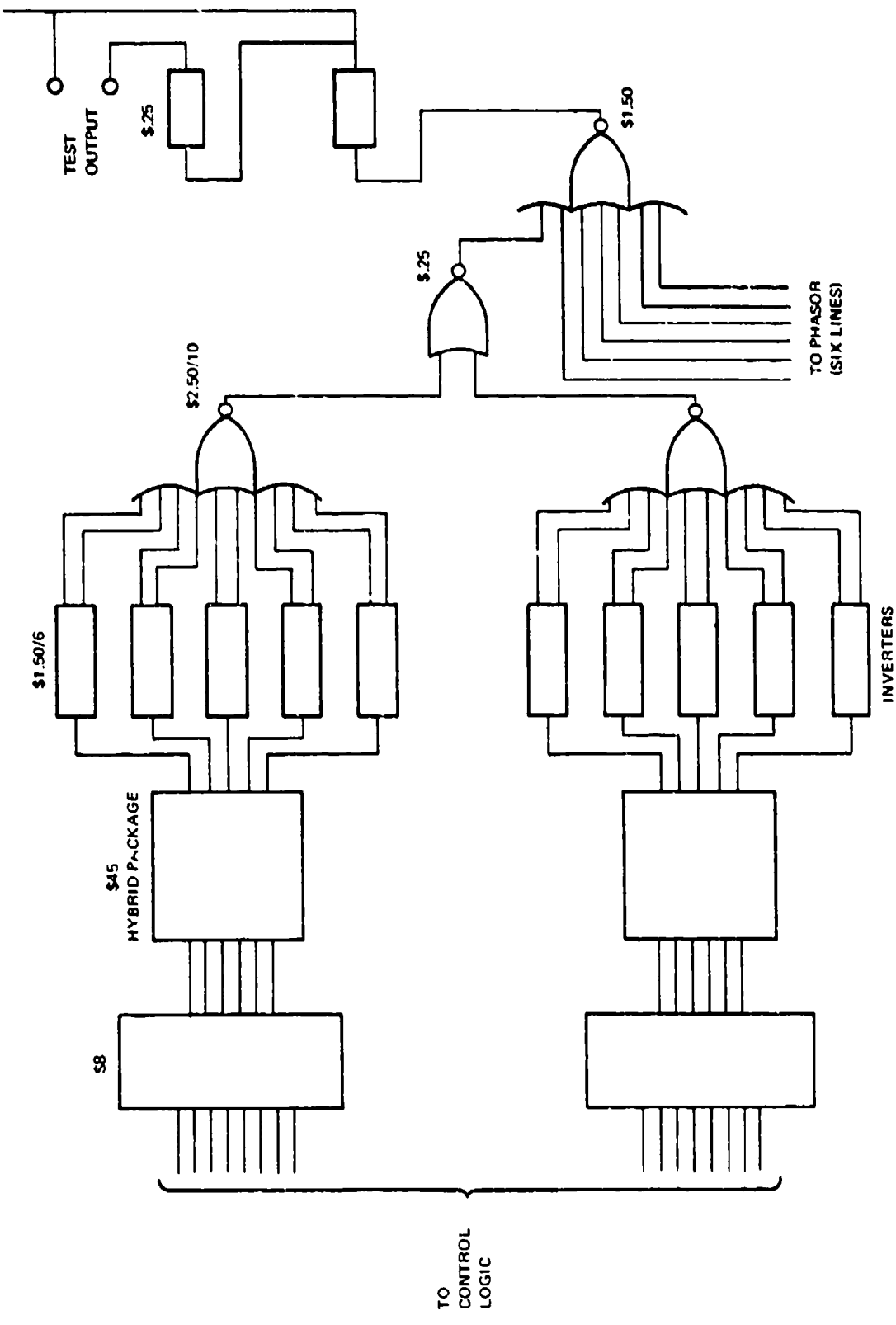

Figure 1-3. Driver and logic for two elements.

3 VERTICAL ARRAY OF SPIRALS FOR HEMISPHERIC COVERAGE

by

J. A. Kaiser

Code 811

Goddard Space Flight Center
Greenbelt, Maryland 20771

for

ARRAY ANTENNA CONFERENCE

Naval Electronics Laboratory Center
San Diego, California

22, 23, 24 February 1972

Vertical Array of Spirals for Hemispheric Coverage

Uniform hemispheric radiation coverage can be considered as a requirement for a spatial square wave where radiation occurs uniformly in the upper hemisphere and there is no radiation into the lower hemisphere. The need for this type of coverage arises when an omni-directional antenna is required to discriminate between a direct signal and its multipath image. Applying a Fourier technique, one can determine the desired radiation pattern analytically as a series of spectral components and then can proceed to generate these components with antenna elements; thus, providing a positive control of radiation coverage. In principle, any radiation coverage with circular symmetry can be synthesized in this manner and under some conditions can be quite broadband.

Mathematically a spatial square wave can be expressed as a series of odd spatial harmonics plus a constant. The harmonic terms are simple cosine variations and can in practice be generated by using uniformly spaced pairs of antenna elements arrayed vertically. The constant can be implemented as a dc or bias term and is generated by a single element at the center of the array.

Consider for example a vertical stack of five isotropic radiators, Figure 1, where four of the elements are equispaced and symmetrically disposed about the array center where the fifth (bias) element is located. The axis of the array (Z axis) is taken as normal to the conventional X-Y plane and the elevation angle, θ, is measured from zenith. The center element in the array, labeled "bias El" in Figure 1, radiates a signal of constant phase for all array aspect angles, making that signal a spatial bias or "dc" contributor or simply A_o, to the total radiation field.

When the innermost pair of elements located about the center of the array, labeled "1st Harm Pair," are excited with equal amplitudes and with phases symmetrical about the center, a field is generated proportional to

$$A_1 \cos \left(\frac{\pi S}{\lambda} \cos \theta + \phi_1\right) \qquad (1)$$

where,

- S is the spacing between a pair of generating elements
- ϕ_1 is the excitation phase of the first harmonic pair of elements
- A_1 is amplitude of excitation of each element of the first harmonic pair
- λ is the wavelength
- θ is the elevation angle.

This field represents the lowest spatial frequency[1] for the array.

In a similar fashion the outermost pair generates a field proportional to

---

[1] R. M. Bracewell, "The Fourier Transform and Its Applications," McGraw Hill Book Co., 1965

$$A_3 \cos\left(\frac{3\pi S}{\lambda} \cos\theta + \phi_3\right) \qquad (2)$$

where, A_3 is the amplitude of excitation of each element of the outer pair and ϕ_3 is the excitation phase of that pair. It can be observed from Equation (2) that the variation in this field is spatially three times faster than the field from the innermost pair, see Equation (1). Thus, the outer pair generates the third spatial harmonic.

Additional pairs with the same spacings will generate higher harmonics. In general, the total field from an infinite array would be proportional to

$$A_o + \sum_{n=1}^{\infty} A_N \cos\left(\frac{n\pi S}{\lambda} \cos\theta + \phi_n\right) \qquad (3)$$

where, n is the index number indicating the odd harmonics, n = 1,3,5...

Figure 2 (a) illustrates the spatial variations of the first two harmonics and Figure 2 (b) the variation of the bias term associated with the array of Figure 1. Relative phases are selected such that when the harmonics are added, a radiation field approaching the shape shown in Figure 2 (b) is produced. The polarity of the bias term determines which radiation hemisphere is being considered, upper hemisphere for a positive bias and lower hemisphere for a negative bias.

In a properly phased finite array, radiation pattern nulls occur whenever the bias term is equal in amplitude and opposite in polarity to the sum of the harmonic terms. Radiation occurring beyond the first null are the sidelobes.

In the experimental setup, the amplitude and the polarity of the bias term was selected to produce minimum sidelobe levels.

The antenna elements chosen for this experiment were four-filament flat spirals as shown arrayed in Figure 3. These spirals were each operated in the third radiation mode, a field configuration where radiation occurs from a circumference of three wavelengths, allowing room in the center through which to route cables. There are six spirals equally spaced and symmetrically disposed about the center of the array where the seventh spiral is located. There is a coaxial cable (RG-223) connecting each spiral input terminal to a corporate feed behind the plate on which the array is mounted. The outer terminals are terminated with resistors to minimize reflected currents from the spiral ends.

Each spiral can be rotated mechanically about the axis by an amount greater than $\pm 15°$. Since the third radiation mode is utilized, a mechanical rotation of $\pm 15°$ produces a change in phase of the radiated field of $\pm 45°$. Thus, fine phasing ($\pm 45°$) is obtained by rotation of the spirals about their axes while coarse phasing (90° increments) is obtained by interchanging input cable connections.

Figure 4 is a picture showing the corporate feed structure used to excite the array. Each of the rectangular printed circuit boards

feeds one filament of each of the seven spirals. The 90° relative phases used to excite the third radiation mode on each spiral is obtained from the circular shaped feed board. This circular feed board is capable of providing, simultaneously, phasings for three additional radiation modes not used in this experiment. The inverted rectangular board shows a microstrip construction used.

Figure 5 shows radiation patterns measured for the array at S-band. The slopes of the radiation patterns near the horizon, i.e., θ near 90°, for both polarizations are fairly steep, approaching 2.5 db per degree change in elevation. The nulls near the axis, i.e., $\theta = 0°$, are those associated with the third radiation mode of the spiral. The fact that they occur off-axis indicates mode impurity, i.e., presence of some first mode energy. The back radiation (sidelobes) is down approximately 20 db. The measured phase center was located along the array axis and approximately 1/2 inch from the array center toward the mounting plate.

Radiation patterns were measured only at the one frequency. Patterns were calculated, however, for spacings of $.9 < \frac{S}{\lambda} < .5$ and for a cutoff angle of $\theta = 90°$. Pattern shape including sidelobe levels and 1st null position remained essentially constant over the entire band.

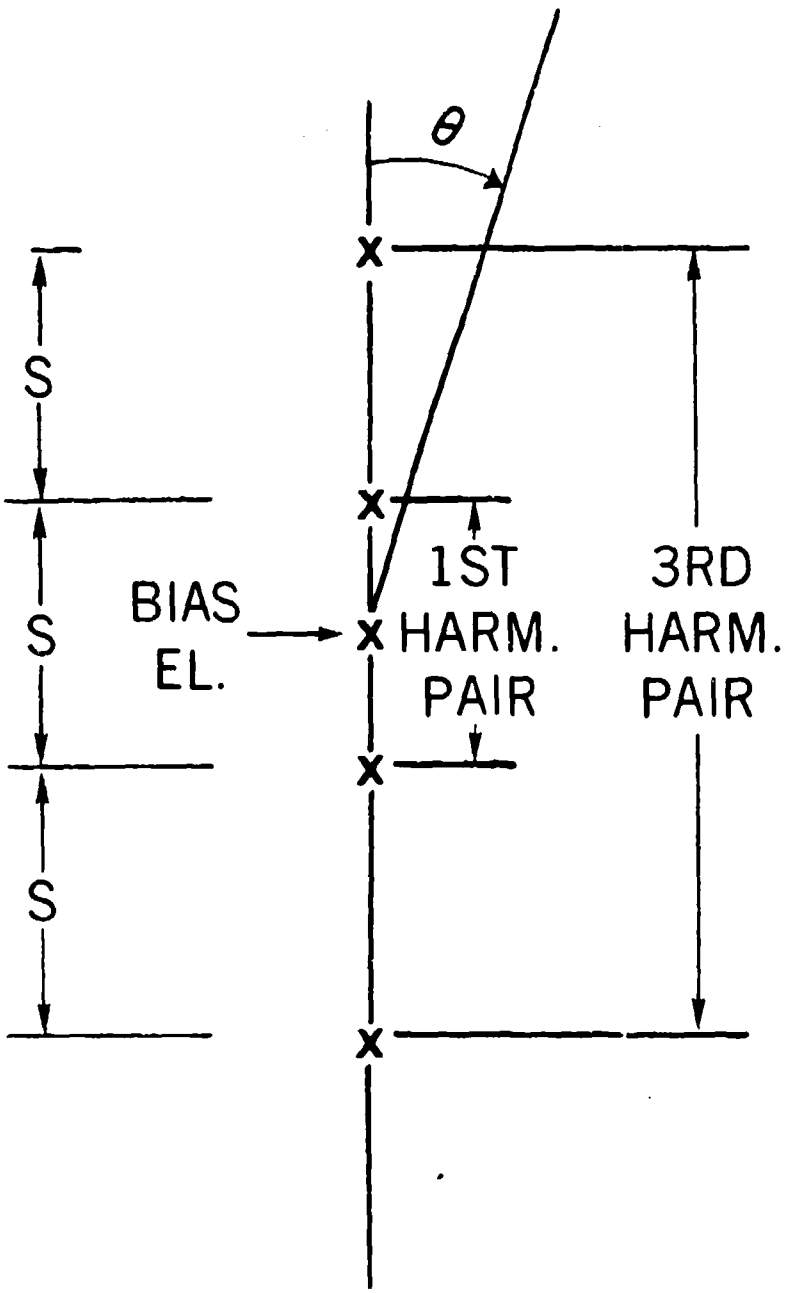

FIG. 1. REPRESENTATION OF FIVE-ELEMENT VERTICAL ARRAY

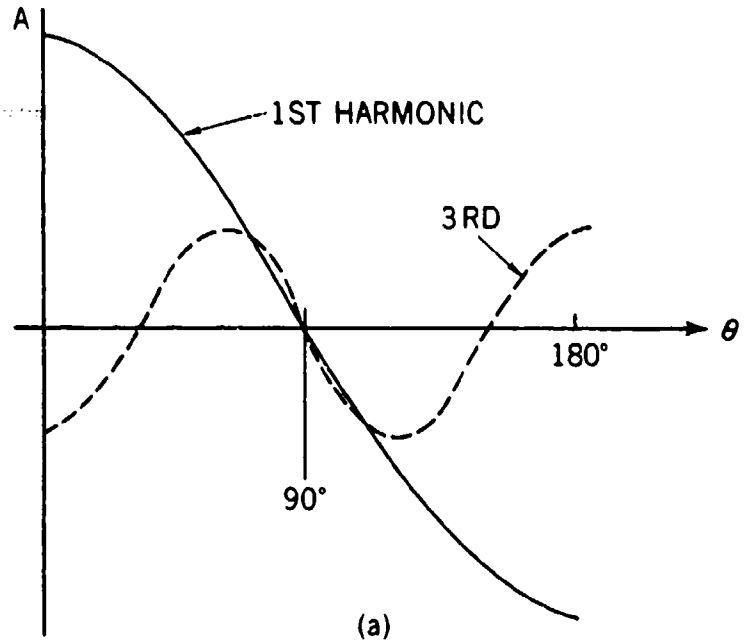

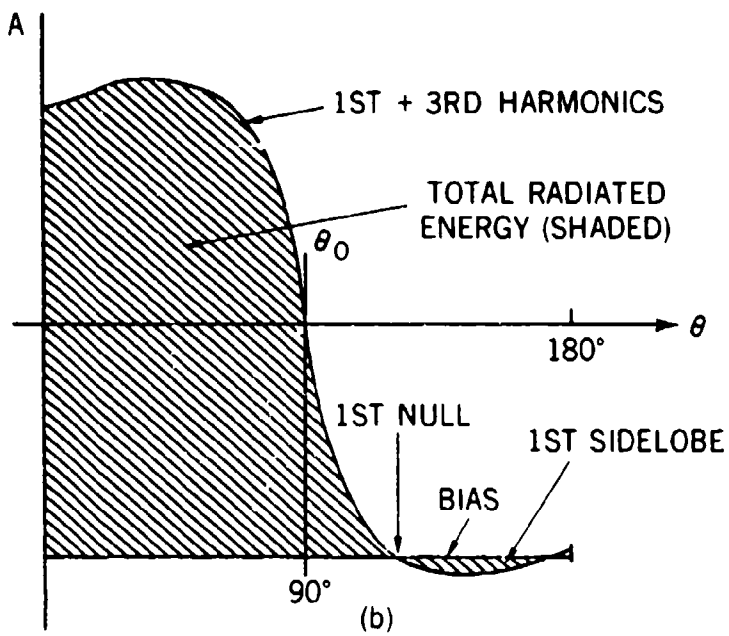

FIG. 2. SYNTHESIS OF A SPATIAL SQUARE WAVE

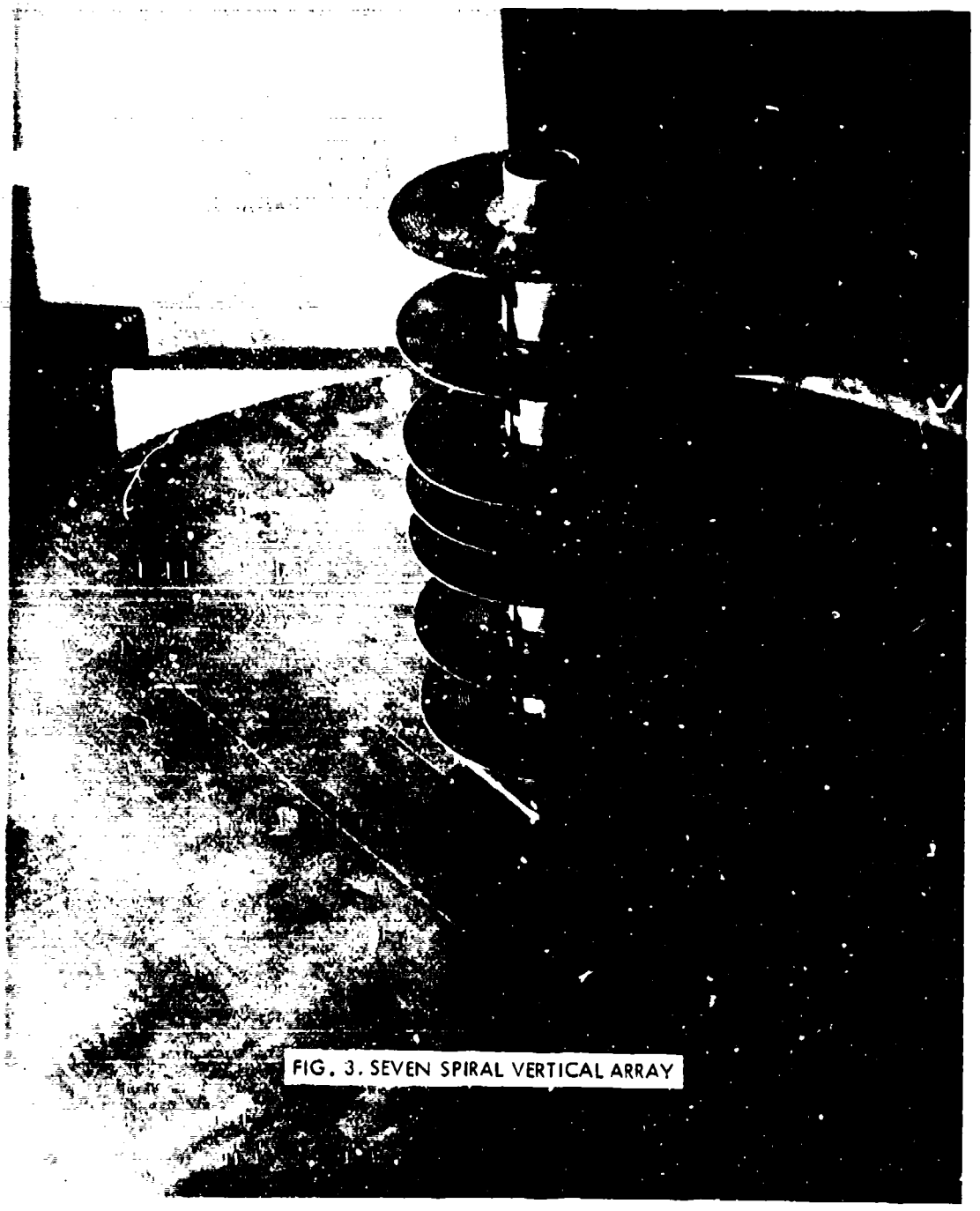

FIG. 3. SEVEN SPIRAL VERTICAL ARRAY

FIG. 4. CORPORATE FEED FOR VERTICAL ARRAY

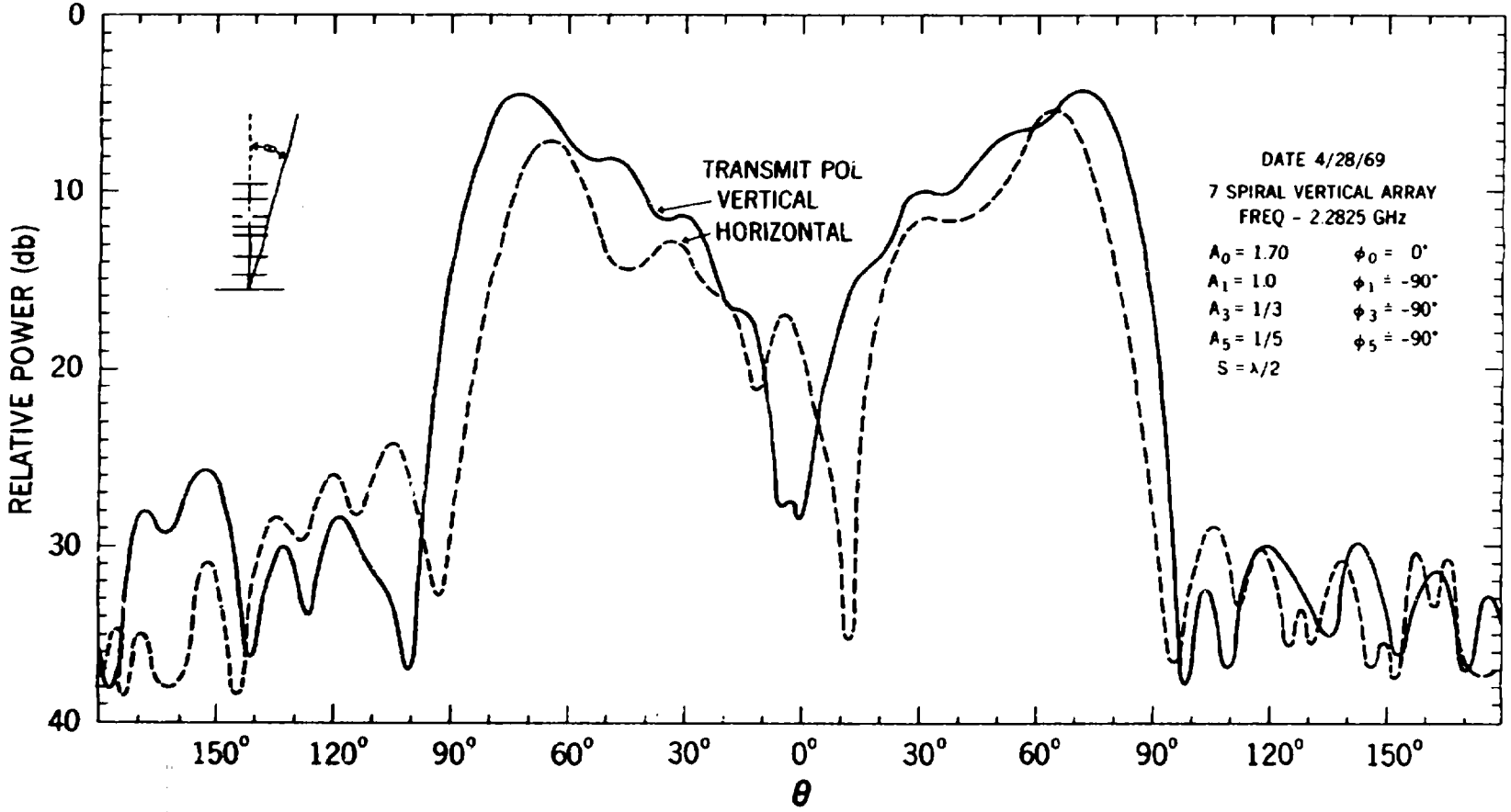

FIG. 5. MEASURED RADIATION PATTERNS

4. CYLINDRICAL AND CONICAL ARRAY INVESTIGATIONS

by

J. E. Boyns

Code 2330

Naval Electronics Laboratory Center
San Diego, California 92152

for

ARRAY ANTENNA CONFERENCE

22, 23, 24 February 1972

Naval Electronics Laboratory Center
San Diego, California 92152

4-1a

INTRODUCTION

Studies resulting in the successful implementation of a circular array which produces a fan beam in elevation and provides 360 degrees in azimuth coverage have resulted in studies aimed at extending the approach to yield three-dimensional data using a pencil beam.[1] A cylindrical array has its optimum performance at the position normal to the cylinder and degrades as the beam is scanned vertically in either direction from this position. In contrast, the conical geometry should have its optimum behavior in a direction normal to the cone angle. If this array can be implemented, then it is clear that this type of antenna will extend the coverage in the elevation plane. The present studies are aimed at a better understanding of the properties of these types of arrays.

The cylindrical array can be considered as a ring array composed of linear array elements, or a stack of ring arrays. The partial array to be described is made up of 42 linear arrays, each with 32 elements, arrayed on a circle 16 feet in diameter. Two different approaches can be used to feed the radiating elements. The first method uses 1:22 power dividers to feed alternate rows of elements in the triangular configuration. Since each of the 64 partial rings has only one phasor board, individual control of the phase at each radiating element is not possible. This results in phase errors as the beam is scanned in the elevation plane and the beam deteriorates. This scheme yields limited elevation-beam data, but can give some indication of the effects of these errors on the elevation beam characteristics.

The other method uses a 3-bit phasor at each radiating element and gives good control of the element phase. This partial array can be scanned in azimuth using conventional linear phase-scanning techniques f step scanning for angles up to about 25 degrees. This array can be used as a test bed to investigate angular accuracy, beam behavior, and performance of the array using short pulses and wideband signals. An indication of the magnitude of the phase tolerances can be obtained in addition to data useful in the design of future systems.[2]

To extend the elevation coverage and retain the advantages of the cylindrical array, a conical shape can be chosen. The use of a conical array is analogous to tilting back the planar array faces of the cylindrical array to extend elevation coverage at the expense of coverage in the region below the horizon. For the configuration chosen the elements are arranged in linear arrays along generators of the cone. This type of arrangement results in unequal element spacings from top to the bottom of the cone. In spite of some possible disadvantages of this type of arrangement, it simplifies the implementation of the logic control required to drive the phase shifters. The type of feed system to be used with this array is of the space-feed type of the unconstrained or feed-through type.

CYLINDRICAL ARRAY ANTENNA

The cylindrical array antenna being investigated at NELC is shown in figure 4-1. The aperture contains 1344 open-ended waveguide radiators arrayed in a 60-degree section of a right cylinder. The elements are arrayed on a triangular grid as shown in figure 4-2. The parameters for the array are listed in table 4-1.

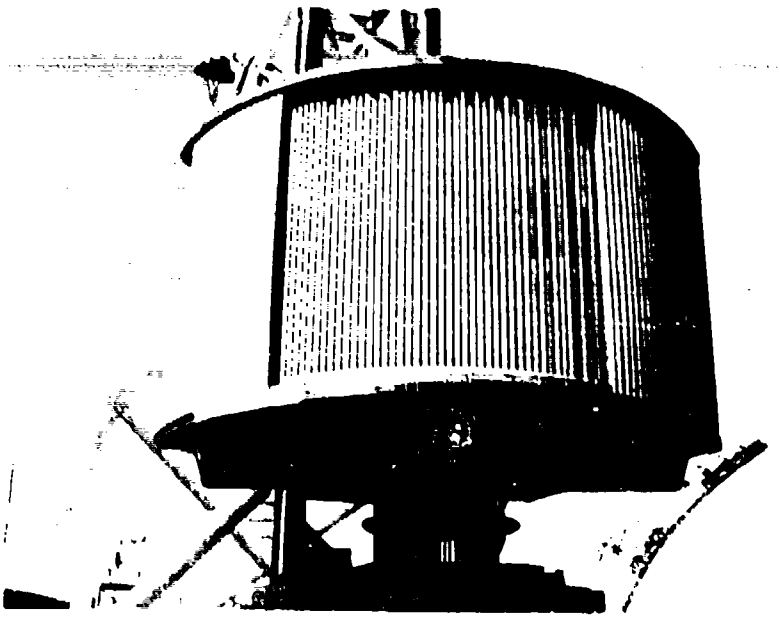

Figure 4-1. 60-degree section of cylindrical array antenna.

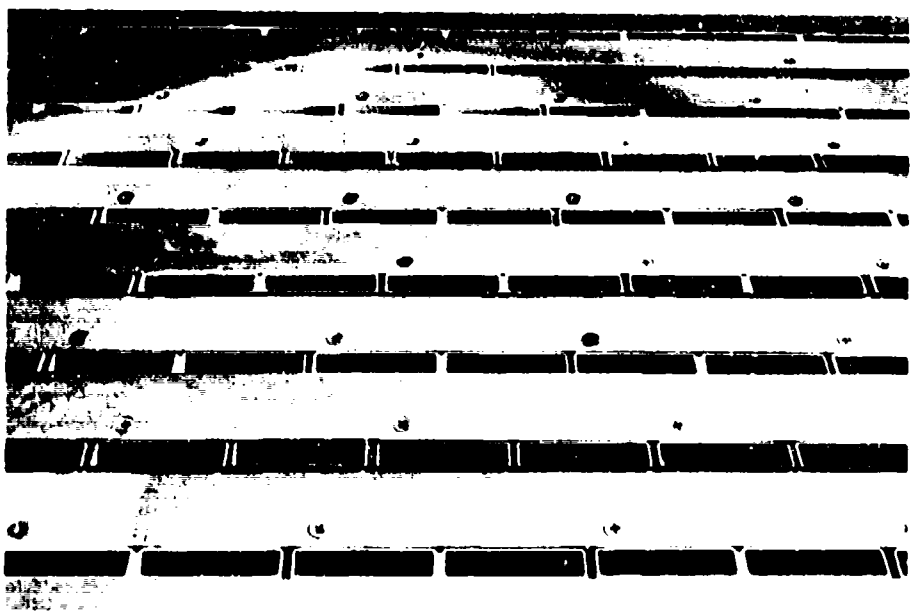

Figure 4-2. Close-up of array aperture.

TABLE 4-1. PARAMETERS FOR CYLINDRICAL ARRAY ANTENNA

Array sector	60 degrees
Configuration	16-foot-diameter cylinder
Elements per column	32
Elements per row	42
Total elements	1344
Type of elements	Open-ended waveguides
Polarization	Horizontal
Frequency band	2.9 - 3.5 GHz
Element spacing in columns	0.72 wavelength
Element spacing in rows	0.64 wavelength
Waveguide width	0.13 wavelength
Waveguide height	0.68 wavelength
Pencil beam	2.5 degrees HPBW
Gain	25 dB over isotropic
Maximum sidelobe level	-25 dB
Scan limits	±25 degrees each plane

FEED SYSTEM I

The first feed system used in conjunction with the cylindrical array antenna section is shown in figure 4-3. This feed system uses 1:22 stripline power dividers with a built-in phase and amplitude taper to feed alternate rows of elements. Each power divider then has a 4-bit stripline phase shifter at its input allowing for scanning of the beam in elevation only. Elemental phase control is not possible in this case. The inputs to the phase shifters are then combined by two 1:32 stripline power dividers which provide an amplitude taper in the elevation plane and allow for monopulse operation.

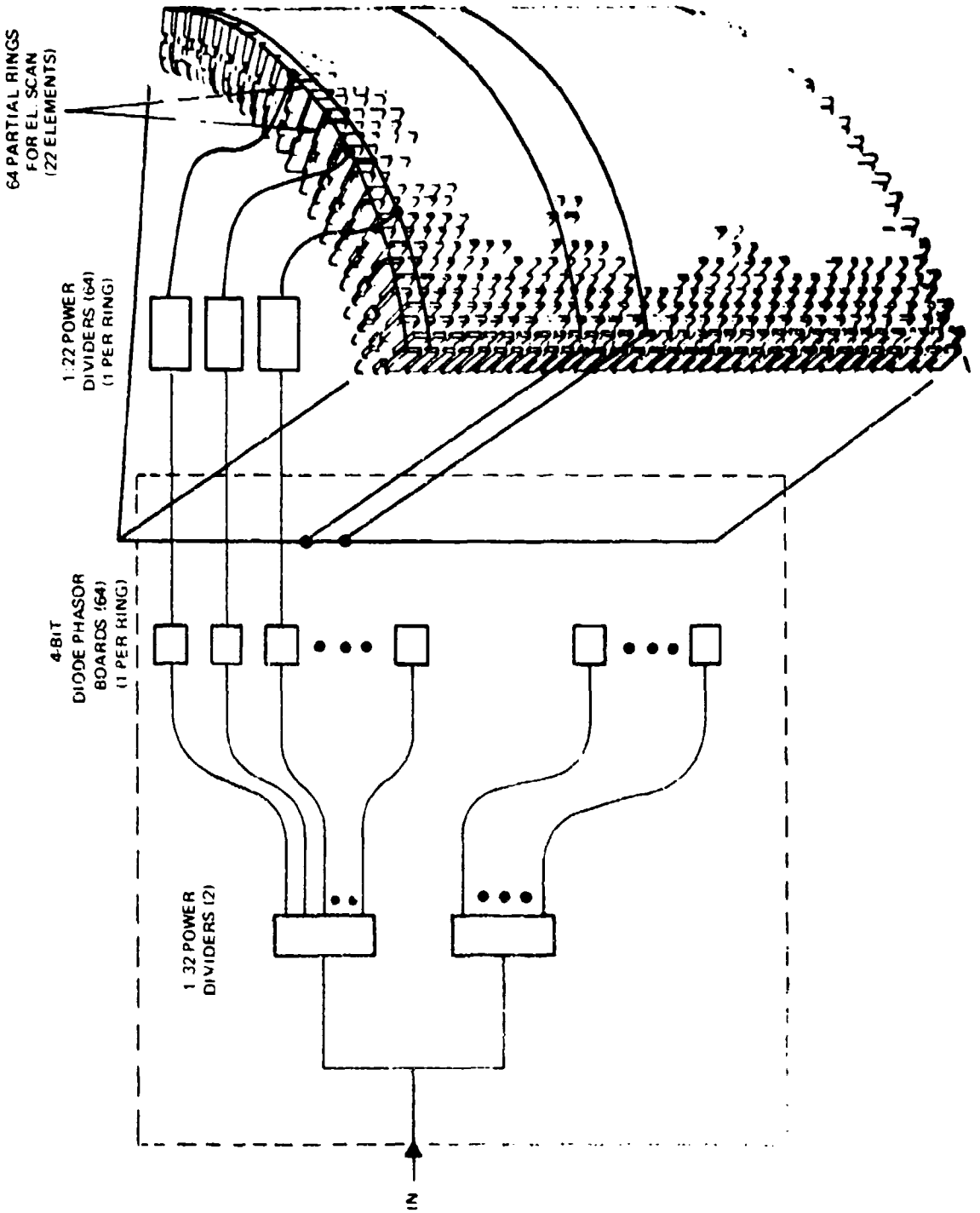

Figure 4.3. Feed system I for cylindrical array antenna.

FEED SYSTEM II

The second feed system for the cylindrical array which is currently being fabricated is similar to that shown in figure 4-3 with changes in the power divider-phase shifter arrangement. The 1:22 stripline power dividers are replaced with 1:21 stripline power dividers having an amplitude taper only. The 4-bit stripline phase shifters are replaced with 3-bit MIC phase shifters at each element. With the phase shifters at each element, control of the phase at each element is possible to allow for scanning of the beam in both the azimuth and the elevation plane.

FEED SYSTEM I COMPONENTS

A portion of the back of the aperture is shown in figure 4-4. The 8-foot semirigid cables which connect the radiating elements to the power dividers are shown in this figure. Figure 4-5 shows the arrangement of the stripline power dividers used in the first type of feed system. The 4-bit stripline phase shifter utilized in the first feed system is shown in figure 4-6. Characteristics for this phase shifter are listed in table 4-2.

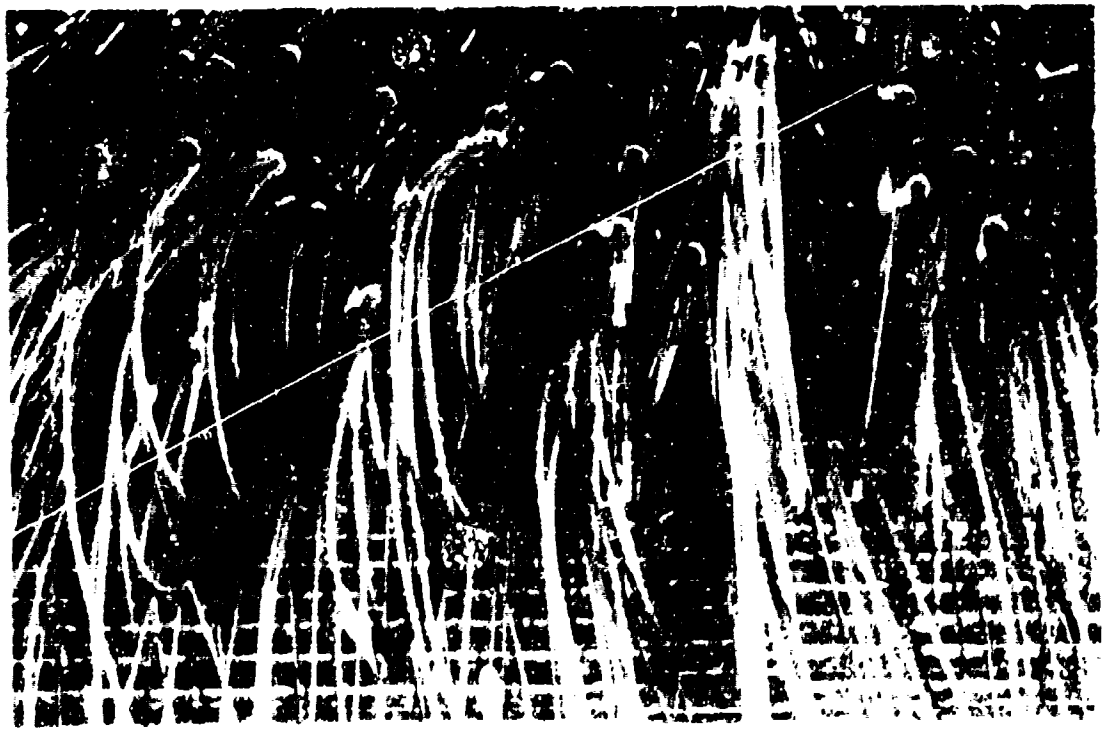

Figure 4-4. Rear-of-the-aperture view of cylindrical array antenna.

Figure 4-5. Stripline power divider arrangement for feed system I.

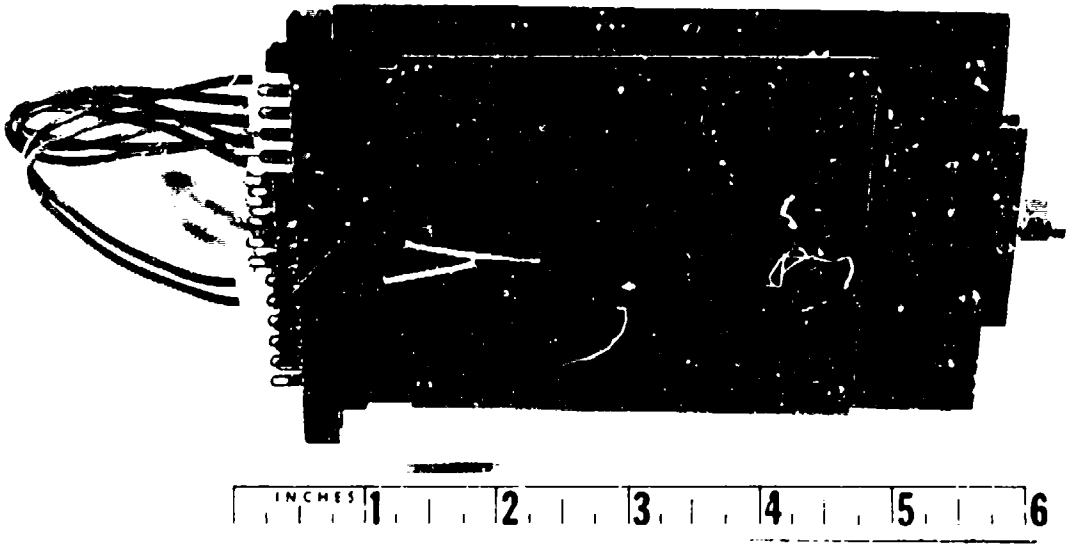

Figure 4-6. 4-bit stripline phase shifter used in feed system I.

TABLE 4-2. CHARACTERISTICS OF 4-BIT STRIPLINE PHASE SHIFTER

- Loss = 2.5 - 3.0 dB
- Freq. = 2.9 - 3.5 GHz
- VSWR = 1.5/1.0
- Power = 5 kW peak

EXPERIMENTAL MEASUREMENTS USING FEED SYSTEM I

Using feed system I, broadside radiation patterns were measured in the azimuth plane. A pattern was measured at 3.5 GHz as shown in figure 4-7. This pattern was measured with all phasors set for zero degrees scan. From figure 4-7 the HPBW is approximately 2.5 degrees and the maximum sidelobe level is -22 dB.

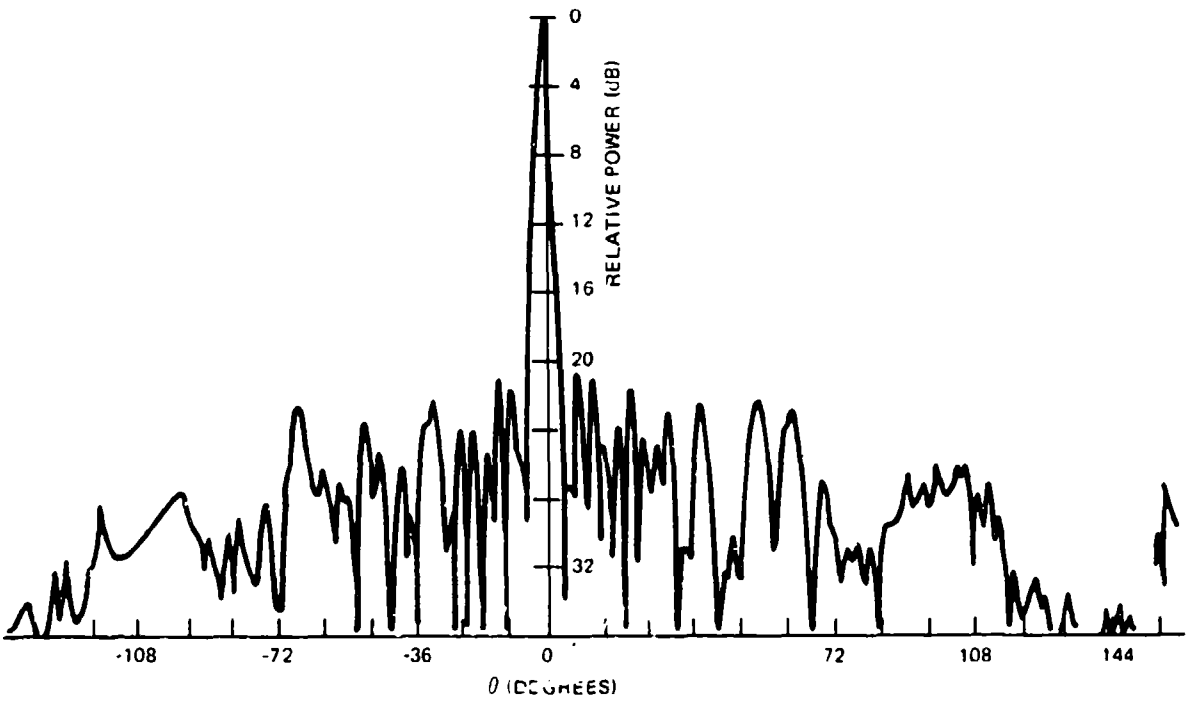

Figure 4-7. Measured radiation pattern in the elevation plane. θ = 0 degree; f = 3.5 GHz.

Elevation radiation patterns were also measured with the phasors set for various angles of elevation. Figure 4-8 shows one elevation pattern with the phasors set for a scan angle of 15 degrees. This pattern was measured at 3.5 GHz. From figure 4-8 the HPBW is 2.5 degrees and the maximum sidelobe level is -13 dB. The sidelobe level is higher than the design level due to systematic errors and lack of elemental phase control. Figure 4-9 shows another elevation pattern at a scan angle of 25 degrees. This pattern was also measured at 3.5 GHz. From figure 4-9 the HPBW is 2.5 degrees and the maximum sidelobe level is -9 dB. The high sidelobe level is again due to the same errors listed for figure 4-8.

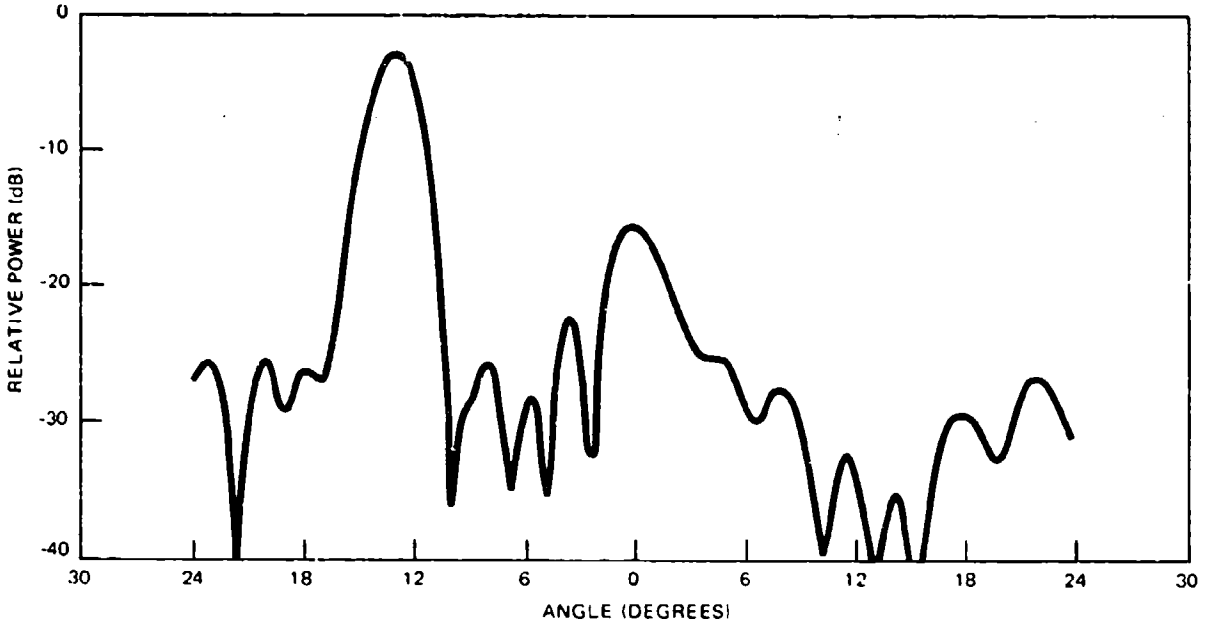

Figure 4-8. Measured radiation pattern in the elevation plane. θ = 15 degrees; f = 3.5 GHz.

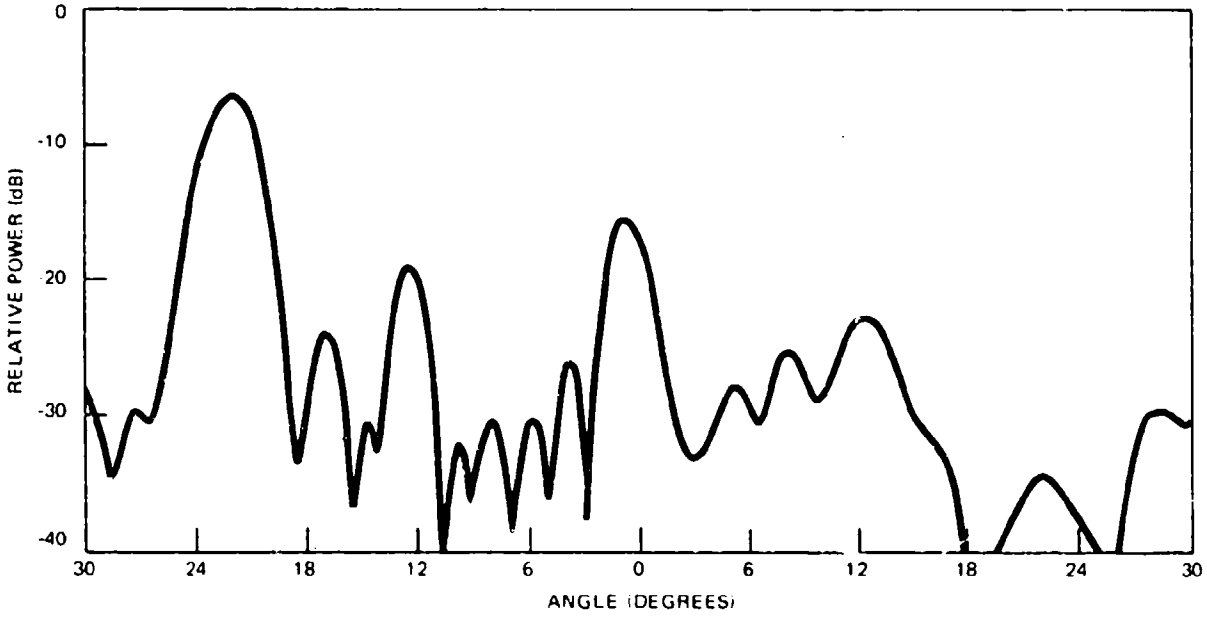

Figure 4-9. Measured radiation pattern in the elevation plane. θ = 25 degrees; f = 3.5 GHz.

FEED SYSTEM II COMPONENTS

The 3-bit MIC phase shifter to be used with the second feed system is shown in figure 4-10. The phasor is fabricated on alumina substrate using PIN diodes. The phasors have been tested up to three kilowatts of peak power at midband before breakdown occurs. Other characteristics of the MIC phasor are listed in table 4-3.

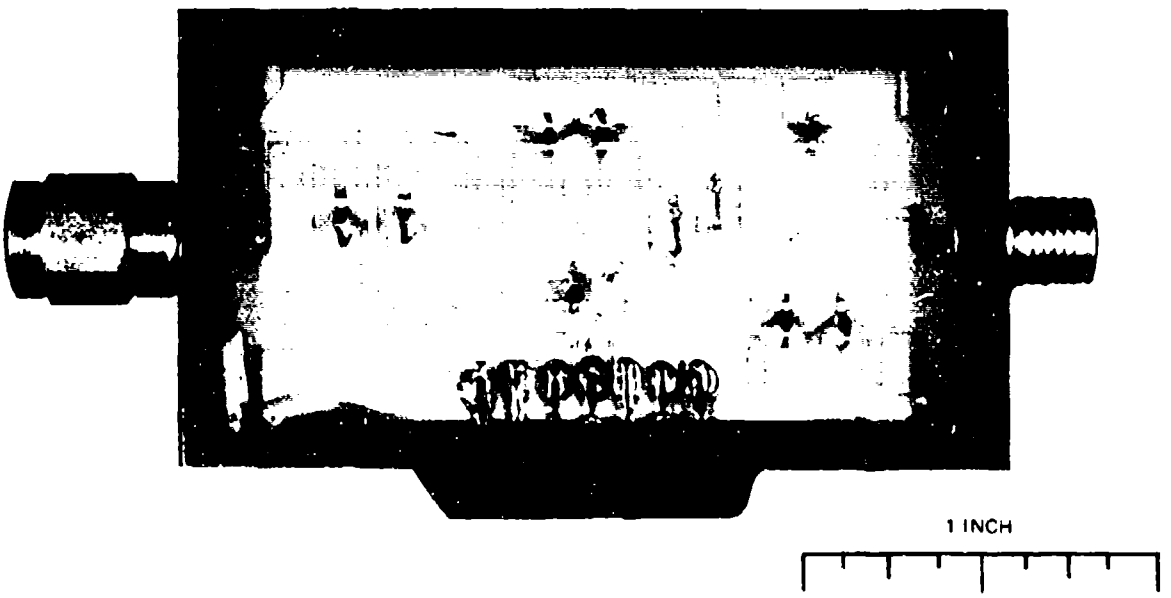

Figure 4-10. 3-bit MIC phase shifter for feed system II.

TABLE 4-3. CHARACTERISTICS FOR 3-BIT MIC PHASE SHIFTER

Three bits	180°, 90°, 45°
Phase tolerance	±10°
Bandwidth	2.9 to 3.5 GHz
Loss	3.0 dB
VSWR	1.5:1
Power handling	2 kW peak
Bias requirements (per diodes)	50 mA, 1 V forward, 90 V reverse
Diodes required	Eight each - Microsemiconductor Corporation (MC1354)
Cost (parts)	$45

The driver-test circuit package for the MIC phasor is shown in figure 4-11. The two circuits are fabricated with thick-film hybrid techniques. Also included in the upper left-hand corner of the package is a 4-bit full adder. Although packaged in a 3-watt package, the circuits draw 70 milliamps maximum per bit and dissipate 2.4 watts maximum. Some of the parameters of the driver and test circuit are listed in table 4-4.

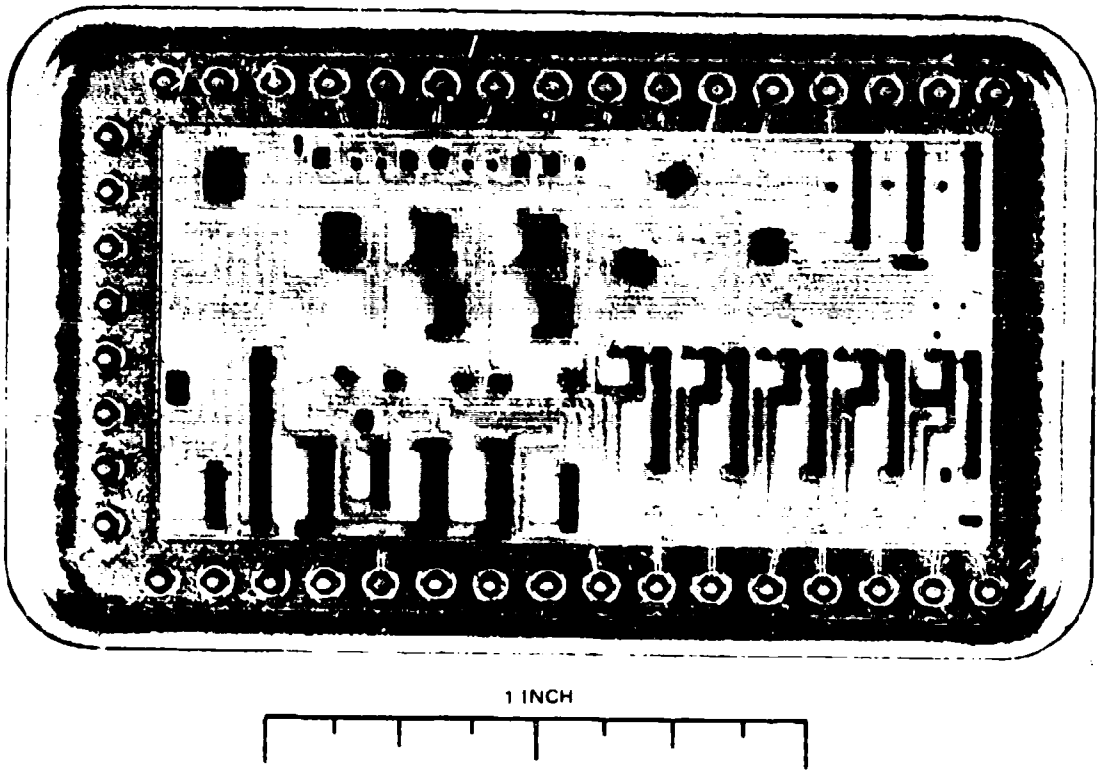

Figure 4-11. Driver-test circuit package for 3-bit MIC phase shifter.

TABLE 4-4. PARAMETERS FOR DRIVER-TEST CIRCUIT PACKAGE

- Fabricated with thick-film hybrid techniques
- Packaged in 3-watt package
- Dissipates 2.4 watts maximum
- Draws 70 milliamps per bit
- Costs $55 per package

Figure 4-12 illustrates the new 1:21 stripline power divider to be used in conjunction with the MIC phasors. This power divider provides only an amplitude taper. Figure 4-12 shows the power divider with 21 phasors mounted in place.

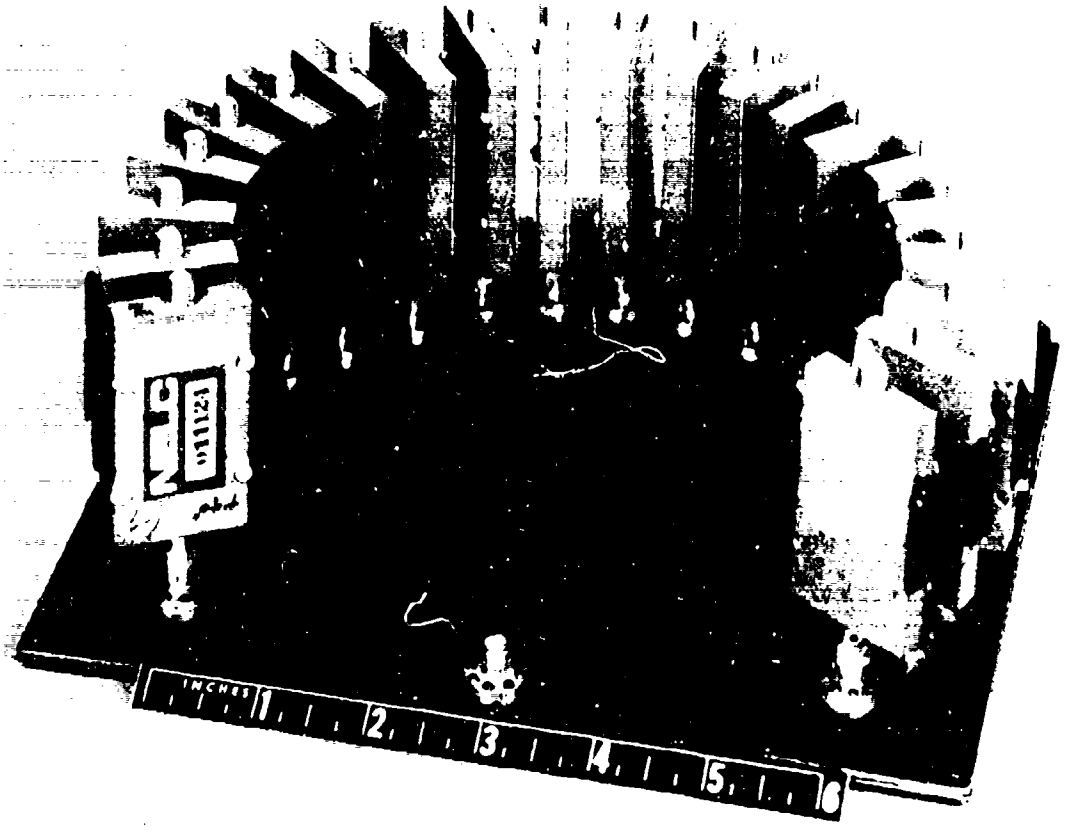

Figure 4-12. 1:21 stripline power divider with 3-bit MIC phasors for feed system II.

CONICAL ARRAY ANTENNA

Because of the limitations of the cylindrical array in regard to elevation scan, NELC is now looking at a conical array section in an attempt to improve the high angle coverage. Table 4-5 illustrates some of the advantages and disadvantages connected with the conical configuration.

TABLE 4-5. ADVANTAGES AND DISADVANTAGES OF CONICAL CONFIGURATION

POSSIBLE ADVANTAGES OF CONE:

- Better scanning properties in elevation
- Possible reduction in some sidelobe levels
- Scan limits imposed by grating lobes may be less severe than for the cylinder
- Interleaving of multifrequency arrays may be easier on a conical surface

DISADVANTAGES:

- Scanning commands could be more complex
- Prediction of performance is more difficult than for the cylindrical array
- Cross-polar lobes will be larger

Methods of feeding the cylindrical array are applicable to the conical array:

1. linear array scan of active columns for elevation scan
2. commutation of distribution in azimuth for azimuth scan

The difference between the cone and cylinder is that in the cylinder all columns are scanned to the same elevation angle, and for the cone, all columns are scanned to a different elevation angle. This results in a decollimation of the sidelobes in the azimuth plane. For the configuration under consideration at NELC the elements are arranged in columns, i.e., equal number of elements in each ring from top to bottom.

Analytical work has been done at NELC for conical arrays with the elements arranged as above. The work has not included mutual coupling as was done with the cylindrical array because of the added analytical complexity.[3]

ANALYTICAL RESULTS

The results of some of the analytical work are given here to illustrate why the particular cone angle was chosen. Figure 4-13 shows the computed elevation beamwidth of a cone-vs.-elevation scan angle for various cone angles as a function of scan angle. As expected, the optimum beam is obtained at the scan angle equal to the cone angle. A maximum beamwidth of 2.5 degrees is desired from this array and for the parameters chosen for this array, figure 4-13 indicates that a cone angle of 20 degrees will provide satisfactory performance from the cone.

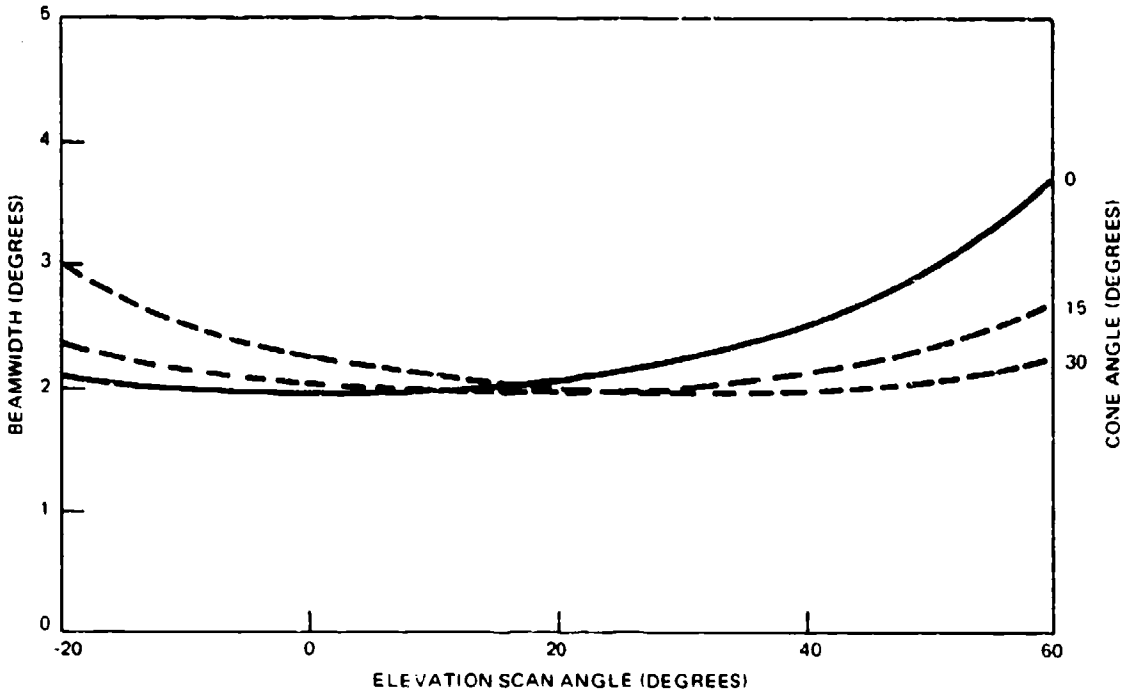

Figure 4-13. Computed elevation beamwidth as a function of scan angle for various cone angles

The effect of cone angle on the azimuth beamwidth was also investigated. Figure 4-14 compares the azimuth beamwidth of a cone with an angle of 30 degrees to that of a cylinder for various elevation scan angles. As shown by figure 4-14, the azimuth beamwidth is independent of the cone angle.

A computed radiation pattern from the conical array is shown in figure 4-15. This particular pattern was computed for an elevation angle of 30 degrees. The pattern in the elevation pattern has well collimated sidelobes but in azimuth they are not collimated by the fact that each column is scanned to a different elevation angle. For the same reason that the azimuth sidelobes are not collimated, any grating lobe tends to be decollimated in the azimuth plane even more so than does the grating lobe of the cylindrical array. NELC does not intend to operate this array in a condition of a grating lobe because of the high VSWR's that can exist due to mutual coupling between the radiating elements.[4]

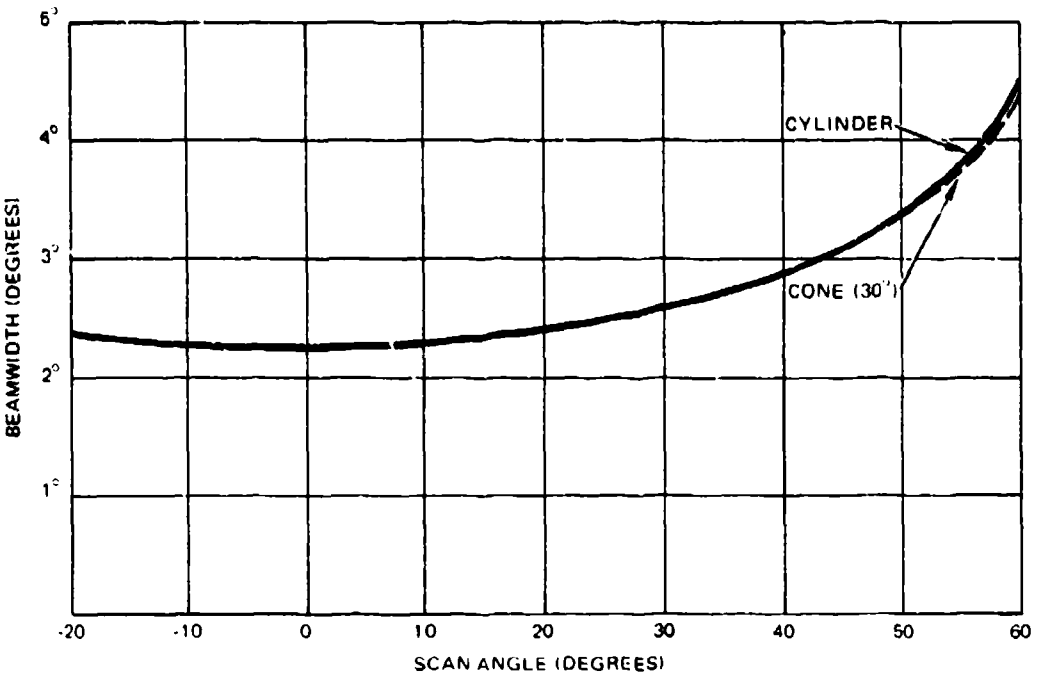

Figure 4-14. Comparison of azimuth beamwidths of conical and cylindrical arrays as a function of elevation scan.

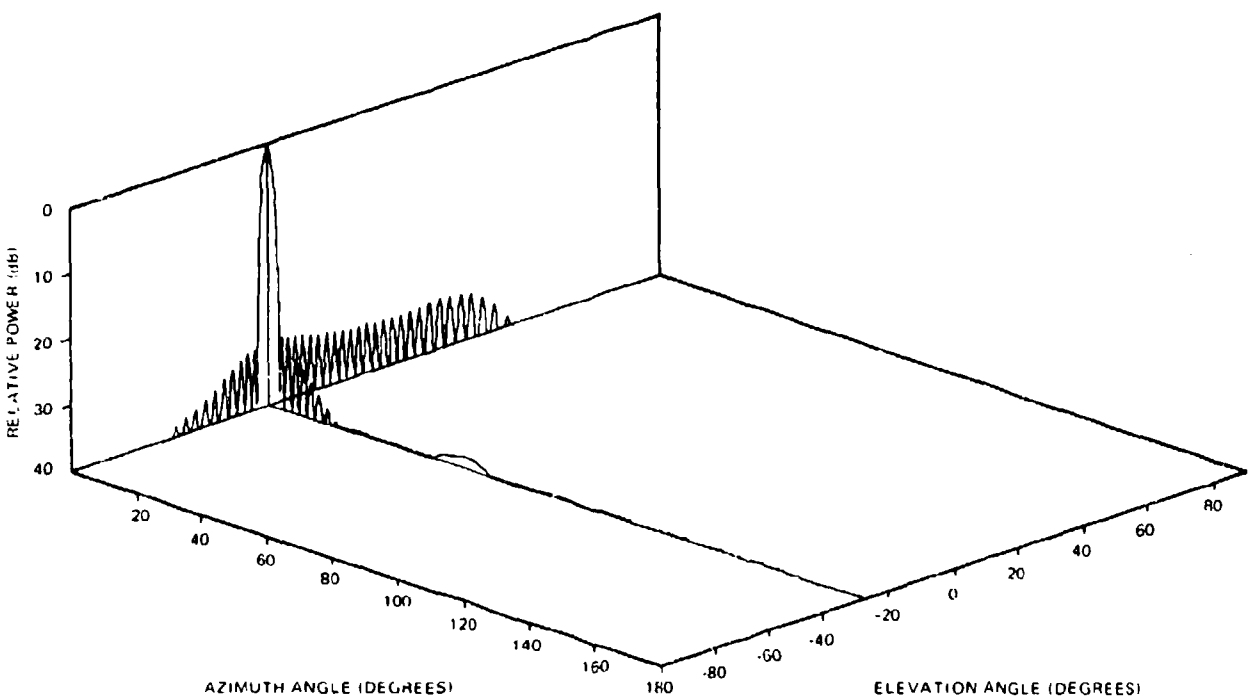

Figure 4-15. Principal computed patterns for a conical array having a cone angle of 15 degrees.

CONICAL ARRAY UNDER STUDY

Figure 4-16 shows the section of a truncated cone that is currently under study. The base of the cone is 16 feet in diameter and the cone angle is 20 degrees. Figure 4-17 illustrates the conical section being fabricated. The arrangement of the printed circuit dipoles can be seen from this figure. The parameters for the conical array are listed in table 4-6.

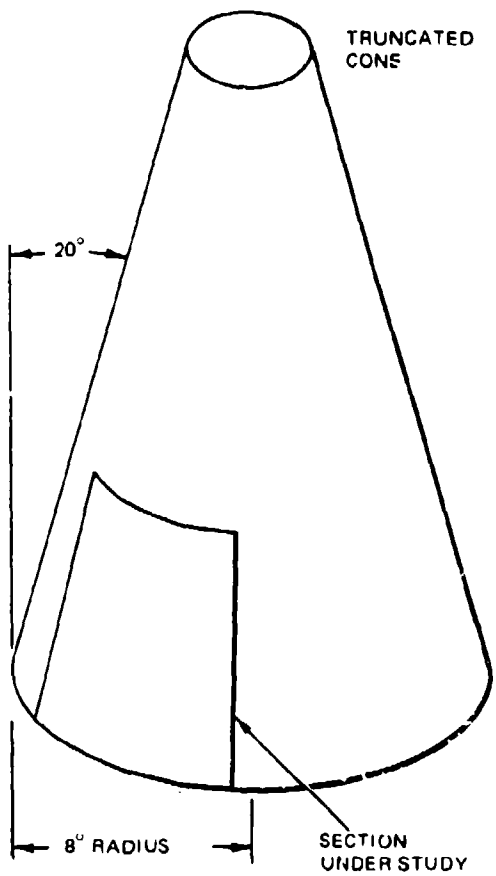

Figure 4-16. Section of truncated cone under study.

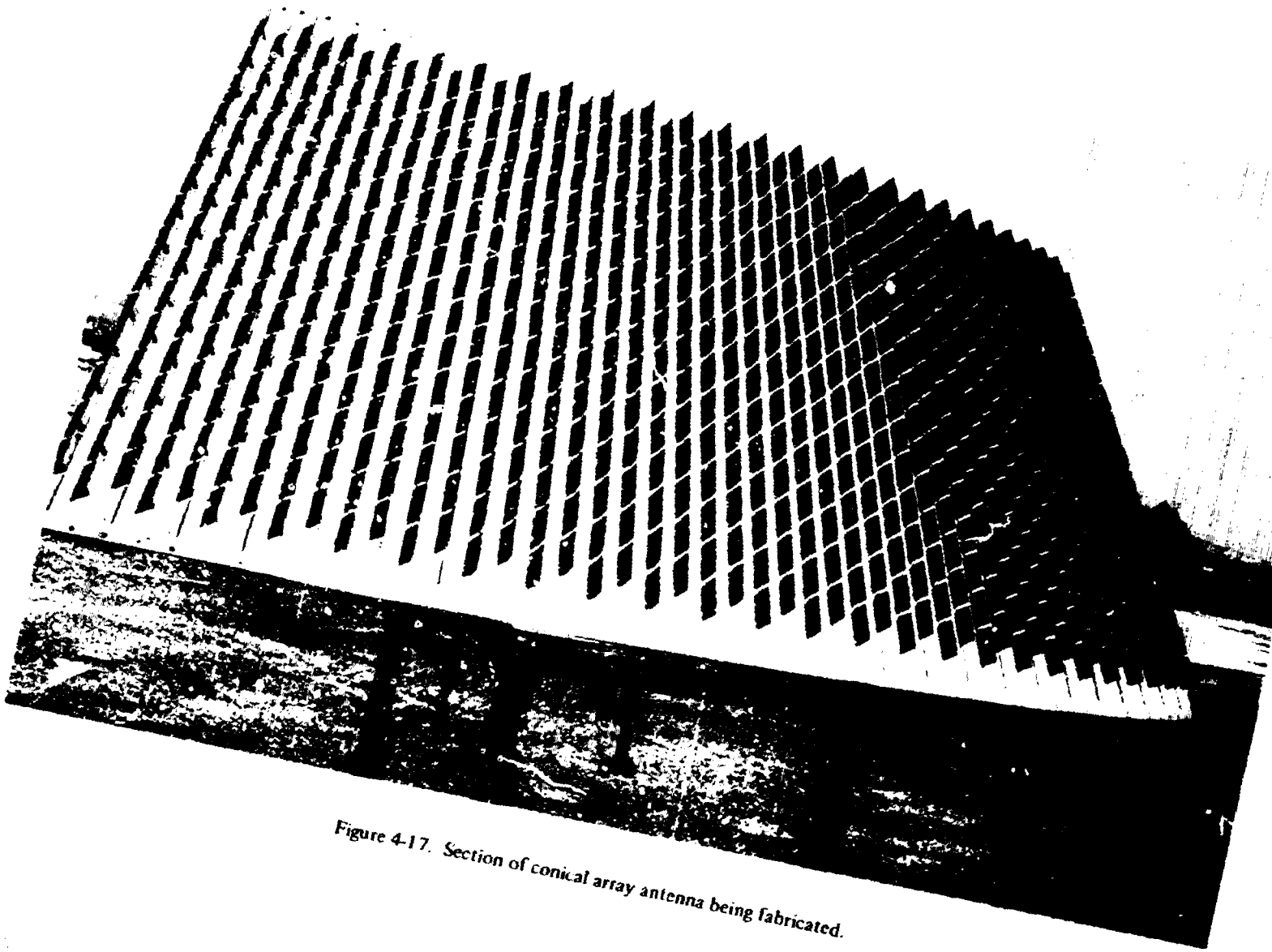

Figure 4-17. Section of conical array antenna being fabricated.

TABLE 4-6. PARAMETERS FOR CONICAL ARRAY ANTENNA

Frequency band	2.9 - 3.5 GHz
Number of elements	750 with single-ended dipoles 950 with feed-through system
Scan limits	+72 degrees to -32 degrees
Polarization	Vertical
Elements	Printed-circuit dipoles
C. .ngle	20°
Sector	75.5°
Radius at top	57.75 in. (15.6 λ)
Radius at base	72.50 in. (19.6 λ)
No. of elements per column	18
Element spacing along a column	2-1/16 in. (0.558 λ)
No. of elements per row:	
Sector	50
Full circle	234
Element spacing along a row:	
Top	1.55 in. (0.418 λ)
Base	1.94 in. (0.525 λ)

CROSS POLARIZATION

A vertical dipole over a cylindrical ground plane gives vertical polarization only. Thus it is fair to assume that an element on the cone gives vertical polarization when referred to a "local" coordinate system, i.e., one which has been tilted to align with the surface of the cone. With this assumption the expected cross polarization can be calculated for the conical array. Figure 4-18 shows the computed vertical and horizontal polarization patterns for the cone which has about 70 degrees of active arc and a 20-degree cone angle. Obviously if either of these parameters is varied, more cross polarization can be expected. The level of the cross polarization stays to less than -22 dB for all scan angles with the largest part appearing under the main beam. The cross polarization from the individual elements contributing to the main beam is larger, but at $\phi = 0$ degrees all horizontal polarizations from the left and right sides of the aperture cancel out. The use of a fast taper provides the low sidelobe level of approximately -40 dB. A slower taper would yield a larger cross polarization. The patterns in figure 4-18 were computed for a single ring. Additional rings would behave similarly.

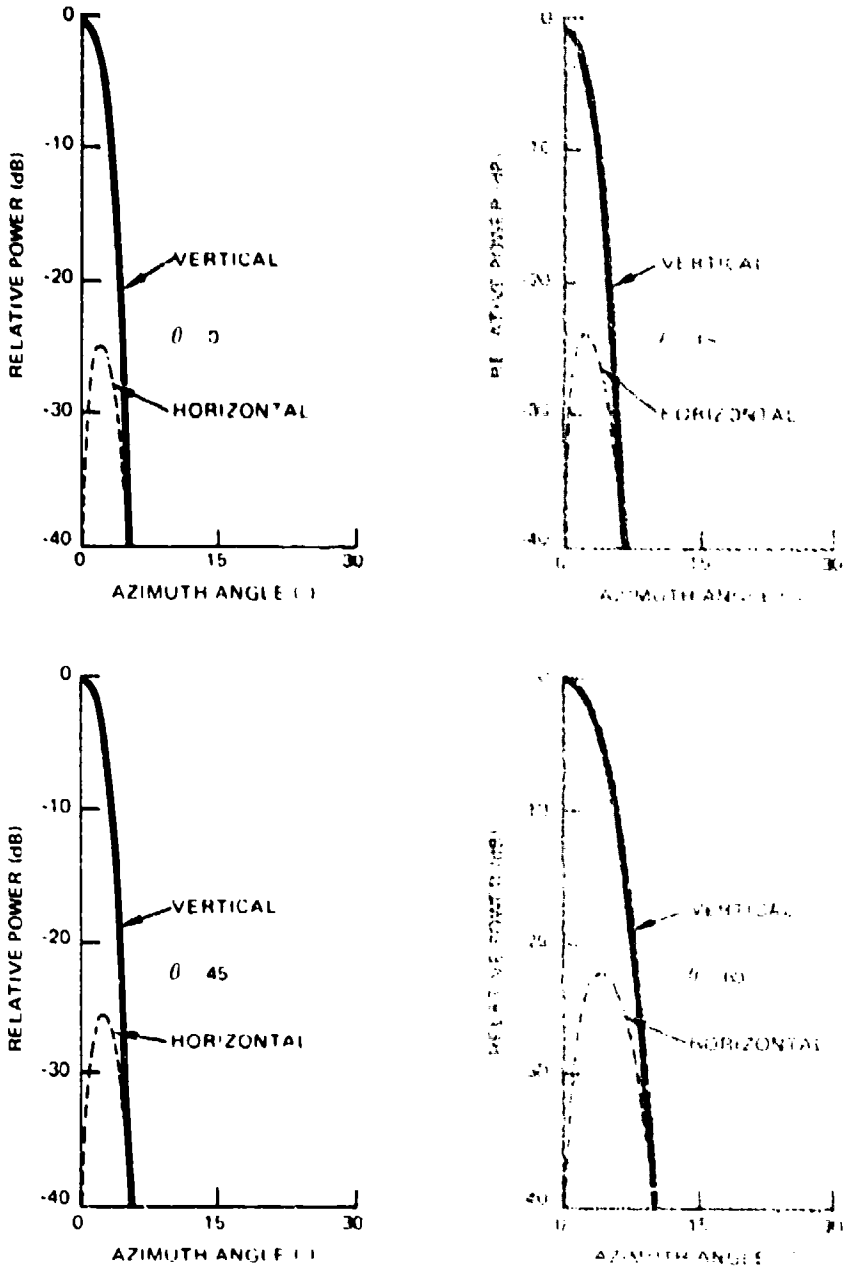

Figure 4-18. Computed vertical and horizontal polarization patterns for conical array antenna

MEASURED RADIATION PATTERNS

Figure 4-19 shows a measured element pattern for the conical array for an elevation scan angle of 0 degrees. The vertical scale used in figure 4-19 is a linear scale to emphasize the details of the pattern on the upper portion (above 10 dB). All element patterns were measured in the array environment with the adjacent elements terminated. Figure 4-20

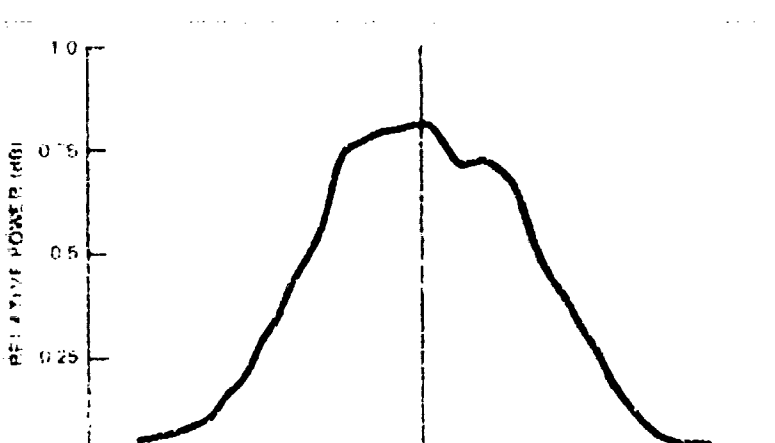

Figure 4-19. Measured element pattern, conical array. $\theta = 0$ degrees, $f = 3.2$ GHz.

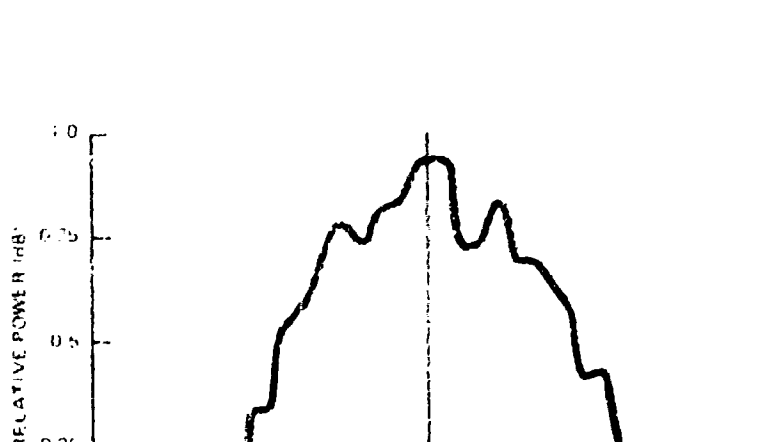

Figure 4-20. Measured element pattern, conical array. $\theta = 25$ degrees, $f = 3.2$ GHz.

shows another measured element pattern for a scan angle of 25 degrees and figure 4-21 shows a pattern for a scan angle of 50 degrees. The element patterns demonstrate the ability of a single column to scan in the elevation plane.

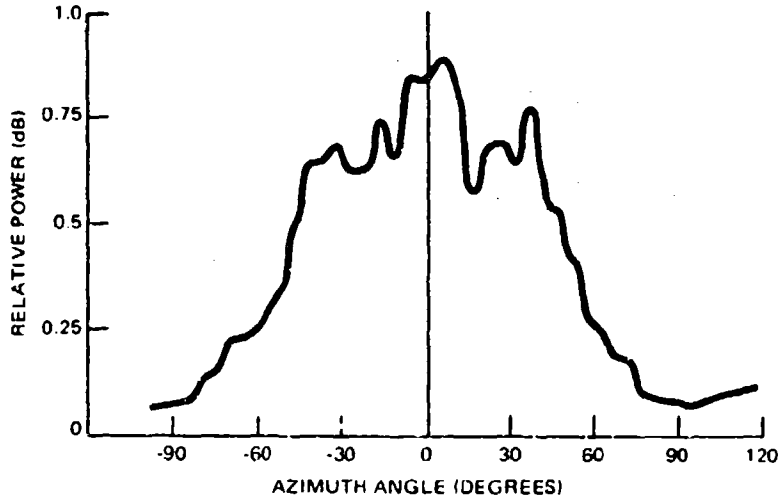

Figure 4-21. Measured element pattern, conical array. θ = 50 degrees; f = 3.2 GHz.

If the activated element is viewed as a member of a linear array, the elevation angles can be roughly predicted at which the pattern gain begins to cut off. It is known that for large planar or linear arrays, the mutual coupling effects can cause large gain loss at the angle of scan where a grating lobe emerges from the invisible to visible space. This loss of gain, then, would show up as a dip in the element pattern. If "d" is the element spacing, then the angles at which the dip should appear are given by

$$\vartheta = \pm \sin^{-1}(\lambda/d - 1)$$

On the elevation patterns, these angles are 28 degrees $\pm\theta$.

FEED SYSTEM

The type of feed system to be used with the conical array is shown in figure 4-22. A feed-through or space feed system has been selected. Table 4-7 lists some of the disadvantages and advantages possible for this type of feed system. Figure 4-23 illustrates the space-feed configuration using a small cylindrical array as the source feed.

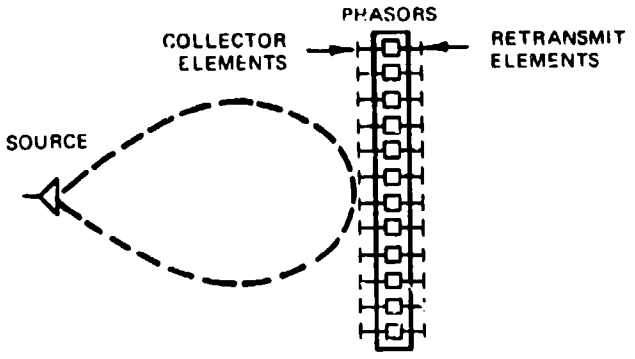

Figure 4-22. Configuration of feed-through type feed system.

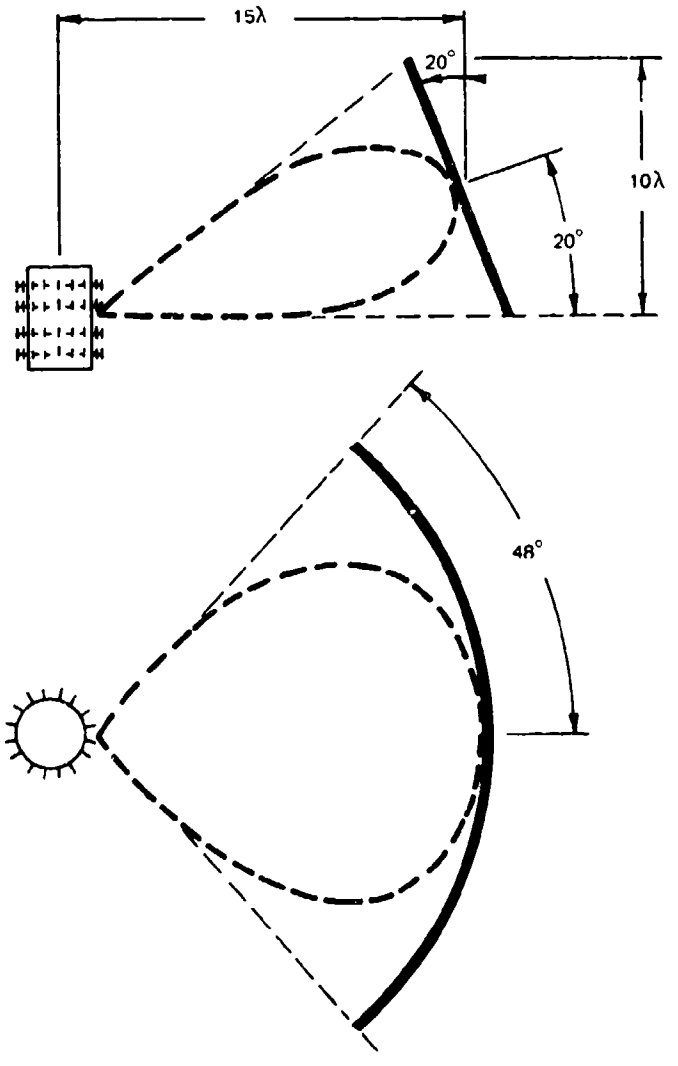

Figure 4-23. Conical array space feed configuration.

TABLE 4-7. ADVANTAGES AND DISADVANTAGES OF FEED-THROUGH TYPE FEED SYSTEM

DISADVANTAGES:

- Space requirement behind aperture
- Power concentrated at one point
- Possible spill-over

ADVANTAGES:

- Simplicity
- Low cost
- Lower losses
- Flexibility
- Dispersion of bit phase errors
- For circularly symmetric arrays:
  - Commute amplitude by steering source beam
  - Multiple beams possible

FEED AND COMPONENT DETAILS

Figure 4-24 shows a stripline module of the radiating element. Shown in this figure are the collector and the retransmit elements on one side of the stripline board with the compensated balun and phasor on the other side. The phasor is nothing more than a fixed line-length. Eight different types of these elements are being fabricated with eight different line lengths to simulate operation of a 3-bit phase scan system. Different beam positions can be obtained by removing the element modules and rearranging them in the aperture according to computed placings.

Figure 4-25 shows the mounting of an element module in the dual ground system. The elements are held in place by spring clips which allows for easy removal and insertion as a new beam position is set up. This approach is an extremely low-cost way of answering questions about the cone.

Figures 4-26 and 4-27 show the dual ground plane system with two different sources for the space feed. Figure 4-26 illustrates a small cylindrical array as the source and figure 4-27 illustrates an array of horn elements on a curved ground plane as the source. Performance of the array using these two sources has been computed and will be compared to measured results when the fabrication of the array is complete.

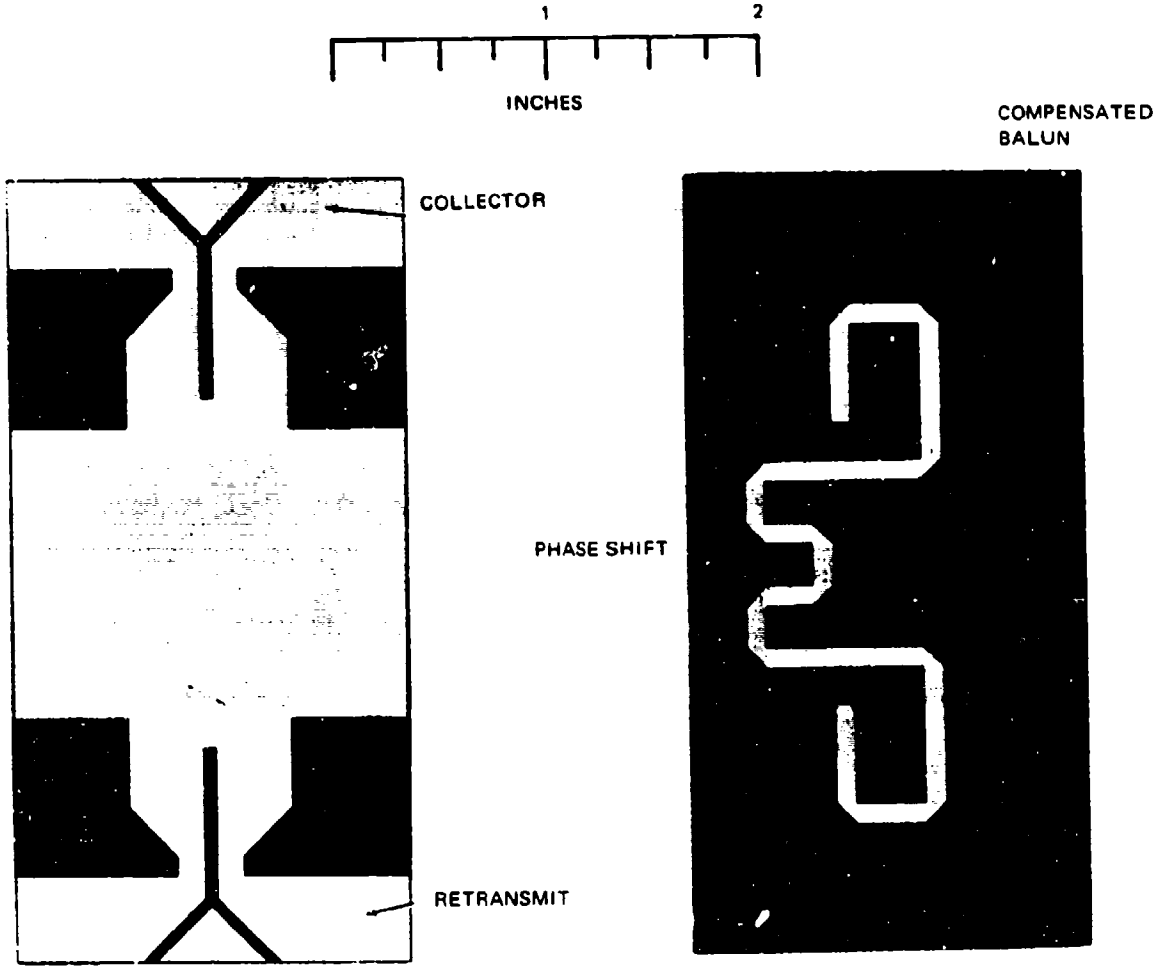

Figure 4-24. Stripline module of radiating element.

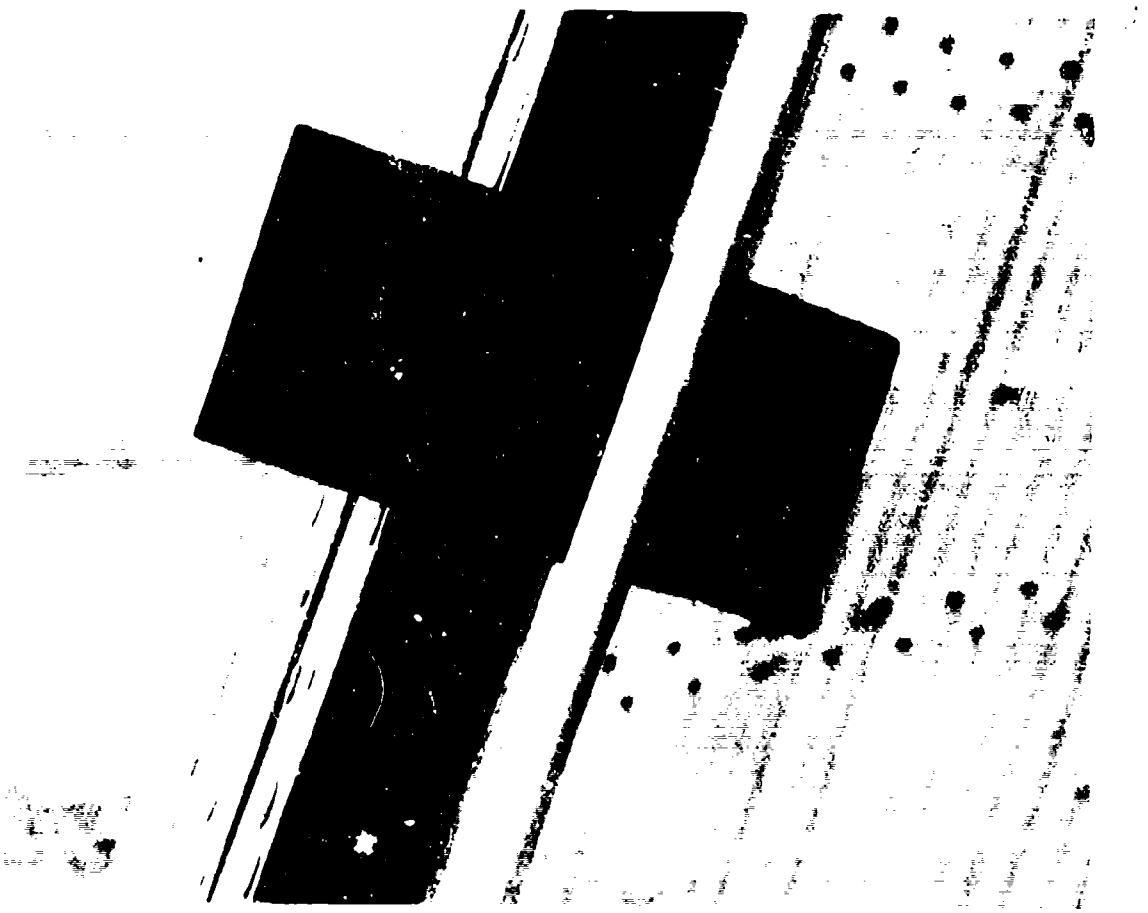

Figure 4-25. Spring-clip mounting of stripline element module.

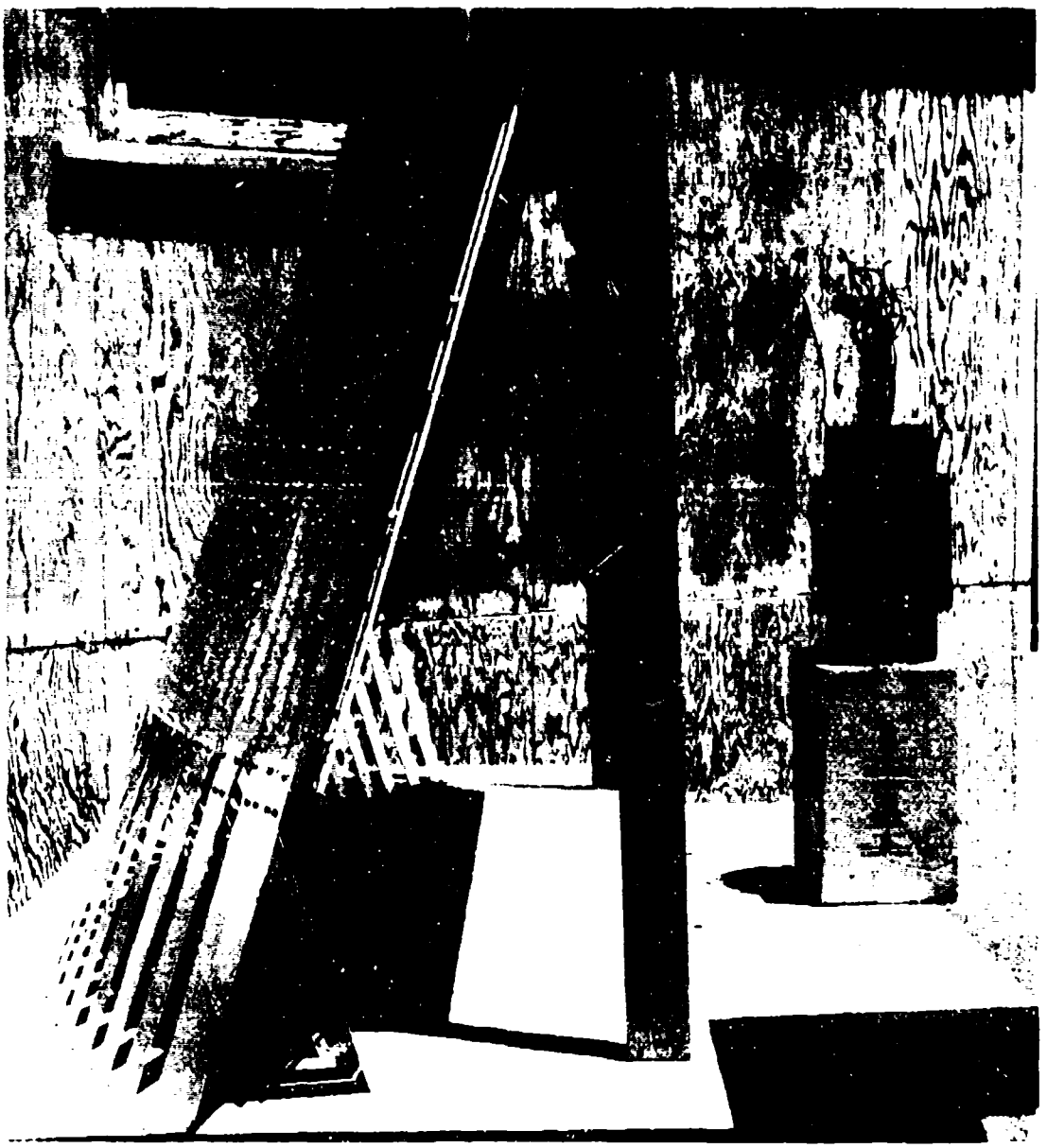

Figure 4-26. Conical array antenna ground-plane system with cylindrical array source.

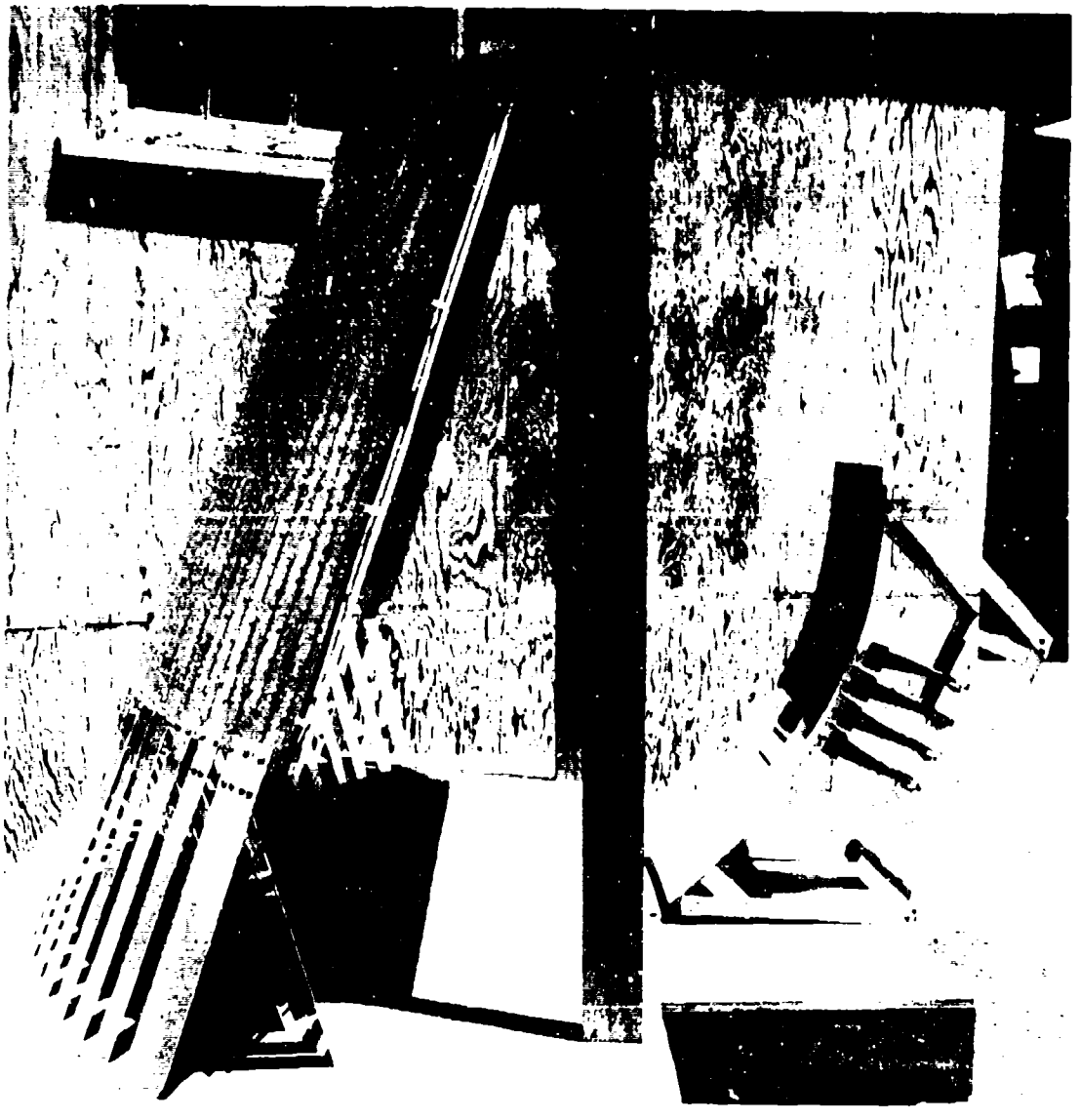

Figure 4-27. Conical array antenna ground-plane system with horn array source.

CONCLUSIONS

A cylindrical array antenna can be used to provide pencil beams and to provide limited elevation coverage, and to give 360-degree azimuth coverage. The cylindrical array has its optimum performance at the broadside position and performance of the array degrades as the main beam is scanned in elevation from broadside.

The conical array can be used to overcome the limitations of the cylindrical array concerning elevation scan. The conical geometry has its optimum performance at a position normal to the conical surface and extends the performance of the array to higher elevation angles at a slight sacrifice of performance below the horizon.

REFERENCES

1. Boyns, J. E. and others, "Step-Scanned Circular-Array Antenna," Institute of Electrical and Electronic Engineers, Transactions: Antennas and Propagation, v. AP-18, No. 5, September 1970

2. Boyns, J. E. and Munger, A. D., "Cylindrical and Conical Array Investigations," International Symposium on Antennas and Propagation, Sendai, Japan, 1-3 September 1971, Proceedings, p. 41-42

3. Munger, A. D., "Mutual Coupling on a Cylindrical Array of Waveguide Elements," Institute of Electrical and Electronic Engineers, Transaction: Antennas and Propagation, v. 19, p. 131-134, January 1971

4. Munger, A. D. and Gladman, B. R., "Pattern Analysis for Cylindrical and Conical Arrays," Conformal Array Antenna Conference, Naval Electronics Laboratory Center, San Diego, California, 13-15 January 1970, Proceedings (NELC TD 95)

NELC PHOTOGRAPHS APPEARING IN THIS PAPER

Figure	NELC Photograph No.
4-1	LSF 973-4-69
4-2	LSF 103-9-68
4-3	LSF 104-9-68
4-4	LSF 1779-5-70
4-5	LSF 2526-9-69
4-6	LSF 91-1-69
4-10	LSF 1580-7-71
4-11	LSF 1577-7-71
4-12	LSF 1581-7-71
4-17	LSF 3262-10-70
4-24	LSF 212-2-71
4-25	LSF 1095-5-71
4-26	LSF 1097-5-71
4-27	LSF 1096-5-71

5. A CYLINDRICAL PHASED-ARRAY ANTENNA FOR AIR TRAFFIC CONTROL

by

R.J. Giannini, J.H. Gutman, P.W. Hannan

Hazeltine Corporation
Greenlawn, N.Y. 11740

for

ARRAY ANTENNA CONFERENCE

Naval Electronics Laboratory Center
San Diego, California

22, 23, 24 February 1972

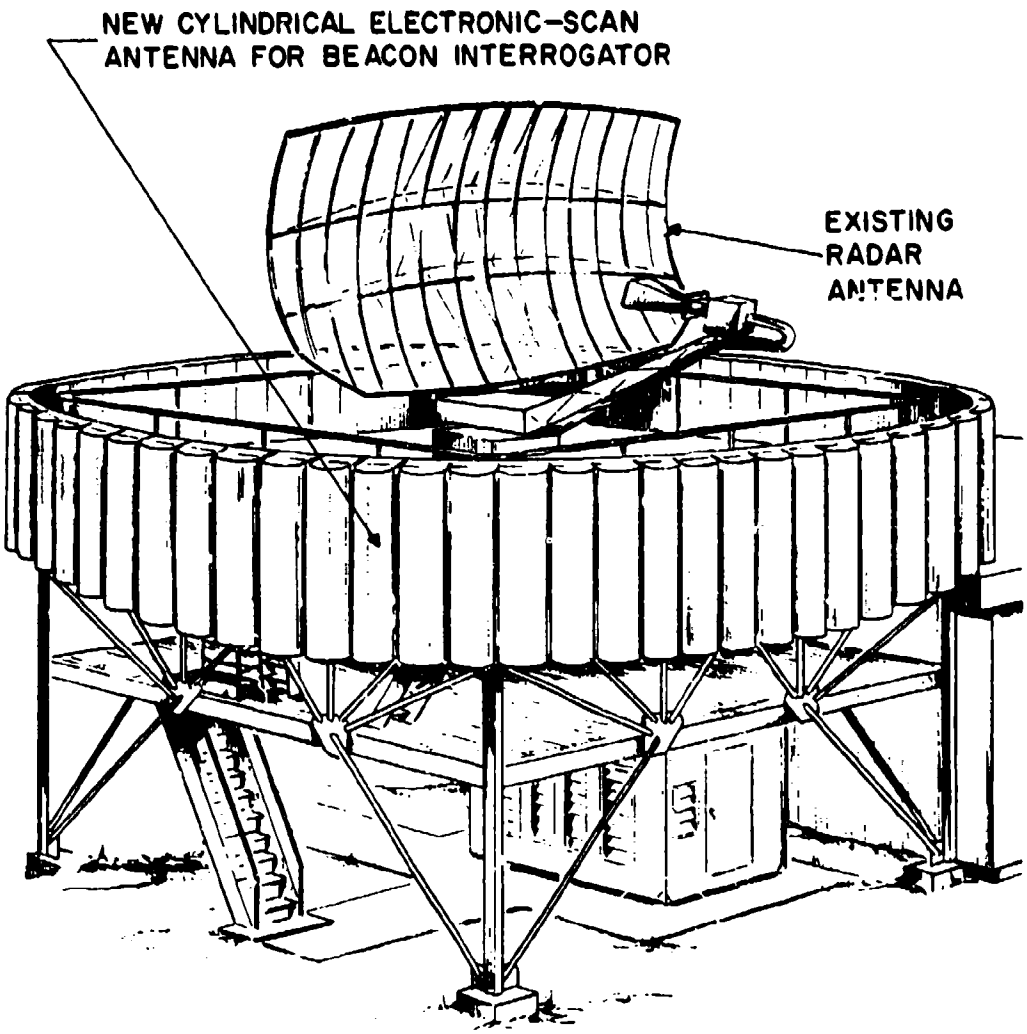

Figure 1. The New Cylindrical Electronic-Scan Antenna

The increasing amount of air traffic that is forecast requires a substantial upgrading of the present Air Traffic Control Radar Beacon System (ATCRBS). A major component of this system is the ground-based beacon-interrogator antenna.

The FAA has launched a program for the development of a new beacon-interrogator antenna. The new antenna is an electronic-scan circular-cylinder array about 40 feet in diameter and 8 feet high. Figure 1 illustrates the new antenna in a typical location under an airport-surveillance-radar (ASR) antenna.

The circular-cylinder array comprises 224 columns; each column contains 16 stripline-dipole radiating elements. Figure 2 indicates how each group of four columns is enclosed in a radome, giving the antenna the corrugated appearance seen in Figure 1. The four-column grouping is also used as the basic module for construction of the array, as illustrated in Fig. 2.

Figure 3 indicates the main fan beam of the antenna. It is used for interrogation of aircraft at 1030 MHz and for reception of their transponder replies at 1090 MHz. The fan beam, which is narrow in azimuth, covers a range of elevation angles from near the horizon to about 35°. The beam scans 360° in azimuth.

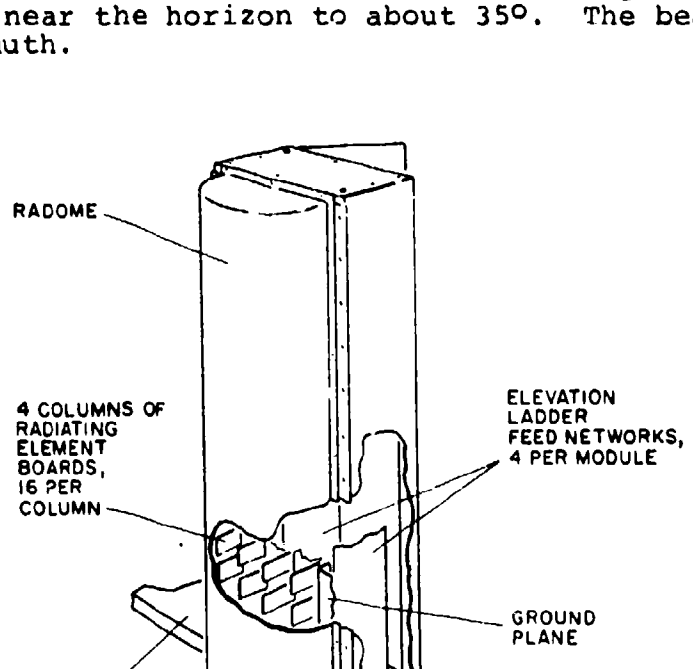

Figure 2. Modular Construction of the Array

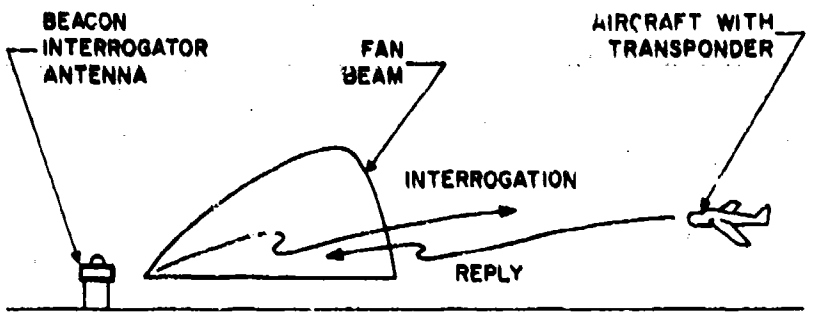

Figure 3. Beacon System for Air Traffic Control

One-quarter of the circular array is active for the fan beam. With tapered excitation of this aperture, an azimuth beamwidth of about 2.3° is obtained near the horizon. However a circular array has a basic defocusing problem that ordinarily would cause a drastic widening of the azimuth beamwidth of the fan beam at higher elevation angles. This would occur because the azimuth focusing (excitation phase) applied to the array aperture for collimated radiation toward the horizon would not be correct for collimated radiation at higher elevation angles. To overcome this problem the antenna employs a two-stage focusing technique.

Figure 4 indicates the principle of this technique, in which the fan beam is divided into two parts in elevation. The lower part is focused in azimuth at a low elevation angle, and the upper part at a high elevation angle. This provides relatively good azimuth focusing over the complete range of elevation angles of the fan beam. The result is an azimuth beamwidth that remains relatively narrow over the fan beam, as indicated in Fig. 4. There is some variation in the beamwidth over the 0 to 35° range of elevation angles; this could be reduced by additional stages of focusing. However the two-stage result is acceptable, and is chosen on a cost-effectiveness basis. The beamwidth variation that would occur if ordinary single-stage focusing were used is also shown in Fig. 4.

Figure 5 illustrates the elevation feed network that distributes power among the 16 dipoles in each column so as to provide the two-part beam in elevation. The network comprises two series feeds in an arrangement called a ladder network. One series feed provides the upper (U) part of the elevation beam, and the other provides the lower (L) part.

Each series feed consists of a series of stripline directional couplers; each coupler is designed to provide a particular current amplitude in its associated dipole. The desired phase of the dipole currents is obtained by properly designing the

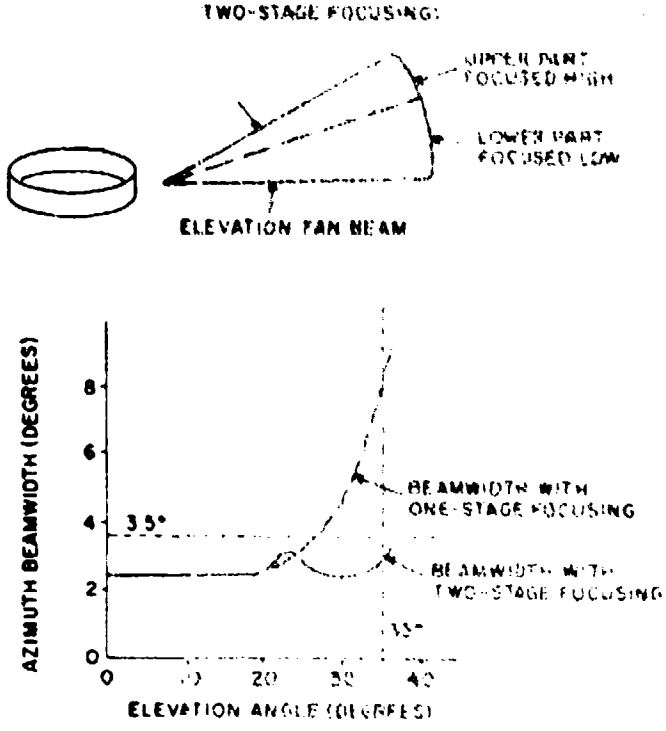

Figure 4. Two-Stage Focusing

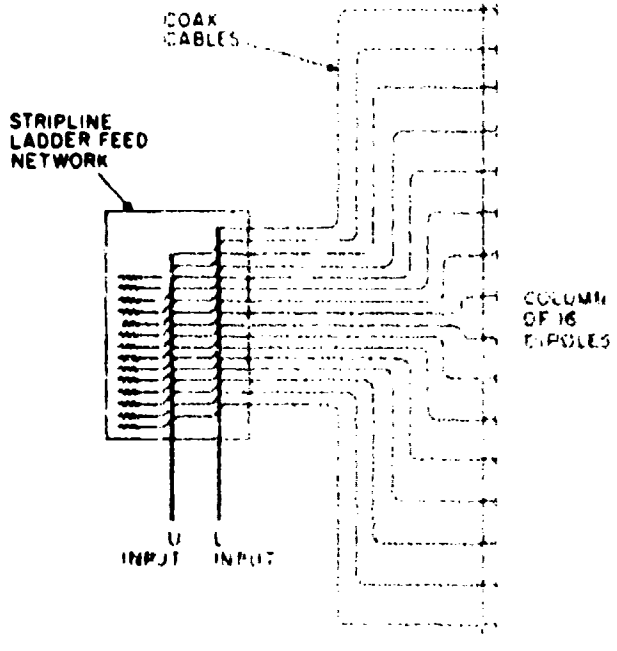

Figure 5. Elevation Ladder Feed Network

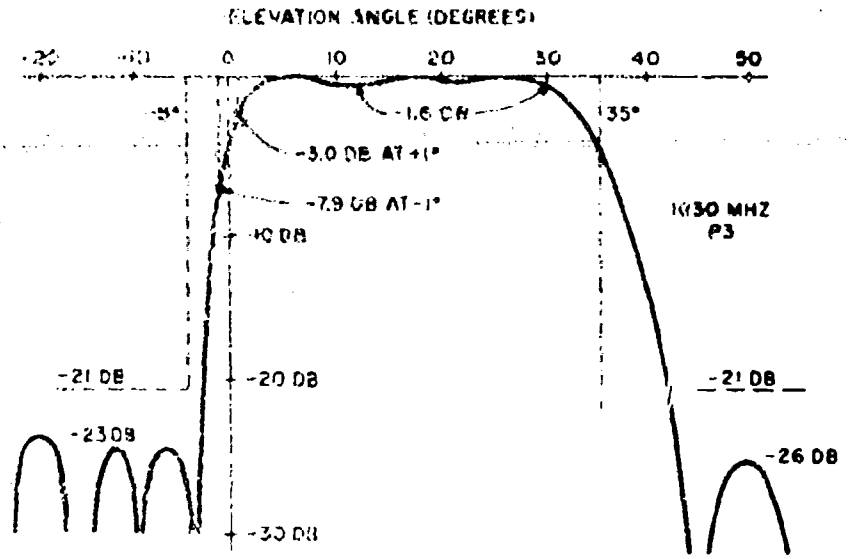

Figure 6. Elevation Pattern

lengths of transmission line in the ladder network and in the coaxial cables leading to the dipoles. The set of 16 currents provided by the U series feed is orthogonal to the set provided by the L series feed; the resulting U and L parts of the radiated beam are also orthogonal to each other. In operation, both parts are radiated simultaneously and blend together smoothly to form the desired elevation pattern of the antenna.

The elevation pattern characteristics are determined by the amplitude and phase of the sum of the U and L currents in the dipoles. A particular set of currents has been determined that provides the elevation pattern shown in Fig. 6. The objectives for the elevation pattern of the beacon-interrogator antenna are (1) constant (within 3 dB) amplitude from just above the horizon to 30° elevation, (2) sidelobes at least 21 dB below the peak, and (3) a sharp cutoff below the horizon such that the level drops from -3 dB at +1° elevation to at least -7 dB at -1° elevation and continues dropping to at least -21 dB at -5° elevation. The computed pattern shown in Fig. 6 meets these objectives with a comfortable margin.

The most important of the [illegible]-pattern objectives is the sharp pattern cutoff. Without a sharp cutoff below the horizon the signal reflected from the ground in front of the antenna causes a serious "vertical-lobing" effect in the net radiated field. This is illustrated at the top of Fig. 7 for the case of a typical conventional beacon-interrogator

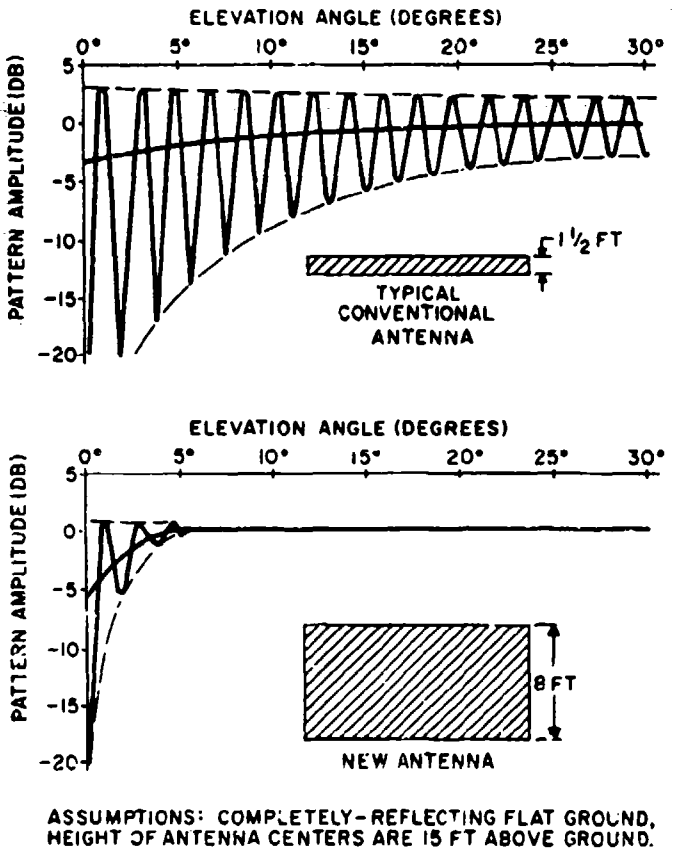

Figure 7. Vertical-Lobing Patterns

antenna having only about a 1-1/2 foot vertical aperture. The poor cutoff obtainable with a small vertical aperture yields a vertical-lobing effect that has deep minima and covers a wide range of elevation angles. With the 8-foot vertical aperture of the new antenna, and with the vertical aperture excitation designed for a sharp cutoff as a major objective, the vertical-lobing effect is much reduced, as indicated at the bottom of Fig. 7.

It was assumed for simplicity in calculating Fig. 7 that the ground is completely reflecting and flat. Actually the ground has a reflection coefficient that varies with angle of incidence and is unity only at grazing incidence and in the absence of vegetation. However the beacon-interrogator antennas are typically located at airports, and there are often large flat areas free of vegetation in front of the antennas. Hence the vertical lobing indicated in Fig. 7 is not unrealistic at the lower elevation angles. At the higher angles, especially near the Brewster angle, Fig. 7 is unduly pessimistic but the comparison of perfor-

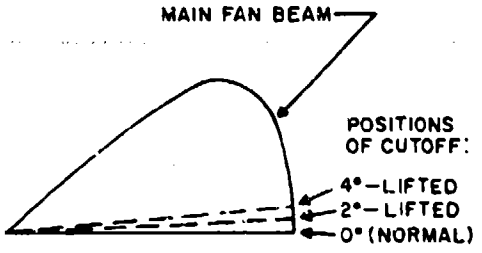

Figure 8. Beam Hopover Patterns

mance between the two antennas is valid. In numerous operational situations with the conventional antenna, particularly at the lower angles, the signal is so weak in some of the minima between vertical lobes that aircraft at those elevation angles become missed targets. A major reduction of the number of missed targets is expected with the new antenna.

An additional feature is provided by the new antenna. As indicated in Fig. 8, the sharp cutoff of the elevation pattern can be electronically lifted 2° or 4° above the normal position. This electronic lifting of the pattern cutoff permits the azimuth-scanning fan beam to "hop over" buildings that are often located near airports in urban areas. At present,with the conventional antenna that has neither a sharp cutoff nor beam hopover, reflections from buildings cause false targets to appear. The new antenna is expected to yield a major reduction of the number of false targets.

Figure 9 outlines the basic parts of the network that provides electronic scan in azimuth. It is a PIN-diode switching-and-phasing network related to (but somewhat different from) the network we described here two years ago for a small circular array [1,2]. At the input port there is a 1 to 56 power divider to provide the proper amplitude distribution across the 56-column active aperture in azimuth. Then there is a set of transfer switches that provide outputs in the particular order needed as the coarse-steering process commutates the excitation around the circular array. Each of the 56 outputs from the transfer switches is then divided into two channels, one for the lower (L) part of the fan beam and the other for the upper (U) part. Each of these 2 x 56 channels contains a four-bit phase shifter and a four-throw switch. The phase shifters provide fine steering and also azimuth focusing, the latter being different for the L and U parts of the fan beam. Each pair of four-throw switches connects to one of the four columns 90° apart on the circular array for coarse steering.

In the original switching-and-phasing network we reported here two years ago, the phase shifters were located below the transfer switches, and the transfer switches required a number

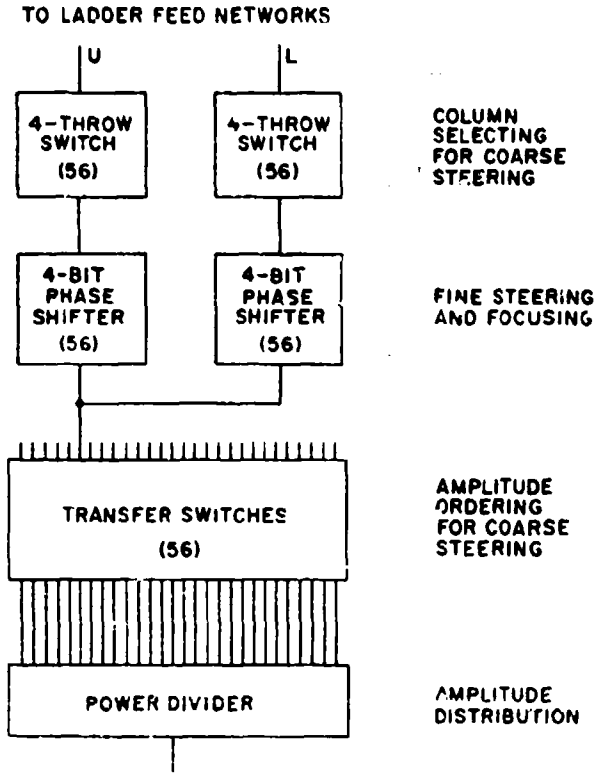

Figure 9. Switching-and-Phasing Network for Azimuth Scan

of layers in series that depended on the number of active elements. With the new, much larger, antenna the number of series layers of transfer switches would be excessive if the earlier arrangement were used. In the new arrangement, the number of series layers of transfer switches depends only on the number of amplitude steps used for the azimuth aperture excitation.

Figure 10 illustrates the difference between the old and the new arrangement. The old arrangement would require five series layers of transfer switches, and would provide full control of the excitation amplitude distribution. For the new arrangement, two series layers of transfer switches are chosen; this requires an excitation amplitude distribution that is quantized in four steps. This stepped excitation yields acceptable performance, and the design is cost-effective.

Figure 11 shows the azimuth pattern calculated from the excitation just described. The angular location of the highest sidelobe is further from the mainlobe than is usually the case; this sidelobe is caused by the excitation amplitude steps. Its level is lower than 25 dB from the peak of

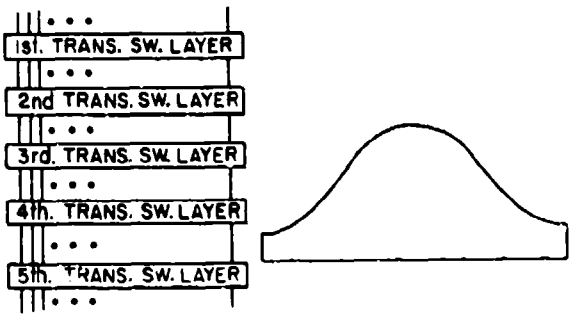

(a) COMPLETE ORDERING NETWORK (OLD ARRANGEMENT)

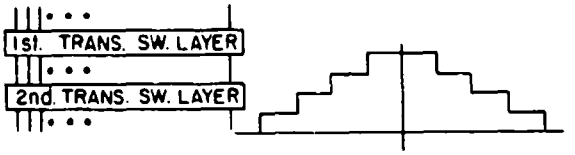

(b) REDUCED ORDERING NETWORK (NEW ARRANGEMENT)

Figure 10. Comparison of the Two Ordering Networks

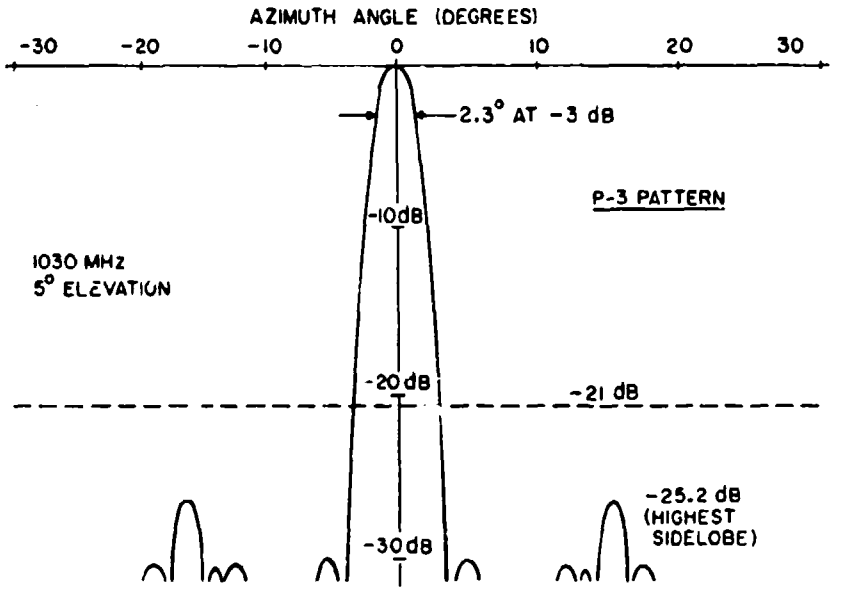

Figure 11. Azimuth Pattern of Fan Beam

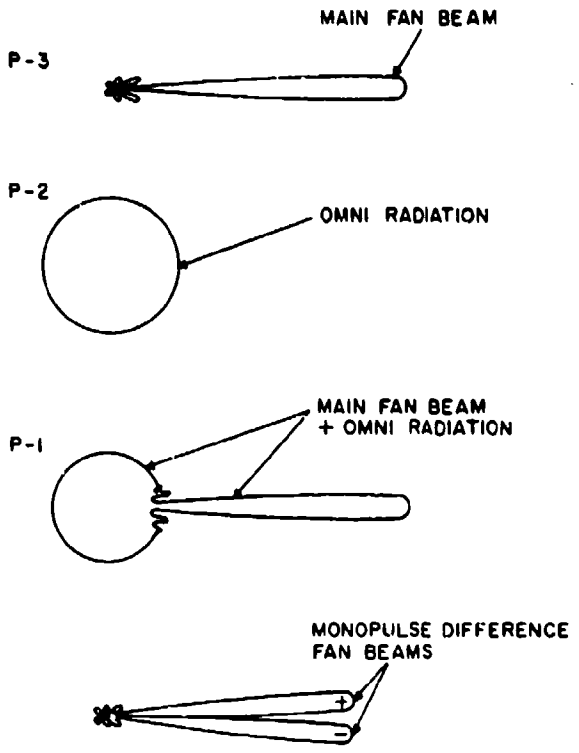

Figure 12. The Four Azimuth Patterns

the main lobe, leaving a comfortable margin below the 21 dB level that is allowed for this antenna.

The power gain of the antenna at the peak of the fan beam is about 17 dB as measured at the transmitter port in the equipment building, and is comparable with that of a conventional antenna installation. This is sufficient for the beacon system using the present transmitter-receiver. The directive gain at the peak is about 27 dB, which is higher than that of the conventional antenna because of the sharp pattern cutoff. The antenna loss of about 10 dB includes cable losses, azimuth and elevation network losses, SLS switch loss, and filter losses.

Figure 12 indicates the four different azimuth patterns that are provided by the new antenna. The first pattern is the main fan beam just described. The next two patterns are required for a side-lobe-suppression (SLS) function. The last is a monopulse difference pattern for azimuth angle determination. All of these azimuth-pattern modes have esentially the same elevation-pattern shape, as given in Fig. 6.

In order to avoid sidelobe interrogation of transponders in aircraft at short ranges, an SLS technique is employed by

the ATC beacon system. Three pulses are radiated by the antenna in each interrogation. The third pulse (P-3) is radiated on the main fan beam, the second pulse (P-2) on an omnidirectional pattern, and the first pulse (P-1) on a main beam pattern which in the latest improved SLS system is combined with an omni pattern. The field strength of the P-2 pattern is greater than that of the P-1 pattern everywhere except in the narrow main-beam portion. If the P-2 pulse received by the aircraft transponder is stronger than the P-1 pulse the transponder does not reply and a short dead-time gate is initiated; this effectively prevents sidelobes of the antenna from causing unwanted transponder replies.

The purpose of the omni component of the P-1 pattern is to trigger the SLS dead-time gate in all transponders within omni range and thereby prevent unwanted transponder replies to reflections from structures less than the dead-time range (about three miles) from the antenna. This technique is complementary to the beam-hopover function in eliminating false targets caused by reflections. Ideally, one or both methods can be used as appropriate, as a function of azimuth.

In the circular-array antenna, the omni pattern required for the P-2 pulse is obtained simply by exciting all the columns of the array with equal-phase equal-amplitude signals. The composite P-1 pattern is obtained by exciting the array with both the omni mode and the fan-beam mode simultaneously. The P-1 and P-2 patterns radiate from the same vertical aperture with the same vertical excitation. This ensures that the residual vertical-lobing effect (see lower part of Fig. 7) is identical for both patterns. As a result, the relative strengths of the net radiated P-1 and P-2 patterns, including the vertical-lobing structure caused by ground reflection, remain the same at all elevation angles. This is important for proper operation of the SLS system [3], and is a significant benefit of the "integral omni" feature of the new antenna as compared with the conventional antenna system that uses a separate antenna for the omni radiation.

For azimuth angle determination, the present beacon system with a conventional mechanically-rotating antenna displays the aircraft transponder replies on a PPI or uses a special-purpose computer to measure the azimuth by determining the center of the group of replies obtained as fan beam rotates past the aircraft [3,4]. With the new antenna the same methods can be used when the fan beam is electronically scanned at a constant rate through 360°. However, in the new discrete-address beacon system (DABS) that is presently being planned to handle increased traffic, an agile-beam mode of operation will be required in high-density areas [5-7]. The new electronic-scan antenna has this capability. It will be highly desirable to determine the target

AZIMUTH ANGLE ERROR FACTORS
A. RF CIRCUIT PHASE ERRORS
1. INITIAL
2. TEMPERATURE INSTABILITY
3. QUANTIZATION OF PHASE SHIFTERS
4. PIN DIODE VARIATIONS
B. STRUCTURAL DISTORTION
1. INITIAL
2. TEMPERATURE INSTABILITY
3. WIND LOADING INSTABILITY
C. INITIAL SITING ERROR FROM TRUE NORTH
TOTAL 3σ ANGLE ERROR = 0.08°

Figure 13. Antenna Beam-Direction Accuracy

azimuth angle from a single reply when using the agile-beam mode; therefore a monopulse receive antenna system would be useful. The new antenna also has this capability by virtue of the monopulse difference pattern that it can provide in azimuth, as indicated in Fig. 12. The monopulse technique could also be used to provide enhancement of azimuth angular measurement in the ordinary rotating-beam mode of operation.

Regardless of which particular angle-determination technique is used in the beacon system, the antenna beam direction must be known within close angular tolerances. This is essential for safety in the ATC system. In the design and construction of the new antenna, the various contributions to azimuth angle error are controlled so as to provide the required angular accuracy of beam direction.

Figure 13 lists some of the factors that produce angle error in the electronic-scan circular array. The main categories are the RF circuit phase errors, the structural distortions that cause the array to deviate from its circular shape and position, and siting error. The procedure followed is (1) to minimize the initial errors by a manufacturing process that involves close tolerances and includes measurement and adjustment of the components and

structure of the antenna, and (2) to minimize later changes by designing the antenna to be as stable as is practical. A careful analysis has been made of this antenna, yeilding an expected 3-sigma azimuth angle error of less than 0.08°.

The new antenna includes a comprehensive system for continuously monitoring all electronic components and all signals to the array columns. Any electrical failure is immediately detected and indicated by this monitoring system. Because of the many parallel paths for radiation in the array, failure of an electronic component often causes only a slight degradation of antenna performance, and the component can be replaced while continuing to use the antenna. Those electronic components that can cause a serious degradation by their failure could be present in duplicate and replaced very quickly or even automatically; this procedure will be studied during the development and test of the antenna.

It is expected that the stationary (non-rotating) antenna will have almost negligible probability of mechanical failure. (In contrast, the conventional beacon antenna, which is attached to the radar antenna and rotates with it, is put out of operation by a failure of the radar rotating mechanism.) Thus the new antenna should be a highly reliable part of the ATC beacon system.

A number of the antenna components have been breadboarded, and some of these are shown in the following figures. Figure 14 shows a breadboard vertical column of radiating elements. Figure 15 shows one of the stripline dipole radiating elements used in the breadboard column. Figure 16 shows a part of the stripline ladder network used with the breadboard column. Elevation radiation patterns of this column have been measured, and the capability for achieving the desired sharp cutoff has been confirmed. Figure 17 shows a breadboard transfer-switch module containing four transfer switches in an arrangement that minimizes the coaxial cable and connectors required in the azimuth electronic-scan network. Figure 18 shows a breadboard antenna control unit in preliminary form; this unit will contain all the circuits that control the electronic scanning and monitoring of the antenna.

In conclusion, as summarized in Figure 19, a major improvement to the ATC beacon system is to be obtained by a new interrogator antenna comprising a cylindrical electronic-scan array. The antenna is presently under development at Hazeltine, and is expected to be under test by the FAA early next year. Mr. Martin Natchipolsky of the FAA is in charge of the project.

Figure 14. Breadboard Vertical Column of Dipoles

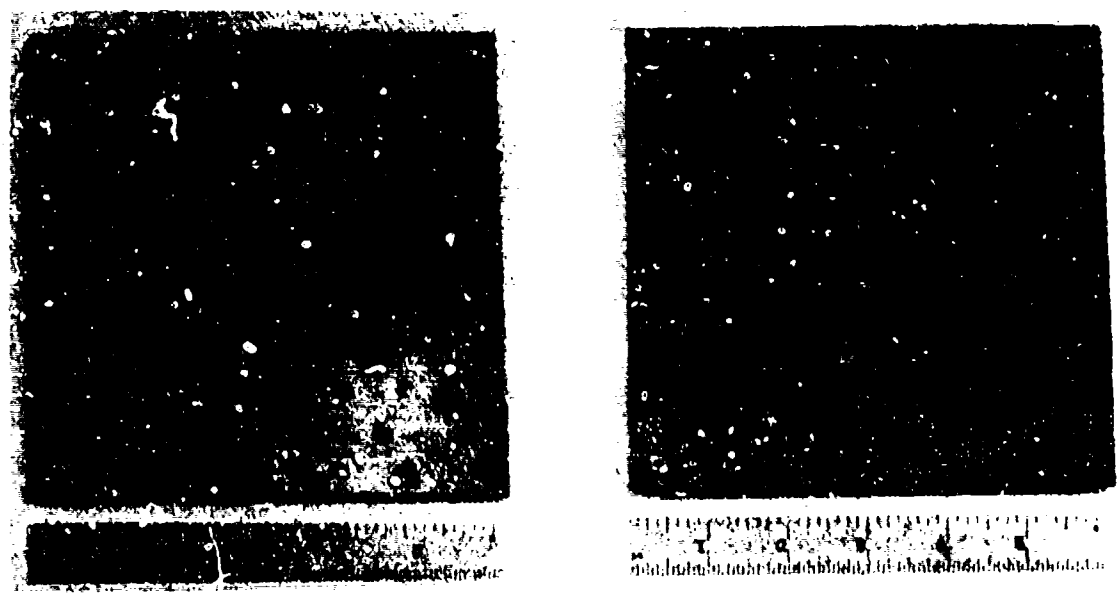

Figure 15. Breadboard Stripline Dipole

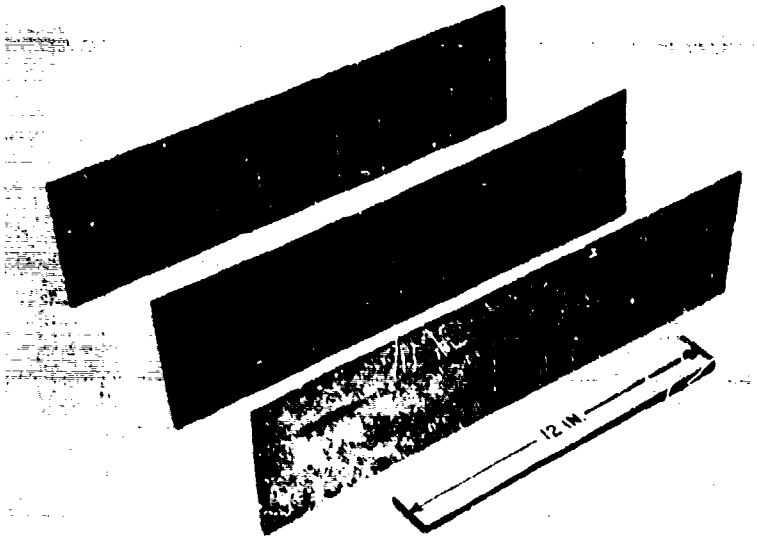

Figure 16. Breadboard Section of Ladder Feed Network

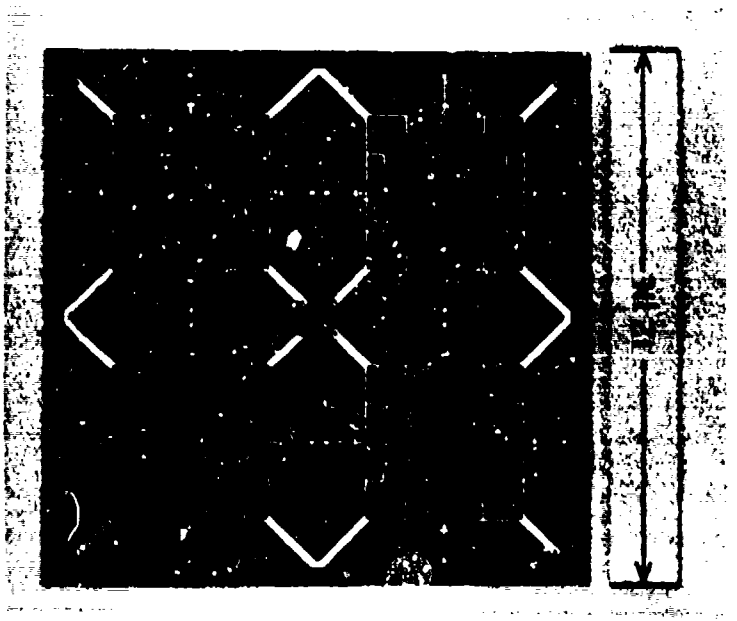

Figure 17. Breadboard Transfer-Switch Module

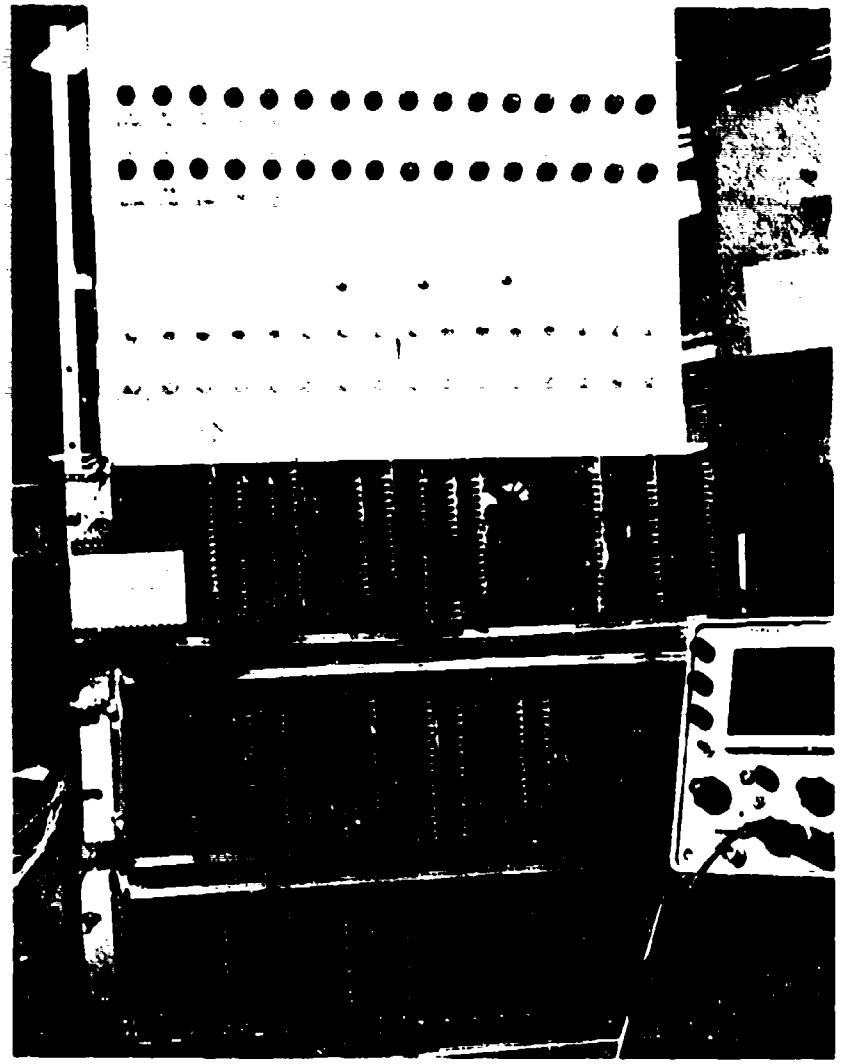

Figure 18. Breadboard Antenna Control Unit (Preliminary Model)

FEATURES OF NEW ANTENNA		RESULTS IN ATC SYSTEM
SHARP PATTERN CUTOFF	•	REDUCED MISSED TARGETS
ELECTRONIC BEAM HOPOVER	•	REDUCED FALSE TARGETS
INTEGRAL OMNI RADIATION	•	IMPROVED SLS OPERATION
ELECTRONIC AZIMUTH SCAN	•	INCREASED TRAFFIC CAPABILITY
MONOPULSE IN RECEPTION	•	INCREASED TRAFFIC CAPABILITY

Figure 19. ATC System Benefits of New Antenna

References

[1] R.J. Giannini, "An electronically-scanned cylindrical array based on a switching-and-phasing technique", Digest of IEEE International Symposium on Antennas and Propagation, pp 199-207; December 1969.

[2] R.J. Giannini, "An electronically-scanned cylindrical array for IFF based on a switching-and-phasing technique", Proceedings of the Conformal Array Antenna Conference, Naval Electronics Laboratory Center, San Diego, California; January 1970.

[3] N.K. Shaw and A.A. Simolunas, "System capability of air traffic control radar beacon system", Proceedings IEEE, vol. 58, No. 3, pp 399-407; March 1970.

[4] S.M. Weinstein, "Beacon target processing for air traffic control", Proceedings IEEE, vol 58, No. 3, pp 408-412; March 1970.

[5] Report of Department of Transportation Air Traffic Control Advisory Committee; December 1969.

[6] N.A. Blake, "System considerations and data processing implications of cooperative conformal array systems for ATC", Proceedings of the Conformal Array Antenna Conference, Naval Electronics Laboratory Center, San Diego, California; January 1970.

[7] R.C. Renick, "An improved ATC radar beacon system", Proceedings IEEE, vol. 58, No. 3, pp 413-422; March 1970.

7. SOLID STATE AIRCRAFT IFF TRANSPONDER ARRAY

by

B. A. Sichelstiel

and

E. L. Frost

Westinghouse Electric Corporation
Systems Development Division
Baltimore, Maryland 21203

for

ARRAY ANTENNA CONFERENCE

Naval Electronics Laboratory Center
San Diego, California

22, 23, 24 February 1972

INTRODUCTION

The omnidirectional antennas used for aircraft tranponders to ensure a response to interrogations arriving from all directions results in an unfortunately large amount of superfluous information at interrogation terminals. If the responses could be made directionally selective through the use of a special antenna subsystem, the burden of sorting through excessive data for a particular response would be reduced. The margin of operational improvement can be justified only if the antenna subsystem is inexpensive, does not reduce aircraft performance, and is compatible with an existing equipment inventory.

This paper describes a low-profile array subsystem that uses microwave integrated solid-state circuits to provide spherical coverage on receive, determine the angle-of-arrival of each valid interrogation and response appropriately with a directional transmit beam. The subsystem uses four linear eight-element arrays equally dispersed about the aircraft roll axis. Each array element contains RF amplification for transmission and reception to avoid the effects of losses in the beam control circuitry. The entire array subsystem is contained within four 3 × 6 × 48 inch antenna packages, except for a sector sum and selection unit at the transponder equipment.

Portions of the array system have been built, and their characteristics are described in the later paragraphs. The next discussion deals with the operating features of the system, the characteristics of the antenna that allow the combination of spherical and directional coverage, and the solid-state module circuit design.

OPERATING FEATURES

The operation of the system is depicted by the block diagram in Figure 1. Each of the four linear arrays contains eight active transmit-receive elements that are combined in a beam-forming network. This network has eight outputs, each of which represents a beam-pointing direction along the aircraft axis.

Once the beams are formed, the signal from each beam is directed in two paths. The first path is to the transmit beam selector, where the beam having the strongest signal is selected as the one that is pointing toward the interrogator. While the interrogator may not be located in this particular sector, further processing by the sector beam selector determines the array that has the strongest signal, thus identifying the sector, and hence, the particular beam that is directed toward the interrogator.

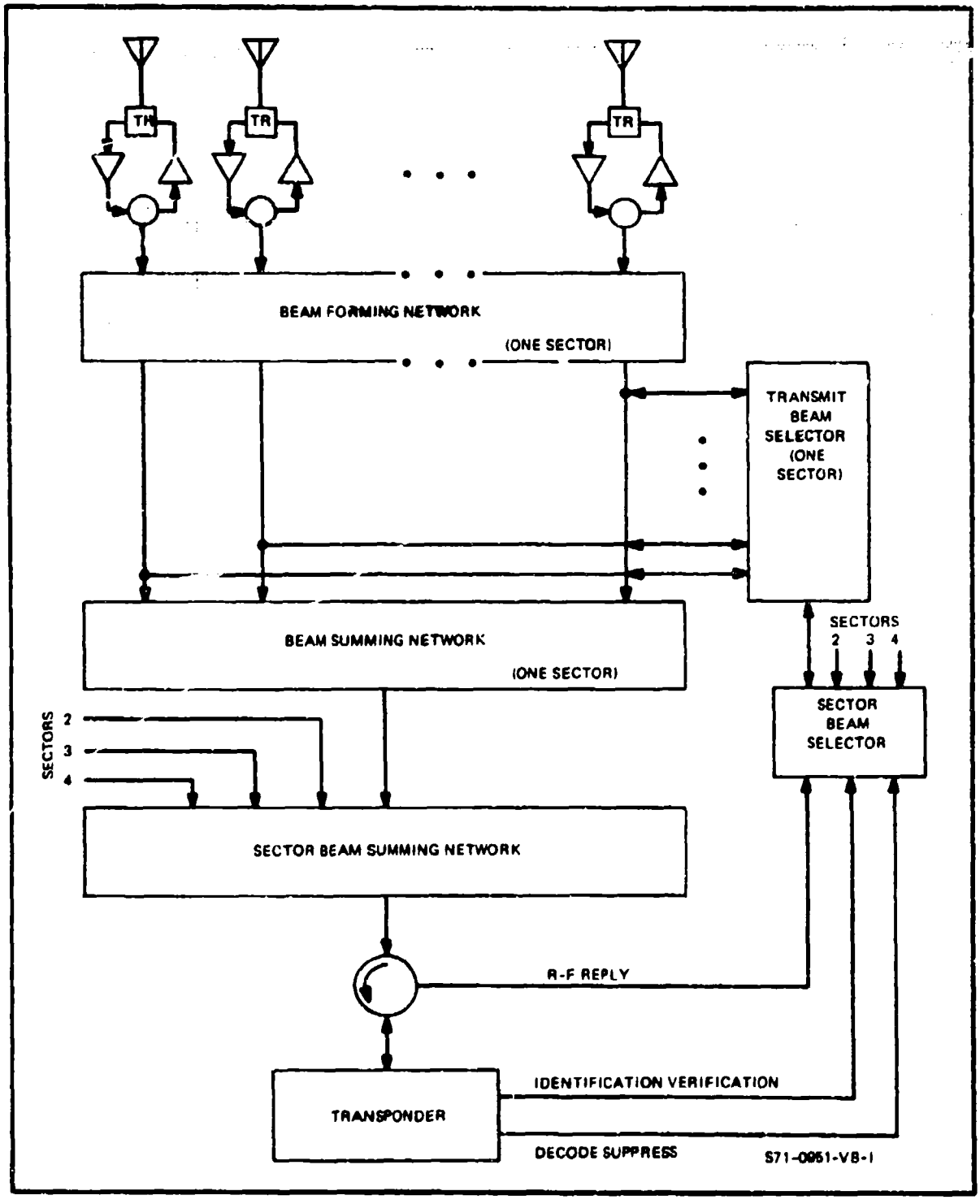

Figure 1. System Operation

The transponder received signal is directed along the second path to the beam-summing network, where the formed beams are recombined so that a nondirectional pattern is obtained from the array. These recombined beams are further combined in the sector beam-summing network to yield an omnidirectional receive pattern. The process of beam summing removes the gain obtained by forming the directional beams, because noise from all the beam-forming network terminals is summed, while the interrogation signal appears at one terminal (or a combination of terminals, with the same amplitude as the single-terminal case). The signal from the summer beams is then fed through a circulator to the RF terminal on the transponder.

The transponder operates on the received RF waveform in its normal manner and, upon identifying a valid IFF interrogation, transmits its reply through the RF terminal to the circulator. The circulator isolates the sector beam-summing network from the relatively high power transponder response.

The transponder must supply the two processing signals required for the selection of the proper transmit beam. There is a signal to identify that a valid IFF interrogation code has been received and also a signal to identify that the transponder is not receiving interrogations it is transmitting.

The transponder RF reply is directed through the sector beam selector by an RF diode switching tree to the proper sector transmit beam selector. Since the proper transmit beam has been selected during the receive waveform, the transponder reply is directed to the desired terminal of the beam-forming network by a single-pole double-throw RF diode switch. The RF response is thereby fed through the array modules, and thus the antenna elements, in the right magnitude and phase to form a beam with the desired directivity.

The system has been designed to offer the same system sensitivity as current transponders. Sensitivity is governed by the transmit beam selector, because a crystal video detection scheme is used rather than a superheterodyne. Crystal video detectors have a notoriously high noise figure due to the 1/f, or flicker noise, at low frequencies. However, a low-noise RF preamplifier is used at each array element to reduce the overall noise figure so that the same system sensitivity can be retained. The calculations in the appendix show that a preamplifier gain of 24 dB is required.

ANTENNA CHARACTERISTICS

The four arrays are mounted on the aircraft along the axes of a 45-degree rotated coordinate in the roll plane as illustrated in figure 2. With 115-degree half-power beamwidths in the E-plane, each array produces a 2 dB crossover along the major elevation and azimuth axis of the aircraft

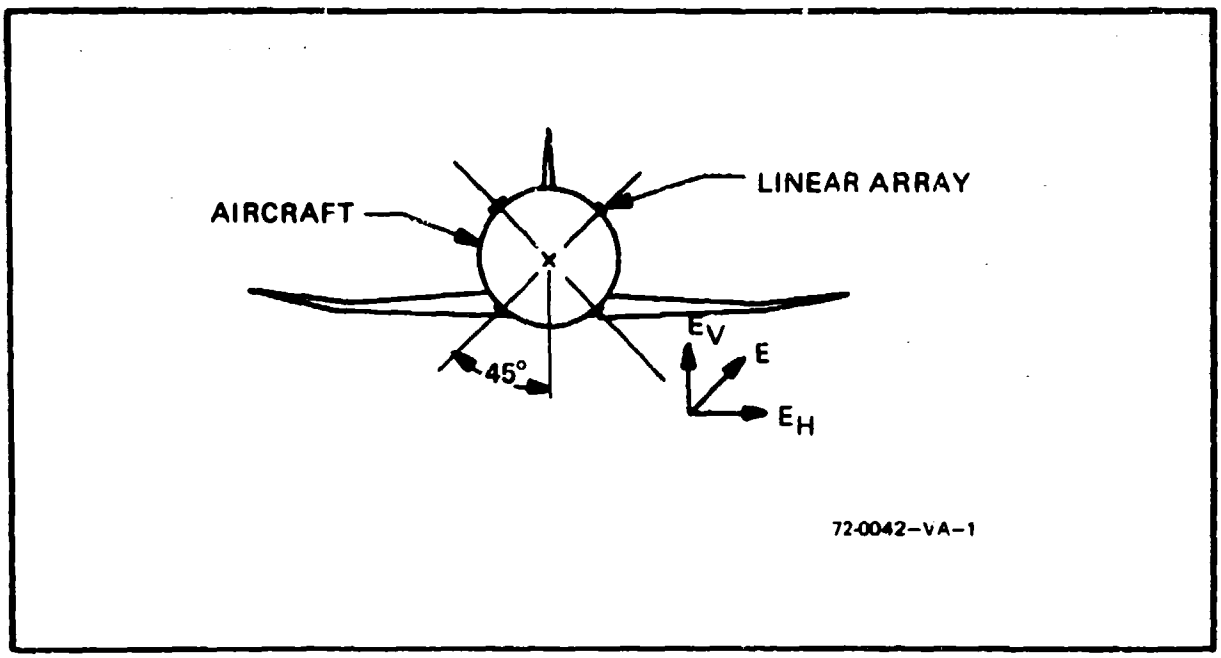

Figure 2. Roll Plane Array Locations

in the roll plane. Figure 3 shows how the four arrays combine to provide the required 360-degree roll plane coverage with a 2-dB gain variation in that plane.

In the azimuth plane in which beam directivity is achieved, the effects of scanning are considered in the array design. The off-broadside beams become wider as the gain drops in accordance with the projected array length in the direction of the beam (array factor) and the H-plane beamwidth of the array elements (element factor). A compensating factor arises in the interpretation of spherical coordinates for solid-angle scanning in that, as the beam is scanned from broadside to endfire, the E-plane beamwidth becomes much narrower.

To cope with the scanning effects and to maintain a nearly constant 30-degree sector width for each beam step and a maximum gain variation of 2 dB, a scheme has been devised whereby the number of elements actually involved in the beam formation varies with the beam direction. Using four elements spaced $\lambda/2$ apart, the beamwidth at 10 degrees from broadside is 26 degrees; at 33 degrees, the width is 30 degrees. For the next step, two additional elements are used to form a beam at 56 degrees with a width of 30 degrees. This choice of beam pointing directions and widths holds the pattern crossover levels at 2 dB as shown in figure 4. The peak directivity for each of these three beams is nominally a constant 11 dB.

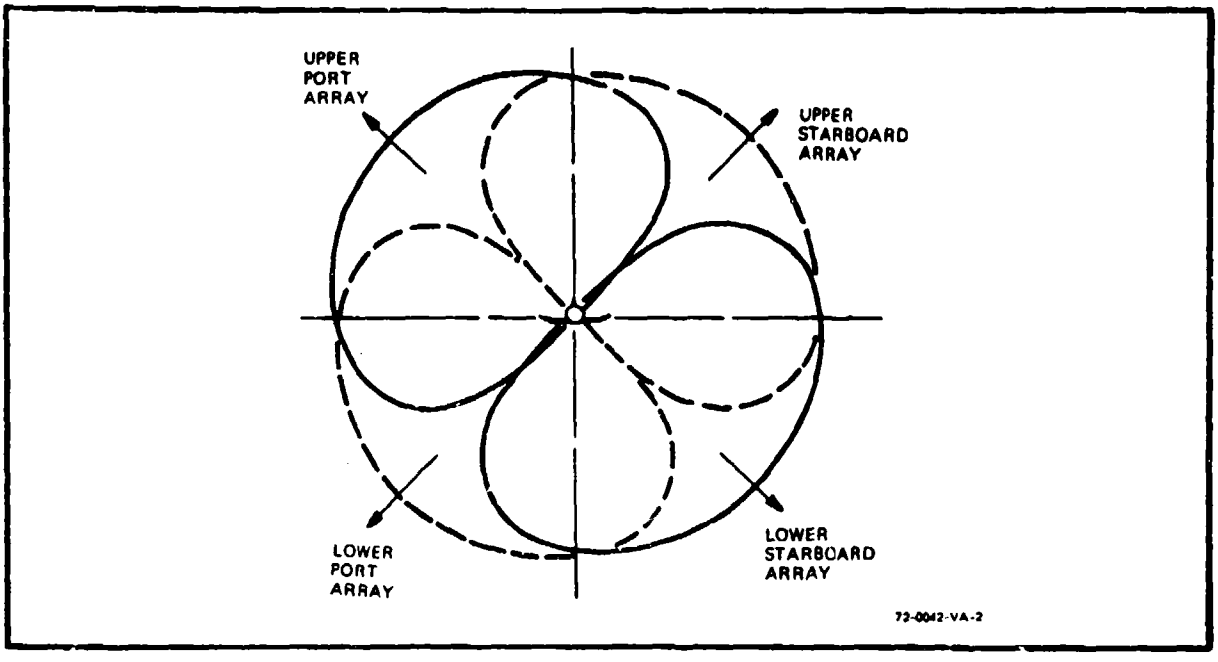

Figure 3. Roll Plane Coverage

The description of the fourth beam is more difficult to predict with any degree of certainty due to the large steering angle involved. However, an angle of 75 degrees seems reasonable to obtain, and this places the cross-over with the adjacent beam and the 90-degree end-fire axis at a level of about 1 dB. Using eight elements for the fourth beam at 75 degrees, the beamwidth is approximately 50 degrees. To achieve a constant stepped azimuth beamwidth of 30 degrees from a single array, about 11 elements would be needed.

Surface waves, higher order modes, and local ground plane effects due to a particular aircraft configuration could dictate the inclusion of some adjustability to customize the final pointing angle to fit a specific aircraft. Further, there is the possibility of enhancing the performance and ensuring coverage toward endfire by combining two, three, or all four arrays for the beam angle closest to the aircraft longitudinal axis.

The formation of multiple beams is realized through the use of a time delay type of beam-forming network as shown in figure 5. Each of the eight beam positions corresponds to an output terminal. For broadside, there is no beam position, but for the line shown, the path lengths to each element are the same. As the beam progresses away from broadside, a time delay

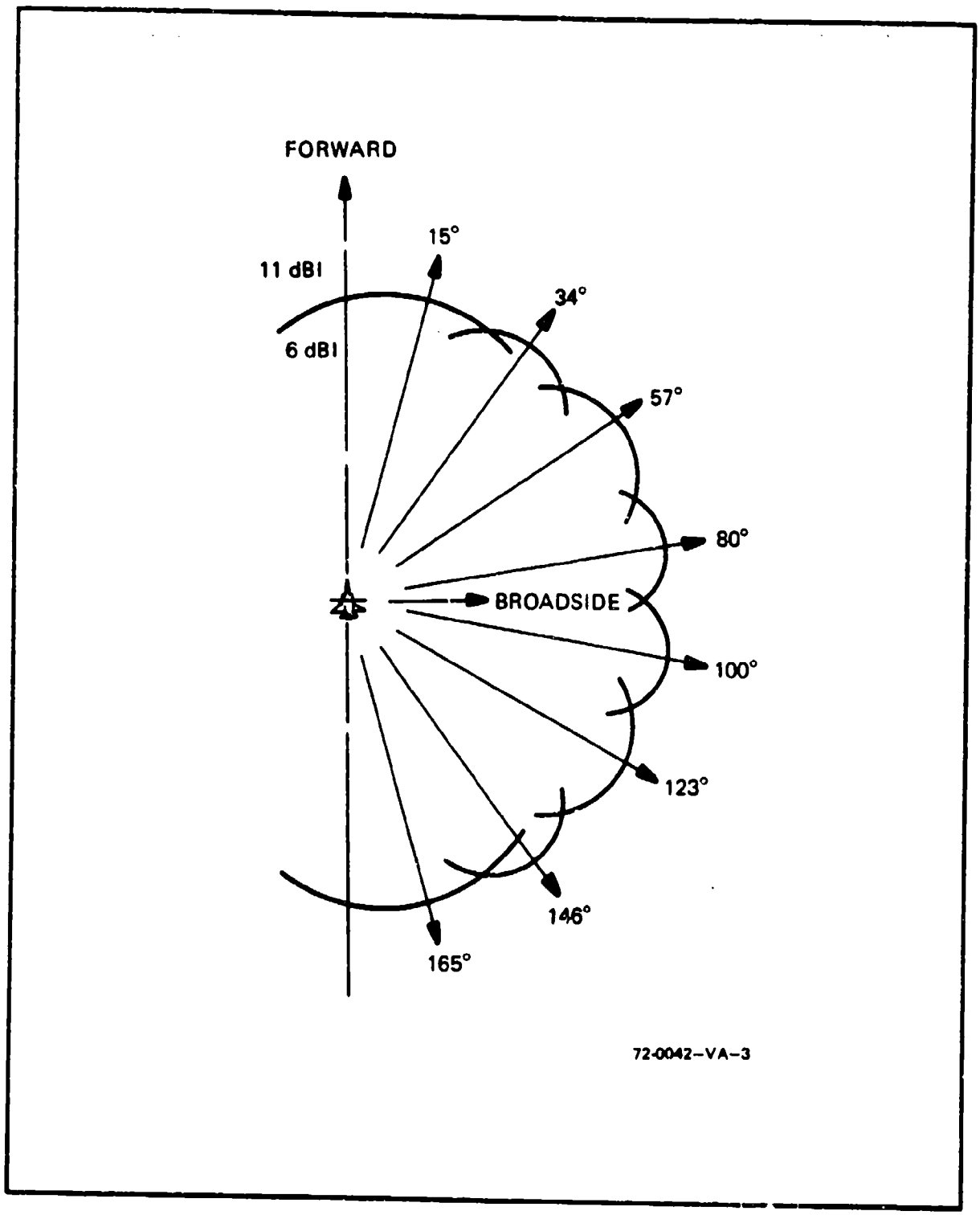

Figure 4. Azimuth Plane Beam Directions

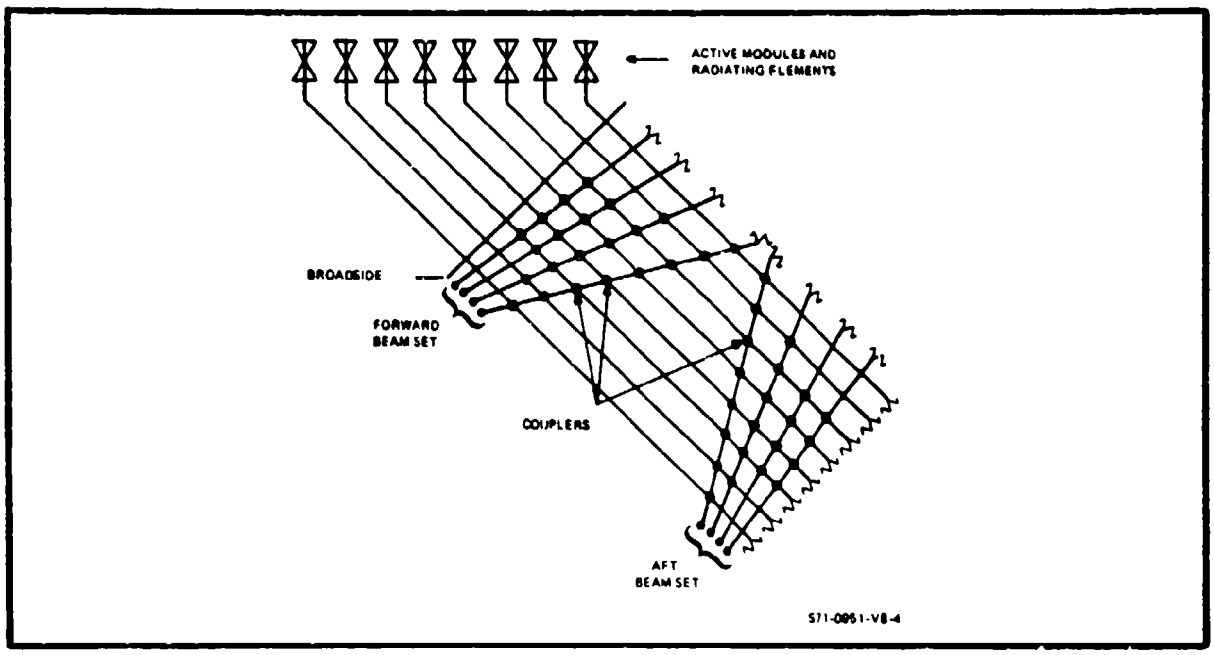

Figure 5. Time Delay Beam-Forming Network

increment is inserted between each two elements through the input line to shift the plane of wavefront emanating from the array. Since some of the energy is unavoidably delivered to the load, this circuit has an effective loss that will vary slightly with the number of elements coupled into the circuit.

The basic antenna is exceptionally simple. It consists of a linear array of eight vertically polarized dipoles $\lambda/4$ in front of a reflector/ground plane as shown in figure 6. The dipoles are situated on the front surface, and the reflector forms a part of the mounting surface to the aircraft. The combination is filled with a low-density foam and covered with fiberglass to form a light rigid package that is impervious to weather.

Each half of the dipoles is fed by a balanced line circuit within the confines of the package. The balanced stripline construction is etched on both sides of a dielectric panel mounted perpendicular to the dipoles and running the length of the package. The proper balanced-to-unblanced line transitions are included ahead of the module electronics, which are also incorporated inside the package.

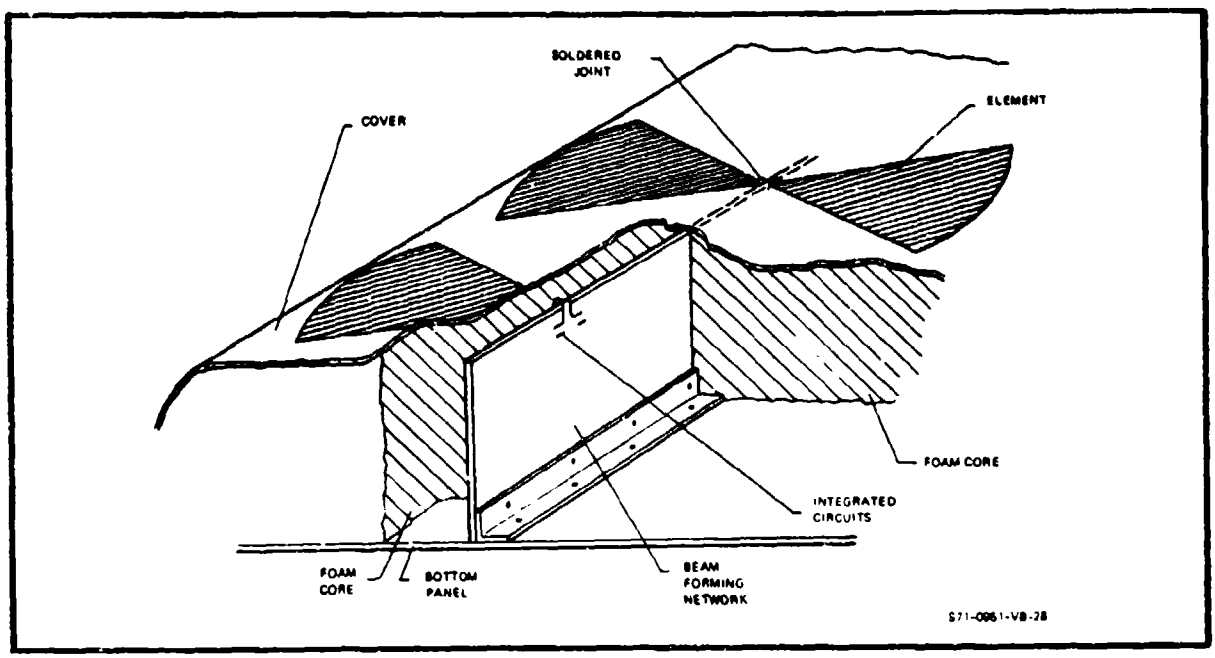

Figure 6. Antenna Construction

The entire array unit is 48 inches long, 6 inches wide, and extends 3 inches above the aircraft surface. Mounting and wiring holes are the only external installation procedures anticipated. This design approach has been used successfully on a low-cost 6-foot linear IFF array built by Westinghouse for the Federal Aviation Administration. The units that have been built have fixed single beams, but they have sum and difference combining circuits and some switching circuits. In models ranging in length from 6 to 10 feet, the weights have followed closely a figure of 0.5 pound per inch.

One of the eight-element arrays is shown in figure 7. The dipoles shown vary in shape from the bow-tie shape used extensively at Westinghouse. This shape was found to produce a VSWR of less than 1.18 over the 1,020 to 1,100 MHz band. Slots etched on a copper clad dielectric also have been considered, and although the interconnections are not quite so simple, their other properties make them equally attractive.

An important factor from the standpoint of operating with an active solid-state power amplifier circuit is the driving point impedance of radiating elements. The changes in this characteristic due to mutual coupling effects that occur with scanning must be kept low for proper transistor operation. Prior analysis based on the periodic nature of a dipole array structure revealed that a theoretical VSWR as high as 9:1 could occur at scan angles

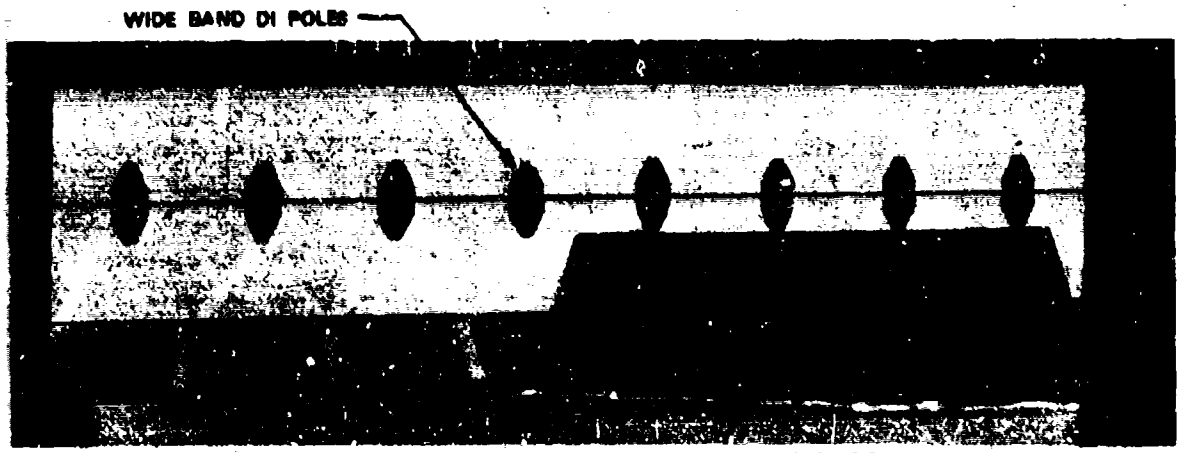

Figure 7. Eight-Element Array

up to 70 degrees for a linear array of dipoles spaced $\lambda/2$ apart and a $\lambda/4$ above a ground plane. The H-plane impedance effect was calculated in terms of the power transmission coefficient where the dipoles are assumed matched at broadside. For a beam at 56 degrees, the VSWR would be 3.5:1. By matching the impedance at an intermediate scan angle, a smaller range of impedance variation is realized.

SOLID-STATE MODULE CIRCUITS

The requirements based on the calculations shown in the appendix and an array gain of 10 dB indicate a module that transmits a peak power of 50 watts, with an input of 6.5 watts. The receiver section must exhibit a gain of 24 dB, with a noise figure of 5.0 dB. The module also must provide transmit/receive signal separation. The selected module circuit, shown in figure 8, uses diode switches for T/R separation instead of circulators, which tend to be larger, and diplexers, which tend to be more lossy and poor in isolation.

The transistor power amplifier is a single-stage design operating with a gain of 9 dB, an overall efficiency of 50 percent, and a peak output of 50 watts. A separate isolator is not included because the amplifier design includes a hybrid coupler isolator as part of the output matching network.

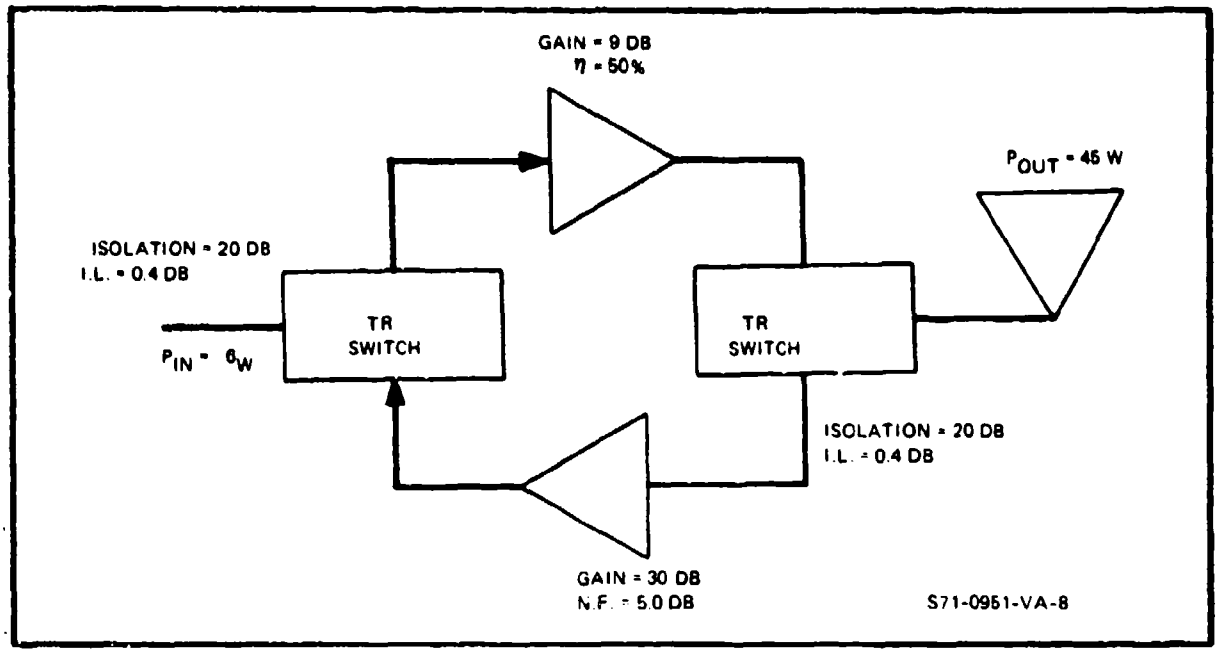

Figure 8. Solid-State Module

Recent developments in semiconductor and packaging technology indicate the possibility of achieving up to 100 watts peak power from a single output transistor. A chip carrier, developed at Westinghouse, has been tested at power outputs of 30 watts at 1.3 GHz with an efficiency of 75 percent. This compares with a power output of 20 watts and an efficiency of 60 percent for the same type semiconductor chip mounted in a conventional package. These chip carriers results are preliminary, but they do indicate that significant improvements in power output and efficiency can be realized through improved transistor packaging.

These increases in power output and efficiency make it possible to operate the power amplifier at a reduced voltage level and thereby take advantage of the improved transistor reliability that results from operating below the normal recommended collector voltage. Using the Westinghouse chip carrier in combination with a transistor chip could provide power outputs in excess of 100 watts at 1.0 GHz operating with a +40 volt collector supply. The 50 watts peak output required for the module could be achieved at a collector voltage considerably below that level (approximately 30 volts).

The low-noise amplifier is a two-stage design to produce a gain greater than 24 dB. Similar designs have been produced at L-band, with gains of

20 dB and noise figures of 2.75 dB. Similarly, diode switches for T/R applications have been built to handle 115 watts peak, 10 watts average, with isolations of 25 dB and a maximum insertion loss of 0.6 dB. A loss of 0.4 dB and isolation of 20 dB are realistic for a PIN diode switch. The entire module circuitry is contained within a package measuring 3.5 inches by 2.5 inches by 0.4 inch.

PERFORMANCE SUMMARY

The electrical performance is summarized in the following table for the case of a single eight-element array operating independently. As stated earlier, proper accounting for phasing between arrays could allow simultaneous operation of arrays at least at end fire if more gain is desired. The figures shown are conservatively based on measured data acquired on similar arrays built at Westinghouse.

ELECTRICAL PERFORMANCE

Parameter	Value
Frequency	1020 to 1100 MHz
Polarization	Linear, H-plane scan
Array Size	48 × 6 × 3 inches
Beamwidths - H-plane	30 degrees (0 to 56 degrees)
E-plane	115 degrees
Sidelobes (grating lobes)	Lower than -12 dB peak
Gain (including BFN loss)	10 dB (0 to 56 degrees)
Gain variation over sphere	<2 dB (0 to ±80 degrees) <4 dB (±80 to ±90 degrees)
Element transmit power	50 watts
Element noise figure	5.0 dB max
Preamplifier gain	24 dB

APPENDIX

DETERMINATION OF TRANSMIT-RECEIVE MODULE REQUIREMENTS

The signal levels required for the system, and hence the RF preamplifier gain, are determined from the available signal at the element module and the sensitivity of the video detector. The detector has a tangential signal sensitivity of -55 dBm, which can be connected to a minimum trigger level (MTL) of -46.8 dBm, for a signal-to-noise ratio of 15.2 dB. Assuming that the same signal intensity is available in space as in current transponder systems, the MTL signal at the module antenna element terminal will be -85.5 dBm, which is determined from an array gain of 1.5 dB and a 9-dB distribution factor for the eight-element array and the original MTL signal of -78 dBm. That is, -78 +1.5 -9 = -85.5 dBm. An additional loss of 0.4 dB in the module T-R device brings the level of the input of the RF preamplifier to -85.9 dBm.

Working back from the video detector, there is a 1.0-dB insertion loss for the RF switch in the transmit beam selector; also a 1.5-dB loss and 18-dB signal gain in the beam-forming network. The gain is due to the coherent addition of the signal from each module of the eight-element array. There is also a 9-dB noise gain because of the incoherent noise addition. Another 0.4-dB loss is incurred in the T-R device at the module output, thus bringing the total losses between the preamplifier and the video detector to 2.9 dB with a gain of 18 dB.

The MTL signal required at the output of the preamplifier is, therefore, -61.9 dBm (that is, -46.8 +2.3 -18 = 61.9 dBm). The required preamplifier gain is then the difference between the input and output signal levels, or 24 dB (-61.9 +85.9 = 24).

The required transmitter power can be determined in a similar manner. The effective radiated power from an array is required to be 500 watts (+27 dBW) to meet transponder distance requirements. The power required at each element of the eight-element array is determined from the array gain of 1.5 dB and the 9-dB distribution factor, or +16.5 dBW (27 - 1.5 -9 = 16.5). The transmission path losses for the T-R devices and beam forming network are the same as before. Additional losses are for the RF switches, three

of them at 1.0 dB each, the transmission line at 0.7 dB; and the circulator at 0.4 dB. Total losses are, therefore, 6.4 dB.

On the other side of the ledger, the gains are 9 dB for the power amplifier and -9 dB for the beam-forming network where the input power is fed to eight elements. The total gain is, therefore, 0 dB, and the transmitter power required is +22.9 dBW, or 195 watts. The transponder transmitter can be used provided a 4-dB attenuator follows the circulator.

The transponder input MTL signal level must be maintained at -78 dBm so that the dynamic range capability will not be exceeded. This level is maintained through the use of a directional coupler at the output of the beam-forming network. This allows the beam-steering signal to be taken off with little loss. The coupling level can be determined by analyzing the remainder of the transponder input path.

The MTL signal at the input to this directional coupler is found from the previously determined -61.9 dBm signal level at the output of the RF pre-amplifier. There is a 0.4 dB T-R loss and a 1.5-dB beam-forming network insertion loss, as well as the 18-dB gain in the beam-forming network. The input to the directional coupler is then -45.8 dBm (-61.9 -1.9 +18 = -45.8 dBm.

Working back from the transponder, there is a 0.4-dB insertion loss for the circulator, a 6.2-dB loss in the sector beam-summing network, a 9.3-dB loss in the beam-summing network, and 0.7-dB loss in the transmission line. Losses of 15 dB are due to the hybrid addition of the RF signals. The total losses are 16.6 dB. Since the MTL required at the transponder input is -78 dBm, the level required at the output of the directional coupler is -61.4 dBm. The directional coupler then requires a coupling of 15.6 dB in the attenuated arm (61.4 - 45.8 = 15.6 dB).

8. SOLID STATE PHASED ARRAYS FOR SATELLITE COMMUNICATIONS

by

D. H. Townsend

Code 5435

Naval Research Laboratory
Washington, D.C. 20390

for

ARRAY ANTENNA CONFERENCE

Naval Electronics Laboratory Center
San Diego, California

22, 23, 24 February 1972

SOLID STATE PHASED ARRAYS FOR SATELLITE COMMUNICATIONS

INTRODUCTION

Modern shipboard satellite communication (SATCOM) systems typically contain high power radio frequency (RF) transmitting tubes with high voltage power supplies, temperature stabilized low noise preamplifiers, mechanically stabilized passive reflector antenna systems, and a wide range of semiconductor devices. This variety of unique circuits precludes extensive use of integrated circuit modules and has caused very high cost for design, fabrication, maintenance, and reliability. The application of traditional design concepts has priced phased arrays out of the SATCOM market for all applications except on the satellites themselves. The point of this discussion is not that conventional phased array designs are wrong or that the cost of acquisition and ownership for mechanically steered antenna systems is high, but rather that new technologies involving solid state microwave circuit integration are available which when logically developed and appropriately combined promise to reduce the cost of acquisition and ownership of SATCOM terminals. For antenna apertures less than 5 square feet, the costs associated with mechanically steered antenna systems are nearly constant, setting a lower bound on the cost of conventional systems (Fig. 1). The application of solid state microwave integrated circuits (MIC) to the transmitter and receiver in a mechanically steered system is limited to a single up converter, down converter, and receiver RF preamplifier. On the other hand, the inherent redundancy of phased arrays with distributed, low power transmitters and receivers permits extensive application of solid state MIC technology. Individual, identical modules consisting of a transmitter with an up-converter and power amplifier capable of delivering 2 watts (W) continuous wave (CW) at X-band and a receiver with a low noise parametric preamplifier and down-converter can be arrayed to obtain aperture gain, electronic steering, and high transmitted powers. It is anticipated that the requirement for large quantities of identical MIC transmit/receive (TR) modules for small aperture phased arrays will substantially lower module costs and, consequently, system costs. Solid state MIC phased arrays, besides reducing system cost of ownership through lower fabrication costs and improved reliability and maintainability, can provide additional performance in areas not readily amenable to solution with mechanically steered antennas.

The primary goal for developing a shipboard SATCOM phased array is to demonstrate how solid state MIC technology can lower the total cost of a small shipboard terminal. To accomplish this objective, a three phase program was established. In phase one, an exploratory model SATCOM phased array composed of solid state MIC transmit/receive modules is developed in order to establish the problems associated with MIC technology for SATCOM applications, to evaluate preliminary design concepts for the T/R modules, and to improve module subsystem performance where

necessary. In phase two, an advanced T/R module mechanically and electrically suitable for direct incorporation into a shipboard SATCOM phased array terminal is developed and tested based on results obtained from improvements to and evaluations of the exploratory array and system tradeoff studies from phase one. In phase three, an advanced development model SATCOM phased array is built for shipboard test and evaluation.

Phase one is nearing completion. A four element MIC phased array has been built to operate through channel one of the Defense Satellite Communications System II (DSCS-II) satellites and is under evaluation at the Naval Research Laboratory (NRL). Four parametric preamplifiers with integral Gunn pumps and preselector filters have been built to provide low noise front ends for each of the module receivers. The MIC module design and system performance studies to be discussed later have, by in large, been completed for phase one. The result has been (1) a complete redesign of the module receiver for lower noise temperature, increased flexibility, and reduced complexity and cost, (2) expanded design of the module transmitter to increase the output power to 2 W CW at approximately 9 percent direct current (dc) to RF efficiency, (3) a complete redesign of the mechanical layout of the module in favor of a dual T/R module with improved form factor, heat dissipation, and reduced module cost, and (4) system studies of methods for increasing array scan volume, to determine the required system effective radiated power (ERP) for working with DSCS-II, to lower system noise temperature, and to predict system power and cooling requirements.

MODULE RECEIVER

Figure 2 shows a block diagram of the prototype exploratory T/R module presently being evaluated at NRL and Fig. 3 shows the receiver and transmitter of an actual prototype module less the radiating element. If the prototype module were to be used in a shipboard SATCOM array, a low noise parametric preamplifier would be added immediately after the receiver preselector filter. In fact, this configuration is to be evaluated when the MIC paramps are delivered to NRL. Since both the paramp modules and the prototype phased array modules contain a preselector filter, the array module filter will become a post-selector filter when the paramp module is connected. In a production module, the paramp would be contained in the same package as the rest of the module receiver and the postselector filter would be eliminated. There are difficulties with the RF/IF module receiver, however. The number of active components in this type of module receiver is large. A large substrate area is needed for the receiver, and an array composed of such modules requires both a receiver IF and local oscillator (LO) manifold. The main advantages of the RF/IF module receiver are the relaxed tolerances required on the IF and LO manifolds.

Due to the limitations of the RF/IF module receiver, future work will concentrate on an all RF module receiver (Fig. 4). The all RF module receiver consisting of a preselector filter, low noise parametric amplifier, and a low

loss wideband phase shifter offers a number of advantages over the RF/IF module receiver. The all RF module receiver has fewer active components than the RF/IF receiver since there is no X3 multiplier, LO amplifier, mixer, IF amplifier, LO connector, or LO manifold for the array. With fewer active components, the production yield and reliability are increased, and the module cost is lowered. In addition, the receiver noise temperature is decreased. The major disadvantage of the all RF module receiver are reduced receiver gain and stricter tolerances required on an X-band receive manifold. Neither of these disadvantages represent a serious problem since an additional parametric amplifier at the output of the receive manifold can supply the additional gain without appreciably degrading the system noise temperature and stripline manifolds of triplate construction have been built at X-band for radar receivers with excellent results. Moreover, the number of ports on a manifold can be cut in half by using the added substrate area in a single all RF module to construct two transmitters driven by power, splitter and two receivers summed in a signal combiner. This not only reduces the T/R manifold cost but also reduces the cost for a single transmitter and receiver as long as the active component costs are low and the module yield is not appreciably affected. The fabrication cost for the passive circuitry is essentially the same for one or two circuits since the process is photographic and the second circuit is an exact copy of the first.

MODULE TRANSMITTER

The greatest change in basic design concept from the prototype T/R module to the advanced module has been in the receiver. The most dramatic change since starting development of the prototype T/R modules, however, has been in the technology for high power transistors at S-band. In little more than 18 months, the power available at S-band using the first production transistors available has increased from approximately 250 milliwatts (mW) to in excess of 5 W CW at 2660 MHz, an increase of 13 dB. The single component having the greatest cost in an MIC module for SATCOM is the high power transistor. For example, the MSC 3005 transistor (5 W CW at 3000 MHz) currently costs approximately $300. From past experience, this cost should drop almost an order of magnitude in the next two years.

Tests at NRL of the transistor amplifier-X3 multiplier technique for generating the desired X-band transmit signal have proven that X3 multiplication of quadriphase, biphase, and frequency modulated signals contributes less than 0.1 dB degradation to the desired communications. Alternate solid state techniques for generating X-band power include injection locked avalanche transit time oscillators (ATTO) and Gunn oscillators and negative resistance avalanche transit time amplifiers (ATTA) and Gunn amplifiers.

These devices and techniques are actively being developed by others for application in SATCOM phased arrays but at present do not generate phase stable power comparable to that available with transistor amplifier-multiplier transmitters. In addition, by multiplying the transmit drive signal in the T/R module, transmit feed manifold tolerances are relaxed and losses are reduced. The prototype module transmitter has an output power of 100 mW, an instantaneous 1.5 dB bandwidth of 125 MHz, and an overall DC/RF efficiency of 6%. The advanced module is to have two transmitters fed by a power splitter, each with an output power of 2 W CW, an instantaneous 1.5 dB bandwidth of 200 MHz, and an overall DC/RF efficiency of approximately 9%. To remove heat from the module, two heat pipes will be press fit into the module case immediately beneath the high power stages of the two transmitters. The heat pipes will pass through openings in the RF manifold to a regulated heat sink. By regulating the heat sink, the module case temperature can be stabilized which, in turn, will help temperature stabilize the module receiver paramp.

ARRAY EFFECTIVE RADIATED POWER

If mechanization losses and mutual coupling effects are neglected, the T/R modules can be assembled in a uniformly illuminated array with an array gain, G_A, and a radiated output power, P_A.

$$G_A = N G_e \cos \alpha$$

$$P_A = N P_e$$

$$G_A P_A = N^2 G_e P_e \cos \alpha$$

where N = number of array elements
G_e = element gain
P_e = power per element
α = scan angle from array broadside

Using an uplink path loss, L_u to the satellite, the uplink carrier to noise (C/kT), Γ_u, is

$$\Gamma_u = \frac{G_{SR} G_A P_A L_u}{k (T_S + T_E)}$$

$$\Gamma_u = \frac{G_{SR} L_u N^2 G_e P_e \cos \alpha}{k (T_S + T_E)}$$

where G_{SR} = satellite receiving antenna gain
G_A = array gain
k = Boltzmann's constant
T_S = satellite receiver temperature, °Kelvin (°K)
T_E = temperature of the earth. (Eq. 1)

For DSCS-II satellites G_{SR} = 16.8 dB, L_u = -203 dB, G_e = 4 dB, P_e = 3 dBW, $\alpha = \pm 60°$, and $T_S + T_E$ = 1200°K. Then

$$\Gamma_u = 15.6 \text{ dB} + 20 \log_{10} N$$

Likewise, for a downlink path loss, L_D, the downlink C/kT, Γ_D, equals

$$\Gamma_D = \frac{G_A\, G_{ST}\, L_D\, P_S}{k\, T_R}$$

$$\Gamma_D = \frac{P_S\, G_{ST}\, L_D\, G_e\, N \cos\alpha}{k\, T_R}$$

where T_R = array receiving system temperature, °K

G_{ST} = satellite transmitter antenna gain

P_S = satellite power. (Eq. 2)

For $G_{ST}\, L_D \simeq G_{SR}\, L_u \equiv G_S\, L$, $T_R = 500°K$, and $P_S = 11.2$ dBW,

$$\Gamma_D = 27.6 \text{ dB} + 10 \log_{10} N$$

The baseband detector input C/kT, Γ_B

$$\Gamma_B = m\, f_D\, (E_B/N_o)$$

where (E_B/N_o) = baseband bit energy to noise density ratio

f_D = data rate, bits/second

m = mechanization loss factor. (Eq. 3)

When coherent phase shift key (PSK) modulation is used, assuming a probability of error of 10^{-3} and a mechanization loss of 2.2 dB,

$$\Gamma_B \approx 8.5 \text{ dB} + 10 \log_{10} f_D .$$

If the satellite repeater bandwidth is greater than or equal to the array receiver bandwidth, the C/kT ratios of the up and downlinks can be combined in order to obtain the overall ratio for a three point satellite relay system (see Fig. 5). Therefore,

$$\Gamma_B = \frac{K\, \Gamma_u\, \Gamma_D}{K\, \Gamma_u + \Gamma_D + B_S}$$

$$\Gamma_B = \frac{0.8\, \Gamma_u\, \Gamma_D}{0.8\, \Gamma_u + \Gamma_D + B_S}$$

where K = 0.8 for a hard limiting repeater when $\Gamma_u/B_S \ll 1$

B_S = satellite repeater bandwidth

and Γ_u 1.25 $\left\{\frac{\Gamma_B (\Gamma_D + B_S)}{\Gamma_D - \Gamma_B}\right\}$ or $\Gamma_u\, \Gamma_D = 1.25 \left\{\frac{1 + \Gamma_D/B_S}{1 - \Gamma_B/\Gamma_D}\right\} \Gamma_B\, B_S$ (Eq. 4)

If $\Gamma_D/B_S \ll 1$ and $\Gamma_B/\Gamma_D \ll 1$ for a wideband repeater and low data rates, respectively, then

$$\Gamma_u\, \Gamma_D \approx 1.25\, \Gamma_B\, B_S .$$

From Eqs. (1) and (2)

$$\Gamma_u \Gamma_D = \left(\frac{G_S G_e L \cos \alpha}{k}\right)^2 \left(\frac{P_e P_S}{T_R (T_S + T_E)}\right) N^3$$

Combining the two above expressions for $\Gamma_u \Gamma_D$ gives

$$\frac{G_e^2 \cos^2 \alpha}{k T_R} P_e N^3 \simeq 1.25 \frac{k (T_S + T_E) B_S}{G_S^2 L^2 P_S} \Gamma_B . \qquad \text{(Eq. 5)}$$

This relationship holds true for a single satellite access so long as operation falls along the linear portions of the plot in Fig. 5. Therefore, the maximum data rate that can be looped through a hard limiting satellite is more sensitive to the number of modules in a filled, uniformly illuminated array than it is to the module power. Fortunately, the cost per element is less for a dual two watt T/R module than for a single one watt T/R module in production quantities within bounds determined by module yield and device costs.

Substituting for the terms in equation (5),

$$P_e N^3 \simeq 1.057 \times 10^5 f_D$$

where

$m (E_B/N_o)$	= 8.5 dB
G_e	= 4 dB
α	= ±60°
T_R	= 500°K
$T_S + T_E$	= 1200°K
$L G_S$	= -187.2 dB
P_S	= 11.2 dBW
B_S	= 125 MHz

For P_e = 2 W and f_D = 75 bits/sec, N ≃ 159. For scans out to α = ±75° for sea state 7, N ≃ 246. This means that at least 123 dual two watt T/R modules are needed for a single satellite access into a similar receiving terminal. An array terminal for N = 246 is approximately a 14 inch by 14 inch square aperture, assuming an element spacing of 0.6 wavelengths. The cosine broadening of the array beam for scans to ±75° decreases the terminal array gain so that a phased array terminal working into itself must reduce its broadside communications capacity by 12 dB in order to operate at extreme scan angles. For operation in the uplink narrow beam of DSCS-II (channel two), communication is improved by approximately 20.2 dB. The conclusion is that for a

large number of small phased array terminals the most effective approach for reducing costs is through reduced satellite channel bandwidths and multiple narrow beam coverage of the earth. Using Eqs. (2) and (3) for Γ_D and Γ_B, respectively, Fig. 6 permits graphical determination of the number of simultaneous accesses possible using a hard limiting repeater.

ARRAY SYSTEM NOISE TEMPERATURE

Arguments have been presented in favor of an all-RF module versus an RF/IF module. Extending these arguments to the array system noise temperature, consider the three configurations in Fig. 7. The well known expression for computing noise temperature is

$$T_S = T_1 + \frac{T_2}{G_1} + \frac{T_3}{G_1 G_2} + \ldots + \frac{T_M}{G_1 \ldots G_{n-1}} \qquad \text{(Eq. 6)}$$

where the noise temperature, T, of an attenuator of loss, L, at a physical temperature T_{LP} is

$$T = (L - 1)\, T_{LP}$$

The three cases all assume an ambient temperature of 300°K. The respective gains, component noise temperatures, and system noise temperatures are shown on Fig. 7 for the respective configurations. Besides excessive complexity, the RF/IF module of case (a) has the worst system noise temperature by almost an additional 300°K. Case (b) has the best system noise temperature but at the expense of requiring two paramps per module. Case (c) has a system noise temperature 31°K greater than case (b) with the same net gain by using a single paramp per module and one paramp at the array summed output. Consequently, case (c) represents the most cost effective approach to a low noise temperature system without undue sacrifice in system noise temperature.

ELECTRICAL AND MECHANICAL INTERFACE REQUIREMENTS

Assuming an array of 250 dual modules or 500 transmitters and receivers, the output radiated power would be one kilowatt. The transmitter logic is expected to require from 50 to 100 milliamperes (mA) at 5 volts (V), the receiver logic from 100 to 150 mA at 5 V, the paramp pump from 200 to 400 mA at 5 V, the transmitter power amplifier from 700 to 800 mA at 28 V, and the transmitter bias supply from 30 to 50 mA at -5 V. Taking the worst case currents, therefore, a single dual T/R module requires 51.80 W of direct current (dc) power at 3 amperes (A). Consequently, 250 dual modules would

require 12.95 kW at 750 A. Since a shipboard SATCOM array would probably be configured as a monopulse automatic tracking system, each of the four panels in an array could be operated on a separate 200 A supply. A dc power supply of this size is often used for computer applications and is generally quite reliable and fairly compact (usually occupying less than 5 cubic feet).

An RF transmit/receive manifold and a dc manifold are required to split the transmit drive signal to the array modules and to combine the received signals as well as to distribute dc power. The most cost effective manifold for this purpose is a seven plate sandwich similar in construction to three back-to-back triplate manifolds. Such a manifold would consist of a ground plane, a dc stripline distribution network, a ground plane, a transmit stripline distribution network, a ground plane, and a receive stripline distribution network. Heat pipes on the modules would pass through the manifold to a heat sink cooled by refrigerated air or ship's chilled water. Modules would plug directly into the manifold/heat exchanger and be fastened in place by a securing screw. To reduce system costs and increase reliability, two module radiating elements will be directly incorporated into the dual modules so that when all modules are plugged into an array the aperture will be complete except for a protective radome. Because the radiating element has not yet been determined for the advanced module, however, the exploratory development of an advanced module will be laid out so as to best approximate the radiating element sites for incorporation at some later time. In the meantime, RF connectors will be located in place of the radiating elements so that existing elements can be connected to the module (see Fig. 8).

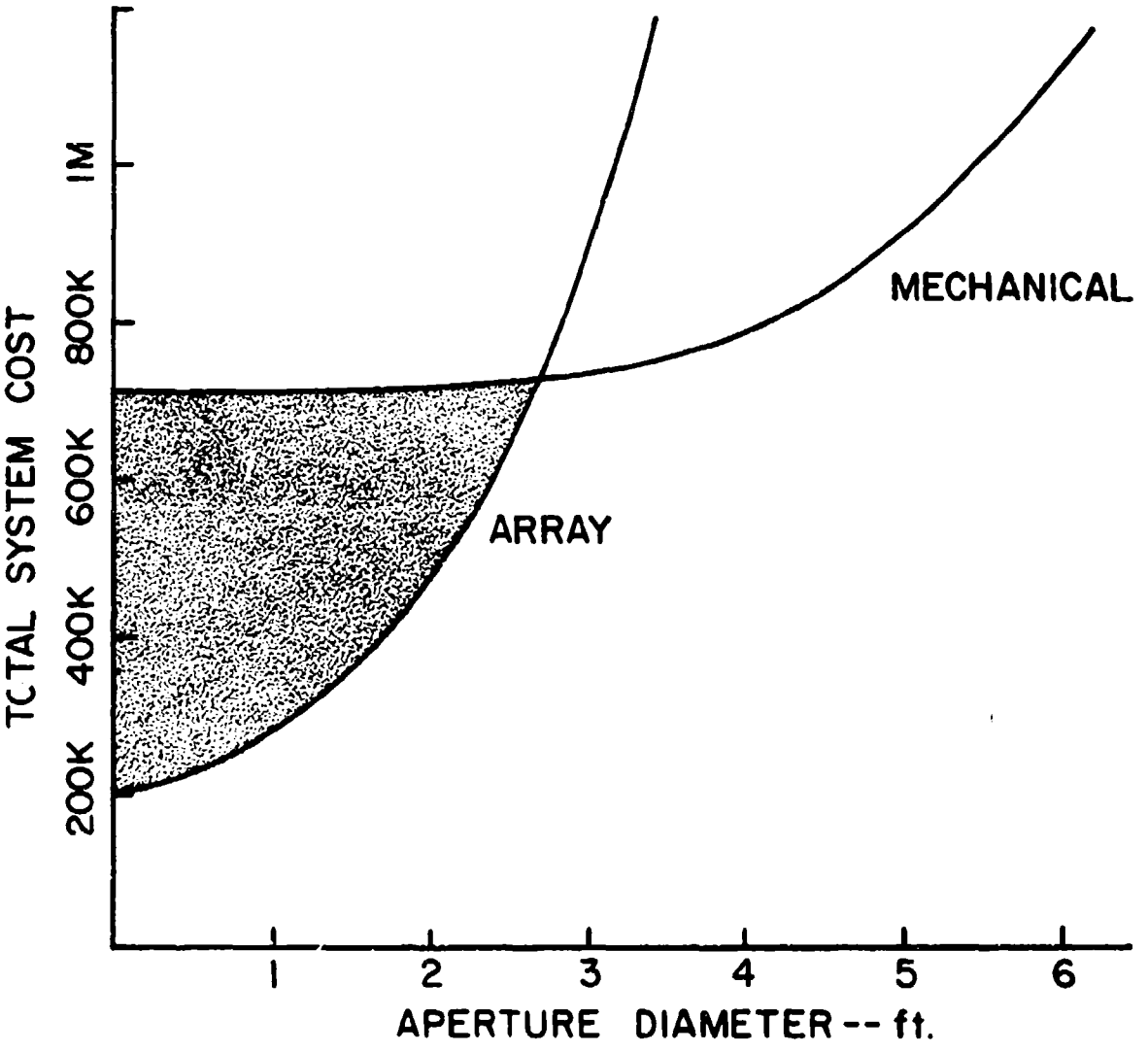

Figure 1. COST vs APERTURE DIAMETER FOR MECHANICAL AND ARRAY ANTENNA SYSTEMS

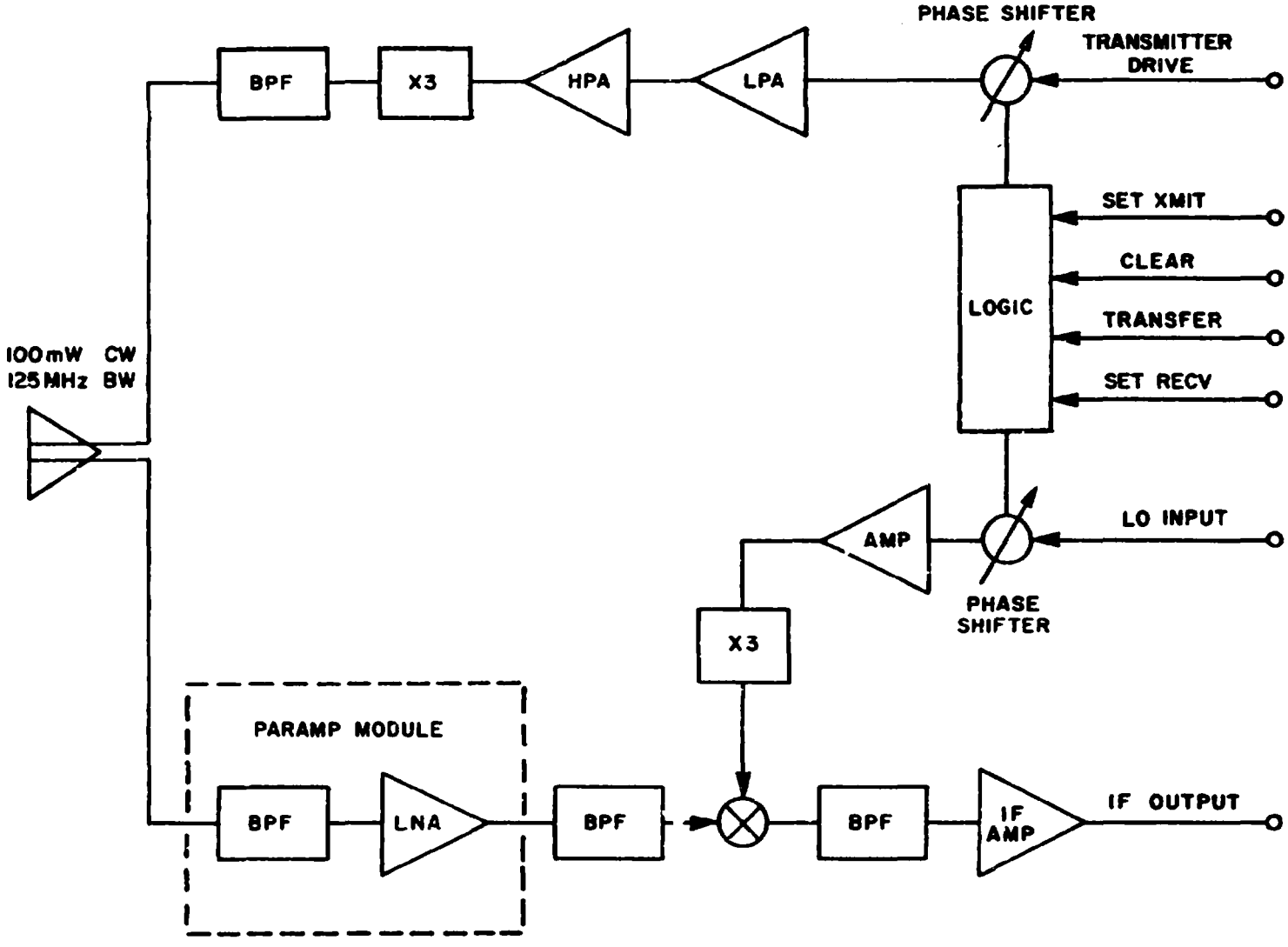

Figure 2. PROTOTYPE MIC TRANSMIT/RECEIVE MODULE AND PARAMP MODULE

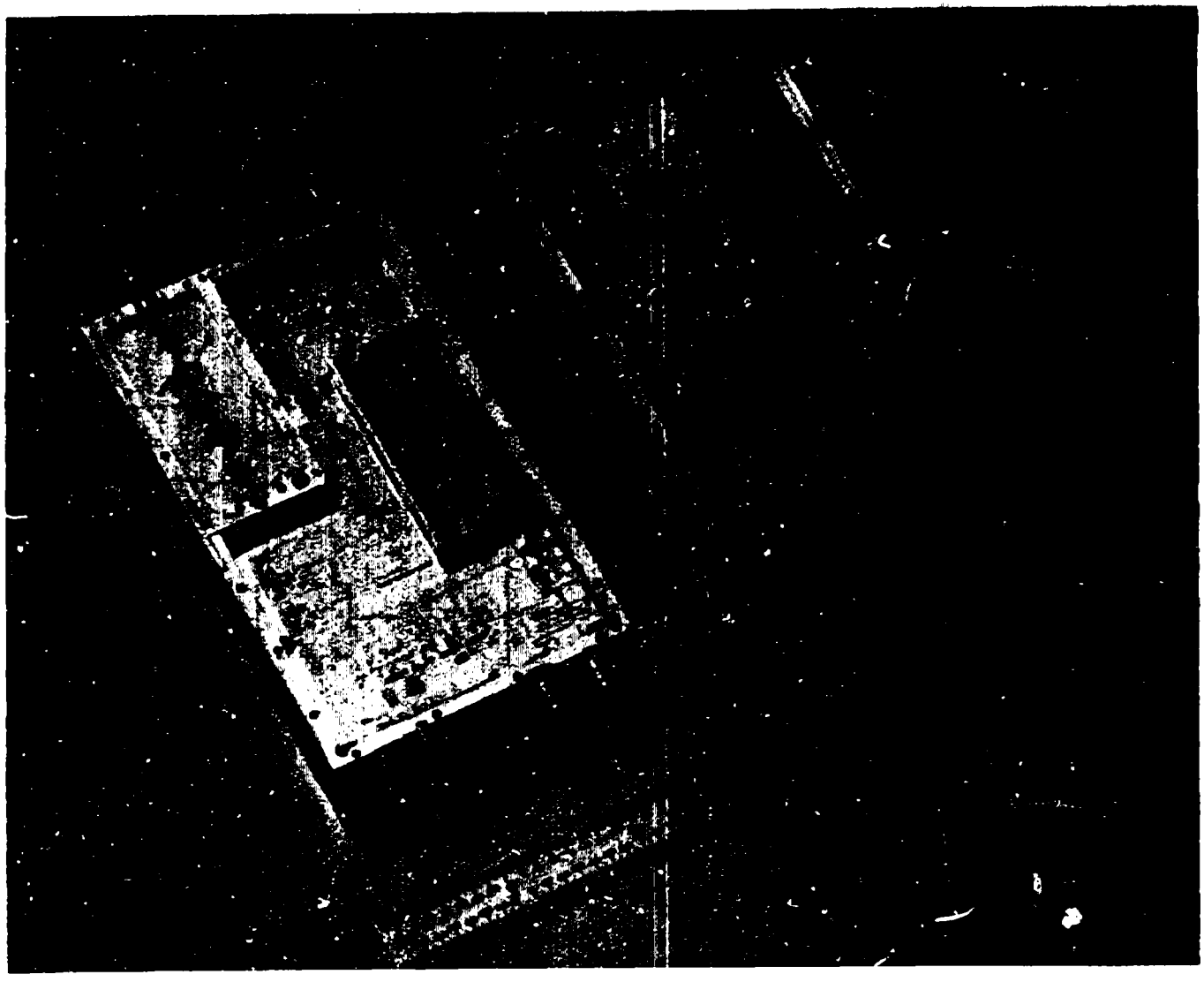

Figure 3. PROTOTYPE MIC MODULE WITH RECEIVER SIDE SHOWN ON THE LEFT AND TRANSMITTER SIDE SHOWN ON THE RIGHT

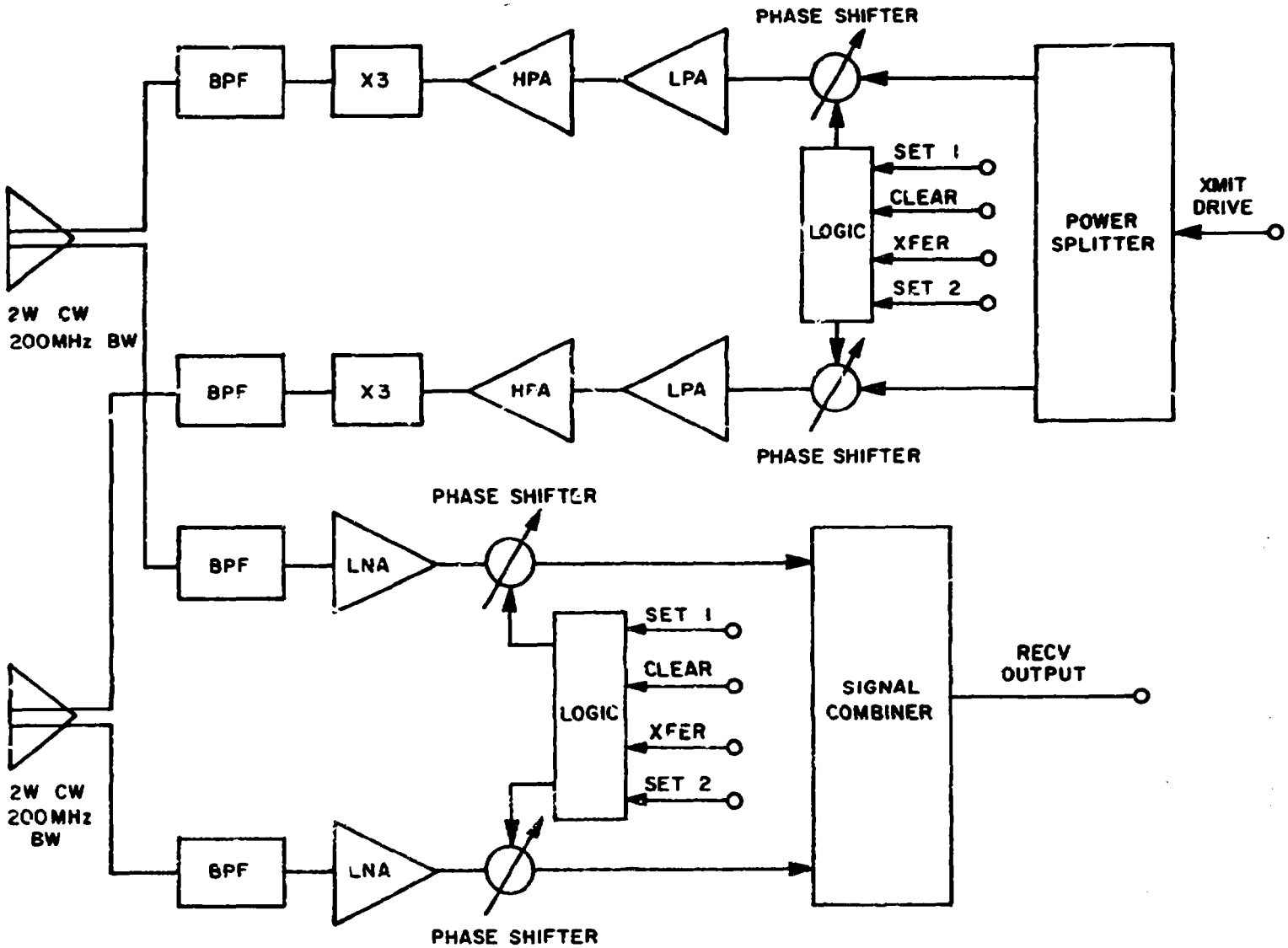

Figure 4. ADVANCED DUAL TRANSMIT/RECEIVE MODULE

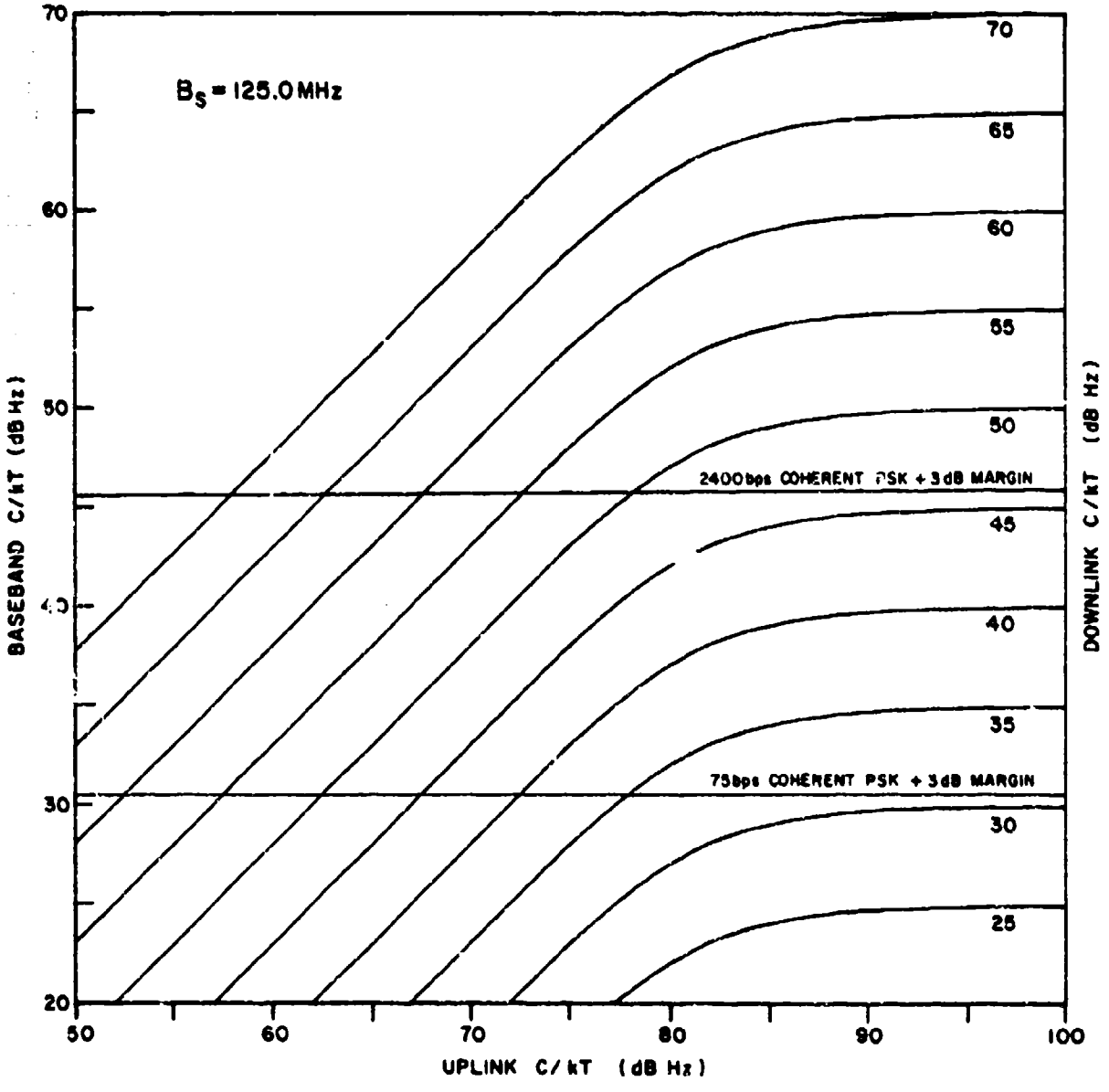

Figure 5. CURVES FOR A THREE POINT SATELLITE RELAY THROUGH A HARD LIMITING REPEATER, SINGLE ACCESS CASE FOR B_s = 125 MHz

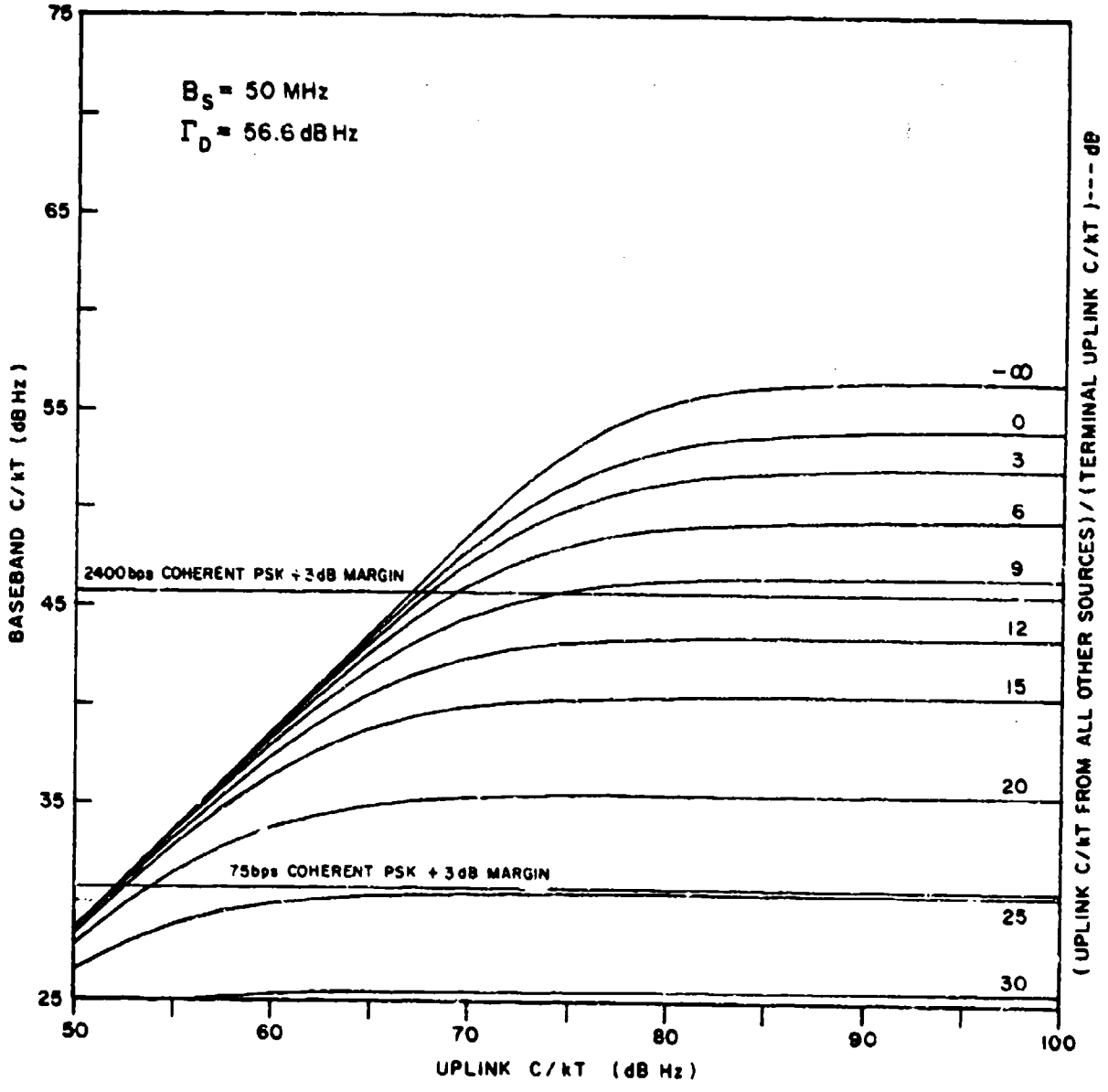

Figure 6. CURVES FOR A THREE POINT SATELLITE LINK THROUGH A HARD LIMITING REPEATER, MULTIPLE ACCESS CASE FOR B_s = 50 MHz and Γ_D = 56.6 DBHZ

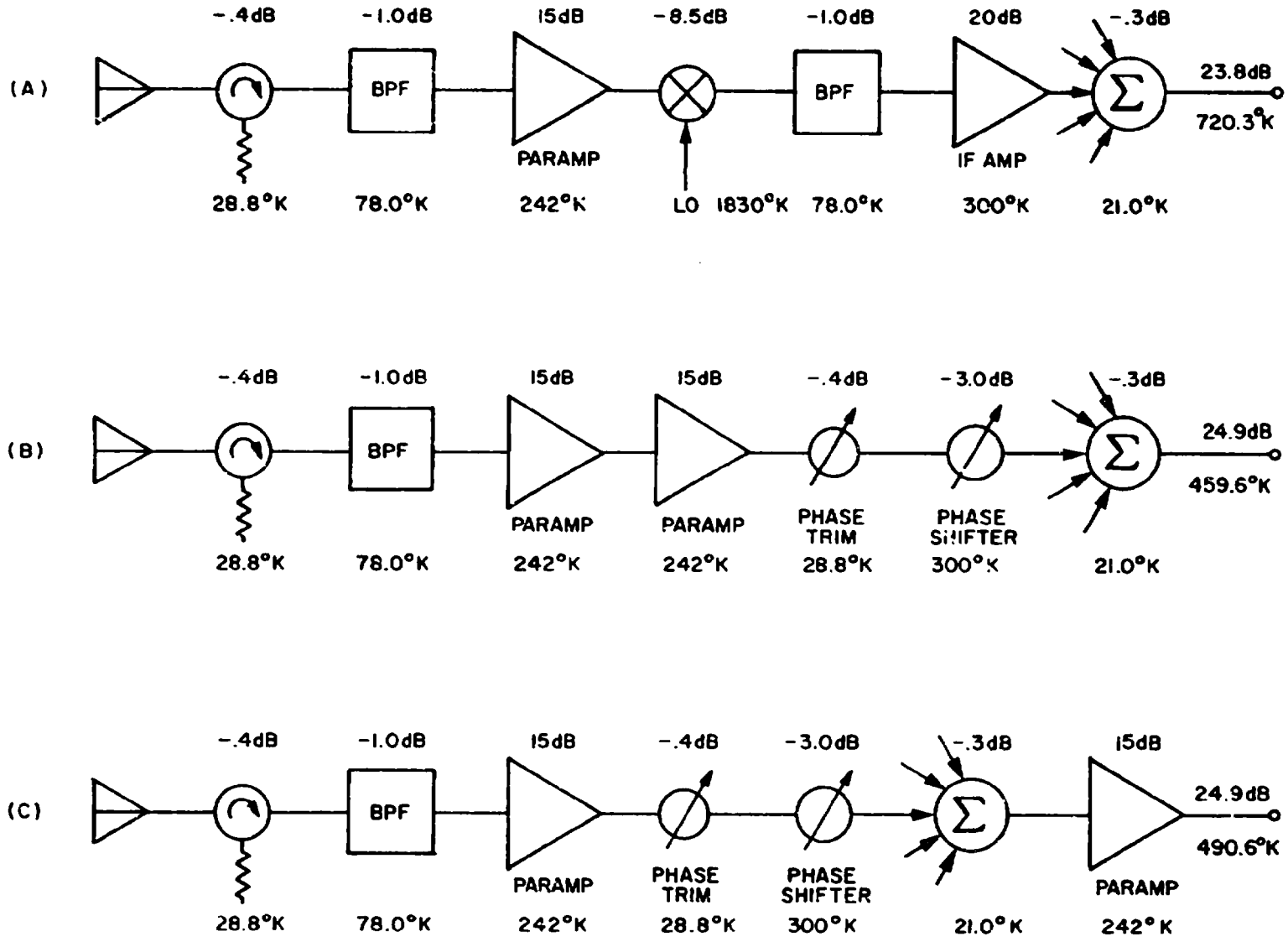

Figure 7. GAIN AND NOISE TEMPERATURE FOR THREE MODULE RECEIVER CONFIGURATIONS

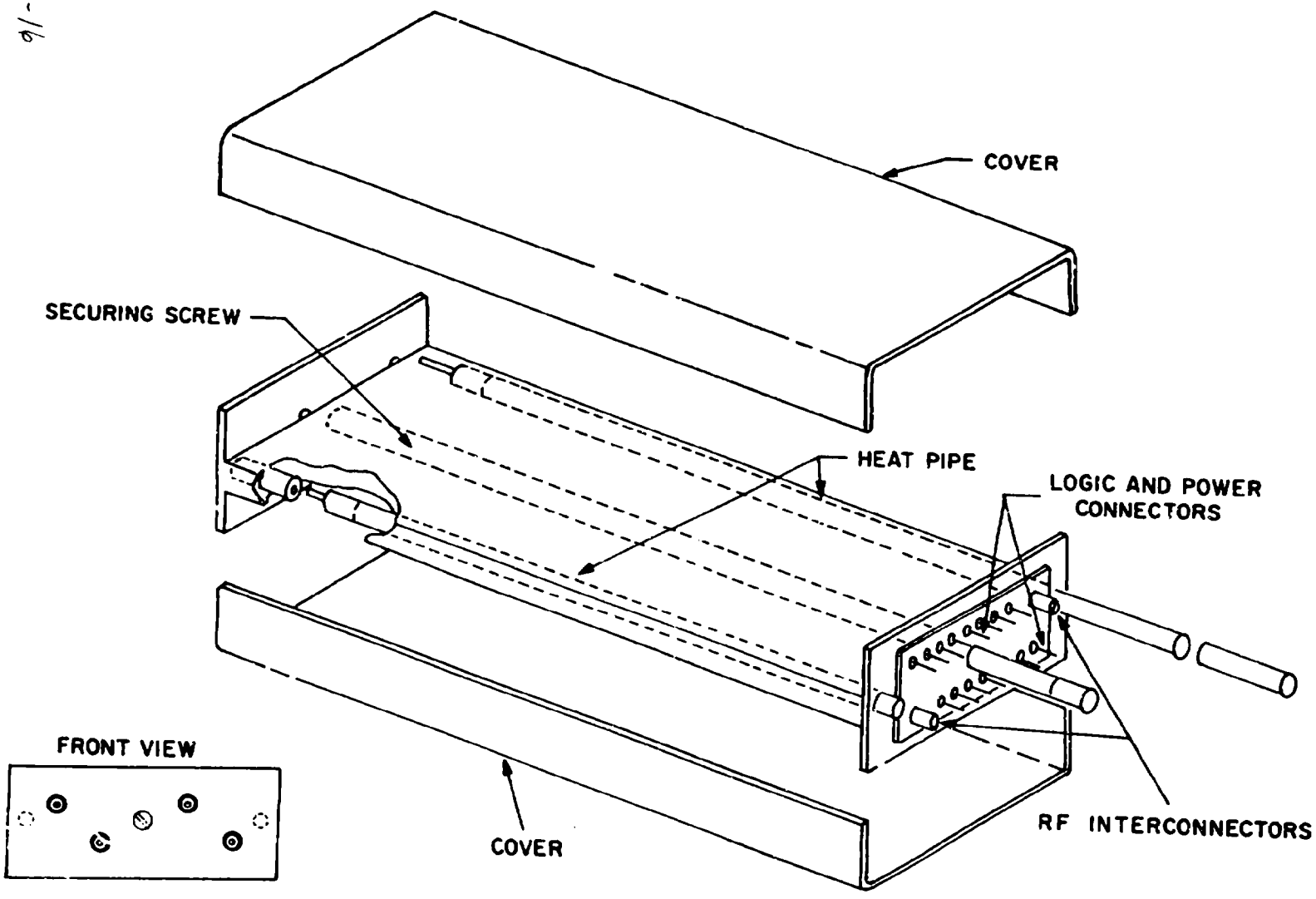

Figure 8. MECHANICAL CONFIGURATION OF THE ADVANCED PHASED ARRAY MODULE, EXPLORATORY DEVELOPMENT VERSION WITH RF CONNECTORS INSTEAD OF RADIATING ELEMENTS

9. SOLID-STATE APERTURE DESPUN ANTENNA

by

D. K. Alexander

Westinghouse Electric Corporation
Systems Development Division
Baltimore, Maryland 21203

for

ARRAY ANTENNA CONFERENCE

Naval Electronics Laboratory Center
San Diego, California

22, 23, 24 February 1972

BACKGROUND

Spacecraft for deep space probes are often spin stabilized to minimize fuel requirements for attitude control. To maintain reliable high-rate data communication with the earth, a high-gain spacecraft antenna is highly desirable because of the limited prime power available on the spacecraft. A directive (typically pencil-beam) antenna must necessarily maintain its alignment toward earth while the spacecraft is spinning. This characteristic is commonly referred to as "despinning" the antenna.

All despun antennas built or proposed to date may be categorized as either mechanically despun (MDA) or electronically despun (EDA). In the mechanically despun approach, the antenna (or parts thereof) is counter-rotated at speed equal and direction opposite to the spinning spacecraft. The antenna totation is provided by an electric motor drive slaved to a rotation rate-sensing electronic drive circuit. Several mechanically despun antennas have compiled notable records of operational service.[1, 2] Nevertheless, the principal disadvantages of mechanically despun antennas, including long term lubrication of moving parts, magnetic disturbances to the scientific package on board, and required location on the spacecraft spin axis cannot be discounted.

Electronically despun antennas avoid the above problems but existing designs [3, 4, 5] introduce some new ones of their own. Electronically despun antennas usually employ a circular array of radiating elements phased to produce a directional radiated beam. As the spacecraft rotates, proper control of the phasing devices keeps the beam directed to earth. Typically, the RF circuitry required to do this consists of power dividers, diode phase shifters with drive circuitry, stripline matrix circuits, and interconnecting transmission lines. The complexity and extent of this circuitry has proven to be a rather severe disadvantage for electronically despun antennas in terms of weight, cost, and, perhaps most important, RF losses. One of the more promising current designs, when built in breadboard form, produced a very low overall antenna efficiency.[6] Having a despun directional antenna beam is of marginal utility if the majority of the transmitter output power is absorbed in the distribution and phasing network.

A NEW APPROACH

In recent years, the increasing interest in solid-state technology, as applied to active aperture phased array antennas, has led to a new concept in packaging. Thus far the concept has been applied primarily to radar sets and involves the distribution of phase shifting, high power amplification, and receiver preamplification functions over the antenna aperture by using many solid-state microwave modules. Each module is mated to a small number of radiating elements (typically one to four). The distributed

solid-state circuits replace such conventional devices as high-power electron tubes, high-power phase shifters, and parametric amplifiers. Studies at Westinghouse have shown this approach to produce significant improvements in the overall efficiency of radar systems. In view of the efficiency shortcomings of despun spacecraft antennas mentioned above, this paper examines the feasibility of its application to satellite communication systems.

A new approach to the despun antenna problem will be described here and involves the application of active solid state-modules to the configuration of a typical spin-stabilized spacecraft. The concept is shown in block diagram form in figure 1. The radiating elements with their associated modules are evenly spaced around a circular cylindrical surface as indicated in the insert. The actual configuration of the radiating elements is quite flexible and may be designed to meet varying antenna performance requirements. For example, beamwidth requirements in the spacecraft axial plane might dictate that the radiating "element" be made up of a linear array of four dipoles. Gain or polarization requirements, on the other hand, could make another configuration more attractive. The modules themselves each contain RF power output stages, low noise amplifiers, a digital phase shifter, logic circuit, and the necessary diplexing devices. A block diagram of the module is shown in figure 2 and will be discussed more fully below. The RF manifold provides for distribution of transmit and received signals to or from the modules. A beam steering computer uses spin rate and earth vectoring information to provide signals to the separate modules, gating them off or on and setting proper phase shift values. A dc power supply provides drive current and other constant voltages to the modules.

In order to direct a beam toward the earth, only the modules on the side of the spacecraft nearest the earth will be gated on. Typically, the number of active modules at any instant would be one-fourth to one-third of N, the total number available. The phase shifter in each module is adjusted to provide a linear phase front perpendicular to the earth position vector. As the spacecraft spins through an angle of 360/N degrees, the digital phase shifters are adjusted periodically to keep the radiated beam properly directed. At the end of the 360/N degree movement, the one active module which has rotated farthest from earth is gated off, the next module on the opposite end of the active group is turned on, and the phase shifting sequence is repeated. It should be noted that the required commands from the computer are repetitive in nature and vary only as the spin rate of the spacecraft. The beam steering computer is thus a relatively simple, low cost component.

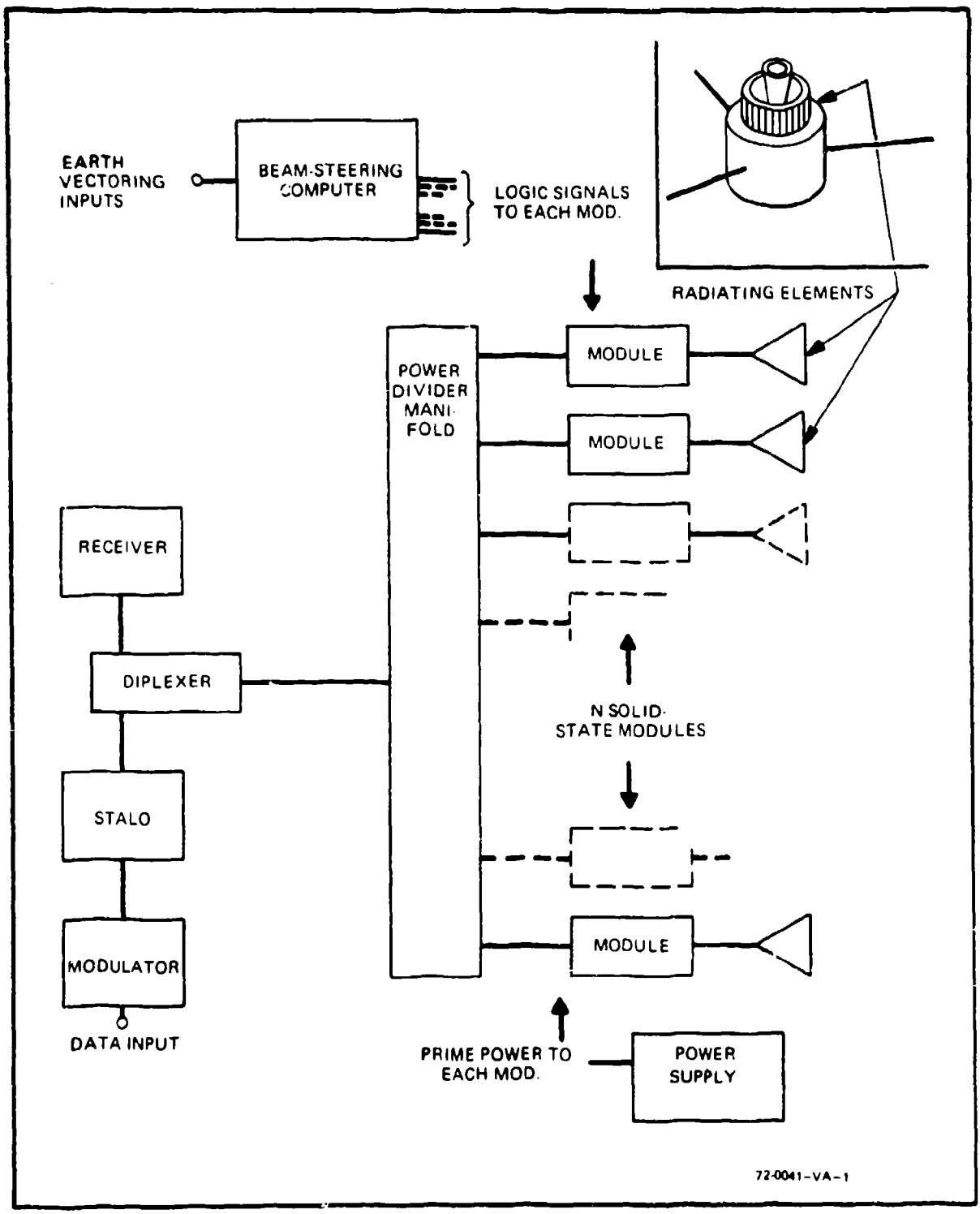

Figure 1. Solid-State Aperture Despun Array Block Diagram

SOLID STATE MODULE

The block diagram of figure 2 shows the basic configuration of the electronic circuit modules which will provide the power amplification, low-noise amplification, and phase shifting functions required to implement the active antenna aperture. By locating both amplification functions immediately adjacent to each radiator, the effect of signal losses in the RF manifold on system efficiency and noise figure are minimized.

The active aperture approach is made possible through the use of microwave integrated circuit techniques which allow the construction of high-performance modules occupying an order of magnitude less space than their conventional counterparts. All module functions are implemented using solid-state devices and hybrid fabrication techniques.

The modules are designed using the "microstrip" approach; that is, distributed transmission lines on high dielectric substrates. The transmission line patterns are produced using high-conductivity, thick-film gold ink printed on 99.5 percent alumina substrates ($E_r \approx 10$). The semiconductor devices are attached using eutectic and thermocompression bonding techniques.

The module configuration indicated by the block diagram is one of several which would be suitable for application to the despun antenna. The basic elements of the module are the following:

Diode Switch - Serves the required on/off switching of the module. Terminates the RF manifold in a 50Ω load when the module is off.

Phase Shifter - Provides the proper signal phasing required for beam steering. A diode digital phase shifter, of the switched line-length variety, with a quantization level of 3 or 4 bits may be used.

Logic Circuit - Interprets the computer code to provide control signals to the phase shifter and diode switch.

Diplexers (2) - Provides transmit and receive signal separation.

Power Amplifier - Generates the required transmit signal signal level. For typical spacecraft applications, 2 to 4 watts CW per module would be required and is within present technology.

Low-Noise Amplifier - Amplifies the receive signal to establish noise figure.

Other module and manifolding configurations may be considered. For example, it might prove advantageous to implement a manifold using a diode switch network and avoid dissipating that portion of the input signal feeding inactive modules. In conjunction with this, the moving of one or more stages of amplification from the module to the manifold could prove beneficial. Options of this type call for detailed analyses which have not been undertaken for this particular application.

ADVANTAGES

As mentioned earlier, in the solid-state aperture approach, the RF power amplifiers and receive channel low-noise amplifiers (LNA) are located immediately adjacent to the array radiating element. This means that losses in the distribution network (or manifold) and phase shifters are much less significant than for the conventional approach of using a single transmitter and receiver. For the transmit case, the manifolding for a solid-state aperture array will have comparable losses, measured in dB, to that of the conventional array. However, since the power level present in the manifold is many times smaller, the absolute power dissipated is likewise much less. Considering the receive channel, there is very little attenuation between the radiating element and the first stage of RF amplification (the LNA). Since this attenuation contributes directly to system noise figure, a considerable improvement is realized. In a later section, the comparative efficiencies of the solid-state aperture and conventional arrays will be discussed in more detail.

An additional advantage of the solid-state aperture despun antenna is versatility in array radiation performance. The beam steering computer can be programmed to control the phase and output of each module. To meet immediate needs, this capability would be used only to provide a despun mode and a failsafe omnidirectional mode. Ultimately, with minor equipment modifications, a broad spectrum of radiation capabilities could be provided. The possibilities include multiple beams to communicate with additional stations and instantaneous changing of illumination functions to suit mission requirements -- sidelobe suppression for secure communications, for example.

Finally, this approach offers reliable operation. The entire RF package employs only solid-state devices. Because the transmitter and initial receiver stages are distributed over the aperture, the failure of these devices, up to some limiting number, is noncatastrophic. Thus, graceful degradation is obtained as an inherent feature of the design.

DISADVANTAGES

The primary disadvantage of the solid-state aperture despun antenna is the state of development of the solid-state components. To date, no solid-state active aperture array has reached production status. In fact, this writer is aware of only two solid-state arrays of usable dimensions that have reached the prototype stage. However, much work has been done in many quarters on the development of microwave integrated circuits suitable for array applications. The Naval Research Laboratory, for example, is presently initiating a procurement for an L-band, solid-state, transmit-receive module. We thus conclude that, although a solid-state module suitable for a despun antenna does not currently exist, such a module is within the present state of the art, and a great deal of research and development now in progress is applicable.

A detailed weight and cost analysis, comparing a solid-state aperture approach with current electronically despun antenna designs, has not been performed. Preliminary estimates indicate that the solid-state aperture approach would, at worst, be competitive in both cases. Current developments in the area of microwave lumped circuit techniques will lead to further weight reductions.

EFFICIENCY COMPARISON

In this section, the efficiency of the solid-state aperture approach will be compared with that of typical electronically despun antennas of conventional design (i.e., having a single, though possibly redundant, transmitter and receiver and employing an electronic beam steering scheme). This comparison involves a number of estimates and assumptions and is not intended to be rigorous but, rather, to show a trend. Satellite communications normally involve frequency separation on the up and down links, and these paths will be considered separately. Ground station parameters (transmitter power, antenna gain and polarization, bandwidth, noise figure, etc.) will be assumed identical in both cases and so will not enter into the comparison. In addition, the actual radiating structure of the spacecraft antenna will be assumed the same for both and will consist of a fixed number of uniformly spaced and excited elements. The latter assumption makes effective radiated power (ERP) proportional to the RF power actually delivered to the aperture face. Because of the limited power available on board the spacecraft, the down link is most important and will be considered first.

Supposing the spacecraft to be transmitting, then, equal effective radiated power (ERP) from both arrays will be assumed and the required prime power to achieve this condition will be compared. As a starting point, a per module

RF output of 4.0 watts CW at S-band frequencies will be assumed for the solid-state aperture approach, a figure well within present state of the art. In table 1, the losses of the transmit circuit for both approaches are tabulated. A generalized block diagram for a conventional EDA is shown in figure 3. For the solid-state aperture array, the table values are based on performance figures for current devices. For the conventional array, the losses are typical of existing designs [3, 4, 5, 6]. Using this data, the prime power necessary to produce equal ERP will be computed for both approaches.

TABLE 1

Transmit Circuit Losses

Conventional Array		Solid-State Aperture Array	
Diplexer	0.6 dB	Diplexer	0.6 dB
Power Divider	1.5	Element Manifold	0.4
Beam Steering Devices (Phase Shifters, Switches, or Matrices)	2.5	Mismatch	0.1
Element Manifold	0.4	Total	1.1 dB
Interconnecting Transmission Lines	0.5		
Mismatch	0.1		
Total	5.6 dB		

Considering first the solid-state aperture, the following additional assumptions will be made.

a. Ten modules are activated at any given time (of a total of perhaps 32 to 40).

b. The RF power output stages are 40 percent efficient.

c. The associated power supplies are 80 percent efficient.

The 10 active modules thus generate 40 watts which, from table 1, is attenuated 1.1 dB reaching the aperture, resulting in an ERP of 31 watts. Using assumptions b and c yields a prime power requirement of 125 watts.

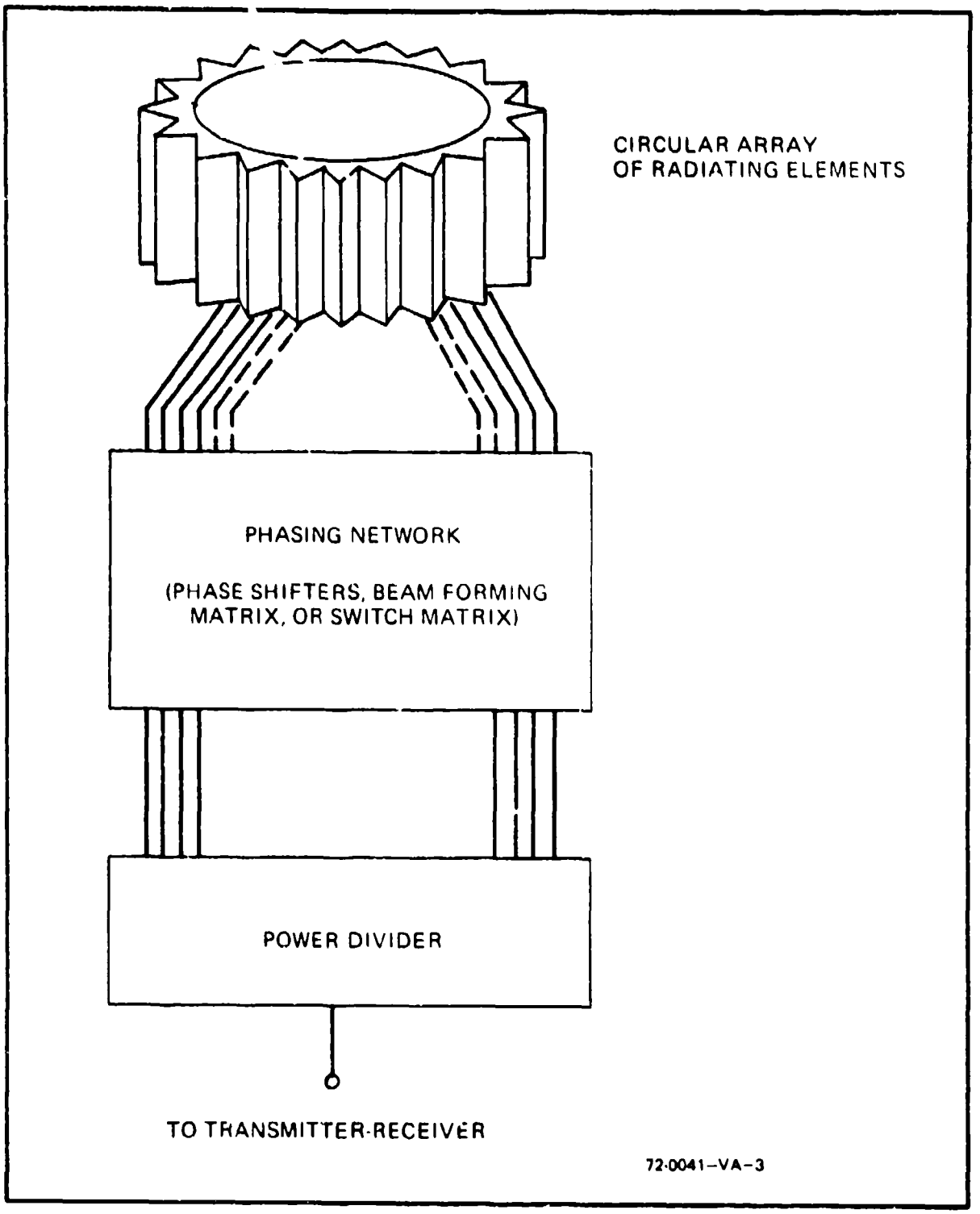

Figure 3. Conventional EDA - Generalized Block Diagram

For the conventional array, the RF power amplifier is assumed to be 60 percent efficient and power supplies, as above, assumed to be 80 percent efficient. In order to achieve the same ERP of 31 watts with 5.7-dB attenuation in the transmit path, 115 watts of RF power must be generated. Applying the stated assumptions concerning efficiencies, we obtain a prime power requirement of 240 watts. This is about 92 percent greater than that of the solid-state aperture or a 2.85-dB difference.

Perhaps the most meaningful way to compare the two arrays for the up link is to compare receive circuit losses plus amplifier noise figure at the first stages of preamplification. It is at this point that system noise figure is essentially established. This comparison is tabulated in table 2. Here again, the solid-state aperture [illegible] showing a 3-dB advantage. If we consider a [illegible] advantage of 5.85 dB is realized.

[illegible] The solid-state aperture [illegible] existing conventional [illegible] assumptions [illegible] would [illegible] different to alter the [illegible]

[illegible]

[illegible]

[illegible]

Conventional Array		[illegible] ate Array	
Element Manifold	[illegible] dB	[illegible]	0.4 dB
Mismatch	0.1	Mismatch	0.1
Beam Steering Devices (Phase Shifters, Switches, [illegible] Matrix)	2.5	Diplexer	0.6
Power [illegible]	1.5	Total Losses	1.1 dB
Diplexer	0.6		
Interconnecting Transmission Lines	0.5		
Total Losses	5.8 dB		
Noise Figure	2.5 dB	Noise Figure	4.0 dB
Losses + NF	8.3 dB	Losses + NF	5.1 dB

SUMMARY AND CONCLUSIONS

A new approach for a despun spacecraft antenna has been presented. It involves the application of solid-state aperture techniques to high gain arrays for spin-stabilized spacecraft. The theory of operation has been discussed along with major advantages and disadvantages. An efficiency comparison shows this array to be responsive to a genuine need. It is felt the solid-state aperture despun antenna holds promise of remedying some of the major shortcomings of current designs.

REFERENCES

1. Blaisdell, Rubin, and Mahr, "ATS Mechanically Despun Communications Satellite Antenna." IEEE Transactions on Antennas and Propagation, Volume AP-17, No. 4, pp. 415-428, July 1969.

2. Donnelly, Graunas, and Killian, "The Design of the Mechanically Despun Antenna for the Intelsat-III Communications Satellite." IEEE Transactions on Antennas and Propagation, Volume AP-17, No. 4, pp. 407-414, July 1969.

3. Chiang, Yaminy, and Jackson, "A Foam Dielectric Matrix-Fed Electronically Despun Circular Array." Proceedings of the 1970 G-AP International Symposium, pp. 29-36, September 1970.

4. Erhardt, H. R., and Subbotin, B. T., "Application of Electronically Phased Antennas for Spin Stabilized Satellites." Hughes Aircraft Co., Space Systems Division, 1966.

5. Sheleg, Boris, "A Matrix-Fed Circular Array for Continuous Scanning." Proceedings of the IEEE, Volume 56, pp. 2016-2027, November 1968.

6. Yaminy, Roger R., "Prototype Electronically Despun Cylindrical Phased Array Antenna, Phase II Technical Report." Radiation Systems Inc., TR-512, April 1970.

10. STRIPLINE STRAP-ON ANTENNA ARRAY

by

A. Waterman and D. Henry

Physical Science Laboratory

New Mexico State University

Prepared for

Array Antenna Conference
Naval Electronics Laboratory Center
San Diego, California
22, 23, 24 February 1972

Physical Science Laboratory

BOX 3549 LAS CRUCES, NEW MEXICO 88001
AREA 505 524-4851 TWX 910-983-0541

STRIPLINE STRAP-ON ANTENNA ARRAY

A. Waterman and D. Henry

Physical Science Laboratory
New Mexico State University

ABSTRACT

The development discussed in this paper was conducted by the Physical Science Laboratory, New Mexico State University, for the Air Force Cambridge Research Laboratory under Contract No. AF 19628-69-C-0177.

The design objectives for this antenna system included the optimization of the following conditions: The array had to be light weight and low profile in order to be strapped-on to the surface of a rocket or placed below the surface of a satellite. The primary frequency of operation was to be in the 2.2 to 2.3 GHz S-band TM region. Coverage was to be omnidirectional, with a maximum 3 dB roll plane variation. The polarization was to be linear, and the gain should be greater than 10 dB below isotropic in all planes except for a 2^{o} allowable null area forward and aft of the vehicle.

The first antenna array constructed was designated as Model No. 55.001, and was flown successfully in May 1971. This array had an 8 slot S-band TM configuration, and a 4 slot C-band beacon. The S-band array was fed in phase with constant impedance 50 ohm striplines using a corporate feed structure. The C-band array was scaled from the S-band design using the same type of feeding system. The S-band slot array was circumferential, however, the C-band system had 2 axial and 2 circumferential slots. Radiation coverage from both systems was adequate, however, the VSWR bandwidth was quite narrow. The 55.001 was flown on a 7.75 inch Niro rocket.

In an effort to increase the VSWR bandwidth, a minor modification to the stripline feed was incorporated in Model No. 55.003. This antenna array is for a 6 inch Astrobee-D rocket, which will be flown in March 1972. The 55.003 is a circumferential 8 slot S-band array. The bandwidth for a VSWR of less than 1.5:1 is approximately 45 MHz, which is a 50% improvement over the 55.001.

The Stripline Strap-On Antenna Arrays mentioned in this report have achieved all of the major design goals. Radiation coverage is at least 96% of the missile area greater than 10 dB below isotropic. Further research is being conducted to increase the VSWR bandwidth, and other vehicle diameters are in the design stages.

Introduction

Stripline antennas have been theoretically proposed since 1954. The construction method and preliminary investigations used in the arrays

discussed in this paper have been previously presented.[1] The main points which led to a successful array design were: a corporate feed structure using constant impedance lines; a $\lambda s/4$ open ended stub ($\lambda s = \lambda/\sqrt{\epsilon}$, ϵ = dielectric constant of the laminate) past the top edge of the slot; a bonding Mylar film to hold the boards together.

Array Design Model 55.001

The calculated acceptable roll pattern variation for the S-band array could be obtained by using a minium of 8 radiating elements.[2] The outer diameter of the configuration, without the radome, was 8 inches and this fixed the circumferential dimension of the cavities at .6 λ. The radiating slots were .45 λ and positioned in the center of their respective cavities. The axial cavity dimension, across the slot, was determined to be .457 λ. Since the impedance at the center of the slots was high and line to slot registration was not extremely critical, the slots were center fed. Four elements were paralleled, and then the two four element sets were again tied in parallel. A $\lambda s/4$ transformer was then added at the center junction for the final impedance matching. The S-band array configuration is shown in Figure 1. Element numbers 1, 4, 5, and 8 are offset slightly, in order to have each element feed point at the correct length from the junction. This same reasoning applied for the area of line around the feed point transformer. VSWR and radiation contour plots are shown in Figures 2 and 3 respectfully. The bandwidth of this array for a VSWR of less than 1.5 was only 30 MHz. The radiation coverage was within specifications, and a typical portion of the flight AGC records is shown in Figure 4.

Using the S-band design information, A C-band beacon array was constructed. Since coverage and VSWR were not critical, a four element array was chosen. Two elements were horizontal and two were vertically polarized. The C-band array configuration is shown in Figure 5. The elements were offset in order to reduce the overall axial length of the array. No attempt was made to transform the final junction impedance because of pressing time commitments. VSWR curves and radiation contour plots appear in Figures 6, 7, and 8.

The flight configuration, for the integrated S- and C-band array, including radome and mounting hardware is shown in Figure 9.

Array Design Model 55.003

The previously discussed design could easily have been scaled to fit the outer diameter of this configuration which is 6.2 inches. However, an attempt to reduce the overall axial length, increase the VSWR bandwidth, and reduce the roll plane variation led us to a few minor design changes.

The roll plane variation was reduced from 3 dB to 2 dB by using 8 radiating slots. This fixed the circumferential dimensions of the cavities at .46 λ, and necessitated reducing the slots to .42 λ. This change in dimensions was easily compensated for by increasing the axial cavity dimension to .48 λ.

The VSWR bandwidth was increased from 30 MHz to 45 MHz by the

combination of three factors. First, a more symmetrical feeding arrangement, starting with two elements in parallel. Each two-element set is then tied in parallel to give four elements. Second, each four-element set is tied in parallel through an odd multiple $\lambda s/4$ line of the same constant impedance previously used. This places the feed point directly in the center of a continuous line rather than near the end of a $\lambda s/4$ stub. Third, the 90° bends in the stripline have been replaced with 45° bends, thereby reducing the fringing discontinuity.

The axial length was reduced by moving the first parallel junctions inside the normal cavity areas without any disturbance to the array resonance. The final configuration is shown in Figure 10.

This model will not include a C-band array and will be flown sometime in 1972. The VSWR curve and radiation contour plot are shown in Figures 11 and 12.

Photographic views of this model are shown in Figures 13 and 14 and are similar to the model 55.001 except for the C-band array and its associated feed point.

Conclusions

The stripline strap-on antenna arrays discussed in this paper can easily be adapted to any size vehicle. Scaling to various frequencies is easily accomplished, and the artennas could be flush mounted if desired. The present designs are for missiles, satellites, and aircraft; however, the techniques could be used on ground based planar arrays.

References

1. A. Waterman and D. Henry, "Stripline Strap-On Antenna Array," Twenty-First Antenna Symposium, University of Illinois, Allerton Park, or Physical Science Laboratory, Report Number PSO0731, October 1971.

2. J. Ricardi, "Directivity of an Array of Slots on the Surface of a Cylinder," Electronic Engineering, September 1967, pp. 578-581.

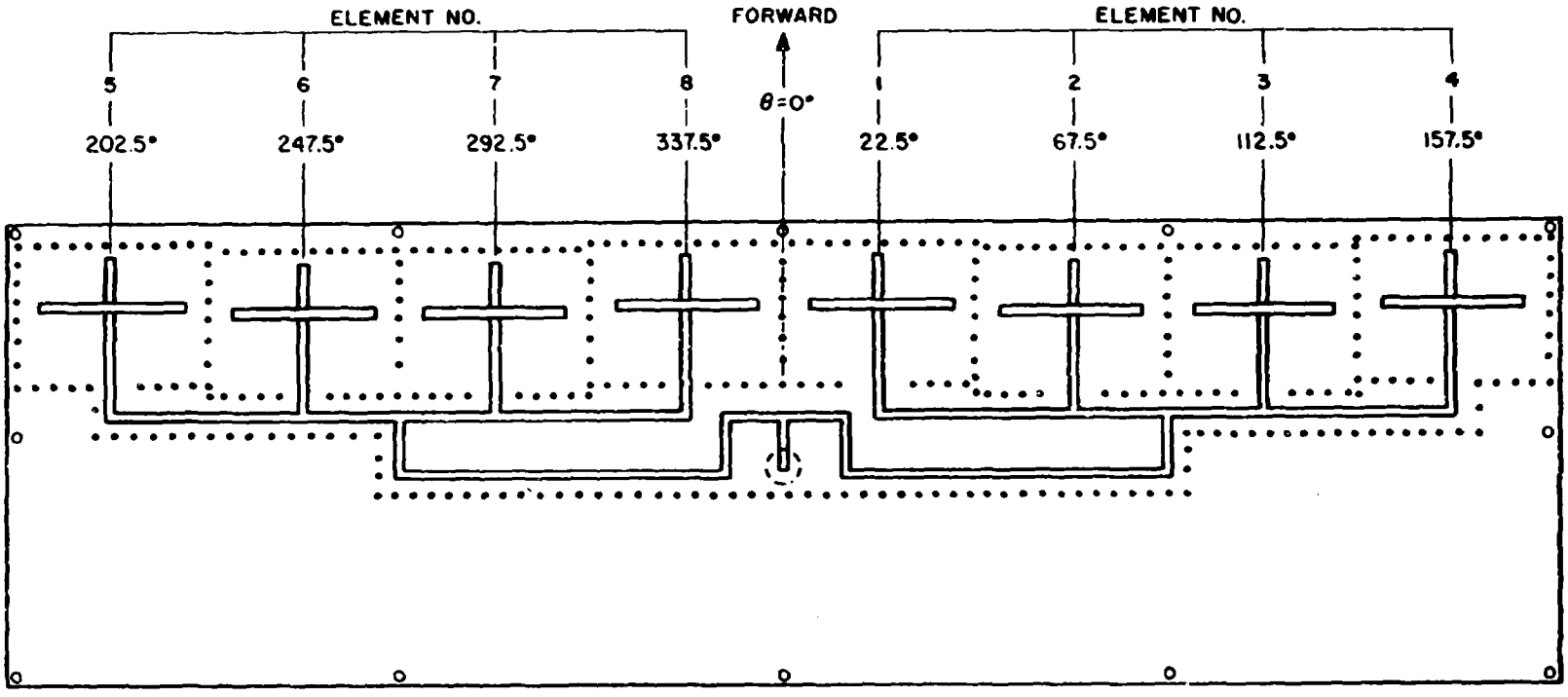

Shown above is the relationship of the slots, rivets and stripline circuit. The slot and rivet locations are on one side of a double clad board, and the stripline feeding arrangement is on the opposite side of the same board. The C-band circuit is shown in Figure 5.

FIGURE 1 S-Band array

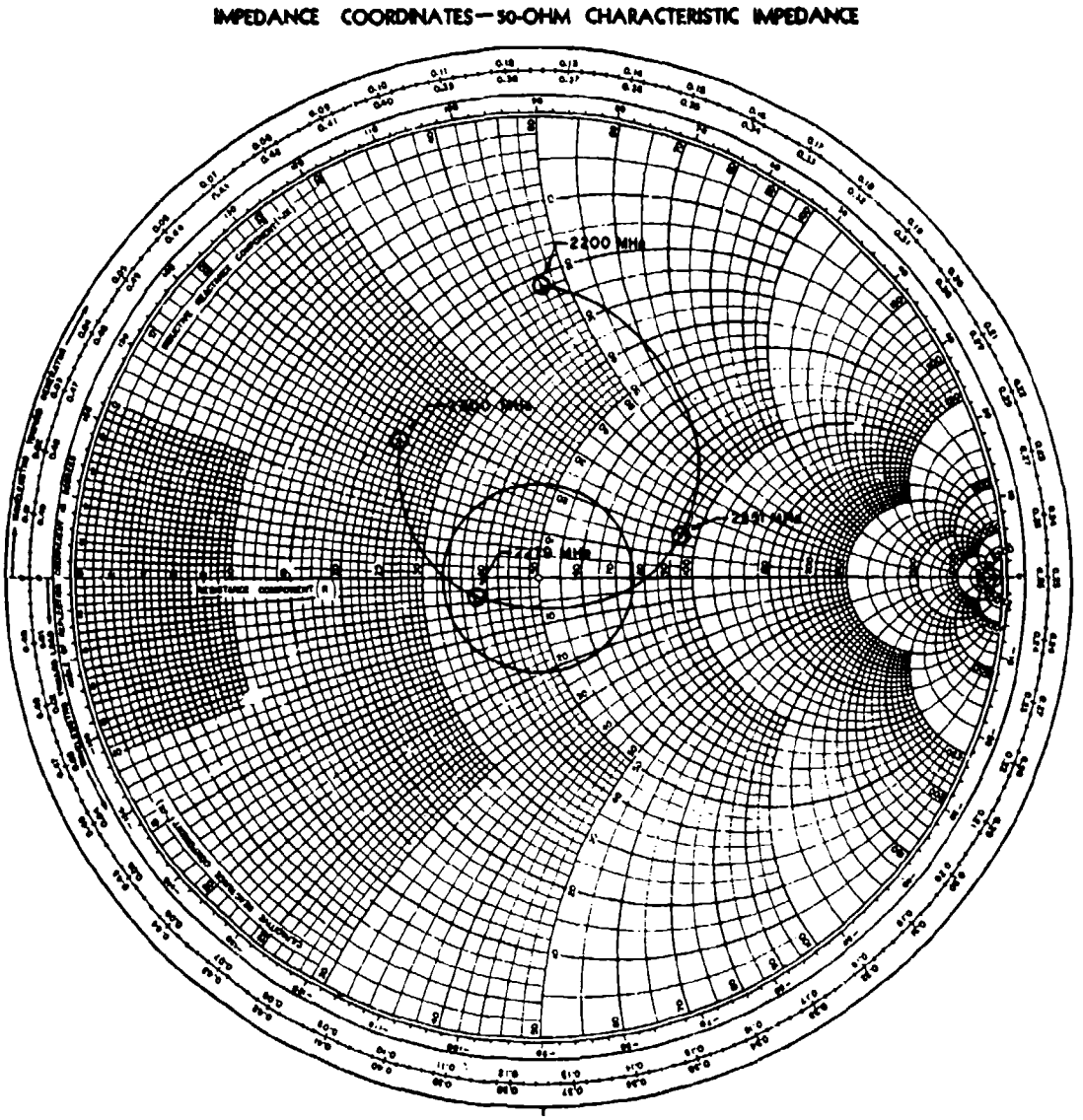

FIGURE 2 S-Band input impedance

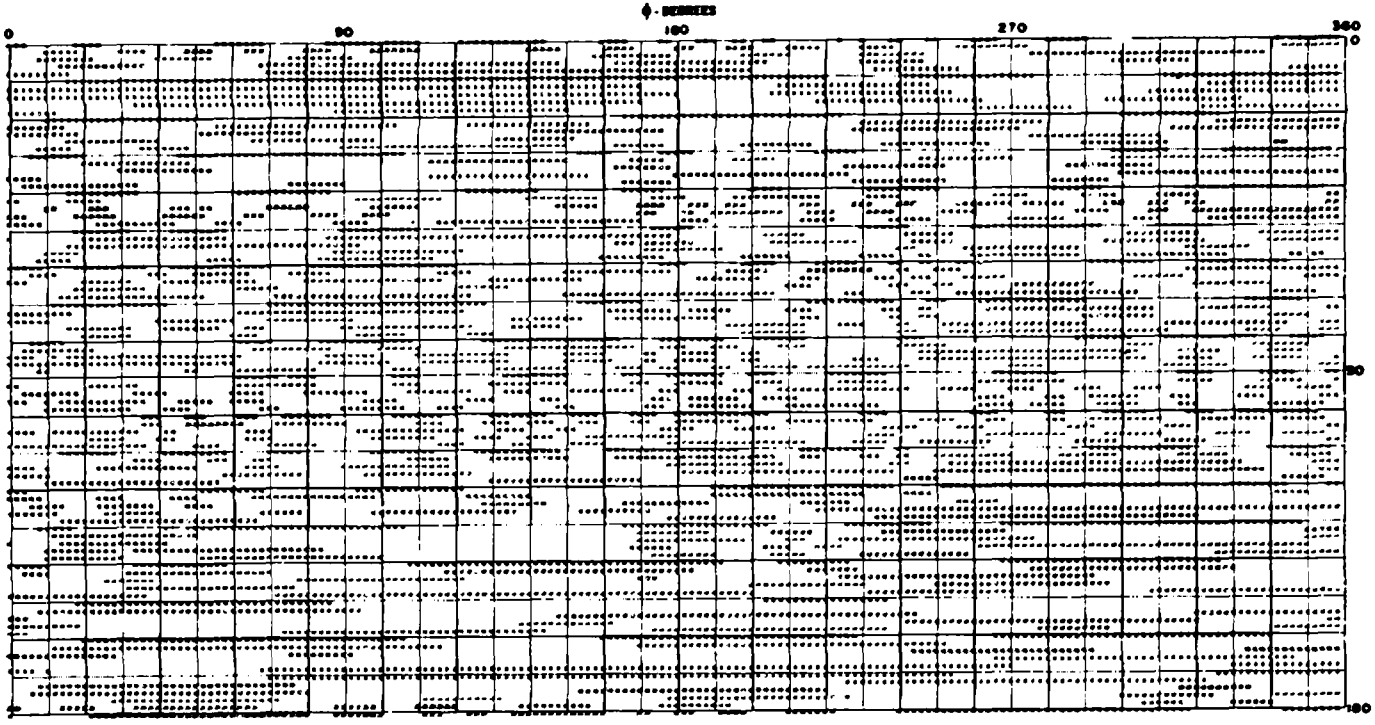

CONTRACT NO: AF 19(628-69-C-0177 PSL FUND NO: 17601 RANGE REQUEST NO: 1779 DATE: 5-16-71

PATTERN MEASUREMENT FREQUENCY: 2264.5 MHz PSL PHOTO NO: N/A ANTENNA MODEL NO: 55.001 MODEL SCALE: 1:1

POLARIZATION COMPONENT RECORDED: RH ARRAY NO: N/A ARRAY PHASING: N/A

GAIN REFERENCE ANTENNA: TYPE AND S/N: SCR 1.7 GAIN OF THE REFERENCE ANTENNA: N/A dB

DESCRIPTION OF TEST ANTENNA: Prototype Integrated S-band and C-band Satellite Array

DESCRIPTION OF VEHICLE MOCKUP: 3' long, 7.75" cylinder with 20° 20" long nose cone

THE NUMBER 10 IN THE POWER CONTOUR GRAPH CORRESPONDS TO -16 dB WITH RESPECT TO THE GAIN REFERENCE ANTENNA.

DESCRIPTION OF THE GAIN MEASUREMENT: Reference PSL Gain Pattern No. 101633

REMARKS: The feed point of the S-band array is designated as θ = 0°.

FIGURE 3 S-Band power contour plot

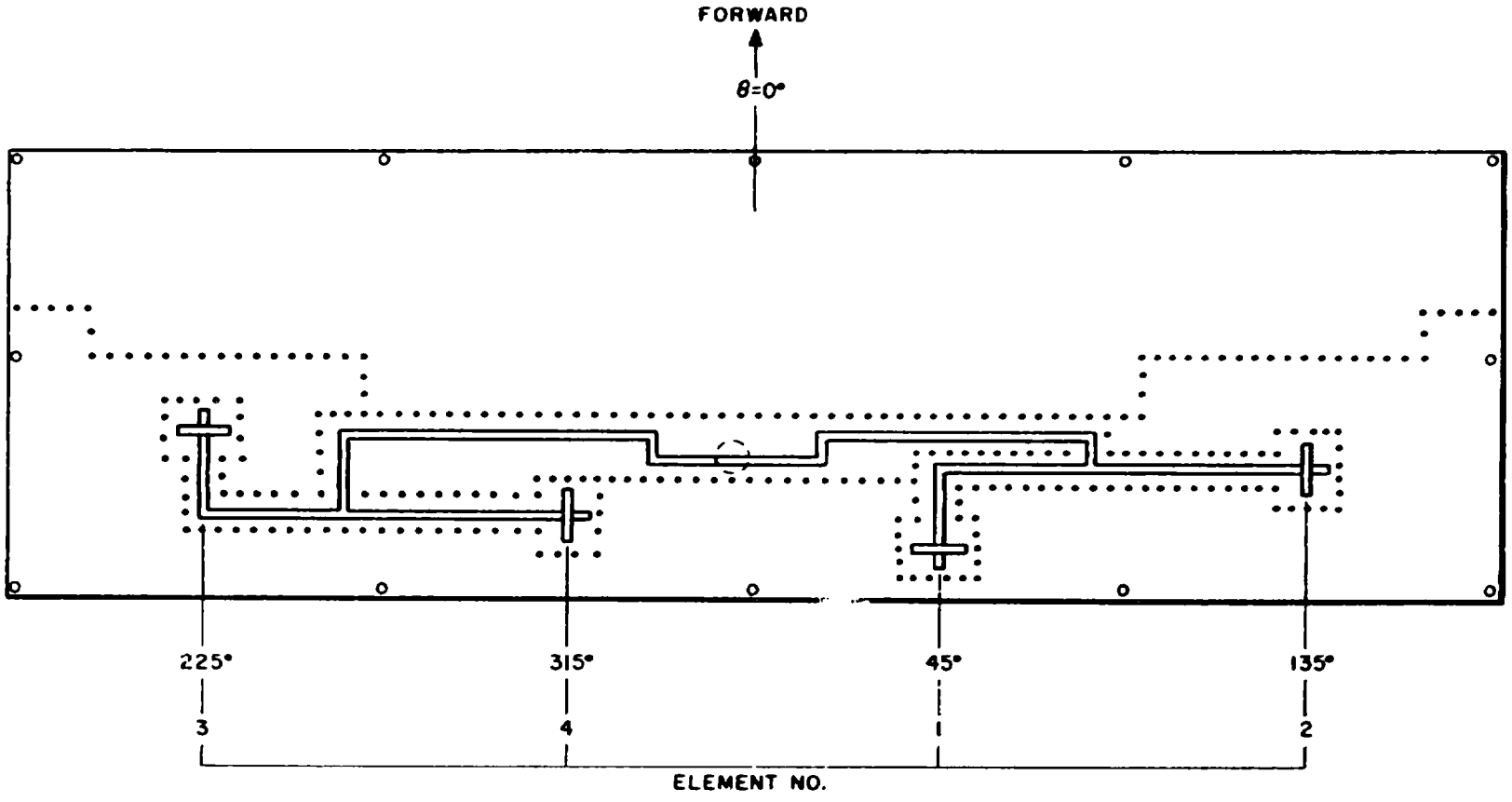

Shown above is the relationship of the slots, rivets and stripline circuit. The slot and rivet locations are on one side of a double clad board, and the stripline feeding arrangement is on the opposite side of the same board. The S-band circuit is shown in Figure 1.

FIGURE 5 C-Band array

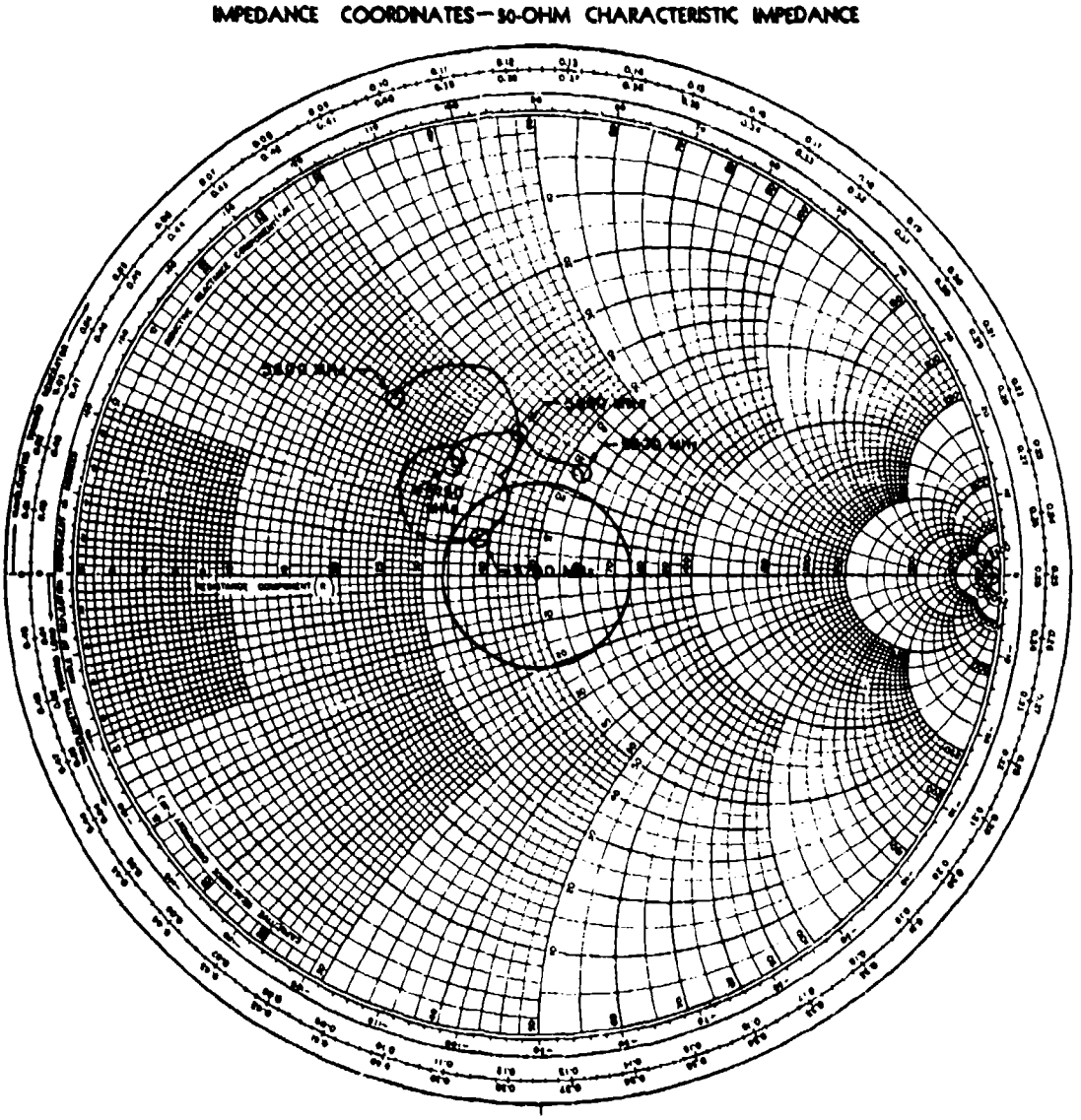

FIGURE 6 C-Band input impedance

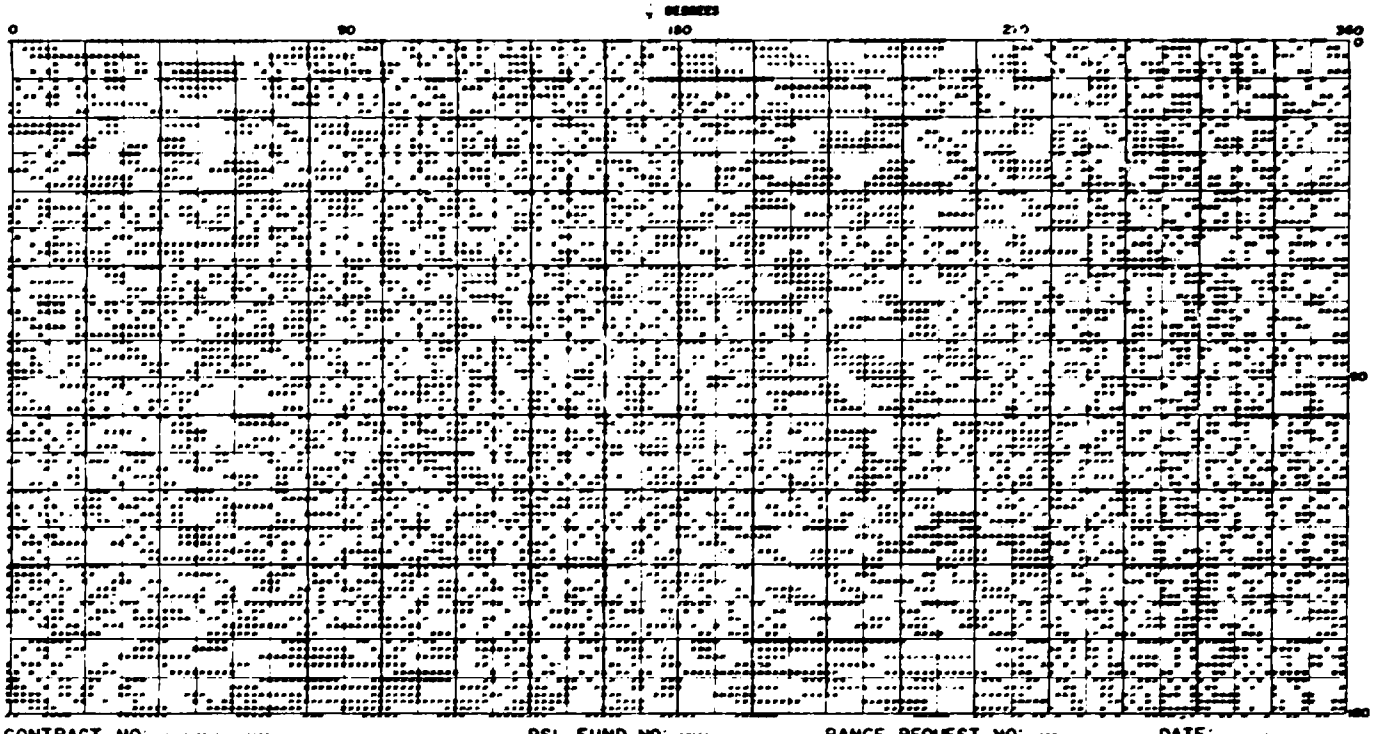

CONTRACT NO: AF 04(694)-69-C-0177 PSL FUND NO: 17661 RANGE REQUEST NO: 1800 DATE: 3 19-71

PATTERN MEASUREMENT FREQUENCY: 5700 MHz PSL PHOTO NO: P/A ANTENNA MODEL NO: 55.091 MODEL SCALE: 1:1

POLARIZATION COMPONENT RECORDED: CP ARRAY NO: P/A ARRAY PHASING: P/A

GAIN REFERENCE ANTENNA: TYPE AND S/N: SCR 1.9 GAIN OF THE REFERENCE ANTENNA: +19 dB

DESCRIPTION OF TEST ANTENNA: Prototype Integrated S-Band and C-Band Slotline Array.

DESCRIPTION OF VEHICLE MOCKUP: 3' long, 7.75" cylinder with 20° 20° long nose cone.

THE NUMBER 10 IN THE POWER CONTOUR GRAPH CORRESPONDS TO -19 dB WITH RESPECT TO THE GAIN REFERENCE ANTENNA.

DESCRIPTION OF THE GAIN MEASUREMENT: Reference PSL Gain Pattern No. 101A55

REMARKS: The feed point of the S-band Array is designated as θ = 0°.

FIGURE 7 C-Band E θpower contour plot

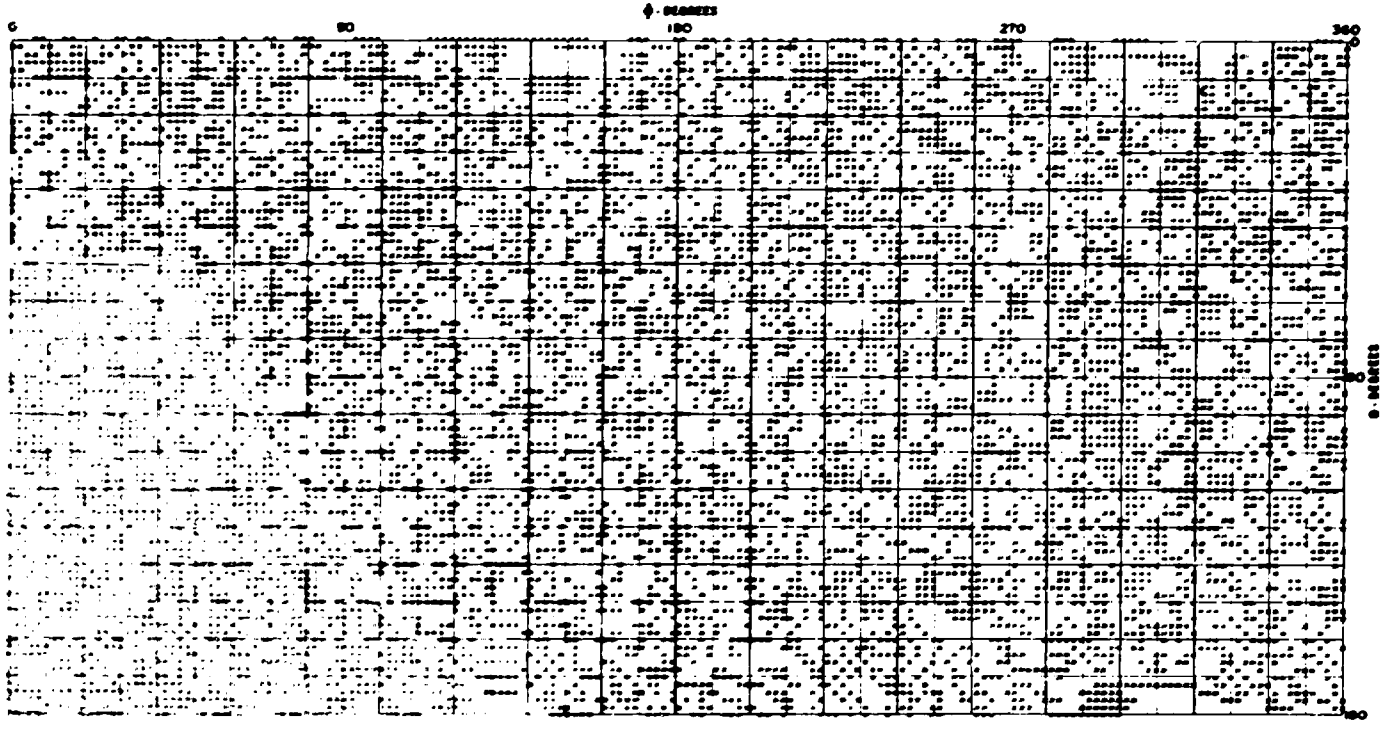

PSL FUND NO. [illegible] RANGE REQUEST NO: 1800 DATE: 3-19-71

PATTERN MEASUREMENT FREQUENCY [illegible] PSL PHOTO NO N/A ANTENNA MODEL NO: 55.001 MODEL SCALE: 1:1

POLARIZATION COMPONENT RECORDED [illegible] ARRAY NO N/A ARRAY PHASING: N/A

GAIN REFERENCE ANTENNA TYPE AND S/N [illegible] GAIN OF THE REFERENCE ANTENNA: +19 dB

DESCRIPTION OF TEST ANTENNA [illegible]

DESCRIPTION OF VEHICLE MOCKUP [illegible]

THE NUMBER [illegible] IN THE POWER CONTOUR GRAPH CORRESPONDS TO [illegible] dB WITH RESPECT TO THE GAIN REFERENCE ANTENNA.

DESCRIPTION OF THE GAIN MEASUREMENT [illegible]

REMARKS [illegible]

FIGURE 9 C-Band L power contour plot

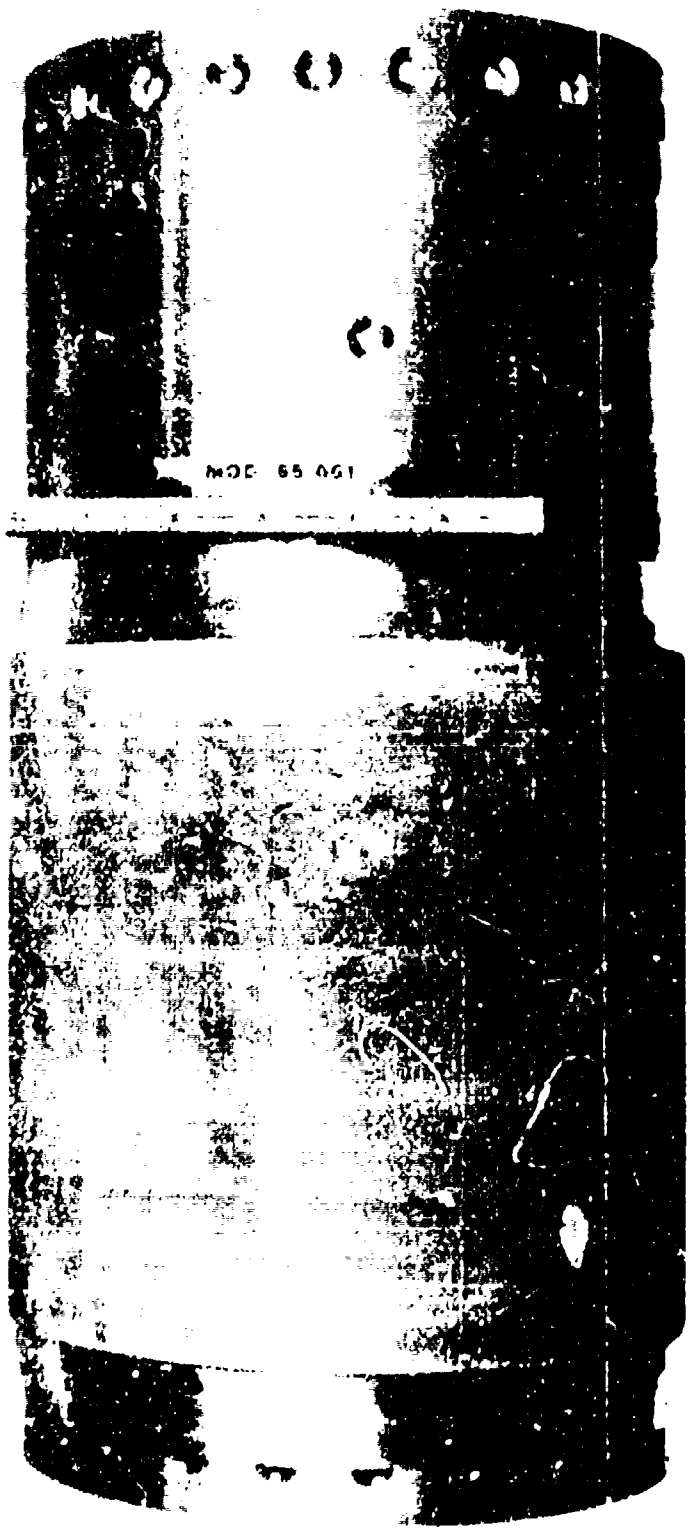
MDE 65 051

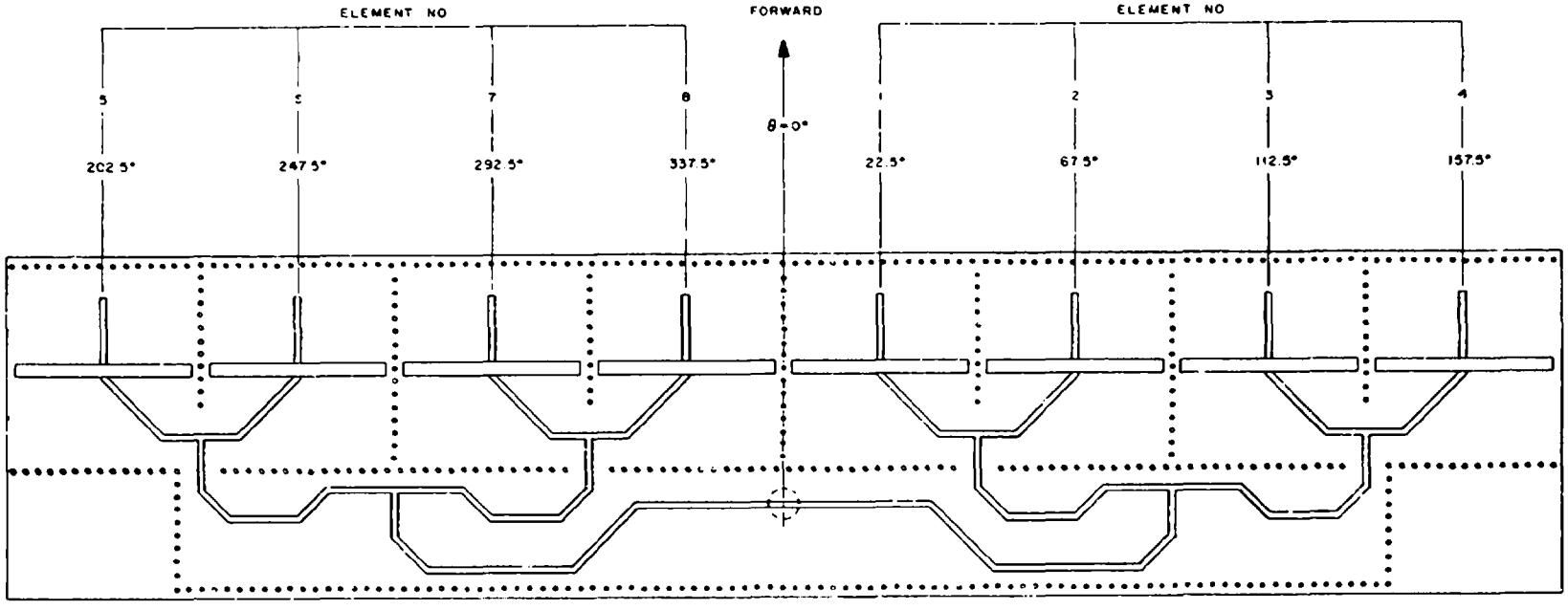

FIGURE 10 Model 55.003

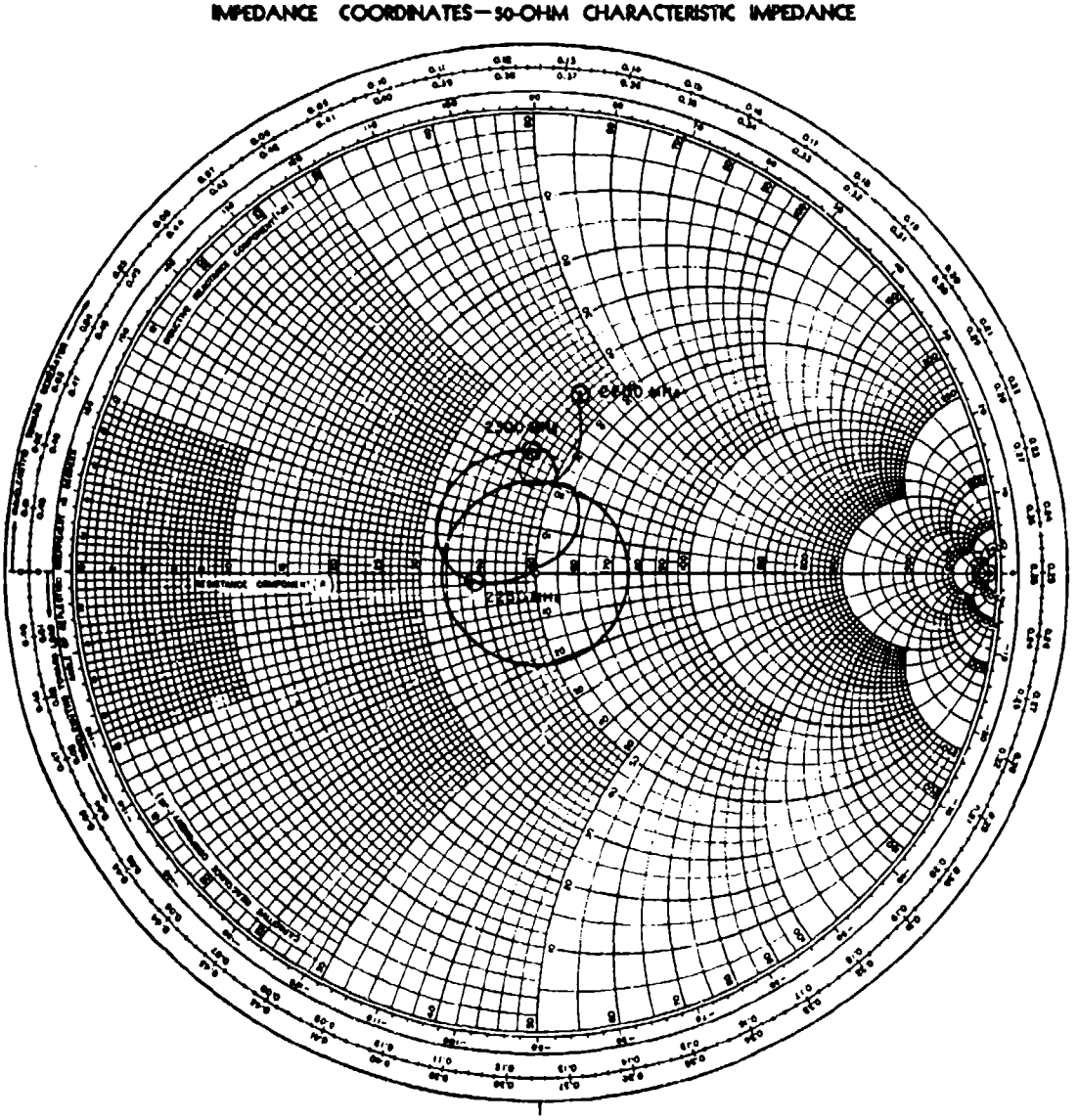

FIGURE 11 Model 55.003 VSWR curve

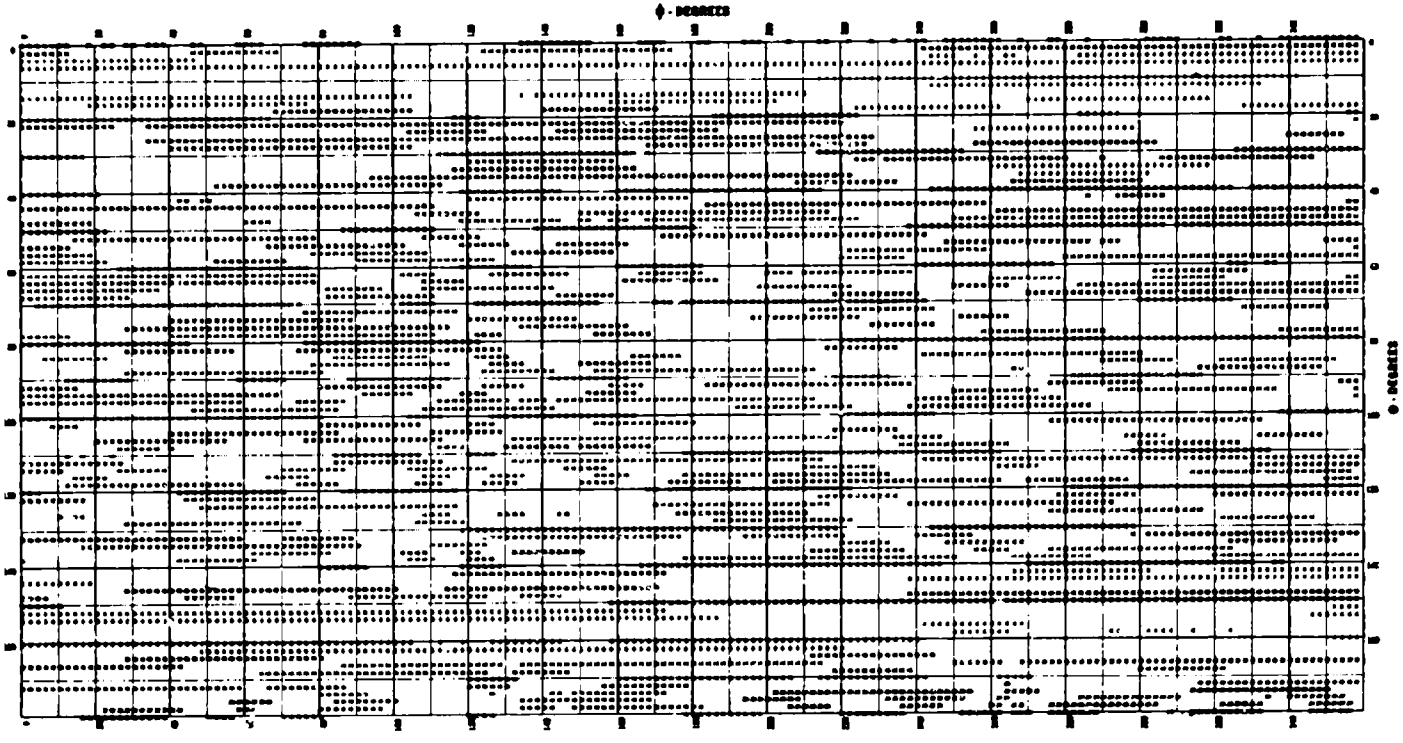

CONTRACT NO: AF 19628-69-C-0177 PSL FUND NO: 17601 RANGE REQUEST NO: 1863 DATE: 10-25-71

PATTERN MEASUREMENT FREQUENCY: 2.25 GHz PSL PHOTO NO: N/A ANTENNA MODEL NO: 55.003 MODEL SCALE: 1:1

POLARIZATION COMPONENT RECORDED: RP ARRAY NO: N/A ARRAY PHASING: N/A

GAIN REFERENCE ANTENNA: TYPE AND S/N: SGH 1.7 GAIN OF THE REFERENCE ANTENNA: +16 dB

DESCRIPTION OF TEST ANTENNA: Prototype S-Band Stripline Array (8 elements)

DESCRIPTION OF VEHICLE MOCKUP: 6" diameter cylinder, Array mounted in center of 6' long mockup

THE NUMBER 10 IN THE POWER CONTOUR GRAPH CORRESPONDS TO -16 dB WITH RESPECT TO THE GAIN REFERENCE ANTENNA.

DESCRIPTION OF THE GAIN MEASUREMENT: Reference PSL gain pattern No. 10464)

REMARKS: The feed point of the array is designated as $\theta = 0^{\circ}$

FIGURE 12 Model 55.003 radiation contour plot

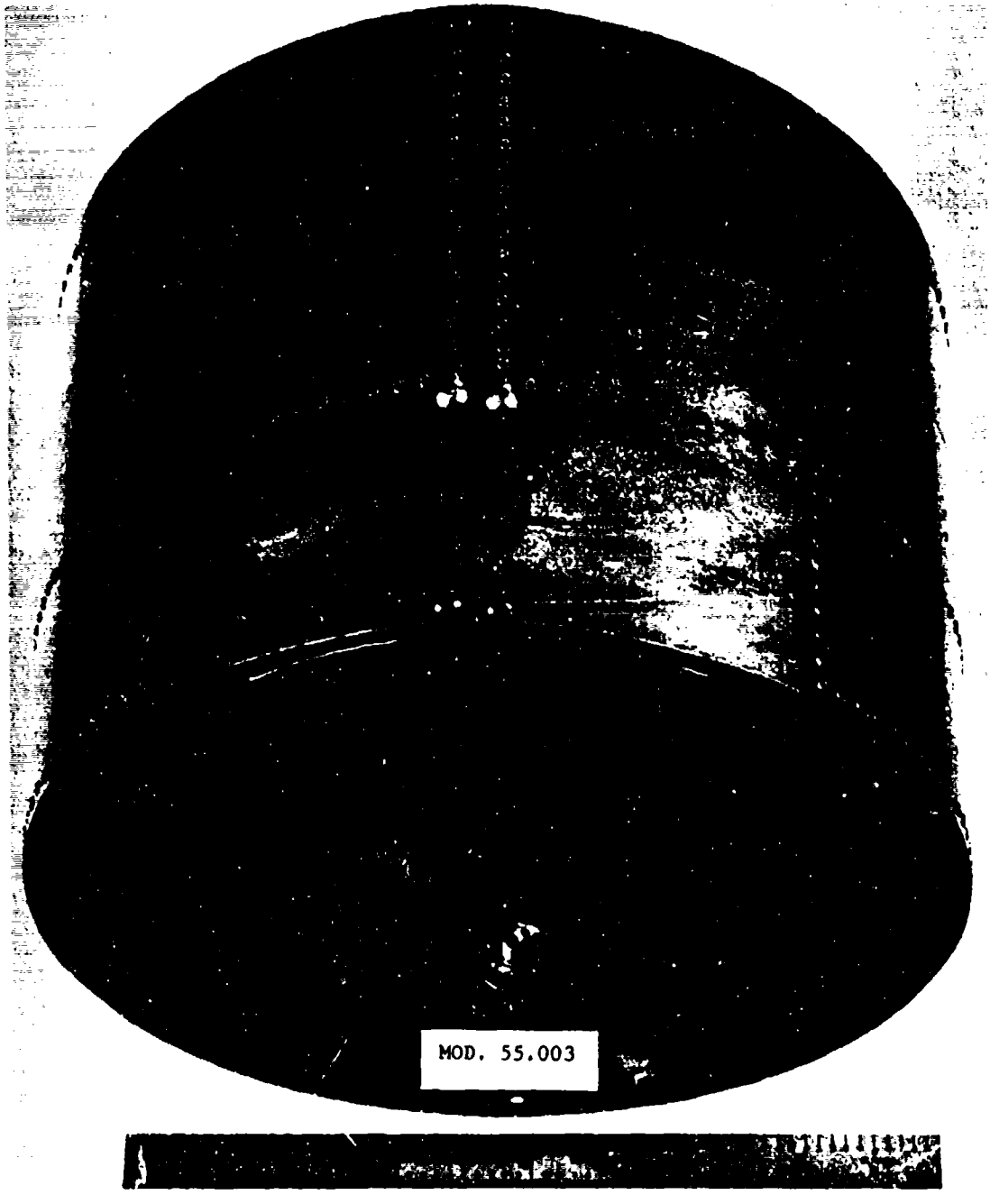

FIGURE 13 Model 55.003 View of the feed point

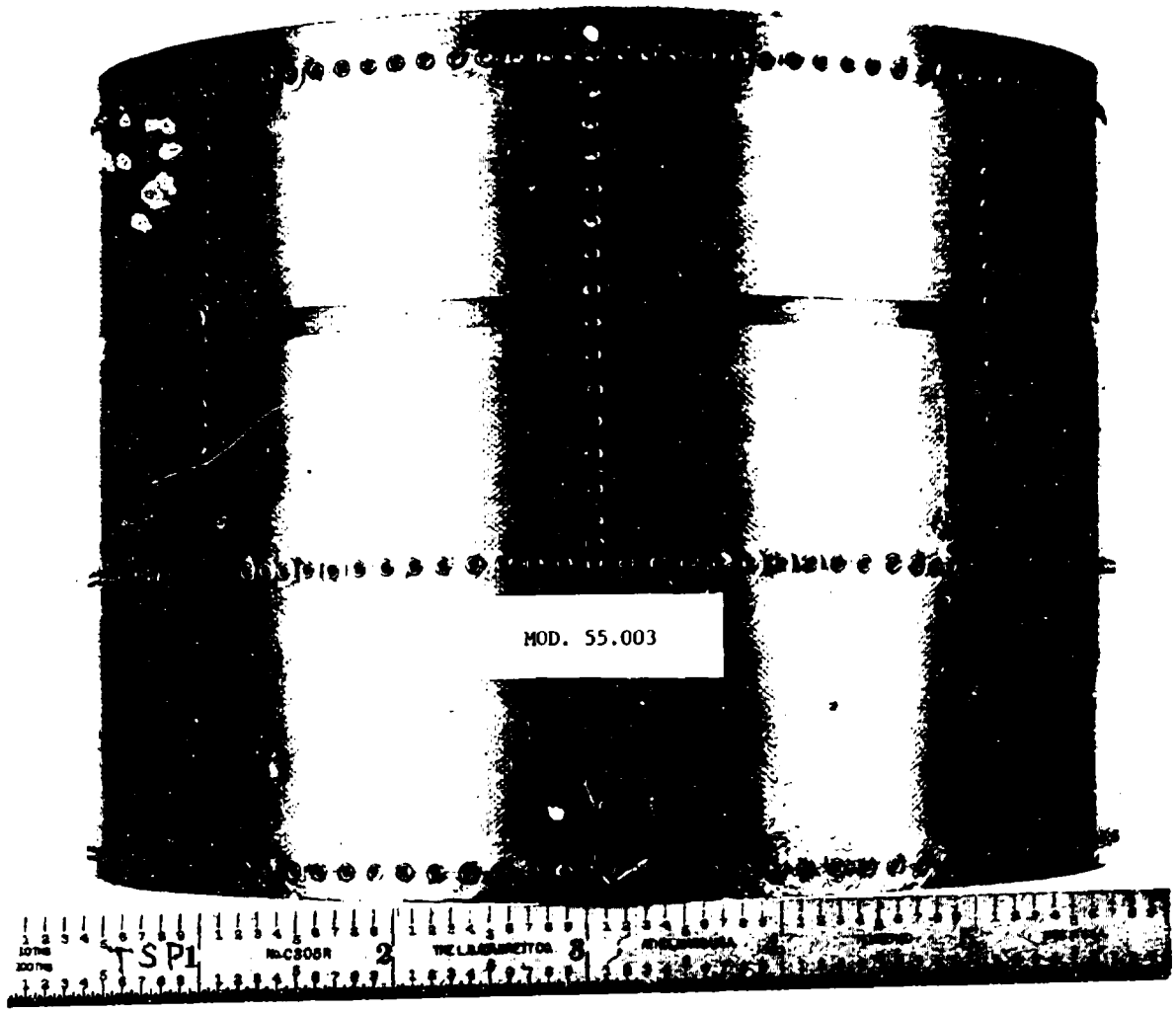

FIGURE 14 Model 55.003 full scale view

11. A NEW SIMULATOR TECHNIQUE FOR PHASED ARRAYS

by

J. J. Gustincic

Chalmers University of Technology
Gothenburg, Sweden

for

ARRAY ANTENNA CONFERENCE

Naval Electronics Laboratory Center
San Diego, California

22,23,24 February 1972

ABSTRACT

The usual methods of measuring infinite array input impedance by means of rectangular waveguide simulators have undesirable features in that a separate simulator must be constructed for each scan angle with no straightforward means of obtaining the input impedance at any general scan angle. This paper describes general measuring techniques and experimental results obtained on a new type of simulator utilizing multiple elements in a multi-mode rectangular waveguide. The technique is valid for element spacings which allow grating lobes and is quite general in that it can be applied to an array with any polarization so long as the elements are symmetric about their vertical and horizontal axes and so long as the array spacing is rectangular or triangular.

The proceedure is demonstrated on a simulator containing 25 stripline slot elements. By measuring one row of the scattering matrix of the input lines to the slots, the reflection coefficient for the infinite array is obtained at 25 angles of scan, 20 of which are in real space. The 25 values of the reflection coefficient are actually the eigenvalues of the scattering matrix of the simulator element feedlines and are used in an eigenvalue expansion to give an interpolation to the input reflection coefficient at any scan angle. The interpolation is shown to have the physical significance of being the reflection coefficient at the center element in a 100 element sub-array when such sub-arrays are arrayed side by side to form an infinite array. It is shown that each of the eigenvectors of the scattering matrix and the individual modes of the simulator waveguide are related as in a reciprocal two-port network allowing sliding load techniques to be utilized during the measurements to eliminate the problems associated with an imperfect load in the multimode simulator guide.

This work was supported by the Swedish Board for Technical Development and the LM Ericsson Telephone Co., MI-Division, Mölndal, Sweden.

BASIC PRINCIPLES

Waveguide array simulators basically fall into two general classes. The first class contains the single active element simulators in which the active infinite array impedance is directly measured at one scan angle by measuring the input impedance to a single excited element radiating into a loaded waveguide. In the second category are the multi-element simulators in which a number of loaded elements are illuminated by a waveguide mode and the mode reflection measured. The array impedance is then obtained through reciprocity by means of an equivalent circuit for the element waveguide interface. One scan angle is simulated for each different waveguide mode incident and a separate high order mode launcher and reflection measuring scheme must be provided for each desired angle.

The measurement technique described here circumvents the problems of high order mode launching and also allows the array impedance to be measured at a number of scan angles in a single simulator. Fundamentally the procedure consists of using a multi-element simulator with the simulator waveguide terminated in a matched load. By determining certain of the scattering coefficients between the simulator elements, the reflection coefficient which would occur if the elements were fed in such a way as to excite a particular high order mode can be calculated by superposition in a digital computer. Once these scattering coefficients have been determined, the computer can be used to "launch" each of the simulator waveguide modes separately so that the array behavior can be determined at all the angles within the range of modes supported by the simulator.

Figure 1 shows a multi-element simulator of the type ordinarily used[1] with a high order mode launcher in the rectangular waveguide. The waveguide has a width a and a height b. The simulator contains N elements with element positions given by x_i, y_i , $i = 1,2,..N$. In the following it will be assumed the elements are vertically polarized with similar results applicable in the case of horizontal polarization. With the output waveguide terminated in a matched load, let the scattering coefficients between the k th simulator element and all the other elements, S_{kj} , $j = 1,2,..N$, be measured. This involves N - 1 transmission coefficient measurements between the k th element and each of the other elements and one reflection coefficient measurement at the k th element. The feedlines of the elements which are not directly involved in the measurements must of course be terminated in matched loads. The results of these N measurements can then be used to compute the infinite array impedance at N scan angles in the following way.

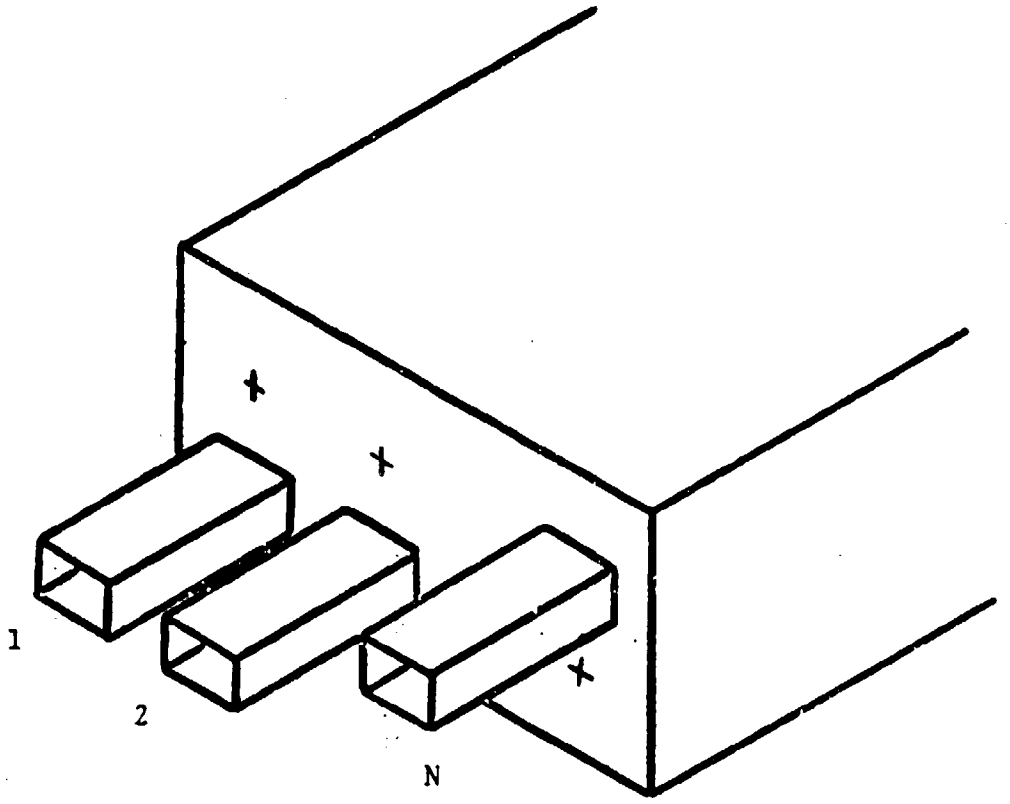

Figure 1. A general simulator consisting of N array elements radiating into a rectangular waveguide.

the infinite array reflection coefficient for the various scan angles simulated are simply the eigenvalues of the scattering matrix of the simulator elements and the a_i are the eigenvectors.

AN H-PLANE SIMULATOR

The first attempt in applying this method was made in a three element H-plane simulator. This simple case for which m = 0 and n = 1,2,3 provides an excellent illustration of the previous concepts. The simulator is shown in Figure 2. The radiating elements are dumbell shaped stripline slots surrounded by mode suppression screws. The measurements were made at a design frequency of 9.5 Ghz. The slot spacing was chosen to be $0.538\lambda_0$ and the waveguide height $0.475\lambda_0$. The element spacing is such that a grating lobe enters real space at a scan angle of 60°. The waveguide width is three times the element spacing so that from (2) it is seen that the simulator can simulate the infinite array at the three H-plane scan angles of $\theta = 18^\circ$, 38° and 68°. The grating lobe radiation is also simulated at the 68° scan angle by the TE_{30} mode. At this scan angle the grating lobe and main beam make the same angle with respect to broadside. The three eigenvector excitations, (a_1, a_2, a_3), which correspond to the three scan angles simulated can be obtained from (1) as

$$\left(\frac{1}{2}, 1, \frac{1}{2}\right) \qquad \left(\frac{\sqrt{3}}{2}, 0, \frac{-\sqrt{3}}{2}\right) \qquad (1, -1, 1)$$

and these are easily seen to be the excitations required to generate the TE_{10}, TE_{20} and TE_{30} modes respectively. With the elements numbered 1,2 and 3 from right to left in Figure 2 and the waveguide terminated in a tapered load, the scattering coefficients for the number 1 element were measured with a network analyzer and found to be

$$S_{11} = .56\angle 42^\circ \qquad S_{12} = .09\angle 168^\circ \qquad S_{13} = .04\angle -36^\circ$$

The input reflection coefficient to the array under scan was then calculated by means of the k = 1 equation in (4) for the three scan angles as follows.

$$\Gamma_{10} = S_{11} + 2S_{12} + S_{13}$$
$$\Gamma_{20} = S_{11} + 0 - S_{13}$$
$$\Gamma_{30} = S_{11} - S_{12} + S_{13}$$

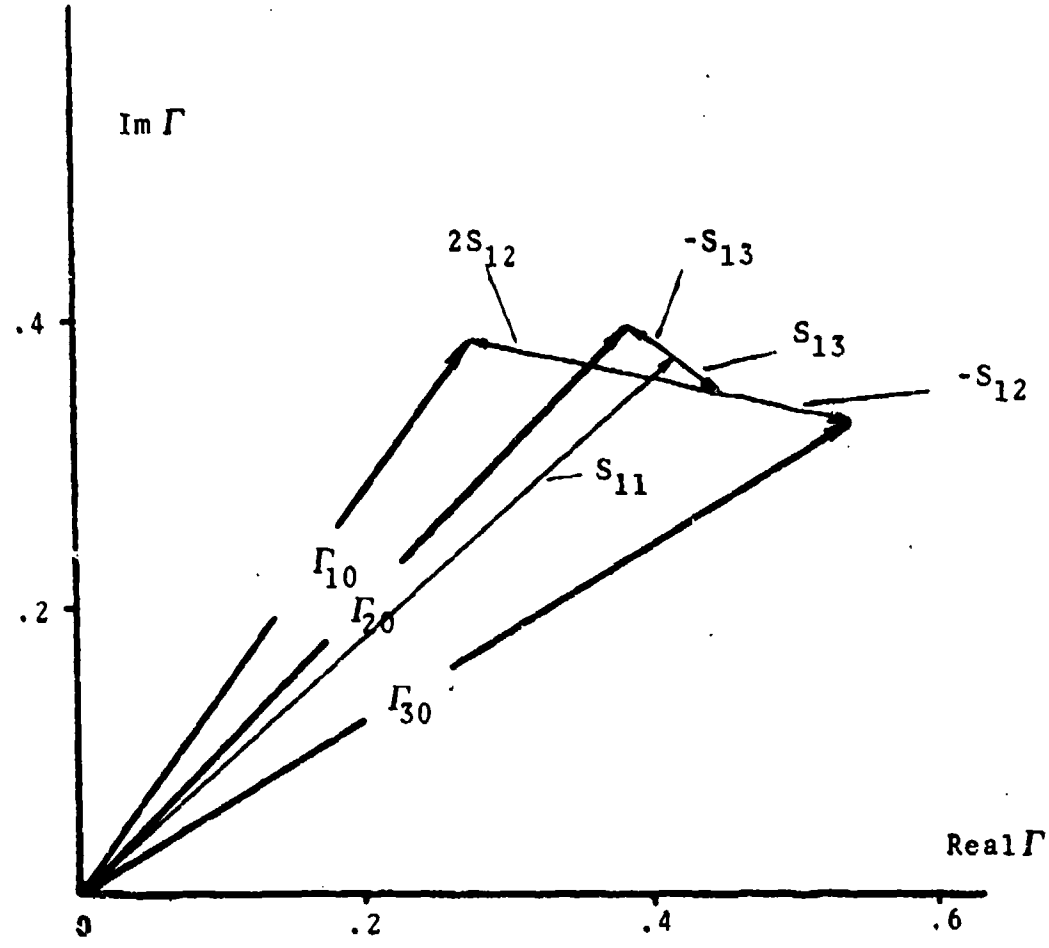

Figure 3. Graphical computation of the input reflection coefficients.

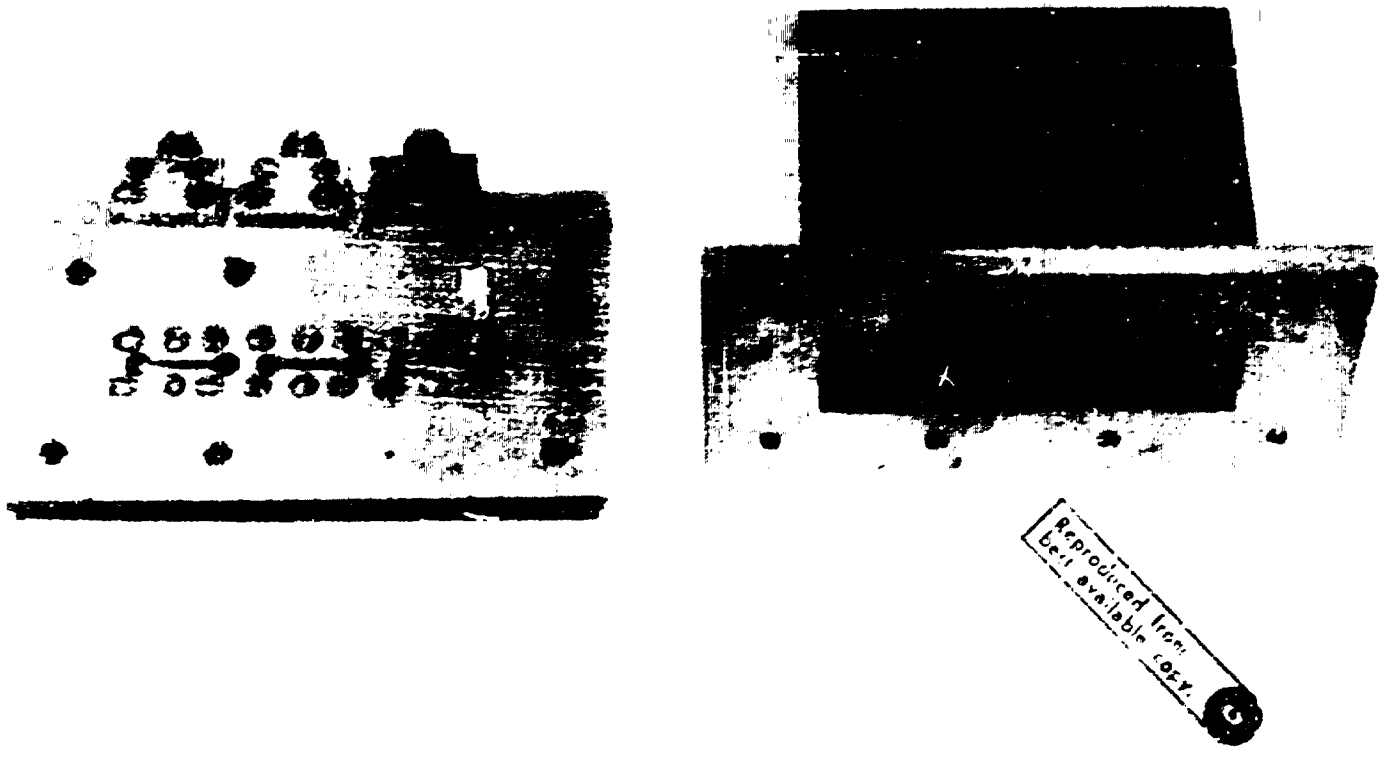

Figure 2. The three element biplane simulator.

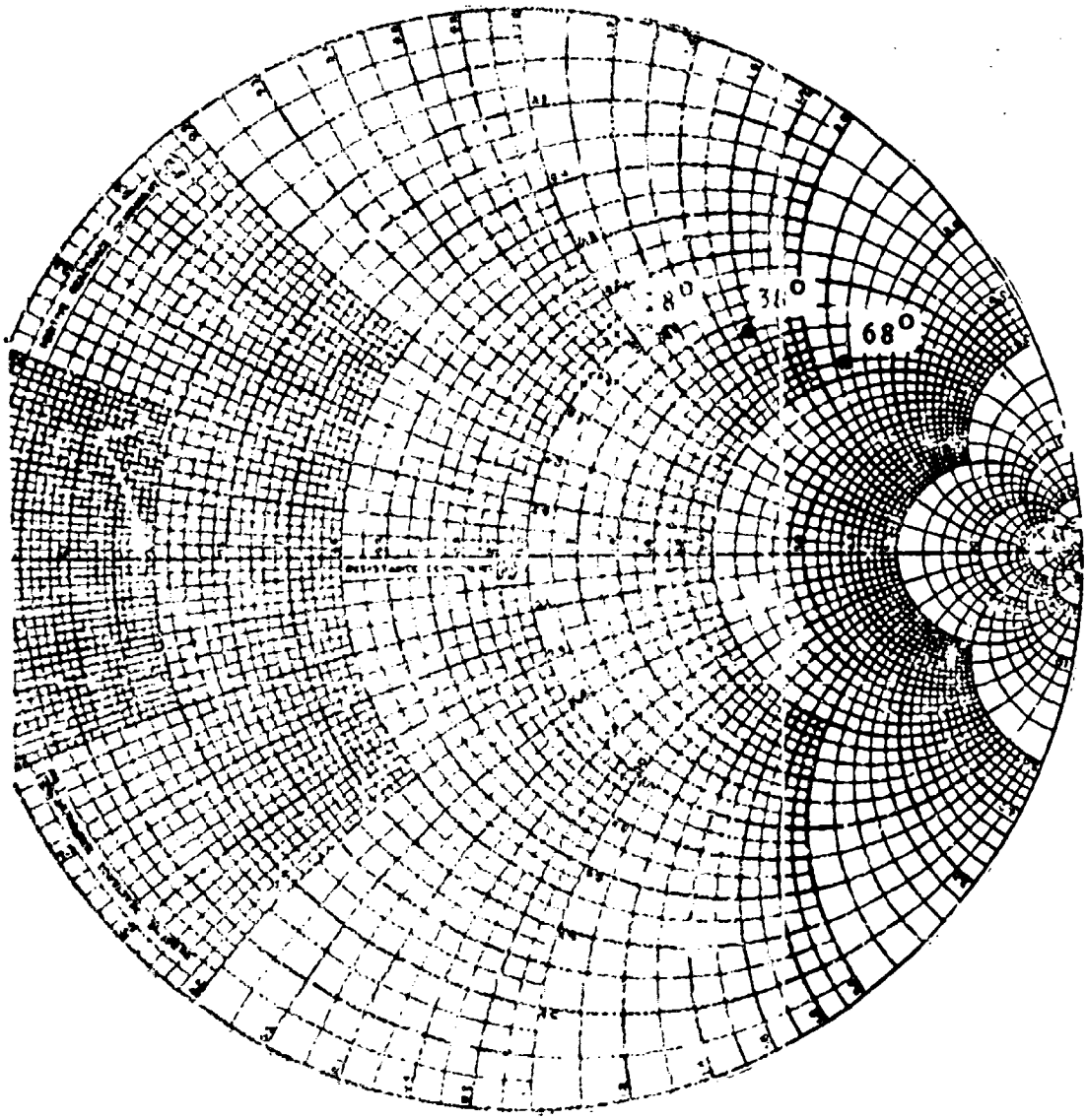

Figure 4. The input impedance to the infinite array at three angles of scan.

This computation is carried out graphically in Figure 3 in order to illustrate how the total reflection occurs. It is seen from this Figure that in this representation the primary component of the Γ_{n0} is S_{11}, the reflection coefficient of port 1 when the other ports are matched. This component of the reflection is mainly due to the mutual coupling in the E-plane between the simulator slot and the infinite array of slots which are the images in the top and bottom walls. The slot used in the simulator is matched and has no reflection when radiating alone on a ground plane. The variation of the reflection coefficient with scan is seen to be associated with the cross coupling between the simulator elements. The input impedance to the infinite array at the three scan angles is shown on the Smith chart of Figure 4. The impedance is referred to the terminal plane where the input feedline crosses the centerline of the slot.

THE TWENTY-FIVE [illegible] T SIMULATOR

With the apparent success of the three element simulator it was decided to proceed with a 25 element simulator in order to obtain information for scan plane angles greater than zero. The simulator elements and output waveguide can be seen in Figure 5. The elements are slots similar to those of the three element simulator and the element spacing is identical. Twenty-three of the elements are terminated in stripline pill terminations which are shown exposed in the Figure. The remaining two elements are provided with coax connectors for use in the transmission measurements. The required 25 measurements were then made by interchanging element positions. Great care had to be taken to adequately electrically seal any cracks between elements in order to obtain consistently repeatable results. The simulator is capable of simulating the infinite array at the 25 scan angles given below along with the corresponding mode numbers.

	m =	0	1	2	3	4
n = 1	θ =	10.6°	16.3	27.4	41.2	59.6
	ϕ =	0.0°	48.7	66.3	73.7	77.6
2		21.7	25.2	34.1	47.1	66.9
		0.0	29.7	48.7	59.7	66.3
3		33.7	36.4	44.1	57.2	-
		0.0	20.8	37.2	48.7	56.7
4		44.7	50.2	58.3	76.5	-
		0.0	15.9	29.7	40.5	48.7
5		67.5	71.4		-	-
		0.0	12.8	24.5	34.4	42.4

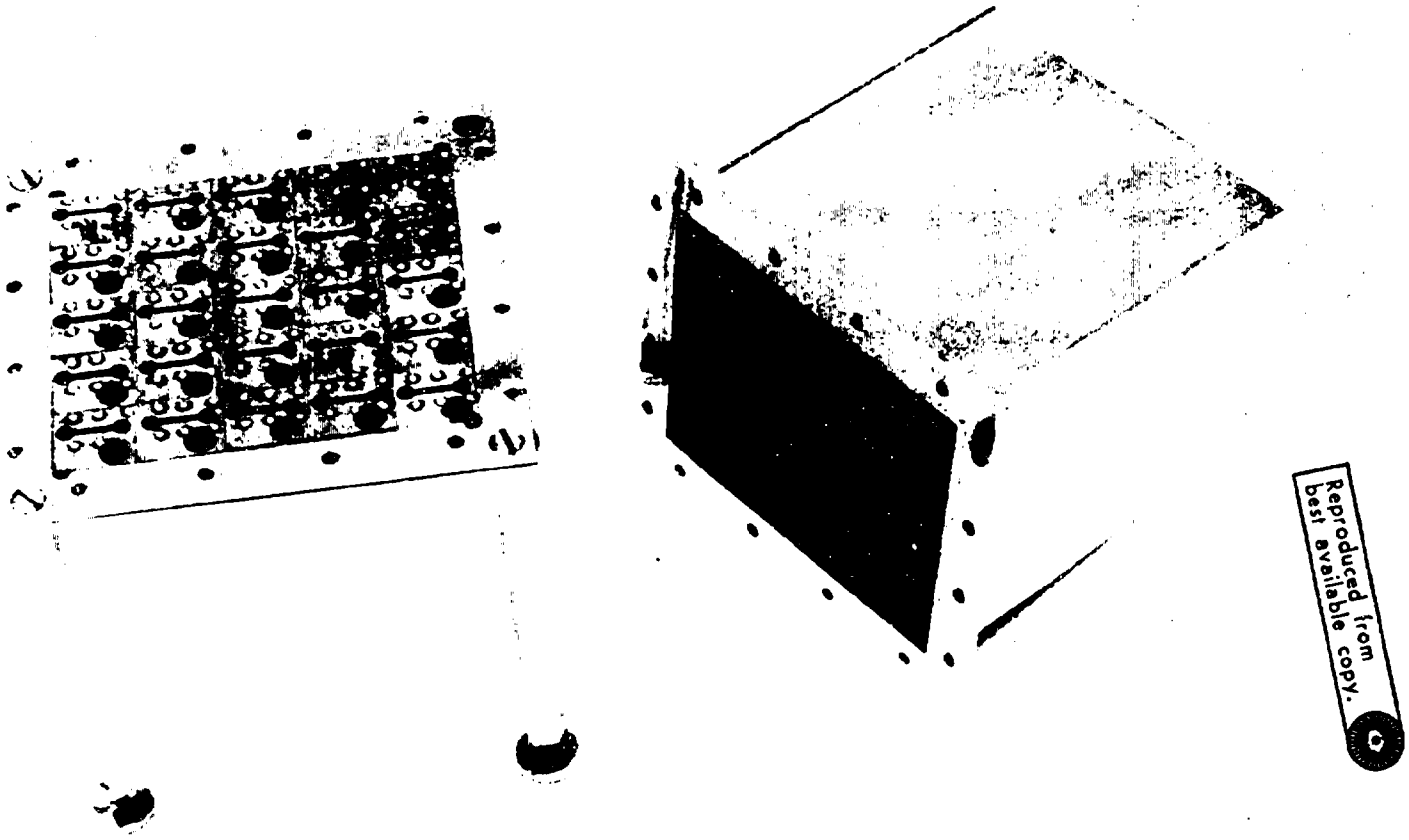

Figure 5. The 25 element infinite array simulator.

The five missing scan angles in this table correspond to cut-off modes where the array is scanned into imaginary space.

With such a large number of waveguide modes the problem of constructing an adequate absorbing termination for the simulator waveguide becomes formidable. To overcome this difficulty a sliding partially reflecting termination was constructed of flat absorber material. The termination can be seen in Figure 6 along with a shorting plate which was used to check for ohmic losses. It is well known[2] that as the sliding termination is moved toward the array elements, the small reflection from this imperfect load modifies the input reflection coefficient in such a way that it approximately describes a small circle about its true value. The center of the circle then gives the reflection coefficient for a perfectly absorbing termination. The rate at which the reflection coefficient goes around the circle for a given movement of the load is determined by the guide wavelength of the mode being reflected by the termination.

The 25 required scattering coefficients of the simulator were measured for five equally spaced load positions and some concern was expressed when the measurements appeared to have a purely random correlation to the position of the load. However, after the computer processing of equation (4), the randomness vanished in a rather dramatic fashion. Figure 7 shows some typical computed reflection coefficient loci with the load positions being numbered 1 to 5 (position 5 being nearest to the radiating elements). For the 1,0 mode, a simple calculation shows that moving the termination from position 1 to position 2 should correspond to a movement around the small circle of 225° while for the 2,4 mode the same movement would correspond to only 89° since that mode is nearer to cutoff and has a longer wavelength. From the loci of Figure 7 it is seen that the computer did indeed launch the 1,0 and the 2,4 mode independently of one another demonstrating the validity of the technique.

Also shown in Figure 7 is the locus of the reflection coefficient for the 3,4 mode which is evanescent in the simulator guide. At position 5 the load is immersed in the reactive fields in front of the simulator elements. As the load is moved away from the elements it absorbs less and less energy until finally the reflection coefficient approaches unity magnitude for the waveguide which is cutoff.

INTERPOLATION

When the excitation (1) is applied to the elements of the

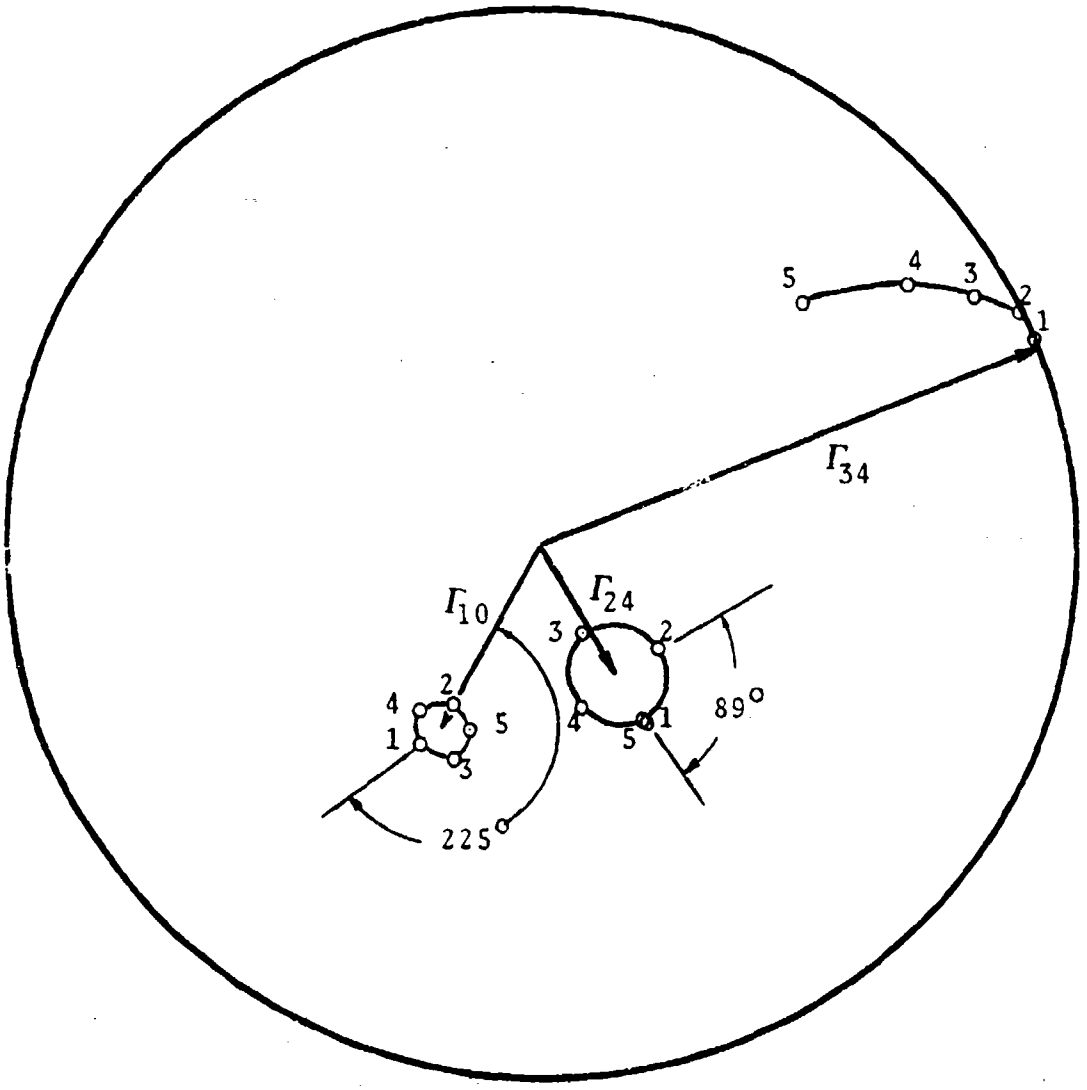

Figure 7. Reflection coefficients as obtained from the computer processing.

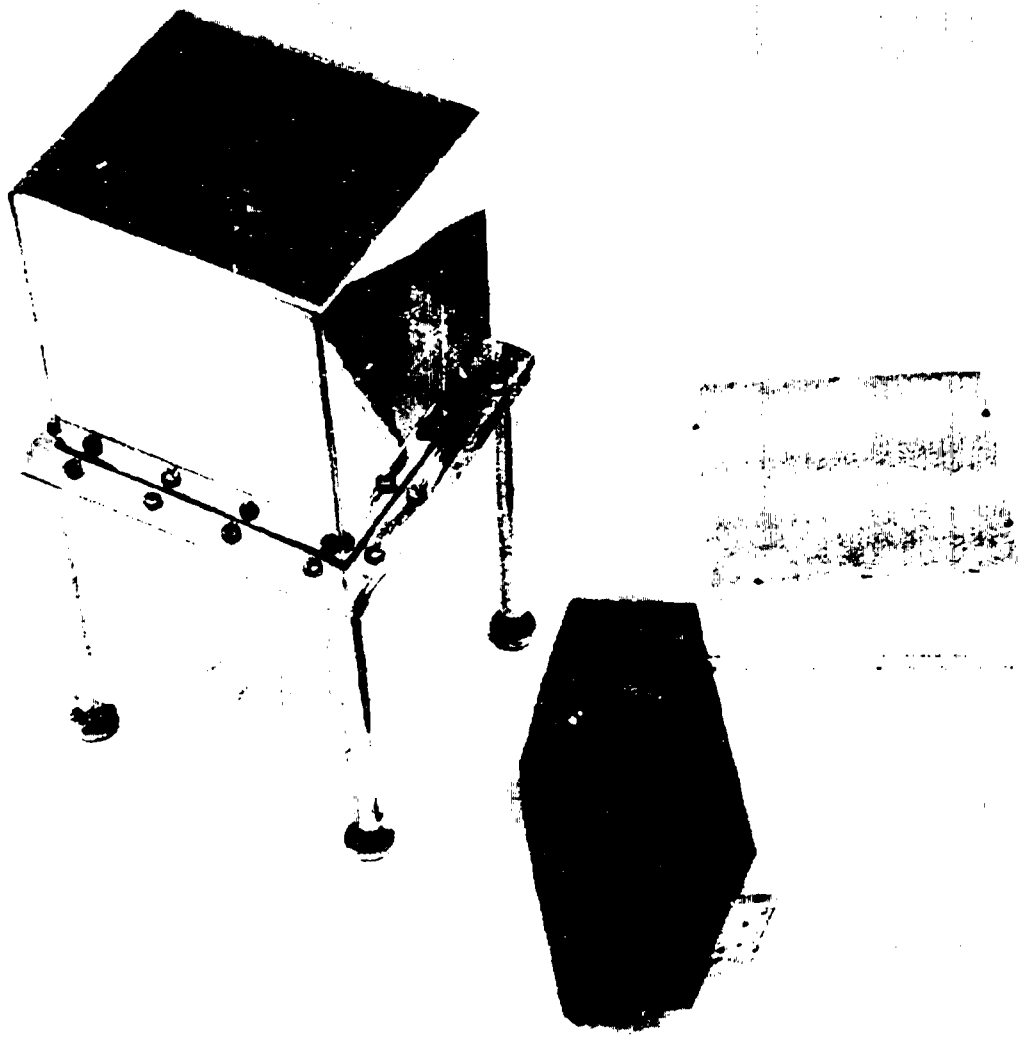

Figure 6.

The sliding load.

simulator, they radiate as if they were in an infinite array because their images in the waveguide walls form the infinite array environment. If a general excitation of the form

$$A_i = \sin ux_i \cos vy_i \qquad i = 1,2,..N \tag{6}$$

is applied to the simulator elements, their images can also be thought of as forming an infinite array. The infinite array in this general case is made up of an infinite number of identical sub-arrays, arranged side by side in the x-y plane. The basic sub-array extends from $x = -a$ to $x = +a$ and $y = -b$ to $y = +b$ with elements located at $\pm x_i, \pm y_i$, $i = 1,2,..N$. The excitation of these elements is given by (6). When excitation (6) corresponds to one of the eigenvalue excitations, i.e., $u = n\pi/a$, $v = m\pi/b$, the excitation from sub-array to sub-array is continuous and the homogeneous infinite array is formed. For values of u and v between these points, amplitude discontinuities exist between the sub-arrays and a zoned infinite array results. If the simulator is large enough, the input impedance to an element near the center of the sub-array should approximate that of an infinite array. This is particularly true when u and v are near the eigenvalue points since at these points the amplitude discontinuities disappear entirely. By choosing

$$u = k_o \sin\theta \cos\varphi \tag{7}$$

$$v = k_o \sin\theta \sin\varphi \tag{8}$$

the simulator can be used to approximately simulate the infinite array at the general scan angles θ and φ. Because the $a_i(n,m)$ are eigenvectors of the scattering matrix of the simulator[3], the general excitation (6) can be expanded in terms of them as follows.

$$A_k = \sum_{n,m} c_{nm}\, a_k(n,m) \qquad k = 1,2,..N \tag{9}$$

where the expansion coefficients are obtained by multiplying (9) by $a_k(p,q)$ and summing over k. The orthogonality property of the eigenvectors then gives

$$c_{pq} = \sum_{k=1}^{N} A_k\, a_k(p,q) \;/\; \sum_{k=1}^{N} a_k^2(p,q) \tag{10}$$

When the excitation (9) is applied to the simulator, each eigenvector is reflected with a reflection coefficient Γ_{nm} so that the ratio of reflected to incident amplitude at the feedline of the k th element is given by

$$\Gamma(\theta,\varphi) = \frac{1}{A_k} \sum_{n,m} c_{nm}\, a_k(n,m)\, \Gamma_{nm} \qquad (11)$$

Equation (11) was applied to the corner element of the 25 element simulator which gave the input reflection coefficients corresponding to one of the center elements in a 10 x 10 = 100 element sub-array. The resulting values of reflection coefficient as a function of scan angle are shown for scan planes for which $\varphi = 0^{\circ}$, 48.7°, 66.3° and 90° in Figures 8 to 11. The first three scan planes contain scan angles of the eigenvalues of the simulator while the E-plane scan at 90° does not.

Figure 8 shows the reflection coefficient for H-plane scan. The interpolation formula (11) is seen to give a smooth curve passing through five of the eigenvalues which are indicated by dots. In Figure 9 the 48.7° scan plane results are given. This curve passes through three of the eigenvalues and a ripple is now observed between these points. In Figure 10 the curves for the 66.3° scan plane pass through only two eigenvalues and considerable fluctuations are evident between the points. Finally in Figure 11 the E-plane scan curves diverge to values with magnitude greater than unity as the strong mutual coupling between sub-arrays reflects more energy into the excited element than was incident. From the behavior of the curves it appears that the sub-array impedance approximates the infinite array impedance fairly well for scan plane angles up to about 45° with decreasing accuracy as the scan plane is tilted up from the H-plane.

ACKNOWLEDGMENT

The efforts of A. Derneryd and P.-I. Jonsson in the computations and experimental work are gratefully acknowledged.

REFERENCES

1. A.A. Oliner, R.G. Malech, "Simulation of Infinite Arrays by Waveguide," R.C. Hansen, Ed., "Microwave Scanning Antennas," vol. 2, New York; Academic Press, pp. 322-335, 1966.

2. E.L. Ginzton,"Microwave Measurements,"New York: McGraw-Hill Book Co., sec. 6.5, 1957.

3. R. Courant, D. Hilbert, "Methods of Mathematical Physics," vol. I, New York: Interscience Publishers, chap. 1, 1965.

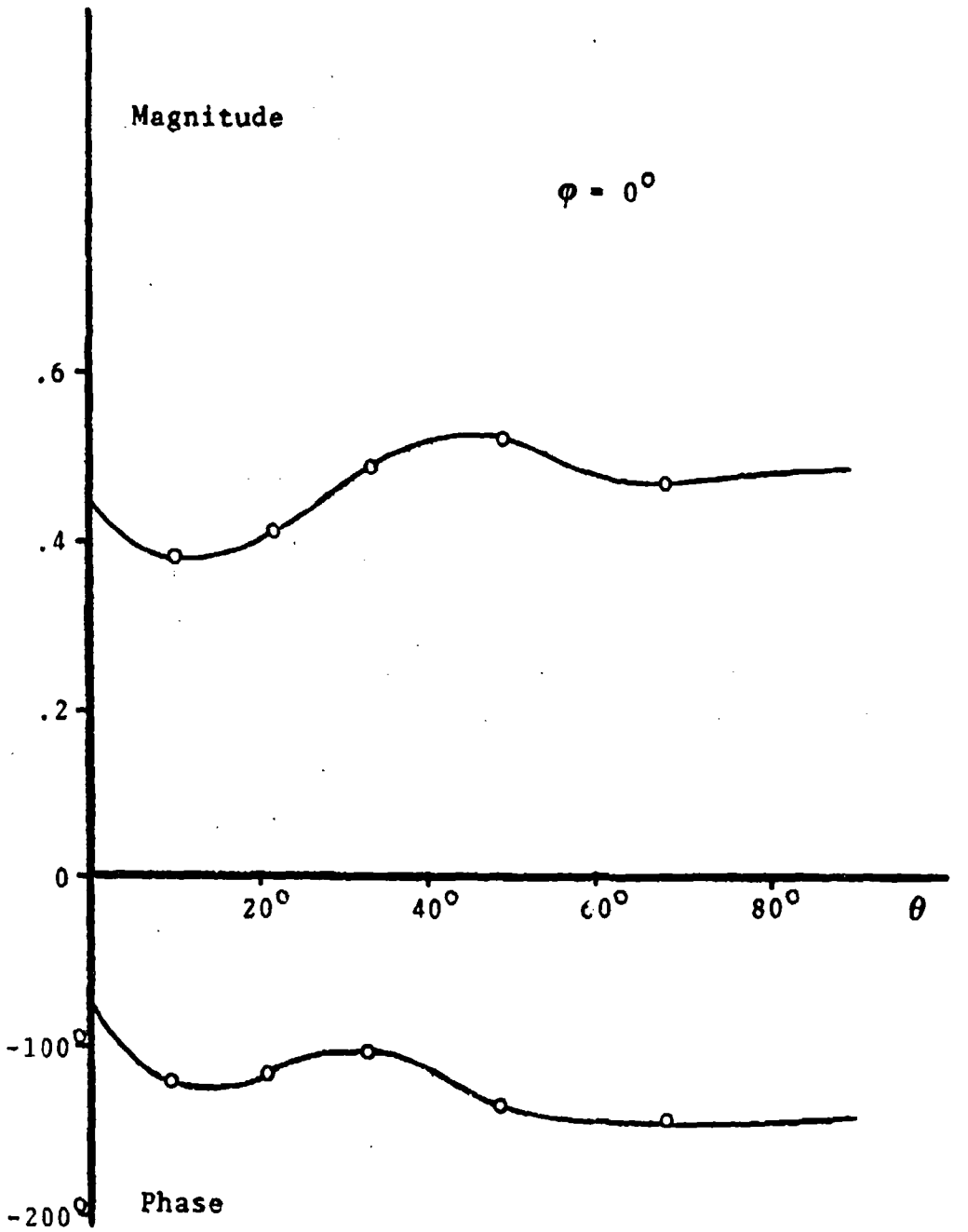

Figure 8. The reflection coefficient for H-plane scan.

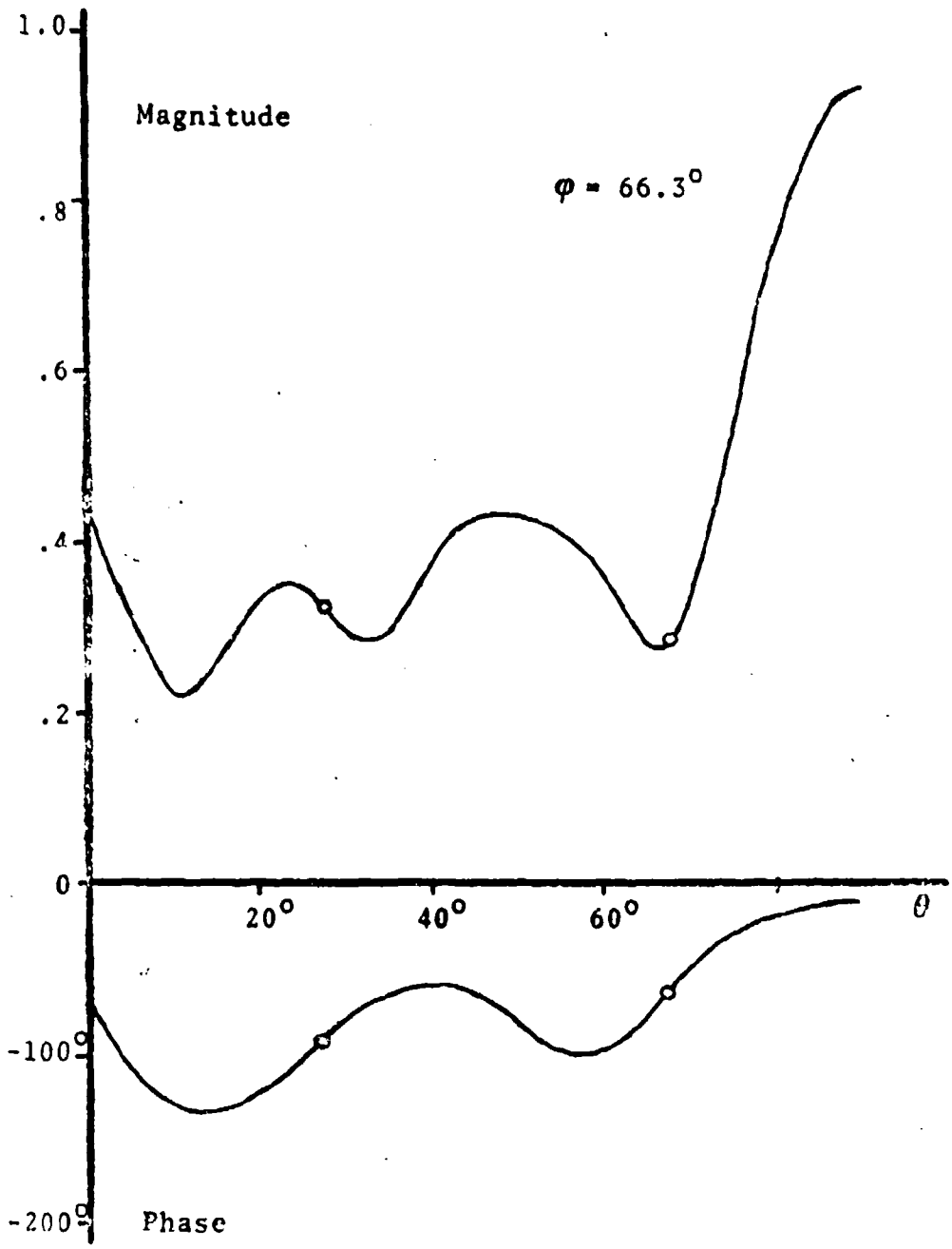

Figure 10. The reflection coefficient for the 66.3° scan plane.

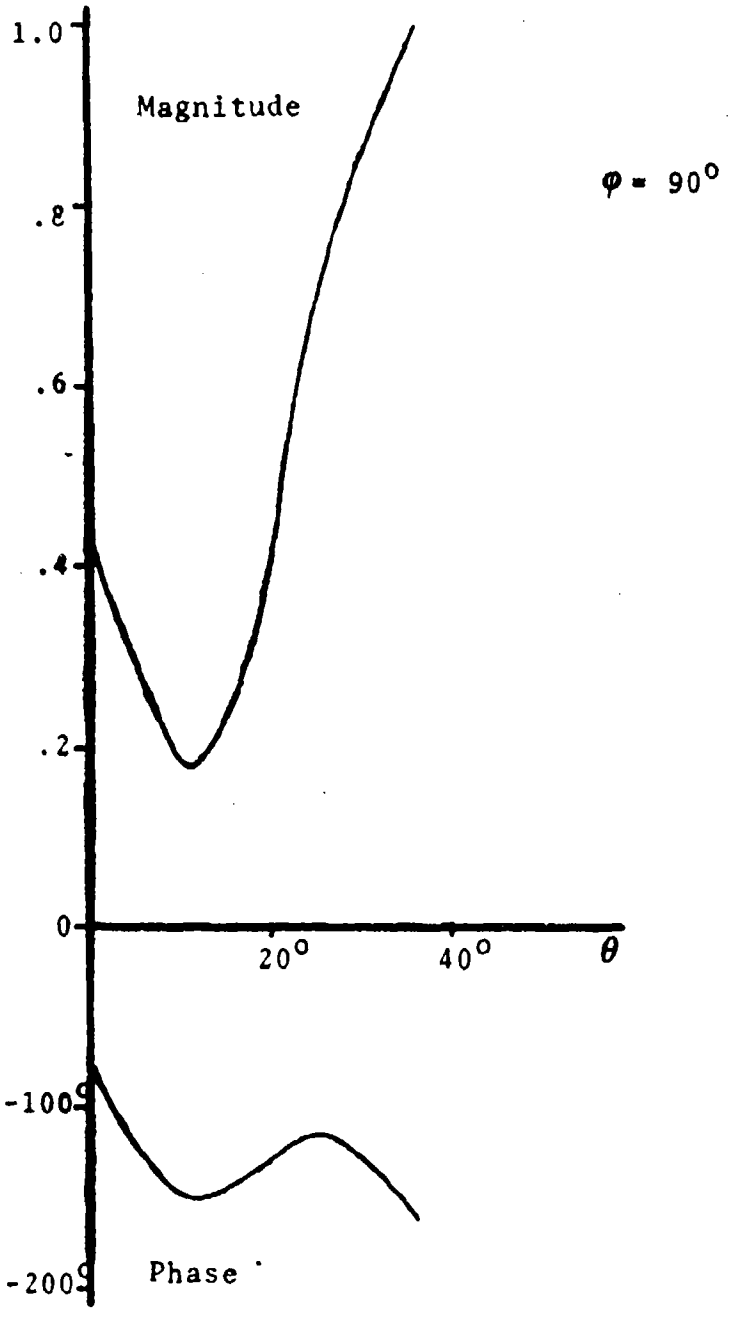

Figure 11. The reflection coefficient for E-plane scan.

12. DECISION-THEORETIC PARALLEL-PROCESSING ARRAYS

by

G. C. Young and J. E. Howard

Radar Division
Aerospace Group

Hughes Aircraft Company
Culver City, California 90230

for

ARRAY ANTENNA CONFERENCE

Naval Electronics Laboratory Center
San Diego, California

22, 23, 24 February 1972

DECISION-THEORETIC PARALLEL-PROCESSING ARRAYS

by G. O. Young* and J. E. Howard**

ABSTRACT

A new class of antenna has been conceived based on the use of a digital processor following a set of antenna elements. Such a processor is programmed to carry out estimation and decision-making procedures as dictated by decision theory. The quality of the estimate or decision depends on the quality of the data available at the time of decision. These data are continually upgraded by observations which update the probability distributions from which the decisions and estimates are made. The quality criterion for optimum multiple-target directing-firing leads to a multimodal, mathematical surface that must be searched for a global maximum. In general, if N sources are to be detected, an N-dimensional search is required. One of the major efforts in this approach has been a reduction in processing complexity and time. The feasibility of the processing has been demonstrated by numerous computer simulations in which the actual software to be used in an eventual system was used to provide a realistic assessment of expected performance. The simulations demonstrated the ability to accurately locate multiple, closely spaced sources.

APPROACH

An antenna can usually be viewed as a set of subapertures whose outputs are summed. The typical antenna is a RF data collector followed by a simple, RF analog computer, in the form of a vector summer. Phased or electronically scanned arrays employ phase shifters that are also simple analog computing devices. In many cases, following frequency translation or video detection of the signal, the analog computer could be replaced by a digital computer. But, more significantly, much more sophisticated processing is possible with a digital computer. Such processing provides improved performance, such as multiple-target resolution well within the conventional Rayleigh limit. Furthermore, continuous observations of the whole field of view are possible with no time delay between looks.

A new class of antennas has been conceived based on the use of a digital processor following a set of antenna elements. The digital processor can make estimates of target parameters (range, velocity, angle, etc.) and decisions (target present or absent, target or clutter, etc.). To accomplish these actions, the processor is programmed to carry out estimation and decision-making procedures as dictated by

---

*Senior Staff Engineer, Aerospace Group, Hughes Aircraft Company
**Staff Engineer, Aerospace Group, Hughes Aircraft Company

decision theory. The quality of the estimate or decision depends on the quality of the available a priori data, i.e., the data available at the time of decision. These data are continually upgraded by using observations to update the probability distributions from which the decisions and estimates are made. Although decision theory had been applied extensively in the time domain, its application to spatial problems, or more generally, to space-time problems, had not. Several basic assumptions were made. The choice for antenna structure was the array because of its flexibility and large number of degrees of freedom. Furthermore, it is ideally suited for parallel processing. Parallel data-gathering and processing was chosen as optimum for decision-theoretic systems.

The typical antenna processing is simple and analog, with the processing usually carried out at RF. It is clear that this same processing could be carried out at lower frequencies, IF or video. Furthermore, the processing could be carried out digitally as well as by analog means. It was decided to use digital processing because of its flexibility, speed, capacity, and convenience for parallel processing. In addition, digital processing makes simulation very straightforward. The expected analog inputs can be simulated and the actual software to be used for processing employed in the simulation. The sole purpose of the associated analog electronics is then to demodulate the element (or module) outputs to a form acceptable by the computer. The computer software is not simply a digitizing of conventional analog antenna processing techniques, however. Instead, it is an optimized program that yields decisions and estimates with low risk in an acceptable amount of time. Individual processing of each antenna element or module provides the greatest flexibility in processing and pattern control.

PARALLEL-PROCESSING ARRAY

Parallel processing has a number of features: (a) It can reduce time to achieve decision or estimate to tolerable risk, since all of the field of view is continuously observed. (b) It does not suffer from errors due to time scintillation between "looks." (c) It is essentially a "track while search" system, since it continuously interrogates the whole field of view, while at the same time it provides continuous parameter estimates of the targets of interest.

The typical parallel-processing system consists of two parts: an analog portion which transforms each element (or module) output to a form suitable for digital inputs, and a special-purpose digital processor which transforms these inputs to least risk decisions and estimates. The RF analog computing of the usual processing array can be replaced by equivalent digital computer processing. It has been found, however, that decision-theoretic processing can provide much better performance than can the digital equivalent of conventional processing. Clever algorithms and software design have very significantly reduced the digital complexity. Current developments in digital,

microwave, and IF hardware have further alleviated this problem so that all-parallel processing is practical. Hybrid systems may also be used to reduce complexity. Full parallel data-gathering requires that the transmitter continuously illuminate the field of view. The loss of power in a given direction that results is compensated for by the fact that the reflector in that direction is illuminated for a longer period of time so that the returned energy is the same.

The typical conventional system gathers data sequentially (by scanning) and processes the data sequentially. The processing is very simple, often amounting to only summing, and is usually done at RF. Electronically scanned arrays are more complicated in that they have phase shifters and sometimes attenuators that must be controlled and driven so as to provide a time-varying linear phase shift and constant amplitude shading across the aperture. The parallel-processing system, on the other hand, may be completely parallel and employ a digital computer for processing. The basic form of a parallel-processing direction-finding system is shown in Figure 1.

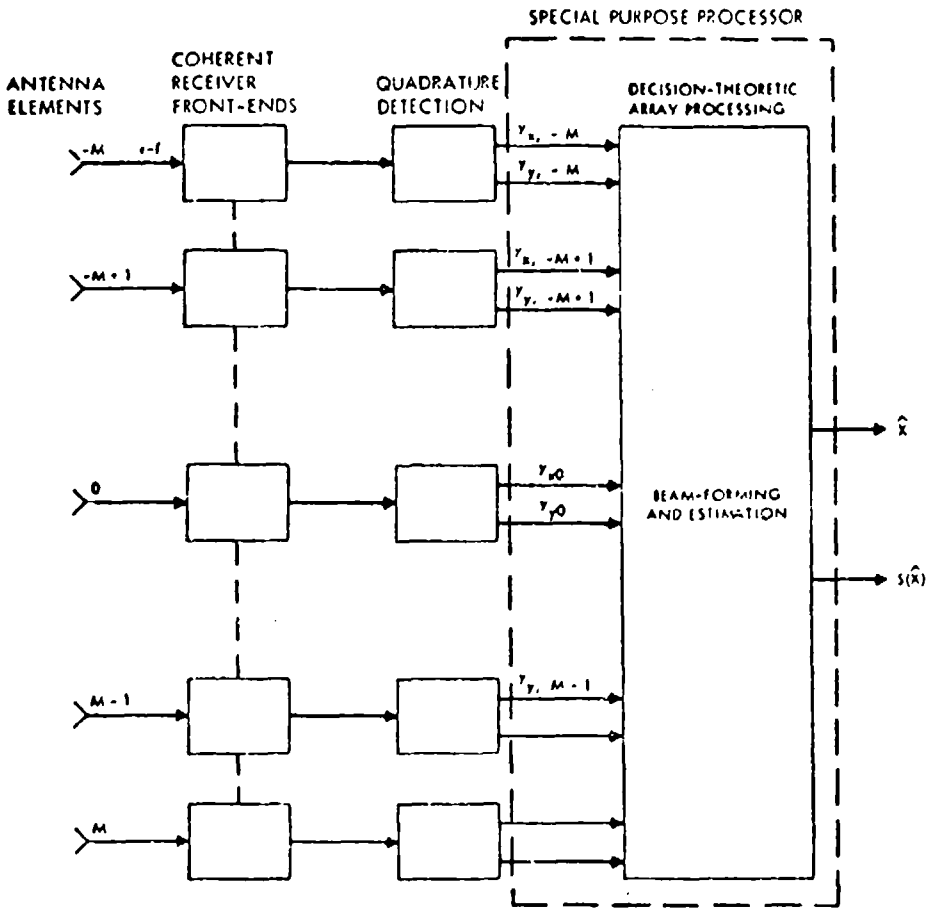

Figure 1. Basic direction-finding system

The coherency requirement on the parallel receiver is not so severe as might be expected. Fixed errors and mismatch in both phase and amplitude can be compensated in the computer. The principal requirement is good tracking, especially in phase, over the expected input and temperature ranges, so that the channels remain matched to within the specified tolerance as a function of time and input level. Beam-forming may or may not occur within the computer, depending on the application. The output is a set of angle estimates.

DECISION-THEORETIC PROCESSING

The antenna processing that is implemented in a digital processor can be derived from a decision-theoretic formulation of the problem of multiple-target direction-finding. The result is unconventional processing that typically involves a multidimensional search for a global maximum. The outcome of this processing is resolution well beyond the Rayleigh limits. In general, if the location of N sources is to be estimated, an N-dimensional search is required. A great deal of time and effort has gone into this problem to reduce convergence time and processing complexity. It has been found that simpler and less time-consuming search procedures can be used if the sources are far apart.

APPLICATIONS

The basic direction-finding system shown in Figure 1 is the central component in a variety of possible applications. If additional estimates or decisions are to be made, this capability is incorporated into the processor. Because of the analogy between multiple-beam processing in the spatial domain and multiple-doppler filter processing in the temporal frequency domain, most of the direction-finding techniques can be carried over into the doppler frequency domain. In addition, learning techniques may be used; these will be discussed shortly. In principle, the general system in Figure 1 is also suitable for communications systems. In addition to the direction-finding system (usually needed, especially for moving systems), there must be a decoder and communications output. The fundamental problem is bandwidth. For the computer to handle large modulation bandwidths, the A/D and computer cycling time must be very short. State-of-the-art computers now have cycling times on the order of 10 ns (100-MHz bandwidth). If larger bandwidths are to be sampled, computers may be paralleled in frequency (i.e., they may sample adjacent bands).

The basic direction-finding system can be supplemented or modified so that a digital computer plus auxiliary sensors and electronics carries out all necessary operations. In addition to those discussed, navigation, mapping, telemetering and many other applications exist for decision-theoretic systems. For example, essentially

all aircraft operations could be performed by a single digital computer so equipped and programmed. An interesting application is in non-planar or conformal arrays. Many of the problems associated with such arrays are resolved because of individual processing of each element output and the fact that no scanning is required.

THE ULTIMATE RADAR SYSTEM

Up to this point receiver processing has been considered, and angular location estimation or direction-finding has been emphasized. These concepts can be generalized to multiple parameter estimation and multiple hypothesis testing (decision and identification). The transmitter as well as the receiver is controlled by probability feedback in which adaptive learning is employed.

The general space-time learning system is shown in Figure 2. Only four channels of the system are shown for convenience. Each

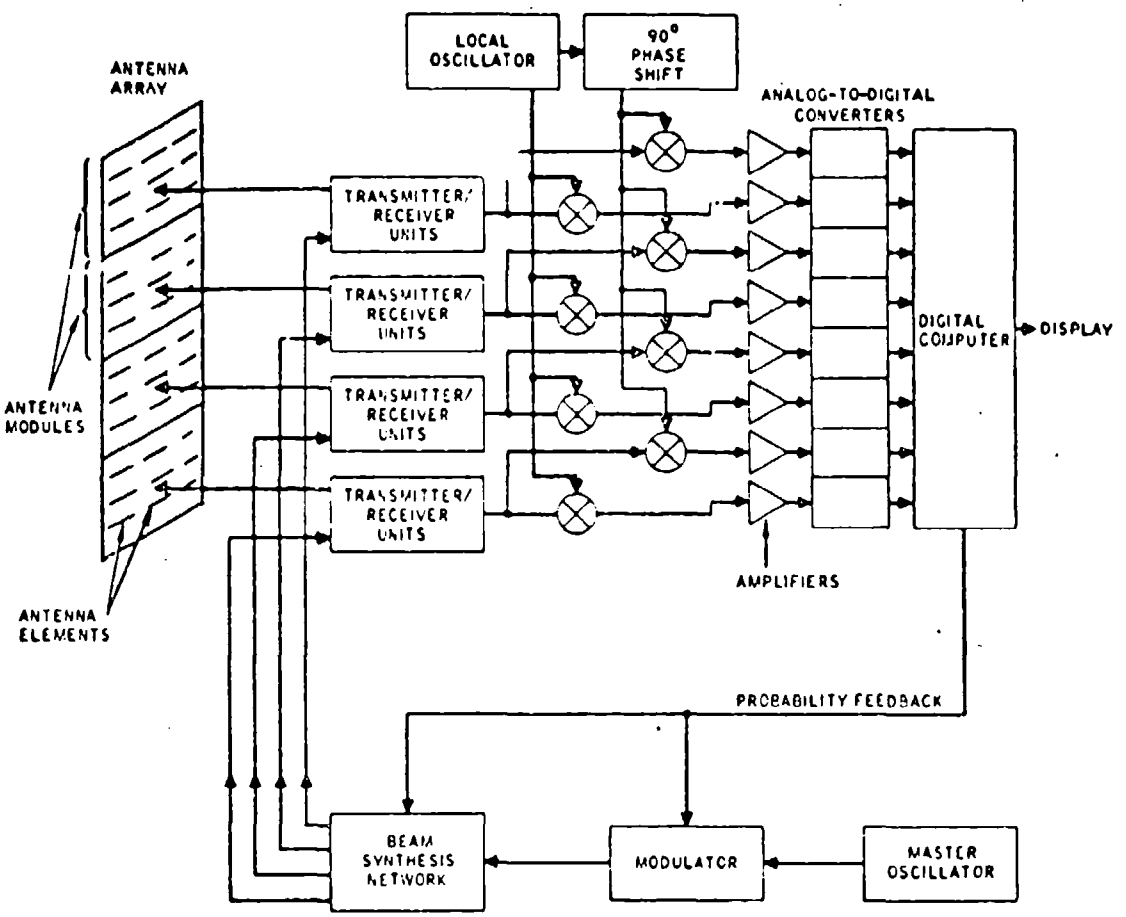

Figure 2. General space-time learning system (four channels)

module is an antenna array, which can be one or more elements. Each module is connected through a transmitter/receiver unit and a conventional receiver with quadrature demodulators down to an analog-to-digital converter. There are eight parallel channels in the system because of the quadrature outputs.

The A/D outputs are fed to the digital computer which carries out decision-theoretic processing such as estimation, decision-making, etc. This information can be displayed or used for automatic weapon firing or for whatever purpose desired. In addition to the display, there is internal feedback, to be described in Figure 3, that

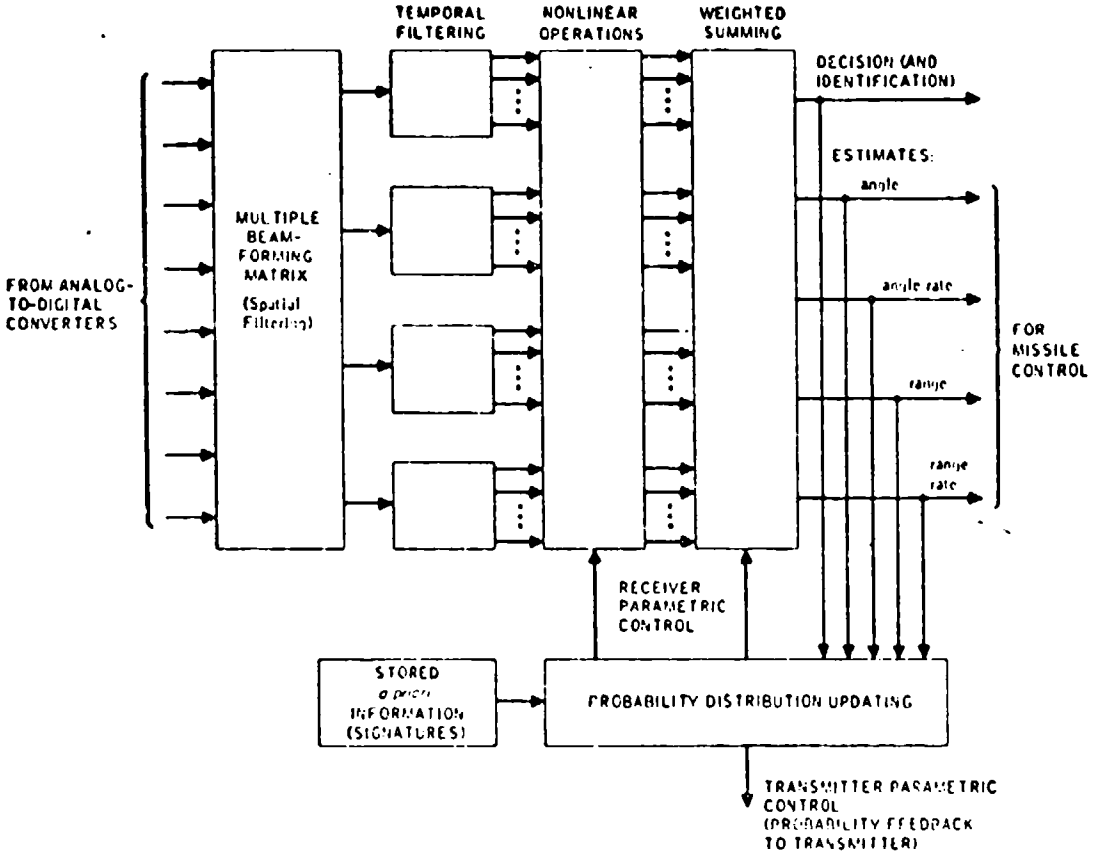

Figure 3. Digital computer processor for receiver

updates or upgrades the probability distributions from which the decisions and estimates are made. This probability feedback is adaptive to the environment and corrects errors in the initial assumptions that were used in making the a priori probability distributions. The revised probability distributions are fed back to the transmitter. For example, suppose that the probability distribution in target location x is available in the computer. This distribution can then be fed back to the beam synthesis network for the transmitter. The master oscillator and modulator

provide the transmitted signal. This beam-synthesis network then modifies the antenna array transmission pattern to conform with the probability distribution in $\underline{x}$. Indeed, the transmitting pattern could have the same shape as the distribution in $\underline{x}$. In any case, it should be related to it in such a way that the major portion of the transmitted energy is concentrated in the region indicated to be most likely by the probability distribution in target location. The feedback is a continuously adaptive process that gradually changes the transmitting pattern from a broad uniform type of coverage, such as used in search, to a narrow peaked type of coverage such as in track.

The internal feedback is shown in Figure 3, which is a diagram of the digital computer processor for the receiver. This figure shows the major operations that occur within the computer. The inputs are from the A/D converter, and generally there is some sort of weighted averaging or spatial filtering such as multiple-beam forming. The various frequencies in the input are then isolated by digital filters, which form the temporal filtering section. This filtering is followed by nonlinear operations such as target location estimation and linear operations such as weighted summing for estimation of parameters, for example, the quadrature component parameters. The estimation and decision operations then yield decisions including resolution and discrimination against clutter (e.g., target identification) and various estimates necessary for reference control or other uses. These estimates principally target(s) position in three coordinates and possibly rates in those coordinates.

The estimates and decisions are also used for probability distribution updating. These estimates are combined in a weighted fashion to form a sampling of parameters, and this random variable, whose distribution is computed from observations, is added in a properly weighted fashion to the a priori random variable that has an assumed distribution. As a function of time, the weighting for the observed probability distribution increases compared with the weighting for the a priori distribution. In other words, as the statistical significance of the observed data increases, the weighting for that term becomes greater and the weighting for the a priori assumed distribution becomes less. Thus, both the estimated parameters and the stored a priori parameters are used in the probability distribution updating procedure. The probability distribution updating is then fed to the computer (receiver parametric control) to update the distribution from which these decisions and estimates are made. At the same time, the probability distribution resulting can be fed to the transmitter as described in Figure 2. This technique is called probability-state-vector feedback but differs from ordinary feedback systems in that the state-vector is not operated on to yield the control vector directly, but rather is used to generate probability distributions and affect the transmitting pattern waveform in such a way that the system performance is greatly improved.

COMPUTER SIMULATIONS

Numerous computer simulations have tested the computer processing and algorithms. These simulations show the direction-finding system to be superior to conventional systems in practically all respects. As an example, consider the results in Figure 4. This figure is a plot of rms error in location versus separation of unequal

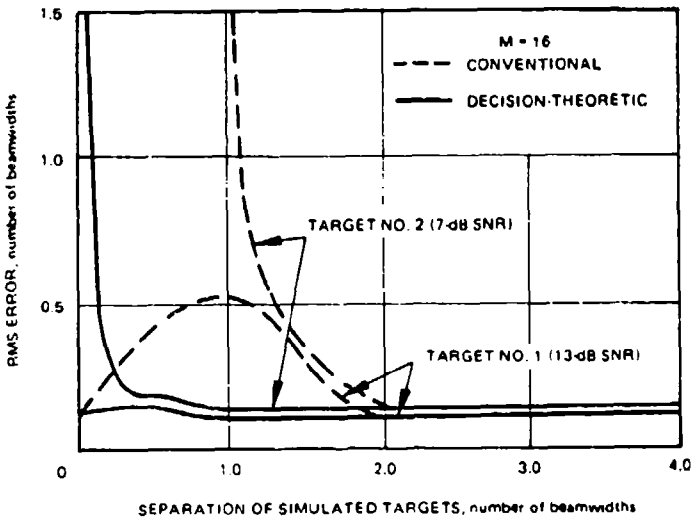

Figure 4. Two-target direction finding

sources. The rms error for both targets remains at approximately 0.1 beamwidth essentially independent of their operation, while the rms error in the conventional system increases markedly for operations less than two beamwidths. In fact, at one beamwidth separation, the error for one target "goes to infinity"; that is, the system no longer recognizes that there are two targets and instead estimates the centroid of the two targets as if it were one target. This figure implies that the resolution capability of the conventional system is one beamwidth whereas it is much less for a decision-theoretic system. Typical design objectives for the decision-theoretic system at high SNR are resolution of 1/10 beamwidth with angular estimation accuracies of 1/20 beamwidth.

Figure 5 shows the accuracy of direction estimates for three very closely-spaced targets at high SNR. A beamwidth for the scale shown is $d/\lambda \sin\theta = 0.25$. The targets are mutually separated by 0.1 beamwidth. As can be seen, the estimates are extremely good, particularly when averaged over several data sets.

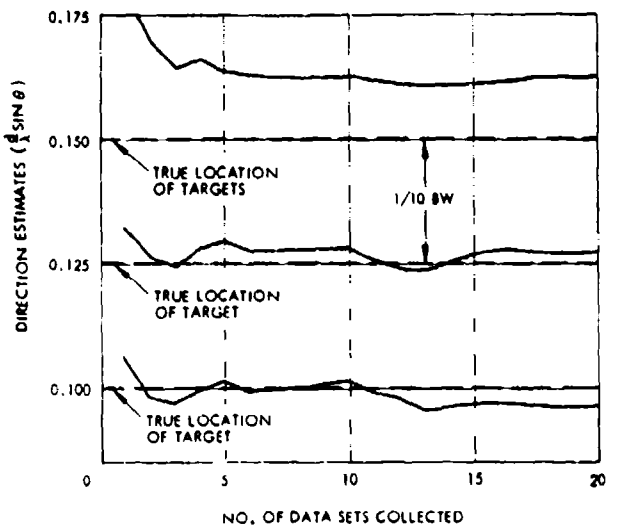

Figure 5. Three-target direction finding (8 element array)

CONCLUSIONS

The direction-finding system can be used as a fundamental building block in the development of systems of various applications. The system can be used as a radar or communications systems and for various other applications. The array need not be planar. The estimation accuracy and resolution capacity are high and can be continually upgraded by space-time learning.

I. Introduction

Chebyshev polynomials are often used to design arrays for optimum patterns. The Dolph-Chebyshev pattern is optimum in the sense that for a given sidelobe level the beamwidth is minimum, or conversely, for a given beamwidth the sidelobe level is minimum. The sidelobes of this pattern are all equal. Although the Dolph-Chebyshev pattern is, in this way, mathematically unique, its sidelobe behavior is not flexible enough for a number of applications. For example, when using directive elements the far-out sidelobes of the array pattern need not be equal to the near-in ones. Also, in order to minimize the external antenna noise effect for the case of non-uniform temperature distribution, the sidelobes of the array pattern should be such as to optimize the signal-to-noise ratio.[1] Therefore, it is useful to provide a synthesis procedure which can give a more flexible sidelobe behavior and still is optimum in the Dolph-Chebyshev sense. Such a technique is discussed in this paper.

II. Optimum Polynomials

A class of optimum polynomials which includes the Chebyshev polynomials as a subclass and is suitable for array synthesis will be given. For our purpose, the pattern of an array is considered to be optimum if for a given peak sidelobe level the beamwidth is minimum, or conversely, for a given beamwidth the peak sidelobe level is minimum. The problem so stated does not have a unique solution as the peak sidelobe can occur anywhere outside the main beam and in the visible range. It becomes well defined when the sidelobe envelope is specified to within an arbitrary constant. For the Dolph-Chebyshev patterns, the sidelobe envelope is always a constant line. Figure 1 shows an example of a general optimum polynomial.

Let $P_n(z)$ be the array polynomial and $Q_m(z)$ the sidelobe envelope, where $n >> m$. The array polynomials $P_n(z)$ which have all the following properties will be denoted as $P_{n,\,m}(z)$:

(i) All zeros of $P_n(z)$ are real, distinct and in a finite interval (a, b).

(ii) All zeros of $P_n(z) + Q_m(z)$ and $P_n(z) - Q_m(z)$ in (a, b) are of multiplicity 2.

(iii) $[P_n^2(z) - Q_m^2(z)]$ has, in addition to (n-1) double zeros, two single zeros at a and b.

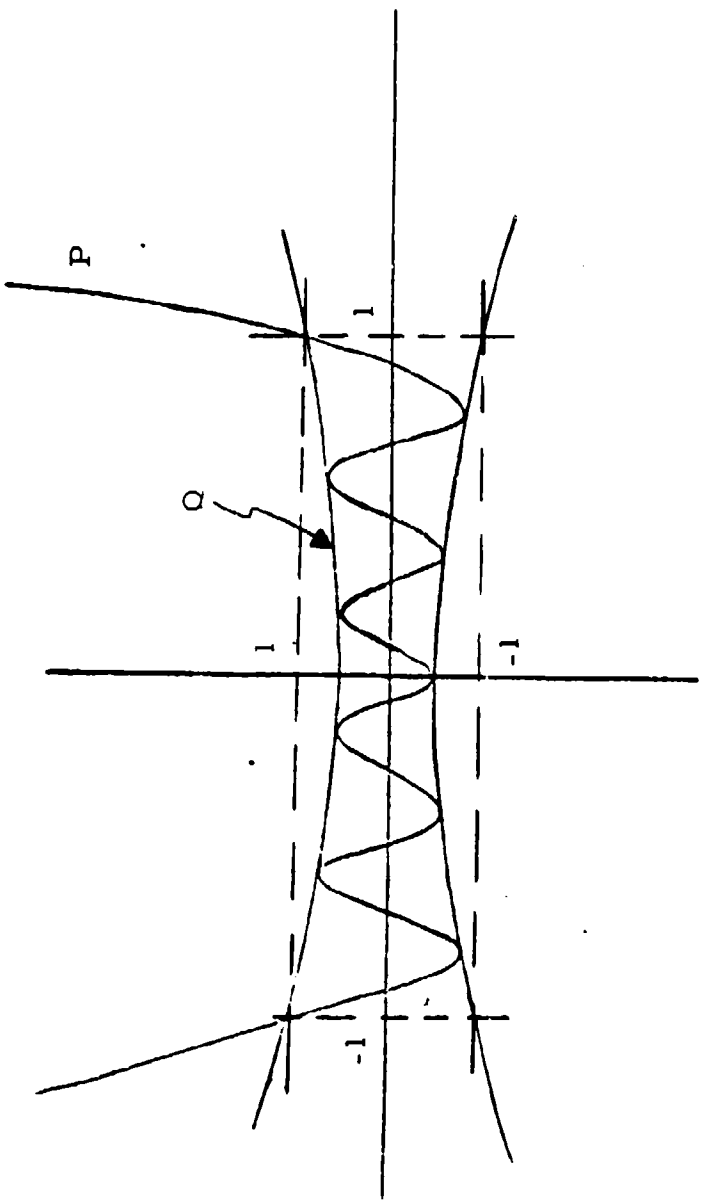

Figure 1. Optimum Polynomial P With Envelope Q

There exists an algebraic procedure for characterizing these polynomials and the procedure is outlined in the Appendix.

III. Special Types of Optimum Polynomials

The algebraic procedure outlined in the Appendix can be used to determine various types of optimum polynomials. In particular, if we let (a, b) = (-1, 1) it can be shown that when $Q(z) = e$, $P_{n,\,o}(z)$ reduces to the Chebyshev polynomials, i. e.

$$P_{n,\,o}(z) = e \cos (n \cos^{-1} z) = e\, T_n(z) \tag{1}$$

The normalization constant can be determined to be

$$e = (1/2)^{n-1} \tag{2}$$

When the envelope $Q(z) = e_o z + e_1$, it is found that the normalization constant should be

$$e_1 = \left(\frac{1}{2}\right)^{n-1} (1 + 4^{n-2} e_o^2) \tag{3}$$

Therefore, it is convenient to let $c = 2^{n-2} e_o$ and write

$$Q(z) = \left(\frac{1}{2}\right)^{n-1} (2cz + 1 + c^2) \tag{4}$$

The corresponding optimum polynomial is then given by

$$P_{n,\,1}(z) = \left(\frac{1}{2}\right)^{n-1} [T_n(z) + 2c\, T_{n-1}(z) + c^2 T_{n-2}(z)] \tag{5}$$

The procedure can be applied to cases of higher degree envelope polynomials. However, for the present study, it is sufficient to give the following special results:

III. 1 If Q(z) is antisymmetric about z = 0, we then have

$$P_{n,\,m}(z) = z\, P_{n-1,\,m-1}(z) \tag{6}$$

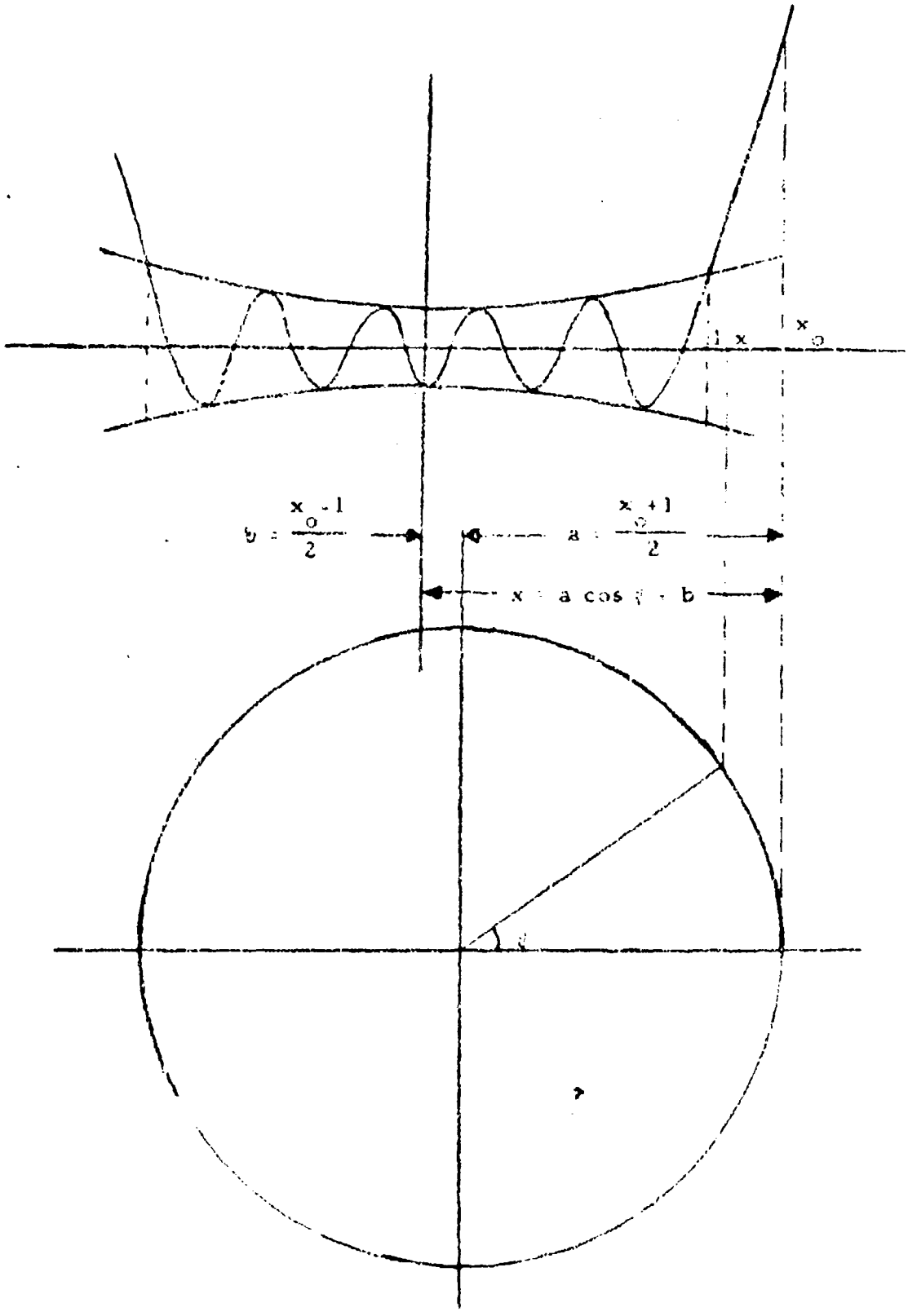

Figure 2. Graphical Representation of Array Transformation

2. If all zeros of $Q_m(z)$ are real and in $(-1, 1)$ i.e. when

$$Q_m(z) = a_0 \prod_{i=1}^{m} (z - z_i), \quad -1 < z_1 \leq z_2 \leq \ldots \leq z_m < 1, \quad (7)$$

then

$$P_{n,m}(z) = Q_m(z) T_{n-m}(z) \quad (8)$$

III. 3. In particular, when $Q_m(z) = a_0 z^m$ then

$$P_{n,m}(z) = a_0 z^m T_{n-m}(z) \quad (9)$$

The polynomials defined by equation (8) can be identified with patterns with monotonically decreasing sidelobes.

IV. Array Application

The polynomials described in II and III can be used to generate array patterns in the following manner. The polynomials $P_{n,m}(z)$ is used with a $2n+1$ element array and the transformation

$$z = a \cos \psi + b \quad (10)$$

where $\psi = kd \sin \theta$ is used to relate the variable z for the polynomial and the variable ψ of the array pattern. Figure 2 shows the above transformation graphically.

For spacing $d = \lambda/2$, DuHamel[2] has shown that

$$a = \frac{1}{2}(z_0 + 1), \quad b = \frac{1}{2}(z_0 - 1) \quad (11)$$

where $z_0 = z(0) = 0$; $a + b$ is determined either by the sidelobe level or by the beamwidth of the array pattern.

As usual, the set of current coefficients (I_i) can be obtained by identifying the polynomial $P_{n,m}(z)$ with the array pattern

$$E_{2n+1}(\psi) = I_0 + 2 \sum_{i=1}^{n} I_i \cos i\psi \quad (12)$$

The directivity of array patterns can be expressed directly in terms of the polynomial P(z). In general, we have

$$D = kd\, P^2(z_o) \Big/ \int_{a\cos kd+b}^{z_o} \frac{P^2(z)\, dz}{\sqrt{(z_o - z)(1+z)}} \tag{13}$$

If the spacing is half wavelength, then

$$D = \pi P^2(z_o) \Big/ \int_{-1}^{z_o} \frac{P^2(z)\, dz}{\sqrt{(z_o - z)(1+z)}} \tag{14}$$

V. Patterns With Monotonically Increasing Sidelobes

The optimum polynomials $P_{n,1}(z)$, given by the expression (5) in III, can be used to obtain array patterns with monotonically increasing sidelobes. For this purpose, we let c be a negative number. The amplitude of the number c should be selected so as to get the desired slope of the sidelobe envelope. Once this is done, the array design can then be carried out according to the procedure outlined in IV.

The class of optimum polynomials $P_{n,1}(z)$ leads to patterns with linear sidelobe envelopes. More general optimum polynomial $P_{n,m}(z)$ can be derived for patterns with non-linear sidelobe envelopes.

VI. Patterns With Monotonically Decreasing Sidelobes

The class of optimum polynomials, given by the expression (9) in III

$$P_{n,m}(z) = e_o z^m T_{n-m}(z)$$

can be used to obtain array patterns with monotonically decreasing sidelobes. Some numerical computations were performed for small arrays ($n \leq 8$). Array properties are evaluated. These include the sidelobe level, the beamwidth, the current coefficients and the directivity. In addition, asymptotic beamwidth expressions together

with an expression relating the beamwidth, the sidelobe level and the effective aperture length are derived for large arrays.

VII. Summary

A class of optimum polynomials which includes the Chebyshev polynomials as a subclass is defined. These polynomials are useful for array synthesis. In particular, the synthesis technique can give a more flexible sidelobe behavior than that obtainable with the Chebyshev polynomials. The application of these polynomials for the array design has been discussed.

References

1. "Optimization of Directivity and Signal-to-Noise Ratio of an Arbitrary Antenna Array", Y. T. Lo et al, Proc. IEEE, Vol. 54 No. 8, August 1966, pp. 1033-1045.

2. "Optimum Patterns for Endfire Arrays", R. H. DuHamel, Proc. IRE, Vol. 41, May 1953, pp. 652-659.

APPENDIX A

ALGEBRAIC CHARACTERIZATION OF OPTIMUM POLYNOMIALS

Let

$$P_n(z) = z^n + a_1 z^{n-1} + \ldots + a_n \tag{A1}$$

$$Q_m(z) = e_o z^m + e_1 z^{m-1} + \ldots + e_m \tag{A2}$$

where the coefficients of the envelope polynomial $Q_m(z)$ are assumed to be given, except for the constant e_m. For the even case, we thus have

$$P_{2n}(z) - Q_m(z) = (z-a)(z-b)(z^{n-1} + b_1 z^{n-2} + \ldots + b_{n-1})^2 \tag{A3}$$

$$P_{2n}(z) + Q_m(z) = (z^n + c_1 z^{n-1} + \ldots + c_n)^2 \tag{A4}$$

which give 2n algebraic equations relating 2n unknowns = $b_1, b_2, \ldots b_{n-1}, c_1, c_2, \ldots c_n, e_m$. The coefficients of the optimum polynomial $P_{2n,m}(z)$ are determined by

$$a_\ell = \sum_{i=0}^{\ell} b_i b_{\ell-i} - (a+b) \sum_{i=0}^{\ell-1} b_i b_{\ell-1-i} + ab \sum_{i=0}^{\ell-2} b_i b_{\ell-2-i} + e_{\ell-2n+m}$$

$$= \sum_{i=0}^{\ell} c_i c_{\ell-i} - e_{\ell-2n+m} \tag{A5}$$

$\ell = 1, 2, \ldots 2n.$

Similarly, for the odd case, we have

$$P_{2n+1}(z) - Q_m(z) = (z-b)(z^n + b_1 z^{n-1} + \ldots + b_n)^2 \tag{A6}$$

$$P_{2n+1}(z) + Q_m(z) = (z-a)(z^n + c_1 z^{n-1} + \ldots + c_n)^2 \tag{A7}$$

which give 2n+1 algebraic equations relating 2n+1 unknowns: $b_1, b_2, \ldots b_n$, c_1, $c_2, \ldots c_n$, e_m. The coefficients of the optimum polynomial $P_{2n+1,\,m}(z)$ are determined by

$$a_\ell = \sum_{i=0}^{\ell} b_i b_{\ell-i} - b \sum_{i=0}^{\ell-1} b_i b_{\ell-i-1} + e_{\ell-2n+m}$$

$$= \sum_{i=0}^{\ell} c_i c_{\ell-i} - a \sum_{i=0}^{\ell-1} c_i c_{\ell-i-1} - e_{\ell-2n+m} \qquad \text{(A8)}$$

$$\ell = 1, 2, \ldots . 2n+1$$

In equations (A5) and (A8), it is assumed that $a_o = b_o = c_o = 1$ and $b_\ell = c_\ell = e_\ell = 0$ where $\ell < 0$.

To show that the above formulation gives the Chebyshev polynomial as a special case, we let all coefficients of the envelope, except $e_m = e$, be zero. Then equations (A5) and (A8) can be summarized as

$$P_n^2(z) - e^2 = (z-a)\,(z-b) \sum_{i=1}^{n-1} (z - z_i)^2 \qquad \text{(A9)}$$

$$\frac{d}{dz} P_n(z) = n \sum_{i=1}^{n-1} (z - z_i) \qquad \text{(A10)}$$

The above two equations can be combined to give the following differential equation

$$\frac{d}{dz} P_n(z) = \pm n \sqrt{[P_n^2(z) - e^2]/(z-a)(z-b)} \qquad \text{(A10)}$$

with the initial condition

$$P_n(b) = e,$$

the solution of the differential equation (A10) is

$$P_n(z) = e \cos \left[n \cos^{-1} \frac{2z-(a+b)}{b-a} \right] \qquad \text{(A11)}$$

which is a shifted Chebyshev polynomial. The following special cases are readily obtained.

(i) $(a, b) = (-1, 1)$, $P_n(z) = e \cos(n \cos^{-1} z) = eT_n(z)$ (A12)

(ii) $(a, b) = (0, 1)$, $P_n(z) = e \cos [n \cos^{-1}(2z-1)] = eT_n(2z-1)$ (A13)

14. BEAM STEERING CONTROL SYSTEM FOR A CYLINDRICAL ARRAY

by

S. A. O'Daniel

Code 2330

Naval Electronics Laboratory Center
San Diego, California 92152

for

ARRAY ANTENNA CONFERENCE

22, 23, 24 February 1972

Naval Electronics Laboratory Center
San Diego, California 92152

BACKGROUND

The antenna requirements for radar, communications, aircraft control and intelligence data have placed severe burdens on space available on ships, aircraft and spacecraft. The packing of many antennas into the limited space has created an additional problem, and has led to the use of one antenna to perform several functions. An obvious requirement under such an arrangement is the ability to rapidly position the antenna beam to various points in space.

Important objectives of the effort to develop shipborne radar systems to satisfy military needs have been broad-spectrum signals, low-sidelobe antennas, and bearing agility. Previous studies have shown that the circular-array type of antenna is effective in meeting these objectives. (See list of references, p. 31.) The use of a linear array as an element of a cylindrical array has been a natural outcome of the wide-spectrum ring-array development. This report presents the results of an investigation into the elevation- and azimuth-scanning properties of such a configuration, and into techniques for array beam steering.

APPROACH

One method of controlling the antenna (that is, steering the pencil beam) is by means of a small digital control computer. The control system is designed to use commercially available integrated circuit devices except for the phasor drivers and test circuits. Logic or control devices to satisfy these requirements were not available commercially; therefore, design details of the driver and test circuit are presented.

The analysis of the cylindrical array is greatly simplified by assuming a separable-aperture distribution and considering the array as a combination of ring and linear arrays. Certain assumptions have been made, and short descriptions of some of the analytical techniques are given.

ANALYSIS OF CYLINDRICAL ARRAY*

GENERAL

The cylindrical array can be considered to consist of a stack of identical ring arrays.[4] We denote the complex excitation of the p^{th} element in the q^{th} ring by $I_{pq} = I(\alpha_p, z_q)$, where α_p is the angular location of the p^{th} and z_q is the z-axis

*Excerpt from reference 4.

location of the q^{th} ring. The coordinate system is shown in figure 14-1. The beam is assumed to be pointed in the $\varphi = 0$ direction in azimuth, corresponding to the $\alpha = 0$ reference point of the element location. The beam is stepped around the cylinder by redefining the $\alpha = 0$ reference to the desired position.

All elements are assumed identical, symmetrical, equally spaced, and pointed along the radius vector. Thus, the azimuth element pattern can be expressed as a function of $|\varphi - \alpha|$. In general, the azimuth pattern depends on the elevation angle θ. The complex element pattern is denoted by $G(\varphi-\alpha, \theta)$, with the phase referenced to the center of the ring in which it lies. Thus, if it is assumed that the phase center is at the element,

$$G(\varphi-\alpha, \theta) = |G(\varphi-\alpha, \theta)| \exp[\, jk\, \rho \cos\theta \cos(\varphi-\alpha)] \tag{1}$$

The far field is

$$E(\varphi, \theta) = \sum_p \sum_q I_{pq}\, G(\varphi-\alpha_p, \theta) \exp[jqu] \tag{2}$$

where

$u = kd \sin\theta$
d = spacing between elements in vertical direction
$k = 2\pi/\lambda$

A beam can be formed in the direction $\varphi = 0$, $\theta = \theta_o$ by exciting all elements to add in phase in that direction (beam cophasal excitation). Thus, in view of (1) and (2) we require

$$I_{pq} = |I_{pq}| \exp[-jk\rho \cos\theta_o \cos\alpha_p - jqu_o] \tag{3}$$

where $u_o = kd \sin\theta_o$.

In (3) the phase terms are separated in α_p and z_q, where $z_q = qd$. This allows us to assume a current distribution of the form

$$I(\alpha_p, z_q) = I^{(a)}(\alpha_p)\, I^{(e)}(z_q) = I_p^{(a)}\, I_q^{(e)} \tag{4a}$$

with

$$I_p^{(a)} = I_p^{(a)} \exp[-jk\rho \cos\theta_o \cos\alpha_p] \tag{4b}$$

and

$$I_q^{(e)} = |I_q^{(e)}| \exp[-jqu_o] \tag{4c}$$

The superscripts (a) and (e) indicate azimuth and elevation distributions, respectively. Note that the azimuth distribution depends on the beam-pointing angle in both azimuth and elevation, whereas $I_q^{(e)}$ depends only on θ_o. Writing the current distribution in the form (4a) allows us to write the pattern (2) in the form

The continuous distribution can be replaced by M elements located at

$$\alpha_p = \frac{2\pi}{M}(p+f) \qquad p = 0, 1, 2, \ldots, M-1$$

where f is a fraction that indicates the position of the beam with respect to the first element. It can be shown[5] that

$$E(\varphi,\theta) = M \sum_{n=0}^{N} \frac{1}{\epsilon_n} I_n^{(\theta_0)} \left| F_n(\theta) \cos n\varphi + \sum_{r=1}^{\infty} F_{rM-n}(\theta) \cos\left[(rM-n)\varphi - 2\pi r f\right] \right| \tag{6}$$

(6) is the desired pattern plus an error term. For spacing $s = \frac{2\pi\rho}{M}$ of less than a half wavelength, only the $r = 0$ term is significant. For spacing less than one wavelength, only $r = 0$ and $r = 1$ contribute, and so forth. The error term's primary contribution to the pattern is in the form of a grating lobe.

STAGGERED ARRAY*

Staggering alternate columns of elements on the cylinder is an effective means of extending the elevation-scanning angle for a given ring-to-ring spacing d and maintaining a small grating lobe.[4]

Consider the staggered array as a superposition of two regular arrays, each with the normal number of rings Q but only half the number of elements in each ring $\frac{M}{2}$. The subarrays are identical except one is rotated by half a spacing in azimuth and is raised by half a spacing in the vertical direction, with the phase compensating for the dislocation. The ring-array patterns for the subarrays can be written as follows, from (6):

Array I - The beam in the direction of the first element; that is, $f = 0$.

$$E\,\mathrm{I} = f(\theta) \sum_n I_n^{(\theta_0)} F_n(\theta) \cos n\varphi + f(\theta) \sum_n I_n^{(\theta_0)} F_{\frac{M}{2}-n}(\theta) \cos\left(\frac{M}{2}-n\right)\varphi$$

$$+ f(\theta) \sum_n I_n^{(\theta_0)} F_{M-n} \cos(M-n)\varphi \tag{7}$$

The $r = 2$ term, which ordinarily would not contribute (for $s < \lambda$) is included, because the spacing is now double the normal spacing.

Array II – The beam is in a direction halfway between two elements; that is, $f = 0.5$.

*Excerpt from reference 4.

$$E\,\mathrm{II} = f(\theta) \sum_n I_n^{(\theta_0)} F_n(\theta) \cos n\varphi - f(\theta) \sum_n I_n^{(\theta_0)} F_{\frac{M}{2}-n}(\theta) \cos\left(\frac{M}{2}-n\right)\varphi$$

$$+ f(\theta) \sum_n I_n^{(\theta_0)} F_{M-n} \cos(M-n)\varphi \qquad (8)$$

If the array were not staggered, each ring would have M elements and a pattern

$$E^{(a)}(\varphi,\theta) = f(\theta) \sum_n I_n^{(\theta_0)} F_n(\theta) \cos n\varphi + f(\theta) \sum_n I_n^{(\theta_0)} F_{M-n}(\theta) \cos(M-n)\varphi \qquad (9)$$

RELATED STUDIES

Two studies have been made of factors which have direct influence on the complexity of the control system – that is, the amount of data to be stored and transferred for each beam and the time required for the data transfer. One study[1] addressed the effect of bit phase errors on array performance. The other study investigated the short pulse behavior of the array.

The results of the bit phase error study led to the selection of 3-bit phase shifters as an optimum choice with respect to array performance, complexity and cost. For example, the type of phasors used affects the costs, since 4-bit phasors require ten diodes, 3-bit phasors require eight diodes, and 2-bit phasors require six diodes. Furthermore, the cost of the control system is dependent on the number of bits that must be controlled. Closely related to cost is complexity, with resulting overall reliability decreasing as the number of phase bits is increased. The study concluded that 2-bit phasors would lead to unacceptably high sidelobes and possible distorted beams. It was determined that the use of 3-bit rather than 4-bit phasors could result in only a slight decrease in performance.

The short pulse behavior study was made to determine the behavior of the cylindrical array antenna for short pulse experiments. In the usual operation of a phased array steered by phase shifters, all phase shift increments are less than 360 degrees, and the transit time of the energy through the array varies due to the omission of wavelength multiples; this omission of delays produces pulse distortion with resulting system degradation. As a result of this study and consideration of power handling capability of the time delay units, the aperture is being divided into 12 subarrays – six for elevation scanning divided into two subarrays for azimuth scanning.

OPERATING CHARACTERISTICS OF CYLINDRICAL ARRAY

The antenna was designed to operate over the frequency range of 2.9 to 3.5 GHz. The array will be steered by phase in both elevation and azimuth. In normal operation of the cylindrical array phase steering is used in elevation only, and azimuth scanning is accomplished by commutation of the excitation distribution.

However, in the system to be described, only a 60 degree arc of the cylinder is implemented; hence azimuth scanning can be accomplished by phasing, as in the planar array, with no commutation of the amplitude distribution.

The antenna consists of 1344 active elements arranged in 42 columns of 32 elements, as pictorially illustrated in figure 14-2. These columns lie along the generators of a cylindrical surface, occupying a 60 degree sector. Alternate columns have a vertical displacement of one-half of the vertical element spacing. This configuration is used because of its superior scanning properties. Each element has an associated diode digital phase shifter with three additive phase units of 180, 90, and 45 degrees. The state of each phase shifter is represented by an integer between 0 and 7, this being the phase shift setting in 45 degree units. The three bits of this number in binary form correspond directly to the 180, 90, and 45 degree units of the phase shifter. Digital control techniques are directly applicable in this method of individual phase control and, hence, in antenna beam steering.

In general, energy incident upon the antenna from a particular direction excites each receiving element with a different phase. The phase shifters behind each element are used to equalize the output phases of all elements so that summation will give maximum signal amplitude. The correct setting of the phase shifters can place the direction of maximum response (the beam position) anywhere within a selected area. In general, each beam that is formed requires a different setting of all 1344 phase shifters. It is clear that even modest beam agility requires some form of automatic control. A photograph of the antenna is presented in in figure 14-3.

The steering circuitry is designed to place the beam in any one of 900 beam positions within the azimuth sector of plus or minus 25 degrees and with elevation limits of plus 30 degrees and minus 15 degrees.

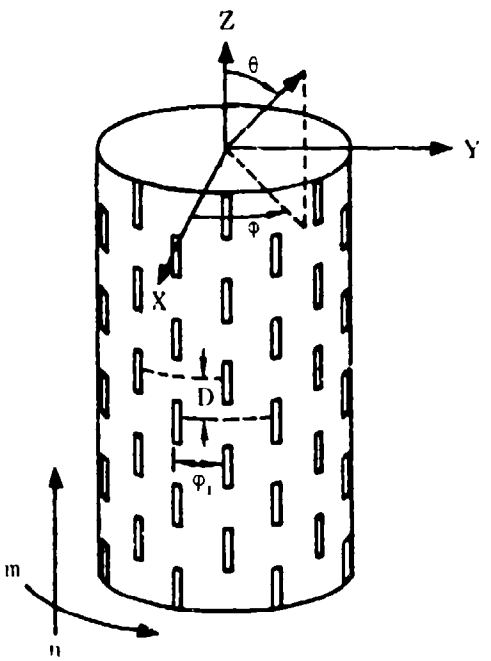

Figure 14-2. Antenna configuration, cylindrical array.

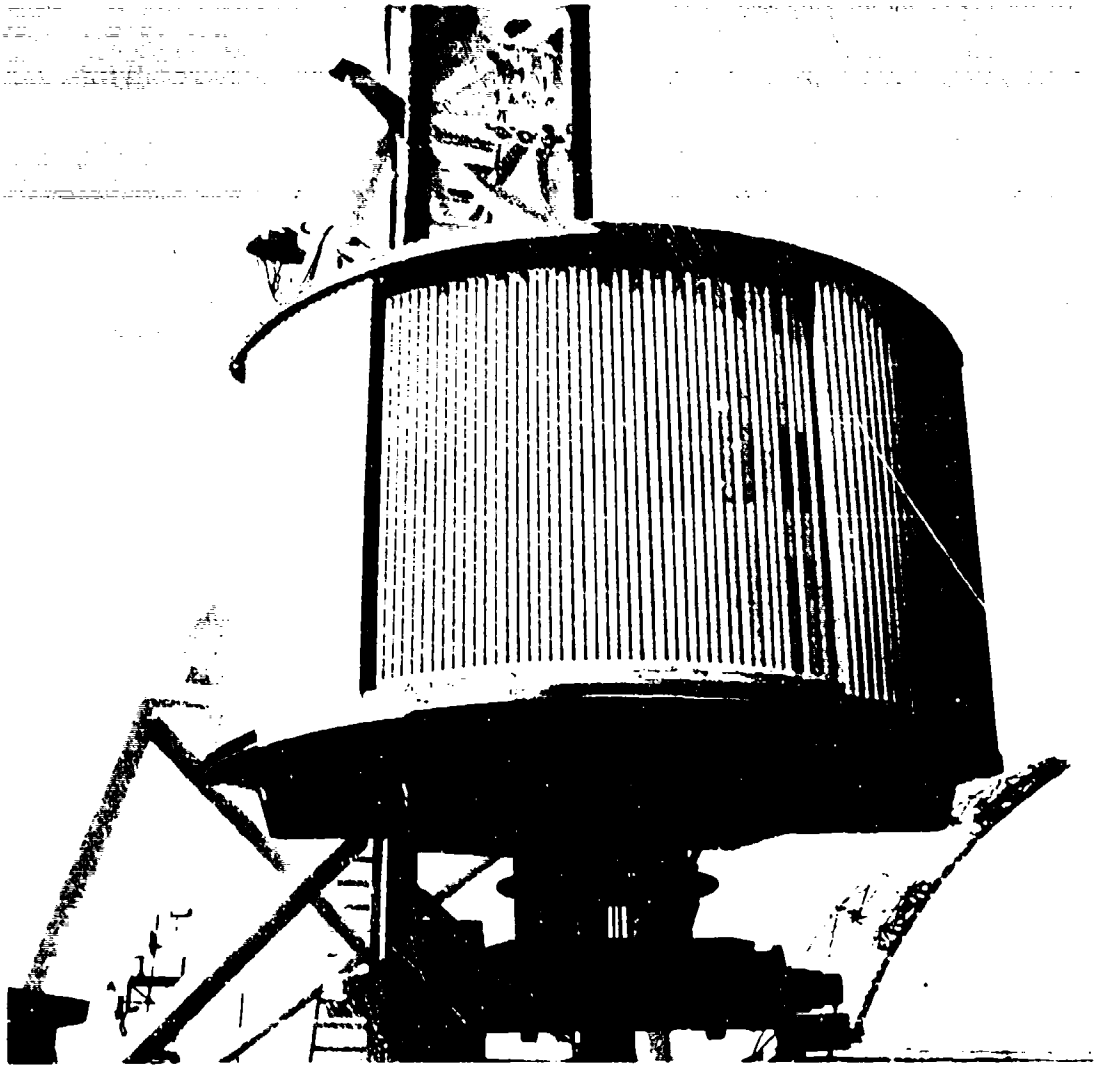

Figure 14-3. Partial cylindrical array.

COMPUTING ELEMENT PHASE VALUES

As illustrated in figure 14-2, the indices m and n give the column and row locations of the elements. The elements lie at locations for which the sum of m and n is even (the choice of this set or the set for which the sum is odd is completely arbitrary). The required phase shifter setting, at the element location (m,n) to form a beam with the coordinates (θ', φ) is given by

$$Pmn = 8nD \text{ Cos } \theta' - 8A \text{ Sin } \theta' \text{ Cos } (\varphi_o + m\varphi_i - \varphi) \qquad (10)$$

The expression is reduced to modulus 8 and rounded to the nearest integer. Symbol definitions are:

Pmn	the digital phase shifter setting at element (m,n).
A	the radius of the cylindrical array in wavelengths. (26.3)
D	the spacing between rows of elements in wavelengths; (0.3625) equivalently, one-half the spacing between elements along columns in wavelengths.
φ_o	Azimuth location of the reference column (m = 0 column).
φ_i	Angular spacing between the vertical columns of elements; ($\doteq$1.4 degrees), equivalently, one-half the angular spacing between elements along rows.

For this antenna, the indices m and n take on 42 and 64 consecutive integer values respectively. The elements lie at lattice locations for which the sum of m and n is even. The indices (m,n) can take on positive or negative values. The range for n is arbitrary, since the addition of a constant value to all n values simply changes all phase values by the same amount. The range of m values, however, must be consistent with the choice of φ_o, the location of the azimuth reference column.

It is apparent that the above equation must be solved for 1344 phase values for each antenna beam position.

BEAM SWITCHING REQUIREMENTS

Once the antenna phasors have been set to form the desired beam, the antenna can transmit radar pulses. The antenna phasors must then remain set for this beam position until sufficient time has passed for the energy to return from the maximum range of the radar if continuous range coverage is desired. The relationship between the waiting time and maximum range is

$$t_w \text{ (microseconds)} = (20/3)R \text{ max. (kilometers)} \qquad (11)$$

A 50-kilometer range (about 27 nautical miles) requires 333 microseconds waiting time.

However, somewhat less time would be available for the computer to transfer the phase values (and other data words) to the antenna for the next beam

position. The computer must also communicate with RADAR control and perform housekeeping and other operations during this time. For shorter ranges of operation, considerably less time may be available to transfer control information to the antenna.

Due to the inherent beam switching capability of this electronically scanned antenna (that is, consecutive beams may be formed in any desired direction within antenna scan limits), many scan patterns are possible and may be implemented under computer control.

DESIGN APPROACH FOR ANTENNA CONTROL

Several methods of setting the phase values onto the antenna were considered. The method to be implemented does not involve memory devices at the individual antenna elements and requires less storage capacity for phase information within the computer.

The method described here, and illustrated in the block diagram of figure 14-4, provides for the summation of two 4-bit binary numbers at each antenna element. Although only three bits of the 4-bit adder output are used to control each phasor, four bit numbers are summed at each element to avoid excessive rounding errors.

Each dot on the element array schematic in figure 14-4 represents the location of an element and the point at which the intersecting data buss values are summed to provide the 3-bit phase value for each element. Note that the rows run horizontally (numbered 1 through 64) and the columns run vertically (numbered 1 through 42). Examination of equation (10) reveals that the phase setting at element (m,n) is the sum of two terms, and that for a given beam (θ', φ) the first term in the expression is linear. That is, the value of this term depends only upon the row in question – n times a constant. This permits a straightforward method of producing all row data from a single number, the number being 8D Cos θ'. The block labeled "Row Multiplier" operates on the number contained in one of the two Row Input Registers and provides a 4-bit number to each of the 64 rows. The second term of equation (10) includes the cosine of a function of m for a given beam (θ', φ). Unlike the row values, this term cannot be readily generated for the column values by a similar technique. The column term is more complex because it includes a correction to compensate for the curvature of the cylindrical surface. The values to be fed along the columns are precomputed and stored in the computer. The values are transferred to the appropriate column shift register, which supplies each of the 42 columns with 4-bit values. Notice that there are four sets of registers in figure 14-4, each set consisting of two identical registers labeled A and B. The block labeled "[illegible]ister Select" will connect the contents of register A or register B to the antenna (or radar) as commanded by the computer control logic.

Two sets of registers are being employed to avoid loss of antenna beam control during the time required to load the registers for a new beam position. The registers will be individually addressable for loading. This will permit greater versatility in antenna control and should reduce the complexity of the control and

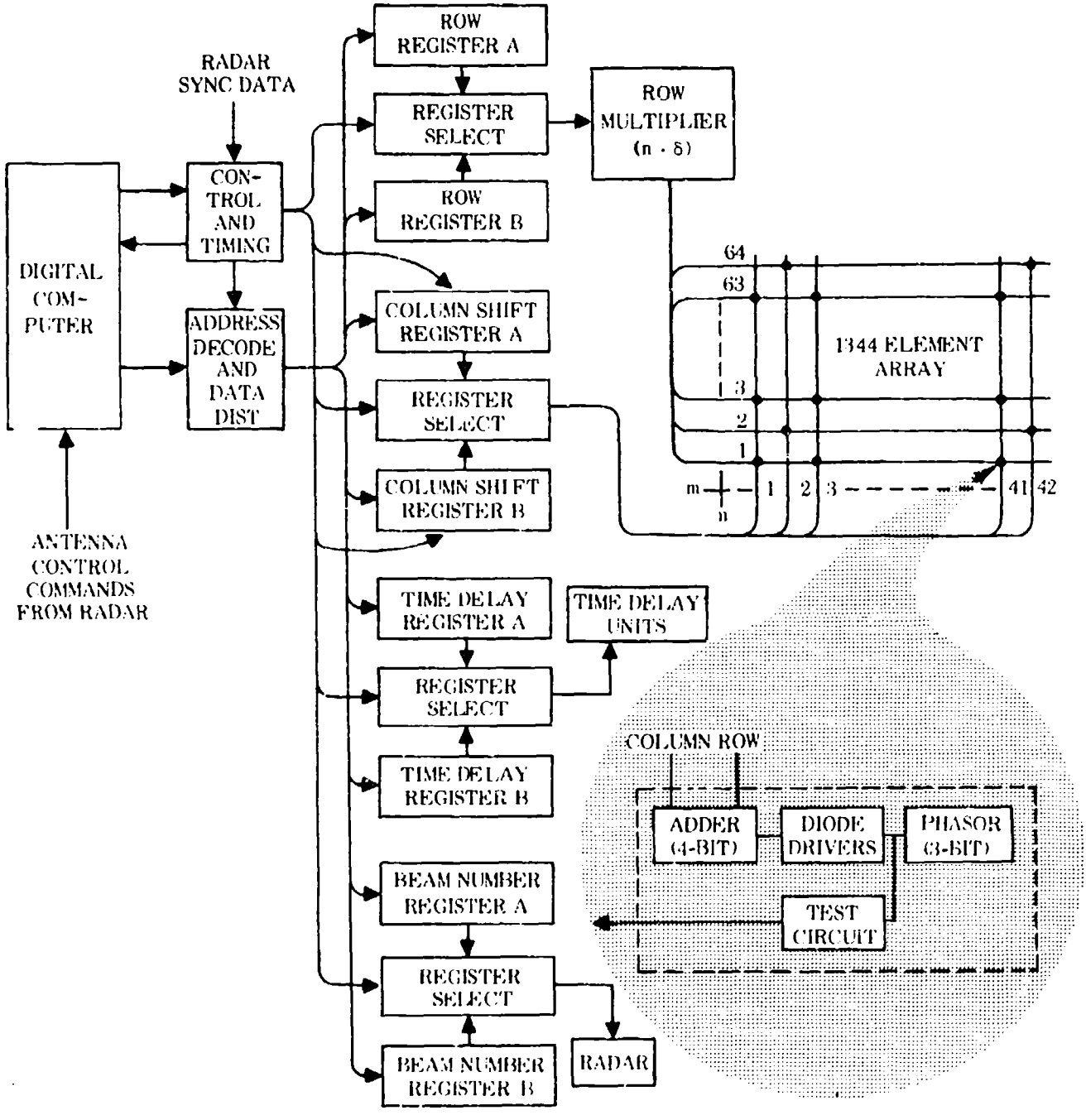

Figure 14-4. Control system block diagram, cylindrical array antenna.

timing logic. As can be seen, the antenna will not be usable during the time required for the data to propagate from the selected register set to the antenna element phasor. The time delay through the row multiplier circuits will be less than 0.5 microseconds.

The radar will send beam control information to the computer. It will also send syncronizing information to the control and timing section to be used to prevent antenna beam switching during radar transmission periods. The current beam number will be constantly available to radar from the selected beam number register.

REQUIRED BEAM POSITIONS/COMPUTER STORAGE

As indicated by equation (10), the number of possible beam positions is essentially infinite. This means that to have all beam positions available requires the on-line computation of phase values for each new beam, since storage of phase values for every beam position is clearly not possible. Study of equation (10) has indicated that several milliseconds are required to compute the phase settings for a new beam, even with the fastest computer. Again, this method is not practical for high-speed antenna scanning.

The method which seems most reasonable is that of storing phase values for a preselected number of beam positions. It is estimated that 900 beam positions, (30 in azimuth and 30 in elevation, which permits about a 45 degree scan in each plane), or less, will provide sufficient accuracy and coverage. Again referring to equation (10), close inspection shows that its value is unchanged if m is increased by one at the same time that ψ is increased by φ_j. This means that the moving of all phase settings on the antenna to the left (or right) by one column moves the main beam in azimuth by φ_j – about 1.4 degrees. This fact is important with respect to the amount of storage space required within the computer. By storing phase value tables over an extended range of m values, it is found that one such table will provide the correct phases for all azimuth beams at the same elevation angle. Therefore, the number of tables in store will be exactly equal to the total number of required elevation beam positions rather than equal to the total number of beams. The length of each table is directly related to the number of required azimuth beam positions. Also, for sequential azimuth scanning the computer is required to transfer only four bits of data into the column shift register that is connected to the antenna (fig. 14-4). This process of transferring four bits of data continues until the beam reaches its azimuth limit. At this time the alternate set of registers (which have been loaded with the next elevation position data) would be connected to the antenna. This procedure would provide a full raster scan. Clearly, a limited raster scan over a specified area can also be achieved by a similar procedure. It should be realized that all other operating modes require the transfer of a complete new set of data for each new beam: the same data transfer time as for random beam positioning.

Figure 14-5 is an example of the actual phase settings required to form a beam at $\theta' = 70$ degrees and $\varphi = 20$ degrees.

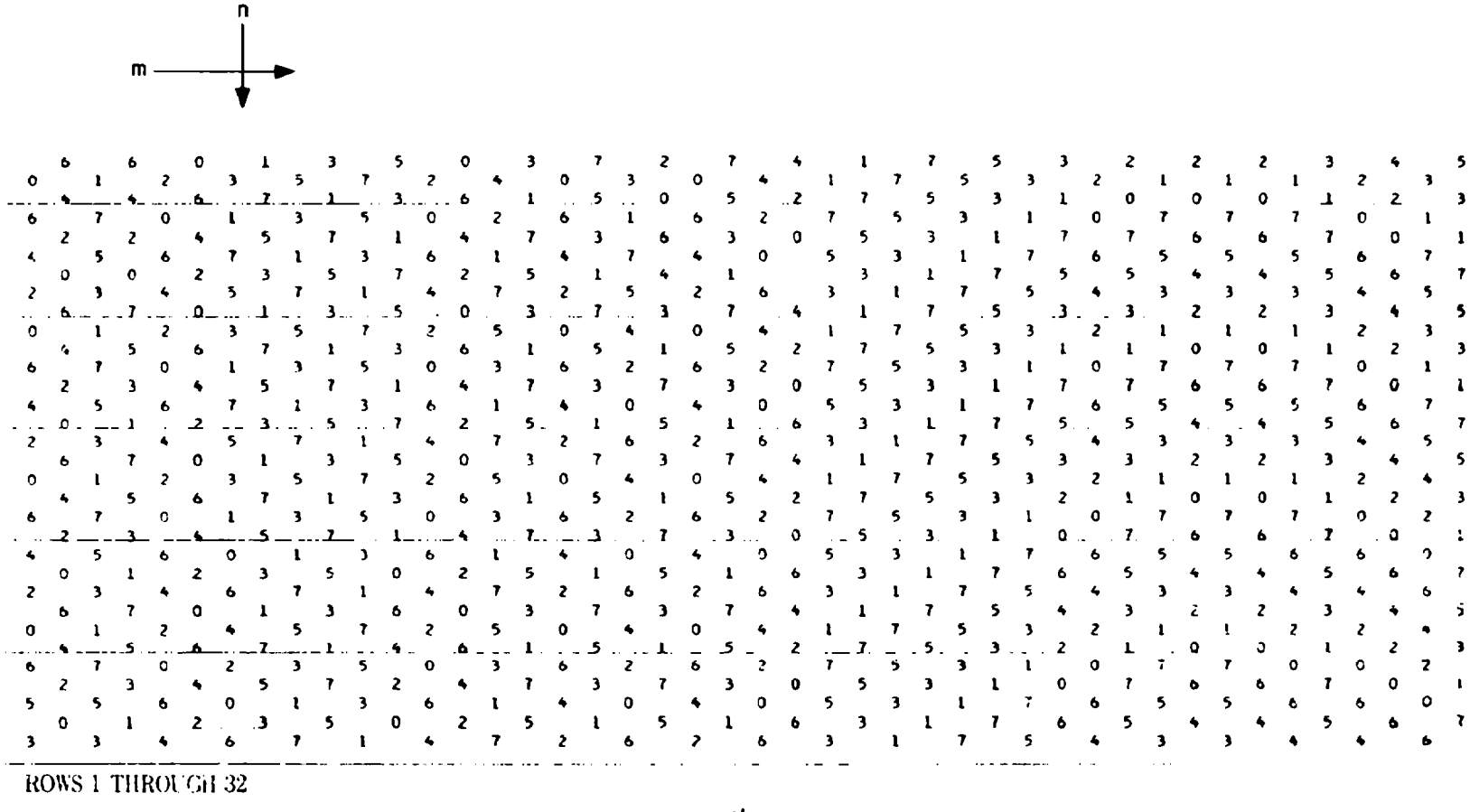

Figure 14-5. Element phase settings, $\theta' = 70$ degrees and $\phi = 20$ degrees.

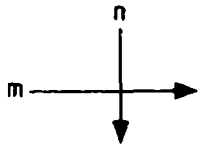

ROWS 33 THROUGH 64

Figure 14-5 (Continued).

DATA STORAGE REQUIREMENTS

Recall that forty-two 4-bit words and one 10-bit word are required to set all antenna phasors for a given beam. Also, additional beams in azimuth (for that elevation position) can be generated for each new 4-bit value that is shifted into the column shift register. This means that for 30 azimuth beams the storage space required is forty-two 4-bit words for the first beam plus twenty-nine 4-bit words for the next 29 beams. Also, twelve 3-bit time delay words must be stored for each beam position.

The storage requirements per elevation position (30 azimuth beams) are,

71	4-bit values (columns)
1	10-bit values (rows)
360	3-bit values (time delay)

Considering a 16-bit computer word, this equates to eighty-seven 16-bit words per elevation position. For 30 elevation positions, the minimum storage requirement for beam data is 2,610 computer words. This assumes maximum packing of data.

The following expression gives the minimum number of 16-bit words required for any selected number of elevation and azimuth beam positions.

$$N = n_{EL} \left[(10n_{AZ} + 45)/4 \right] * \tag{12}$$

Where

n_{EL} = Number of elevation beams

n_{AZ} = Number of azimuth beams

N = Number of 16-bit words

Storage requirements for the running programs are not as easily computed at this time. However, it is quite reasonable to expect the total core requirement will exceed 4000 words. Since computers generally are not available with less than 4000 word blocks of memory, this application then will require an 8000-word memory computer. Provision will be made for additional memory if required.

SPEED/OUTPUT REQUIREMENTS

As previously indicated, the general requirement is for twenty 16-bit data words to be transferred for each beam. This data will be divided among four separate registers. Therefore, the output sequence will be to address a register and then output its data until the 20 words are transferred.

Once the computer program has interpreted the command from radar and found the block of data to be transferred to the antenna, it must make several more

---

* The factor $(10n_{AZ} + 45)/4$ is computed and rounded to the next higher integer before multiplying by n_{EL}.

memory references to output the phase data and control words. The instruction execution time (for one particular computer) to transfer the 20 data words, address the specific registers and output one required control command, requires up to 103 microseconds. The memory cycle time of this machine is 0.86 microseconds. The 103-microsecond time is for programming each word out through the central processing unit. If the optional buffer channel feature is considered for this machine, the same transfer takes 48.9 microseconds. The data for the column shift register could be transferred via such a buffer channel at memory cycle speeds. A small machine with this memory speed and a suitable output section should be adequate to control the antenna for any desired function.

CIRCUIT DESIGN AND PACKAGING

PHASOR DRIVER CIRCUITRY

The schematic diagrams of figure 14-6 illustrate both the driver circuitry required to control each 3-bit diode phase shifter and the 3-bit phasor. A photograph of the phasor is shown in figure 14-7. The phasor is designed with PIN diodes three diodes each for the 180-degree and 90-degree phase bits. The 45-degree phase bit uses two diodes. The 180-degree and 90-degree phase bits are of the switched-line form. The 45-degree phase bit is of the periodically loaded-line form. As indicated, the diodes in this bit are stub mounted across the main line.

Control requirements for the 180-degree and 90-degree phase bits are identical. Referring to the 180-degree bit, note that two diodes are labeled D. This phase bit requires complimentary control – that is, when diodes A are reverse biased, diode D must be forward biased. This condition produces the long delay path (180-degree phase shift). The diodes are physically located a distance equivalent to a quarter-wavelength from the T junctions of the phase bit. The low impedance of a conducting diode is transformed to a high impedance at the T junction by the quarter-wave-length line. The two diodes of the 45-degree bit are controlled in parallel, either both on or both off. When the diodes are reverse biased (off state), the 45-degree phase shift is introduced.

For satisfactory operation, the PIN diodes are driven with a forward current of 30-35 milliamperes or a reverse voltage of 90 volts. The diode driver was designed to interface directly with transistor transistor logic (TTL) and to operate at the TTL power supply voltage, +5 volts. The base reference voltage, +3V, can be derived from the regulated +5-volt supply through a simple series pass regulator.

Assume the 180-degree input shown in figure 14-6 is the in the "logic 0" state (about 0.2 volts). Q_1 conducts and the common emitter voltage becomes about 2.5 volts, which is sufficiently low to hold Q_2 off. About 70 milliamperes is delivered to the two parallel PIN diodes. The current through D_1 develops a reverse bias from base to emitter of Q_3 and holds it off. Since D_2 is not conducting, Q_4 provides a low impedance path from -90 volts to point D, the anode of the

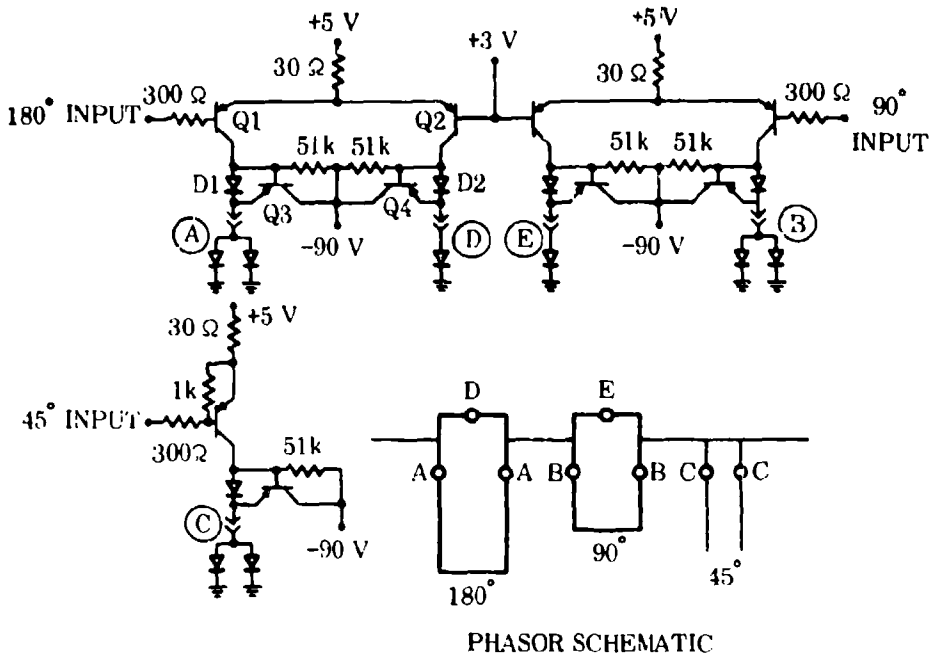

Figure 14-6. Phasor driver and phasor schematics.

single PIN diode. As the input rises to the "logic 1" state turning Q_1 off, the common emitter voltage rises until Q_2 conducts (about 3.6 volts). About 35 milliamperes is delivered to the single PIN diode. The voltage across D_2 turns Q_4 off. Since D_1 is not conducting, Q_3 applies reverse bias to the pair of PIN diodes. Switching waveforms are illustrated in figure 14-8. The waveforms illustrate the voltage and current for the two-diode side of the phase bit (point A). Figure 14-8 illustrates the "turn-off" characteristics of the circuit. This switching is initiated when the input signal changes from the "logic 0" state. As indicated, the current delivered to the diode pair changes from 70 milliamperes to zero in about 0.4 microseconds. About 0.1 microsecond later Q_3 begins conducting and a reverse current flows through the pair of PIN diodes to the -90-volt supply. This current reaches a maximum of 140 milliamperes and then begins decreasing toward zero. Diode current flow is essentially zero after about one microsecond. The diode reverse voltage reaches its maximum of -90 volts in less than 2 microseconds. Figure 14-8 illustrates a complete switching cycle. Note that the time required to switch the diodes into conduction is considerably less than the time required to reverse bias them.

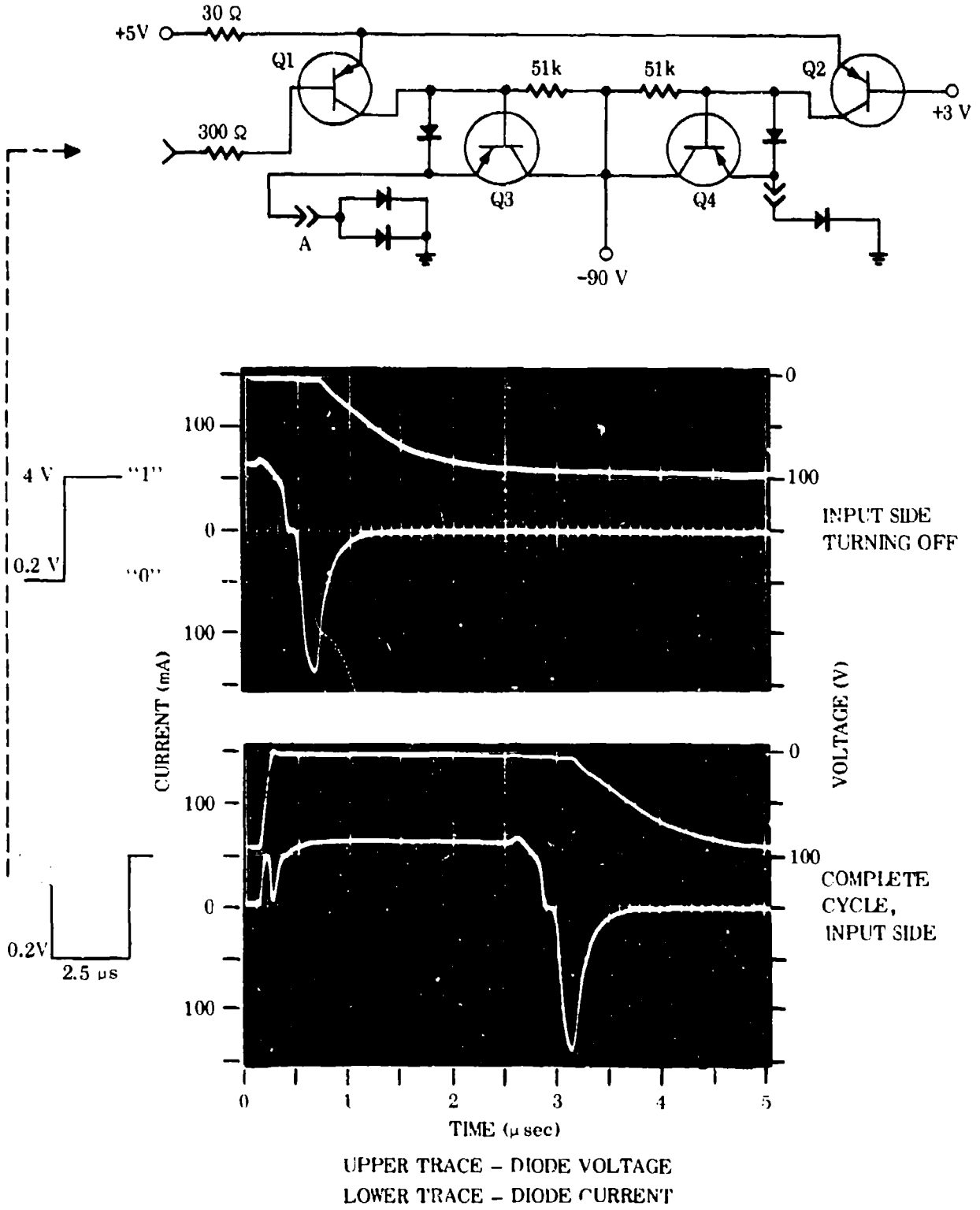

Figure 14-8. Driver switching schematic and waveforms (upper trace - diode voltage; lower trace - diode current).

ELEMENT TEST CIRCUITRY

Test circuitry has been designed as an integral part of the antenna control logic. For large arrays it is necessary to provide a method of testing for defective or inoperative control components. Random failure of elements of phased arrays is a characteristic which has been called "graceful degradation." This means that array performance degrades gradually as more and more radiating elements cease to operate fully or fail completely. Indeed, the capability of detecting and repairing these components as they fail should be available. Alternatively, one could perform some sort of periodic manual test and/or inspection or simply wait until antenna degradation is reflected in overall poor system performance.

In order to exhaustively test the antenna it would be necessary to sample radiated energy at each element and measure phase and power. This method would be quite expensive and would introduce additional rf losses in the system due to the additional components required.

The test method being implemented for this array provides a "GO-NO GO" test output from each phasor. Each element of the array has a test circuit which is designed to detect faulty control information up to and including the PIN diodes in the phase shifter. The test circuit monitors the five control inputs to the phasor, points A, B, C, D, and E (fig. 14-6). During normal circuit operation the voltage level at any test point is +0.9 volts or -90 volts. The test circuit is designed to provide a measurable output for only two unique sets of driver input commands; that is, minimum phase shift (all inputs low) and maximum phase shift (all inputs high). This is sufficient to examine all phasor diodes, drivers, and related control circuitry. The amount of test circuitry is considerably less than that required to check all eight possible states. Assume that all three driver inputs are low. The voltages at points A, B, and C should be high (+0.9 volts), and at points D and E the voltage should be low (-90 volts). If the three inputs are raised to the high state, the opposite should be true; points A, B, and C low (-90 volts), and points D and E high (+0.9 volts). The logic expression representing these two conditions is

$$A\,B\,C\,\overline{D}\,\overline{E} + \overline{A}\,\overline{B}\,\overline{C}\,D\,E = X \qquad (13)$$

This logic will also detect a shorted PIN diode, since a shorted diode will hold that point at zero volts under all input conditions.

TEST CIRCUIT INTERFACE

In order to implement this test circuit with integrated circuit logic, the voltages monitored must be scaled up to compatible levels. A simple resistive voltage divider, in conjunction with the integrated circuit input clamp diode, is used to accomplish this and is shown as the Type 1 input in figure 14-9. The resistors are so chosen that -90 volts at the test point (point 1, fig. 14-9) produces a slightly negative voltage at point 2. The clamp diode prevents this voltage from becoming more negative than -0.6 volts. This is the "logic 0" level. When point 1 is +0.9 volts, point 2 rises to the "logic 1" level, about +4 volts.

As indicated above, five of these interface circuits are required per phasor. One circuit for each of the phasor control inputs, points A through E of figure 14-6. This will permit detection of a control circuitry malfunction and will also detect shorted PIN diodes. Also, this circuit will detect open PIN diodes at points A and B of figure 14-6. By examining driver circuit operation it is seen that if point A is open (because of open PIN diodes or connector failure), the PIN diode connected to point D will be forward biased for both input logic states. Correspondingly, the same is true for the 90-degree driver.

Additional circuitry to detect open diodes is required for points D, E, and C only. The interface circuitry to accomplish this is illustrated in figure 14-9, Type 2. Point 3 of this circuit rises to the "logic 1" level if the PIN diode or associated connector opens.

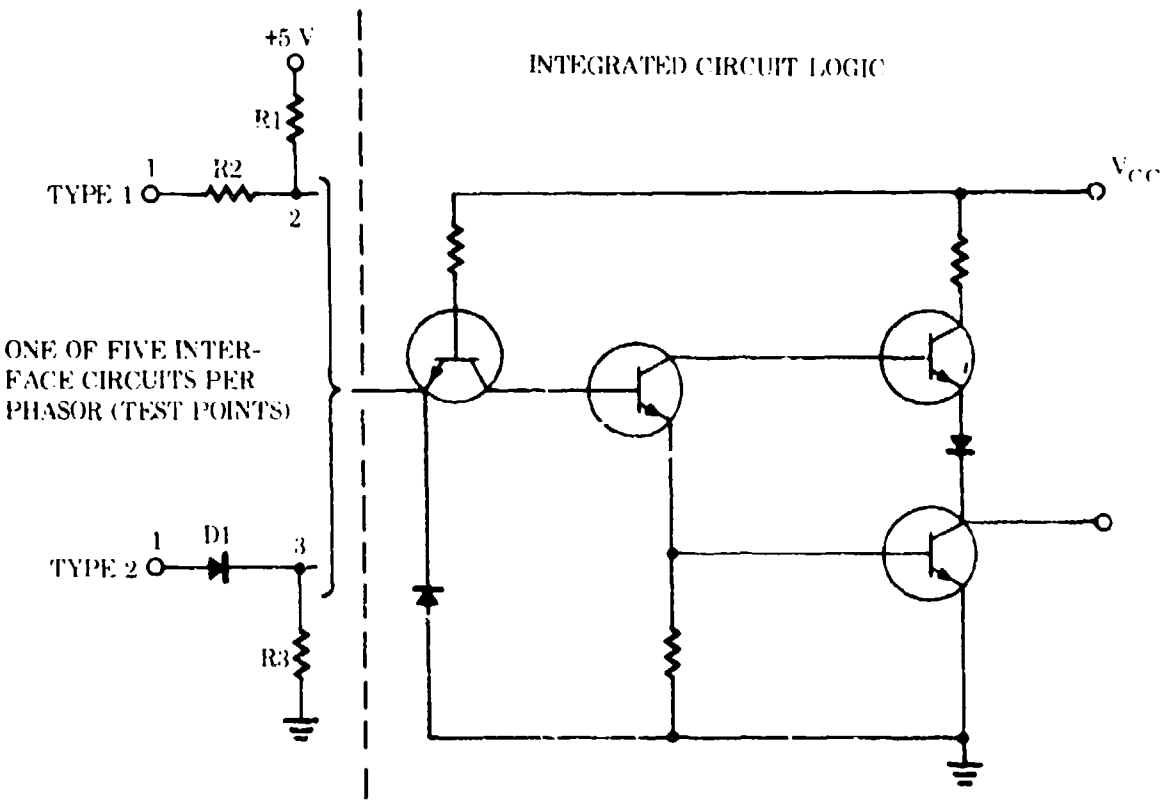

Figure 14-9. Test circuit interface schematics, Types 1 and 2.

TEST CIRCUIT LOGIC

The complete equation to be implemented for testing an antenna element consists of eight variables

$$A\,B\,C\,\overline{D}\,\overline{E}\,\overline{F}\,\overline{G}\,\overline{H} + \overline{A}\,\overline{B}\,\overline{C}\,D\,E\,\overline{F}\,\overline{G}\,\overline{H} = Y \qquad (14)$$

The variables F, G, and H are contributions of the three interface circuits designed to detect open PIN diodes (fig. 14-9). Note that point 3 of figure 14-9 is always at the "logic 0" level under normal operation.

The logic function of equation (14) may be realized directly with and-or logic, converted to its NAND or NOR equivalent, or perhaps a combination of the above. Equation (14) expressed in NAND and NOR form is as follows:

$$\overline{\overline{A\,B\,C\,\overline{D}\,\overline{E}\,\overline{F}\,\overline{G}\,\overline{H}} \cdot \overline{\overline{A}\,\overline{B}\,\overline{C}\,D\,E\,\overline{F}\,\overline{G}\,\overline{H}}} = Y \qquad (15)$$

$$\overline{\overline{A}+B+C+D+E+F+G+H} \cdot \overline{A+B+C+\overline{D}+\overline{E}+F+G+H} = \overline{Y} \qquad (16)$$

Equation (15) requires thirteen inverters to produce the complements of the variables A through H and to avoid driving more than one logic gate from any resistive interface circuit. Also, two eight-input NAND gates and one two-input NAND gate are required. This requires three inverter chips and three NAND chips, or a total of six chips to implement the circuit. Equation (16) could be implemented with five open collector inverter chips using the "wired OR" technique to produce the NOR gates. Eight-input NOR chips are not readily available.

Both the above require too many chips and too many interconnections to be attractive. Implementing equation (16) would require 124 wire bonds to interconnect the five integrated circuit (IC) chips.

Another expression which requires three IC chips, less than half the wire bonds, and less IC chip cost has been found. This circuit uses one MSI chip and two SSI chips. The equation is more complex, and more logic is utilized; yet the IC cost is less, and the circuit is easier to implement. Equation (17) is the logic expression for this circuit.

$$(\overline{A} \oplus B)\,(\overline{A} \oplus C)\,(A \oplus D)\,(A \oplus E)\,\overline{F}\,\overline{G}\,\overline{H} = Y \qquad (17)$$

or

$$(A \odot B)\,(A \odot C)\,(A \oplus D)\,(A \oplus E)\,\overline{F}\,\overline{G}\,\overline{H} = Y$$

Equations (14) and (17) are shown to be equivalent as follows:

$$Y = (\overline{A}\,\overline{B}\,\overline{C}\,D\,E + A\,B\,C\,\overline{D}\,\overline{E})\,\overline{F}\,\overline{G}\,\overline{H} \qquad (14)$$

adding zero value terms to permit factoring,

$$Y = (\overline{A}\,\overline{B}\,\overline{C}\,\overline{A}\,D\,E + \overline{A}\,\overline{B}\,\overline{C}\,A\,\overline{D}\,\overline{E} + A\,B\,C\,\overline{A}\,D\,E + A\,B\,C\,A\,\overline{D}\,\overline{E})\,\overline{F}\,\overline{G}\,\overline{H}$$

$$= (\overline{A}\,\overline{B}\,\overline{C} + A\,B\,C)(\overline{A}\,D\,E + A\,\overline{D}\,\overline{E})\,\overline{F}\,\overline{G}\,\overline{H}$$

again, adding zero value terms to each factor,

$$= [\bar{A}\,\bar{A}\,\bar{B}\,\bar{C} + \bar{A}\,A\,\bar{B}\,C + \bar{A}\,A\,B\,\bar{C} + A\,A\,B\,C)]\,[(\bar{A}\,\bar{A}\,D\,E + \bar{A}\,A\,D\,\bar{E} + \bar{A}\,A\,\bar{D}\,E + A\,A\,\bar{D}\,\bar{E})]\,\bar{F}\,\bar{G}\,\bar{H}$$

$$= [(\bar{A}\,\bar{B} + A\,B)\,(\bar{A}\,\bar{C} + A\,C)]\,[(\bar{A}\,D + A\,\bar{D})\,(\bar{A}\,E + A\,\bar{E})]\,\bar{F}\,\bar{G}\,\bar{H}$$

$$Y = (\bar{A} \oplus B)\,(\bar{A} \oplus C)\,(A \oplus D)\,(A \oplus E)\,\bar{F}\,\bar{G}\,\bar{H} \qquad (17)$$

The test circuit logic diagram with the phasor-driver interface circuits is shown in figure 14-10. The circuit utilizes all logic functions on the three IC chips except for one input to the 8-input NAND gate. As indicated, a single test output Y will be provided for each of the 1344 elements. Under the two input test conditions, this output should be the same at all elements.

Recall that the antenna is constructed in rows and columns of elements, much the form of a matrix. This suggests that the 1344 element test output points could be combined in such a way that row-column indicators would pinpoint the faulty element. This would require one AND circuit for each row and one AND circuit for each column of the antenna with appropriate row and column indicators for each of the 106 AND circuits. A faulty element test output would cause the row and column indicators which include the faulty element to illuminate. However, if two elements are simultaneously indicating a fault, the row-column circuits could indicate up to four elements. Assume the elements circled in figure 14-11 are

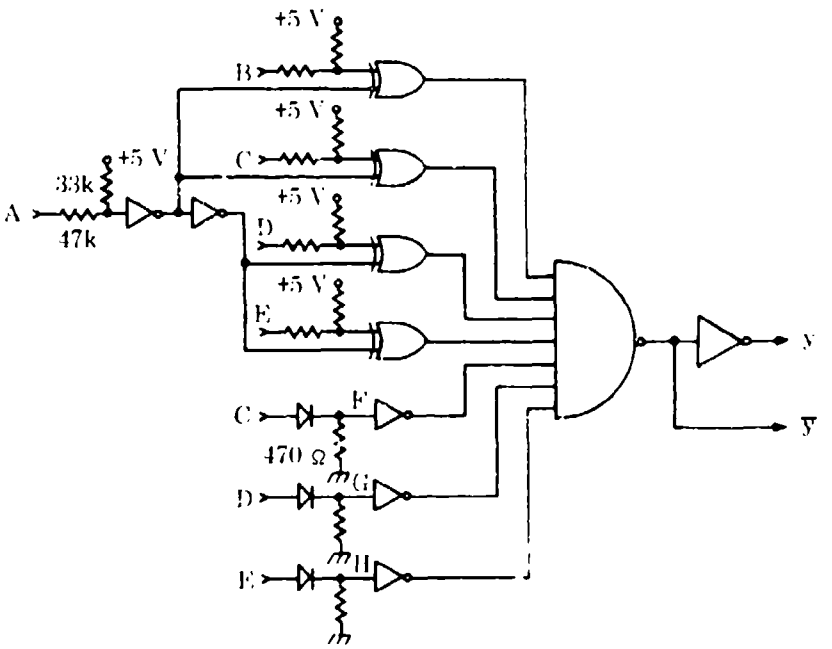

Figure 14-10. Test circuit logic.

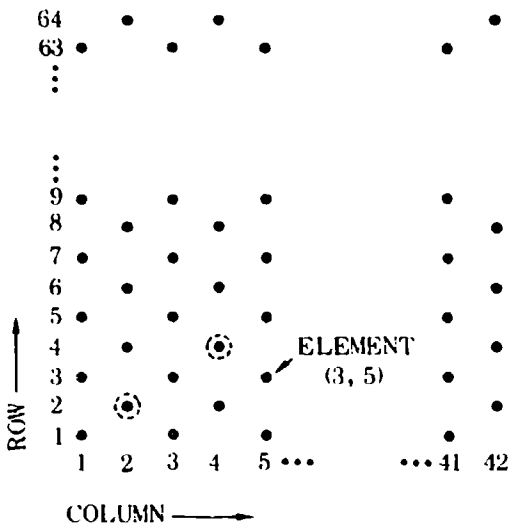

Figure 14-11. Antenna element locations.

outputting fault indications, elements (4, 4) and (2, 2). There are also row-column intersections for the good elements (4, 2) and (2, 4). Due to the empty array locations, the ambiguity occurs only when the elements lie in rows (or columns) for which the sum is even and are not located in the same row or column.

The presence of ambigious indications is obvious by inspection, when they occur, and may be isolated quickly by checking the element test circuit outputs (Y, fig. 14-10).

The row and column AND circuits will be implemented as shown in figure 14-12. Single AND gates are not available with the required number of inputs. The test procedure could be completely automated by returning the row and column signals to the control computer. Periodic testing could then be performed under operational conditions with brief interruption of antenna operation.

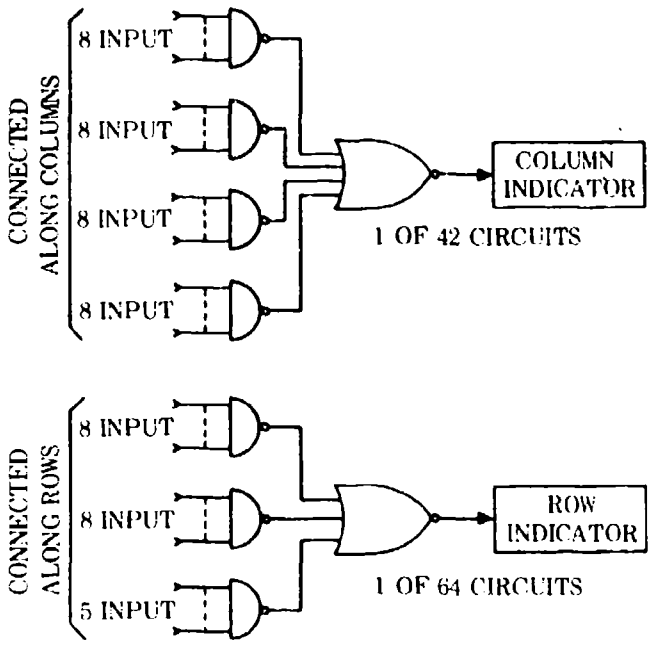

Figure 14-12. Row and column logic diagrams, test circuitry.

PHASOR DRIVER AND TEST CIRCUIT PACKAGING

Twenty drivers and twenty test circuits were designed and packaged using the thin-film hybrid-circuit technique. Photographs of the driver and test circuit are shown in figures 14-13 and 14-14. The information obtained from the design and test of these circuits was useful in designing a thick-film hybrid which includes the control and test electronics required at each element in the array. A block diagram of this circuit, the adder-driver-test circuit (ADT), is shown in figure 14-15. A photograph of the completed ADT is shown in figure 14-16.

Low-level TTL logic was used in the test circuit design to reduce power consumption. This permitted the interface circuits (fig. 14-9) to be designed with higher values of resistance. The maximum power dissipation for the ADT is 2.4 watts. This occurs when the circuit is switched to produce minimum phase delay.

The thick-film technique was considered more desirable for this application because of lower substrate cost and more rapid production, which resulted in a substantial overall savings. In thick film, the resistors and conductive paths are screen-printed on a relatively inexpensive substrate. The active devices are mounted in discrete chip form. In the thin-film circuits referred to above, a gold-clad ceramic substrate was etched leaving the conductor paths and bonding pads. The resistors and active devices were mounted in chip form, then interconnected by wire bonding. Although thin-film conductors and resistors can be constructed by a deposition process, this approach was not considered practical for this application.

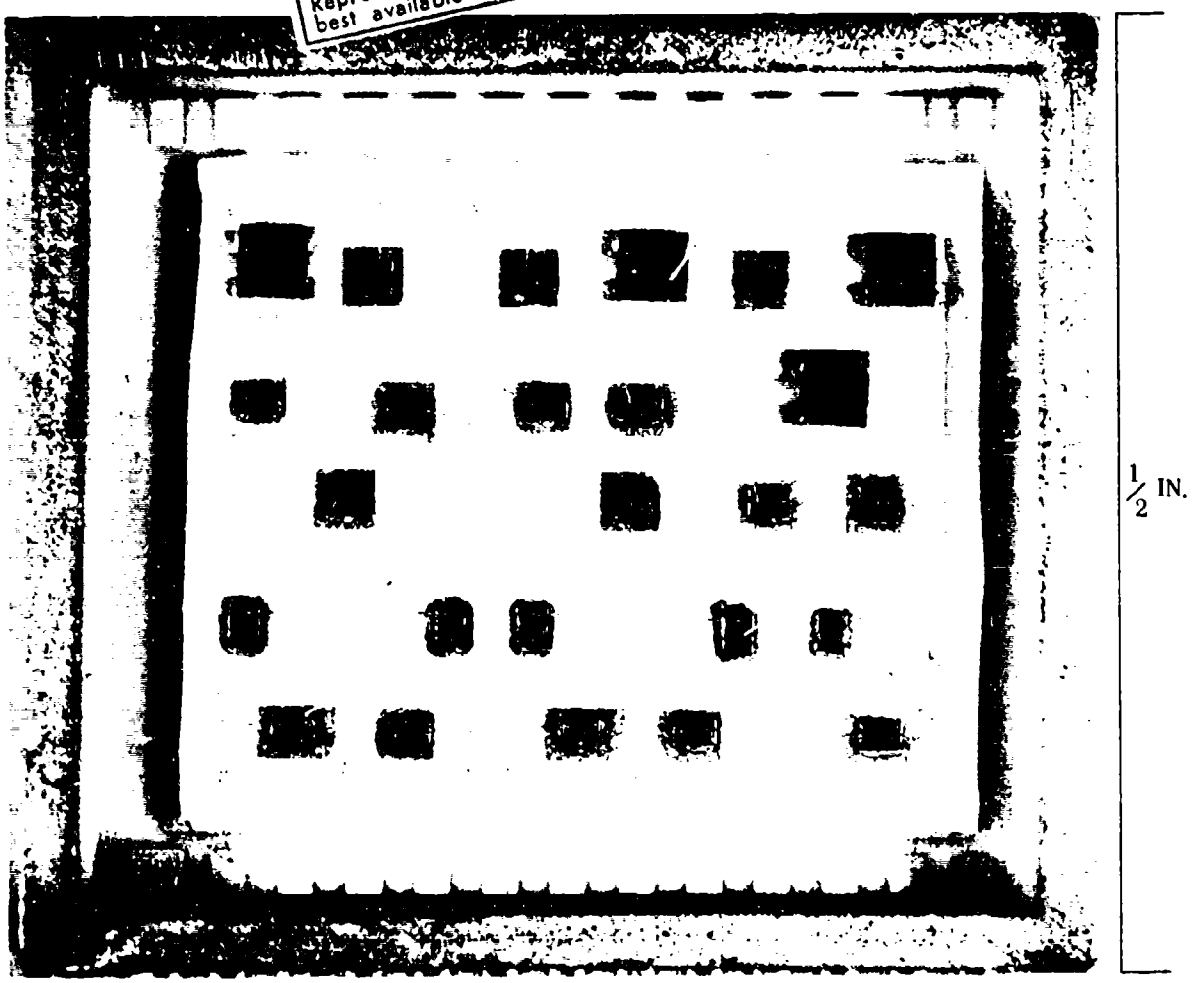

Figure 14-13. Phasor driver.

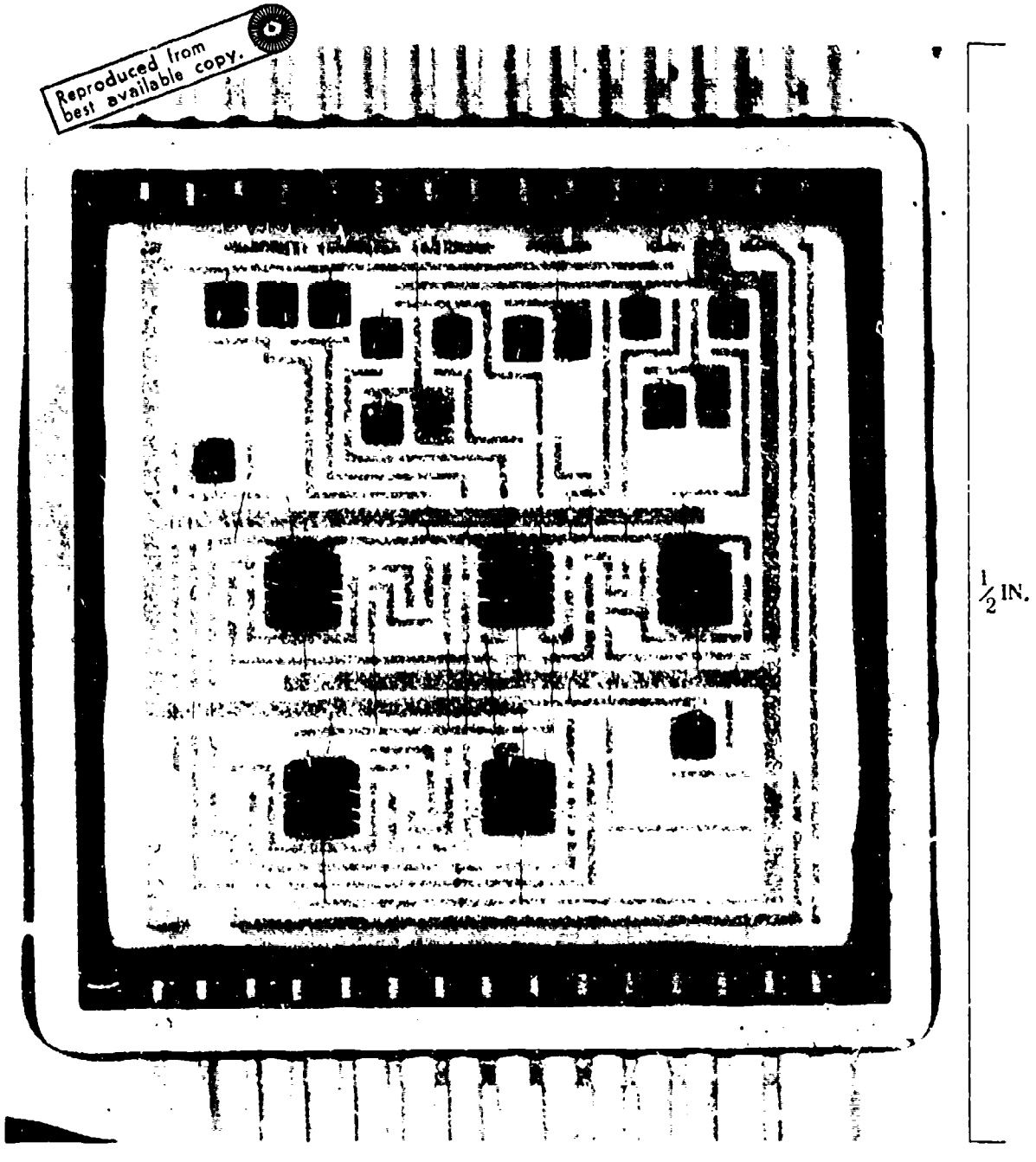

Figure 14-14. Test circuit.

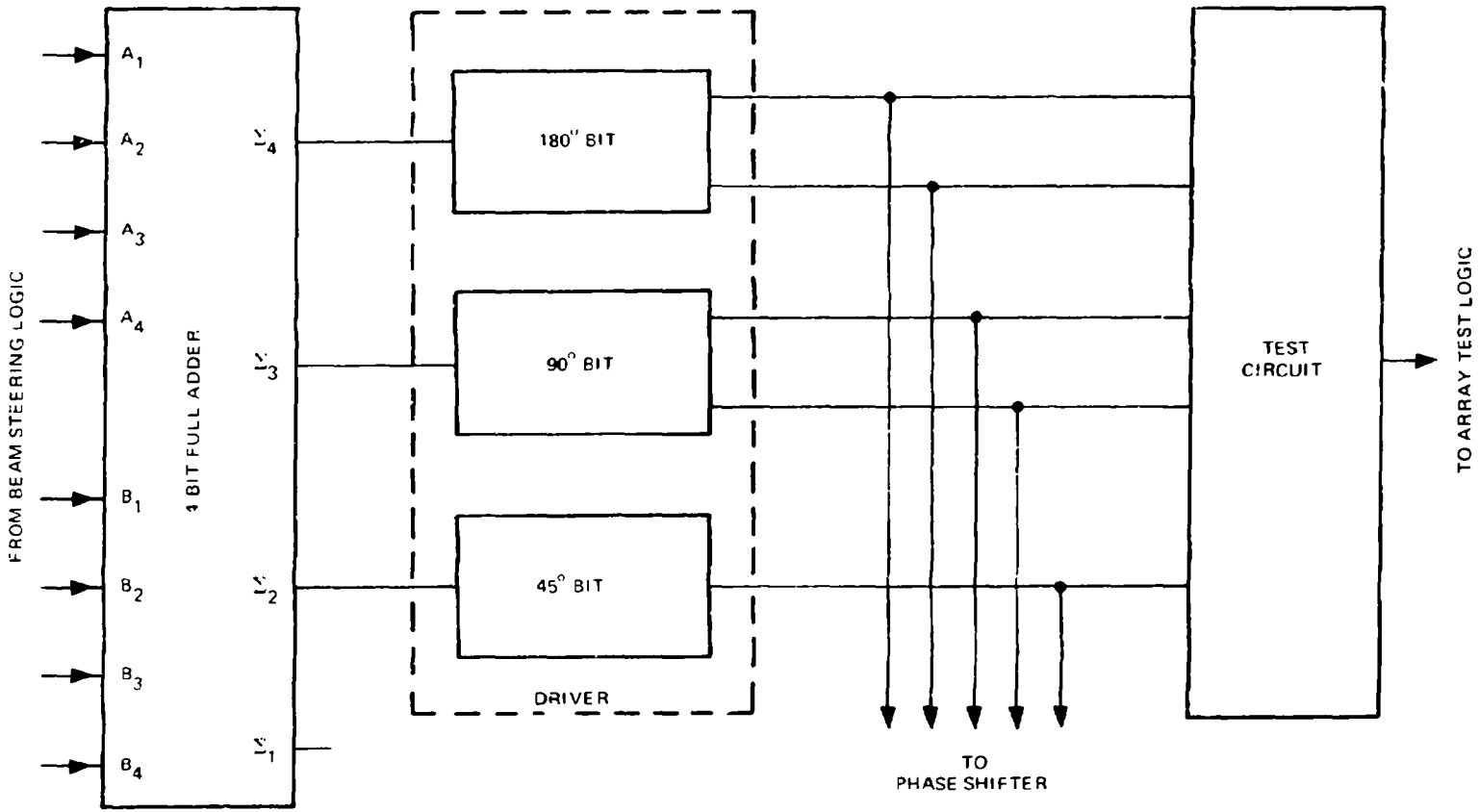

Figure 14-15. ADT block diagram.

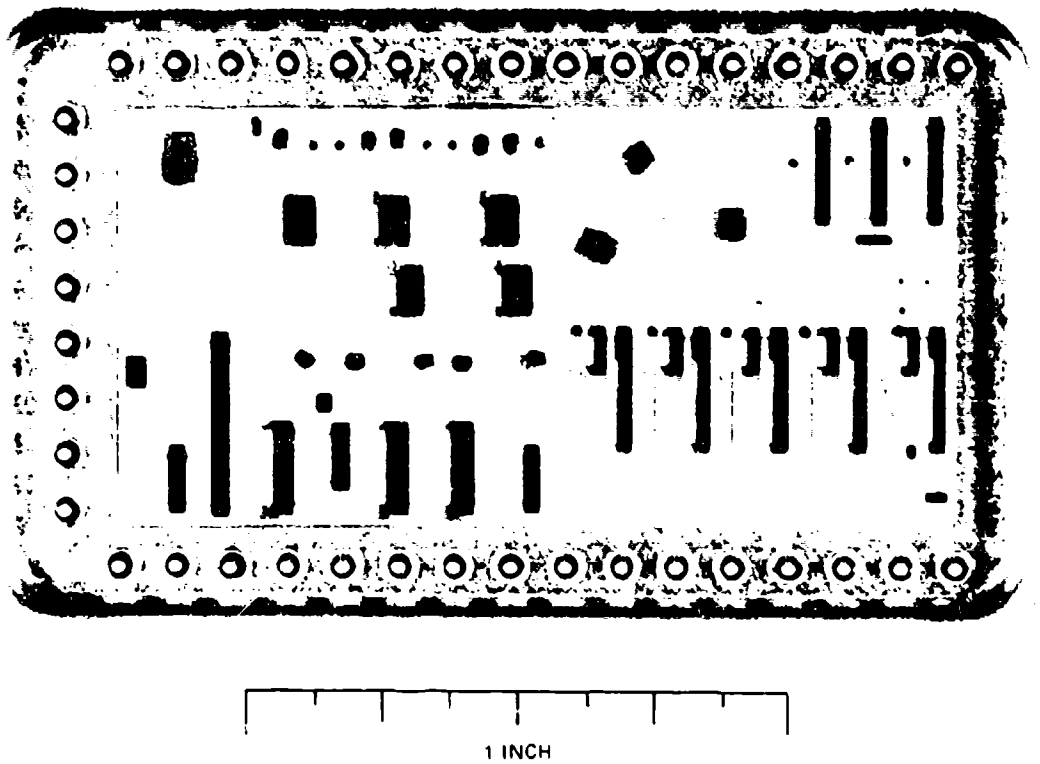

Figure 14-16. Adder-driver-test circuit, thick film.

CONCLUSIONS

A small general-purpose computer is found to be acceptable for steering the beam for many random beam positions of a cylindrical array. A general-purpose controller can also be used for system testing and evaluation because of its programmable versatility. Set-up time for random beam positioning is on the order of 100 microseconds.

The use of binary adders at each antenna element to produce the element phase values eliminates three disadvantages of storage devices (flip-flops): (1) the method using flip-flops to form shift registers along rows or columns requires much more data storage capacity in the control computer; (2) the set-up time to transfer data for a given beam is longer, and (3) packaging considerations are more stringent. By keeping storage devices electrically remote from the antenna elements, and in small quantity, they can be compactly packaged and well shielded. The control method described allows this, and, as a result, noise is less likely to be a problem.

The application of thick-film microcircuit techniques to produce the phasor driver and test circuit in a common package is expected to improve reliability and reduce cost of these components.

REFERENCES

1. Munger, A. D. and Gladman, B. R., "Pattern Analysis for Cylindrical and Conical Arrays," Conformal Array Antenna Conference, Naval Electronics Laboratory Center, San Diego, California, 13-15 January 1970, Proceedings

2. Boyns, J. E. and others, "Step-Scanned Circular-Array Antenna," Institute of Electrical and Electronic Engineers, Transactions: Antennas and Propagation, v. AP-18, no. 5, September 1970

3. Munger, A. D., "Mutual Coupling on a Cylindrical Array of Waveguide Elements," Institute of Electrical and Electronic Engineers, Transactions: Antennas and Propagation, v. 19, p. 131-134, January 1971

4. Gladman, B. R. and others, "Cylindrical and Conical Array Investigation," 21st USAF Antenna Symposium at Allerton Park, Urbana, Illinois, 12-14 October 1971. Proceedings

5. Naval Electronics Laboratory Center Report 1521, Current Distributions and Radiation Patterns for Circular-Array Radar Antenna: Theory, by A. D. Munger, 26 October 1967

6. Naval Electronics Laboratory Center Report 1672, Mutual Coupling in Cylindrical-Array Antenna, by B. R. Gladman, 17 December 1969

7. Naval Electronics Laboratory Center TN 1583, Effect of Bit Phase Errors on Cylindrical Array Radar Antenna, by A. D. Munger, 13 November 1969

15. PATTERN ANALYSIS OF WIDEBAND CIRCULAR SECTOR ARRAYS

by

K. G. Schroeder

The Aerospace Corporation*

San Bernardino, California 92408

for

ARRAY ANTENNA CONFERENCE

Naval Electronics Laboratory Center

San Diego, California

22, 23, 24 February 1972

*The views expressed in this paper do not reflect those of The Aerospace Corporation, or the official opinion, or policy, of any of its governmental or private sponsors.

Pattern Analysis of Wideband Circular Sector Arrays

1. Introduction

Because of their low silhouette, high gain directional circular antenna arrays are natural candidates for communication and radar antenna systems in space-limited installations such as ships and aircraft. Flat circular arrays have the lowest possible silhouette and thus present minimum cross-section to the air drag and the shock wave created by hypersonic flight or by explosion of either nuclear or conventional weapons.

A basic advantage of circular arrays is their theoretically constant gain with azimuth beamsteering. Gain variation with elevation steering can be reduced by thinning of multi-ring concentric arrays.

If single-ring circular arrays are excited co-phasally so that they form a pencil beam, their patterns are Bessel functions of the first kind and zeroth order, so long as the element spacings are small. (Ref. 1) The first sidelobes of this pattern are only 7.9 db below the main beam maximum, which accounts for the few radar applications of this antenna type. However, excitation of one or more rings using an "arc sine feed" allow reduction of near-in sidelobes of directional circular arrays. (Ref. 2).

Because of the basic high cost of a circular array it becomes necessary to minimize the number of elements required to achieve a certain electrical performance, such as angular resolution. Also, the effects on this performance of random element removal due to catastrophic failure have to be studied. The complexity, and cost, of a circular array can also be reduced by feeding only a narrow sector instead of the full circle of elements.

In this paper, the use of a digital computer program is described to study sidelobes for large element spacings. Various beam steering aspects of circular arrays are discussed, and beamwidth data are shown for sectorized modular arrays. Results for large circular arrays are presented, and hardening approaches for various radiator types are included. (See Ref. 3). Due to the possibility of ablation of protective coatings used for the antenna elements under thermal load of, e.g., re-entry, these elements may have to be designed for a considerably larger bandwidth than that required by the signal being transmitted by the array, and broadband matching approaches are therefore discussed. As a practical example, a hardenable multi-ring circular array is described which has 3:1 bandwidth and the potential for full hemispherical coverage, and a beam steering system is shown which allows 360 degree azimuth steering with little gain variation. Beamwidth adjustment is possible by varying the feed sector angle. Monopulse tracking is readily provided by virtue of simultaneously available even and odd aperture excitations.

2. Circular Array Pattern Formulas

2.1 Basic Gain Formulas for Multi-Ring Arrays*

*The same formulas are applicable, of course, for single rings also, in which case no summation is necessary.

For small element spacing (equal or less than half a wavelength) and a large number of elements per ring, we get the following approximate formula for the relative gain of a ring array at a distant point: (for isotropic radiators)

$$E(\theta,\phi) = 2\pi \sum_{m=1}^{M} A_m r_m J_o\left(\frac{2\pi\rho_m}{\lambda}\right) \tag{1}$$

where $$A_m \neq f(\phi) \tag{2}$$

is the amplitude weight on ring m, M is the total number of rings, r_m is the radius of ring m

and $$\rho_m = r_m \left[(\sin\theta\cos\phi - \sin\theta_{om})^2 + (\sin\theta\sin\phi - \sin\theta_{om}\sin\phi_{om})^2\right]^{1/2}$$

with θ, ϕ = general co-ordinates,

(θ=0: Beam pointing towards zenith) (3)

θ_{om}, ϕ_{om} are the angles of the beam direction of a ring m, and do not have to coincide for the various rings. As a matter of fact, for operation near horizon, the rings will have to get a different ϕ_{om} in order to compensate for the beam broadening in elevation, if equal beamwidths in azimuth and elevation are desirable.

2.2 Approximation for Beam Pointing Near Zenith

With $\theta_{om} = 0 = \phi_{om}$ we get

$$\rho_m = r_m\left[\sin^2\theta\cos^2\phi + \sin^2\theta\sin^2\phi\right]^{1/2} = r_m\sin\theta \tag{4}$$

The pattern is:

$$E(\theta,\phi) = \sum_{m=1}^{M} 2\pi A_m r_m J_o\left(\frac{2\pi r_m}{\lambda}\sin\theta\right) \tag{5}$$

By varying θ and ϕ by small increments the sidelobes can be studied near zenith, and by varying these angles by large increments (up to θ = 45°; $0 \leq \phi \leq 360°$) the actual pattern and its possible variation can be studied for the upper portion of the desired hemispherical coverage.

2.3 Approximation for Beam Pointing Near the Horizon

With $\theta_{om} = \frac{\pi}{2}$; $\varphi_{om} = 0$ we get (for $\varphi = o$)

$$\rho_m = r_m \left[(\sin\theta \cos\varphi - 1)^2 + (\sin\theta \sin\varphi)^2 \right]^2 \qquad (6)$$

$$= r_m \left[\sin\theta - 1 \right]$$

and the elevation pattern becomes (7)

$$E_2(\theta, o) = \sum_{m=1}^{M} 2\pi A_m r_m J_o \left| \frac{2\pi r_m}{\lambda} (1 - \sin\theta) \right|$$

For $\theta = \frac{\pi}{2}$ the azimuth pattern becomes:

$$E_2\left(\frac{\pi}{2}, \varphi\right) = \sum_{m=1}^{M} 2\pi A_m r_m J_o \left| \frac{4\pi r_m}{\lambda} \sin\frac{\varphi}{2} \right| \qquad (8)$$

Here we get a considerably broader elevation pattern than azimuth pattern. If we were to achieve equal beam width for $E_2\left(\frac{\pi}{2}, \varphi\right)$ and $E_2(\theta, o)$ we have to assume different φ_{om}'s, until the azimuth pattern becomes as broad as the elevation pattern.

The beam broadening is very small for elevation angles down to about 45 degrees, and a 10:1 broadening occurs at $\theta = 85$ degrees from Zenith. This broadening is a function of the diameter, however, and has to be studied for each ring diameter separately. However, both for the study of beam broadening of the elevation pattern near the horizon and for investigation of the dependence of the azimuth or elevation pattern on element thinning, no simplification of the pattern equation is possible. Since the investigations will be run on a computer, it appears thus generally advantageous to use a summation formula for the contributions from the individual radiators, rather than the Bessel function approximation. This approach is mandatory for the study of sector arrays.

3. Pattern Computation for Multi-Ring Arrays of Isotropic Sources Using Summation of Vector Contributions

3.1 Plane Ring Array

The summation of the contributions of all elements in the case of a plane ring array leads to the following general equation:

$$E(\theta, \varphi) = \sum_{m=1}^{M} \sum_{I=1}^{L_m} A_m \exp j \left| \psi_{lm} - \frac{2\pi r}{\lambda} \sin\theta \cos(\varphi - \varphi_{lm}) \right| \qquad (9)$$

here ψ_{lm} is the phase of the illumination of element l on ring m

If we make $\psi_{lm} = \frac{2\pi r_m}{\lambda} \sin\theta_{om} \cos\left(\phi_{om} - \phi_{lm}\right)$ (10)

then the array pattern has its maximum value for $\theta = \theta_m$; $\phi = \phi_{om}$ and the pattern equation is

$$E(\theta, \phi) = \sum_{m=1}^{M} \sum_{l=1}^{L_m} A_{lm} \exp j \left\{ \frac{2\pi r_m}{\lambda} \left[\sin\theta_{om} \cos\left(\phi_o - \phi_{lm}\right) - \sin\theta \cos\left(\phi - \phi_{lm}\right) \right] \right\} \quad (11)$$

where θ_{om}, ϕ_{om} are the angles of the beam maximum for ring m

L_m = total number of elements on ring m

3.2 Generalized Array With Arbitrary Ring Envelope

If all rings are horizontal and concentric, but are not located on one plane, we can write the formula in the following way:

$$E(\theta, \phi) = \sum_{m=1}^{M} \sum_{l=1}^{L_m} A_m \exp j \left\{ \delta_{lm} - \frac{2\pi}{\lambda} d_{lm} \right\} \quad (12)$$

Where A_m = Amplitude of m_{th} ring, $A \neq f(\phi)$

$$d_{lm} = r_m \left[\cos\theta_m \cdot \cos\theta \cos\left(\phi - \phi_{lm}\right) + \sin\theta_m \sin\theta \right] \quad (13)$$

with

$$\phi_{lm} = \frac{2\pi}{\lambda} \cdot l + \phi_{lmo} \quad (14)$$

and ϕ_{lmo} = angular displacement of first element (l = 1) on each ring with respect to main beam direction,

$$\delta_{lm} = \frac{2\pi}{\lambda} d_{lm}\left(\theta_o, \phi_o\right), \text{ where } \theta_o, \phi_o = \text{angles of main beam} \quad (15)$$

θ_m = angle of envelope of ring array with horizon at the point where the envelope touches ring m as shown in Figure 1.

In order to facilitate multiple pattern investigations on a digital computer, the pattern can be written as:

$$P(\theta, \phi) = \left[\sum_{m=1}^{M} \sum_{l=1}^{L_m} A_m \cos\left(\delta_{lm} - \frac{2\pi}{\lambda} d_{lm}\right) \right]^2 + \left[\sum_{m=1}^{M} \sum_{l=1}^{L_m} A_m \sin\left(\delta_{lm} - \frac{2\pi}{\lambda} d_{lm}\right) \right]^2 \quad (16)$$

for $\theta = \theta_o$, $\phi = \phi_o$ we get

$$P(\theta_o, \phi_o) = P_o = \left| \sum_{m=1}^{M} \sum_{l=1}^{L_m} \right|^2 A_m \quad (17)$$

And the normalized pattern equation is:

$$P^*(\theta, \phi) = \frac{1}{P_o} \cdot P(\theta, \phi), \text{ where } P^*_{max} = P^*(\theta_o, \phi_o) = 1 \quad (18)$$

The actual far-field pattern of the array can then be found by taking the square root of the values in the power pattern above (Formula 16) and multiplying the resulting gain pattern by the element pattern of the chosen antenna element.

4. Symmetrically Phased Flat Circular Arrays

4.1 General

Based on the summation formula described in the preceding section, a computer program was written (Ref. 4). This program is equally useful for the investigation of single-ring or multi-ring circular arrays, with arbitrary element weights and ring amplitudes, and for any array envelope function. Because of the lowest silhouette and maximum aperture in elevation, only flat (planar) ring arrays were studied. The approach chosen was to assume eventual use of either vertically polarized elements for coverage from horizon to about 45 degrees, or endfire radiators with circular polarization for the angular volume from zenith down to about 45 degrees. Since the latter case is equivalent to a broadside planar array with circular boundary, and does not really utilize the unique features of the ring array, the emphasis of the investigation was placed on ring arrays with operation near horizon.

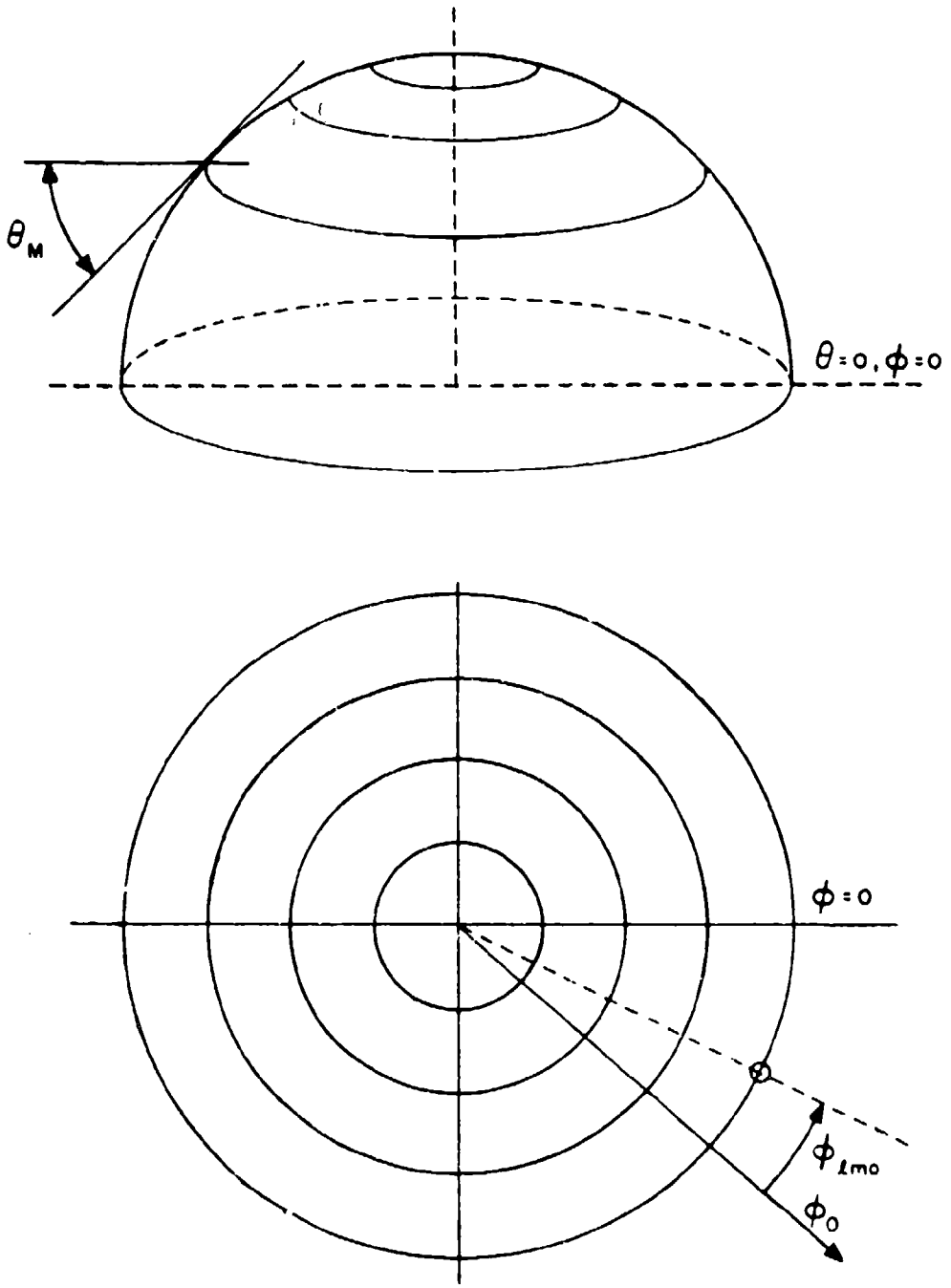

Fig. 1: Multi-Ring Array with Spherical Ring Envelope

4.2 Directional Mode Full Circular Array

If all the contributions from the individual elements are to be in phase at a distant point, then the elements have to be phased according to

$$\psi_1 = \frac{\pi D}{\lambda} \cdot \cos \phi_1 \text{ (Radians)}$$
$$= 360\ R_\lambda \cdot \cos \phi_1 \text{ (Degrees)} \qquad (19)$$

where ϕ_1 is the angle in azimuth of the element 1 with respect to the desired beam direction (Figure 2) and R_λ the radius in wavelengths.

If all the elements are placed equidistantly around the total circumference, we have a full circular array, with a first sidelobe level of -7.942 db, corresponding to the second maximum of the zeroth-order Bessel function of the first kind. The array factor is given by (see previous section):

$$G(\phi, \tfrac{\pi}{2}) = J_o \frac{2\pi D}{\lambda} (\sin \tfrac{\phi}{2}) \qquad (20)$$

and $$G(0,\theta) = J_o \frac{\pi D}{\lambda} (\sin \theta - 1) \qquad (21)$$

where (20) is the azimuth pattern in the horizontal plane, and (21) the elevation cut, both for a beam pointing at $\phi = 0$, $\theta = 90$ degrees.

The formulas hold if $N \leq \frac{2\pi D}{\lambda} + 2$ which corresponds to an element spacing of half a wave-length or less. (N = number of elements)

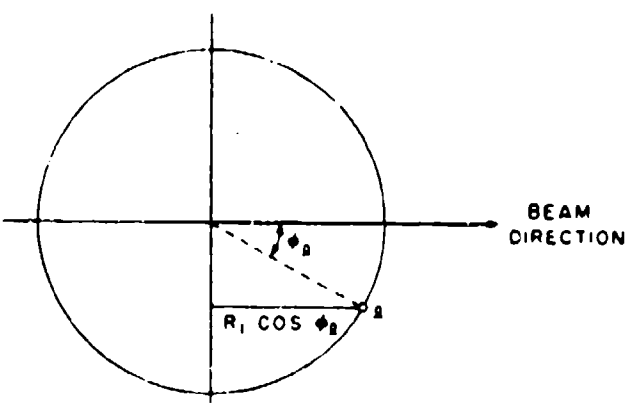

Fig. 2: Element Phasing for Directional Mode (Cophasal Excitation with Phase Reference at Ring Center

4.3 Element Arrangement for Optimum Feed Structure Having Even Symmetry of Elements

When elements are phased according to formula (19), the phase center of the array coincides with the geometrical center. For a directional array, this means that elements diametrically opposite on the circle have phases of equal magnitude and opposite polarity. If now, in addition the elements are placed (or selected) symmetrically with respect to the beam axis, such that the axis falls either halfway between two elements or directly on an element, then two elements each have the same phase (ψ_k and ψ_k' in Figure 3) with either an even or odd number of elements for each half array. The even-numbered case is better from the standpoint of power division, and shall be treated exclusively in the following chapters, even though all conclusions apply equally well to the odd-numbered configuration. By giving the elements, in addition, an amplitude weight such that $A_1 = A_1' = A_{-1} = A_{-1}'$; $A_2 = A_2' = A_{-2} = A_{-2}'$ and so on, a first sidelobe other than the -7.9 db for a uniform ring array can be chosen, at the expense of an increasing backlobe. Examples of amplitude weights are $\cos \frac{\pi}{2} x$, Tchebycheff or Ramp. Other methods of nearbeam side-lobe suppression are discussed in connection with a practical array.

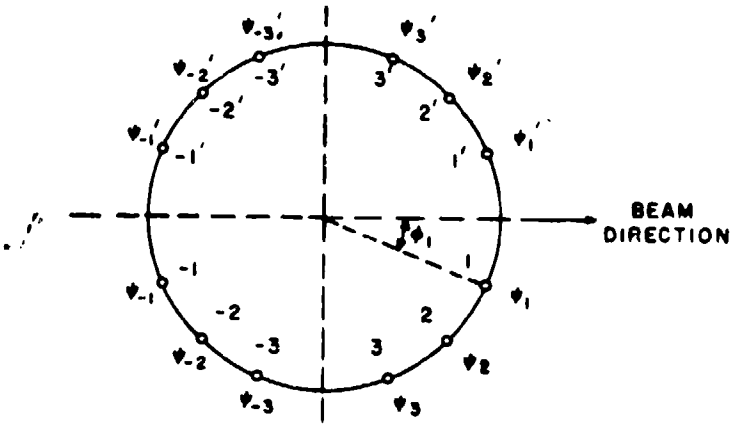

Fig. 3: Symmetrical Phasing of Circular Array

Note: $\psi_k = \psi_{k'} = -\psi_{-k} = -\psi_{-k'}$

if $\phi_{k'} = -\phi_k$, $\phi_{-k'} = -\phi_{-k}$

and $\phi_{-k} = 180 - \phi_k$

4.4 Beamwidth Variation in Symmetrical Circular Arrays

For certain applications it is desirable to change the azimuth beamwidth on a given antenna configuration in order to meet changing operational

requirements. There are two ways of achieving varying beamwidth with a circular array:

1) Change of ring diameter

2) Change of sector angle

If a fairly continuous coverage of beamwidths is attempted using method 1), the ring diameters have to fall close together. The following table shows the ring diameters and the associated beamwidths for an array containing one center element and up to six rings around it, where the element spacing within each ring is exactly 0.25λ.[1)]

TABLE I

(Beamwidths to 20 db points)

Number of Rings	Number of Elements	Maximum Diameter	Beamwidth (degrees)
1	5	0.318	124
2	13	0.636	74
3	25	0.955	56
4	41	1.272	39.1
5	61	1.59	36
6	85	1.91	26.3

It should be noted that for the narrower beamwidths all the interior rings have to be used simultaneously, thus resulting in a large number of elements. Feeding one ring at a time is problematic for concentric ring arrays with such close spacing because the other rings get excited parasitically. In method 2), the beamwidth of the array is changed by letting the elements cover only a limited sector of the ring. This reduces the effective aperture D_λ^* according to Figure 4:

$$D_\lambda^* = D_\lambda \cdot \sin \frac{\alpha}{2} \tag{22}$$

where α is the sector angle, D_λ , D_λ^* are the numeric diameters of the array in multiples of wavelengths. The azimuth beamwidth of the array is then (for constant element weight)

$$B = 4 \text{ arc sin } \frac{1.13}{2\pi D_\lambda^*} \tag{23}$$

---

1) From: H. P. Neff and J. D. Tillman, "Electronically Scanned Circular Antenna Array", 1960 IRE Convention Record, pp 41-47.

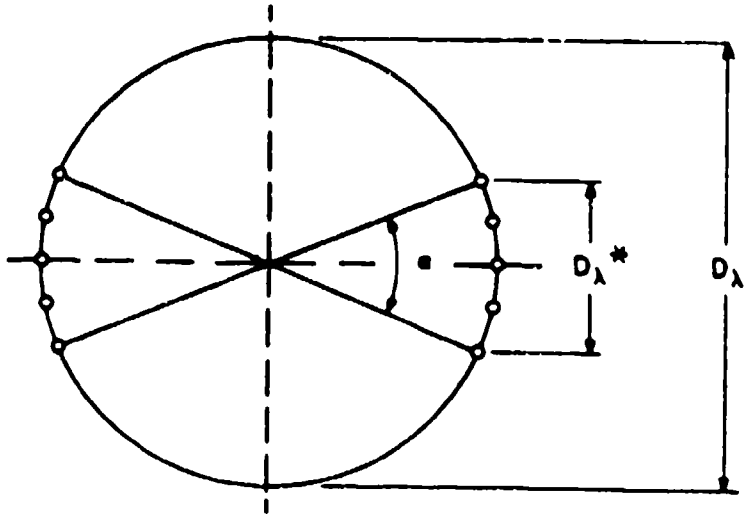

Fig. 4: Double-Arc Circular Array

This formula holds with good approximation for sector angles between 180 degrees and about 60 degrees. From here on down the double-arc configuration acts more like a linear double aperture, its beamwidth thus being

$$B = 2 \cdot \text{arc sin} \frac{k\, f(\alpha)}{D_\lambda \sin \frac{\alpha}{2}} \tag{24}$$

where k is a constant depending on the degree of uniformity achieved in the projected aperture, and $f(\alpha)$ a correction term such that

$$\lim_{\alpha \to o} \sin^{-1} \frac{f(\alpha)\, k}{\sin \frac{\alpha}{2}\, D_\lambda} = \cos^{-1} \frac{\pi}{2D_\lambda} \tag{25}$$

which is determined by the maximum beamwidth obtainable by two point sources D_λ apart.

The azimuth beamwidth can thus be varied in increments dictated by the element spacing. As the beamwidth is increased, the sidelobes in the elevation pattern increase also, until they are as large as the main lobe, which happens for $\alpha < 22$ degrees. At the same time a backlobe develops in the azimuth pattern which has almost equal magnitude as the forward beam, but narrower beamwidth. Because of this backlobe, the limiting sector angle for unidirectional operation is $\alpha \approx 45$ degrees, with a corresponding beamwidth of about 27 degrees. Bi-directional operation is possible, with good sidelobe suppression, down to $\alpha \approx 20$ degrees, with a beamwidth of about 38 degrees. (These values are for uniform amplitude distribution. Small increases in beamwidth can be achieved by varying the amplitude taper across the arcs.)

Figure 5 shows the beamwidth variation which can be expected for certain sector angles. In curve I the theoretical beamwidth is shown for a full-ring circular array with equidistant element spacing and uniform amplitude weight, where the diameter decreases with $\sin \frac{\alpha}{2}$. The narrowest beam, for a 4λ diameter array, is 10.2 degrees.

For Curve II the element spacing in the ring was corrected so that it would produce a fairly uniform linear projected aperture for the larger sector angles. The element weighting was also constant. The values for the beamwidth were then computed using formula (17) and are shown in Curve II. Curve III shows the values of $\frac{f\left(\frac{\alpha}{2}\right)}{\sin\left(\frac{\alpha}{2}\right)}$ for the use of formula (24) as deduced from the computed beamwidth values.

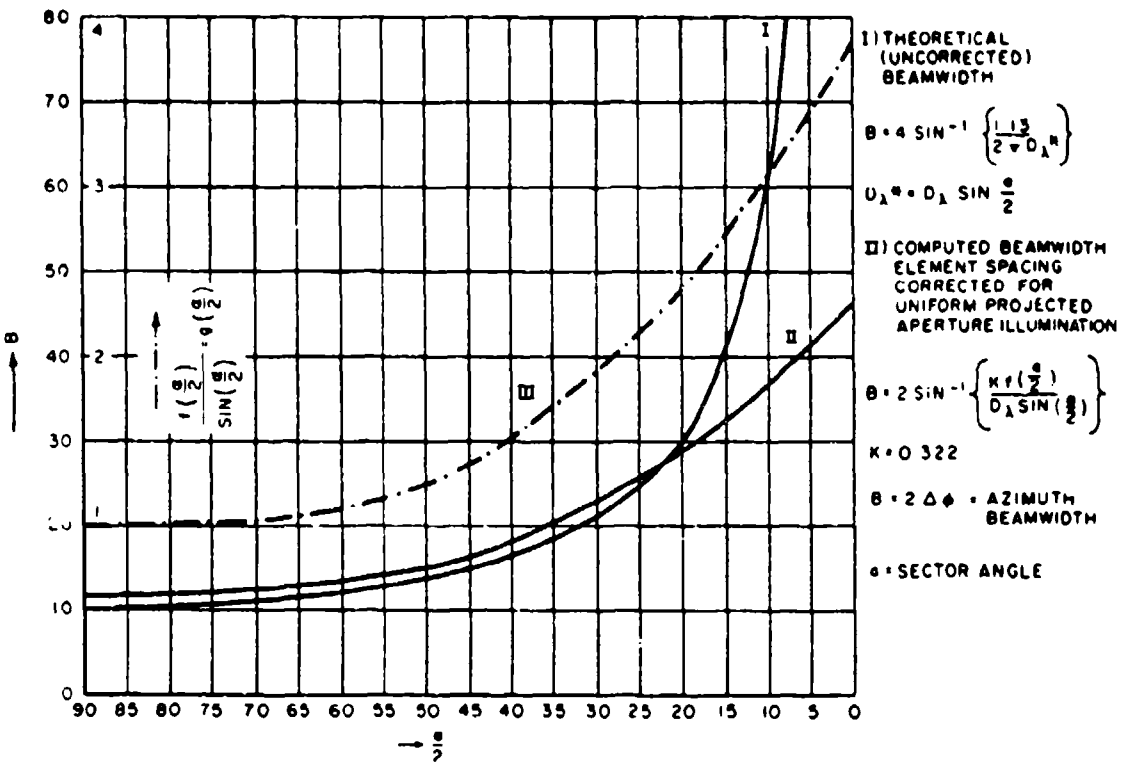

Fig. 5: Beamwidth Variation With Sector Angle for Circular Array, D=4λ

5. Pattern Computations for Circular Sector Arrays of 4λ Diameter

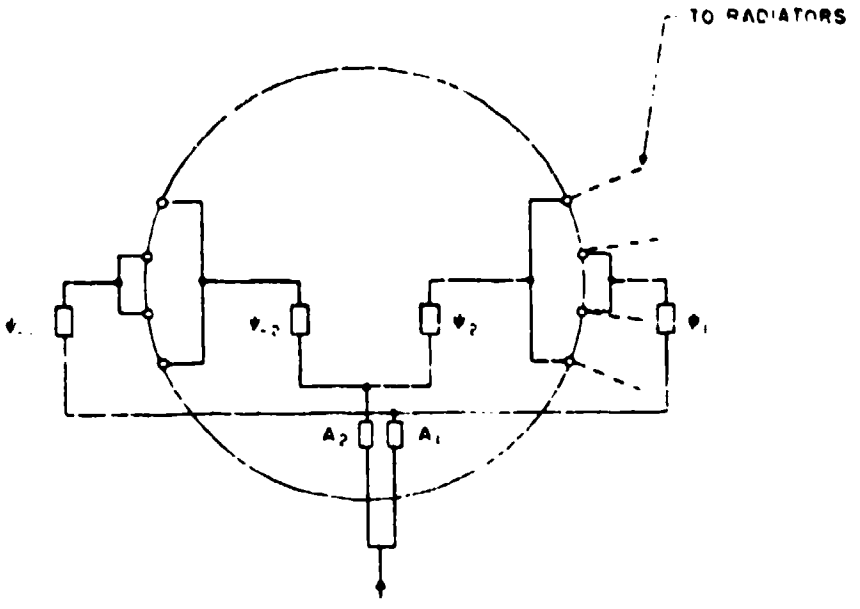

Fig. 6: Double-Arc Feed

5.1 Full Circular Array (180 Degree Sector)

A single beam is obtained if the elements are phased according to equation (10). (See Fig. 6) The narrowest possible beam is produced by an array having a certain minimum number of elements spaced equidistantly around the full circumference, with all elements excited by currents of equal amplitude. The beam thus obtained has an azimuth 3 db width of about 10.2 degrees, and the first sidelobe is down -7.9 db from the maximum.

The minimum number of elements is dictated by the maximum spacing between elements which does not result in excessive deviation of the resultant azimuth pattern from the J_0 pattern. This maximum spacing has been computed to lie between 0.25 and 0.5λ. Figure 7 shows that for 0.5λ element spacing sidelobes of -16 to -19 db appear in the azimuth range from 160 to 180 degrees. The elevation pattern (Fig. 8) is constant up to an element spacing of about 0.75λ and, therefore, does not have to be considered here. (The first sidelobes are smaller than -7.9 db, because the angular increments were not taken fine enough).

If the total number of elements required for a perfect J_m pattern is distributed equidistantly around the circumference, the available number of elements, and their positions, are predetermined. In Figure 9 the arrangement of 48 elements is shown, with symmetry of the feed structure determining the assumed beam direction, and Figure 10 and Figure 11 shows two possible equidistant arrangements of elements using less than the total number. If every other element is used (Figure 10) we have a spacing of 0.524λ, and slightly increased backlobes can be expected (Fig. 12). If every third element is used

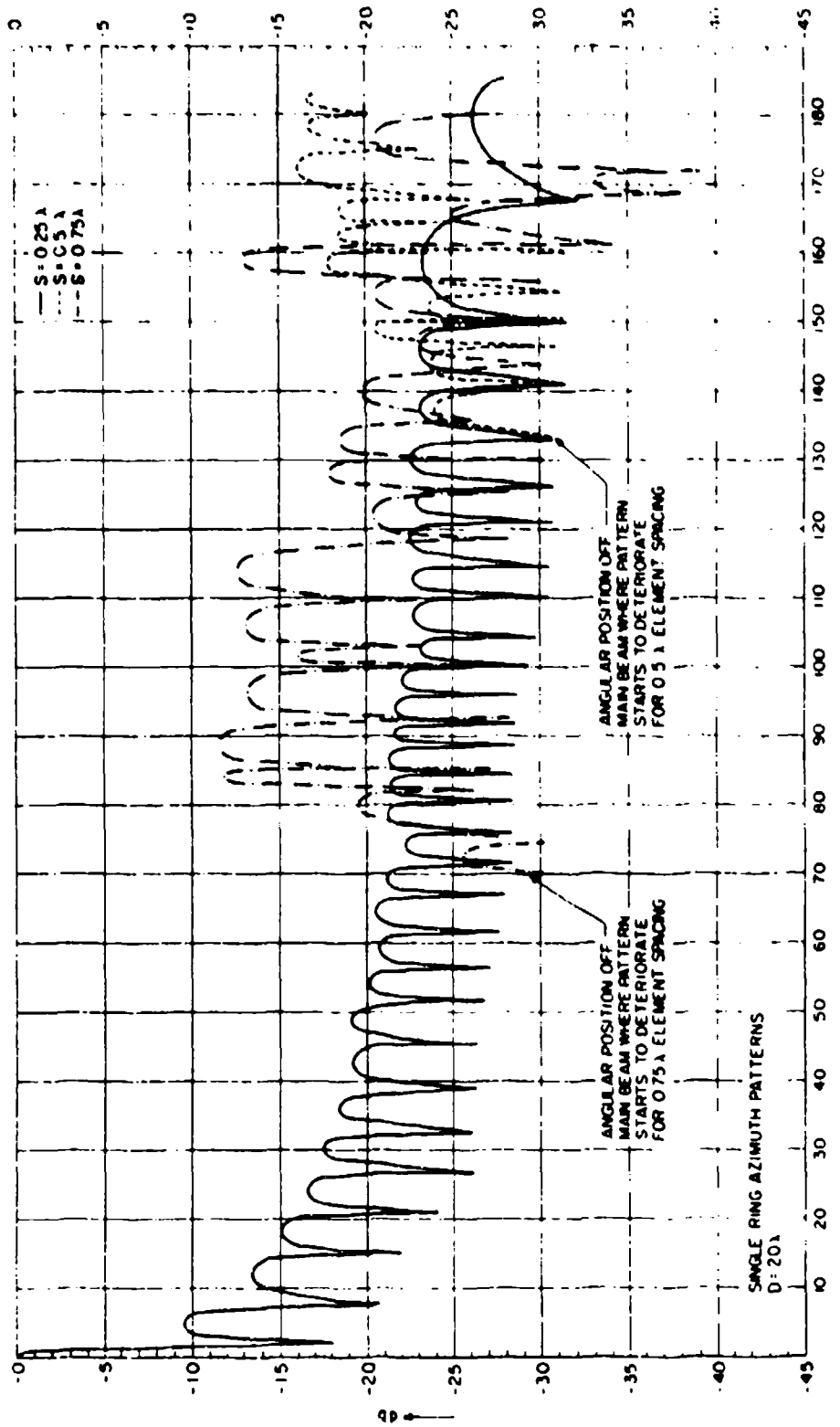

Fig. 7: Single-Ring Azimuth Patterns, D = 20λ

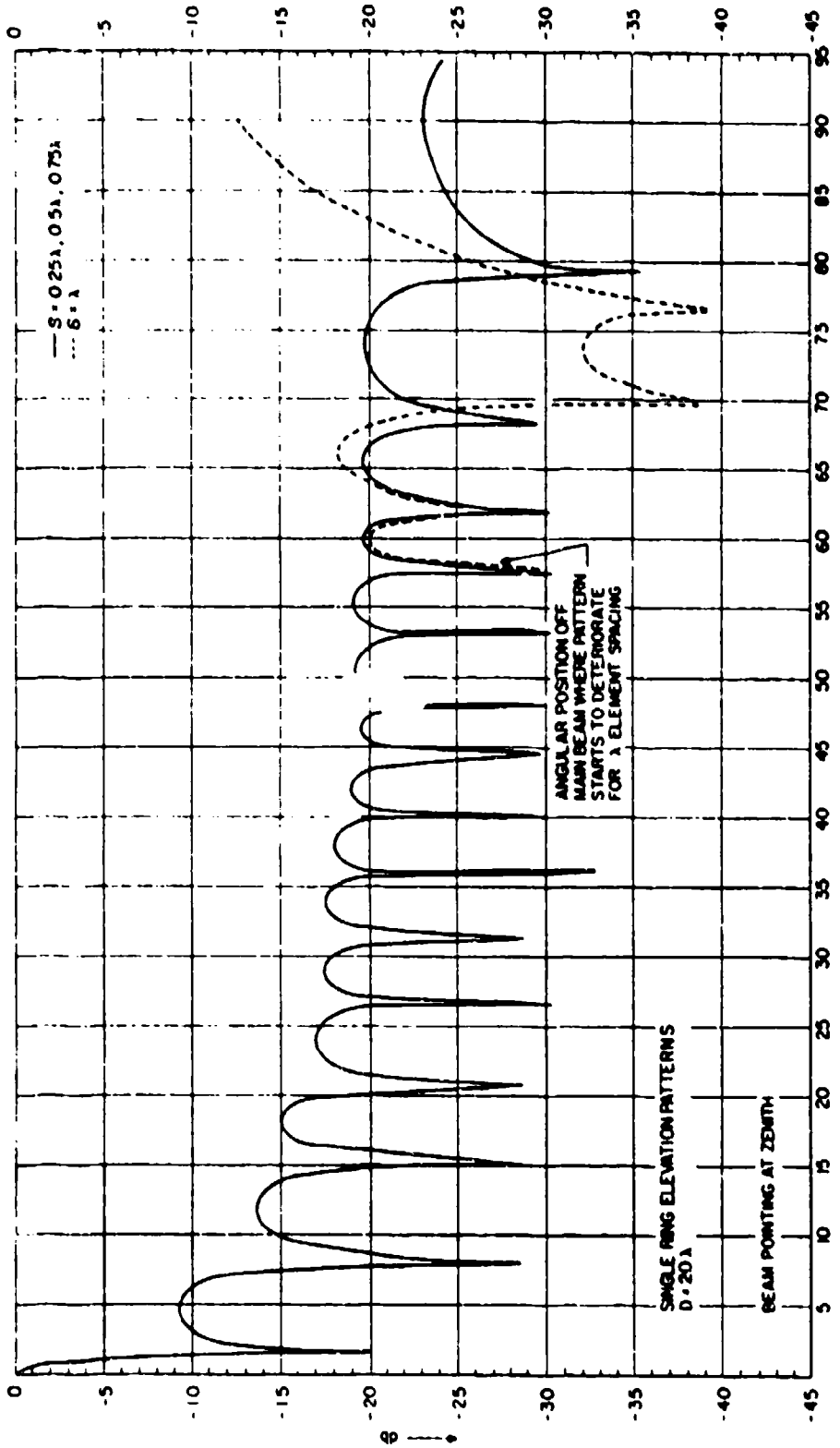

Fig. 8: Single-Ring Elevation Patterns, D = 20λ

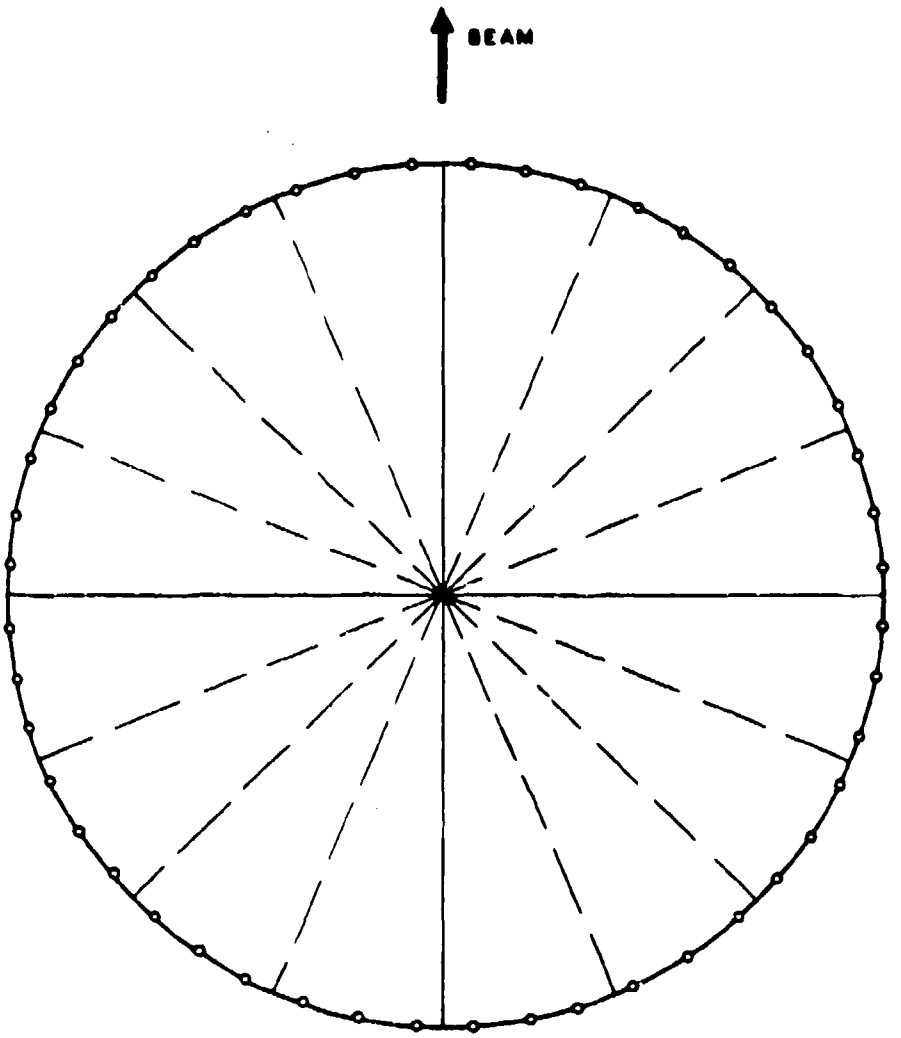

Fig. 9: 48-Element Array Configuration; Beam Direction Half Way Between Two Elements

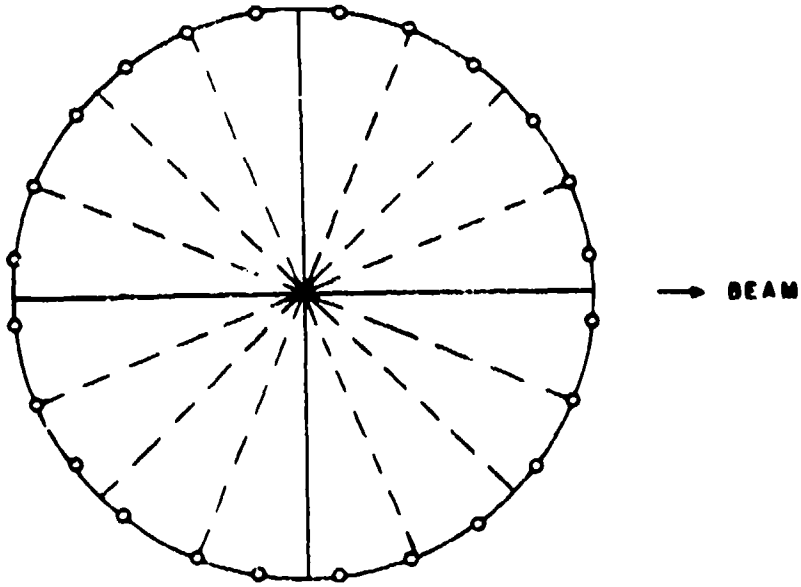

Fig. 10: 48-Element Array, 24 Elements Selected

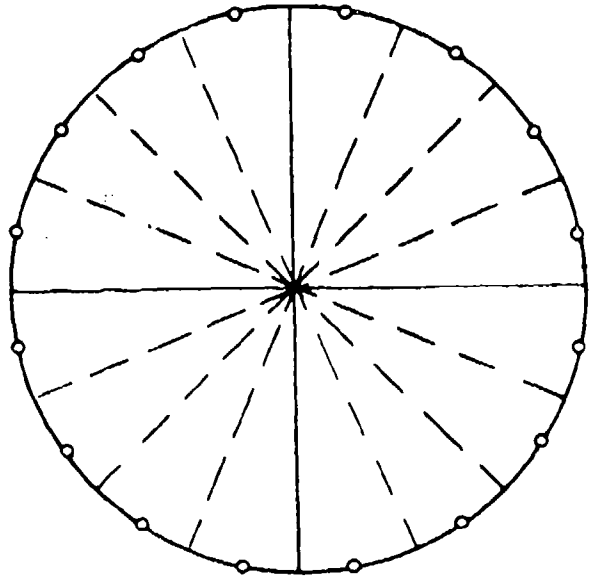

Fig. 11: 48-Element Array, 16 Elements Selected

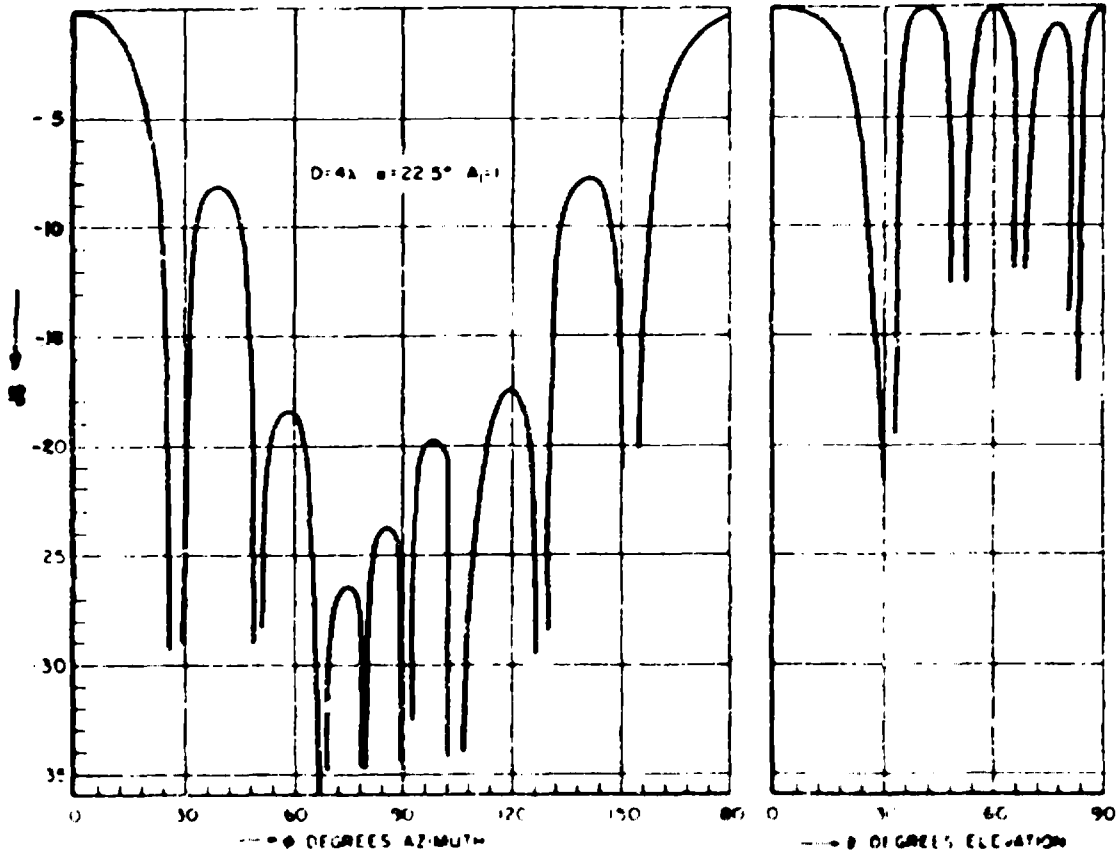

Fig. 12: 4×4 Element Array

(Fig. 11), a strong sidelobe of about -5 db appears at 90 degrees azimuth and is practically invariant of any amplitude weight over the array. (Fig. 13).

5.2 Space-Tapered Sector Array

The first sidelobe can now be improved by amplitude weighting of the elements, or by non-uniform element spacing, the latter being essentially a non-uniform amplitude distribution over a uniform array.* Figure 14 shows how 32 elements can be selected in the 48-element array, thus preserving even symmetry in the feed structure, and reducing the element spacing to a value where the residual terms in the Bessel approximation of the ring array pattern are negligible, and also reducing the mutual coupling in those portions of the array which have large phase differences. Figure 15 shows the computed patterns for the array of Figure 14. The effect of non-uniform element spacing in circular arrays becomes evident if we consider the change in projected element spacing. Whereas a straight, uniform linear array would have a -13.5 db first sidelobe for uniform amplitude distribution, the projection of the elements in a circular array shows increasing element density towards the outer edges of the array. This is a type of spacing which is directly opposite to the type of spacing required for reduced first sidelobe level. Consequently, the first sidelobe is only -7.9 db down from the main beam. In order to re-establish uniform element spacing in the projection of a circular array with symmetrical feed structure, the element spacing within the ring has to be (Figure 16):

$$S_c = S_L \cdot \sec \phi_m \tag{26}$$

where

S_C = required circular (polygon) spacing between element (n) and (n+1)

$$\phi_m = \text{mean angle off broadside, such that} \tag{27}$$

$$\phi_m = \frac{\phi_n + \phi_{n+1}}{2}$$

with

$$\left.\begin{aligned} \phi_n &= \sin^{-1}\left[\frac{(n-1)\,S_L}{R}\right] \\ \phi_{n+1} &= \sin^{-1}\left[\frac{n\,S_L}{R}\right] \end{aligned}\right\} \quad \begin{aligned} &0 \le n\,S_L \le R \\ &n = 1, 2, 3 \ldots \frac{N-1}{2} \\ &N \text{ odd} \end{aligned} \tag{28, 29}$$

*See: Roger F. Harrington, "Side Lobe Reduction by Non-uniform Element Spacing", Report No. EL 492-6008 T 11, Syracuse University Research Institute, Task Report No. 11, under RADC Contract No. TN-60-115, August, 1960.

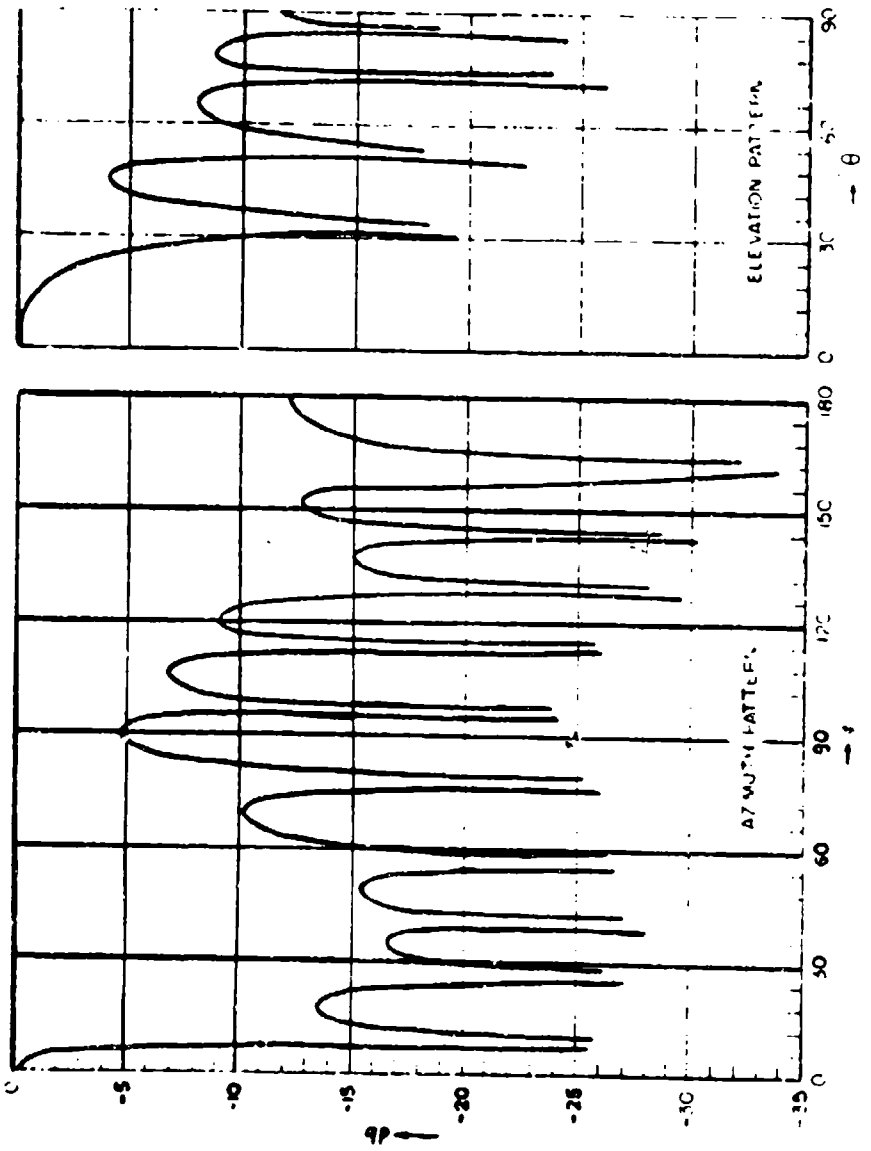

Fig. 13: 48-Element Array, 16 Elements Selected, S.0.786

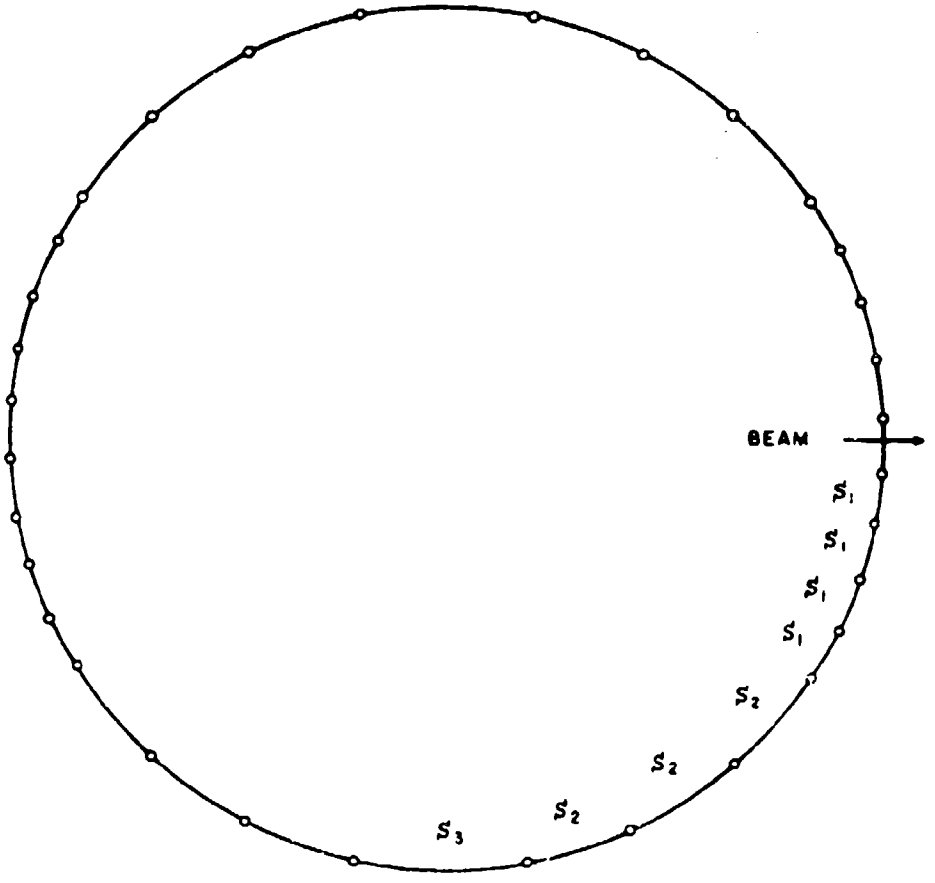

Fig. 14: 48-Element Array, 32 Elements Selected, Non-Uniform Element Spacing

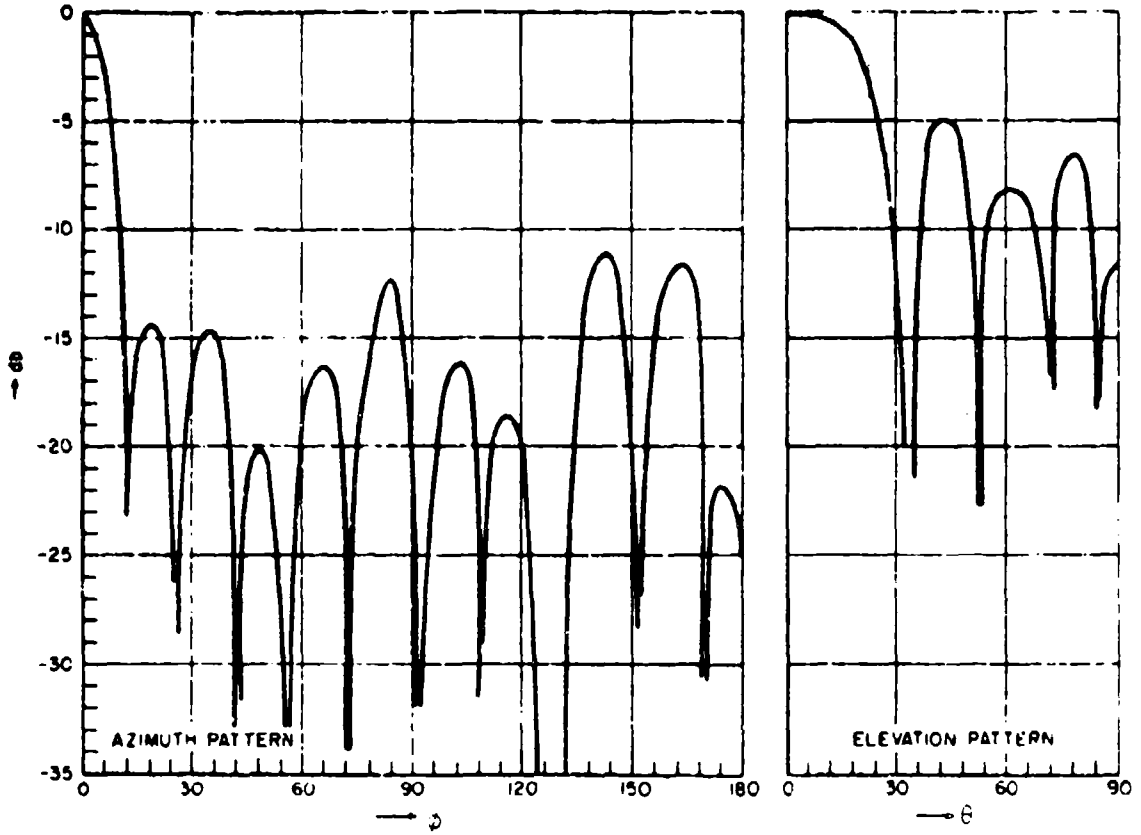

Fig. 15: 48-Element Array, 32 Elements Selected, Non-Uniform Element Spacing

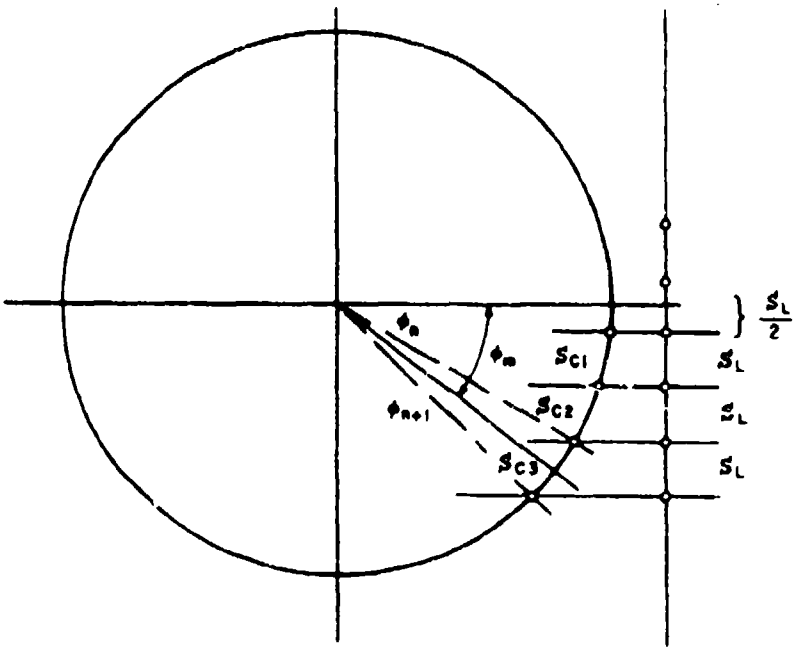

Fig. 16: Circular Array With Uniform Linear Element Projection

for an odd number of elements per arc,

$$\text{and} \quad \phi_n = \sin^{-1}\left[\frac{(n-1/2)\,S_L}{R}\right] \quad \left.\begin{array}{l} 0 \le n\,S_L \le R \\ n = 1, 2, 3 \ldots \frac{N}{2} \end{array}\right. \qquad (30)$$

$$\phi_{n+1} = \sin^{-1}\left[\frac{(n+1/2)\,S_L}{R}\right] \quad \left.\begin{array}{l} \\ N \text{ even} \end{array}\right. \qquad (31)$$

for an even number of elements.

With only discrete element positions available, the optimum positions according to (26) could only be approximated anyway. If additional nonuniformity for near-angle sidelobe suppression is desired, an increase in spacing is chosen which is larger by a certain amount, such that the required amount of increase in consecutive projected element spacing is achieved. Thus,

$$S_c^{\,1} = S_L \sec\phi_m + \Delta S(\phi) \qquad (32)$$

where $\Delta S(\phi)$ is the additional progressive increase indicated by the sidelobe suppression technique.*

It should be mentioned here that this technique will decrease the near-beam sidelobes, but it will also increase the sidelobes at large angles off beam. A compromise is indicated, therefore, and with the limited number of element positions available in the 48-element array, not too fine a control of the projected spacing is possible. Both (26) and (32) can be approximated with increasing accuracy as the total number of elements in the array is increased.

5.3 Single Beam Array with Double-Arc Feed of Reduced Sector Angle

The azimuth beamwidth can be increased according to formula (II-11) by reducing the sector angle of that portion of the array which is covered by the feed structure. For example, in the case of 4 λ diameter, a 90 degree double-arc array has a beamwidth between 16 and 20 degrees, depending on the uniformity of the projected aperture and/or the amplitude taper across the arcs, and a 45-degree double-arc array has a beamwidth of 25 to 30 degrees in azimuth. For a 48-element array, we have to choose other sector angles than exactly 90 or 45 degrees. Figure 17 shows a 112.5 degree array, and Figure 18 a 52.5 degree array. The patterns of these arrays are shown in Figures 19 and 20. These two sector angles are covered by 16 and 8 elements respectively, thus providing even symmetry in the feed network and avoiding 3:1 power dividers. The beamwidths are accordingly narrower - about 13 degrees minimum for the 112.5-degree array, and about 24 degrees for the 52.5-degree array.

*Since the elements close to the center of the array have a smaller spacing than in the case of the uniform array, S will take on negative values for these elements.

The patterns of two sets of adjoining 22.5-degree double arcs (Figure 21) will overlap approximately at the 3 db points, if one element between each arc is not used so that it can act as a buffer element against mutuals. This means that, by arranging the feed into several double-arc feeds, which can be selected separately, it is theoretically possible to cover a 360-degree range in azimuth with 10 discrete bi-directional (figure-eight) beams, each having 37-degree beamwidth and accordingly reduced gain as compared to the full ring. The arrangement of the feeds and their beam directions are shown in Figure 22.

The gain reduction is due to

1. the increase in azimuth beamwidth

2. the increase in elevation sidelobe levels, the gain in elevation almost entirely being determined by the element pattern

3. the increased backlobe in azimuth, which for a 22.5-degree double arc is only down -0.5 db from the forward beam, and has a beamwidth of ~28 degrees.

Amplitude tapers across the array for narrow sector angles have a tendency to further increase the backlobe, and improve the near sidelobes as in a linear array due to the fact that the projection is almost uniform anyway.

The full ring (=180-degree double-arc configuration) has a gain of about 18 db, the 90-degree double arcs have a gain of at least 15 db, and the 45-degree double arcs lie in the neighborhood of 12 db. (The double arcs shown have higher gains, of course, because of the narrower beam widths as compared to the exact "90-degree" and "45-degree" double arcs). Directive gain was computed for a slightly different diameter (even 13λ circumference). Figs. 23 and 24 summarize azimuth and elevation main beams for various sector angles.

As the sector angle is decreased, below 52.5 degrees in the 48-element case, the behavior of the array approaches that of the double-element configuration, which has 16 lobes (for a diameter of 4λ) of equal magnitude, the beamwidth of the front and back lobes being a maximum 46.2 degrees. This is, therefore, the limiting main beamwidth which can be achieved with a circular array of 4λ diameter in the double-arc configuration. Needless to say, it is impractical to approach this beamwidth because of the power radiated in undesirable directions. Even if the backlobe were useful, the 14 sidelobes would represent a prohibitive gain reduction and invite jamming. When larger azimuth coverage than approximately 30 degrees is desired, it is thus necessary (for this array size) to use several simultaneous beams.

5.4 Multi-Ring Arrays of Large Diameter

5.4.1 General

As the diameter of a single-ring array is increased, and if the sidelobes are to be kept reasonably low, concentric interior rings of elements can be added. This is particularly advantageous when steering to higher elevation angles is desired. As an example, the same flat ring array configuration might

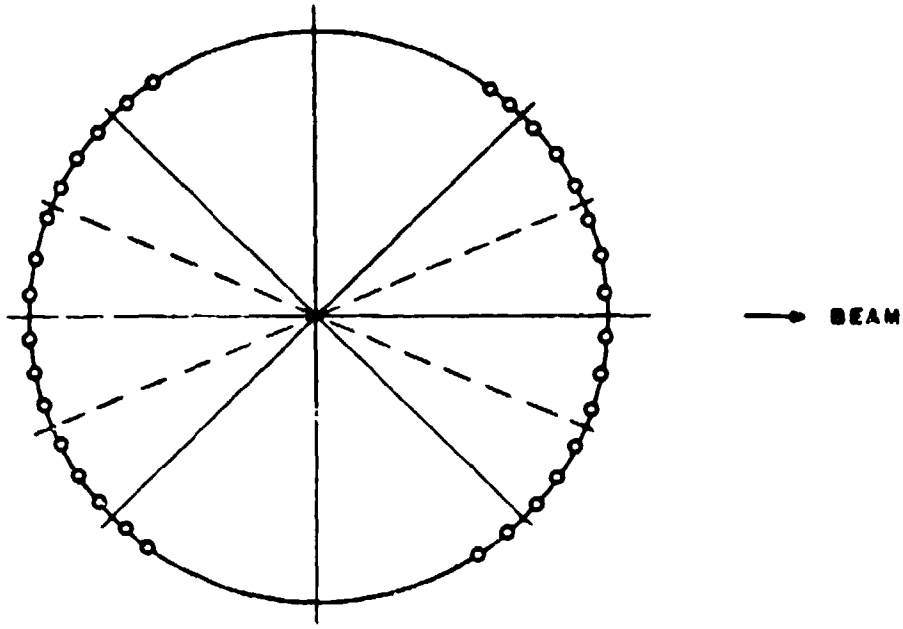

Fig. 17: 48-Element Circular Array, 32 Elements Selected in "90-Degree Double-Arc" Configuration

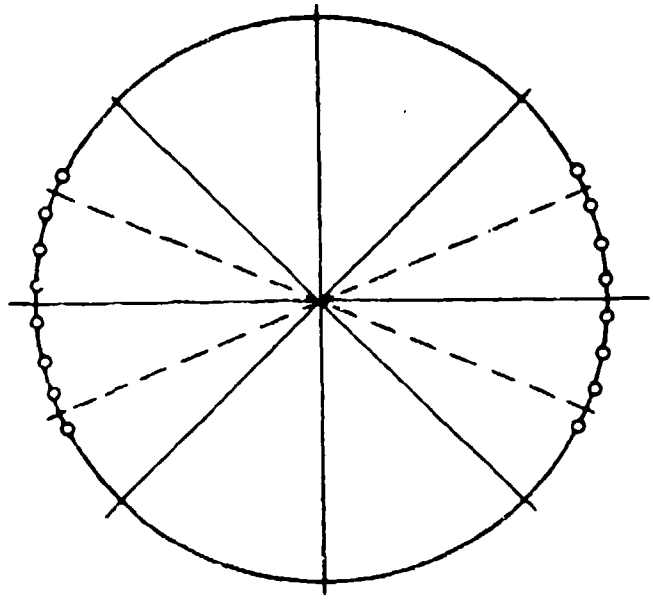

Fig. 18: 48-Element Circular Array, 16 Elements Selected in "45-Degree Double-Arc" Configuration

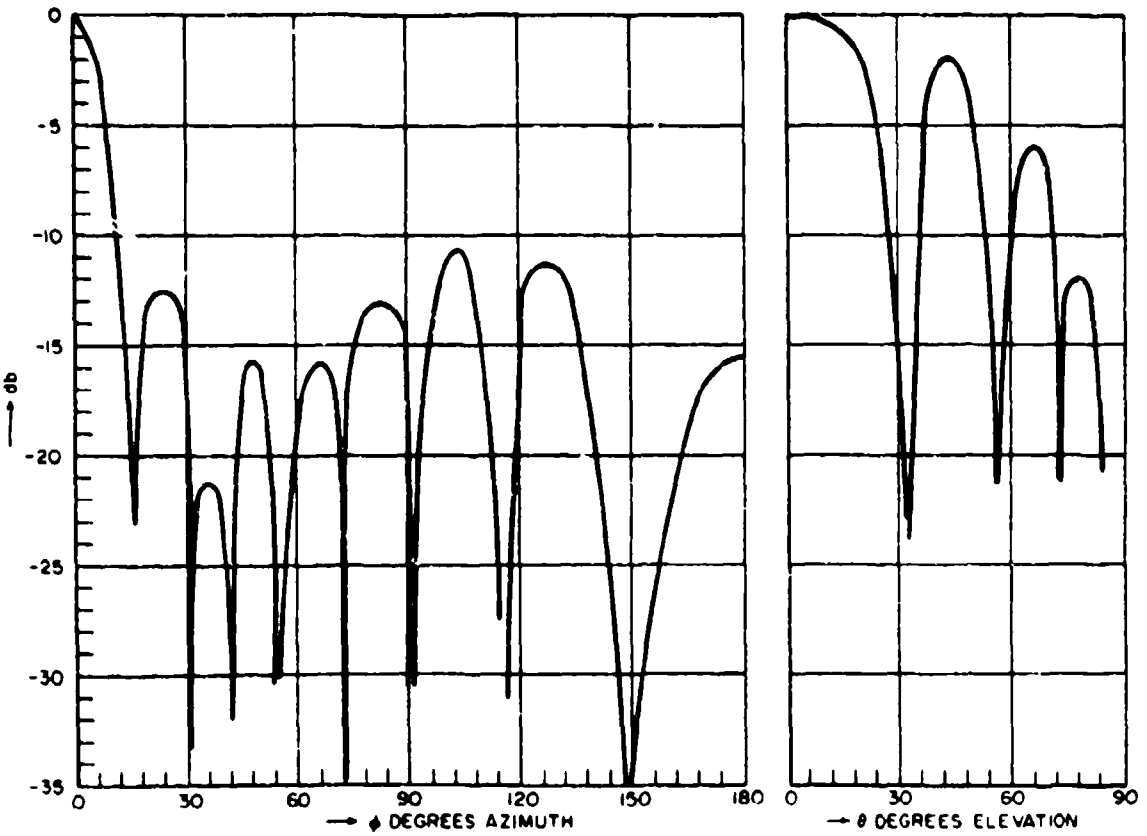

Fig. 19: 48-Element Array, 32 Elements Selected in 112-5-Degree Configuration S=0.26 Uniform Amplitude Distribution

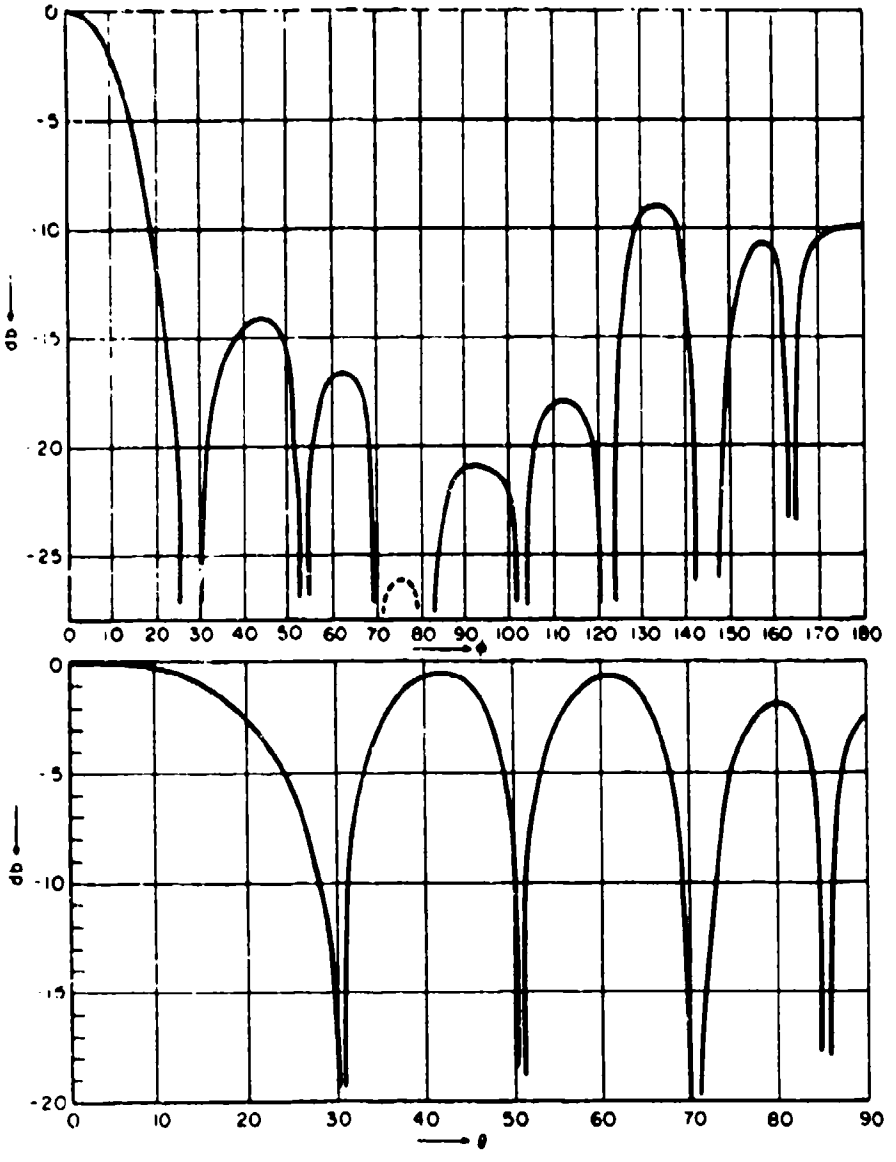

Fig. 20: 48-Element Array, 16 Elements Selected in 52.5-Degree Configuration

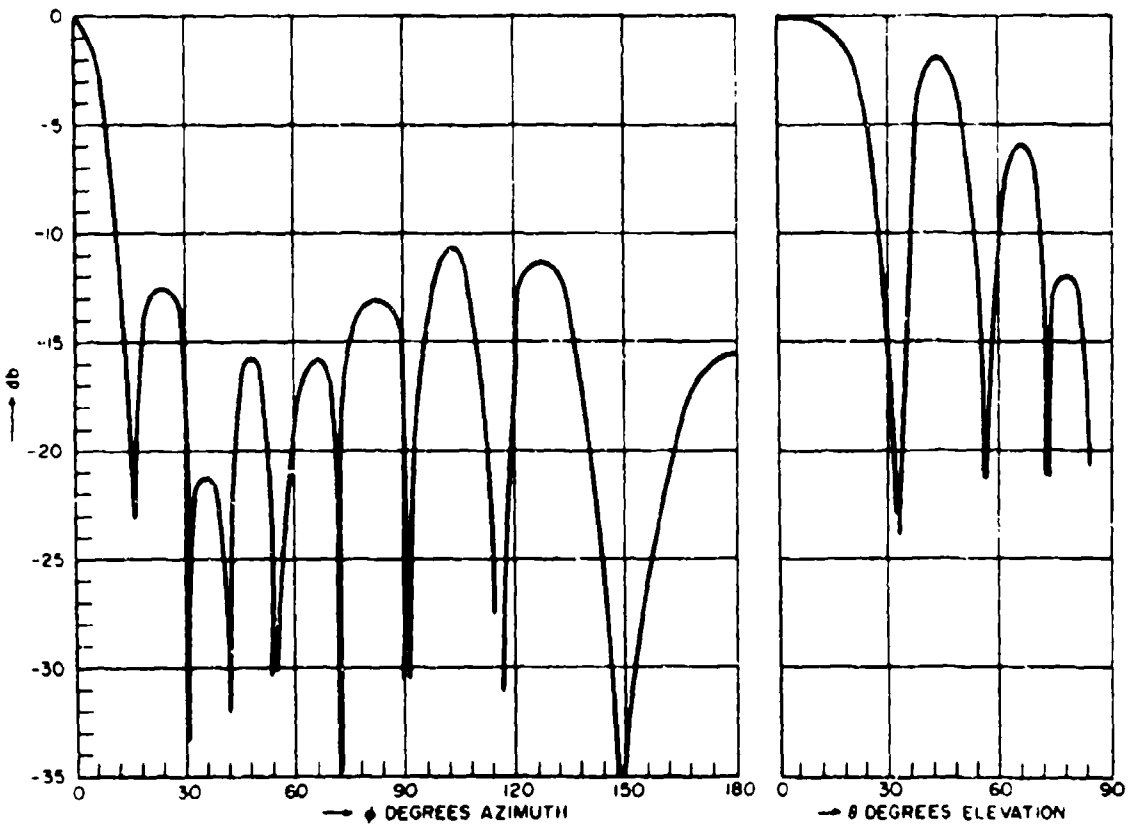

Fig. 21: 48-Element Array, 8 Elements Selected in 22.5-Degree Double-Arc Configuration

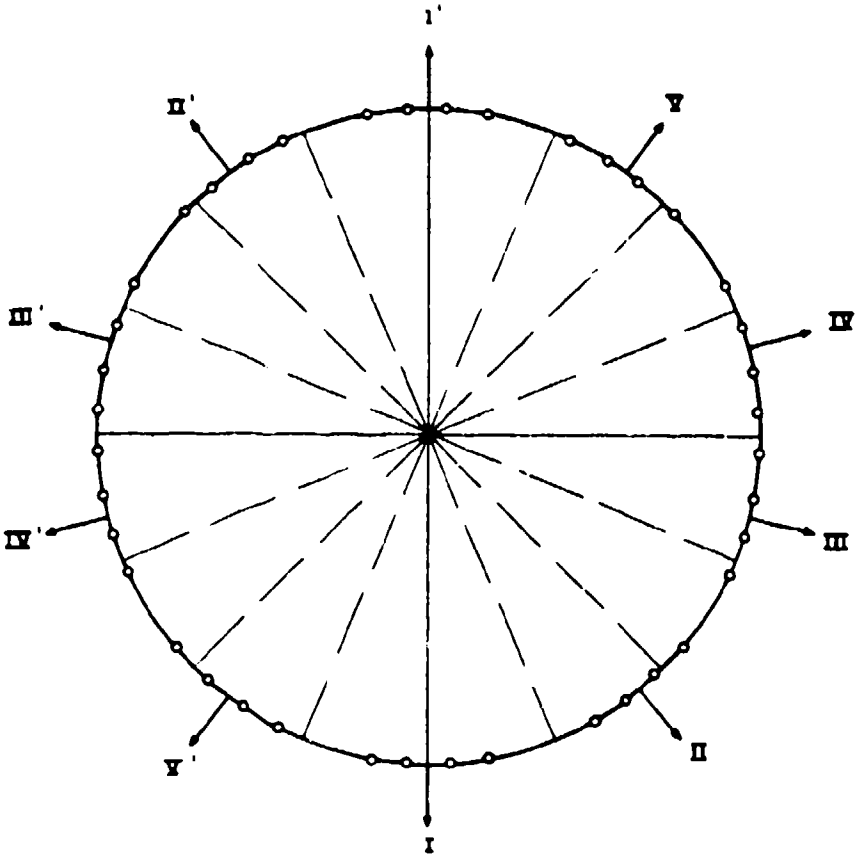

Fig. 22: 48-Element Circular Array

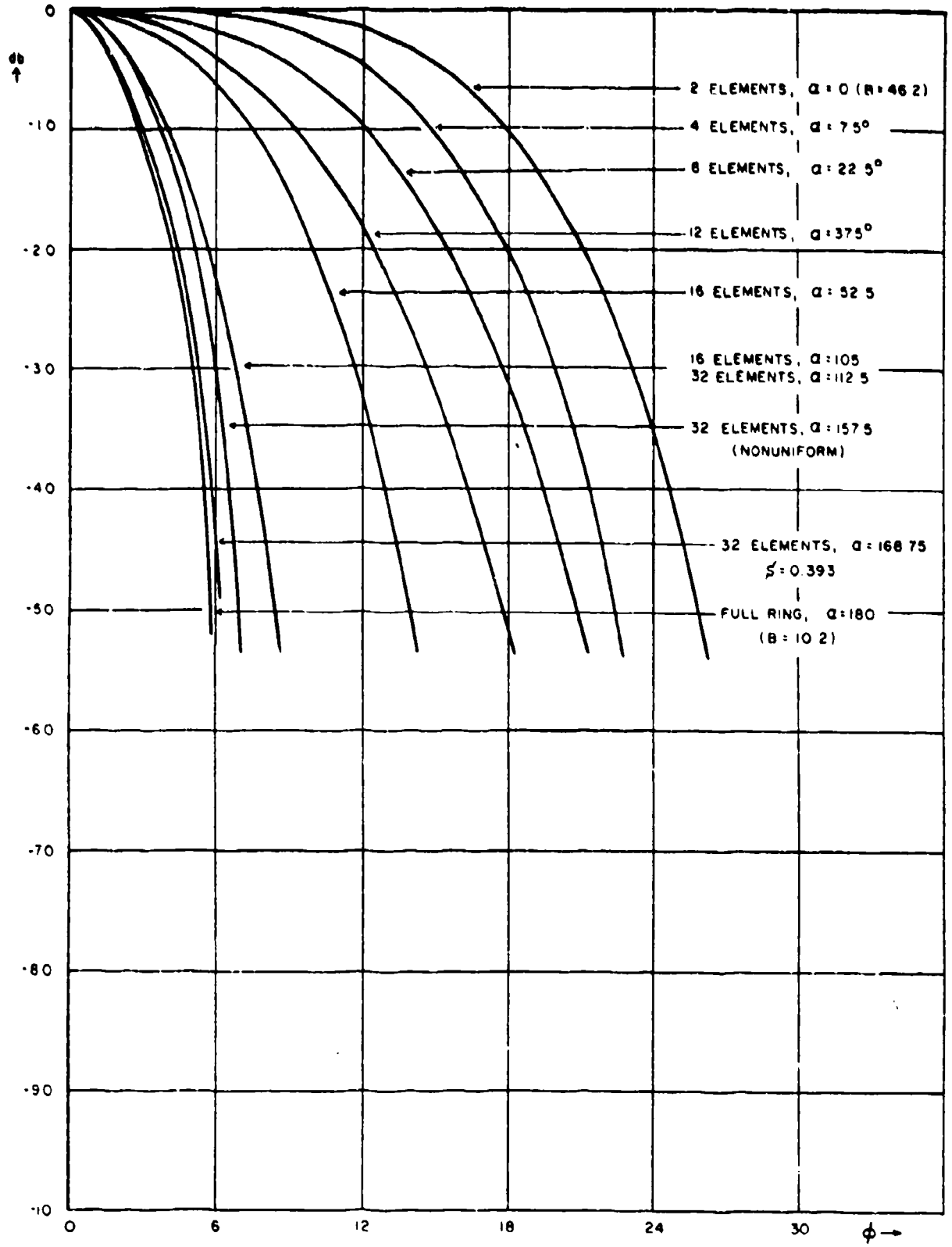

Fig. 23: 48-Element Circular Array, Azimuth Main Beamwidths, Double-Arc Configuration, $\Delta S = 0.262\lambda$, Isotropic Sources with Constant Amplitude

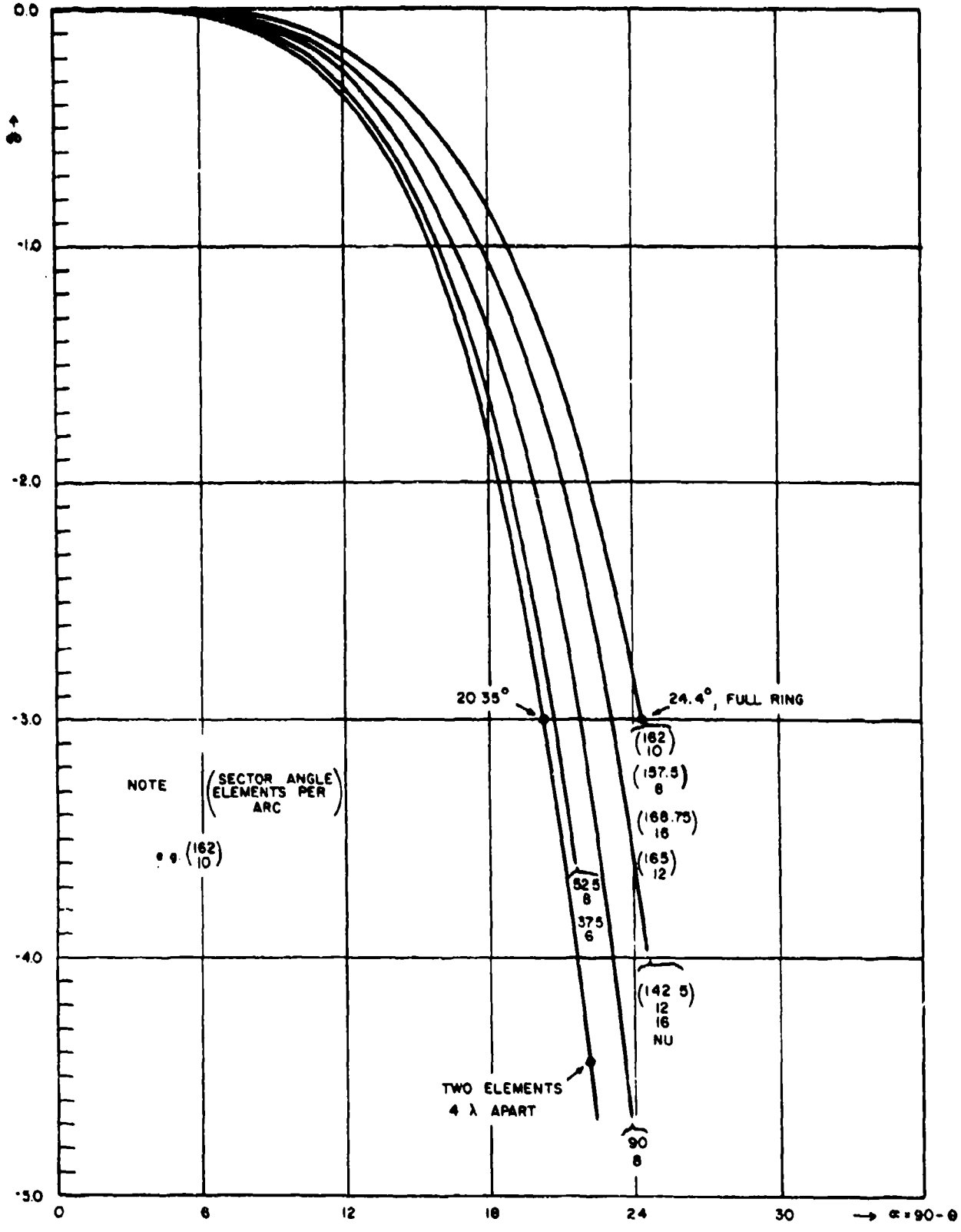

Fig. 24: 48-Element Array, Elevation Main Lobe, Double-Arc Configuration, Isotropic Sources with Constant Amplitude

be used at angles near the horizon for radar and terrestial communications, and at angles near zenith for satellite communications. (Assuming, of course, the array has the required bandwidth capability.) By using a combination of elements, e.g., an endfire dielectric antenna and a caploaded folded monopole, essentially hemispherical coverage can be achieved, one set of elements being scanned to ± 30 degrees from zenith, the other from there on down to horizon. If both elements were at the same location, a minimum-mutual-coupling element arrangement could be found, for instance, by feeding the dielectric endfire elements through the folded portion of the folded monopole.

The two elements would not have to operate at the same frequency.

For optimum sidelobe conditions, it also may be required to use a different array configuration for the two extreme cases of beam position, operation at zenith and operation at horizon.

Since a single ring of the diameter required for the desired beamwidth would have -8 db sidelobes around zenith, and can only be improved to ~ -15 db at horizon, it is more or less imperative to use a continuous circular aperture for good sidelobe suppression. For a circular grid of elements spaced half a wavelength, the number of elements becomes very large for any reasonably large diameter. For instance, if we have an array of 20 wavelengths diameter, which would result in a beamwidth at zenith of about 2 degrees, then we need 20 rings, spaced half a wavelength apart, with a total number of 1261 elements. This number is obtained by assuming 20 rings with a diameter

$$D_m = m\lambda \tag{53}$$

and a number of elements per ring:

$$N_m = 6m + 1 \tag{54}$$

with

$$m = 0, 1, 2, 3 \ldots M$$

the total number of elements is then

$$\sum_{m=o}^{M} N_m \quad N_M = \frac{M+1}{2} \quad (2 + 6M) \tag{55}$$

The formula for N is obtained by dividing the circumference of the consecutive rings by the element spacing on the rings, or half a wavelength, and then taking the next higher integer in order to assure that the element spacing on each ring is a little smaller than half a wavelength.

Preliminary investigations showed that there is no advantage in non-uniform ring spacing and that amplitude weights applied to the aperture from ring to ring (each ring having the same amplitude for all elements) only improve the sidelobes in the broadside case, i.e., when the beam is pointing at zenith.

In this case, for a "grid spacing" of up to 0.75λ no pattern deterioration will occur, and the near-angle sidelobes can be improved over the -17.5 db for a continuous circular aperture by applying the necessary amplitude weights. The behavior of various arrangements of rings and elements on the rings have been investigated theoretically by using the computer program, for a 5-ring array with 20 wavelengths maximum diameter. The results are summarized in Tables 2 and 3.

The various problems arising for systematic element thinning are discussed in the following section.

5.4.2 Systematic Element Thinning in Multi-Ring Arrays

In any array of many rings, spaced a certain constant distance apart, sidelobe enhancement will occur in azimuth for a certain angle off the main beam direction at which the path difference from the elements on the ring diameters perpendicular to the beam direction becomes equal to one wavelength. This path difference is given by

$$d_\lambda = \Delta R_\lambda \sin\theta \sin\phi \tag{36}$$

where

d_λ = path difference in wavelengths

ΔR_λ = ring spacing in wavelengths

ϕ = azimuth angle off the beam axis

θ = elevation angle of the beam axis off zenith

The critical angle at which the secondary lobes occur (for a critical path difference $d_{crit} = 1\lambda$) is then given by

$$\phi_{crit} = \sin^{-1}\left[\frac{1}{\Delta R_\lambda \sin\theta}\right] \tag{37}$$

As an example, the sidelobe patterns for a 20λ maximum diameter, 5-ring circular array with the beam pointing at horizon all showed secondary lobes at ± 30 degrees, which agrees with the critical angle from the above formula for $\theta = 90°$, $(\Delta R_\lambda = 2\lambda)$. There is also a secondary lobe close to 60 degrees, which is due to enhancement of contributions from elements on the beam axis. (In this particular computer run, the first element in each ring was placed on the beam axis, i.e. $\phi_1 = \phi_0 = 0$. This points out the necessity of avoiding any element accumulations.) A third enhancement took place at approximately ± 90 degrees (actual angle varied with element spacing) because here all the elements on the maximum diameters perpendicular to the beam direction are about 2λ apart, and a fourth group of secondary lobes appears at 180 degrees off the beam axis. These four types of sidelobes can all be explained from the above formula, the azimuth angle at which they occur generally increasing as the beam is moving up from horizon.

These four types of secondary lobes are not as strong as the primary beam, of course, because their enhancement is based on a majority group of elements in line with the beam axis and at right angle with the beam axis; in other words, concentration of elements in the areas of the greatest ring diameters. If those groups would deteriorate into two perpendicular linear arrays (e.g. Mills Cross), the echelon lobes would be of the same amplitude as the main beam.

A general increase in backlobes is observed for 1λ element spacing versus 0.25λ, but this has been shown to be a general property of single rings also, and is independent of the echelon lobe formation.

The elevation patterns of the multi-ring array also showed two secondary lobes which exceed the ordinary sidelobe pattern.

In an attempt to eliminate all these secondary lobes, elements were arranged in a completely symmetrically thinned configuration, so that the element spacing was smaller than one wavelength in the critical areas pointed out above. From single ring investigations it is safe to increase the element spacing v the rings up to about one wavelength, as far as the elevation pattern rned, and up to half a wavelength with respect to the azimuth pattern. One possible configuration, leaving the element spacing in the radial direction fixed at half a wavelength and varying it around the circumferences, is shown in Figure 25. Here, the element spacing within the rings varies from a maximum of 1.24λ (ring number 4 from outside) to a minimum of 0.35λ (ring number 10, or innermost ring.)

The resultant patterns show a much greater uniformity of the sidelobe levels (Figures 26 and 27). The total number of elements is greater than in the case of a multi-ring array as described previously, but this configuratio may have to be chosen in cases where the sidelobe requirements do not allow the type of sidelobe enhancement present in the multi-ring array.

5.4.3 Conclusions

If sidelobes of a certain maximum level can be allowed, either because the system requirements are not so much demanding low sidelobes but rather high directive gain, or because the angular regions in which they occur are being eliminared by the element pattern, then a multiple-ring array, i.e. an array with large spacings in terms of wavelengths between the rings and small spacings within each ring, will provide solutions to a given gain requirement which have a minimum number of elements and still have the low first sidelobe (or close to it) characteristic for a continuous circular aperture.

If larger volumes have to be covered, or certain maximum sidelobes have to be observed, either random thinning, or a symmetrically-thinned array configuration can be chosen, the amount of thinning possible again depending on the sidelobe levels that can be tolerated.

Table 2

MULTI-RING ARRAY

5 RINGS, CONSTANT SPACING: $D_{max} = 20\lambda$

S = Element Spacing Within Rings
N = Number of Elements

Sidelobe Levels And Angles At Which They Occur

S = 0.5λ, N = 377				S = 0.75λ, N = 262			
AZ		ELEV.		AZ		ELEV.	
Angle (deg.)	Level (db)	Angle (deg.)	Level (db)	Angle (deg.)	Level (db)	Angle (deg.)	Level (db)
10°	25.6	22°	16.9	10°	25.5	22°	17
20°	26.8	28°	24.2	20°	26.7	28°	24.2
26°	18	34°	25.2	26°	18	32°	25.1
30°	15.6	38°	30.2	30°	15.6	38°	30.2
34°	26.97	42°	27.9	34°	27.1	42°	27.9
44°	34.90	46°	32.2	40°	35.1	46°	32
50°	31.2	50°	26.3	50°	31.1	50°	28.2
56°	23.4	56°	19.5	56°	23.3	56°	19.5
62°	20.4	62°	17.7	62°	20.4	62°	17.6
66°	31.7	68°	30.9	66°	31.96	68°	31
72°	34.02	76°	32.3	72°	32.9	76°	32.3
78°	34.42	82°	30.6	94°	16.7	82°	30.5
86°	33.5	90°	21	98°	17.9	90°	21.1
94°	24.24			104°	24.2		
98°	20.58			110°	24.98		
104°	29.7			116°	17.1		
108°	35.62			124°	19.5		
124°	34.4			138°	21.9		
130°	36.4			146°	22.3		
136°	30.4			150°	21.9		
144°	29.3			158°	23.8		
152°	20.9			164°	23.8		
158°	24.85			168°	20.8		
162°	21.2			176°	18.4		
166°	23.95						
172°	18.2						
176°	21.6						

Table 3

MULTI-RING ARRAY

5 RINGS, CONSTANT SPACING; $D_{max} = 20\lambda$

S = Element Spacing Within Rings
N = Number of Elements

Sidelobe Levels And Angles At Which They Occur

S = 2λ, N = 95				S = 5λ, N = 39			
AZ		ELEV.		AZ		ELEV.	
Angle (deg.)	Level (db)	Angle (deg.)	Level (db)	Angle (deg.)	Level (db)	Angle (deg.)	Level (db)
10°	25.4	24°	16.8	14°	11.2	22°	17.5
20°	28	30°	24.6	20°	17.7	28°	23.1
26°	19.1	36°	24.8	24°	16.3	40°	9.7
34°	14.1	40°	29.9	30°	25.4	50°	13.8
42°	21.5	44°	27.5	36°	15.2	56°	10.6
46°	18.9	48°	32.9	42°	15.1	62°	13.96
52°	18	52°	24.7	48°	18.2	66°	11.7
60°	13.6	58°	18.5	52°	22.2	70°	11.1
70°	18.4	64°	12.1	56°	17.7	78°	13.2
76°	19.96	72°	13.3	60°	13.3	86°	7.4
82°	19.2	80°	18.1	64°	15.5		
90°	20.2	84°	22.1	68°	18.5		
94°	15.9	88°	19.6	76°	18.97		
102°	16.9			84°	18.7		
106°	21.8			90°	10.8		
110°	20.7			96°	15.5		
122°	19.7			100°	13.8		
130°	21.4			108°	17		
134°	17.9			114°	14.97		
140°	16.5			124°	8.5		
146°	17.6			134°	23.1		
150°	17.6			140°	16.3		
160°	22			144°	17.5		
166°	25.5			152°	11.3		
174°	16.2			162°	12.97		
180°	17.98			172°	7.99		

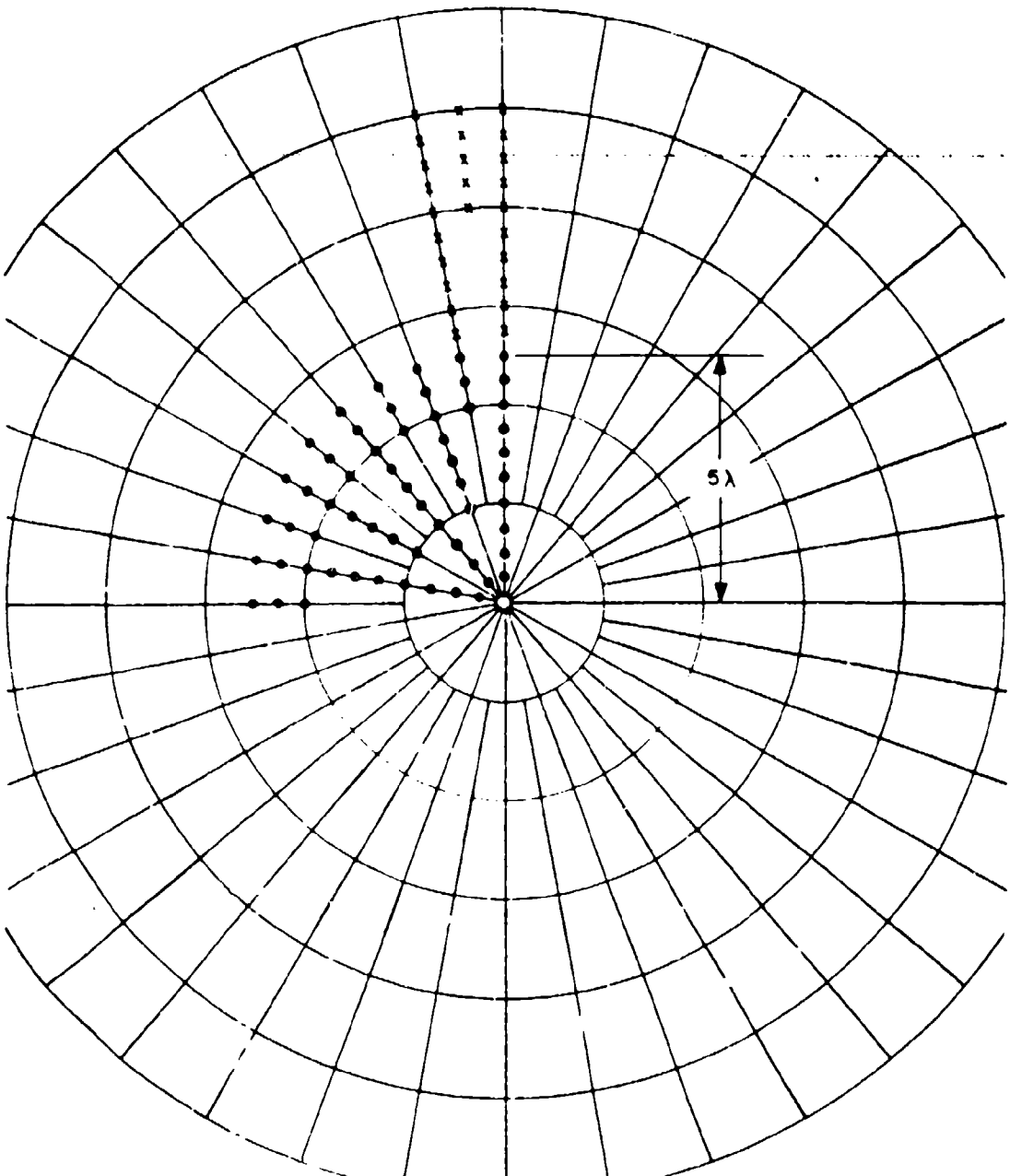

Fig. 25: Element Arrangement for Quarter of 10-Ring Array, $D_{max} = 10\lambda$ (Extension to 20λ Diameter Indicated)

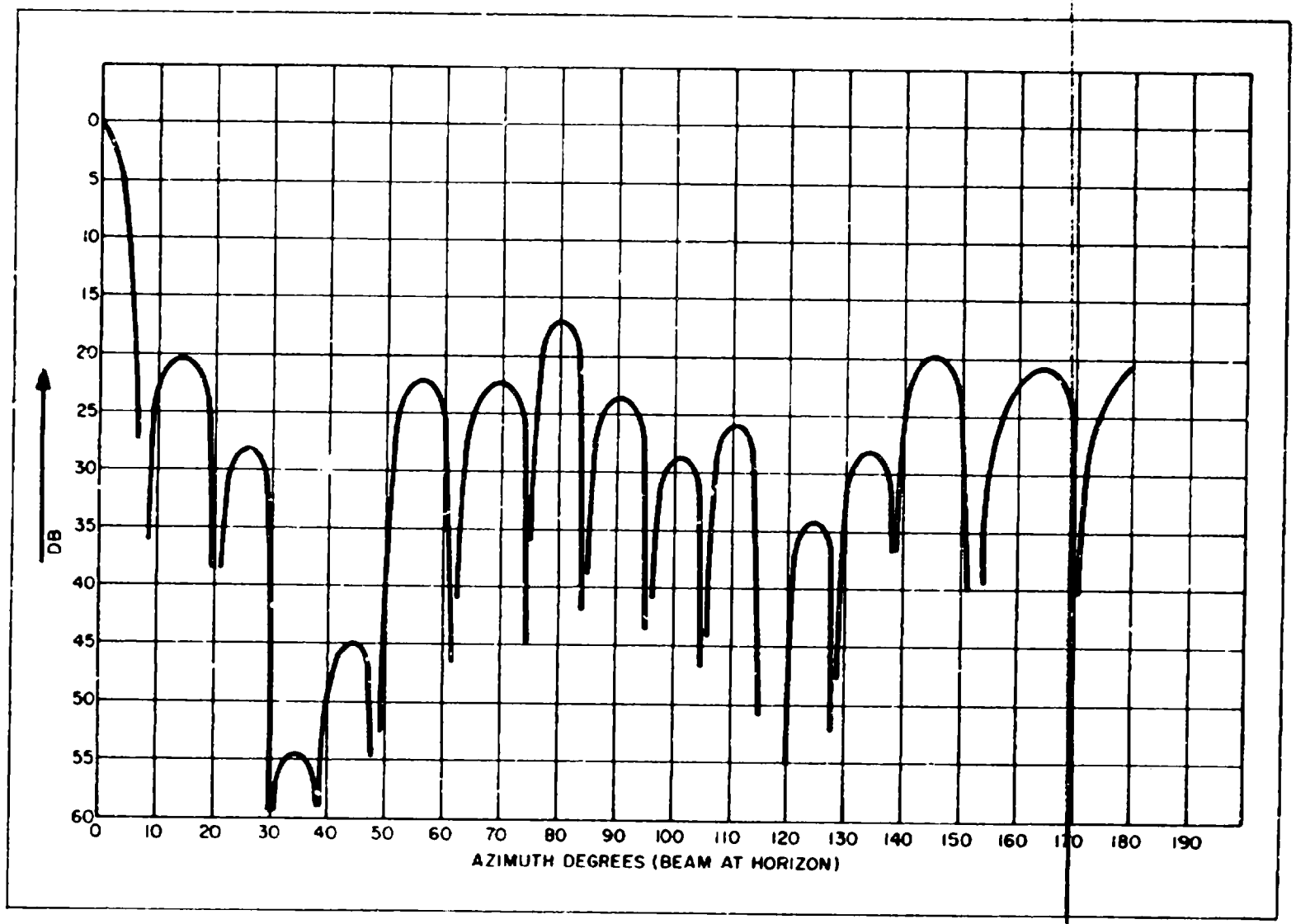

Fig. 26: Star Array, (10-Ring Circular Array), $D_{max} = 10\lambda$, Elements per Ring: 36, 36, 36, 18, 18, 18, 18, 9, 9, 9, (Azimuth)

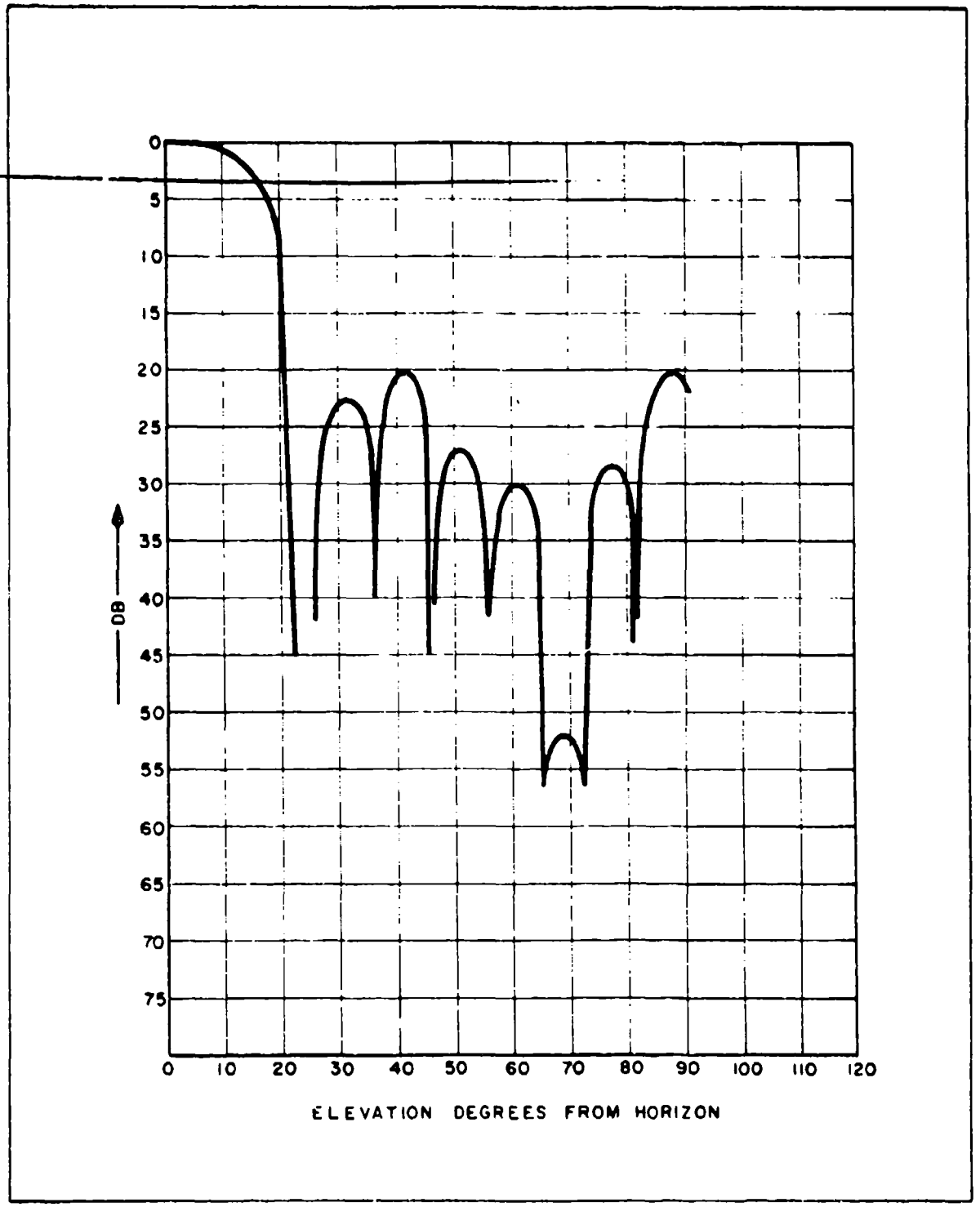

Fig. 27: Star Array, (10-Ring Circular Array), $D_{max} = 10\lambda$; Elements per Ring; 36, 36, 36, 18, 18, 18, 18, 9, 9, 9, (Elevation)

6. Scanning, Bandwidth and Mutual Coupling Considerations

6.1 Comparison of Scanning Approaches

A Wullenweber antenna is usually scanned with a mechanically rotated capacitive coupling structure. The same approach is possible for a full ring array, but it may not be desirable because of the relatively low scanning speeds possible, and the mechanical wear of the system. Two other scanning techniques are the sequence current concept and modulation scanning.

Both use a sampling gate to allow observation of a particular beam direction, because the beam is scanning continuously. The modulation scanning technique has the disadvantage of low element utilization (because the backlobe has to be blacked out), of poor elevation directivity and a large signal processing bandwidth. (The bandwidth is approximately $N \cdot \Delta f$, where N is the number of array elements, and Δf the information bandwidth.) For these reasons a fourth method, the incremental beamsteering (or beam switching) technique is suggested in connection with a broadband binary symmetrical beamforming network.

For a requirement of 360° azimuth scanning or beam steering (either for search or for varying operating conditions and directions, as in mobile applications,) this type of circular array shows a definite advantage in gain-bandwidth product, as we shall see below, provided that true time delay is employed, rather than modulo 2π phasing. With true time delay, and broadband radiating elements, the array factor is the only limitation to the bandwidth of the array as compared to the modulo 2π phasing schemes, where the instantaneous bandwidth is approximately given by

$$\Delta f \approx \frac{f_o}{D_\lambda} \tag{38}$$

which means it cannot exceed the center frequency divided by the aperture in wavelengths. In the case of e.g., a 5λ - diameter array, the maximum bandwidth with this type of phasing arrangement would be approximately 20%, whereas a true time delay phased array has at least octave, and conceivably 3:1 frequency range. This array is, therefore, very useful for multifunction systems accommodating direction finding, communications, data and control links, and radars within the same aperture.

6.2 Scanning of Ring Arrays with Binary Symmetrical Feed Structure

The binary symmetrical feed network allows a maximum of beam forming flexibility. The possibility of operating a single-ring array either in an omnidirectional mode, or covering one or more directions with narrow, high-gain beams has been investigated (Ref. 4) and numerous beam combinations with their associated directivity gains were synthesized. In all cases, the assumed beam forming matrix consisted of a signal combining (or dividing) network with binary distribution, and phasors which could be either of the modulo 2- type, or true delay lines such as coax or stripline. For simultaneous beams into different directions one has the option of either having several

beams formed by using several double-arc configurations, in which case the directivity (and the absolute gain) is reduced by 3 db each time the beam number is doubled, or by using signal dividers at the elements, in which case the directivity is preserved, but the absolute gain is reduced as above. (The latter case obviously requires much more complex feed structures, and would only pay off if directivity is of importance.)

Broadband operation is possible through the use of true time delay, even though modulo 2π phasing is always possible, of course. Unless the aperture is very large, or the frequency is very low, the required delay times can easily be accomplished with coaxial or strip transmission lines. The required time delay is given by

$$\tau = \frac{d_n}{V} \tag{39}$$

or

$$\tau = \frac{D}{2V}\,(1 + \cos \phi_n) \tag{40}$$

where ϕ_n is the angular position of element n relative to the beam axis, from the center,

d_n is the distance of element n to the phase reference

V is the phase velocity of the received signal in free space (usually the speed of light.)

D is the diameter of the ring (in the same units of length used for V).

Since negative time delay is impossible, the phase reference will be at the periphery of the ring, and the maximum delay line length required (for the element located opposite the phase reference) is given by (Fig. 28):

$$V \times \Delta T_{max} = L = \frac{1}{\sqrt{\epsilon_r}}\ D \tag{41}$$

where ϵ_r is the relative dielectric constant in the cable, (for most cables $1/\sqrt{\epsilon_r} = 0.69$.) An array phased in this manner ('co-phasal' excitation) can now be operated over a large bandwidth and is limited only by sidelobe performance and gain variation dictated by the array factor. By proper distribution across the aperture an optimum trade-off between sidelobes in azimuth, sidelobes in elevation and gain can be achieved.

This type of array, with fixed phasing for a certain beam direction, can now be steered in azimuth by switching the antenna element feed lines to different output ports of the feed network. For N antenna elements and M output ports N x M switches are required to cover 360 degrees in azimuth with

N overlapping beam positions. In general, a 3 db overlap will be sufficient, but if a smaller gain variation is desired, a larger number of elements can be used. (Fig. 29).

6.3 Array Bandwidth Considerations

The bandwidth of the binary symmetrical corporate feed can easily be as high as 10:1 using broadband techniques such as ferrite-core hybrids at frequencies up through UHF, and log-periodic structures at microwave bands. This includes fixed delay lines. The bandwidth limiting components are thus switches used in the commutator, amplifiers (if used, e.g., to improve the transmit efficiency), the array elements themselves, and the array factor.

Using ordinary monopoles or dipoles, even with small length-to-diameter ratios, less than an octave bandwidth can be expected from the array elements. Considerable improvement is possible by using two elements in a complementary pair configuration (Ref. 5). One possible configuration consists of two identical monopoles in an endfire pair, the impedance of one being externally complementarized with respect to the other. Another configuration would be a slot-monopole or slot-dipole pair. Depending on the allowable efficiency, in excess of 10:1 bandwidths have been reported. (Ref. 6).

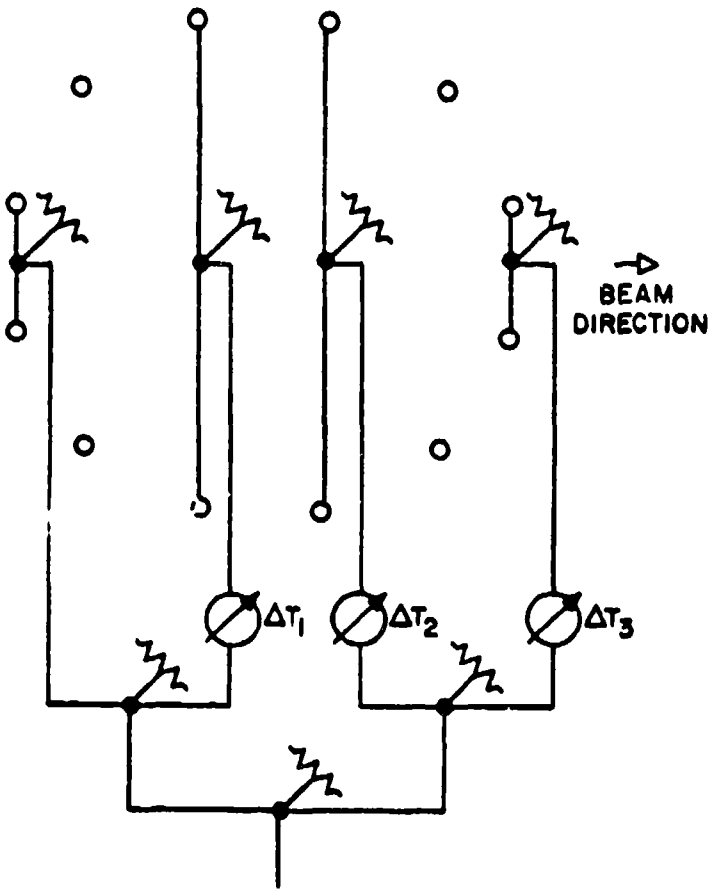

Fig. 28: 8-Port Binary Symmetrical Beam Forming Network for Space-Tapered Excitation of 12-Element Circular Array Using Time Delay Phasing

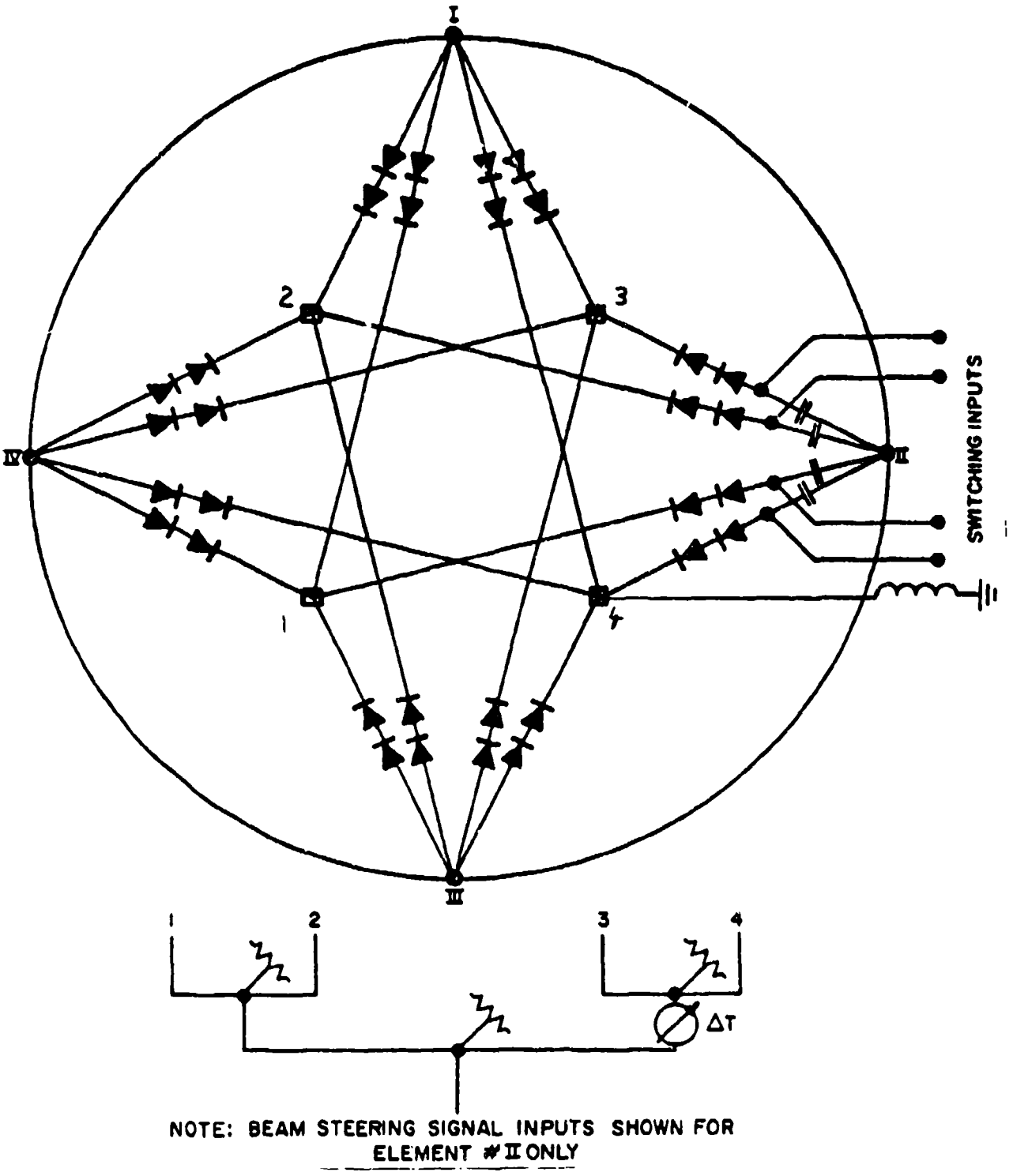

Fig. 29: Solid-State Commutator for Four-Element Array

The array factor bandwidth, finally, depends at one extreme on the number of elements one is willing to use within a given aperture, i.e., the tolerable element cost, and at the other extreme on the maximum tolerable sidelobe level, at a certain elevation angle.

For sidelobe levels around 10 dB, the computer analysis presented in this paper has shown that element spacings of several wavelengths can be tolerated. From Table 3, e.g., we find that the 5-ring array (with a ring-to-ring spacing of ~2.2 wavelengths) will exhibit a maximum azimuth pattern sidelobe of ~12 dB for 2 wavelengths element spacing on each ring. Since gain variation with frequency is inevitable in broadband fixed-aperture antennas, the conclusion is that for 12 dB sidelobe level this array can be thinned to about 10% element density at the highest frequency, amounting to about 40% density at the lower end of an octave band. For more stringent sidelobe requirements, the element density at the high end will have to increase, until the array is denser than the conventional half-wave grid at the low end of the band. Multifunction broadband arrays in general, and circular arrays in particular, will thus have to be designed so that their most sidelobe-sensitive functions are occupying the lowest operating frequencies of the available array bandwidth. This means that, generally, radar functions will have to be accommodated at the low end of the band. In any event, the near-normal element densities at the low frequency end will give rise to significant mutual coupling. Of all radiating elements tested so far, only externally complementarized complementary pair configurations have exhibited the required mutual coupling resistance for spacings of less than half a wavelength, measurements being available for spacings as low as 0.1 wavelengths.

Electrically large radiating elements, such as log-periodic monopole arrays, are relatively poorly suited for use in circular arrays, because their performance deteriorates rapidly in strong mutual coupling environment, and because their phase centers move along the log-periodic structure as a function of frequency. This aggravates the frequency dependence of the beamwidth further, the maximum effective array aperture coinciding with the maximum frequency, so that the aperture in terms of wavelengths increases almost with the square of the frequency.

To determine the practical performance of endfire complementary monopole pairs, an eight-pair circular array was designed, which is now described.

7. Broadband Circular Array Test Results

A dual-ring array of eight elements per ring and one wavelength diameter at 400 MHz was designed. (Ref. 7.) Two adjacent elements were grouped together to form an endfire monopole pair. (Fig. 30.) The individual directional patterns are very broad, so that only a small amplitude taper results from the fact that the edge pairs are not operating at the peak of their cardioid patterns. (Fig. 31). The monopoles used for the model had a height-to-diameter ratio of 3.2:1 for the center ring, and a ratio of ~4:1 for the outer ring. The spacing between rings was a quarter wavelength at 400 MHz, and the spacing between elements in the outer ring was 0.38 wavelengths at 400 MHz. The element spacing at the lowest frequency measured, i.e., 200 MHz, was thus 0.19 for the elements in the outer ring. The spacing between elements on

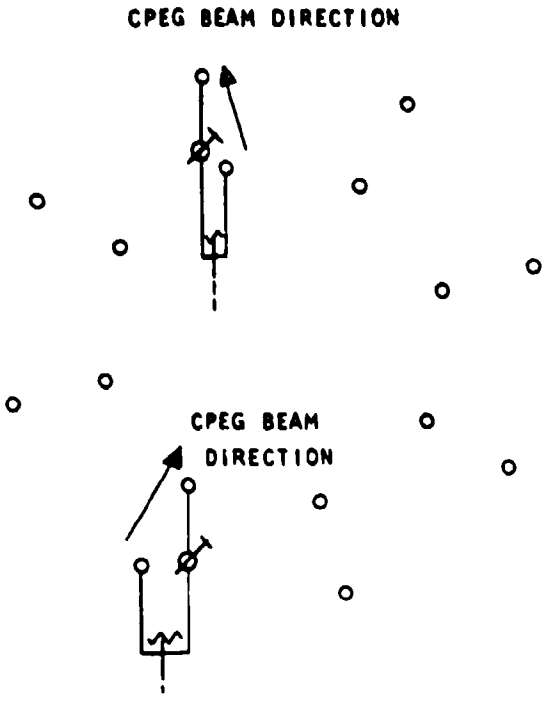

Fig. 30: CPEG Phasing Principle

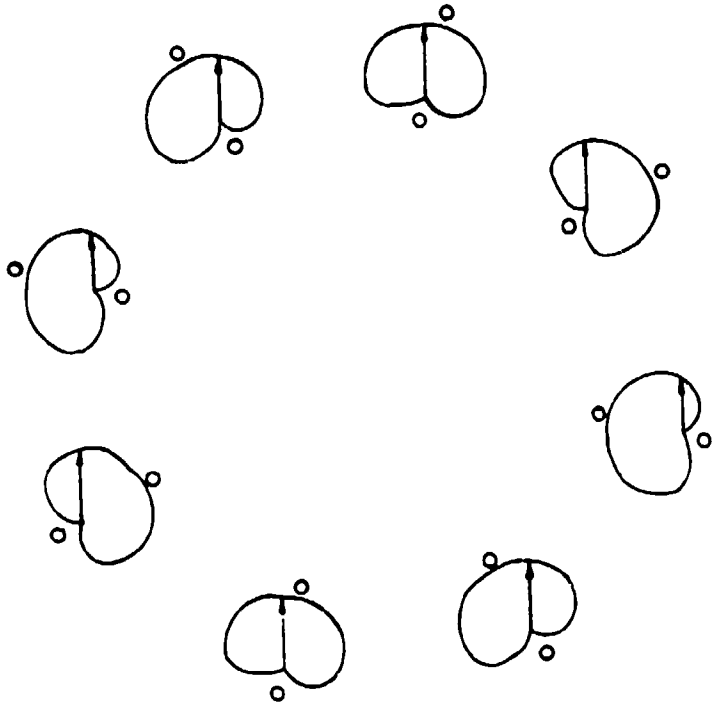

Fig. 31: CPEG Pattern Utilization

the inner ring was about 0.1 wavelengths at 200 MHz. The measured input impedance of an eight-port hybrid feed network feeding the eight complementary pairs, with time delay compensation in the direction of propagation as shown in Fig. 28, is depicted in Fig. 32. The impedances were somewhat improved by the loss of the feed network, which was about 2 dB at the highest frequency, and about 1 dB at the lowest frequency.

Sum patterns for the array are shown in Figs. 33 to 35, and difference patterns (obtained by feeding the two halves of the array perpendicular to the sum beam direction 180 degrees out of phase) are given in Figs. 36 and 37.

The sidelobe performance is about as would be expected for the small element number (8 effective elements in a virtual 4-element broadside array configuration). To determine array matching efficiencies, all powers in the CPEG (= Complementary Pair Element Group) hybrid difference ports, and in the feed network difference ports, were measured and added up. Net efficiency (excluding feed network ohmic losses, which could be eliminated by using amplifiers at each CPEG input) was ~90% at 200 MHz, and about 70% at 400 MHz.

8. Element Hardening Aspects

To protect the radiating elements from environmental damage, some studies were performed on potential hard radiator designs. (Ref 3, 4.) Fig. 38 shows a proposed electrically small hard cap-loaded folded monopole, which can be used over a fairly wide band by tuning, and can be stored mechanically for maximum protection. Similar units could be designed for near-resonant size, and broadbanded by using them in complementary pairs. A more conventional broadband hard radiator configuration is shown in Fig. 39. Obviously, ultimate configurations will depend heavily on frequency band, bandwidth, overpressure level, and elevation steering requirements.

9. Acknowledgments

Credit is due General Electric Co., Heavy Military Electronics Department, Syracuse, N. Y., for sponsoring part of the circular array computer study. The author wishes to express his gratitude to Hal Schroeder for his programming efforts, and to F. R. Ruterman and W. T. Whistler for their support and advice. The majority of the patterns were also calculated during employment at General Electric under U.S. Air Force Contract AF 19(604)-7469, with Mr. Otto Kerr of the Cambridge Research Laboratories as Program Manager.

The Complementary Pair circular array development and testing was performed while the author was employed at Collins Radio Co., Dallas, Texas, under an inhouse phased array research program. The basic endfire complementary pair element group ("CPEG") was first reduced to practice for the V.O.A., U.S. Information Agency under contract No. I.A. - 12183. Thanks are due Preston Law, Sid Kessler, George Jacobs and Julius Ross of the Voice of America International Broadcasting Service for their encouragement and financial support.

Also acknowledged are the continued suggestions and inspirations provided by Frank Boyd, Jim Headrick, Rus Brown and Paris Coleman of the Naval Research Laboratories, especially while monitoring an Office of Naval Research study under contract N0014-67-C-0106.

10. References

(1) H. Stenzel, "Uber die Richtcharakteristik von in einer Ebene angeordneten Strahlern" Elektrische Nachrichtentecimik, Vol. 6, May 1921, pp. 165 - 181.

(2) "Near Sidelobe Suppression In A Single-Ring Directional Array with Horizontal Beam Direction", U.S. Patent No. 3, 3808,058 (Assigned to U.S. Air Force)

(3a) W. T. Whistler, K. G. Schroeder, et al, Semi-Annual Report, "Hardened Point-to-Point Communication Antenna Configurations," Contract No. AF-19(604)7469, G. E. Syracuse, June 1961 (Unclassified Chapter: "Design Criteria for Circular Arrays").

(3b) Final Report, "Hardened Point-to-Point Communication Antenna Configurations," G.E. Syracuse, May 1962.

(4) K. G. Schroeder, "Analysis and Synthesis of Ring Array Antennas," G. E. Technical Information Series, No. R 62 EMH 55, Syracuse, Dec. 1962.

(5) "Complementary Pair Element Groups", U.S. Patent No. 3,449, 751. (Assigned to Collins Radio Co.)

(6) P. E. Mayes, W. T. Warren, F. M. Wiesenmeyer, "The Monopole-Slot: A Small Broadband, Unidirectional Antenna", IEEE 1971 G-AP International Symposium Digest, pp. 109-112.

(7) K. G. Schroeder, "Wideband Circular Arrays of Complementary Pair Element Groups," IEEE Transactions on Aerospace and Electronic Systems (Supplement) Vol. AES-3, No. 6, Nov. 1967, pp. 309-323.

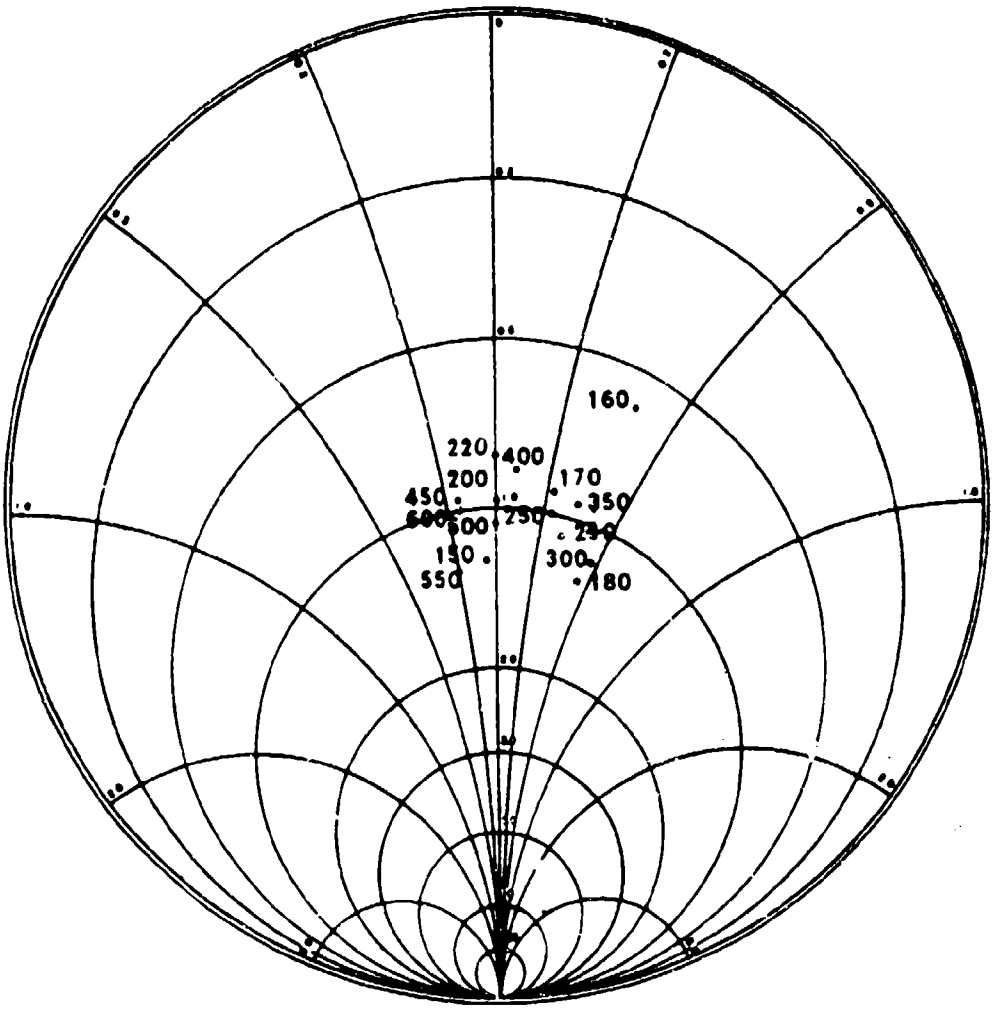

Fig. 32: 8-CPEG Circular Array Beam Input Impedance

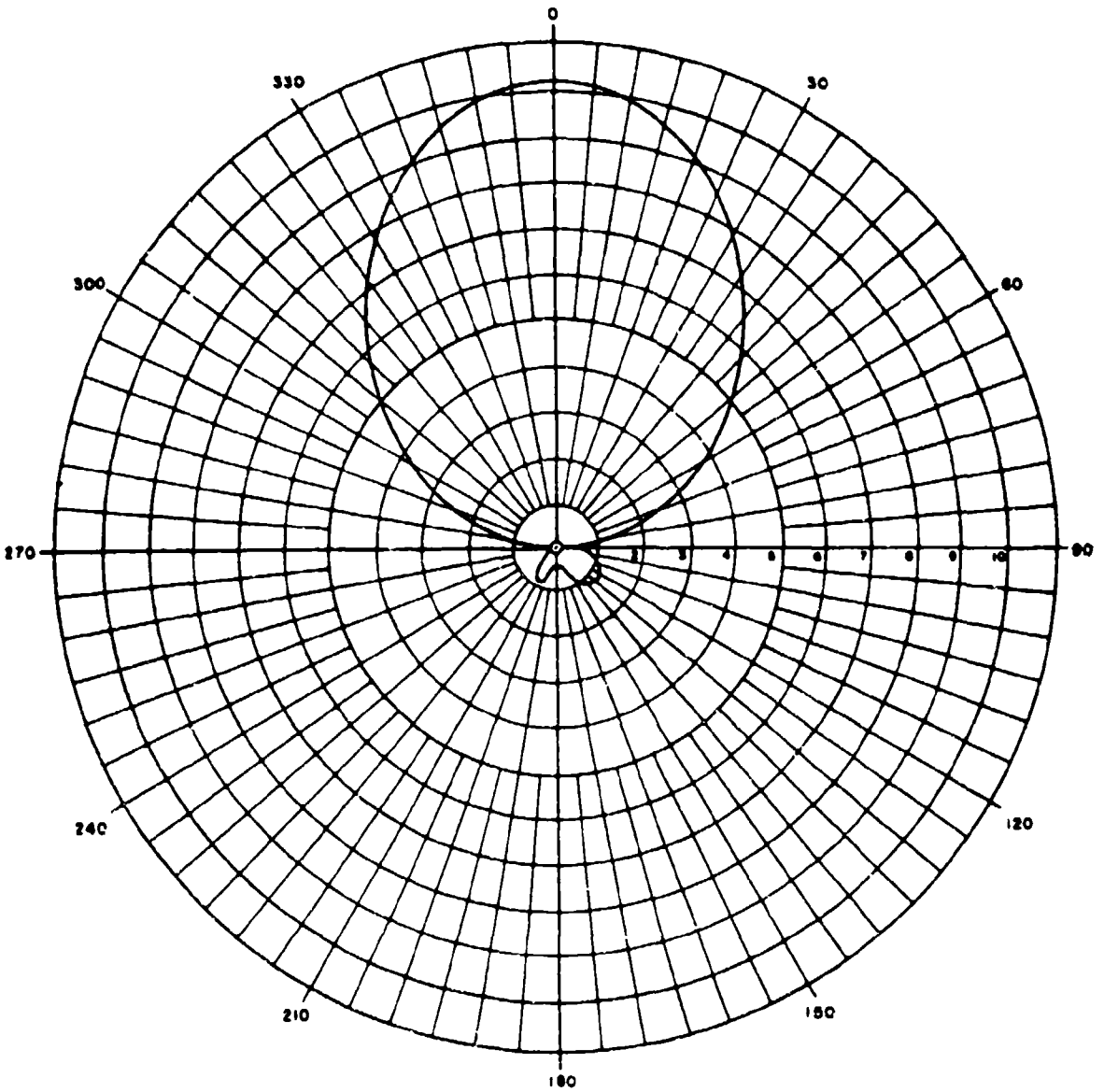

Fig. 33: 8-CPEG Circular Broadband Array Directional Far-Field Voltage Pattern. Azimuth Pattern, θ = 0, F = 220 MC

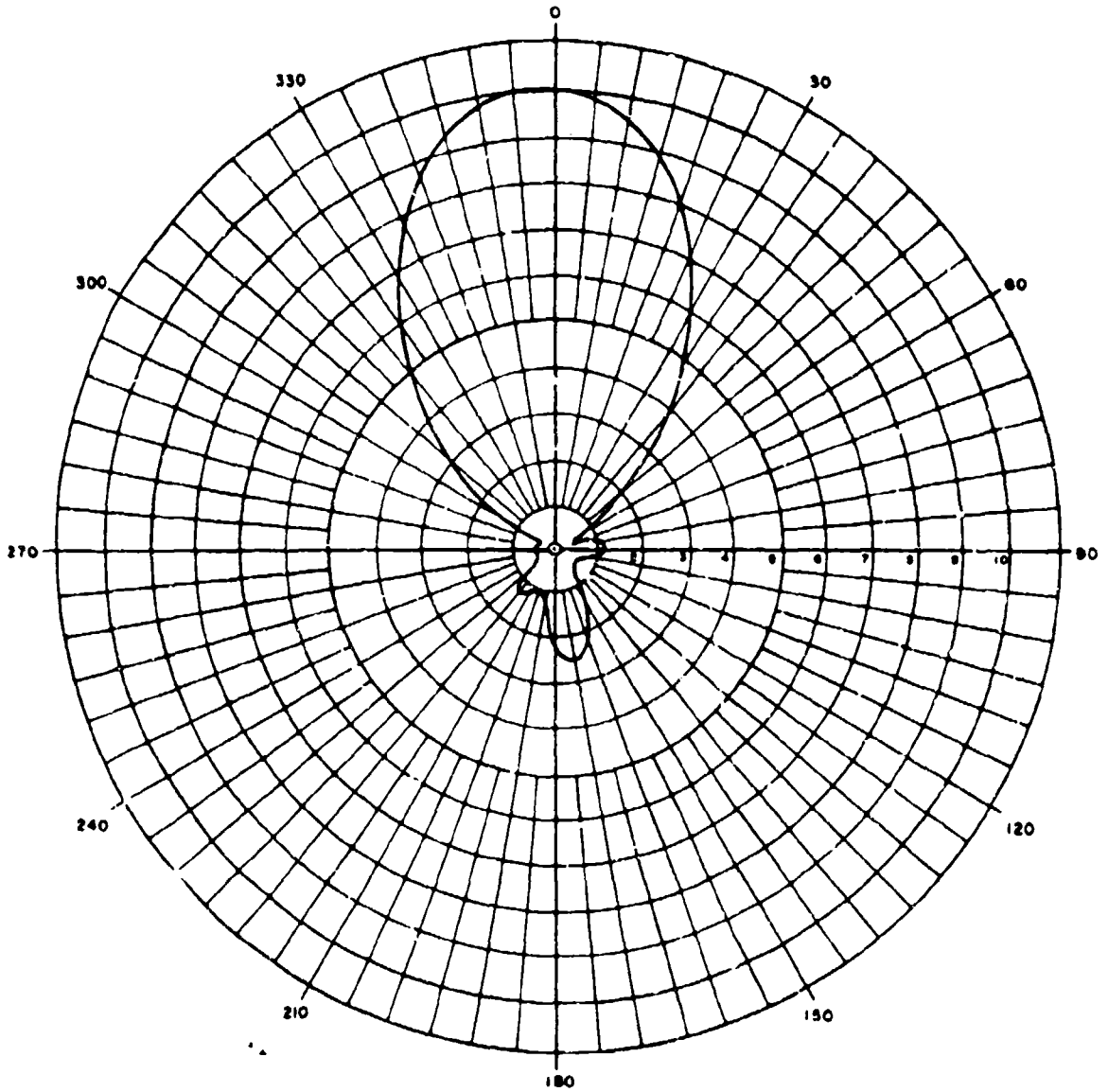

Fig. 34: 8-CPEG Circular Broadband Array Directional Far-Field Voltage Pattern. Azimuth Pattern, $\theta = 0$, F = 300 MC

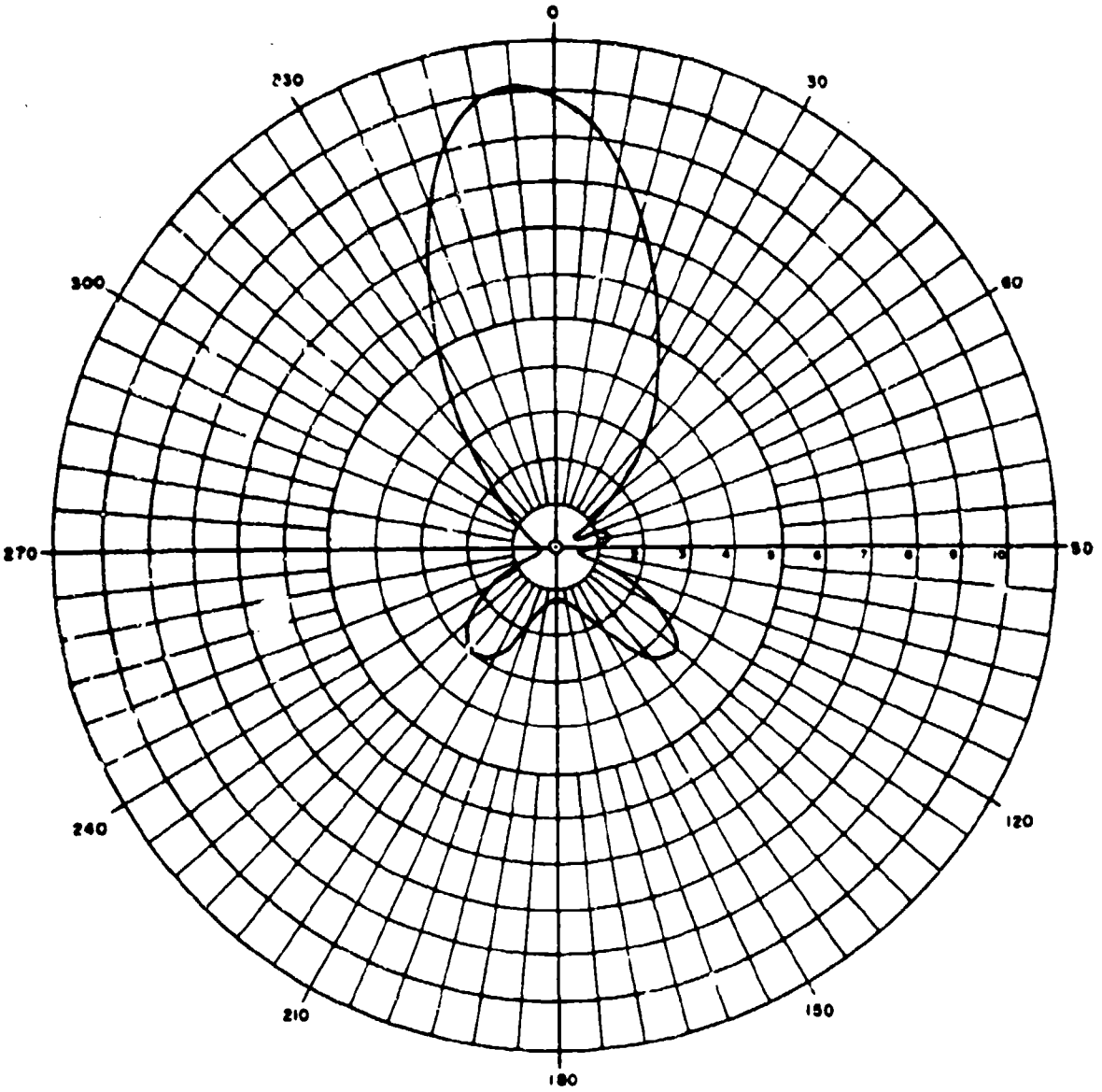

Fig. 35: 8-CPEG Circular Broadband Array Directional Far-Field Voltage Pattern. Azimuth Pattern, θ = 0, F = 400 MC

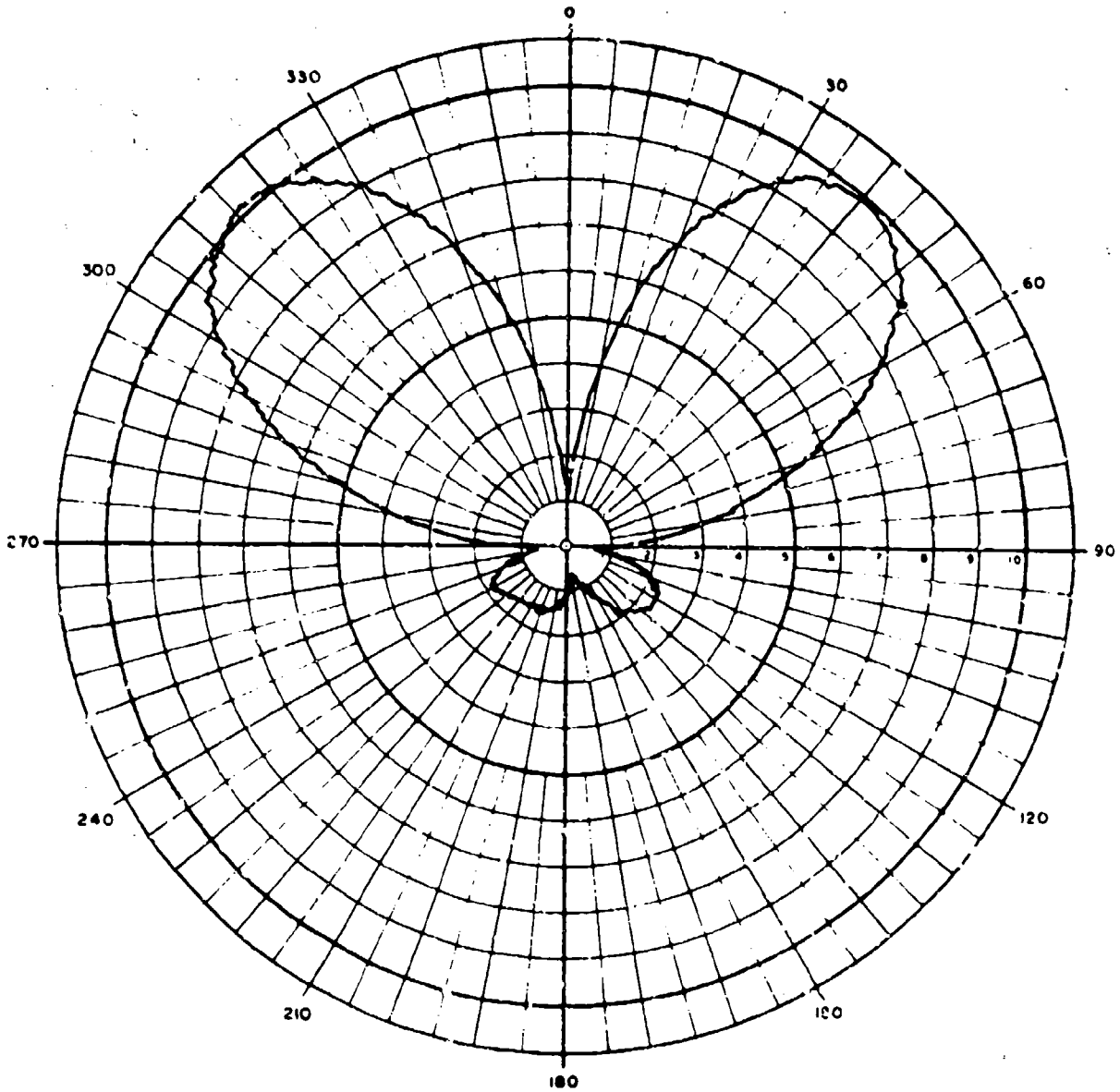

Fig. 36: Difference Pattern of 8-CPEG Circular Broadband Array, f = 300 MHz

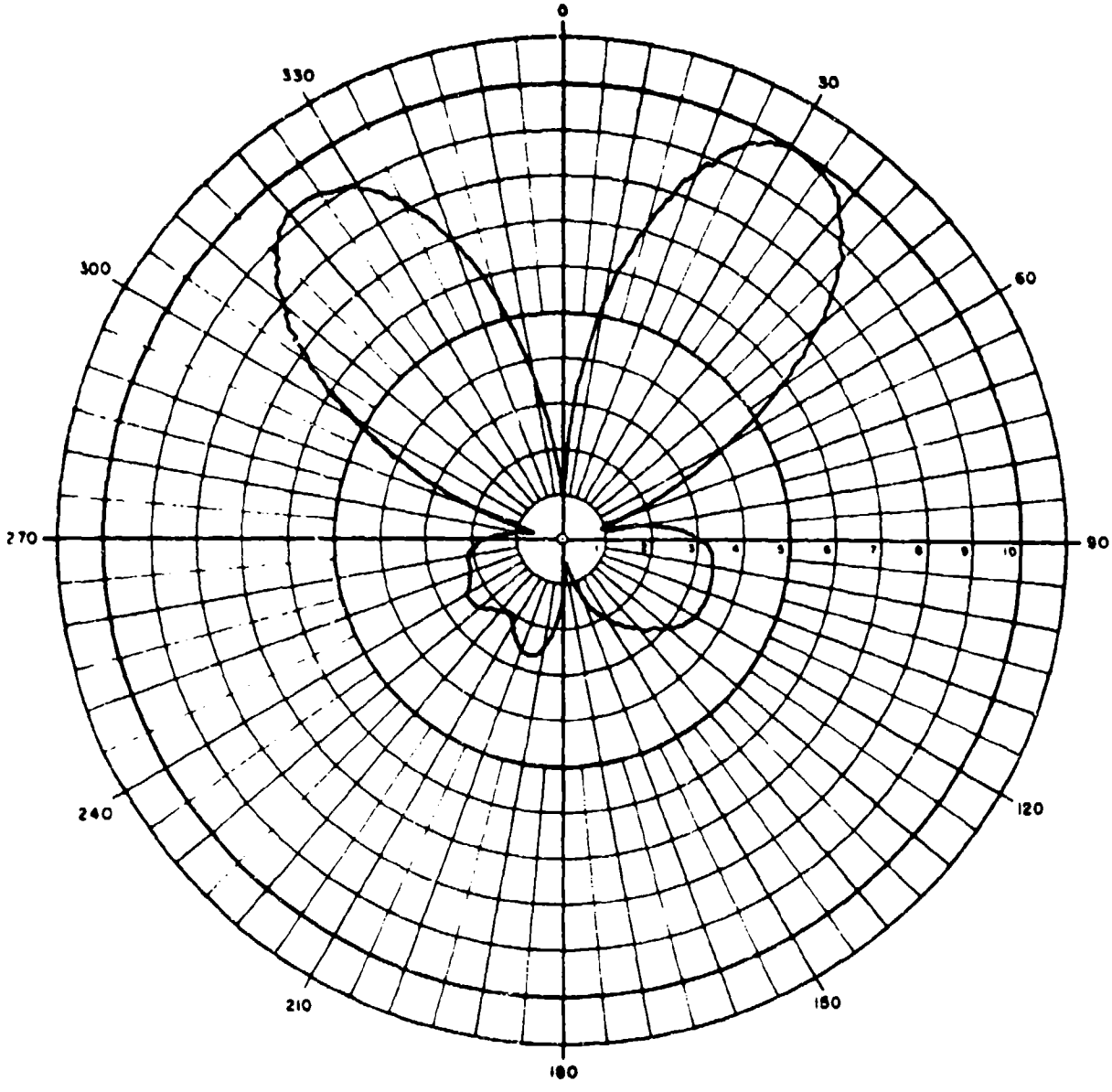

Fig. 37: Difference Pattern of 8-CPEG Circular Array, f = 400 MHz

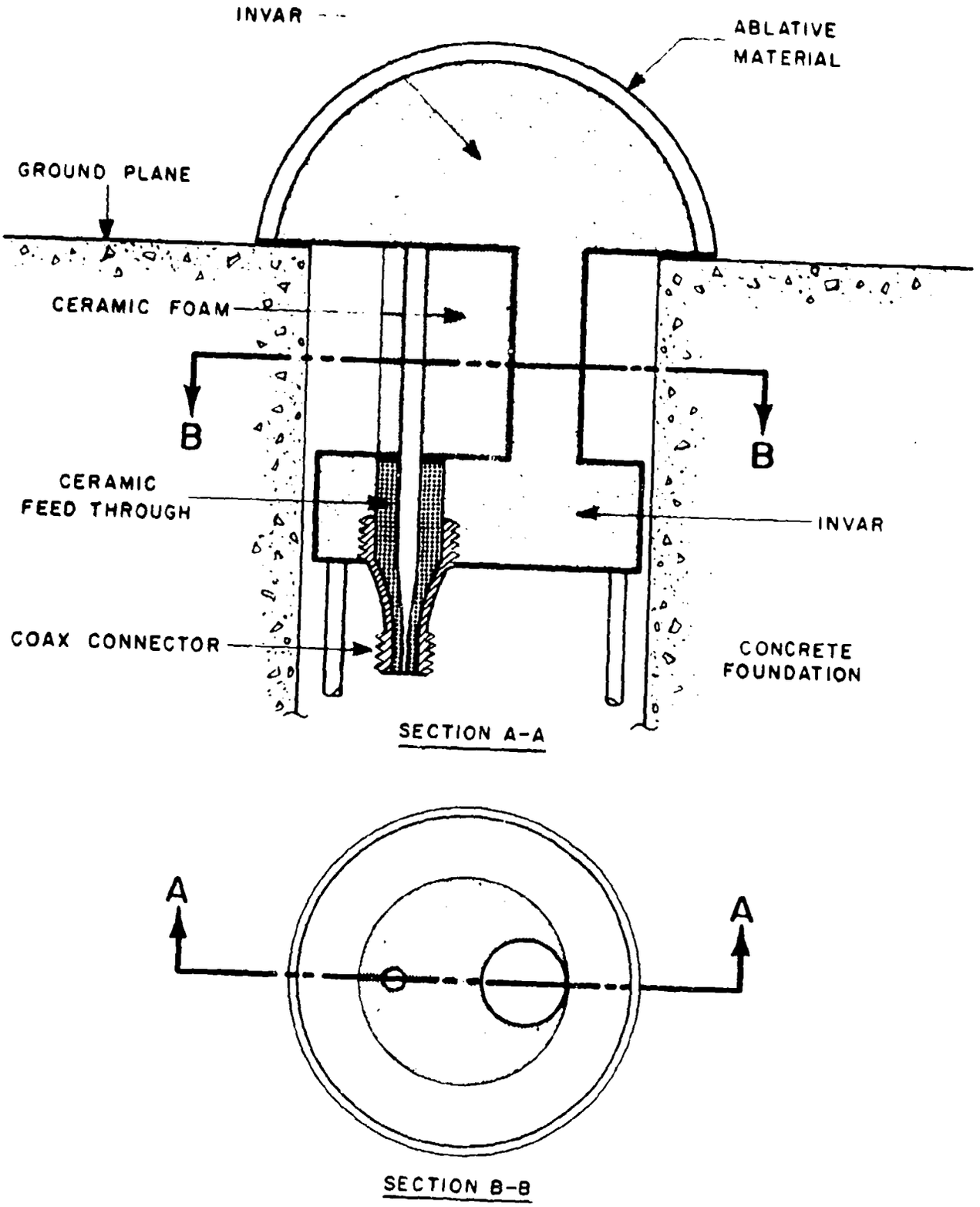

Fig. 38: Hardened Cap-Loaded Folded Monopole (Stored Position)

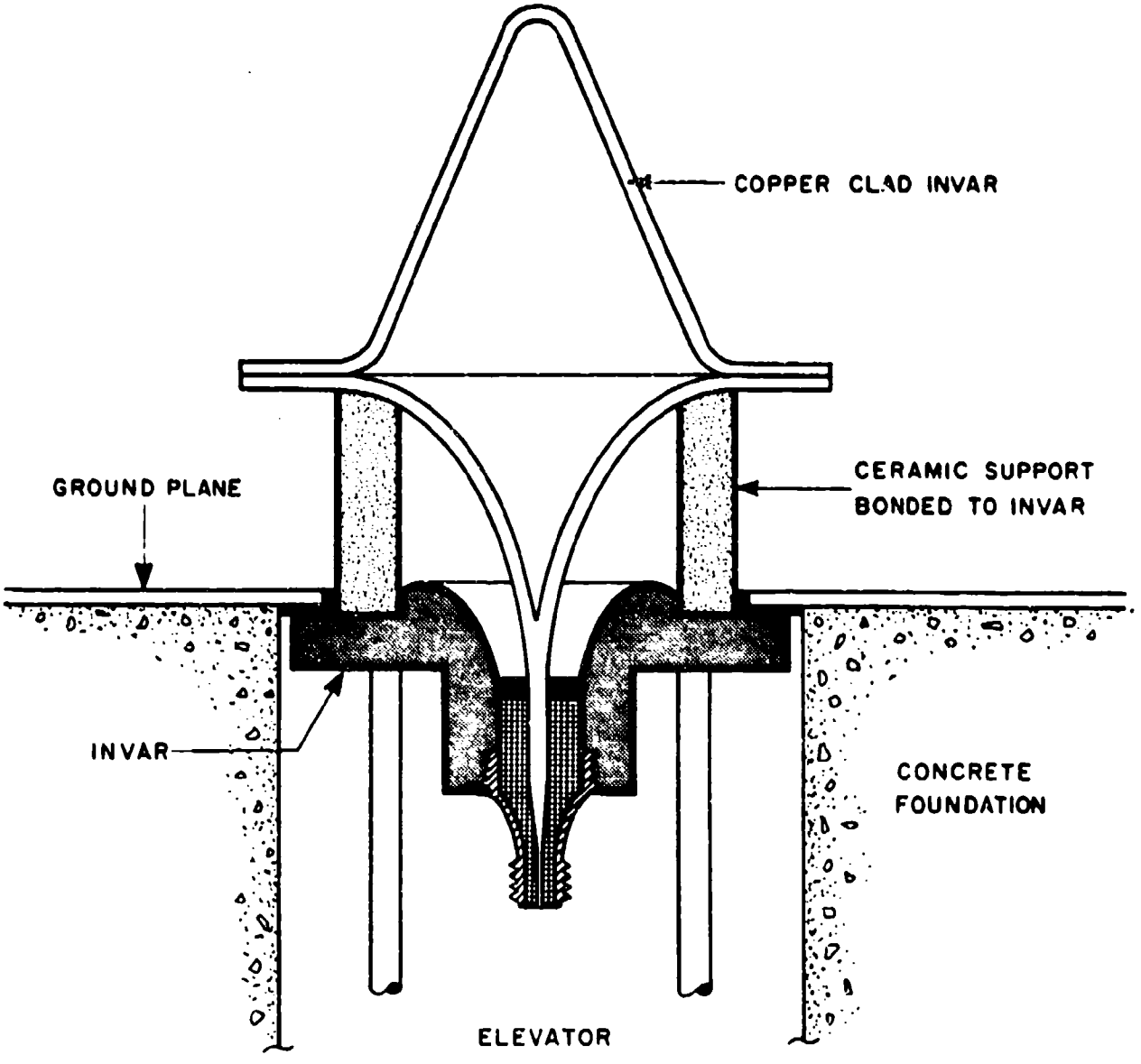

Fig. 39: Hardened Exponential Monopole

16. IMAGES OF ANTENNAS BY SPECTRUM ANALYSIS OF MICROWAVE HOLOGRAMS

by

E. L. Rope and G. P. Tricoles

General Dynamics Electro Dynamic Division
P.O. Box 127, San Diego, Calif. 92112

for

ARRAY ANTENNA CONFERENCE

Naval Electronics Laboratory Center
San Diego, California

22-24 February 1972

1. INTRODUCTION AND SUMMARY

1.1 INTRODUCTION

Holography originated in optics, as an imaging process, but it is now being developed for microwaves. In holography, images are formed in two, distinct steps. In the first step, called hologram formation, an object is illuminated and scatters a field onto a detecting surface, which is a photographic plate for optical holography. The detector is also illuminated by a coherent beam that bypasses the object. The developed plate is an interferogram but is called a hologram because it contains both amplitude and phase data. The phase is encoded through positions of the interference fringes. Images are produced in the second step when the hologram is illuminated; this step is called wavefront reconstruction. Optical holography is useful in data processing and vibration analysis as well as for image formation.

Microwave holography is being developed for many applications. These include image formation, especially for objects in optically opaque regions. Holographic methods have been used in diagnostic studies of antennas and of wave propagation through radomes and plasmas. In diagnostic work images are frequently useful for locating reflecting surfaces; however, in some cases, the holograms yield more information than do images. The development of microwave holography seems reasonable because holograms are interferograms and because interferometers are useful for measuring diffracted microwave fields. Complex-valued, nearfield data are well known to be useful in computing farfield patterns of antennas; this application clearly involves the sampling and transform methods that are utilized in holography. Holography is also related to inverse scattering.

Microwave holography offers an approach to studying the field distributions of aperture antennas and arrays as well as those induced on reflecting objects. This kind of application motivates the work described in this paper. If the resolution capabilities of microwave holography can be developed sufficiently, then it would be useful in determining the fields near an antenna without placing a probe in the near-field. This paper describes an approach to improving and simplifying microwave holography for applications to antenna and radome diagnostics.

Although microwave holography is still being developed, it has already been applied to many problems, with a variety of techniques. Probably the first application was to forming images of the ionosphere by illuminating scale-reduced radio-wave sounds.[1] Several procedures and displays have been developed to form visible images when metallic and dielectric objects are illuminated with microwaves.[2,3,4] Images are usually formed with laser light from scale-reduced transparencies that

represent interference patterns scanned by a probe antenna and represented by an array of lights or by an oscilloscope. Binary, detour-phase, microwave holograms have also been developed.[5] Images have been formed of concealed weapons that were illuminated by millimeter waves.[6] Multipath propagation in radomes has been studied by forming images of reflecting regions; the technique does not use an explicit reference beam.[7] The double exposure method, developed in optics, has recently been applied to study deformations of large structures.[8]

Probably the earliest diagnostic application of microwave holography was made in 1950 by Koch, who produced visible displays of interference patterns formed by a radiating antenna and a reference beam. However images were not formed in this early work.[9] More recently, microwave holograms have been used to measure radome boresight error.[10]

Several problems remain in doing microwave holography. There is apparently no sensitive and convenient, continuous detector analogous to photographic film. Discrete antennas and conventional detectors are most common although liquid crystals and specially processed films are being investigated.[11, 12] The use of discrete antennas introduces sampling notions; for example, a probe antenna must be moved on paths that are sufficiently close to prevent aliasing in images. Scanning an area with a single probe antenna is time consuming and requires apparatus that is sufficiently stable; consequently, a single antenna is rapidly scanned or a linear array is used.[13]

The reconstruction procedure is especially significant in microwave holography because the wavelengths of light and microwaves differ by approximately four orders of magnitude. Microwave holograms must be scale-reduced for reconstructions with visible light. However, practical reductions are appreciably smaller than the ratio of wavelengths so that alternate reconstruction methods are being considered to eliminate scale-reductions. Reconstructions have been computed in both acoustic and microwave holography.[14, 15, 16] Inverse scattering has been investigated theoretically and numerically.[17] Reconstructions have also been made with microwaves to simulate antennas through simpler holograms and also to study the effects of approximations made in sampling and representing the microwave field.[18, 19]

Computational reconstruction procedures seem attractive because they eliminate the time delays and non-linearities that occur in using photographic film.[20] The non-linearities occur in recording the fringes and in scale reduction; they generate higher order images that can reduce image quality. The time delays occur in developing and scale reducing the film.

1.2 SUMMARY

This paper describes a new technique that accelerates microwave holography through the computation of reconstructions with an analog spectrum analyzer. The spectrum analyzer forms images by processing detected fringes that are scanned by a moving probe antenna in the formation step of a microwave hologram formation experiment. Computational reconstructions accelerate holography by eliminating the delays in developing and scale reducing films for reconstructions with visible light. The images are formed in almost real time; the delays are approximately 50 seconds, the interval needed to scan the fringes.

Computational reconstructions can also improve image quality by eliminating two sources of distortion. One source is the non-linearity of film that records the fringes and copies the holograms in photographic, scale reductions. The other source is the partial scale reduction of microwave holograms to produce optical holograms. Because wavelengths differ by factors approximately 10^4, only partial scaling is practical.

Computational methods have some limitations. They may be restricted to relatively simple objects because computer storage is limited. The approach described in this paper is further limited because the spectrum analyzer has a single channel and operates on the voltage from a square-law detector. To see this limitation, consider sampling the field over an area. An antenna array is used, and the fields from the array elements are summed, prior to detection. The quadratic detector forms a sum that contains products of the fields from the elements. Consequently, higher order images, higher sidebands, are generated. The magnitude of this problem is evaluated for a receiving array with two elements.

Neither limitation, storage nor higher order images, is expected to be a serious problem because many diagnostic applications involve a relatively small number of sources. Moreover many practical, radiating structures have dimension that have orders of magnitude comparable to the wavelength of centimeter waves so that the number of resolution cells is small. Our experimental results verify that the method is satisfactory for studying antennas with a small number of elements, for locating defective elements, and for measuring the size of aperture antennas.

This paper describes the analysis of the reconstruction procedure, and it describes our initial experiments for simple objects. Initially we considered either one or two small antennas the object to study resolution. The radiation was coherent, so phase, as well as amplitude, was controlled. A reference beam was used and arranged to produce Fourier transform holograms (lensless Fourier transform or point-reference method). Fringes were sampled with a single antenna and power was detected with a crystal. The detected voltage was the processed by an analog spectrum

analyzer. From the computed spectrum the region of space in which the amplitude exceeds a threshold value defines the spatial extent of the image and hence object. That is, the spectrum analyzer performs an inverse transform.

The detection process is analyzed experimentally and theoretically to evaluate the magnitudes of second-order images, which can degrade the first-order image. Proper experimental conditions gave the second-order image amplitude 1/20 that of the first, this value is negligible.

The method was extended to include a receiving array of two elements connected to a hybrid junction. The baseline is orthogonal to the direction of motion. Consequently, we perform an arithmetic operation in waveguide, then detect in the crystal, and finally Fourier transform in the spectrum analyzer. The squaring operation (to express microwave power) generates a number of product terms from the summation generated by the receiving array. Higher order terms were evaluated. It is experimentally shown that for two receiving antennas the amplitude of the second-order term is 1/10 that of the first order; this value is also negligible.

The reason for using a receiving array, of course, is to obtain information about the object's height. The width is determined by the breadth of the spectrum.

2. ANALOG COMPUTATION OF RECONSTRUCTIONS

2.1 EXPERIMENTAL ARRANGEMENT

The microwave apparatus is shown in Figure 2-1 and 2-2. A klystron oscillator K supplies 15.30 GHz microwaves to two identical dielectric antennas H_1 and H_2, shown in Figure 2-2, and to antenna R that radiates a reference field. The intensities of the fields radiated from each antenna are adjustable with attenuators A_1, A_2, and A_R. The energy supplied to all antennas can be adjusted separately by attenuator A. The relative phase of the fields from H_1 and H_2 can be adjusted with the phase shifter S. C and C′ are directional couplers. A receiving, probe antenna P is moved on a continuous, horizontal path by a motor. Vertical motion is provided by a second motor. The field is detected by a crystal detector, D.

The arrangement of Figure 2-1 produces an intensity (power) distribution of fringes that contains the Fourier transform of the source distribution. In optics, the arrangement is called the lensless Fourier transform method, or the point reference method. The Fourier transform is obtained subject to restrictions on positions of the sources. To see the transform relationship mathematically approximate the object source by a single point at the origin of the rectangular coordinate system in Figure 2-3. Let the reference source also be a point at $(0, y_r, 0)$ at the observation point P (x, y, z), let the reference field be

$$u_r = a_r e^{i\varphi_r} \tag{1}$$

and let the object field be

$$u_o = a_o e^{i\varphi_o}, \tag{2}$$

The field at (x, y, z) is then

$$u = u_r + u_o \tag{3}$$

$$= a_r e^{i\varphi_r} + a_o e^{i\varphi_o}, \tag{4}$$

Let us assume and suppress time dependence $e^{-i\omega t}$. Let us assume that a_r and a_o are constants; this assumption omits the inverse radial dependence of amplitude. Further, let us assume that a_r and a_o are real.

Moreover let us assume that

$$\varphi_o = kr_o \tag{5}$$

and

$$\varphi_r = kr_r \tag{6}$$

where k is $2\pi/\lambda_o$, with λ_o the wavelength.

From Equation 4 the intensity is proportional to

$$|u|^2 = a_o^2 + a_r^2 + a_r a_o e^{i(\varphi_o - \varphi_r)} + a_r a_o e^{-i(\varphi_o - \varphi_r)} \tag{7}$$

Next consider $\varphi_r - \varphi_o$. Now

$$r_o = (x^2 + y^2 + z^2)^{1/2} \tag{8}$$

and

$$r_r = [x^2 + (y-y_r)^2 + z^2]^{1/2} \tag{9}$$

If we expand r_o and r_r with the binomial formula, then to second order

$$\varphi_o - \varphi_r = (ky_r x^{-1}) y = \frac{1}{2} kx^{-1} y_r^2. \tag{10}$$

From Equation (10) we see that $\varphi_o - \varphi_r$ is linear in the observation point coordinate y. That is, in Equation 7, we have

$$|u|^2 = b[1 + c \cos(ay + \alpha)] \tag{11}$$

where α is $-ky_r^2/2x$, a is ky_r/x, b is $(a_o^2 + a_r^2)$, and c is $2a_o a_r/(a_o^2 + a_r^2)$. From Equation 11 we see the intensity contains a cosine term, with argument linear in y. If we recall the Fourier transform of a delta function is a plane wave, then we can consider $|u|^2$ in Equation (11) as a Fourier transform, using spatial frequency variables.

The detection and display is sketched in Figure 2-4. As the probe samples the intensity in the probing plane, a spectrum analyzer performs a second Fourier transform to produce reconstructed amplitudes.

2.2 ANALYSIS OF RECONSTRUCTION

Let us assume that the microwave intensity in the hologram plane has the form given in Equation 11. Now the input to the spectrum analyzer is a voltage V. In order to describe the non-linearities introduced by the crystal and amplifier let us write

$$V = (|u|^2)^{\gamma} \tag{12}$$

The exponent γ depends on the intensity incident on the detecting crystal; ideally, γ has unit value for small signals. Its value will be considered in another subsection. From Equations 12 and 11

$$V = c' [1 + c \cos (ay + \alpha)]^{\gamma}, \tag{13}$$

where c' is $(a_o^2 + a_r^2)^{\gamma}$, and c, a, and α were defined just after Equation 11. Expanding V in a binomial expansion, and using trigonometric identities, we have on retaining second-order terms that

$$V = c' \{V_0 + V_1 \cos (ay + \alpha) + V_2 \cos [2(ay + \alpha)]\} \tag{14}$$

where

$$V_1 = \gamma c \{[(\gamma-1)(\gamma-2) c^2/8] + 1\} \tag{15}$$

and

$$V_2 = c^2 \gamma (\gamma-1)/8. \tag{16}$$

The reconstructed image is obtained by Fourier transforming V. We obtain

$$u' = c' \int_o^T V e^{-i\omega t} dt, \tag{17}$$

where T is the duration of the scanning interval and ω is $2\pi\nu$, where ν is the temporal frequency.

Carrying out the integration, with $y = W[1-(2t/T)]$ and 2W the hologram width, we obtain for the spectrum, which is a section of the image, that

$$u' = U_0 + U_1 + U_2, \tag{18}$$

where

$$U_0 = c\,[\,1 + \alpha\,(\alpha - 1)\,(c/2)^2\,], \tag{19}$$

$$U_1 = c\;V_1\,(T/2)\exp[-\,iky_r^2/x - i(\omega T/2)]\;\operatorname{sinc}\;[aW + (\omega T/2)] + \ldots, \tag{20}$$

$$U_2 = c\;V_2\,(T/2)\exp[-iky_r^2/x - i(\omega T/2)]\;\operatorname{sinc}\;[2aW + (\omega T/2)] + \ldots, \tag{21}$$

The dots indicate terms with negative frequencies, and $\operatorname{sinc} x = x^{-1} \sin x$.

We can now estimate the amplitude of the second-order image as a fraction of the amplitude of the first-order image. Now the functions of the form x sinc x have maxima at unequal frequencies, but their maxima are equal. Therefore the amplitude of the second-order image relative to that of the first order is

$$|U_2/U_1| = \frac{1}{2}\,(\gamma - 1)\,(a_o/a_r)\,[1 + (a_o/a_r)^2\,]^{-1} \tag{22}$$

Equation 22 shows that second-order images are reduced as γ tends to unit value and as (a_o/a_r) is reduced. Figure 2-5 shows $|u_2/u_1|$ for typical values of γ and a_o/a_r. The anticipated amplitude of $|U_2/U_1|$ is less than 0.05; consequently, the second order image should be negligible.

Typical values of γ were determined by measuring the voltage from the spectrum analyzer with an oscilloscope for a range of values of the power radiated by antenna H_1 in Figure 2-1, while H_2 and R were fully attenuated. Results are shown in Figure 2-6. Values of γ near 1 are certainly possible. However, when all three antennas radiated, the amplitude of each was reduced to retain approximate linearity.

2.3 EXPERIMENTAL RESULTS: ONE-DIMENSIONAL IMAGES

Figure 2-7A shows a reconstruction made with H_2 attenuated so that only H_1 and R radiated. The spectrum is shown in a linear scale on the left and again on the right but plotted with voltage proportional to the logarithm of the linear voltage. The frequency at the peak is 0.16 ± 0.01 Hertz. From the definition that a is ky_r/x and from Equation 20,

$$\nu = \omega/2\pi = -2\,\frac{(2W)}{T\lambda_o}\,\frac{yr}{x} \tag{23}$$

Now λ_o is 1.980 cm, 2W is 45 cm, T is 50 sec., x is 152 cm, and y_r is -51.3 cm. Therefore ν is 0.16, in good agreement with measurement.

Figure 2-7B shows a reconstruction for H_2 radiating with H_1 attenuated. Notice that the peak of the spectrum occurs at a lower frequency when H_2 radiates. This result is reasonable because H_2 is closer to the reference antenna than is H_1.

Figure 2-8 shows reconstructions for both antennas radiating when they are in phase and out of phase.

Reconstructions were computed with only H_1 radiating for several attenuation settings of A_1 in Figure 2-1 with a constant power level radiated by the reference antenna R. The effect can be described as varying a_o/a_r in Equation 4. In optics, this procedure is called varying the beam-balance ratio. The reconstructions resembled those in Figure 2-7A except that the magnitude of the second order image, relative to that of the first order, depended on a_o/a_r. Figure 2-5 shows measured values of $|u_2/u_1|$. The form of the curve verifies the analysis. We estimate $|\gamma| = 0.85$.

The spectra are plotted with amplitude as ordinate and frequency as abscissa. They are one-dimensional spectra, not the two-dimensional images we would expect for the small, localized antennas shown in Figure 2-2. Clearly we cannot expect information about the height of the transmitting antennas when the receiving antenna has negligible vertical extent. In order to obtain data about height we use two antennas, as described in the following subsection.

2.4 EXPERIMENTAL RESULTS: TWO-DIMENSIONAL IMAGES

Figure 2-9 shows a pair of receiving antennas separated by a vertical distance and translated horizontally to scan the microwave fringe pattern. The two antennas are connected by a hybrid junction. The hybrid junction performs an arithmetic operation, summation of the complex-valued fields received by each antenna. Note that the summation precedes detection. Consequently the approximately square-law detection generates products of the summed fields. These products can increase the level of higher order images. However, experimental data for a single radiating, object antenna (H_2) show the level of the second order to be 0.1 that of the first order. Recall that for one receiving antenna the relative magnitude was between 0.02 and 0.04. When these values are squared, the intensity is rather low. If further reduction is needed, for complicated objects, then γ could be reduced to obtain some further reduction. It is reasonable to expect the second-order images to be a limiting factor for some objects.

To obtain an image that has height information, we introduce phase shifts into the paths between the receiving antennas and the hybrid junctions. In computing Fourier transforms from hologram data we have

$$u' = \iint u_H \, e^{ik(y \sin \theta \sin \text{of} + z \cos \theta)} dydz$$

for the reconstructed field, where θ and φ are spherical polar co-ordinate angles. (See Figure 2-3; z is orthogonal to the page.)

In the spectrum analysis procedure, data are obtained continuously in y but for two narrow bands about $\pm z^A$, where $\pm z^A$ are the positions of the receiving antennas. In order to compute images in the direction θ, we can introduce (equal and opposite) phase shifts, but of course must change the magnitude of the shift for each value of θ. Now θ is approximately 90°. Let us use instead of θ, the elevation angle $\beta = 90° - \theta$. Consequently, β is small and in the phase term $k (y \cos\beta \sin\phi + z \sin\beta)$, we have approximately $k (y \sin\varphi + z \sin\beta)$. Thus we ignore the effect of elevation on the y transformation that is done by the spectrum analyzer. However, we introduce phase shifts in the amount $\pm kz^A \sin\beta$.

The phase shift corresponding to the elevation angle β was inserted by changing the vertical position of the center of the array. The proper magnitude can be intuitively derived. For an antenna spaced by distance s/2 from the xy plane and then elevated by distance $\bar{z}$ the phase change is $k (s/2) \bar{z}/x$. This value follows because (s/2x) is approximately the angle from the receiving antenna to the object. The result follows more formally by analyzing the computed reconstruction. It can be shown that the spectrum is, for the first order,

$$u_1' = 4\gamma T D^{-1} (2a) \cos^2 (ks\bar{z}/2x) \operatorname{sinc} \Omega$$

where D is $[A + B \cos(\alpha_1 - \alpha_2) + 2 \cos(\beta_1 - \beta_2)]^{\gamma}$, and where A, B, α_1, α_2, β_1 and β_2 depend on the amplitudes and phases of the object wave and reference wave. Ω is $ky_r 2W/Tx$. Clearly the factor $\cos^2 (ks\bar{z}/2x)$ is the power pattern of the vertical pair of antennas.

Figure 2-10 shows spectra for four heights of the receiving array. Notice that the amplitude falls off as $\bar{z}$, the height of the center of the array is increased. Figure 2-11 shows the angular regions through which the amplitude of the spectra in Figure 2-10 exceeded 0.7 times the highest spectrum amplitude.

The factor $\cos^2 (k\Delta\bar{z}/ax)$ may appear surprising. Should the spectrum amplitude vary as the first power of the consine? To answer this question measurements of spectral amplitude were made as a function of the vertical displacement of the array. Figure 2-12 shows the data for 7.5 cm separation of the antennas; i.e., s/2 = 3.75 cm. The measured points follow the cosine squared curved better than the cosine. The measurements were repeated for s/2 = 7.5 cm; agreement with the cosine squared curve was even better. That the discrepancies depend on s/2 suggests that our expression is approximate. In addition to the approximations used in the quadratic expansions for distances and by non-linearities, the phase change introduced by height is approximate antenna interraction. Phase shifters could, of course, be used.

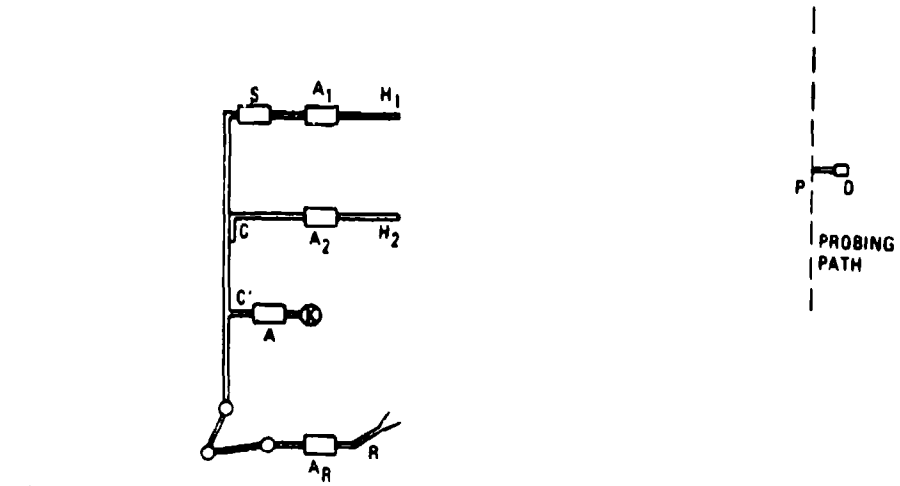

Figure 2-1. Microwave Apparatus for Fourier Transform. The dashed line shows a probing path for the receiving antenna P; D is a crystal detector. S is a phase shifter; A_1 and A_2 are attenuators for antennas H_1 and H_2. R is a reference beam antenna, and C and C' are directional couplers.

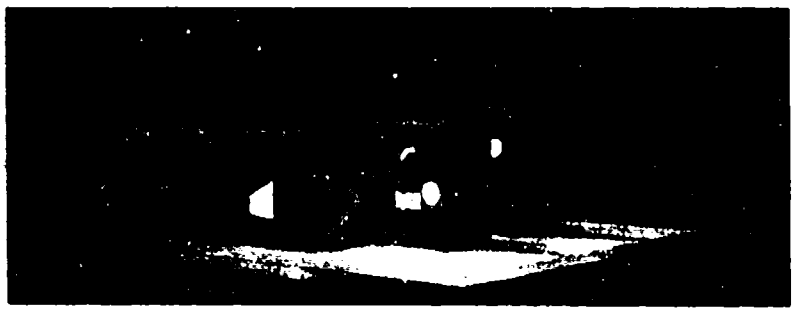

(A) TRANSMITTING ANTENNAS

(B) OVERALL VIEW

MJ002

Figure 2-2. Photographs of Microwave Apparatus for Fourier Transform.

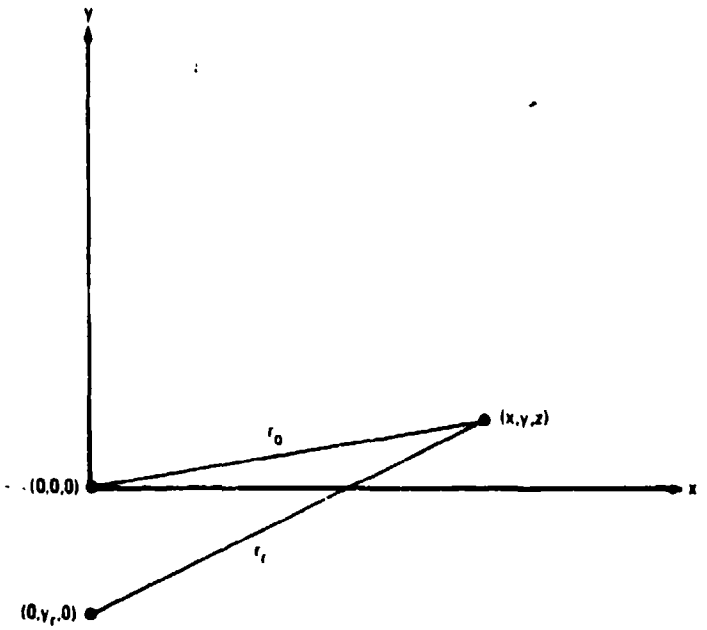

MJ003

Figure 2-3. Geometry of Coordinate System

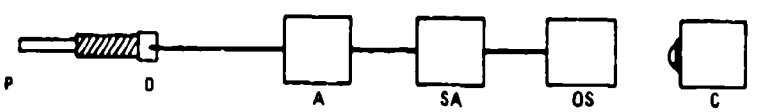

Figure 2-4. Detection and Transform Apparatus. P is a receiving antenna; D a crystal detector. A is a Hewlett Packard 415E Amplifier and SA is a Spectral Dynamics Corp., Real Time Spectrum Analyzer. OS is an oscilloscope and C a camera.

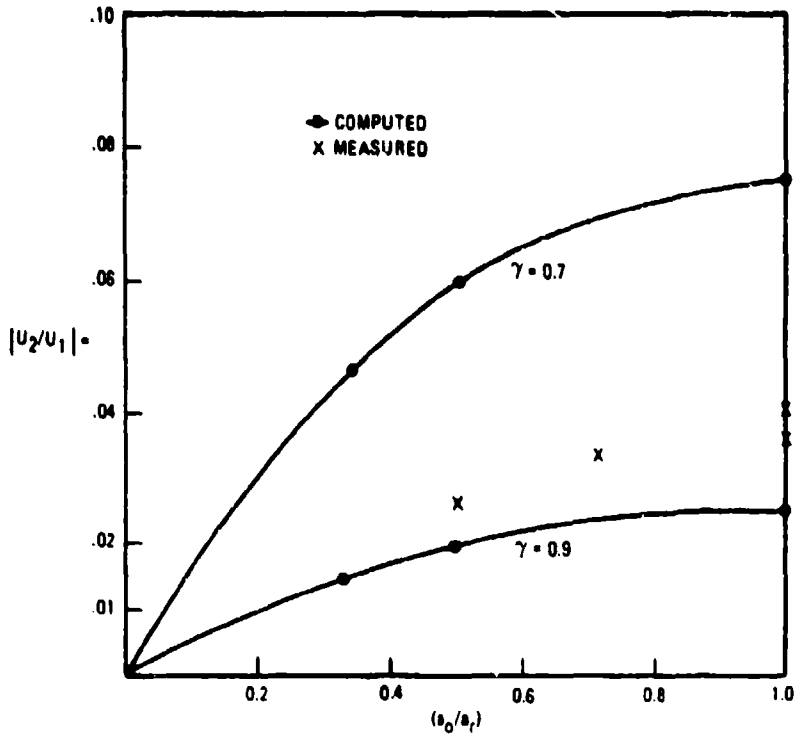

Figure 2-5. Relative Magnitudes of 2nd and 1st Order Images for a Point Object, a Point Reference source, and a Single Detector.

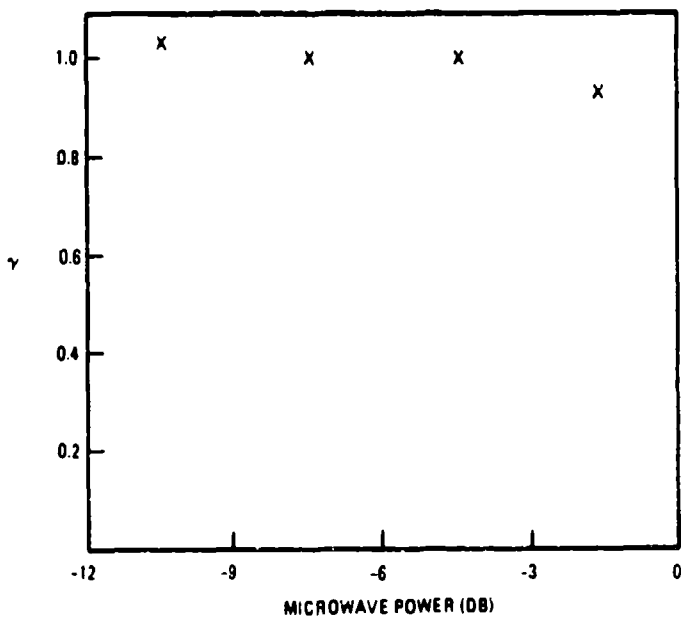

Figure 2-6. Values of γ Determined Experimentally. Power radiated by H_1 was reduced in 3-dB steps with H_2 full attenuated. Each value of γ is plotted at the mean power level, between the two values used to determine γ.

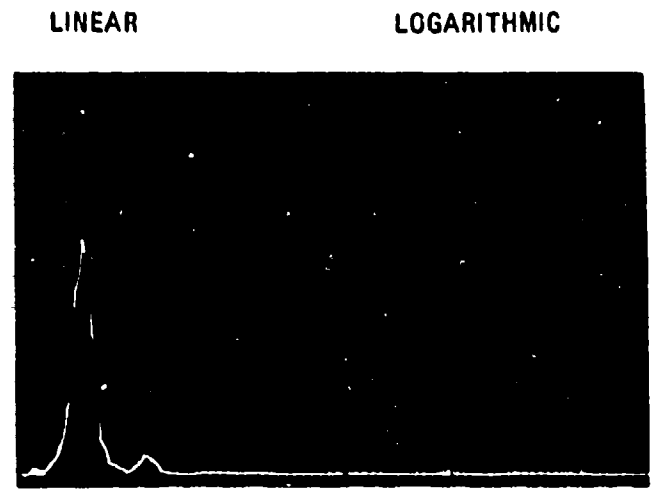

MJ007

Figure 2-7. Reconstruction Computed by Spectrum Analyzer. Only one antenna radiated for each reconstruction. Both H_1 and H_2 (Figure 2-1) were present with their centers separated by 6.3 cm.

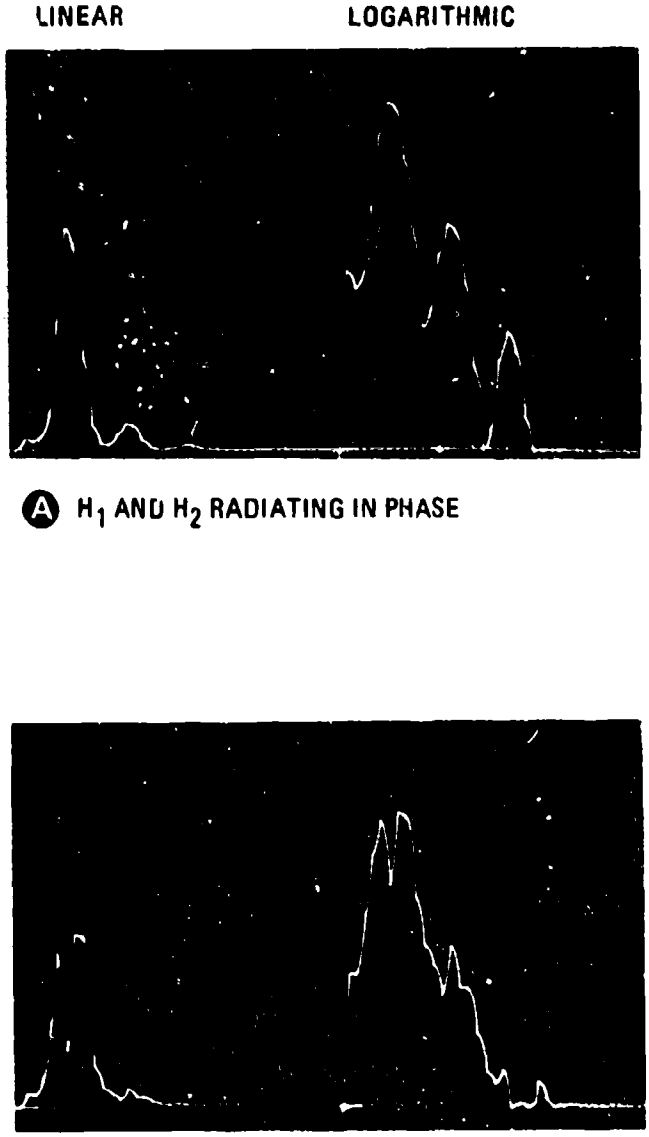

Figure 2-8. Reconstruction Computed for both Antennas Radiating

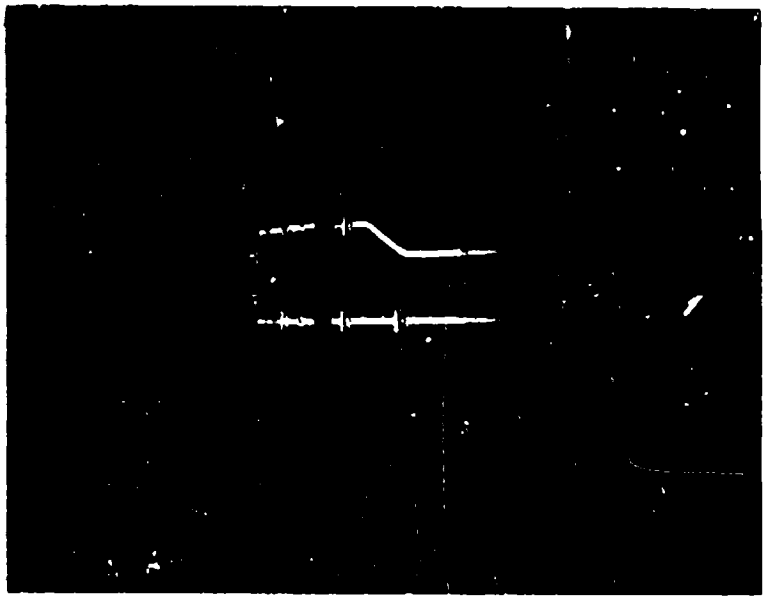

MJ008

Figure 2-9. Receiving Array Vertically Spaced and Translated Horizontally.

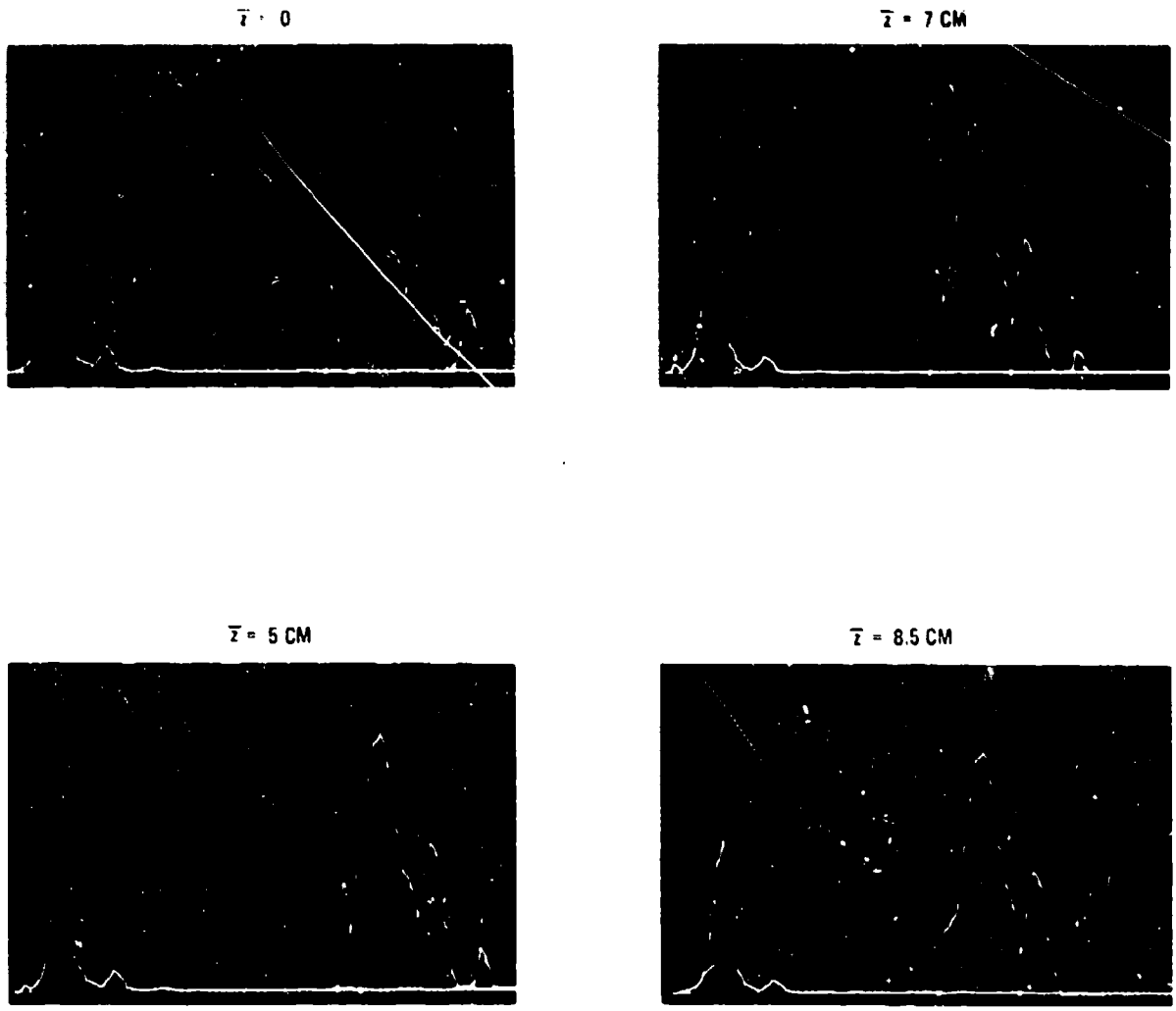

Figure 2-10. Reconstruction with two Receiving Antennas Separated by 7.5 cm. Four vertical positions of the receiving array shown; object was single radiating antenna.

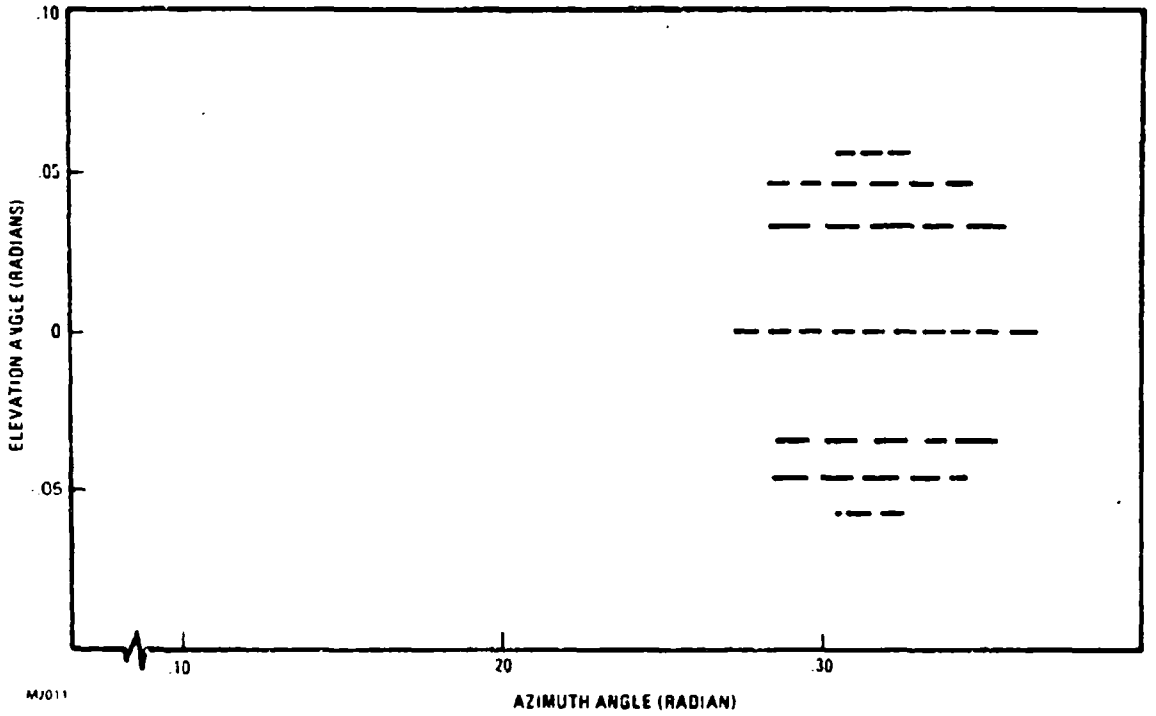

Figure 2-11. Reconstructed Image of one Antenna. The dashed lines shown regions in which the spectra of Figure 2-10 exceeded a value 0.7 times their highest value.

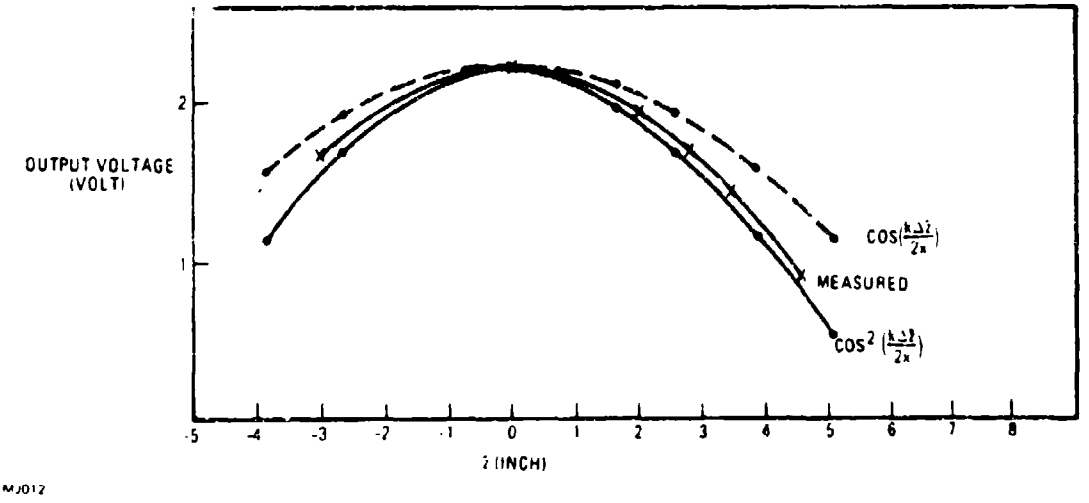

Figure 2-12. Measured and Computed Voltage at Spectrum Maxima for Several Elevation Positions of the Two-Antenna Receiving Array.

REFERENCES

1. G. L. Rogers, Nature, 177, 613 (1956).
2. R. P. Dooley, Proc. IEEE 53, 1733 (1965).
3. G. Tricoles and E. L. Rope, J. Opt. Soc. Am. 56 (542A) 1966; 57, 97 (1967).
4. Y. Aoki, Proc. IEEE 56, 1402 (1968).
5. G. Tricoles and E. L. Rope, Digest IEEE/G-MTT Symposium, 1970 (IEE Cat. No. 70c 10-MTT, p. 124.
6. N. H. Farhat and W. R. Guard, Proc. IEEE 59, 1303 (1971).
7. G. Tricoles and E. L. Rope, J. Opt. Soc Am. 61, 1571 (1971).
8. G. Papi, V. Russo, and S. Sottini, IEEE Trans. AP-19, 740 (1971).
9. W. E. Kock, Microwaves, p. 46, Nov., 1968.
10. G. Tricoles and E. L. Rope, Digest IEEE/G-AP Symposium, 1971 (IEE Cat. No. 71 c 39 ap) p. 160.
11. C. F. Augustine, Electronics, June 24, 1968, p. 118.
12. K. Iizuka has investigated specially processed Polaroid film. A description of recent applications to plasma diagnostics is given in Electronics, Dec. 1971, p. 10.
13. See References 8 and 10.
14. Y. Aoki, J. Ac. Soc. Am.
15. M. M. Sondhi, J. Ac. Soc. Am., 46, 1158 (1969).
16. G. Tricoles and E. L. Rope, Digest IEEE/G-AP Symposium, Oct. 1967, p. 194, IEEE Cat. No. 3C52.
17. W. A. Imbriale and R. Mitha, IEEE Trans. AP-18, 633 (1970).
18. E. L. Rope and G. Tricoles, Digest IEEE/G-AP Symposium. Dec. 1960.
19. P. F. Checcacci, V. Russo, A. M. Scheggi, Alta Frequenza, XXXVIII, 378 (1969).
20. A. Lohmann and O. Bryngdahl, J. Opt. Soc. Am.

ACKNOWLEDGEMENT

The work described in this report was supported by the U.S. Navy Air Systems Command under Contract N00019-71-C-0065.

17. ANALYSIS OF ANTENNAS ON AIRCRAFT

by

Walter D. Burnside, Chong Long Yu,
and Ronald J. Marhefka

The Ohio State University ElectroScience Laboratory
Department of Electrical Engineering
Columbus, Ohio 43212
20 December 1971

for

ARRAY ANTENNA CONFERENCE

Naval Electronics Laboratory Center
San Diego, California

22, 23, 24 February 1972

The strength of these analyses lies in their representation in terms of the propagation of rays, as each individual contribution to the E-M field can be easily identified. In a practical sense this is useful because the negligible contributions can be easily neglected. This results in a simplified picture of the physical processes and reduces the computational effort required to obtain a solution.

Another useful property of these analyses is that they provide for the incorporation of existing solutions. For example, if the basic properties of an antenna in terms of a classical modal solution[16] are known, this solution can be cast in the ray-optics form and used in a diffraction analysis. Thus the solution to a complicated problem can be "built-up" from known solutions to the individual parts of the complicated problem using the ray optics representation. In this way the various interactions between the component parts can be analyzed separately and then put into a complete solution in the final step. Also the effects of any given scatterer upon the radiation pattern can be identified. Such identification could lead to the development of corrective measures.

Using the techniques described above, the radiation patterns in the three principal planes have been determined for various aircraft models. Basically the type of aircraft model analyzed is illustrated in Fig. 6, with the source mounted on the fuselage in the plane of symmetry which includes the vertical stablizer. Due to the nature of ray optics solutions, one is limited to models that are large in terms of the wavelength. On the other hand, these ray optics solutions allow arbitrary locations of the various aircraft parts provided these parts do not become too close together. In addition, our solutions are based on delta function sources for each of the three mutually orthogonal polarization vectors. Thus, a complex antenna system mounted on a complicated aircraft structure can be analyzed using our computer modeling solutions. This gives our solutions a very wide range of coverage in terms of aircraft models, aircraft structure locations and bulk, frequencies, and antennas.

THEORETICAL APPROACH

The wedge diffraction technique is based on the canonical problem of the diffraction by a conducting wedge[17,18] as depicted in Fig. 7. This technique was developed as an extension of the Geometrical Theory of Diffraction;[2] cylindrical wave diffraction and superposition approaches were specifically introduced to permit successful application of the geometrical diffraction approach to antenna problems.[3] The applicability of this technique is illustrated in Fig. 8 which shows the radiation pattern of a slot antenna as influenced by a finite ground plane structure. An application involving a simulated aircraft wing cross section is shown in Fig. 9.

The creeping wave technique is based on the canonical problem of the diffraction by a cylindrical surface,[19-21] as shown in Fig. 10. An example of the accuracy of this technique is illustrated in Fig. 11.

A problem where both wedge diffraction and curved surface diffraction are utilized is shown in Fig. 12. This figure compares calculated and measured patterns for a horn antenna mounted on the leading edge of an F-14 wing section.[22]

Our solutions are based on the aircraft model illustrated in Fig. 6, in which the aircraft is modeled by cylinders, cones, spheres, and flat plates. The location of the source has been limited to the surface of the fuselage in the plane of symmetry which contains the vertical stabliizer. With these constraints to our solutions, it was found that the existing modal solutions[23] for the three mutually orthogonal delta sources mounted on an infinite cylinder was the most practical solution in the roll and azimuth planes. For the elevation-plane, it was found that the shape of the fuselage had a great effect on the radiation patterns and, thus, had to be handled differently. In fact a new approach has been developed in which the fuselage cross-section is described by a set of points to give a very good model representation.

The various components of the aircraft structure act as near field scatterers. These near field scattering problems require new techniques in that previous scattering solutions were mainly based on far-field constraints. In any event, the overall aircraft solution is handled nicely under our ray optics format in that each of the scattering mechanisms can be isolated and analyzed individually. For example, the isolated finite cylinder (engine) scattering is solved using the modal solution, wedge diffraction theory, and physical optics. This solution in turn is then applied to our aircraft model simply by adjusting the incident field appropriately. Similarly, scattering from the wing is first introduced in terms of an isolated finite plate using three dimensional wedge diffraction techniques and then adapted to our aircraft model. Consequently, the solutions for the radiation patterns in the three principal planes with an arbitrary source mounted on a complex aircraft model are solved by breaking up the model into its component parts which are examined and analyzed separately. These isolated scattering mechanisms are, then, adapted to our complete aircraft model, which makes the solutions extremely versatile in terms of the location and the bulk, or size, of these structural components. In addition, since the several components of the total pattern are developed, one can examine various alternatives to enhance the desired radiation pattern. This can be accomplished analytically in terms of the source frequency, antenna type, antenna location, and the aircraft structure. It should also be possible to analyze the pattern effects of appropriately placed and designed absorbers.

RESULTS

The overall problem has been divided into three parts, these being each of the three principal planes. In each case models have been analyzed which give a realistic and workable solution to the problem.

In most cases the "Geometrical Theory of Diffraction" was applied because it is the most practical approach. However, modal solutions as well as physical optics techniques have been used in some instances to expedite the analysis.

Solution for the pattern in the roll plane (or x-y plane in Fig. 6) was initiated using a simple two-dimensional model as illustrated in Fig. 13a. This model was chosen so that available techniques could be directly applied before attempting to solve the much more difficult three dimensional problem. The modal solutions[23] were used for the three mutually orthogonal delta sources mounted on a cylinder (fuselage). This gave us a so-called pseudo - Green's function solution in that an arbitrary antenna system could be handled by numerically integrating our solution over the antenna aperture. Image theory was applied to our model to account for the wing, and wedge diffraction handled the wing tip. As illustrated in Fig. 14, our solution compares very favorably with measured results taken on our two-dimensional aircraft model.

The effect of the engines was added to our model by two cylinders as shown in Fig. 13b. To include this effect in our analysis, the two-dimensional near-field modal solution was adapted to our previous solution. It is again seen in Fig. 15 that very good agreement was obtained between our measured and calculated results. One should also note that the experimental results are approaching the limit of validity of our solution and yet the agreement is quite good. Note that our solution is valid provided the dimensions are large in terms of the wavelength.

In order to include the three-dimensional wing effect in our solution, the near-field scattering from an arbitrary finite rectangular plate was studied. Using this solution the plate (or isolated wing) is specified by its four corners and the source by its far-field pattern and location. The total scattered field is then given for any direction in space. This solution was then adapted to our aircraft model by introducing the additional source variation due to the creeping waves on the surface of the fuselage. A calculated roll plane pattern using this complete roll-plane model is illustrated in Fig. 16.

In addition to frequency domain pattern plots, pulse waveforms have been examined for the three basic elements mounted on our roll plane model of Fig. 13. This provides one with an excellent means of observing the effects of the various scattering mechanisms over a very wide range of frquencies as illustrated in Fig. 17. Using this solution, one can investigate the time response for an arbitrary pulse provided that the lower frequency limit is not greatly exceeded.

The major effect on the radiation pattern in the azimuth plane (the y-z plane in Fig. 6) is due to the fuselage, which is simply modeled by a cylinder. Again, the modal solutions for the radiation patterns of the three basic sources mounted on an infinite cylinder is known. Applying these solutions, the resulting azimuth patterns are illustrated in Fig. 18. Secondary contributors to this pattern

are the engines, which, for our initial study, are modeled by finite cylinders. An approximate solution for the far-zone scattering from a finite cylinder is not difficult using GTD and physical optics. The accuracy of this solution is depicted in Fig. 19.

In order to analytically apply the finite cylinder to our model, the near zone scattering had to be determined. The main difficulty with this problem was analytically handling the scattering from the long cylindrical portion, neglecting the edges and end caps. After examining various alternatives, the two-dimensional near-field solution was cast into our ray optics form and applied to our soulution. An example of this solution after it was adapted to our aircraft model is illustrated in Fig. 18, where it is found to compare favorably with measurements.

The elevation plane (x-z plane in Fig. 6) was initially studied using a basic model composed of cylinders, spheres, and cones. The solutions for these problems were, again, based on the two-dimensional analysis which, as shown by Ryan,[15] is valid for the three-dimensional elevation plane solutions. Some of the results of this study are illustrated in Fig. 20. Even though this solution is valid for our simple model, this model really is not general enough to include the wide variety of aircraft fuselages encountered in practice. Consequently, a new approach was developed in which the fuselage is described by a set of points. In this way any convex fuselage shape can be included in our computations. In addition, more general fuselage models were developed using a more rigorous "GTD" solution, the most general being a composite (back-to-back) ellipse. Some of the results of this study are illustrated in Fig. 21. In any event, combining these various techniques, one should be able to cover a very wide variety of fuselage configurations.

In summary, for each of the three principle plane radiation patterns studied, a model was chosen which could not only be analyzed but was representative of a wide variety of modern aircraft structures. These solutions also allow, within limits, for arbitrary locations and size of the various structural components (wing size and location, engine size and location, etc.). In addition, the three mutually orthogonal delta sources were considered which allows for an arbitrary antenna system to be analyzed provided it is mounted on the fuselage in (or near) the plane of symmetry which includes the vertical stabilizer. Finally, wherever possible, our solutions were verified by measured results.

REFERENCES

1. Baender, R. and Jue, J., "A Computer Program for Calculating the On-Aircraft Characteristics of Antennas," Sylvania Electronic Systems Western Division SESW-G896 prepared for the Naval Air Development Center under Contract N62269-69-C-0386.

2. Keller, J.B., "Geometrical Theory of Diffraction," Journal of the Optical Society of America, 52, (February 1962), pp. 116-130.

3. Rudduck, R.C., "Application of Wedge Diffraction to Antenna Theory," Report 1691-13, 30 June 1965, ElectroScience Laboratory, Department of Electrical Engineering, The Ohio State University; prepared under Grant No. NsG-448 for National Aeronautics and Space Administration, Washington, D.C. Also published as NASA Report CR-372.

4. Yu, J.S., Rudduck, R.C., and Peters, L., Jr., "Comprehensive Analysis for E-plane of Horn Antennas for Edge Diffraction Theory," IEEE Trans. Antennas and Propagation, Vol. AP-14, (March 1966), pp. 138-149.

5. Yu, J.S. and Rudduck, R.C., "H-plane Pattern of a Pyramidal Horn," IEEE Trans. on Antennas and Propagation Comm., Vol. AP-17, No. 5, September 1969.

6. Ryan, C.E., Jr. and Rudduck, R.C., "Calculation of the Radiation Pattern of a General Parallel-Plate Waveguide Aperture for the TEM and TE_{01} Waveguide Modes," Report 1693-4, 10 September 1964, ElectroScience Laboratory, Department of Electrical Engineering, The Ohio State University; prepared under Contract N62269-2184 for U.S. Naval Air Development Center, Johnsville, Pennsylvania.

7. Ryan, C.E., Jr., and Rudduck, R.C., "A Wedge Diffraction Analysis of the Radiation Patterns of Parallel-Plate Waveguides," IEEE Trans. on Antennas and Propagation Comm., Vol. AP-16, No. 4, July 1968.

8. Wu, D.C.F., Rudduck, R.C., and Pelton, E.L., "Application of a Surface Integration Technique to Parallel-Plate Waveguide Radiation Pattern Analysis," IEEE Trans. Antennas and Propagation, Vol. AP-17, (May 1969), pp. 280-285.

9. Ryan, C.E., Jr. and Rudduck, R.C., "Radiation Patterns of Rectangular Waveguides," IEEE Trans. Antennas and Propagation Comm., Vol. AP-16, (July 1968), pp. 488-489.

10. Burnside, W.D. and Pelton, E.L., "Wedge Diffraction Theory Analysis of Parallel-Plate Waveguide Arrays," Report 2382-14, 25 September 1969, ElectroScience Laboratory, Department of Electrical Engineering, The Ohio State University; prepared under Contract F33615-67-C-1507 for Air Force Avionics Laboratory, Wright-Patterson Air Force Base, Ohio. (AD 860 082)

11. Burnside, W.D., Pelton, E.L., and Peters, L., Jr., "Analysis of Finite Parallel-Plate Waveguide Arrays," to be published as a Communication in IEEE Trans. Antennas and Propagation.

12. Balanis, C.A. and Peters, L., Jr., "Analysis of Aperture Radiation from an Axially Slotted Circular Conducting Cylinder using Geometrical Theory of Diffraction," IEEE T-AP-17, January 1969, pp. 93-97.

13. Balanis, C.A. and Peters, L., Jr., "Aperture Radiation from an Axially Slotted Elliptical Conducting Cylinder using Geometrical Theory of Diffraction," IEEE T-AP-17, July 1969, pp. 507-513.

14. Balanis, C.A. and Peters, L., Jr., "Radiation from TE_{10} Mode Slots on Circular and Elliptical Cylinders," IEEE T-AP-18, No. 3, May 1970, pp. 400-403.

15. Ryan, C.E., Jr., "Analysis of Radiation Patterns of Antennas on Finite Circular Cylinders and Conically-Capped Cylinders," Report 2805-2, ElectroScience Laboratory, Department of Electrical Engineering, The Ohio State University; prepared under Contract DAAA21-69-C-0535 for Picatinny Arsenal.

16. Harrington, R.F., Time Harmonic Electromagnetic Fields, McGraw Hill Book Co., New York, 1961.

17. Pauli, W., "On Asymptotic Series for Functions in the Theory of Diffraction of Light," Physical Review, 54, (1 December 1938).

18. Hutchins, David L. and Kouyoumjian, Robert G., "Asymptotic Series Describing the Diffraction of a Plane Wave by a Wedge," Report 2183-2, 15 December 1969, ElectroScience Laboratory, Department of Electrical Engineering, The Ohio State University; prepared under Contract AF19(628)-5929 for Air Force Cambridge Research Laboratories.

19. Keller, J.B. and Levy, B.R., "Decay Experiments and Diffraction Coefficients for Surface Waves on Surfaces of Non-Constant Curvature," Symposium on Electromagnetic Theory, Professional Group on Antennas and Propagation, IRE, December 1959, pp. 552-561.

20. Voltmer, D. and Kouyoumjian, R.G., "Higher Order Terms in the Diffraction by Curved Surfaces," paper to be published.

21. Kouyoumjian, R.G. and Burnside, W.D., "The Diffraction by a Cylinder-Tipped Half Plane," IEEE, AP-18, No. 3, May 1970, pp. 424-426.

22. "Low-Profile Scanned-Beam IFF Antenna System Development Study," Final Report 2836-4, 11 August 1970, ElectroScience Laboratory, Department of Electrical Engineering, The Ohio State University; prepared under Contract N62269-69-C-0533 for Naval Air Development Center.

23. Sinclair, G., "The Patterns of Antennas Located Near Cylinders of Elliptical Cross Section," Proc. IRE, Vol. 39, No. 6, June 1951.

24. Ross, R.A. and Price, E.L., "Radar Cross Section of Finite, Right-Circular Cylinders," Report ER/RIS-11, October 1966, Cornell Aeronautical Laboratory.

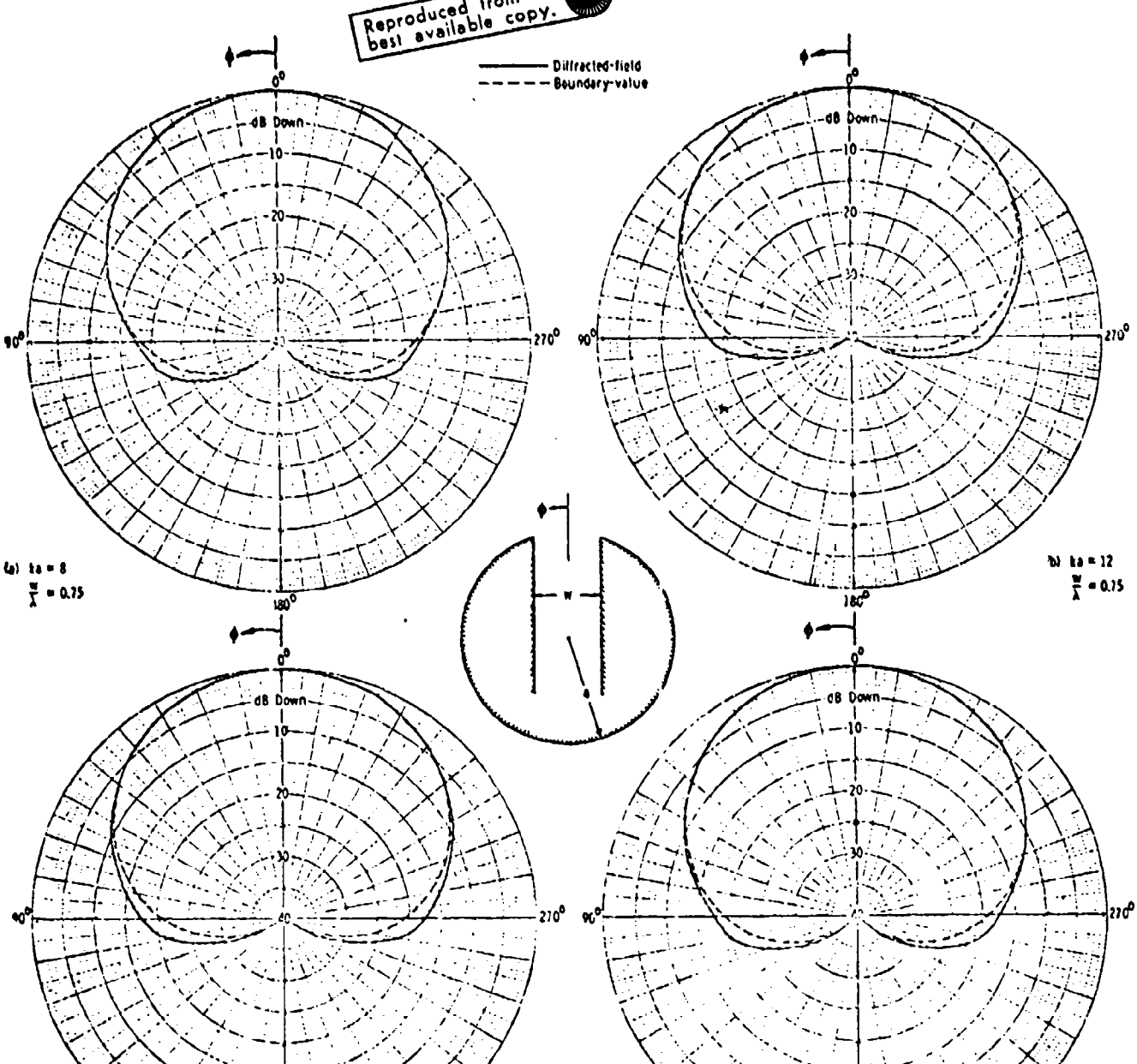

Fig. 1. Radiation patterns of a TE_{10} Mode slot on a circular conducting cylinder.

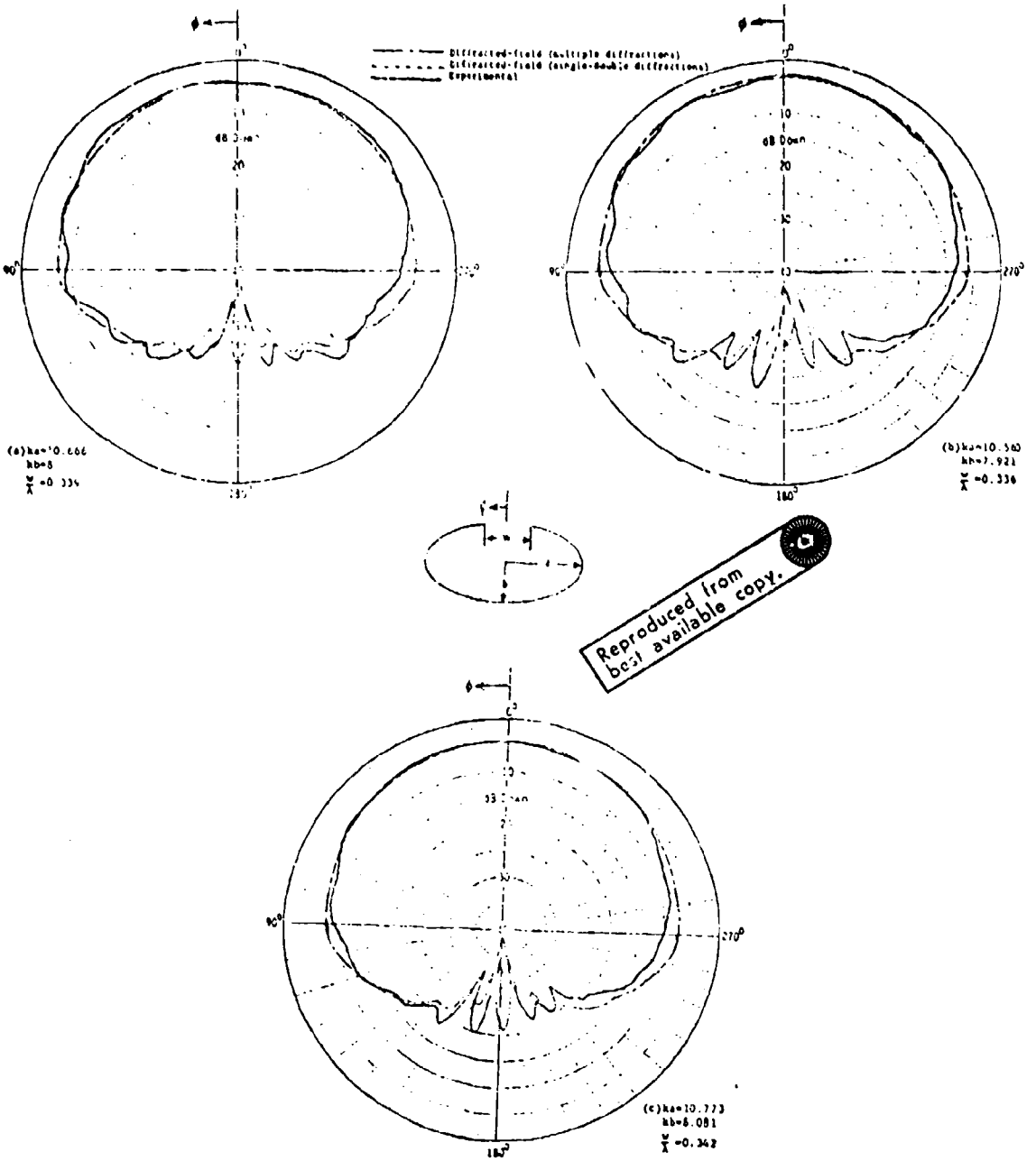

Fig. 2. Comparison of radiation patterns for smaller size elliptical cylinders (TEM Mode).

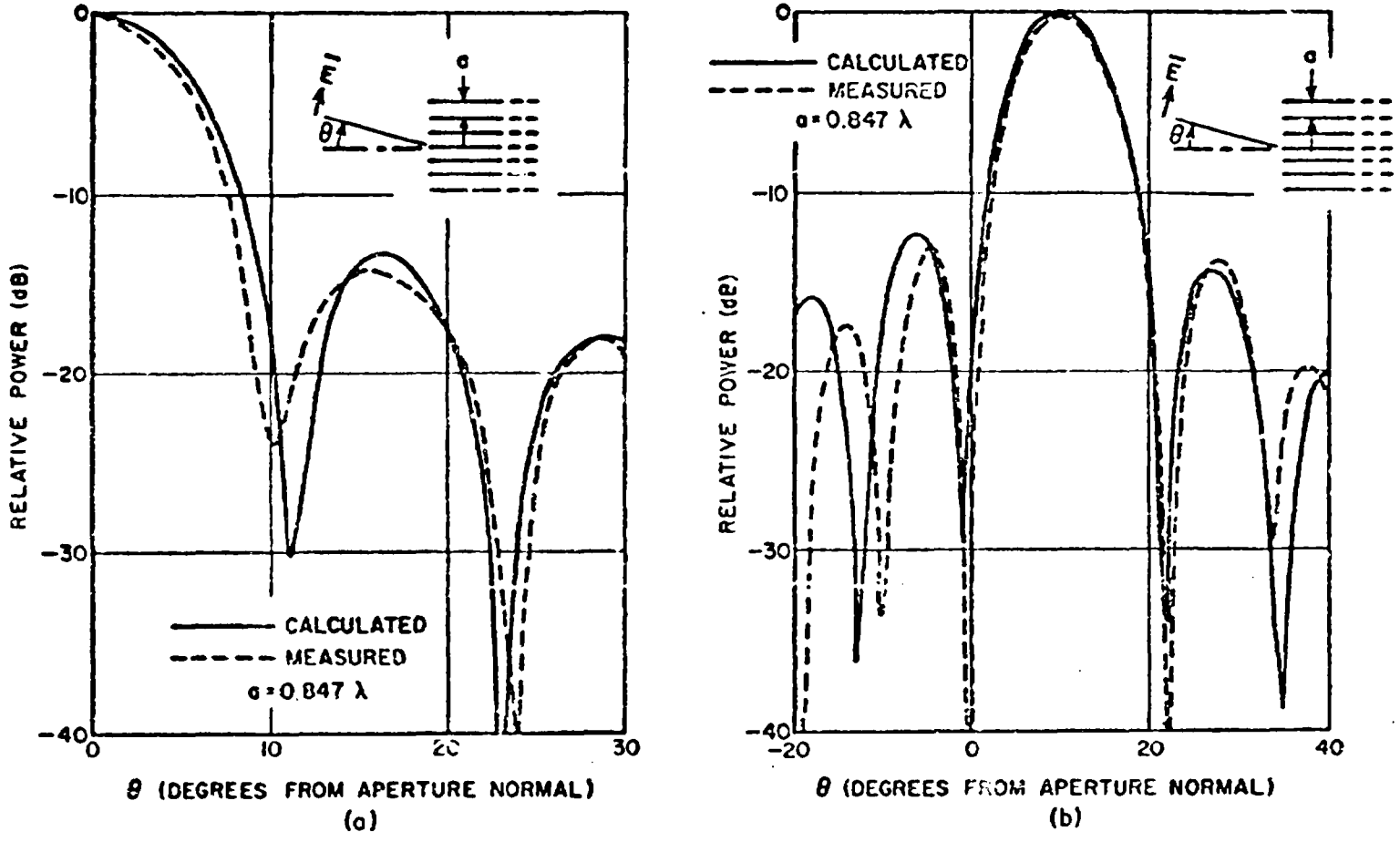

Fig. 3. The TEM radiation pattern of a six-element planar parallel-plate array for scan angles of 0° and 10°.

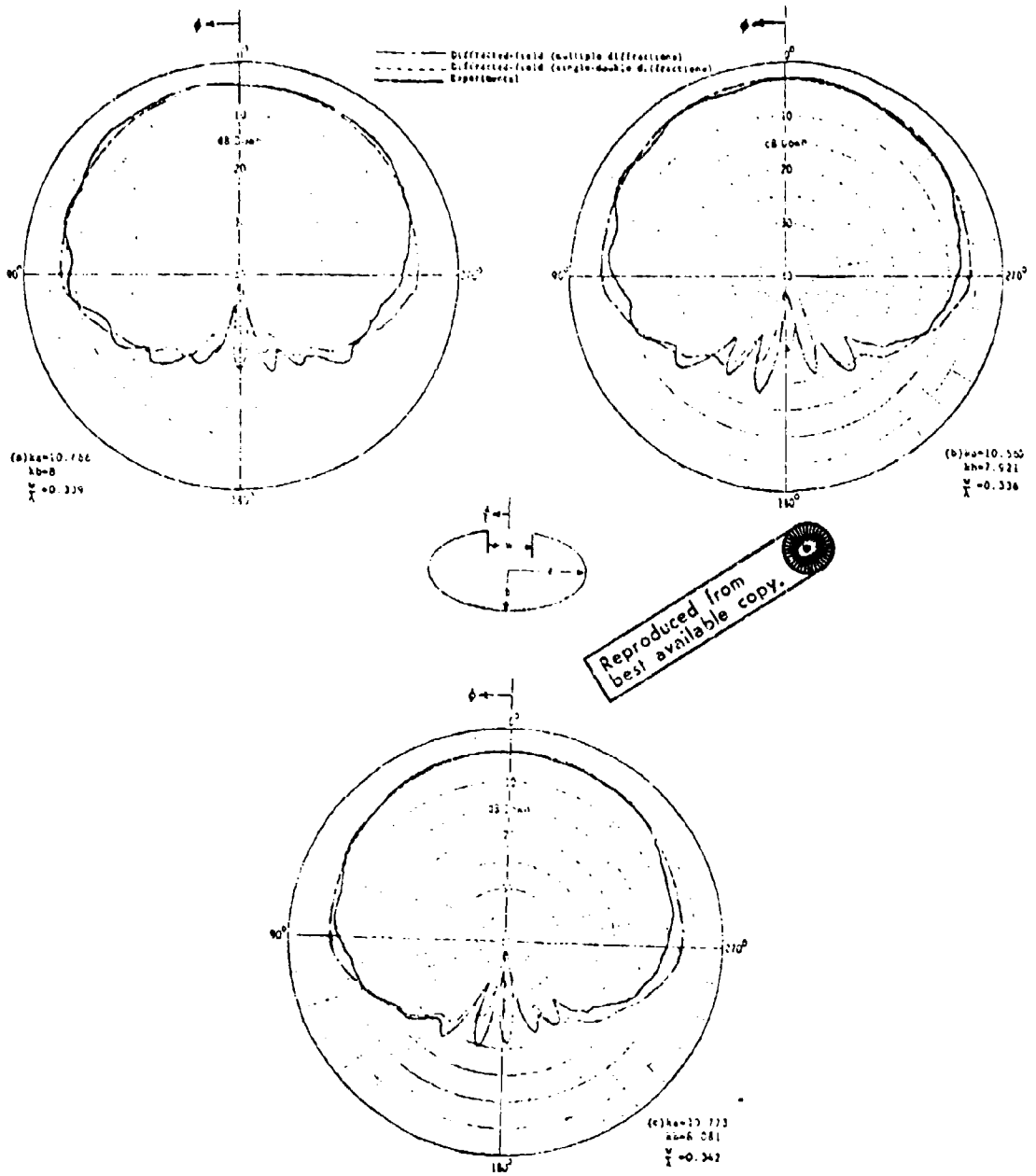

Fig. 2. Comparison of radiation patterns for smaller size elliptical cylinders (TEM Mode).

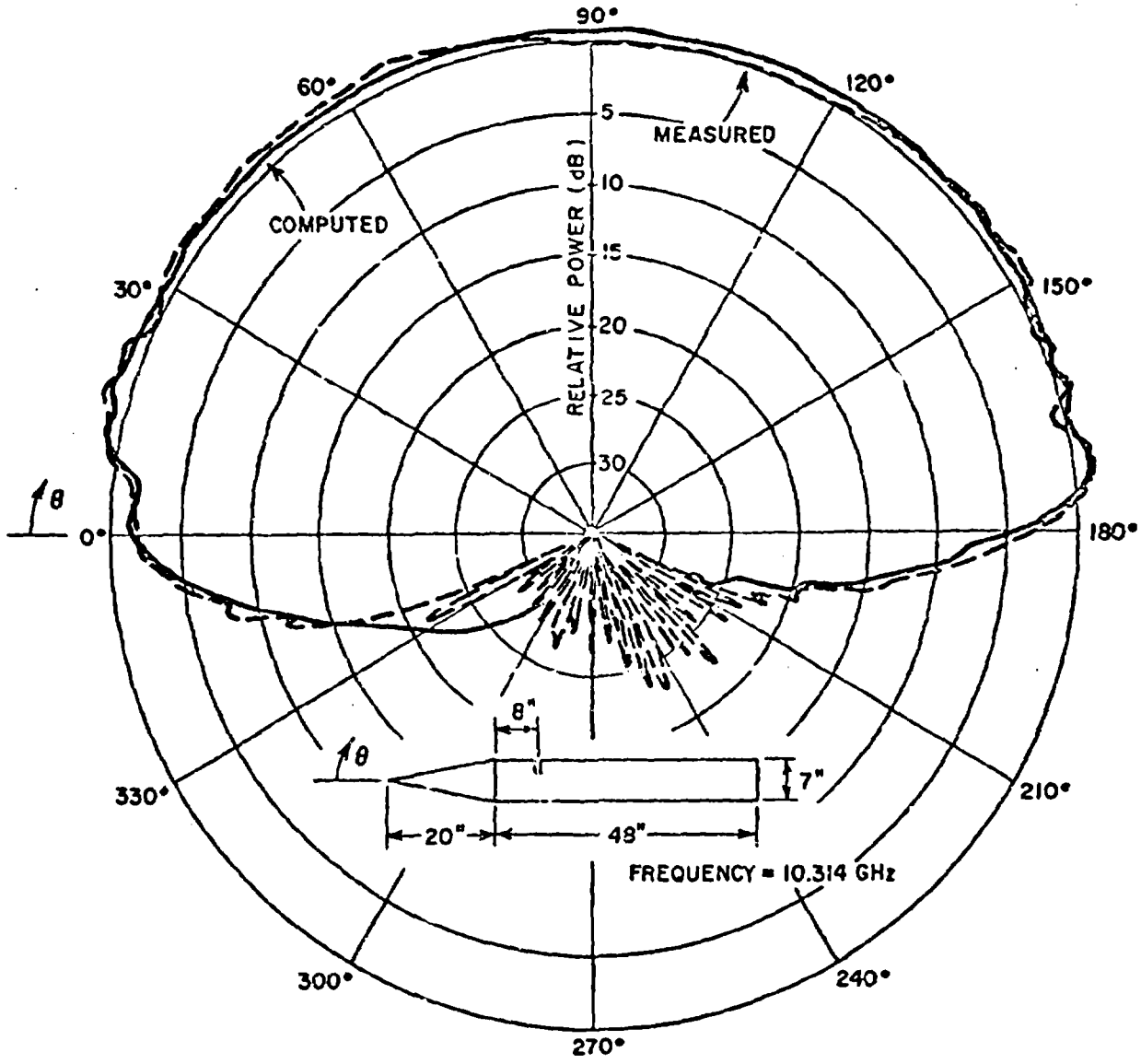

Fig. 4. Elevation pattern of a circumferential slot on a conically-capped cylinder.

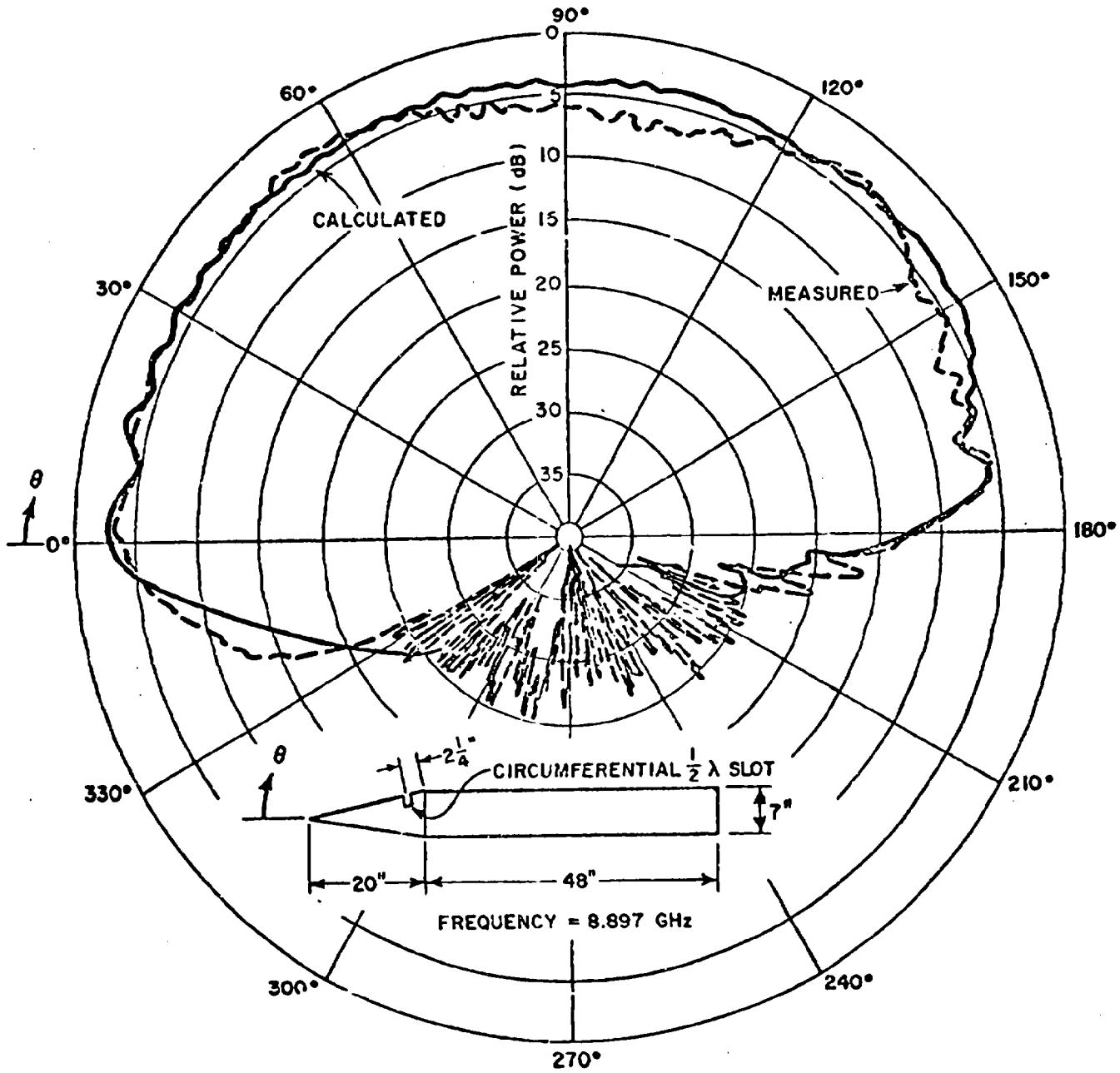
90°
0
60°
120°
10
CALCULATED
15
RELATIVE POWER (dB)
30°
20
MEASURED
150°
25
30
35
θ
0°
180°
θ
2¼"
CIRCUMFERENTIAL ½ λ SLOT
330°
210°
7"
20"
48"
FREQUENCY = 8.897 GHz
300°
240°
270°

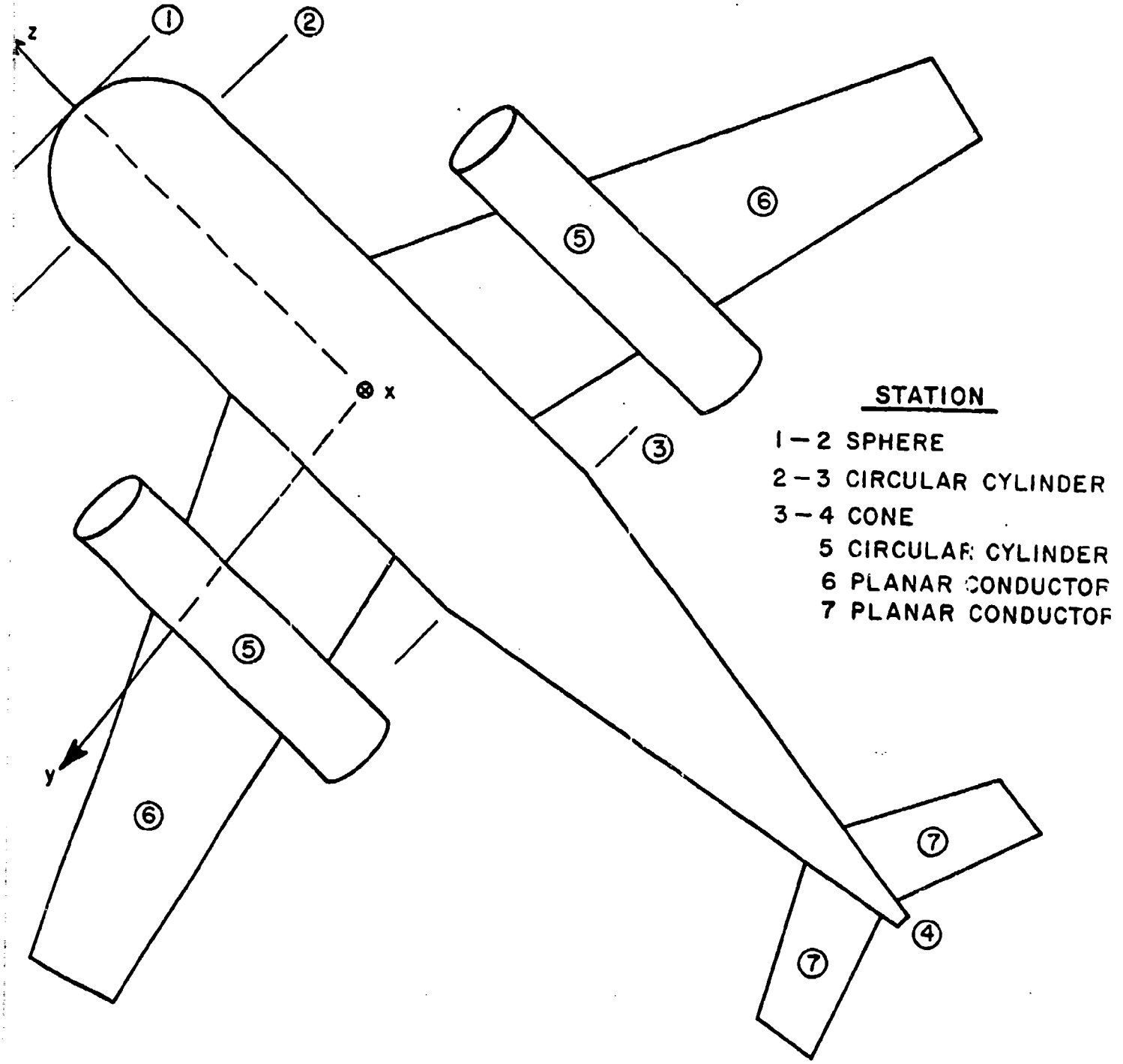

Fig. 6. Simplified aircraft model.

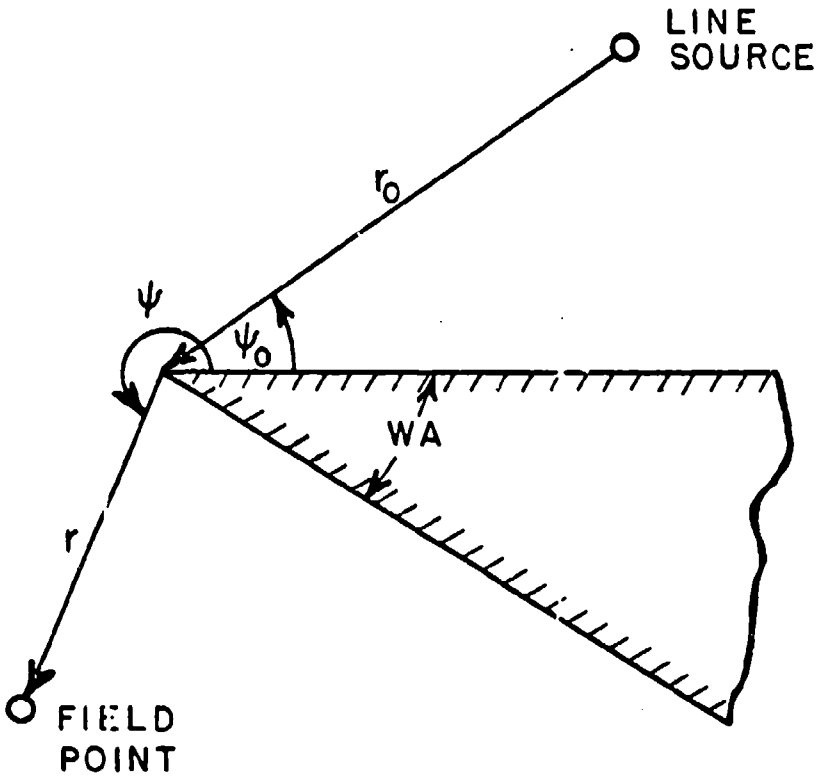

Fig. 7. Diffraction by a wedge.

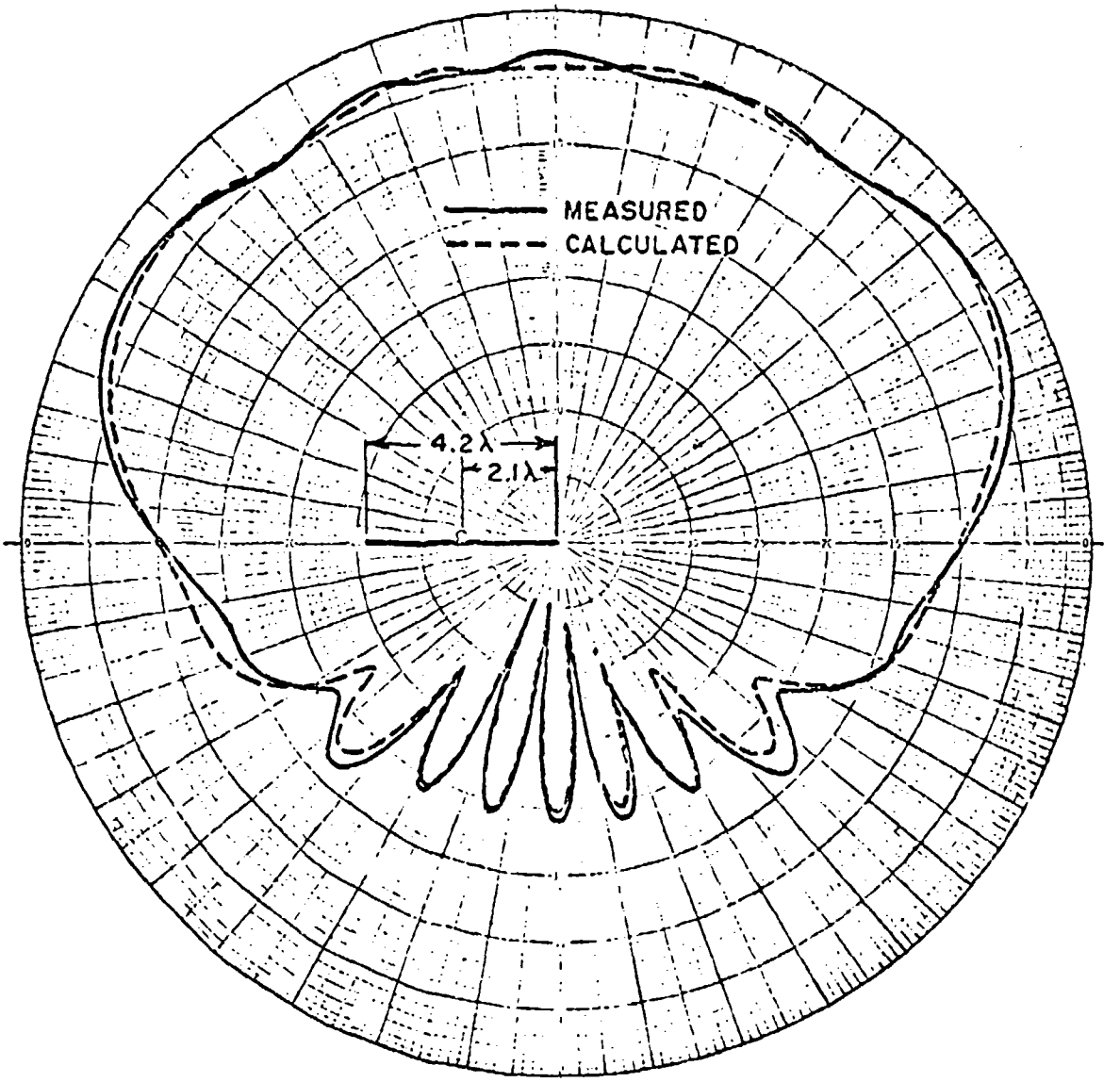

Fig. 8. Radiation pattern of a slot mounted on a finite ground plane.

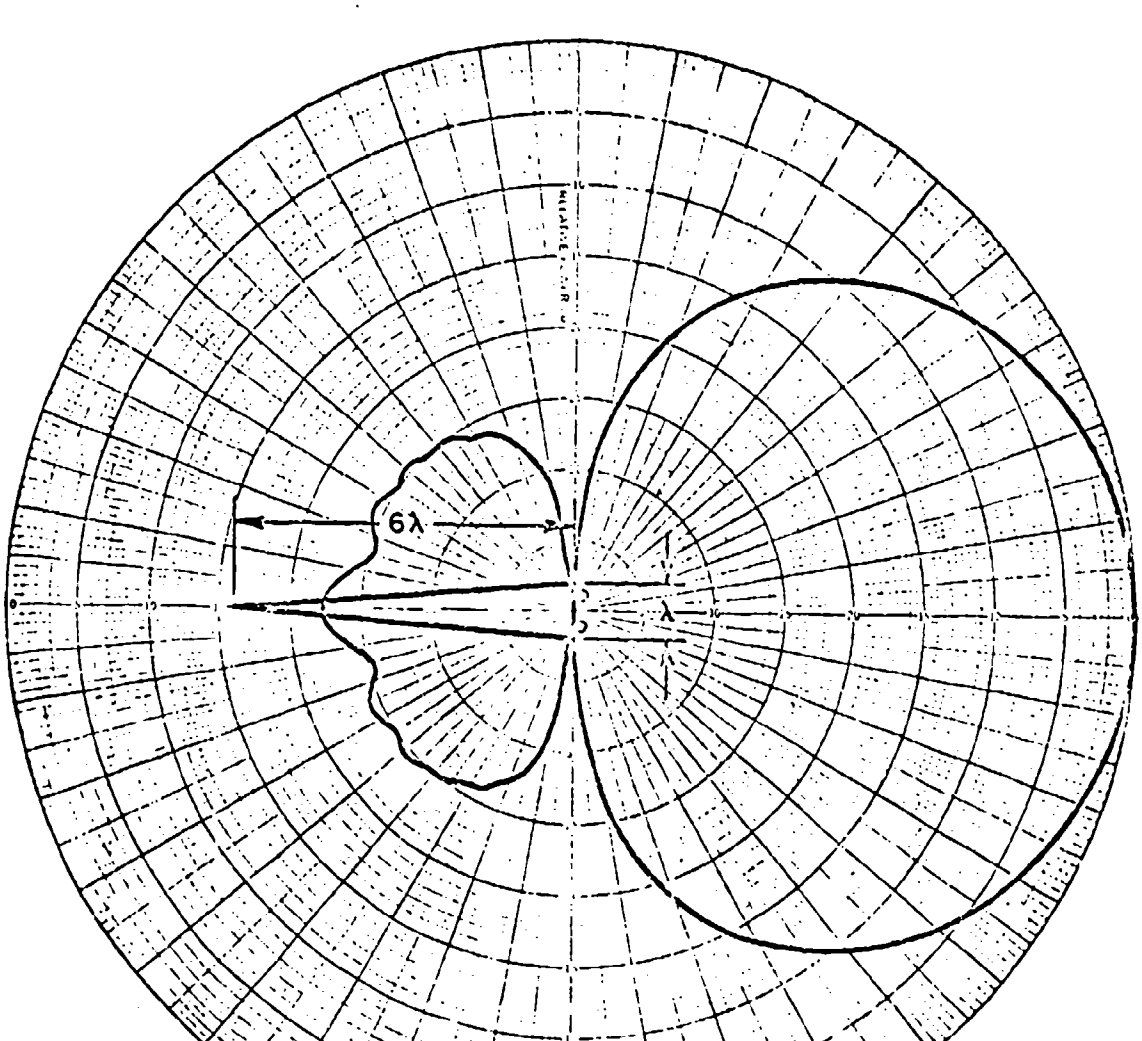

Fig. 9. Elevation pattern of a two element array mounted on the leading edge of a glove section model.

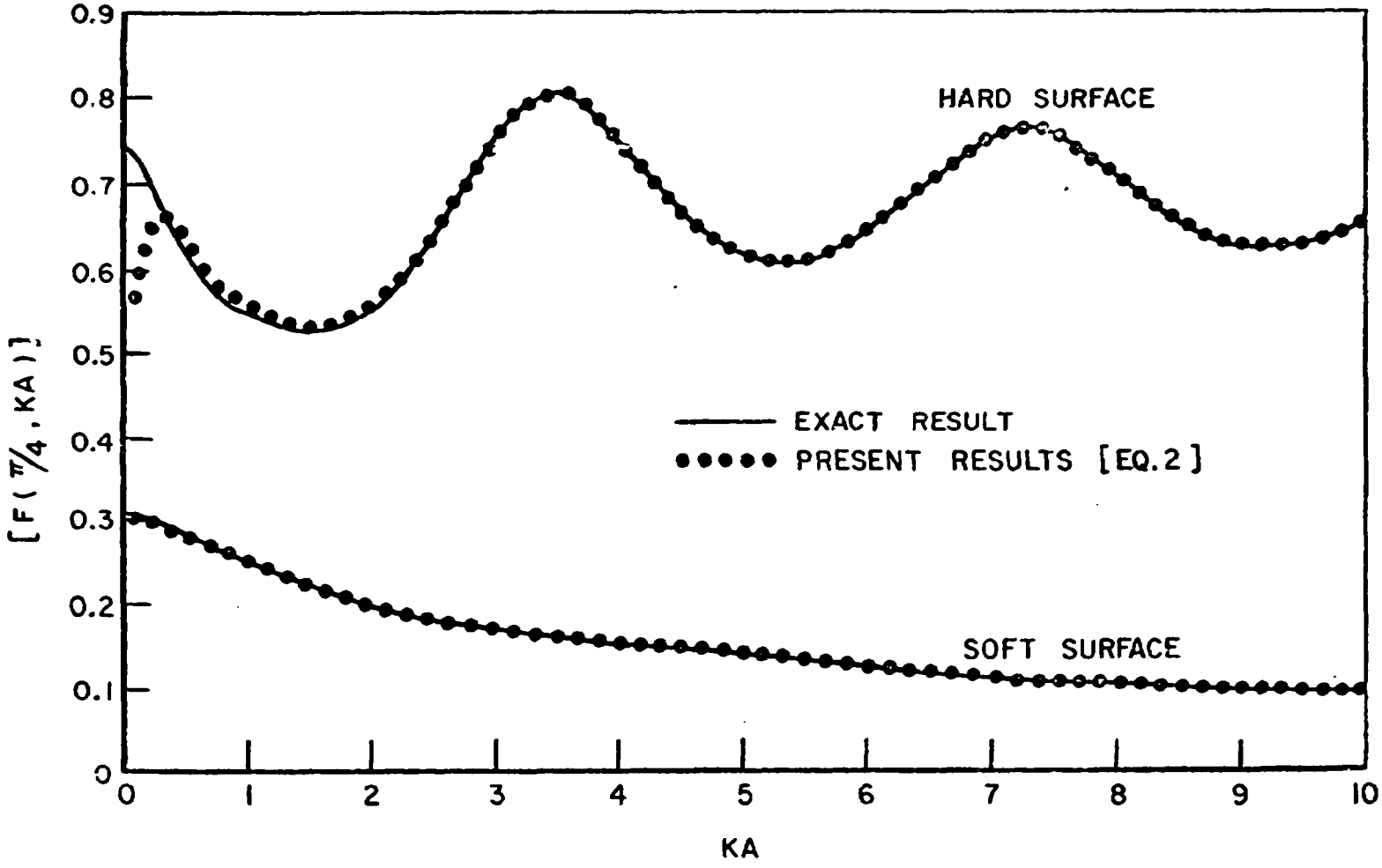

Fig. 11. Magnitude of the pattern function from a cylindrically-tipped half plane versus circumference (ka).

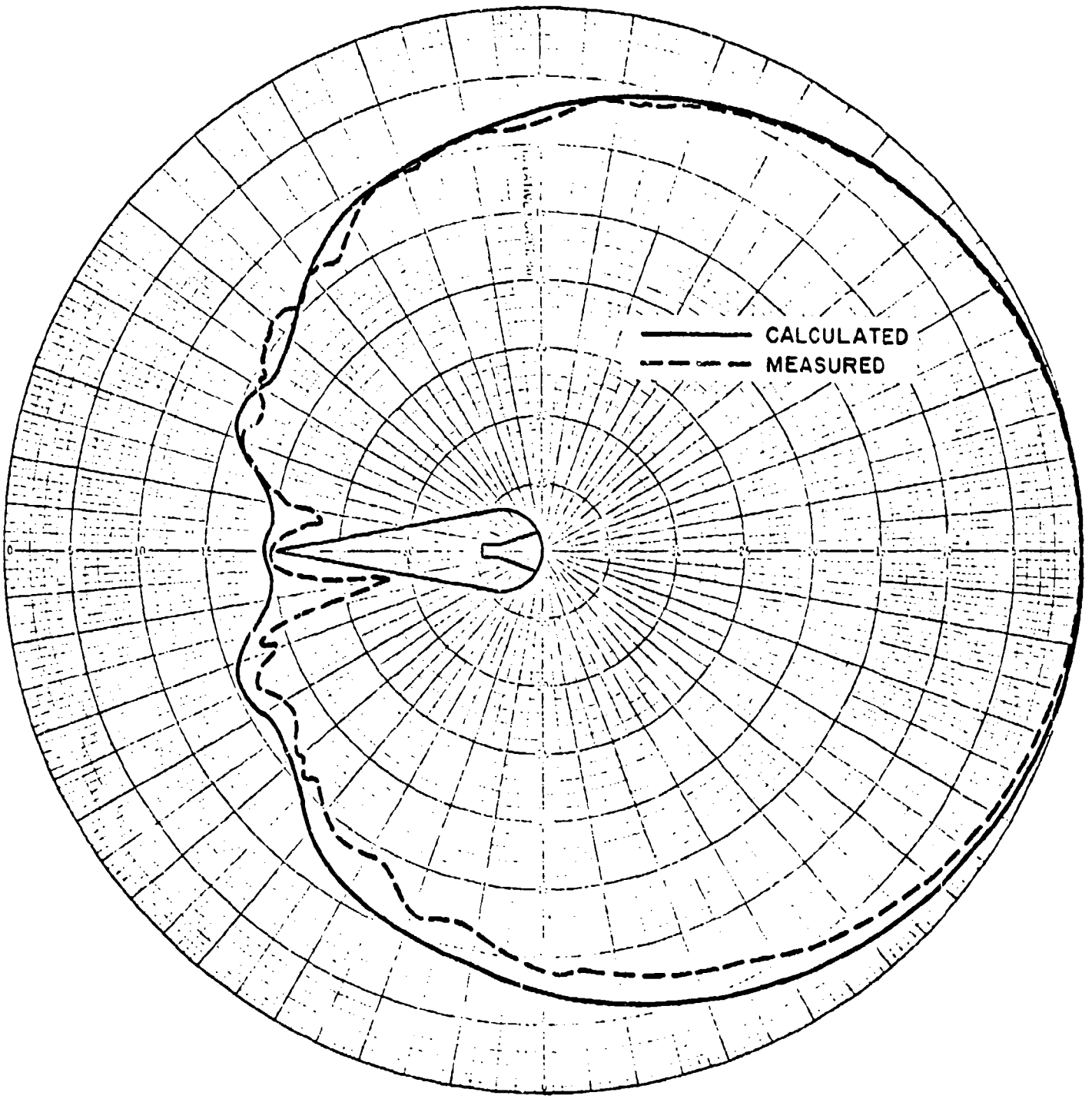

Fig. 12. Calculated and measured elevation pattern of a sectoral horn mounted on a glove section mock-up.

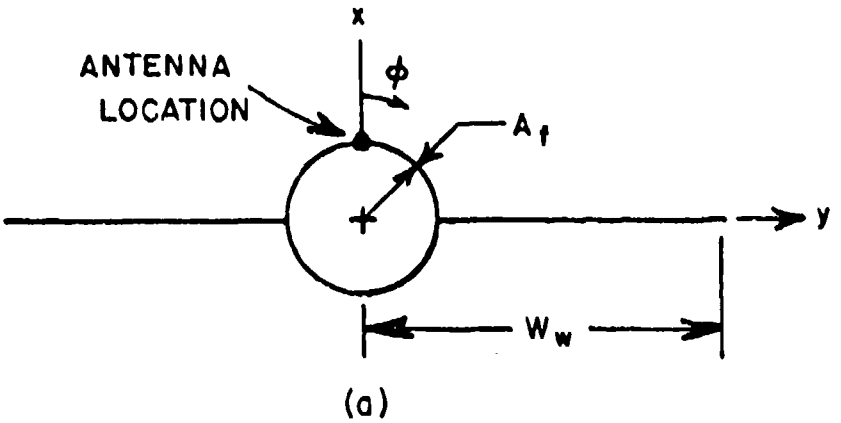

Fig. 13a. Two dimensional model for the roll plane W/O engines.

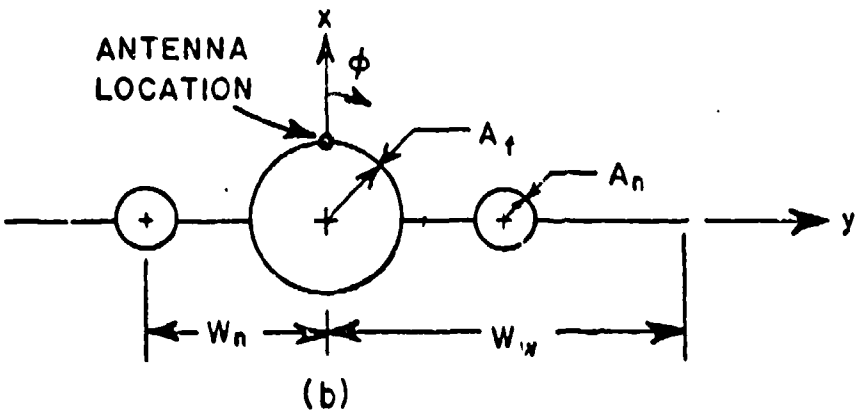

Fig. 13b. Two dimensional model for the roll plane W/ engines.

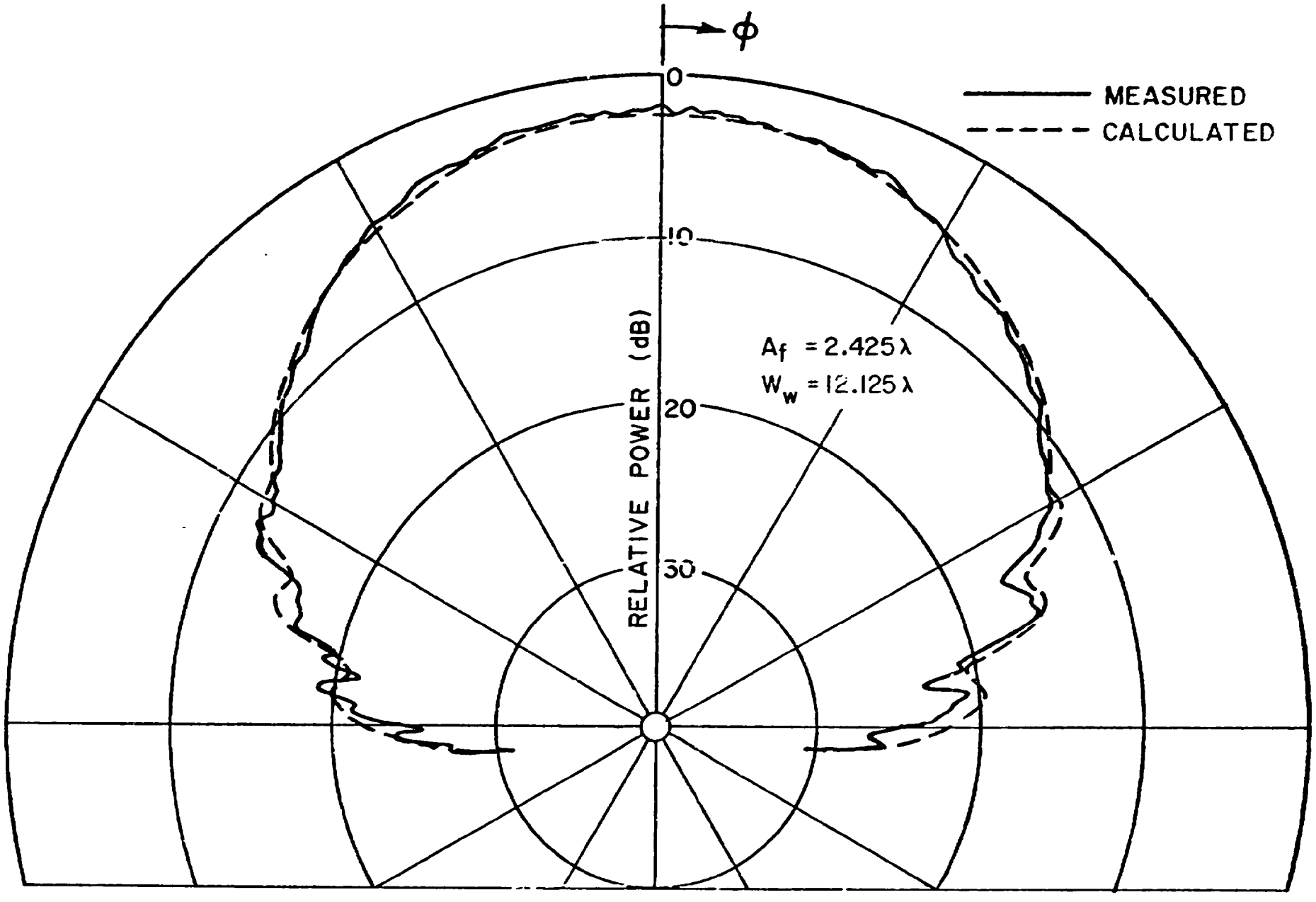

(a) CIRCUMFERENTIAL SLOT

Fig. 14a. Roll plane patterns.

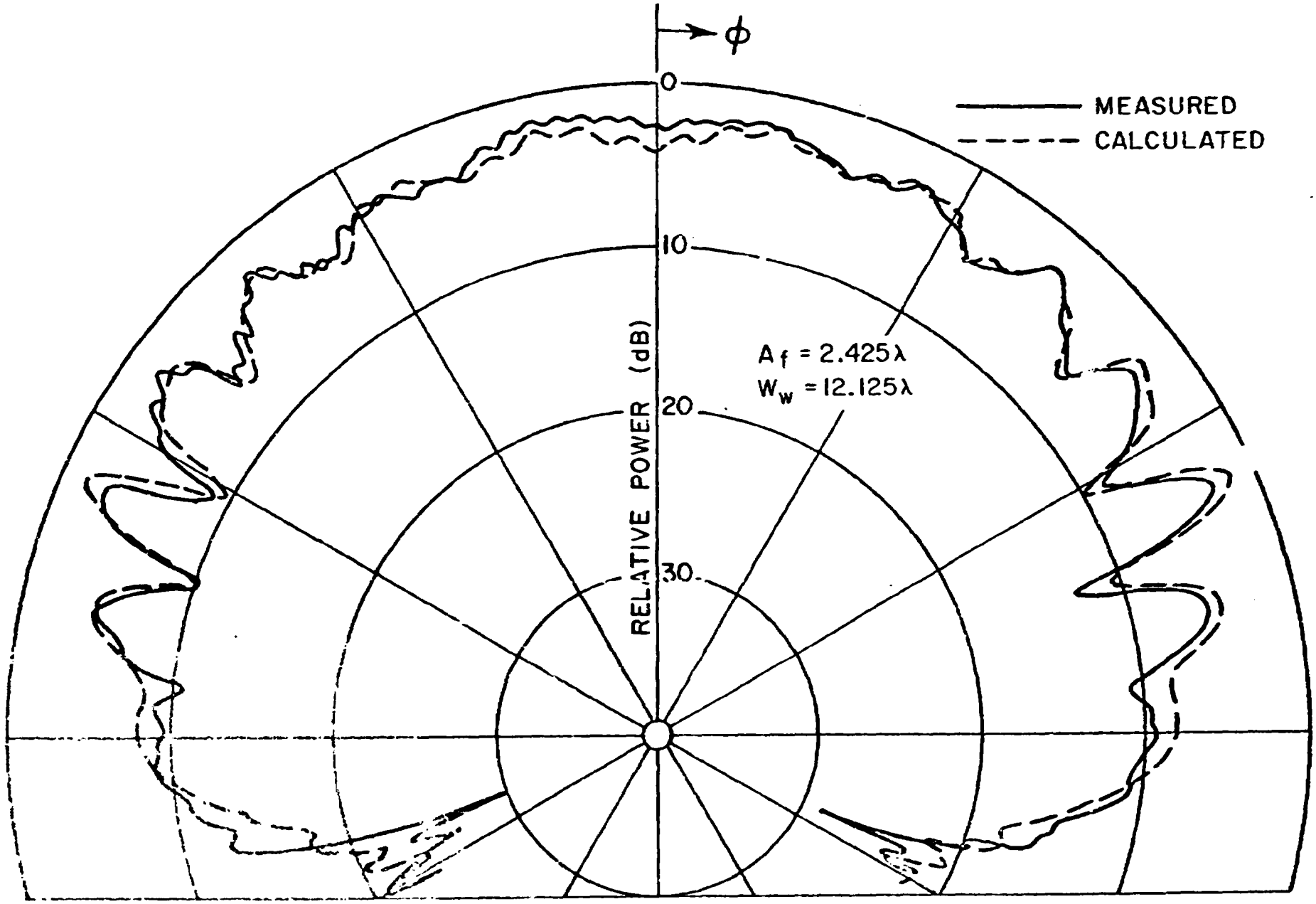
φ
0
10
20
30
RELATIVE POWER (dB)
MEASURED
CALCULATED
$A_f = 2.425\lambda$
$W_w = 12.125\lambda$

(b) AXIAL SLOT

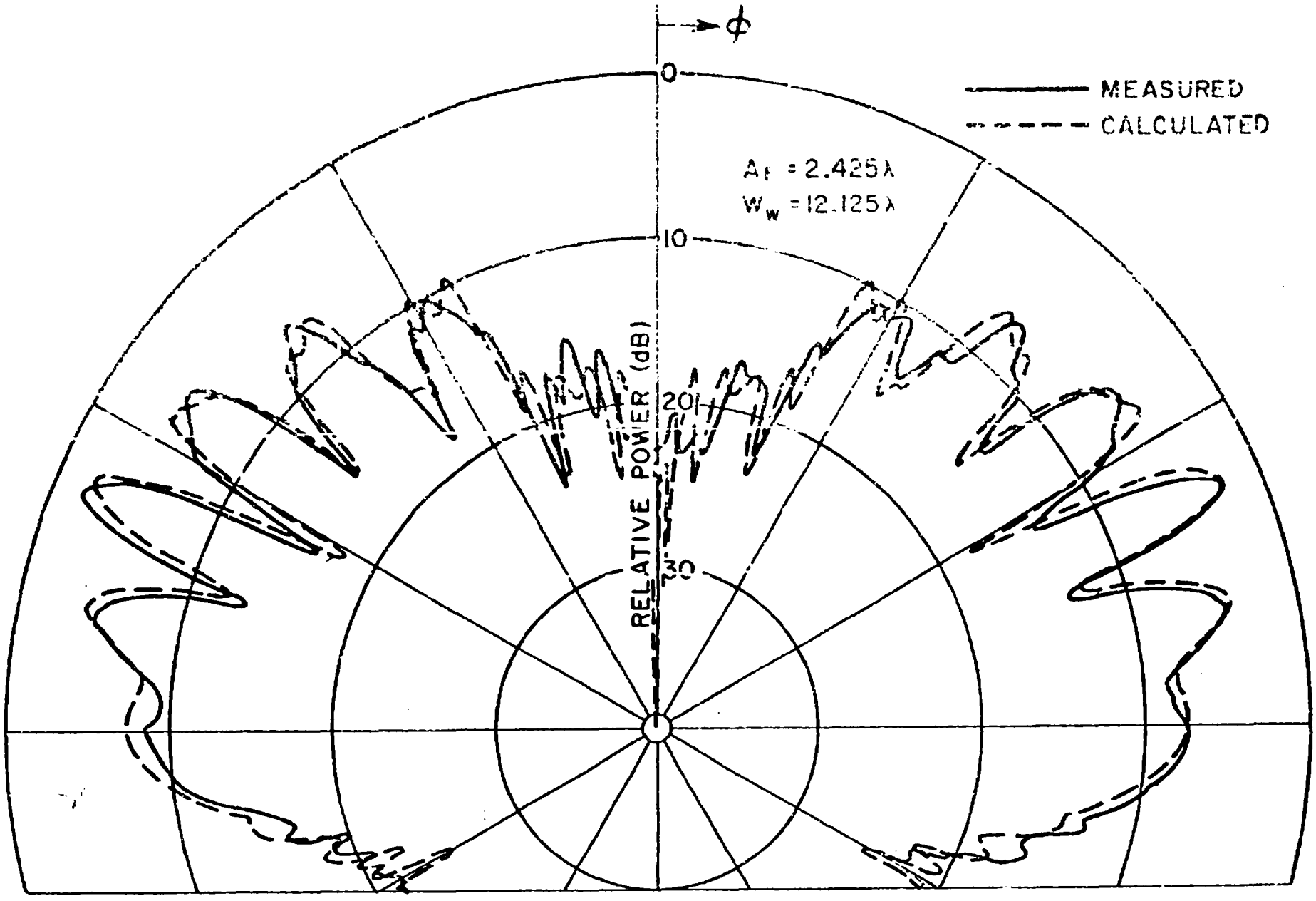

(c) MONOPOLE

Fig. 14c. Roll plane patterns.

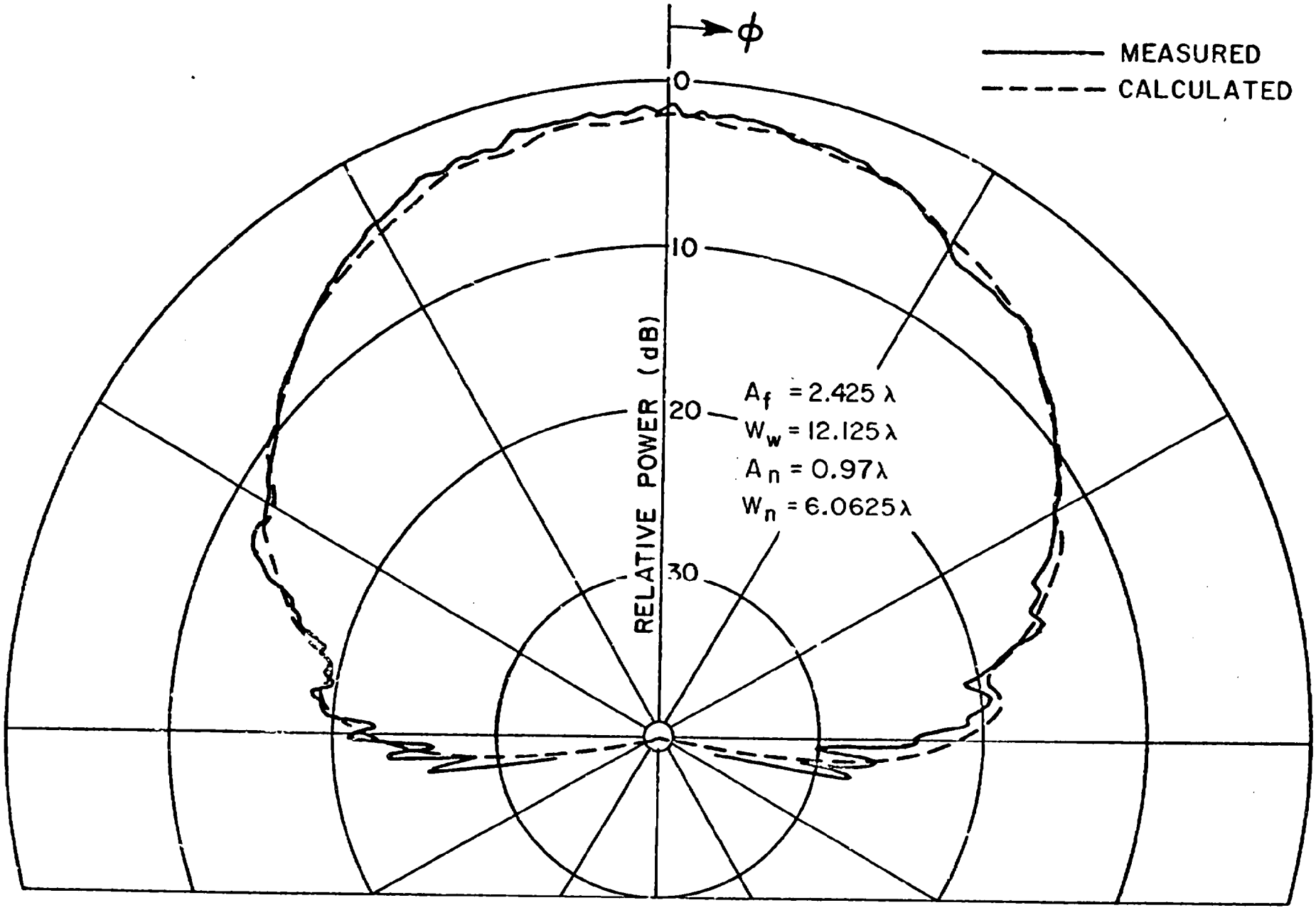

(a) CIRCUMFERENTIAL SLOT

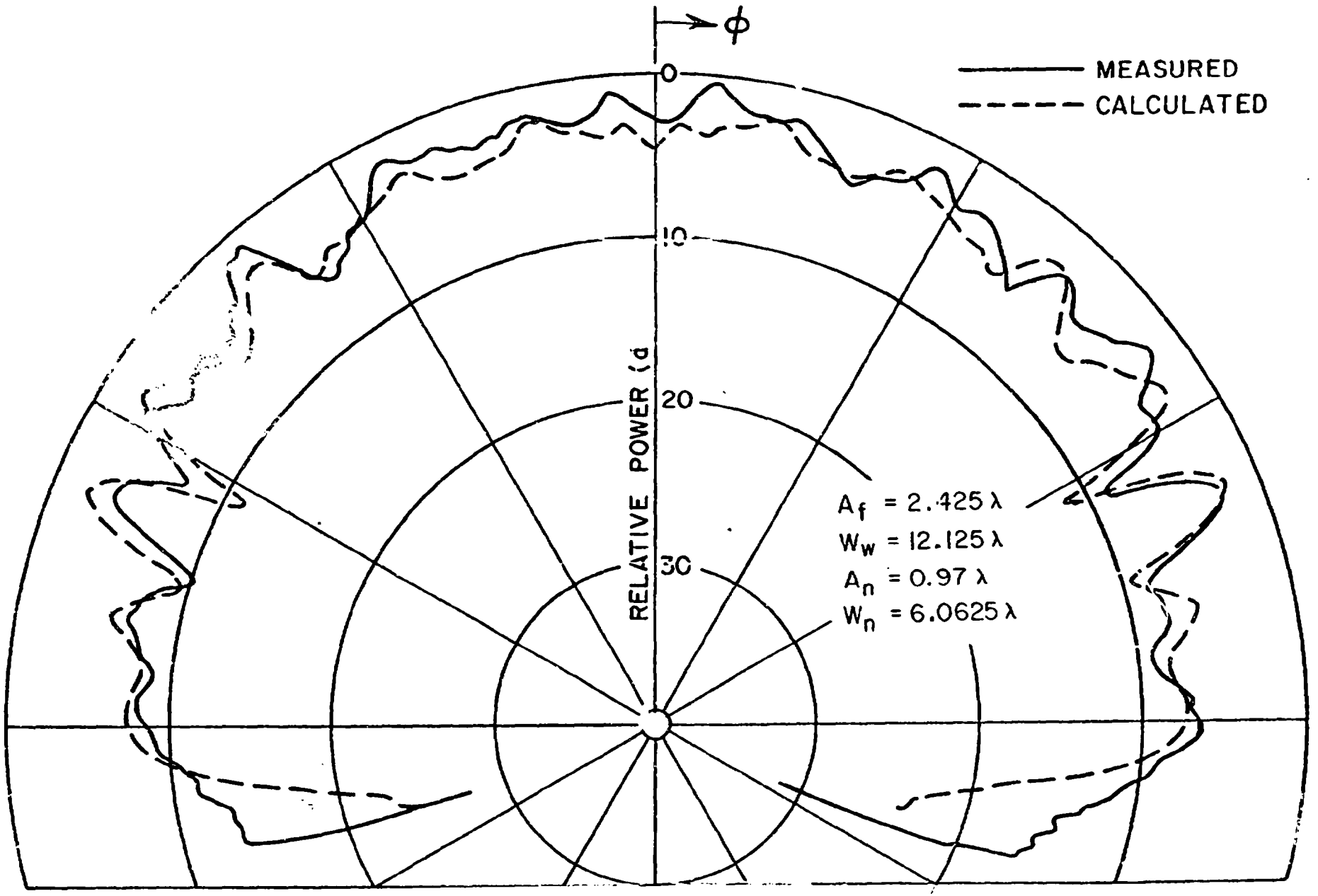

(b) AXIAL SLOT

Fig. 15b. Roll plane patterns.

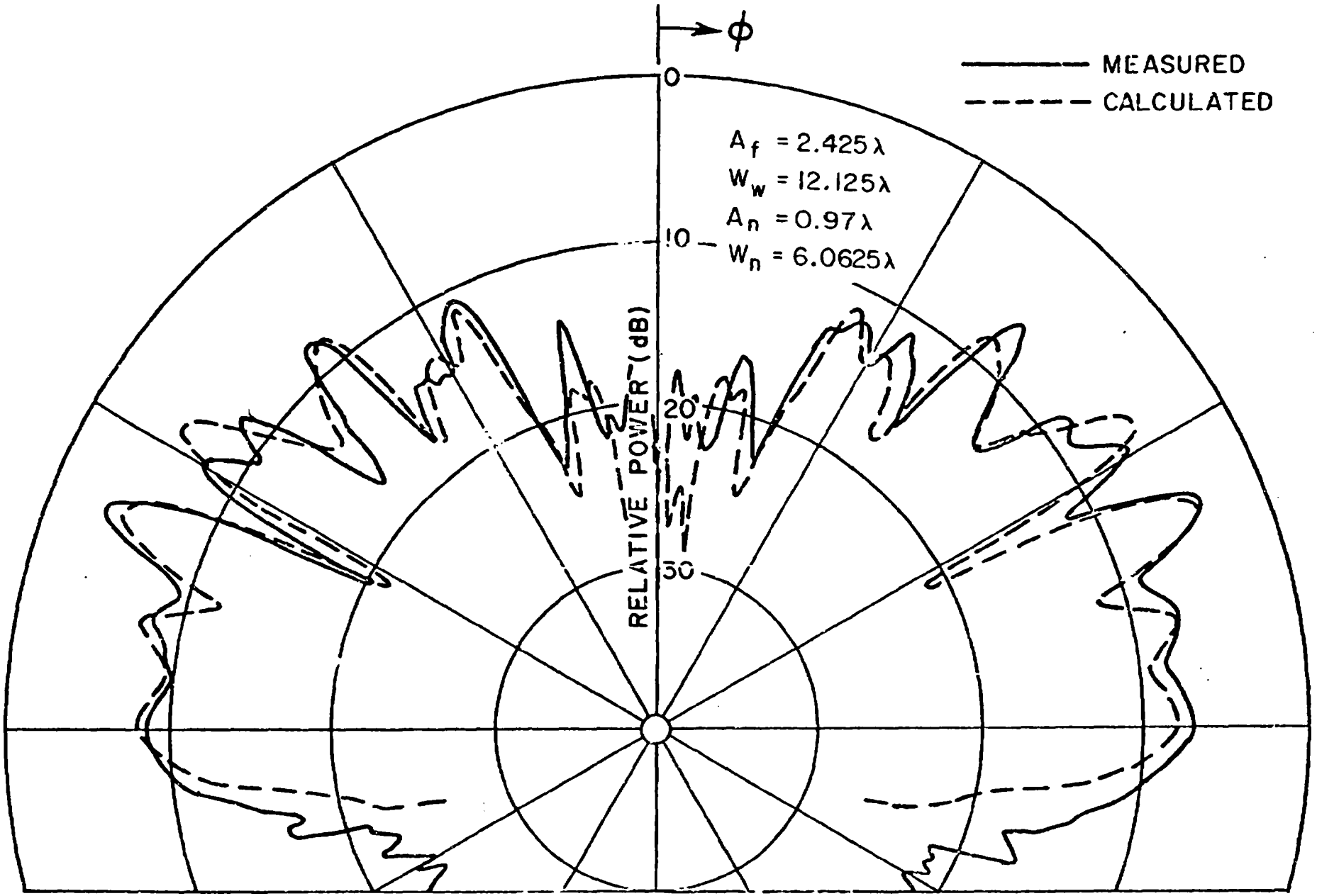
φ
0
10
20
30
RELATIVE POWER (dB)
MEASURED
CALCULATED
A_f = 2.425λ
W_w = 12.125λ
A_n = 0.97λ
W_n = 6.0625λ

(c) MONOPOLE

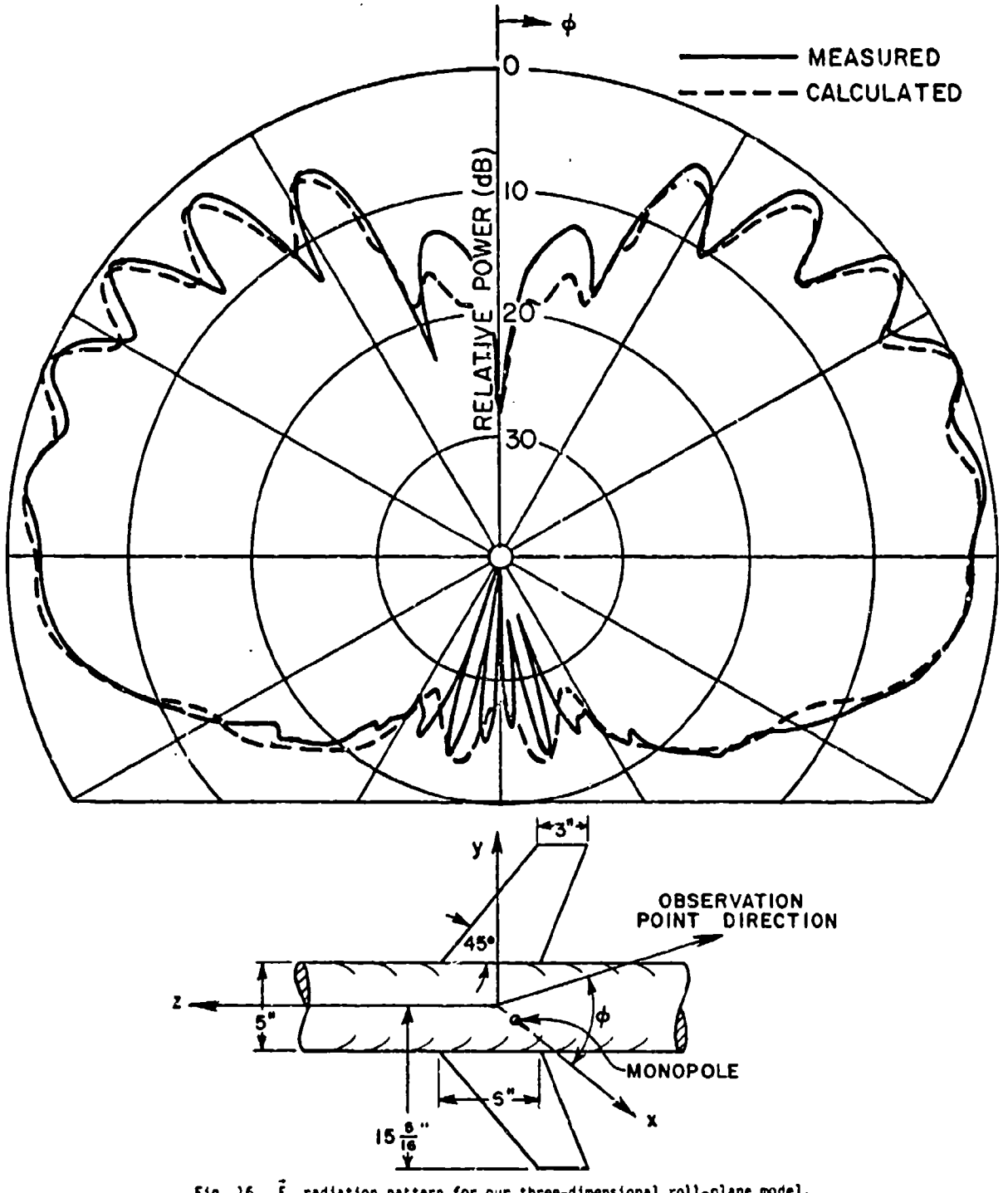

Fig. 16. $\vec{E}_\phi$ radiation pattern for our three-dimensional roll-plane model.

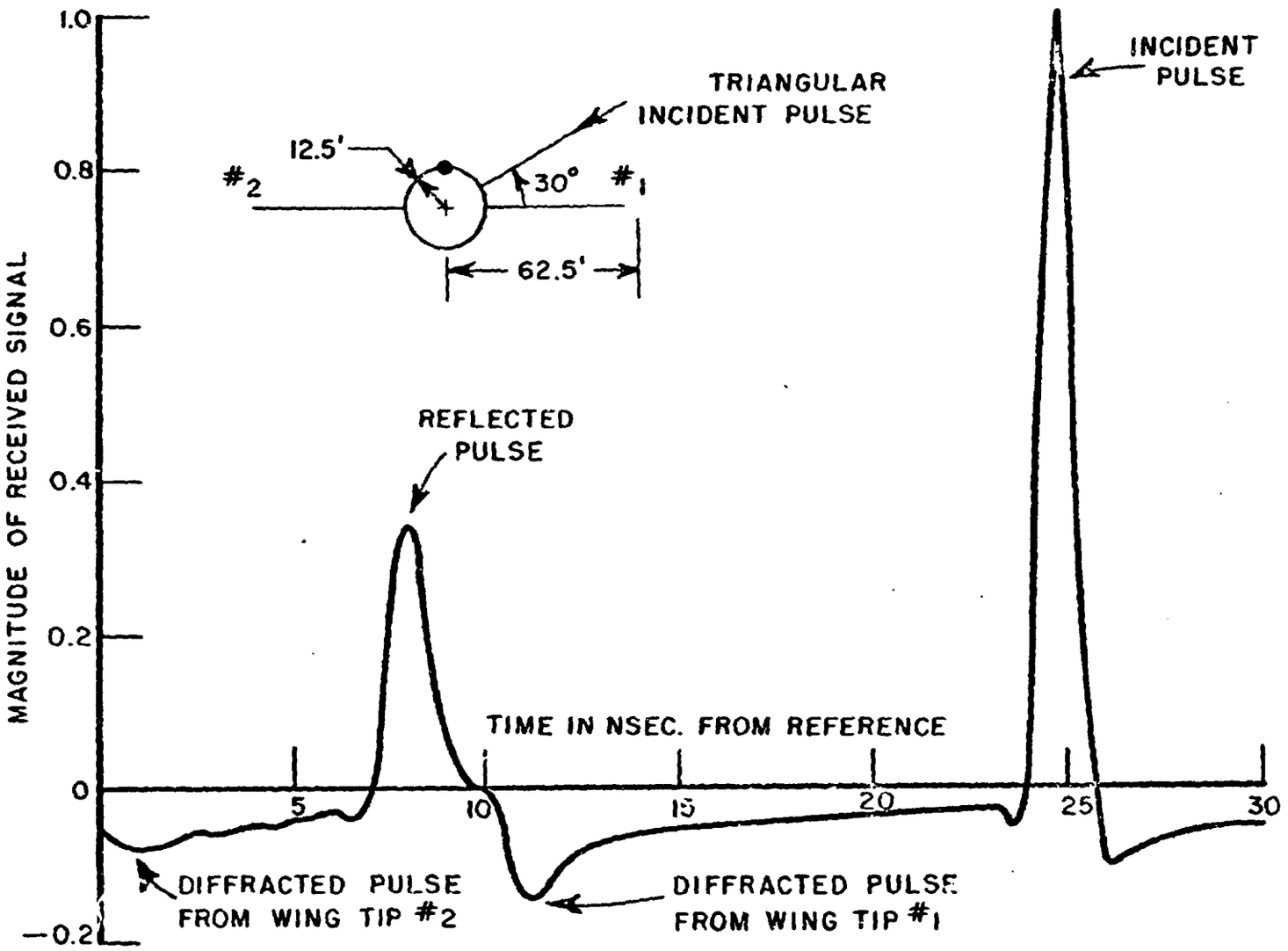

Fig. 17. Received waveform from infinitesimal axial slot on the roll plane model.

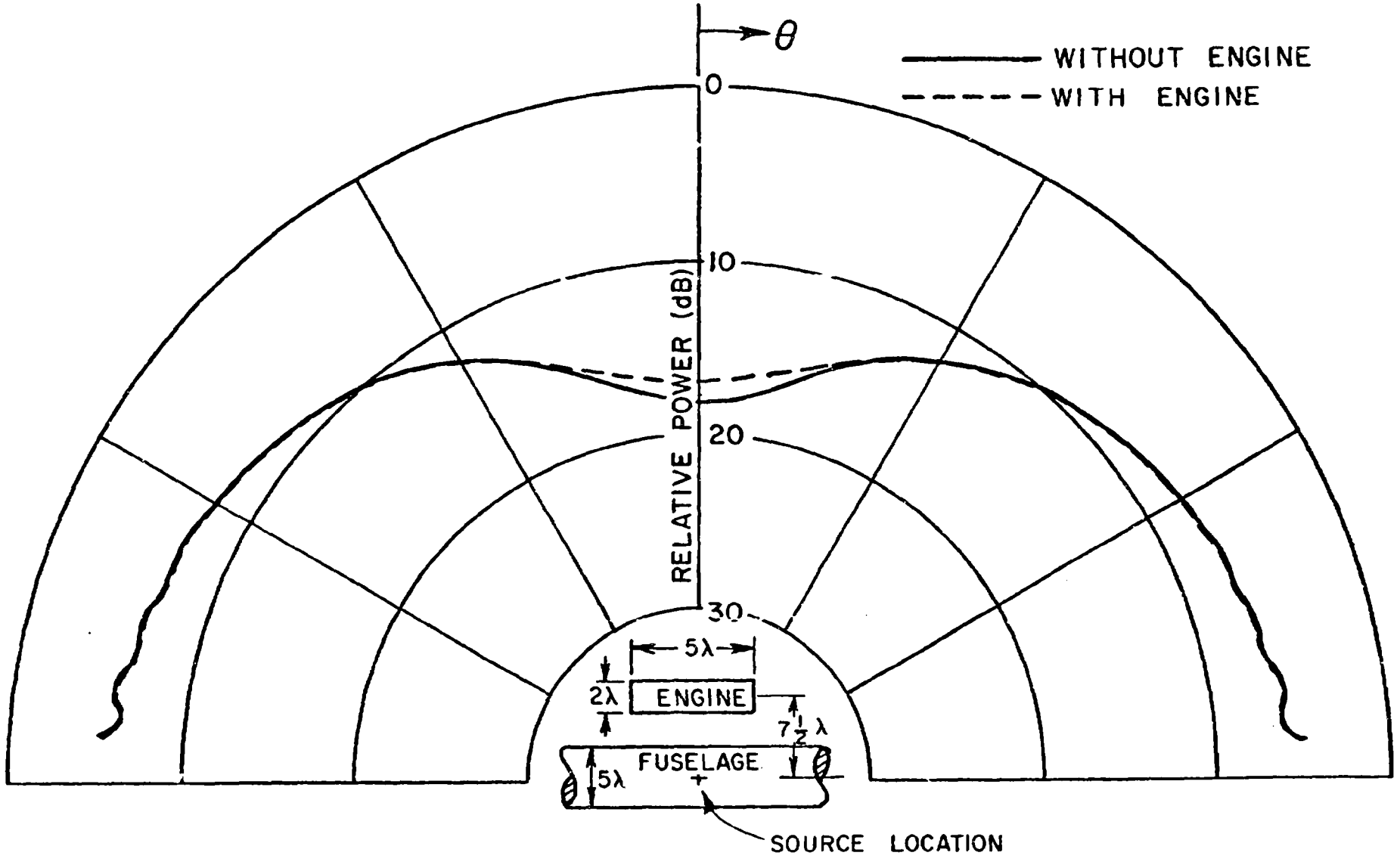

(a) CIRCUMFERENTIAL SLOT

Fig. 18a. Azimuth plane pattern.

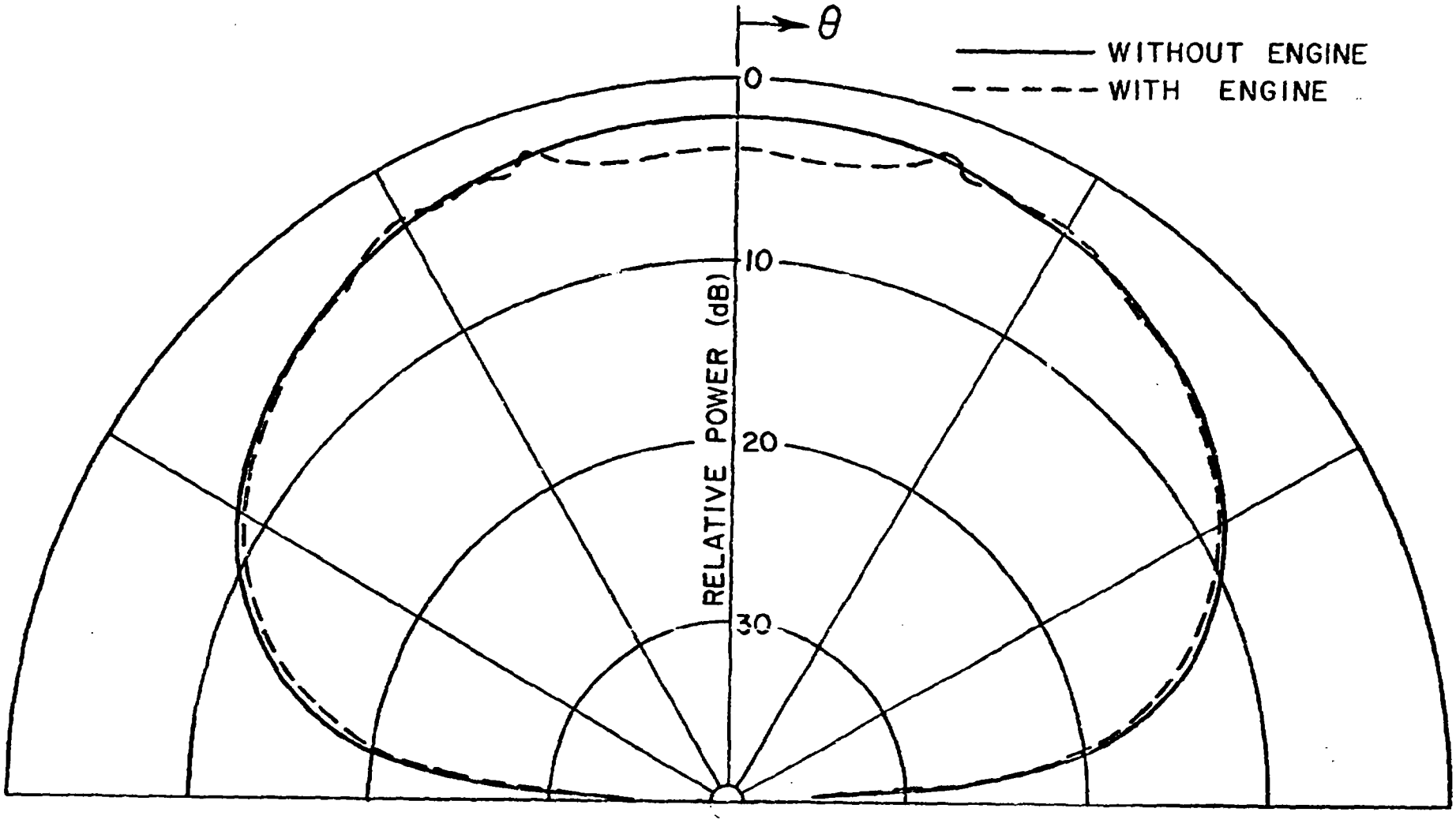

(b) AXIAL SLOT

Fig. 18b. Azimuth plane pattern.

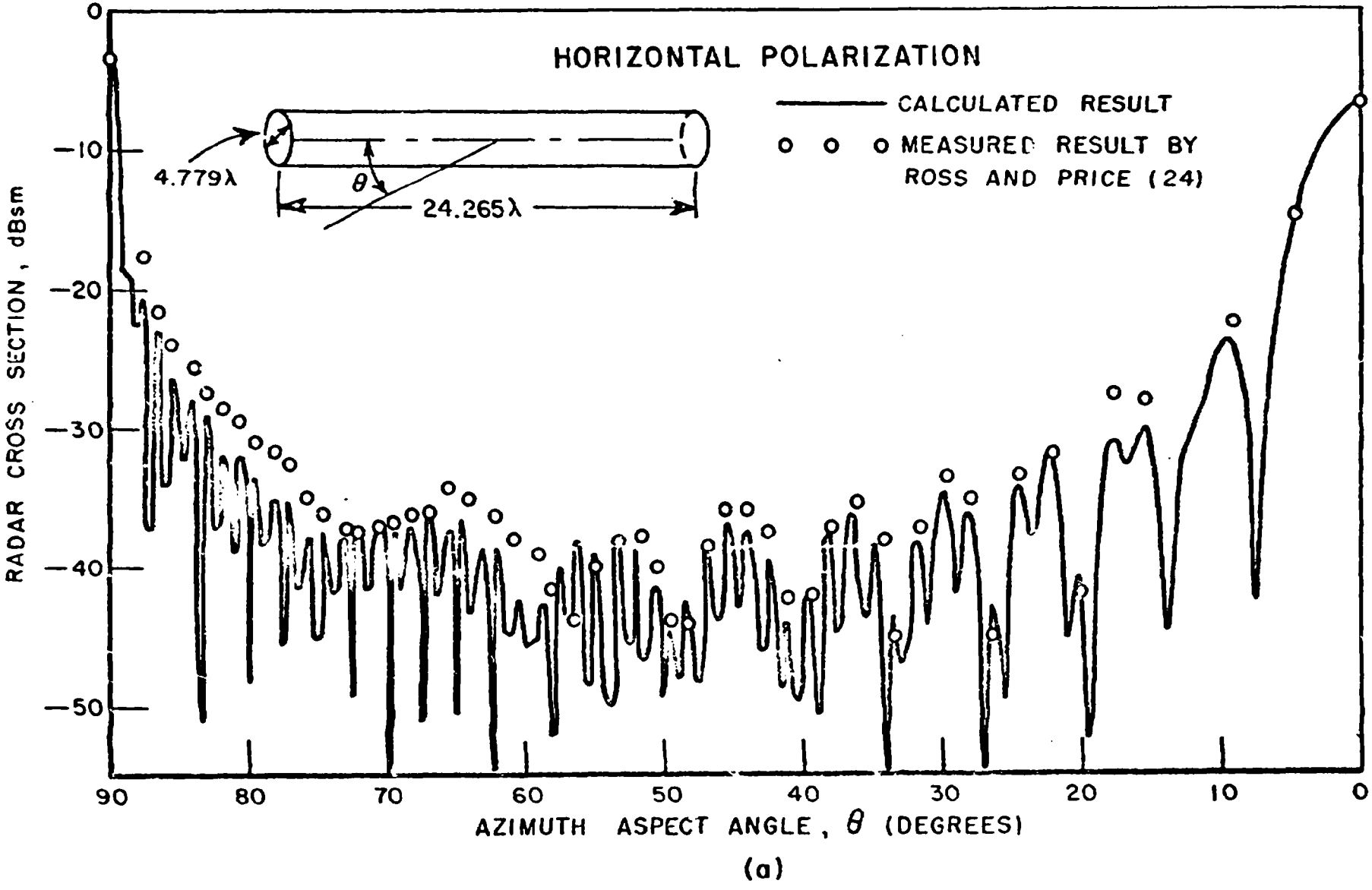

Fig. 19a. Far field radar cross-section from a finite cylinder.

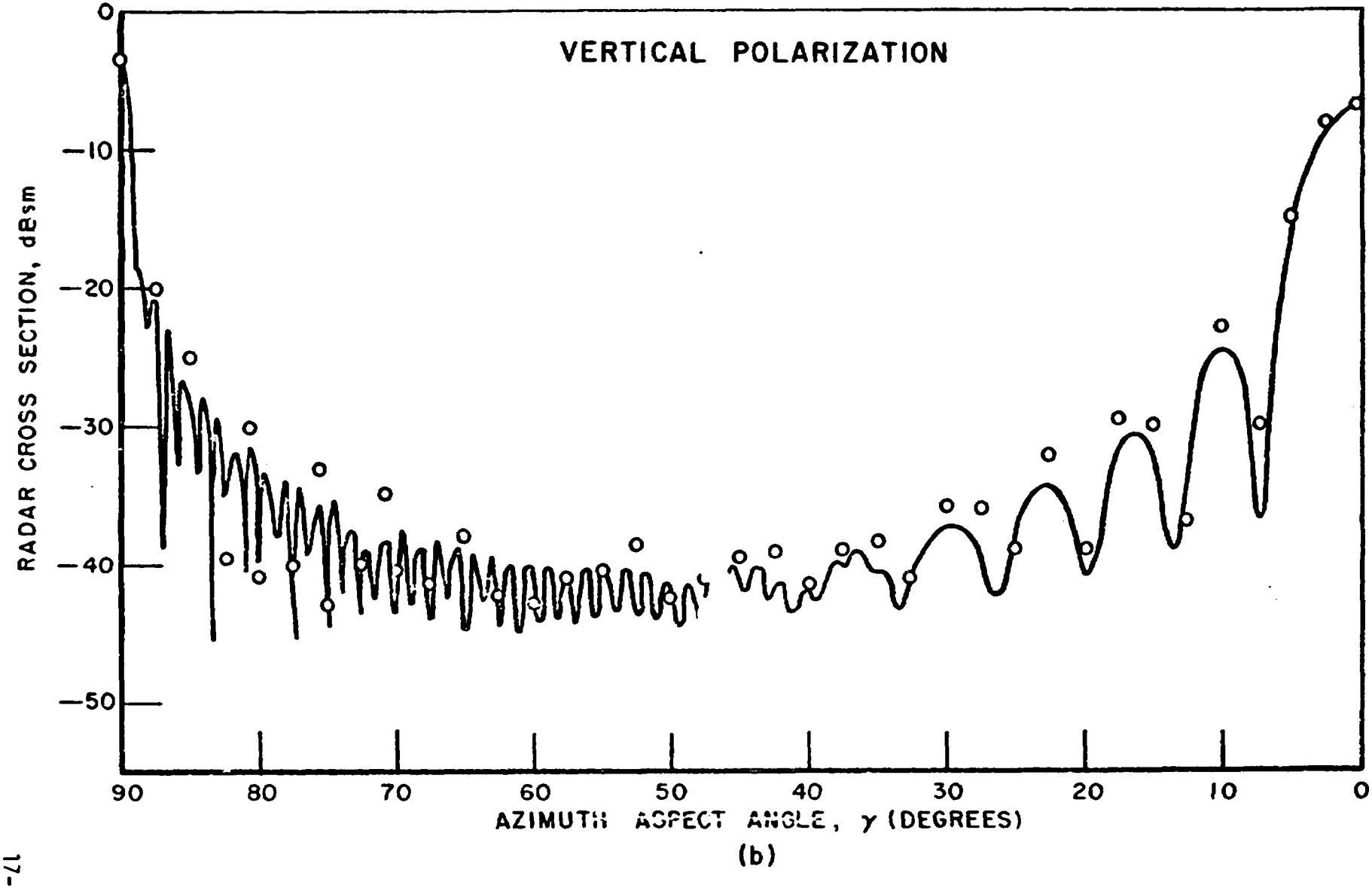

Fig. 19b. Far field radar cross-section from a finite cylinder.

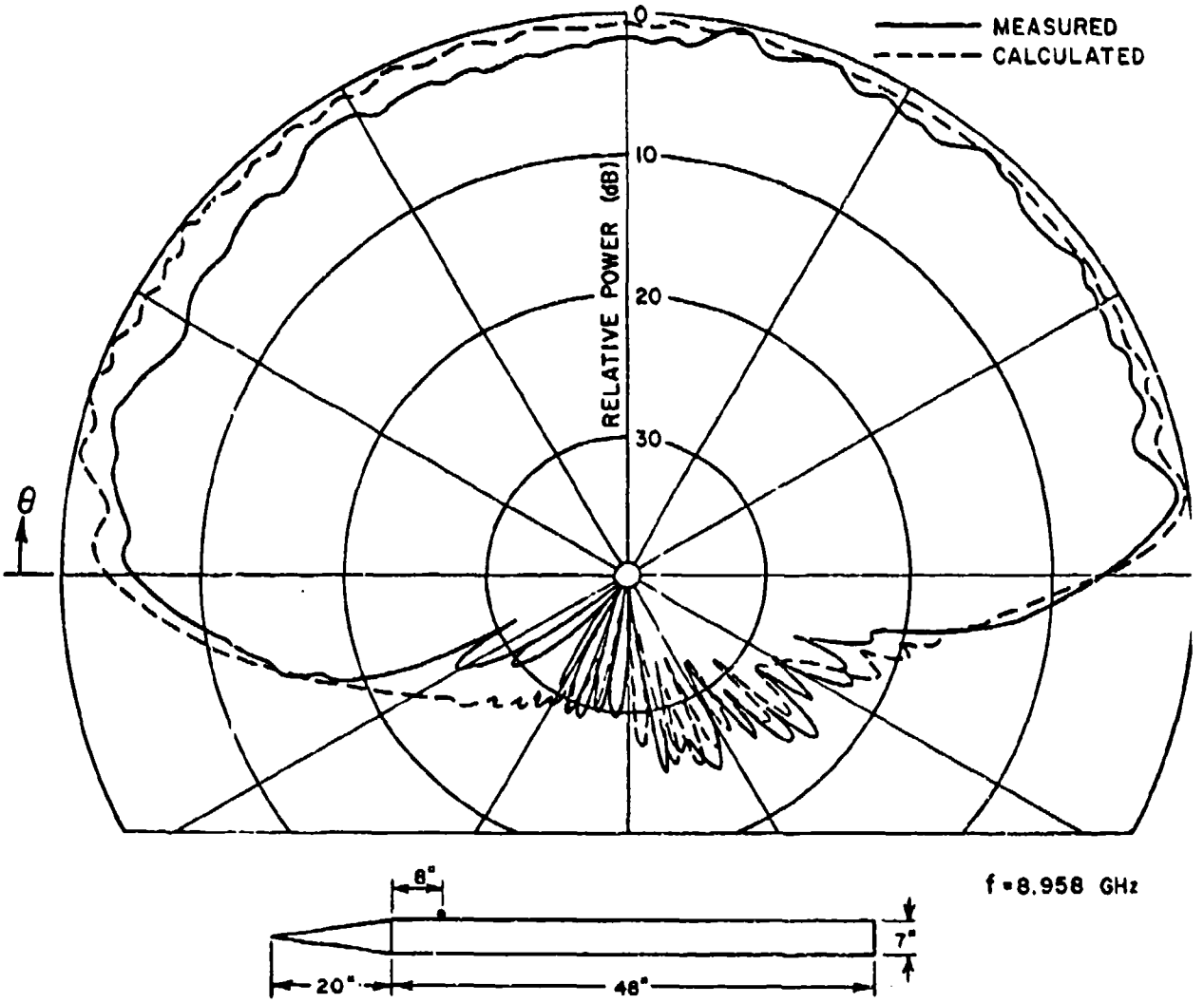

(a) CIRCUMFERENTIAL SLOT

Fig. 20a. Elevation plane patterns.

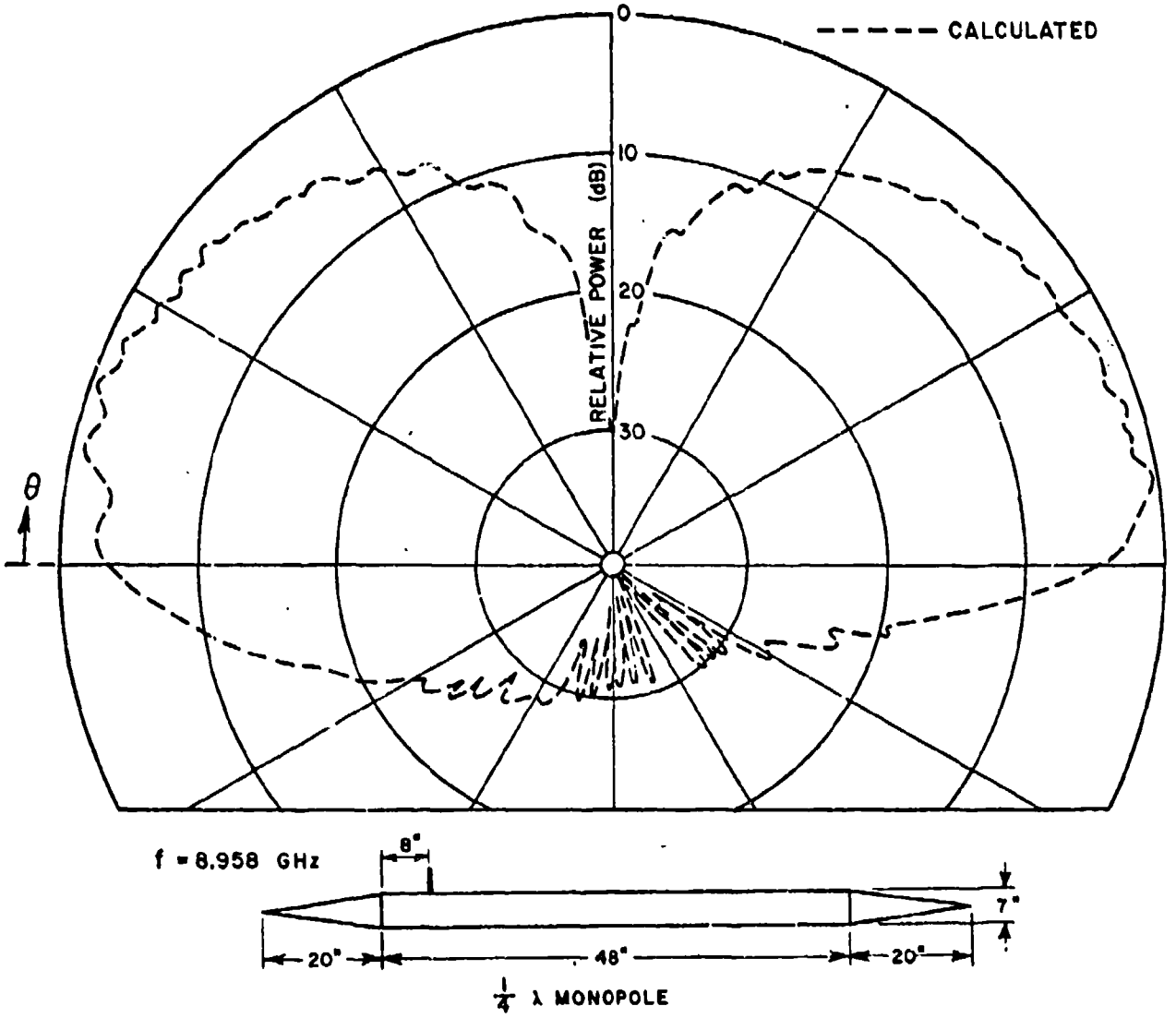

(b)

Fig. 20b. Elevation plane patterns.

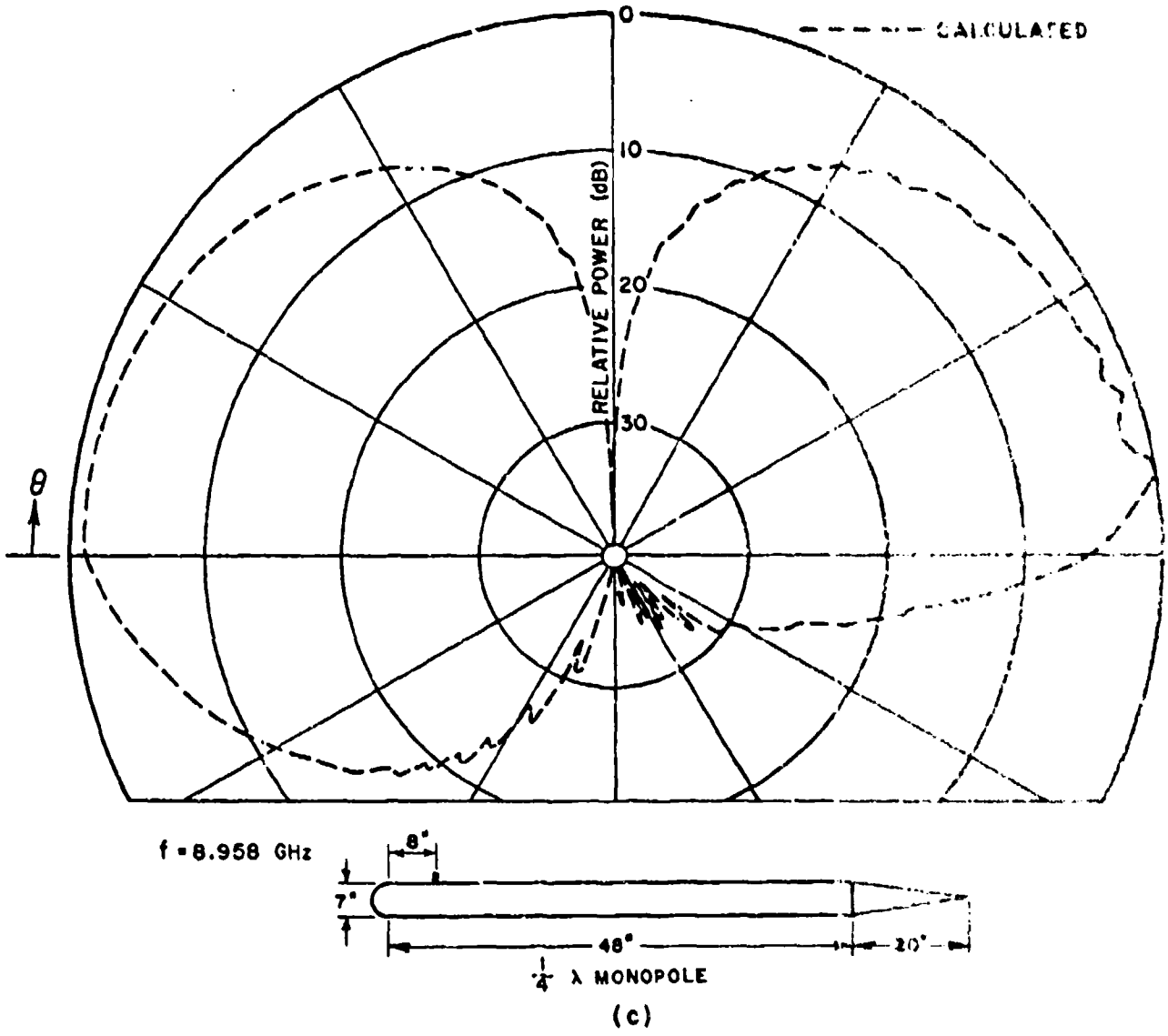

Fig. 20c. Elevation plane patterns.

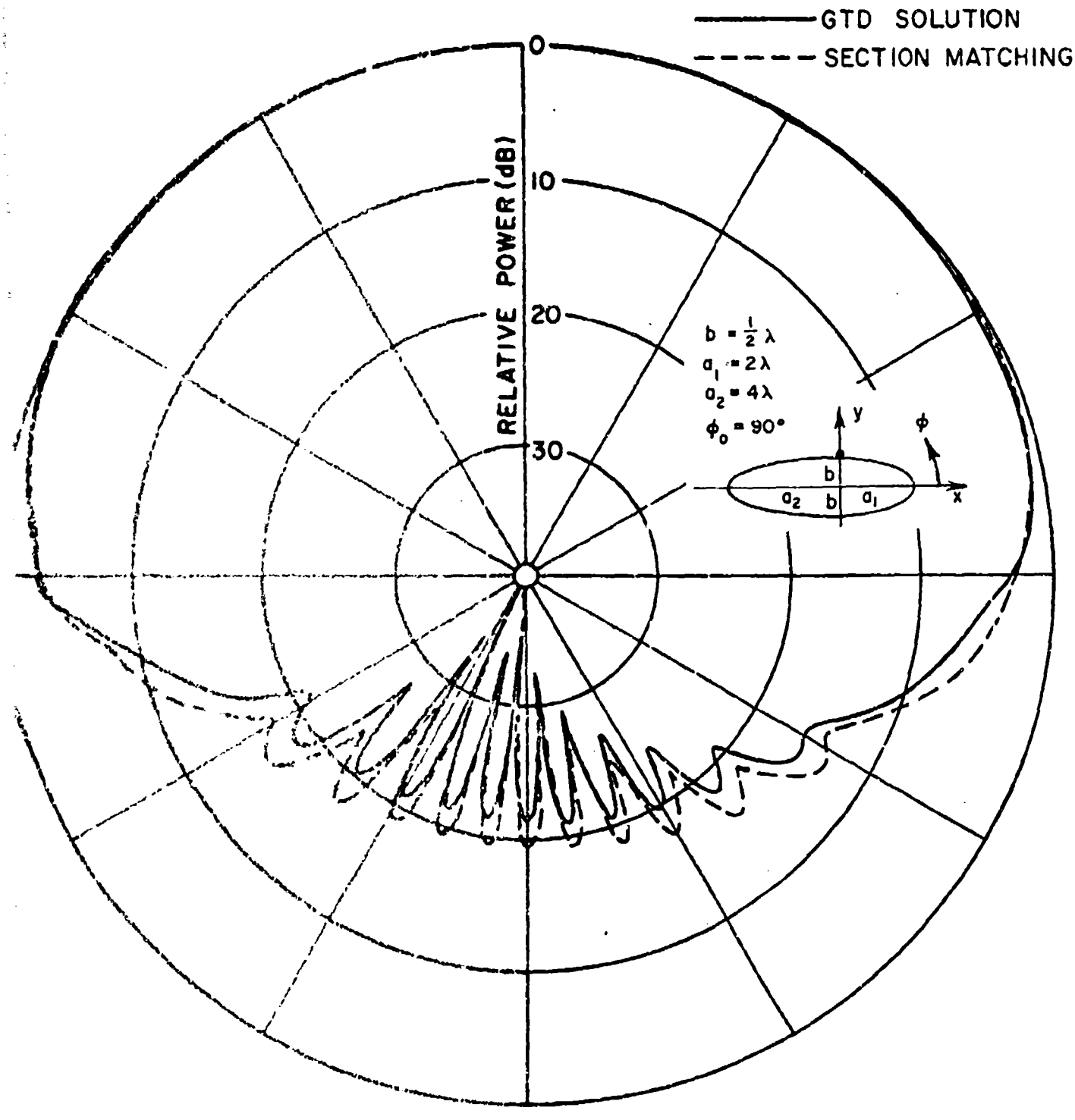

(a)

Fig. 21a. Elevation plane pattern with a circumferential slot mounted on a composite ellipse model.

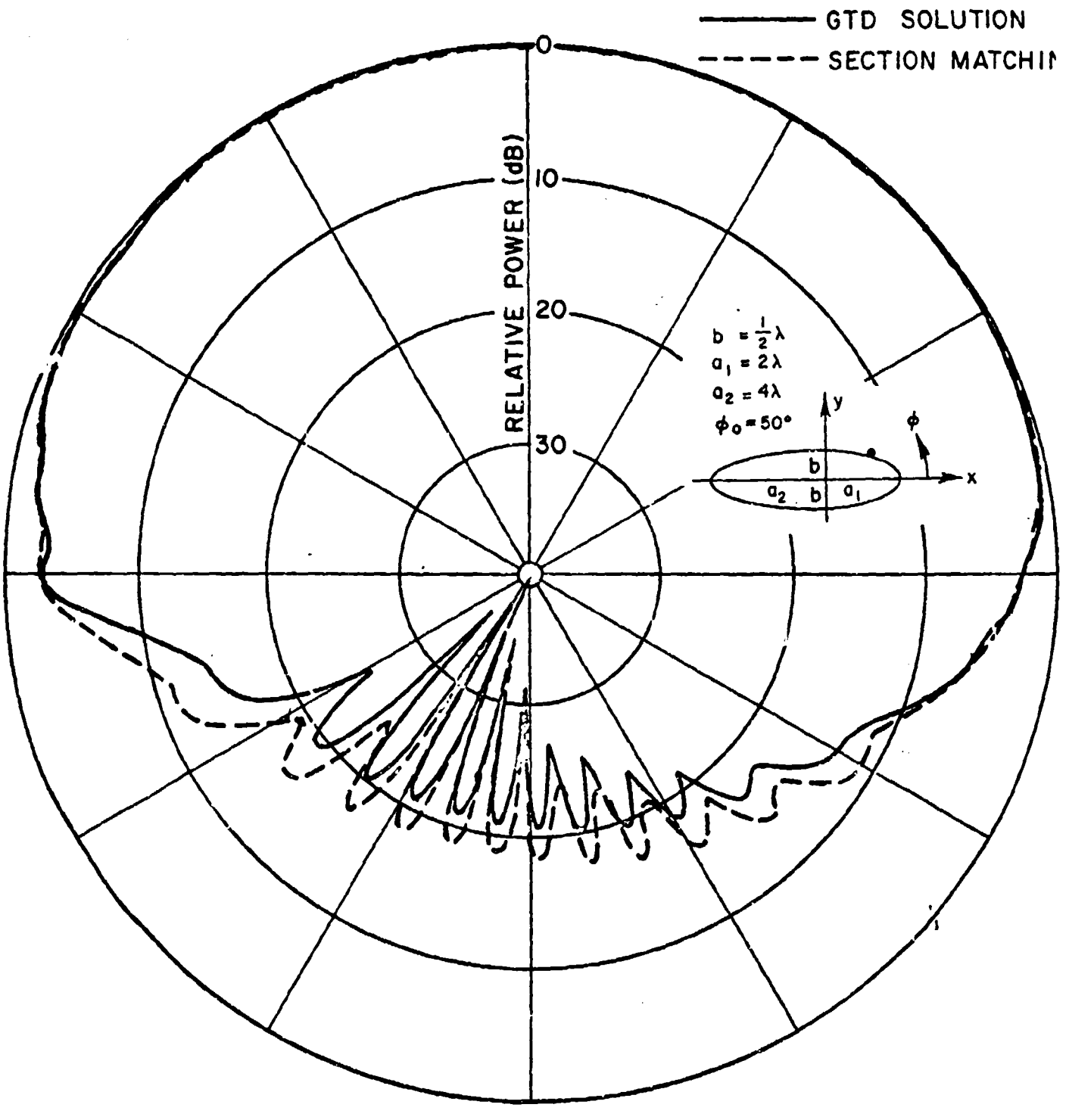

(b)

Fig. 21b. Elevation plane pattern with a circumferential slot mounted on a composite ellipse model.

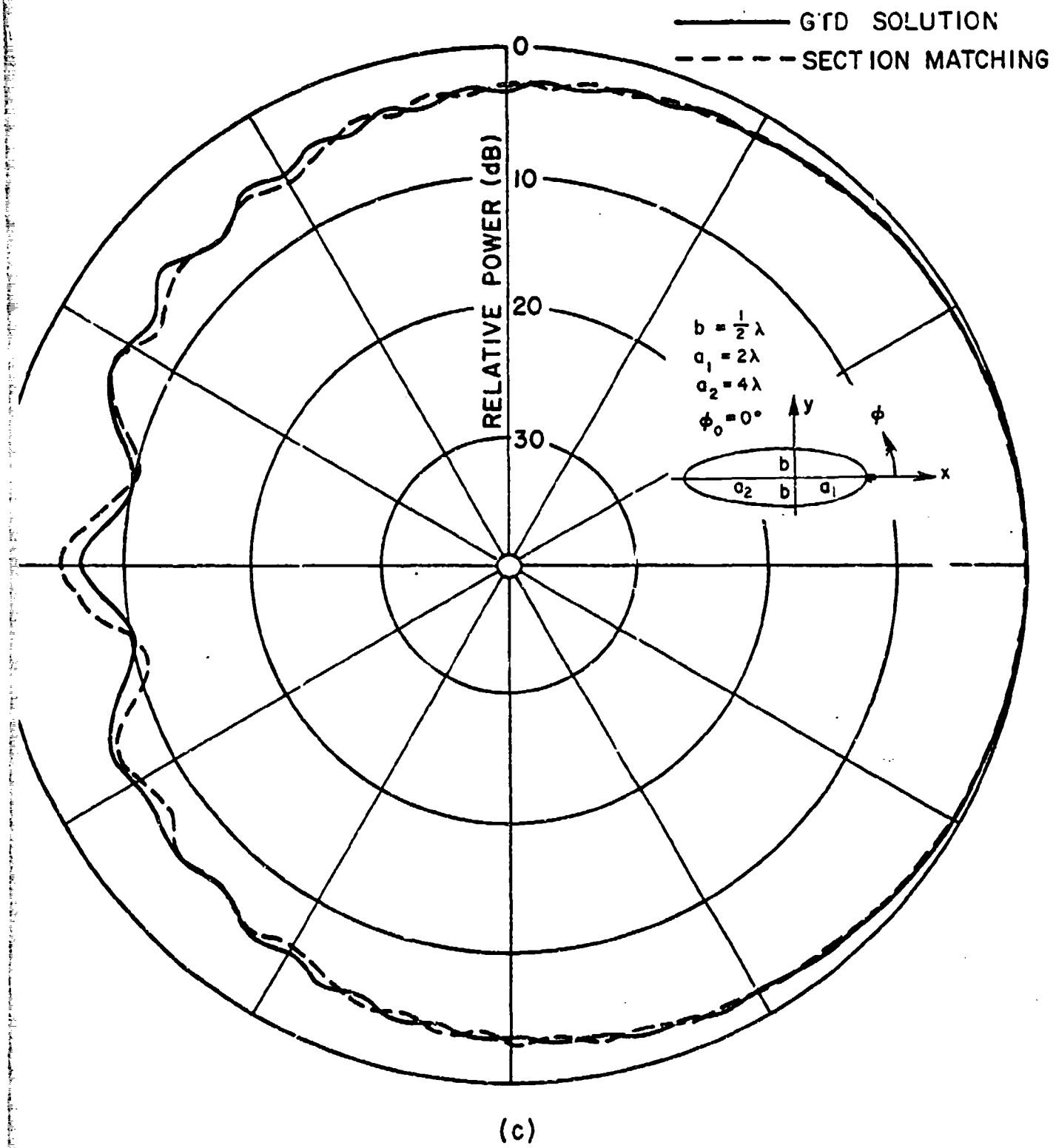

(c)

Fig. 21c. Elevation plane pattern with a circumferential slot mounted on a composite ellipse model.

18 A 16 ELEMENT FREQUENCY LOCKED BULK EFFECT ARRAY

By

J. C. POLK AND C. A. NEWKIRK

ITT GILFILLAN
7821 Orion Avenue
Van Nuys, California 91409

For

ARRAY ANTENNA CONFERENCE

Naval Electronics Laboratory Center

San Diego, California

22, 23, 24 February 1972

1. INTRODUCTION

Endeavoring to significantly advance the state of the radar art in 1967, ITT Gilfillan established the SPAR (Solid State Phased Array Radar) program.

Our approach was to perform an overall systems analysis to determine an optimum configuration and a most desirable source device. The results of our study indicated that solid state sources could be classified into two groups that we chose to call peak power limited and energy limited devices. We found that the radar parameters could be met by either class, but energy limited sources were clearly the cost effective choice. At the time of the study, no satisfactory energy limited device existed, so we initiated a program for the development of a suitable bulk effect device with Standard Telecommunications Laboratories, our ITT central research establishment.

For the past five years ITT Gilfillan, working with STL and supported by NAVSEC, NRL and RADC has brought the bulk effect device from the position of a laboratory curiosity to the threshold of a technique which shows great promise for application in the next generation solid state radars. The work to be discussed is our first effort to demonstrate the radar capability of energy limited source technology.

2. EXPERIMENTAL RADAR SYSTEM

The radar system chosen to demonstrate the application of energy limited devices to the distributed transmitter problem consists of sixteen solid state modules incorporated into a linear array configuration, together with a control system, receiver and displays. The array is shown in Figure 1 and a block diagram of the full system is shown in Figure 2. Because the intent was to demonstrate use of Gunn oscillators, much of the system was built from available hardware. Components specifically designed and built for this program, in addition to the modules, were the master timing control, automatic beam steering network, frequency agility network and corporate feed. Peak transmitter power was 160 watts excluding phase shifter and line losses.

Figures 3 and 4 are B-scope displays of the Los Angeles skyline. Scan range in azimuth is $\pm 45^{\circ}$ (horizontal coordinate on the scope), and the range to targets is up to 5 km (vertical on scope). Range markers occur at 1 km intervals showing on the scope as horizontal bars. In the display of Figure 3, beam normal is northeast; i.e., the beam scan is from north to east, and in Figure 4, beam normal is due north. Targets were identified by noting azimuth and range from the display and looking up the location on a U. S. Geodetic Survey map. Major identifiable targets are labeled. Since there is

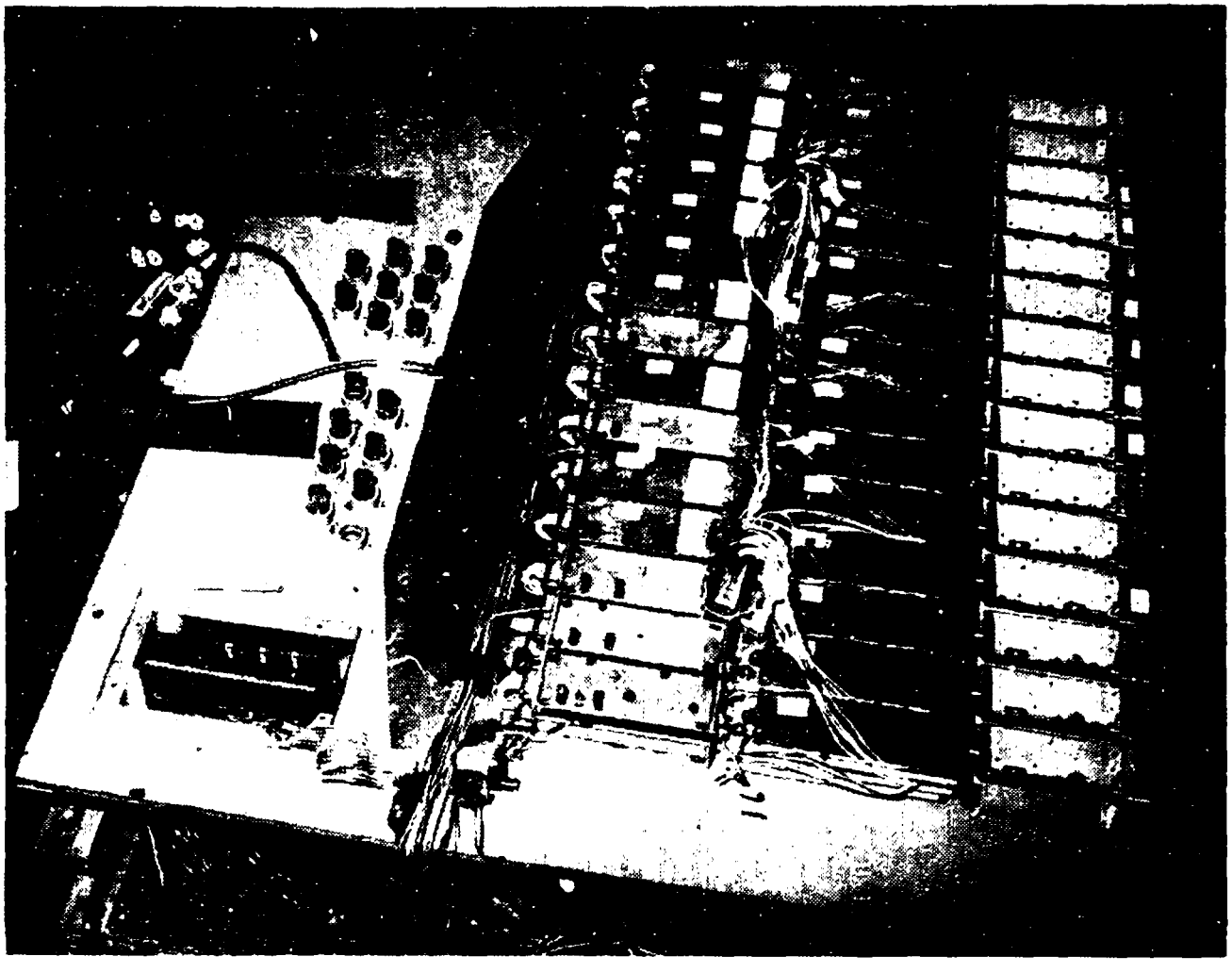

Figure 1. Solid-State Active Array Assembly

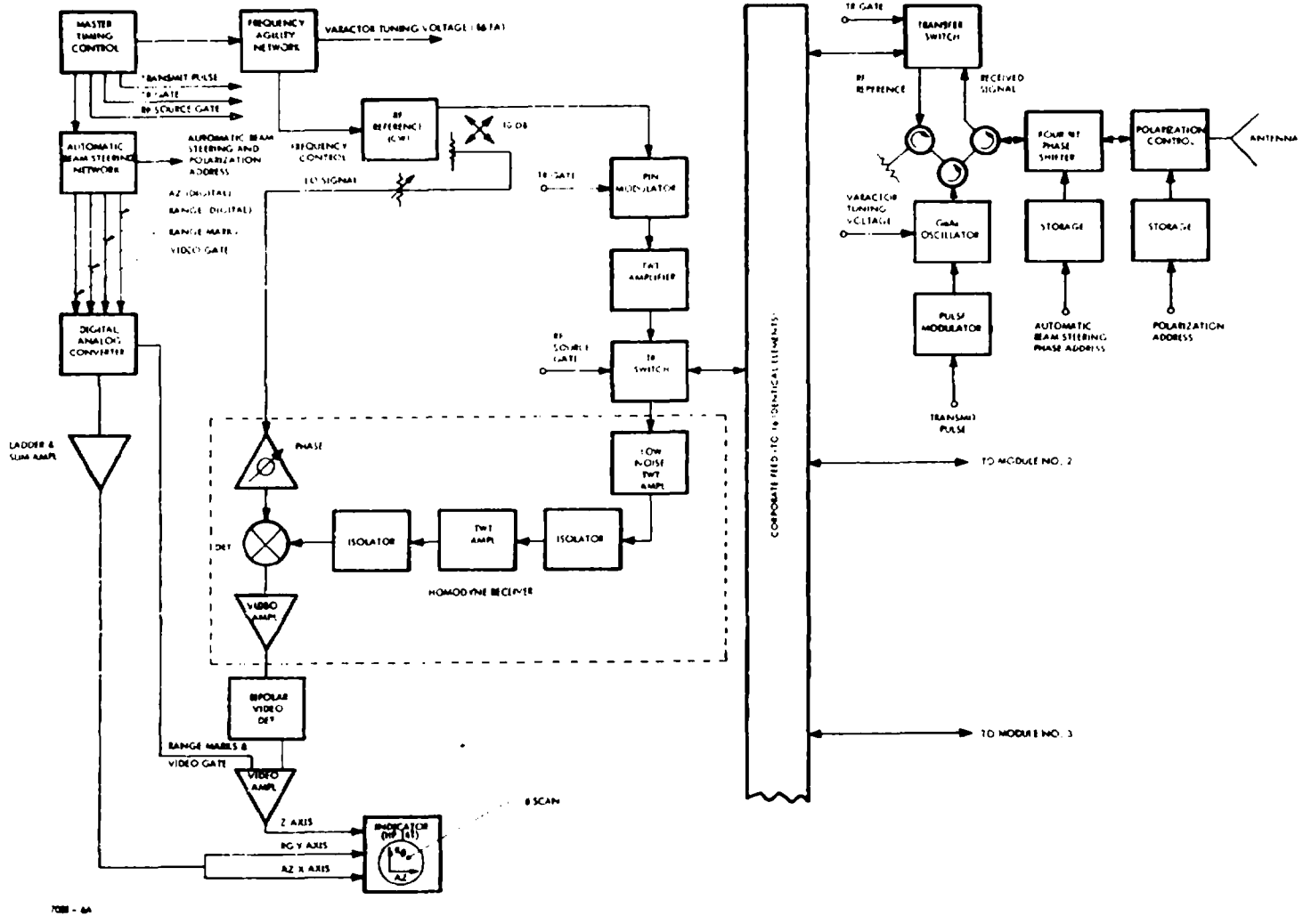

Figure 2. System Block Diagram

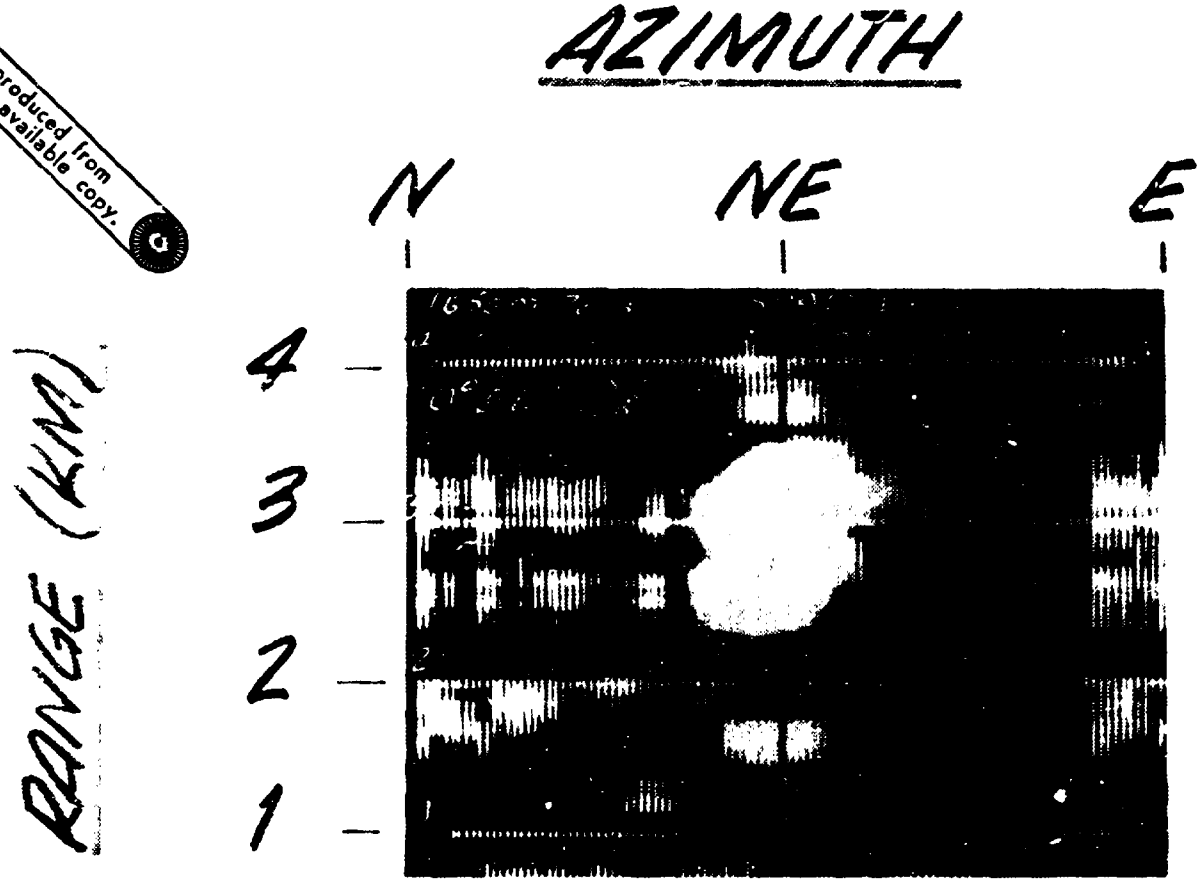

Figure 3. B-Scope Display of Downtown L. A. (SPAR Radar)

a 45° overlap in azimuth between the two pictures, the left half of Figure 3 should be the same as the right half of Figure 4. The differences are attributed mainly to sidelobe returns, particularly in the vicinity of 3 km range in Figure 3.

Performance of the unit using an A-scope display is illustrated in Figure 5. Range marks show as periodic signals at 6.7 μsec (1 km) intervals. The large signal in the first 6 μsec is due to clutter; returns at 12 μsec are high rise buildings. (When these data were taken, there was a 4 μsec error in the range gate that was later corrected.) A target is clearly visible at 68 microseconds (10.2 km).

Although only five range markers were used (up to 5 km), the A-scope display had an indefinite maximum range that could be changed by varying the sweep time of the scope. The B-scope was limited by blanking to 5 km maximum range and basically was less sensitive. The two displays therefore complemented each other, the A-scope giving better sensitivity and longer range, and the B-scope giving the azimuth angle information.

During the test program, numerous radar pictures of the area were obtained, and the location of the Van Nuys Airport 2 km due west of ITT Gilfillan's plant afforded an ideal opportunity to watch moving targets.

A sequence of pictures of a small aircraft during takeoff is shown in Figure 6. The beam scanner was programmed so that the beam stays in one position for sixteen consecutive pulses before moving to the next position. With the runway oriented north and south, the range is virtually constant over the visible angular sector. The radar return from the aircraft moves south (left) between the returns from hangars on either side of the runway. Moving aircraft were detected at ranges up to 4 km. One fixed target was detected at 11.7 km, the maximum range from which any returns were seen. Based on the classical radar equation, the expected range of the system on a 20 square meter target was computed to be 2200 meters, without allowing for improvement due to integration of pulses. Theory shows that for sixteen successive pulses on target, received signal could be enhanced as much as 10 dB, thus increasing range to over 4,000 meters. In fact, many targets were detected at well over 4,000 meters range, but their radar cross-sections were not known. A calibrated range to target measurement was not carried out.

As shown in the block diagram of Figure 2, each solid state module contains the Gunn oscillator, a pulse modulator, TR switching, phase shifters for beam steering and polarization control, and logic and driver circuits. The TR switching allowed the corporate feed to be used for both transmit and receive functions.

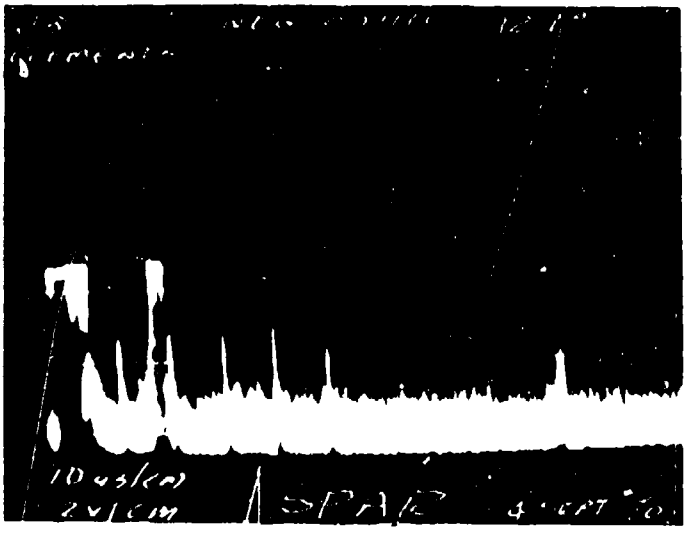

6000-62A

Figure 5. A-Scope Display of SPAR Radar

LIGHT AIRCRAFT DURING TAKEOFF

AS OBSERVED WITH THE SPAR SYSTEM

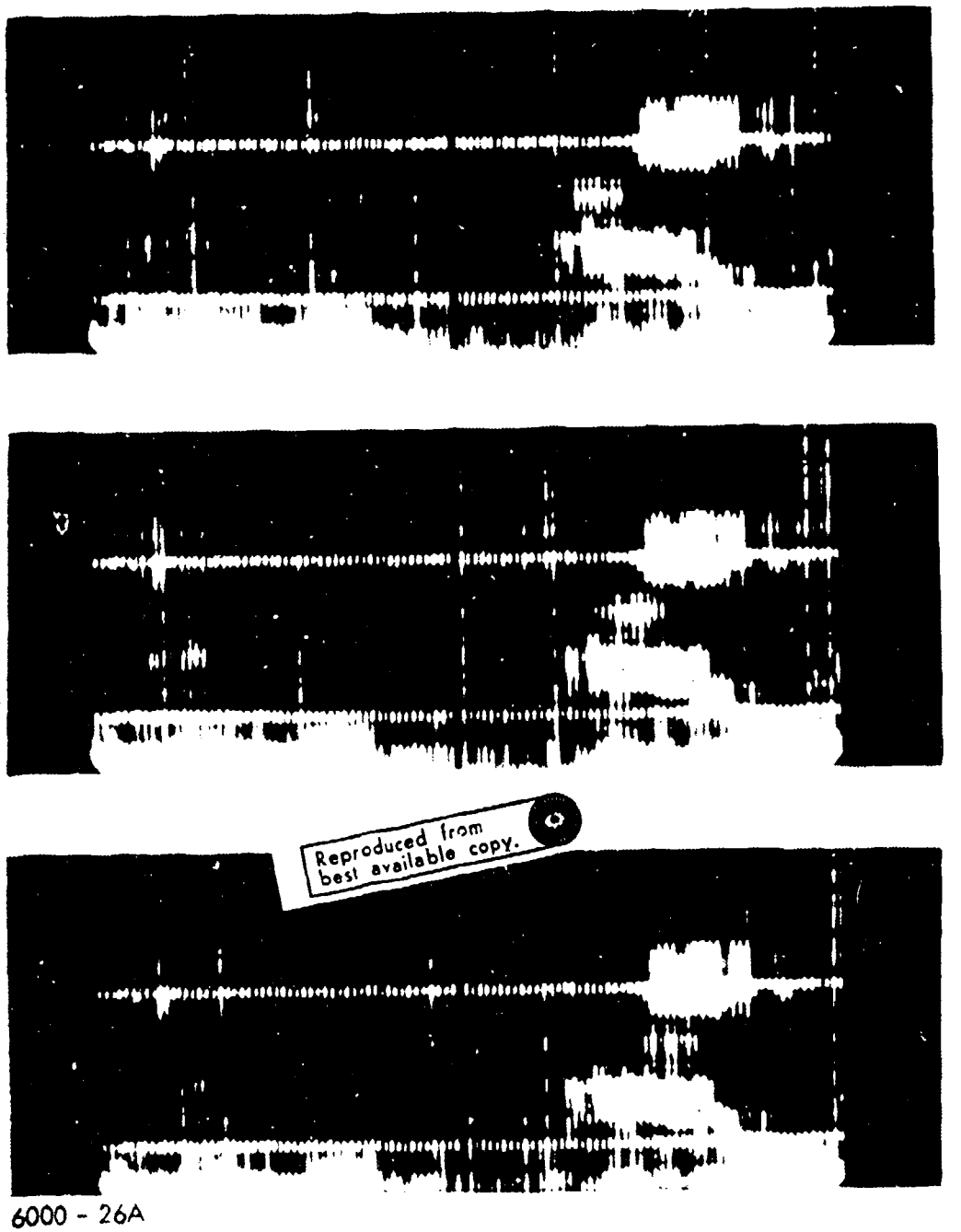

6000 - 26A

Figure 6. Sequence of Photographs Showing Moving Target

The injection locking signal was applied to the oscillator before the bias pulse. This was governed by the master timing control circuit, and the locking pulse was set to straddle the Gunn bias pulse. Locking power for the Gunn oscillators comes from a CW rf reference oscillator, whose output is modulated, amplified, and distributed to each module. Conventional laboratory equipment was used for these components.

Phase distribution across the aperture is a major factor in determining pattern shape. A specific allowable phase error was not established, but a general target was one-half of the least significant bit, or $\pm 11\text{-}1/4^{\circ}$. At a specific fixed frequency, the phase could be adjusted to virtually zero error, but phase was quite sensitive to temperature and tended to drift slightly. Phase distribution across the array aperture was measured using a conventional phase bridge with a pickup horn to probe the aperture.

Phase errors across the aperture can be corrected by three methods:

a. Increasing locking power -- this was carried out and gave a decrease in locking gain from 18 dB to 13 dB.
b. Tuning the oscillator frequency by changing the varactor voltage or by mechanical tuning.
c. Phase trimming external to the oscillator.

Since oscillator temperature was critical, a monitoring system of thermocouples was set up so that oscillator temperatures could be read individually. The cooling system was simply a box enclosure that fit over the array with a fan that pulled air in at the center with exit at the ends. To stabilize phase, it was necessary to allow the array to warm up to stabilize temperature. More recent oscillators have been built with greatly reduced sensitivity to temperature variations.

Scanning performance of the array was close to theoretical prediction. The beam scan program was $\pm 48^{\circ}$ in azimuth, with grating lobe effects becoming pronounced at scan angles beyond 40°, as predicted by theory. A shaped ground plane was used to increase directivity in the elevation plane, giving array gain of 22 dB.

3. GUNN OSCILLATORS

Operating parameters of a typical Gunn oscillator in this system are as follows:

Power Output	10 watts peak
Pulsewidth	1 microsecond
Duty Cycle	0.001
Mechanical Tuning	250 MHz

Electronic Tuning	250 MHz
Center Frequency	3.55 GHz
Efficiency	3%
Locking Gain	13 dB
Locking Figure of Merit	0.08

Best performance achieved in this circuit was 32 watts power output, electronically tuned over a 5% frequency band, and 5 watts tuned over a 34% bandwidth. Performance of these oscillators is uniform enough so that the array was highly successful; however, considerably more effort is required to improve consistency. (Significant advances in GaAs and Gunn device technology have been made since these oscillators were fabricated and power outputs have increased more than an order of magnitude.)

The oscillator and its schematic circuits are shown in Figures 7 and 8. The circuit is fabricated in microstrip transmission line on alumina substrate. The Gunn device is placed in shunt across a section of 20-ohm line, approximately one-tenth wavelength from the short circuit point created by the resonator band stop filter. A tuning varactor is located in series with the line between the Gunn device and the short circuit.

Characteristics of particular importance for a phased array application are locking performance and frequency tracking over the band.

Locking performance was found to agree closely with the theory of Adler.* Locking gain and bandwidth are related by the equation:

$$2\,\Delta f_L = k\, f_o \left(\frac{P_L}{P_o}\right)^{1/2}$$

where

$2\,\Delta f_L$ is the lock-in bandwidth

f_o is the frequency of the locking signal

P_L is the locking signal power

P_o is the output power of the oscillator to be locked

k is a constant, which may be denoted a locking "figure of merit"

Figures of merit measured on this system for all 16 oscillators varied between 0.015 and 0.15.

---

*R. Adler, "A Study of Locking Phenomena in Oscillators", Proc. of the IRE, Vol. 34, pp 351-357, June 1946.

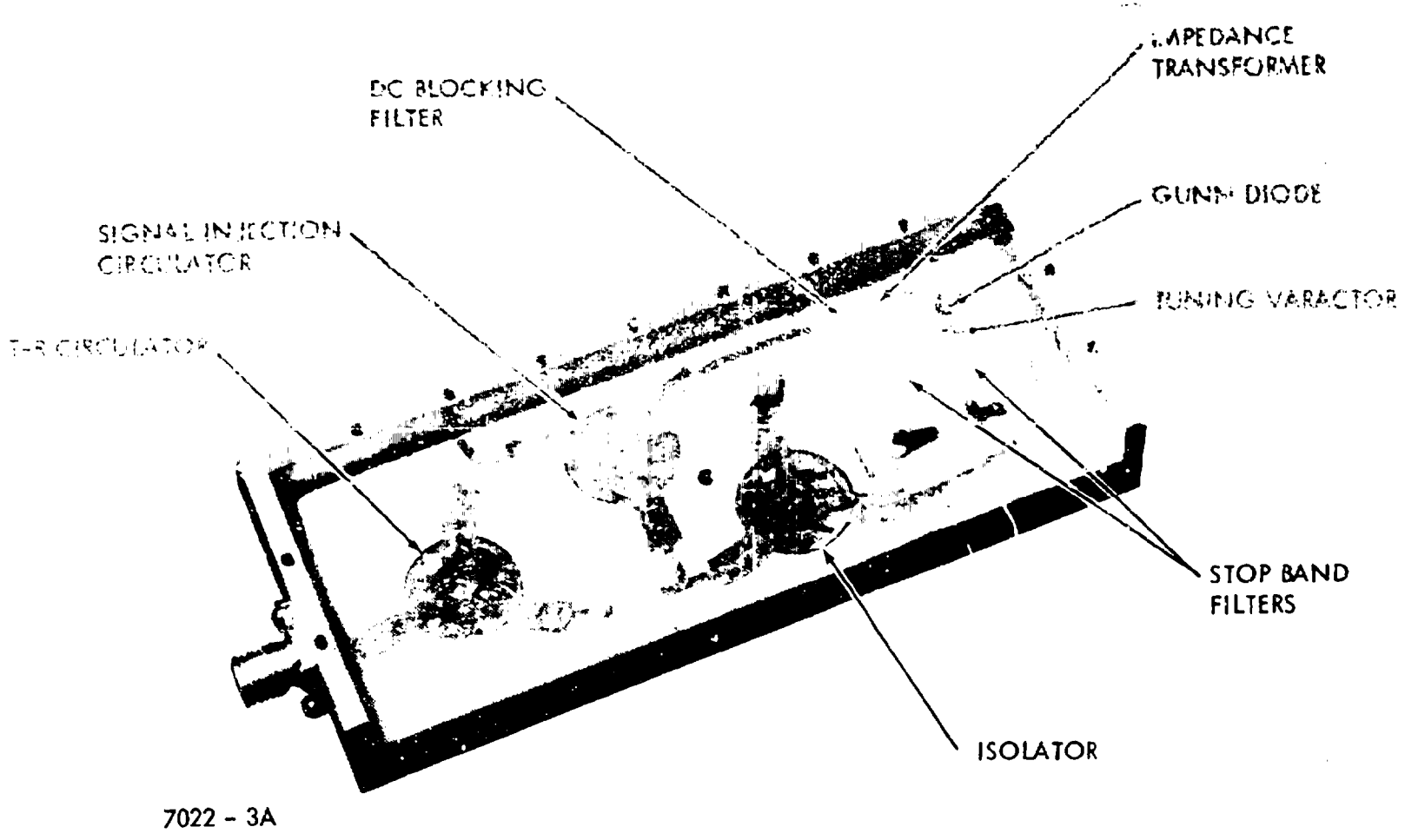

Figure 7. Gunn Oscillator

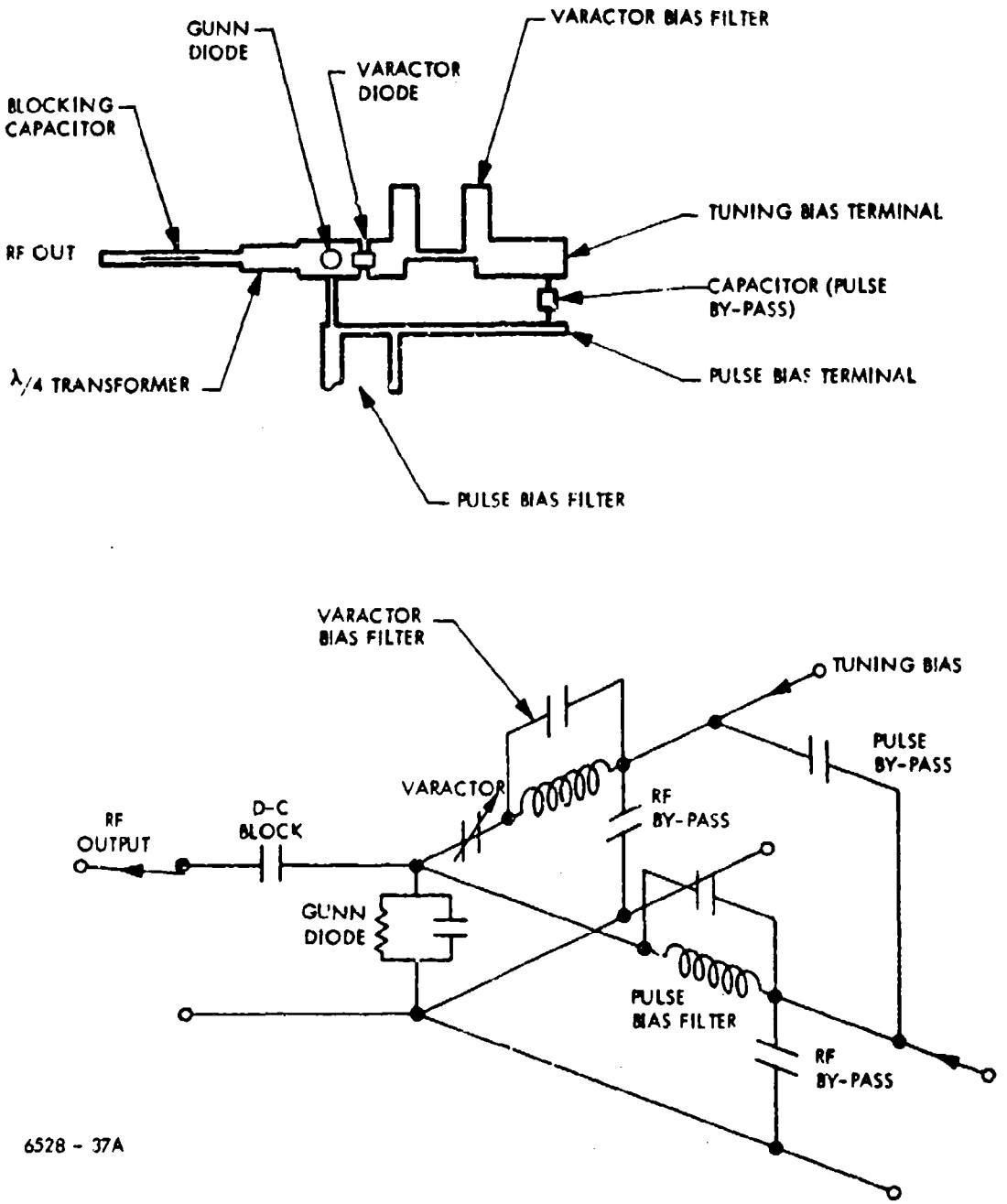

Figure 8. Oscillator Schematics

The oscillator is tuned electronically by varying the varactor bias voltage. Obviously, it is critical for the frequency response vs tuning voltage to be similar for all oscillators. Tuning characteristics were satisfactorily similar; the oscillators tracked each other to within ±15 MHz over most of the tuning band, compared to a locking band of ±25 MHz. Difficulty in achieving close frequency tracking arose from the differences in tuning varactors, typically 10%, and in the Gunn devices themselves. For this reason, the common tuning band for all oscillators was less than the typical band for one oscillator, i.e., 140 MHz for all oscillators, vs typically 250 MHz for one. A mechanical tuning adjustment was designed to compensate insofar as possible for differences between oscillators, and the mechanical tuning range was 250 MHz. The tuning band finally selected for array work was 3.48 - 3.62 GHz.

4. HIGH POWER TRANSMITTER

Having illustrated usefulness of the locked oscillator as a source for the distributed transmitter array, the question of feasibility quickly becomes one of transmitter performance. In support of the locked bulk effect array, we have carried on a program under Navy sponsorship for the development of high performance bulk oscillators. The results of these efforts to date have been encouraging. Emphasis of our program has been placed on maximizing average power performance while maintaining a ratio of peak-to-average power greater than 100:1.

Significant results have been:

Peak Power	260 watts @ 3500 MHz
Average Power	1 watt
Pulse Energy	1000 μjoules
Efficiency	10% S-band
	25% L-band
Tuning Range	20%

Development of the devices is continuing with a kilowatt of peak power and 10 watts of average power at S-band expected within a year.

A brief reference should be made to the theoretical efficiency of the bulk effect transmitter source. Figure 9 is a curve of efficiency plotted as a function of inverse peak-to-valley ratio for the semiconductor. β is the overdrive voltage or the ratio of bias to threshold voltage for the device in question. Parameters for our current best result are plotted on the curve. Because measurement of actual peak-to-valley ratio is extremely difficult, the results indicated must be considered as a lower bound for the device measured rather than an indication that optimum circuitry has been obtained. The significant conclusions to be drawn from this chart are:

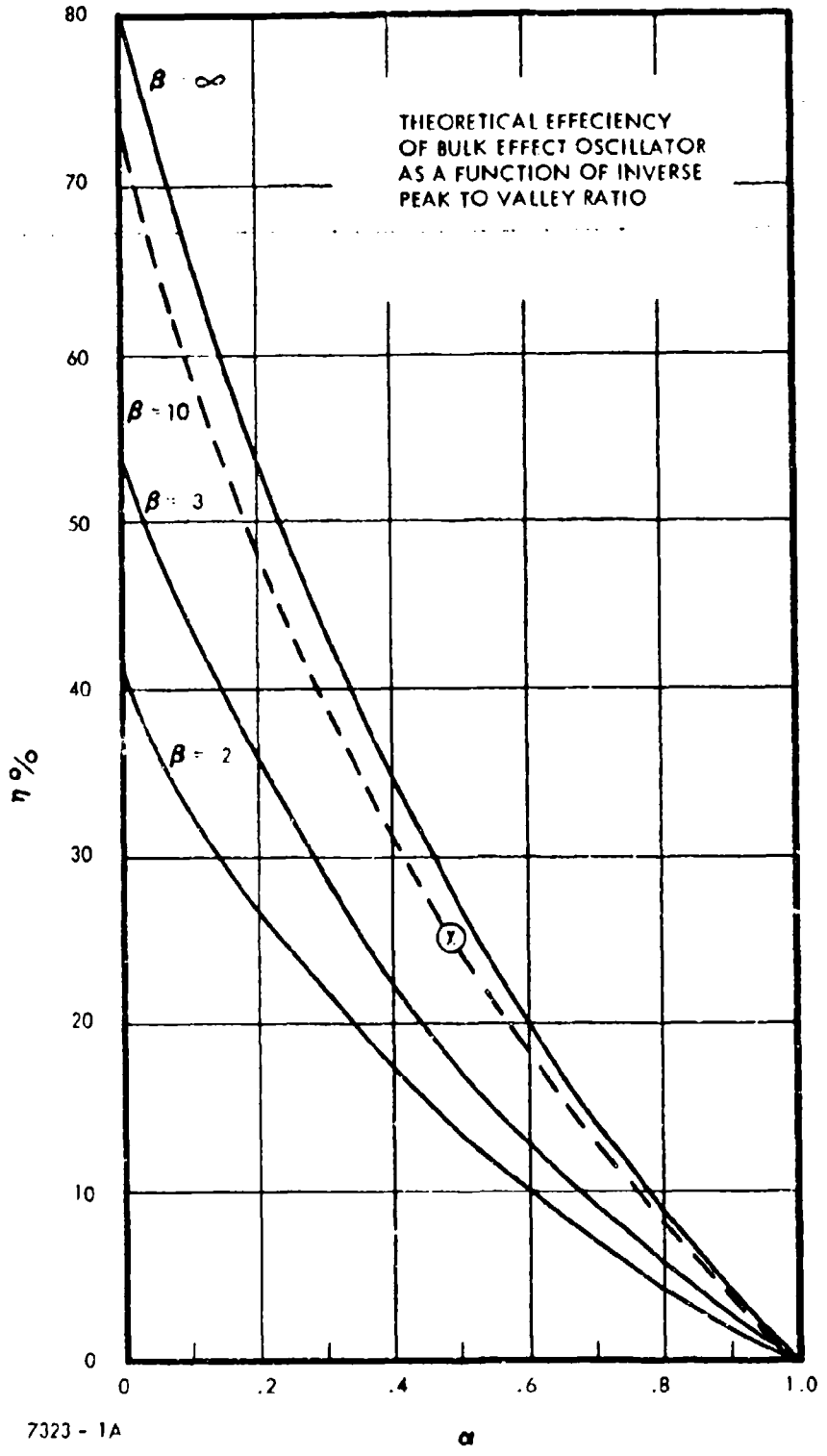

Figure 9. Efficiency

Even small improvements in semiconductor quality will make a significant impact on bulk oscillator efficiency. Since all other performance factors are already quite acceptable, the future of this device as a source for distributed transmitter arrays appears to be very bright.

5. CONCLUSION

This program successfully achieved its original objectives. It has been demonstrated that Gunn oscillators can be injection locked to perform in a scanning radar system. An experimental radar system was built that detected small aircraft up to a 4 km range and stationary targets up to a 12 km range. System characteristics were electronically programmed and controlled, and expected performance was met or exceeded.

Much improvement is still required before it will be feasible to build a large scale tactical system. Increases in power output and efficiency have been mentioned. Improvements are also needed in phase and frequency control, and the reduction of temperature sensitivity. The degree of recent progress in Gunn oscillator performance is shown in Table 1. Large scale cost reductions are required to establish economic feasibility.

Obviously there were, and are, major problem areas in a system of this complexity. Some of these are of a mundane nature; for example, because of the many interconnections throughout the system, reliability of connectors proved to be a problem. Noise in the logic circuits was another problem area. Both of these will require careful design in a large phased array system.

This program has provided a great deal of information and has opened many new areas of study. It represents a major step forward in development of solid state radar systems.

TABLE 1.

PROGRESS IN GUNN OSCILLATORS

	SPAR Osc.	Recent lab results
Peak power	10 w	260 w
Average power	50 Mw	1.02 w (102 w peak at 1% duty)
Pulse energy	0.06 MJ	1.02 MJ (114 w - 9 μsec)
Efficiency	3%	10%
Phase change during a 1 μsec pulse	20%	1.5°
Temp. coefficient of freq. change	-2 MHz/°C	-.2 MHz/°C

Acknowledgments

This program is representative of what can be accomplished through industry working closely with the services. Early in the program we received requirements guidance from the Navy and invested Corporate IR&D funds. Shortly thereafter, Mr. Paul Taylor of the Naval Ship System Command and other personnel within the Naval R&D community recognized the potential and sponsored developmental efforts, particularly in the area of bulk effect devices and associated circuitry. Rome Air Development Center supported us in the areas of modulation and locked oscillator techniques.

The consistency and tenacity of the scientists at STL have yielded impressive results. Similarly, a score or more of my colleagues at ITT Gilfillan have devoted their many talents toward the success of this program.